Modified Poly(lactic acid) sheets manufactured by One-Step Reactive Extrusion-Calendering: Thermal, Rheological, Mechanical and Fracture Behaviours

Dissertation Submitted to the

Technical University of Catalonia ▪ BarcelonaTech

In Partial Fulfilment of the Requirements for the

Degree of Doctor of Philosophy

in **Materials Science and Engineering**

Dissertation realized by:

Dipl.-Ing. Jonathan Cailloux

Director:

Dr. Orlando Onofre Santana Pérez

Department of Materials Science and Metallurgy

November-December 2015

“*Learn how to see. Realize that everything connects to everything else*”
- Leonardo da Vinci

Acknowledgement

Undertaking this research work has been a truly life-changing experience for me and it would not have been possible to successfully accomplish it without the support and guidance that I received from many people throughout these five years.

First and foremost, I would like to thank my supervisor Prof. Dr. Orlando Onofre Santana Pérez for the possibility to draw up this PhD thesis, for his valuable advice and support in all the scientific research activities. He has been actively interested in my work and has always been available to advise me. I am very grateful for his motivation, enthusiasm but also for his patience in my beginnings. It is not sufficient to express my gratitude with only a few words.

Special thanks are also given to Prof. Dr. Maria Lluïsa Maspoch and Prof. Dr. Antonio Martinez for giving me the opportunity to undertake a doctoral program at the *Universitat Politècnica de Catalunya* (UPC) in the R&D *Centre Català del Pàstic* (CCP) in Terrassa, Spain. I also gratefully acknowledge the funding I could benefit from the *Spanish Ministry of Science and Innovation* (MICINN) during the whole research activities.

Thanks to Prof. Dr. Jordi Bou and Prof. Dr. Antxon Martinez de Ilarduya (*Department of Chemical Engineering, Universitat Politècnica de Catalunya*) for the numerous *SEC* and *NMR* experiments and their analysis.

I would like to express my appreciation to Dr. Jean-Marie Raquez and Mr. Sébastien Moins (*Laboratory of Polymeric and Composite Materials, University of Mons, Belgium*) who have offered me their time for the numerous SEC-multiple detectors measurements and their evaluations.

Many thanks should be given to Lucas, Maxime, Maria Corrina, Jonathan and Ruben, who helped me during the accomplishment of this PhD study. I am especially grateful to them for their contribution in my experimental activities. My deep appreciation goes out to the present and past members of the CCP research team: Prof. Dr. Marcelo, Prof. Dr. Miguel Sanchez, Prof. Dr. José Ignacio Velasco, Dr. Edgar, Dr. Sylvia, Dr. Vera, Dr. Julio, Ing. Angelica, Ing. David, M. Sci. Gabriel, M. Sci. Hooman, M. Sci Javier for their valuable advices, for their friendship during my time in the CCP and finally for always making me feel so welcome.

My gratitude is also extended to Dr. Tobias Abt. He was one of the first friendly faces to greet me when I began this challenging experience and has always been a tremendous help no matter the task or circumstance. Letztlich, vielen Dank für unsere Freundschaft, für all jene Momente des Lachens, der Freude und Wahnsinn in Barcelona.

I am also very grateful to all those of the CCP administration and especially to Anna (also called "*La Morena*®"). Muchas gracias por tu amistad y por tu gran ayuda administrativa en mi vida tanto a nivel profesional como privada, sin olvidarme de estos cinco años de comidas y cafés compartidos a diario. Nunca hay que olvidar que *todos los días sale el sol chipirón!*

Enfin, ces remerciements seraient incomplets si je n'en adressais pas à l'ensemble des membres de ma famille pour leur soutien logistique et moral, ainsi que pour avoir cru en moi et m'avoir encouragé à poursuivre mes rêves durant cette longue et rude période. Encore mille fois merci pour tout.

Jonathan Cailloux
Terrassa, 2015

Abstract

The purpose of this PhD thesis was to investigate the sensitivity of the rheological, thermal, mechanical and fracture behaviours on the topological changes induced in two commercial PLA grades. PLA 2002D and PLA 4032D (NatureWorks, Belgium) with a D-lactide content of 4.25 and 2 %, respectively, were reactively modified in the melt with predetermined concentrations of a multi-functional epoxide agent (Joncryl 4300F, BASF, Germany). In a preliminary study, the evolution of the coupling reactions was followed by monitoring the torque versus time in an internal mixer device. Once all parameters were optimized, reactive extrusion was performed in a co-rotating twin screw extruder with a screw diameter of 25 mm (L/D=36). The main emphasize of this work was on the production of modified PLA sheets (thickness: 1 mm, width: 100 mm) through a **one-step reactive extrusion-calendering process** in pilot plant (maximum production capacity of 5 $kg.h^{-1}$).

Under similar processing conditions, the higher the D-lactide content, the lower was the reactivity of the PLA type towards the reactive agent. During processing, a competition between degradation and chain extension/branching reactions took place which led to a stabilization of the melt properties and an increase in the molecular weight (MW). Classical spectroscopic (FT-IR, NMR) and chromatographic (SEC-multiple detectors) methods failed to highlight structural differences between unmodified (PLA) and modified (PLA-REX) samples.

On the other hand, rheological properties were significantly modified and suggest the formation of non-uniform branched structures, which include sparsely long chain branching (LCB) macromolecules. Both the melt elasticity and the melt response time increased. Bi-modal molecular weight distribution (MWD) spectra were inferred from the complex viscosity functions of PLA-REX samples which exhibit a double curvature in the shear-thinning regime. Based on these MWDs, a procedure is suggested to quantitatively estimate the amount of modified PLA chains from solely melt measurements. Thus, rheological measurements turned out to be a valuable tool for the detection and the quantification of small contents of topological changes in the work at hand.

Thermal properties were slightly modified with the modification of the chain architecture. Upon constant heating, the maximum rate of conversion declined for PLA-REX samples; thus leading to a decrease in the degree of cold-crystallization. Thermal fractionation, according to the *successive self-nucleation and annealing* methodology, suggests a modification of the length distribution of crystallisable PLLA chain segments. In the present work, These trends mainly accounted from the increase in MW coupled with the enhanced concentration of defects into the polymeric chains (*e.g.* branch point). In the T_g region, the rate of enthalpy relaxation was found to

decrease with increasing the entanglement network density under controlled aging periods at 30 °C.

For a given thermal history, PLA-REX yielded comparative mechanical properties as those of PLA samples under uniaxial tensile loading. This is an important finding, because rheological properties (*i.e.* melt elasticity, viscosity, etc) may be controlled independently of the mechanical properties according to both the processing conditions and the concentrations of reactive agent used in the current study. While de-aged samples behaved in a ductile manner, aged samples were brittle. This behaviour was attributed to the effect of the physical aging process on the mechanical behaviour which commonly promotes the ductile/brittle transition.

Regarding de-aged samples, the *essential work of fracture* analysis revealed no changes neither in the work required for the onset of crack propagation nor in the work associated to the resistance of crack propagation. Regarding aged PLA-REX samples, the energy consumed up to the onset of crack propagation was found to decrease due to an apparently decreased network extensibility, promoting a premature craze-crack transition.

Resumen

El principal propósito de esta tesis doctoral ha sido investigar los efectos inducidos por cambios topológicos en dos grados comerciales de PLA en sus comportamientos reológicos, térmicos, mecánicos y a fractura. PLA 2002D y PLA 4032D (NatureWorks, Bélgica) con un contenido de enantiomero D igual a 4,25 y 2%, respectivamente, fueron modificados a través de un proceso de extrusión reactiva con concentraciones predeterminadas de un agente multifuncional con grupos epóxidos reactivos (Joncryl 4300F, BASF, Alemania). En un estudio preliminar, la evolución de las reacciones de acoplamiento fue registrada a través del seguimiento del par de fuerzas en función del tiempo de mezcla en un dispositivo de mezclador interno. Una vez todos los parámetros optimizados, el proceso de extrusión reactiva se realizó en una extrusora doble husillo co-giratorio con un diámetro de usillo igual a 25 mm (L/D = 36). El principal objetivo de este trabajo, fue la producción de láminas de PLA modificadas estructuralmente a través de un proceso simultáneo de extrusión reactiva-calandrado en un solo paso (capacidad máxima de producción de 5 $kg.h^{-1}$).

Bajo condiciones similares de procesamiento, cuando el contenido de enantiomero D sea mayor, la reactividad del tipo de PLA será menor hacia el agente reactivo. Durante el procesamiento, una competición entre degradación, extensión de cadenas y reacciones de ramificación conlleva a una estabilización de las propiedades del fundido y a un aumento en el peso molecular (MW). Los métodos clásicos de espectroscopia (FT-IR, NMR) y cromatográfico (SEC-múltiples detectores) fallaron en resaltar las diferencias estructurales entre las muestras modificadas (PLA-REX) y las no modificadas (PLA).

No obstante, las propiedades reológicas resultaron modificadas significativamente sugiriendo la formación de estructuras ramificadas no uniformes, que incluyen escasamente la presencia de ramificaciones largas (LCB). Tanto la elasticidad como la respuesta del fundido en el tiempo aumentaron. Los espectros de distribución de peso moleculares (MWD) bi-modal se infirieron de las funciones de viscosidad compleja de las muestras de PLA-REX las cuales presentan una doble curvatura en el régimen pseudo-plástico. En base a estos MWD, se sugiere un procedimiento, para estimar cuantitativamente la cantidad de cadenas de PLA modificadas a partir de mediciones realizadas únicamente en el fundido. Por lo tanto, las mediciones reológicas, resultaron ser una herramienta valiosa para la detección y la cuantificación de pequeñas cuantidades de cambios topológicos en el trabajo a mano.

Por otra parte las propiedades térmicas se vieron ligeramente alteradas con la modificación de la arquitectura molecular. Tras un calentamiento constante, la tasa máxima de conversión para las muestras de PLA-REX se redujo; lo que conlleva a una disminución en el grado de cristalización en frío alcanzable. El fraccionamiento

térmico, de acuerdo con la metodología de *auto-nucleación y recocidos sucesivos* (SSA), sugiere una modificación de la distribución de la longitud de los segmentos cristalizables de cadena de PLLA. En el presente trabajo, esas tendencias están atribuidas principalmente al incremento en MW, juntamente con la mayor concentración de defectos en las cadenas poliméricas (punto de ramificación). En la región de T_g, los resultados sugieren una reducción de la cinética de envejecimiento físico con un aumento en la densidad de enredos físicos bajo períodos de envejecimiento controlados a 30 °C.

Para una historia térmica dada, las muestras de PLA-REX exhiben propiedades mecánicas comparativas a las muestras de PLA bajo una carga de tracción uniaxial. Este podría ser considerado un hallazgo importante, puesto que las propiedades reológicas (elasticidad del fundido, viscosidad, etc.) pueden ser controladas de forma independiente a las propiedades mecánicas de acuerdo a las condiciones de procesamiento y a las concentraciones de agente reactivo utilizadas en el estudio actual. Mientras que las muestras rejuvenecidas presentaron un comportamiento dúctil, las muestras envejecidas resultaron frágiles. Este comportamiento, se atribuyó al efecto del proceso de envejecimiento físico en el comportamiento mecánico que promueve la transición dúctil/frágil.

En las muestras rejuvenecidas, el *trabajo esencial de fractura* no reveló ningún cambio ni en el trabajo necesario para el inicio de la propagación de grietas ni en el trabajo asociado a la resistencia de propagación de grietas. Por otra parte las muestras envejecidas de PLA-REX, la energía consumida hasta el inicio de la propagación de la grieta disminuyó debido a una disminución de la extensibilidad aparentemente de la red molecular, promoviendo una transición prematura "*craze-grieta*".

Table of contents

List of Figures

List of Tables

Abbreviations and Symbols

The abbreviations and symbols are classified alphabetically.

Abbreviations

a.u.	Arbitrary unit
ar	Aromatic
as	Asymmetrical
Bio-PE	Bio-Polyethylene
CCP	Centre Català del Plàstic
CRYSTAF	Crystallization Analysis Fractionation
CTOD	Crack-Tip-Opening Displacement
CY	Carreau-Yassuda model
CY-Ext	Extended Carreau-Yassuda model
DDENT	Deeply-Double-Edge-Notched Tensile
DENT	Deeply-Edge-Notched Tensile
DSENT	Deeply-Single-Edge-Notched Tensile
DIC	Digital Image Correlation
DOPZ	Diffuse Outer Plastic Zone
DSC	Differential Scanning Calorimetry
DSENT	Deeply Single Edge Notched Tension
e.g.	For example
EPFM	Elastic Plastic Fracture Mechanics
ESIS-TC4	European Structural Integrity Society-Technical Committee 4
EWF	Essential Work of Fracture
GRAS	Generally Recognized as Safe
HDPE	High-density Polyethylene
HDT	Heat Distortion Temperature
HIPS	High Impact Polystyrene
HMW	High Molecular Weight
HN	Havriliak-Negami model
HN-Ext	Extended Havriliak-Negami model
i.e.	That is
IFPZ	Inner Fracture Process Zone
IR	Infrared spectroscopy
IV	Intrinsic viscosity
LA	Lactic Acid
LCB	Long Chain Branching
LDPE	Low-Density Polyethylene
LEFM	Linear Elastic Fracture Mechanics
LVE	Linear Viscoelastic regime

MWD	Molecular Weight Distribution
n/a	Not available
NMR	Nuclear Magnetic Resonance
oop	Out-of-plane
OP	Optical Purity
OPDZ	Outer Process Deformation Zone
PB	Polybutadiene
PBAT	Poly(Butylenes Adipate-co-butylene Terephthalate)
PC	Polycarbonate
PCL	Polycaprolactone
PDI	Polydispersity index
PE	Polyethylene
PEG	Polyethylene Glycol
PET	Polythylene Terephthalate
PHA	PolyhydroxyAlkanoate
PLA	Poly(Lactic Acid)
PMMA	Poly(Methyl Methacrylate)
PP	Polypropylene
PPF	Primitive Path Fluctuations
ppm	Parts Per Million
PS	Polystyrene
PVC	Poly(Vinyl Chloride)
PYFM	Post-Yielding Fracture Mechanics
RDA	Rheological Dynamic Analysis
RH	Relative Humidity
ROP	Ring Opening Polymerization
s	Symmetrical
SCB	Short Chain Branching
SEC-DRI	Size Exclusion Chromatography with Differential Refractive Index detector
SENB	Single-Edge-Notched Bend
SENT	Single-Edge-Notched Tension
SME	Specific Mechanic Energy
$Sn(Oct)_2$	Tin octoate
SSA	Successive Self-nucleation and Annealing
st	Stretching
TEM	Transmission Electron Microscopy
THF	Tetrahydrofuran
TMW	Time-molecular weight superposition principle
MDSC	Modulated Differential Scanning Calorimetry
TNPP	Tris(nonylphenyl) Phosphate
TREF	Temperature rising Fractionation

TTS	Time-Temperature Superposition
US FDA	US Food and Drug Administration
vGP-plot	van Gurp-Palmen plot

Symbols

A_0	Transversal section of the tensile samples	m^2
a_T	Horizontal shift factor (TTS principle)	-
b_T	Vertical shift factor (TTS principle)	-
C_1, C_2	Constants from curve fitting (WLF equation)	-
C_∞	Characteristic ratio (measure of the chain stiffness)	-
E	Elastic or Young's Modulus	Pa
E', E''	Storage and loss modulus (DTMA analysis)	Pa
E_a	Activation energy for flow (Arrhenius equation)	kJ/mol
G', G''	Storage and loss modulus (RDA analysis)	Pa
G_c	Crossover modulus (RDA analysis)	Pa
G_c	Critical strain energy release rate (fracture analysis)	$J.m^{-2}$
G_e	Modulus at infinite times	Pa
$\|G^*(\omega)\|$	Absolute value of the complex modulus as a function of the angular frequency	Pa
G_n^0	Plateau Modulus (RDA analysis)	MPa
h	Height of the OPDZ zone (DDENT specimens)	mm
H	Enthalpy	$J.g^{-1}$
$H(\tau)$	Relaxation spectrum	Pa
J	Nonlinear energy release rate per unit area	$J.m^{-2}$
$J(t)$	Time-dependent creep compliance	Pa^{-1}
J', J''	Storage and loss compliance (RDA analysis)	Pa^{-1}
J_0	Energy consumed to initiate crack propagation (CTOD analysis)	$kJ.m^{-2}$
J_0	Spontaneous elastic part of the compliance (RDA analysis)	Pa^{-1}
J_e^0	Linear steady-state elastic compliance	Pa^{-1}
$J_r(t)$	Time-dependent recoverable compliance	Pa^{-1}
$\|J^*(\omega)\|$	Absolute value of the complex compliance as a function of the angular frequency	Pa^{-1}
K	Amount of modified PLA chains (NMR analysis)	%
K	Stress-intensity factor (fracture analysis)	$Pa.m^{1/2}$
L	Length	mm
l	Ligament length	mm
$L(\lambda)$	Retardation spectrum	Pa^{-1}
L_0	Initial gauge length of the tensile specimens (50 mm)	mm
m, n	Number of curvatures in both extended viscosity models	-
M_a	Molecular weight of a long chain branch (arm MW)	$g.mol^{-1}$

M_b	Critical branch molecular weight for entanglement	g.mol^{-1}
M_c	Critical molecular weight for entanglements	g.mol^{-1}
M_e	Molecular weight between entanglements	g.mol^{-1}
m_i	Reduced molecular weight	-
M_i	Molar mass of the component molecules of type *i* (SEC experiments)	-
M_n	Number-average molecular weight	g.mol^{-1}
M_p	Molecular weight at the MWD spectrum maximum	g.mol^{-1}
M_r	Molecular weight of the repeat unit	g.mol^{-1}
M_v	Viscosity-average molecular weight	-
M_w	Weight-average molecular weight	g.mol^{-1}
M_z	z-Average molecular weight	g.mol^{-1}
n_i	Fraction of the component molecules *i* (SEC experiments)	-
n_v	Number of real or virtual repeating bond per monomer unit around which the polymer chain is able to rotate	-
P	Pressure	Pa
P_i	Load at a given deformation *i*	N
R	gas constant	J.K^{-1}.mol^{-1}
R_g	Radius of gyration	nm
r_p	Size of the plastic zone at the crack tip	mm
t	Thickness	mm
t	Time	s or min
T_0, T	Reference temperature and temperature of measurements	°C
T_a	Aging temperature	ºC
T_b	Bulk temperature	ºC
t_a	Aging time	min
$Tan\ \delta$	Loss factor	-
T_b	Brittle/ductile transition temperature	ºC
T_c, T_{cc}	Crystallization and cold crystallization temperature	°C
t_{eq}	Equilibrium time	min
T_g, T_{gm}	Glass transition and midpoint glass transition temperature	°C
T_m, T_{me}	Melting and end melting temperature	°C
T_s	Self-seeding temperature (SSA analysis)	ºC
t_s	Annealing time at T_s (SSA analysis)	min
V_{crack}	Crack propagation rate	mm.s^{-1}
$V_{craze\text{-}growth}$	Craze growth rate	mm.s^{-1}
v_f	Free volume	-
W	Width	mm
w_e	Specific essential work of fracture	kJ.m^{-2}
W_e	Essential work of fracture (per area unit)	kJ
w_f	Specific work of fracture	kJ.m^{-2}

W_f	Work required for the whole fracture process	kJ
w_i	Weight-fraction of the component molecules i (SEC experiments)	-
w_p	Specific nonessential work of fracture	$MJ.m^{-3}$
W_p	Nonessential work of fracture (per volume unit)	$MJ.m^{-1}$
X_c	Degree of crystallinity	%
Z	Number of entanglements per molecule	-
ZG	Distance between grips	mm
ΔH_m^0	Melting enthalpy for a 100 % crystalline PLA	$J.g^{-1}$
ΔH_{cc}	Cold crystallization enthalpy	$J.g^{-1}$
ΔH_m	Melting enthalpy	$J.g^{-1}$
ΔL_x	Increase in specimen length between gauge marks during tensile experiments	mm
$\Gamma(t)$	Torque trace as a function of the mixing time	Nm
α, α_1, α_2	Parameters describing the width of the "knee" in the different viscosity models	-
β	Shape factor of the OPDZ zone (DDENT specimens)	-
β	Distribution of relaxation times (physical aging analysis)	-
β_H	Rate of physical aging	$J.g^{-1}$ per decade
βw_p	Non-essential work of fracture or plastic term	$MJ.m^{-3}$
δ	Phase angle	°
δ_c	Critical crack-tip-opening displacement	mm
δ_H	Enthalpy recovered or enthalpy loss	$J.g^{-1}$
$\delta_{H\infty}$	Equilibrium enthalpy relaxation for infinite aging time	$J.g^{-1}$
δ_i	Crack-tip-opening displacement (CTOD)	mm
$\delta\eta_i(\omega)$	Shift function to correct the complex viscosity raw data	-
$\dot{\varepsilon}$	Strain-rate	s^{-1}
ε_b	Strain at break	%
ε_x	Engineering strain	%
ε_y	Yield strain	%
$\dot{\gamma}$	Shear rate	s^{-1}
$\gamma(t)$	Time-dependent shear deformation	%
$\gamma_r(t)$	Time-dependent recoverable deformation	%
η_0	Zero-shear rate viscosity	Pa.s
$\lvert\eta^*(\omega)\rvert$	Absolute value of the complex viscosity as a function of the angular frequency	Pa.s
ν	Wavenumber (FT-IR experiments)	cm^{-1}
ν_e	Entanglement density	$mmol.m^{-3}$
(ν-1), (ν_1-1), (ν_2-1)	High frequency constant slope $d\log\lvert\eta^*\rvert/d\log\omega$ in the different viscosity models	-
ρ	Polymer melt density at the temperature of measurement	$g.m^{-3}$
ρ_a	Amorphous density of the polymer	$g.m^{-3}$

σ_b	Brittle fracture stress	Pa
σ_i	Engineering stress at a given deformation *i*	Pa
σ_y	Yield strength	Pa
τ	Shear stress	Pa
τ_0, τ_1, τ_2	Characteristic relaxation times fixing the position of the transition regions in the different viscosity models	s
τ, λ	Relaxation time of the retardation and relaxation spectrum, respectively	s
τ_0	Characteristic relaxation time (physical aging analysis)	min
τ_0	Constant shear stress applied during the creep phase	Pa
ω	Angular frequency	$rad.s^{-1}$
ω_c	Critical frequency	$rad.s^{-1}$
$\psi(t)$	Delayed viscoelasticity function	Pa

Chapter 1: Introduction

With an annual rise of approximately 5%, the current worldwide consumption of plastics amounts to about 200 million tonnes per year. It represents the largest field of application for petrochemical feed stock. Around the globe, more than a third of this plastic volume is converted into packaging, representing a quantity of about 20 million tonnes in the European Union alone. For a long time, conventional petrochemical-based plastics such as polyethylene (PE), polystyrene (PS), polypropylene (PP), polyethylene terephthalate (PET) have been used extensively as packaging materials.

These polymers were placed at the forefront of the plastic industry for their good mechanical properties, thermal stability, good barrier to oxygen as well as being safe for use in food-contact articles. However, the actual depletion of fossil fuels, the awareness of increasing environmental pollution and global warming has led to more interest in turning plastic packaging into a more sustainable product. As a result of these economic and ecological issues, the development of the concept of biopolymers has been accelerated since the early 1980s.

In 2011, the global manufactured volume capacities of biopolymers were estimated to be 1.2 million tonnes, with approximately 40% used in the packaging market. Consequently, it represents the biggest field in the bioplastics industry. In 2016, the research institutes foresee the global production of bioplastic multiplied by a factor of six and optimized for innovative packaging solutions as well as specific application demands [1].

The intense development of these new eco-friendly materials offer three main outstanding advantages over finite fossil polymers: manufacturing from renewable resources, biodegradability and a reduction of the carbon footprint. In addition, the properties and quality of certain bioplastic packaging may be comparable to conventional polymer products. Nevertheless, over time the concept of biopolymers has become a buzzword making it necessary to precisely define the qualities and characteristics of this type of polymer.

1.1. What are Biopolymers?

Over the years, the concept of a biopolymer has been established as a polymeric resin that fulfils at least one of the two following conditions [2-4]:

- Partially or completely consisting of "**bio-based**" raw materials. This means that the polymer should be derived from biomass (sugarcane, corn, etc)

- **Biodegradable** or **compostable** under environmental influences. The polymer matrix is converted to natural substances over time (water, compost and/or carbon dioxide). The concept of biodegradability is directly correlated to the chemical structure of the polymer and not from its origin. ISO 17088, EN 13432/14995 or ASTM 6400 or 6868 standard references as well as certification and labelling (seedling label or OK compost via VinÇotte or DIN CERTCO) has been established for these materials.

Four basic groups of polymers are distinguished when their origins are plotted against their biodegradability whereby three of them correspond to biopolymers, as illustrated in *figure 1.1*.

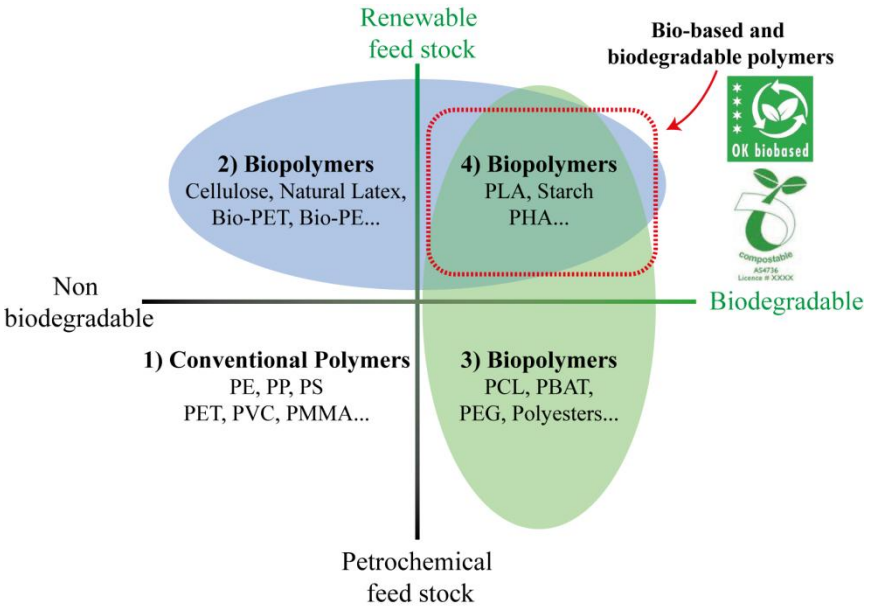

Figure 1.1. Polymer classification related to their origins and biodegradability (Adapted from ref. [2, 4, 5]).

1) Conventional polymers are related to the conventional thermoplastic resins such as PE, PP, PET, PS or even Poly(vinyl chloride) (PVC). They are obtained from petrochemical raw materials (non renewable) and are not biodegradable. Two years

ago, this group represented approximately the 74% of the global demand in polymers [2, 4, 6].

2) Non-Degradable bio-based polymers are related to the oldest manufactured biopolymers. Cellulose and natural latex were the first two engineering polymers based on renewable feed stocks. More recently, a new synthesis development called "drop-in solutions" attempts to replace the fossil feedstock used in the traditional synthesis processes of conventional polymers with renewable feed stock. The main goal is to manufacture bio-based conventional polyolefins (bio-PE) which could be transformed by well-known processing technologies (extrusion, injection, foaming). For illustration purposes, bio-PET is already used for technical applications and for packaging (*e.g.* beverage bottles by "*Coca-Cola*®"). Nowadays, the high cost of production of these bio-polyolefins as compared to their petrochemical-based counterparts affects their competitiveness in different markets [2, 4].

3) Bio-degradable polymers from petrochemical feed stock are related to degradable petro-based biopolymers such as polycaprolactone (PCL), poly(butylenes adipate-co-butylene terephthalate) (PBAT), polyethylene glycol (PEG) as well as various polyesters. Usually, they are used as blend components with other bioplastics to enhance their application-specific performances. While these biopolymers are still manufactured in petrochemical production processes, the depletion of petrochemical feedstock has led to a decrease in usage in different markets [4, 7-9].

4) Bio-degradable polymers from renewable resources are related to polymers which are compostable and bio-based such as poly(lactic acid) (PLA), starch or polyhydroxyalkanoates (PHA). Due to their low environmental impact, this category of polymers is actually of the highest interest to the different markets which look for environmentally friendly materials. Currently, they are produced on large scales due to a significant decrease in production costs over the last few years. In terms of volume, the most famous among them is PLA [4, 10].

While this last category of bio-based and biodegradable polymers is currently manufactured on large scales and in high demand, its development and commercialization were not straightforward and were established over various generations.

1.2. Building a bio-based Future

Since the end of the 1980s and the beginning of the 1990s, an increasing number of compostable and bio-based polymers were developed, essentially based on starch and PHA [3]. Independent of finite fossil resources, these innovative biopolymers were produced by fermentation and then introduced in the market for the first time. The "**first generation of biopolymers**" was thereby born. Despite encouraging

predictions and a certain enthusiasm, the unfavourable political and commercial conditions coupled with medium material properties led to an unsuccessful debut in the market of these new materials [2].

More recently, the "**second generation of biopolymer materials**" has been able to establish itself commercially as a result of the development and optimization of a wide variety of biopolymers. They are comparable with petrochemical-based polymers due to their similar processing and handling properties. In the United States of America and in Europe, the use of this second generation of biopolymers is exclusively focused on degradable, compostable packaging applications and "short-live" uses. Until now, whereas some of these biopolymers suffered economical disadvantages due to limited production capacities, others such as PLA or degradable polyesters have reached an industrial scale [2, 3].

Finally, a "**third generation of biopolymers materials**" turned towards long-life uses and resistance is becoming more prevalent. In this generation, the term of compostability is no longer the main criterion. Currently, due to a depletion of the petrochemical resources, the long-term availability of the renewable resources for the production of polymers is one of the main considerations. This third generation is mainly focused on engineering applications in areas such as the automotive, textile and fibre industries [2].

1.3. PhD framework and objectives

Even though the second generation of biopolymers has reached large-scale production, it is still missing relevant rheological and industrial processability data from the perspective of polymer engineering. That is, the information related to this biopolymer field is still incomplete. In terms of industrial interest, one of the most promising bio-based and compostable biopolymer of the second generation is PLA, belonging to the thermoplastic aliphatic polyester family.

In the beginning, PLA was solely considered for the bioabsorbable/biocompatible medical device market due to significant production costs. Nowadays, due to a decrease in the manufacturing costs, PLA is widely used in short-life eco-friendly applications such as rigid and flexible film packaging, cold beverage containers, bottles, cutlery, etc [10, 11]. Over the past 10 years, it has gained much attention as a replacement for conventional non-biodegradable packaging polymers due to numerous advantages:

- It is bio-based, giving rise to a possible worldwide enhancement of the agriculture economy [11-13].
- It is recyclable and compostable under industrial conditions, leading to a reduction in the worldwide pollution caused by plastic items [12, 14-16].

- The manufacturing process sequesters quantities of carbon dioxide, reducing its overall carbon footprint [17, 18]
- Its mechanical and thermal properties may be tailored through changes to the polymer chain architecture [19-21].
- In the case of food packaging items, the concentration of lactic acid that may migrate to food is below the amount of lactic acid used in common food ingredients, making PLA officially recognized as safe for use in food-contact articles [10, 15, 22].
- It can be processed using conventional thermoplastic processing methods [14, 15, 23].
- It is recognized as an economically advantageous material to use as a packaging polymer [14, 15, 23].
- It can be made as a transparent material under specific processing conditions [24, 25].

High molecular weight (HMW) PLA is a high strength, high modulus thermoplastic biopolymer. Its mechanical properties range between those of crystal PS and PET. However, some other properties such as the melt viscosity, impact strength, heat deflection temperature and barrier properties are not sufficiently optimized to employ PLA in specific applications. Currently, PLA is widely used in the food packaging sector, however its poor thermal resistance and its advanced brittleness have been its principal drawbacks for large-scale commercial applications [7, 26-28].

PLA can be easily processed with standard thermoplastic equipments. However, it does not possess sufficient thermal stability to prevent degradation and maintain its original molecular weight (MW) during large-scale processing [14, 29]. Processing conditions of 185-190 ºC are yet in excess and hydrolysis, unzipping and chain scission degradation reactions occur; leading to a relevant reduction of its initial MW [12, 30, 31]. This loss of MW affects the final properties and leads to unfavourable consequences in several applications fields. The poor melt strength of PLA also limits its processability using specific processing techniques (*i.e.* film extrusion, blown moulding, foaming and deep thermoforming).

HMW PLA items are usually amorphous due to the relatively fast cooling rates of industrial processes as compared to the crystallization rate of current commercial biopolymers [11, 19, 32]. Therefore, its relative low glass transition temperature ($T_g \approx$ 60 ºC) affects the efficiency of the shaped items during applications. Its poor thermal resistance and brittle behaviour are commonly overcome by improving the degree of crystallinity. To get such results, either commercial grades with high stereoregularity are melt blended with nucleating agents or further specific thermal treatments are applied [33-36].

A second approach for solving these drawbacks is the preparation of PLA nanocomposites by melt intercalation in organically-modified layered silicates. While interesting mechanical properties and oxygen permeability were achieved for PLA nanocomposites, several extrusion steps were necessary to reach sufficient clay dispersion. A severe degradation of the polymeric matrix was measured due to both the several processing steps and the presence of the clay organo-modifier (bearing hydroxyl groups). Consequently, the MW significantly decreased; thus affecting the final properties [30, 37-39].

The extrusion process can take advantage of these degradation reactions when it is combined with multi-functional reactive agents, as already reported by numerous authors [40-47]. In the melted state, chemical reactions of high performance may be obtained in a continuous reactive extrusion process with relatively short reaction times. This reactive process is usually considered economically and eco-friendly due to both the absence of diluents and its chemical efficiency. This processing method can be transferred or perfectly practiced in commercial processes [48]. Consequently, it presents an interesting solution to control the degradation of PLA during processing and to enlarge its processing windows.

Resulting from the above considerations, the main objectives of this PhD are listed below:

a) Evaluation of the degree of modification in two commercial grades of poly(lactic acid) modified through reactive extrusion using a multi-functional epoxide agent.

b) Implementation of a sheet manufacturing process using a "one-step reactive extrusion-calendering process" at pilot plant-scale (maximum production capacity of 5 kg.h^{-1}).

c) Investigation of the structure-thermal, rheological, mechanical and fracture properties relationships in manufactured PLA sheets obtained at pre-industrial scale.

Most of the research activities which are carried out in the duration of this PhD project are framed in the whole project entitled: "**Architectural modifications of a PLA matrix through a one-step reactive extrusion-calendering process to enhance the processability, the fracture behaviour and the preparation of biodegradable nanocomposites**" (*Ref*: MAT2010-19721-C02-01). This R&D project is supported and financed by the Spanish Ministry of Science and Innovation. Throughout its duration, most of the activities are realized in the installations of the *Centre Català del Pàstic* (CCP) in Terrassa (Spain). In addition, several companies such as BBraun Surgical® S.A., NUPIK International®, S.L., Zobele group® or Bioglutamic® S.L. are following the progress of the project and are interested in the final conclusions.

1.4. Specific objectives

To successfully complete this study, the present work has been divided in two main steps. Listed below are the specific objectives.

Step 1. Reactive processing at laboratory-scale (internal mixer, 50 g/batch)

- Determination of the processing conditions (temperature, residence time, reactive agent concentration, etc).
- Evaluation of the D-lactide content on the degree of topological changes.

Step 2. Reactive processing at pilot plant-scale (up to 5 kg.h^{-1})

2.1) Scaling up of the reactive processing conditions (determined in step 1) towards the twin-screw extrusion process

2.2) Modified PLA sheets manufacturing via a "one-step reactive extrusion calendering process"

2.3) Physical-chemical characterisation

- Determination of the molecular weight distribution (MWD)
- Estimation of the degree of architectural modifications

2.4) Rheological characterisation

- Determination of the rheological master curves and melt dynamic mechanical spectra
- Estimation of the chain architecture and calculation of parameters related to the molecular structure
- Inversion of the viscoelastic data to MWD spectra

2.5) Thermal characterisation

- Standard calorimetric and thermo-mechanical evaluations (thermal transitions and degree of crystallinity)
- Influence of the reactive modifications on the physical aging kinetics

2.6) Mechanical characterisation

- Evaluation of the topological modifications on the mechanical parameters under uniaxial tensile loading

2.7) Fracture characterisation

- Assessment of the structural fracture behaviour using the postulate criteria of the *Elastic-Plastic Fracture Mechanics* (*EPFM*) and the *Post-Yielding Fracture Mechanics* (*PYFM*)
- Investigation of possible changes in the micromechanisms of deformation

Chapter 2: Theoretical aspects

This chapter presents the theoretical aspects of different concepts which are likely to be influenced by the structural modification of PLA, starting with an overview of physical aging in glassy polymers. Then, a thermal fractionation technique to investigate the heterogeneous nature of the chain structure in polyolefins is analyzed and discussed for its applicability to PLA. Rheological methods with emphasis on the prediction of the complete viscoelastic properties and the estimation of the molecular weight distribution spectrum are described. This chapter concludes with a literature survey of the micromechanisms of deformation and the fracture postulate criteria for polymers.

2.1. Physical aging and enthalpy relaxation

The physical aging process can be best explained through an understanding of both the molecular packing and the free volume decrease that take place when a melted polymer is cooled from above to below T_g. The relative or specific volume of a polymer (V), which is composed of the occupied volume (V_o) and the free volume (v_f), varies with temperature, as shown in *figure 2.1*. The main difference between V_o and v_f is that the occupied volume is the portion of the polymer containing polymer chains, while the free volume represents the regions within the polymer that are not occupied by polymer chains [49].

V decreases linearly with temperature until the glass transition temperature (T_g) is reached. At this point, the rate of change of specific volume is slowed down because the molecular mobility, which maintains a melted polymer in its conformational equilibrium, is suddenly frozen-in. The exact location of the T_g depends upon the cooling rate, with a faster cooling rate corresponding to a higher T_g, as shown in *figure 2.1*. Manufacturing processes often involve rapid cooling; thus leading to both a possible increase in T_g and an excess of v_f below T_g. Consequently, the manufactured glassy polymer is thermodynamically unstable, and its physical properties may vary with time as it approaches an equilibrium state [49].

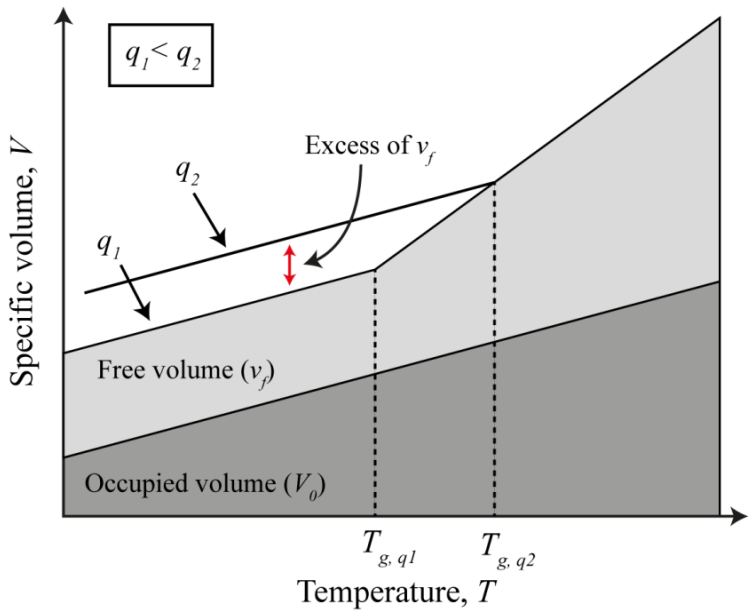

Figure 2.1. Specific or relative volume as a function of temperature for a polymer cooled at two different rates ($q_2 > q_1$) (adapted from *ref.* [49]).

These modifications are achieved by restricted molecular motions below T_g, leading to a configurational rearrangement of chain segments from a totally disordered configuration for unaged materials to locally ordered ones for aged glasses. The rate of change toward equilibrium is related to the level of segmental mobility which is controlled by v_f and how far below T_g the glass is aged. Regarding glasses, this structural relaxation process is referred to as physical aging in order to distinguish glassy state relaxation from other time-dependent processes (*e.g.* recrystallisation, chemical degradation) [50-53].

The physical aging process underlies the accompanying decreases in v_f and in enthalpy (H), which decreases grow in magnitude with time (self-retarding process). This phenomenon has profound impact on polymeric products during their service life and long-term performances. The loss of ductile behaviour on aged or annealed glasses at temperatures below T_g constitutes a major issue for large scale productions. Regarding mechanical properties, while the material stiffness and yield stress increase, creep-, stress-relaxation rates, ductility and toughness decrease.

Below are listed the basic aspects of physical aging below T_g in glassy polymers according to Struik [50, 53].

- **Relaxation times are affected by physical aging**. Aging below T_g induced a continuous decrease in segmental mobility, which slows itself down with time (self-delaying effect). In glassy polymers, since relaxation times are directly related to segmental mobility, mechanical properties will be influenced by a modification in relaxation times.
- **Physical aging solely is effective in the "*aging range*"**. Struik provided data showing that aging is important in glasses between the highest secondary transition temperature T_β and the upper bound of T_g (free-volume theory). Since the segmental mobility decrease with decreasing the temperature below T_g, physical aging is suppressed at T_β, while between T_β and T_g segmental motion is only hindered and aging occur.
- **Physical aging does not affect secondary relaxation processes below T_β.** Even though v_f decreases during physical aging, v_f remains sufficiently large to admit highly localized secondary relaxations.
- **Physical aging is a general phenomenon in glasses**. In the aging range, physical aging is a basic feature of the glassy state due to its thermodynamically unstable state. Regardless of the chemical nature, it should be found in all glasses (*e.g.* monomers, polymers, inorganic glasses, ect.) and should actuate in a similar way. Since the kinetics of this self-retarding process is dominated by the self-retarding effects, the type of the process or the nature of the glass only plays a minor role.
- **Aging time (t_a) is the relevant physical aging parameter.** Struik established that relaxation times increase proportionally to t_a. Therefore, t_a is a parameter of major importance in determining the behaviour of a glass.
- **Physical aging process persists for very long times.** According to the free volume theory, the time (t_∞), required to attain equilibrium at an annealing temperature, $T_a < T_g$, increases exponentially with (T_g-T_a). Struik reported a change in t_∞ at T_g by a factor of about 10 for each 3 °C. Physical aging persists for the entire life of a plastic product, which rate decreases with increasing aging time.
- **Aging is completely thermoreversible.** By heating a glassy polymer above T_g, it reaches it respective thermodynamic equilibrium and any aging that occurred below T_g is erased.

Based on the assumption that changes in v_f and H are time-dependent with similar relaxation time scales, differential scanning calorimetry (DSC) has been used

extensively to measure the kinetics of the enthalpic relaxations at T_g. Upon heating, an endothermic peak in the T_g region is a frequent manifestation of enthalpic relaxation [54, 55]. Based on a large variety of experimental data set, it has been reported that endothermic peak position and magnitude were clearly dependent on annealing conditions [50, 53, 56].

2.1.1. Effect of annealing conditions on endotherm position and magnitude

Glassy polymers, which are isothermally aged at a temperature well below T_g ($T_a < T_g$ - 20 °C), exhibit sub-T_g endothermic maxima in the subsequent DSC heating scans [57-59]. This relaxation effect has been attributed by Hodge and Berens [57] to the nonexponentiality (*i.e.* distribution of relaxation times) and nonlinearity of the glass transition kinetics of samples annealed well below T_g. The peak temperature (T_{max}) increases linearly with the annealing temperature (T_a) and annealing time (t_a). For T_a near but below T_g, and/or long annealing times (t_a), the sub-T_g peaks merge with the glass transition and an endotherm is superimposed on the ΔC_p at T_g (referred to as "T_g overshoot") [52, 56, 60].

In the melted state, the enthalpy of a polymer is solely a function of temperature (T) and pressure (P). When an amorphous polymer is cooled through its T_g, the magnitude of the enthalpy relaxation depends on T, P and on the previous thermal history that it experienced before aging. An increasing rate of thermal quenching, tensile or compressive mechanical stressing and/or previous exposition to a swelling vapour would freeze the segmental configuration in a higher level of enthalpy; thus enhancing enthalpic relaxations over time [27, 57, 59, 60].

The observed effects are illustrated on the schematic "volume, enthalpy-temperature" diagram, as shown in *figure 2.2*. For a sample cooled into its glassy state along the path "ABC" and thereafter annealed at T_1 ((T_g - 20 °C) < T_1 < T_g), V and H relaxes along "CD". Upon reheating, both parameters are recovered to above the transition range along the path "DEB" and the well-know T_g overshoot is observed (*c.f. figure 2.2.a*) [59].

For a sample cooled at a lower annealing temperature T_2 (T_2>T_g-20 °C) along the path "ABF", the enthalpy relaxation (along "FG") is recovered along the path "GHB" and a sub-T_g endothermic peak is thereby observed in a subsequent DSC heating run, as shown in *figure 2.2 b*.

The area or magnitude of the endothermic peaks provide a quantitative measure of the enthalpy loss or enthalpy recovered (δ_H) in glassy polymers. With aging, the segmental mobility causes volume relaxation and a reduction of the v_f [27]. Upon reheating, more energy is required for T_g; leading to an increase in δ_H. Additionally, T_{max} shifts to higher T as the polymer ages in order to complete the morphological

rearrangement occurring at T_g [27, 51, 53, 59, 60]. Accordingly, T_g also increases with aging time.

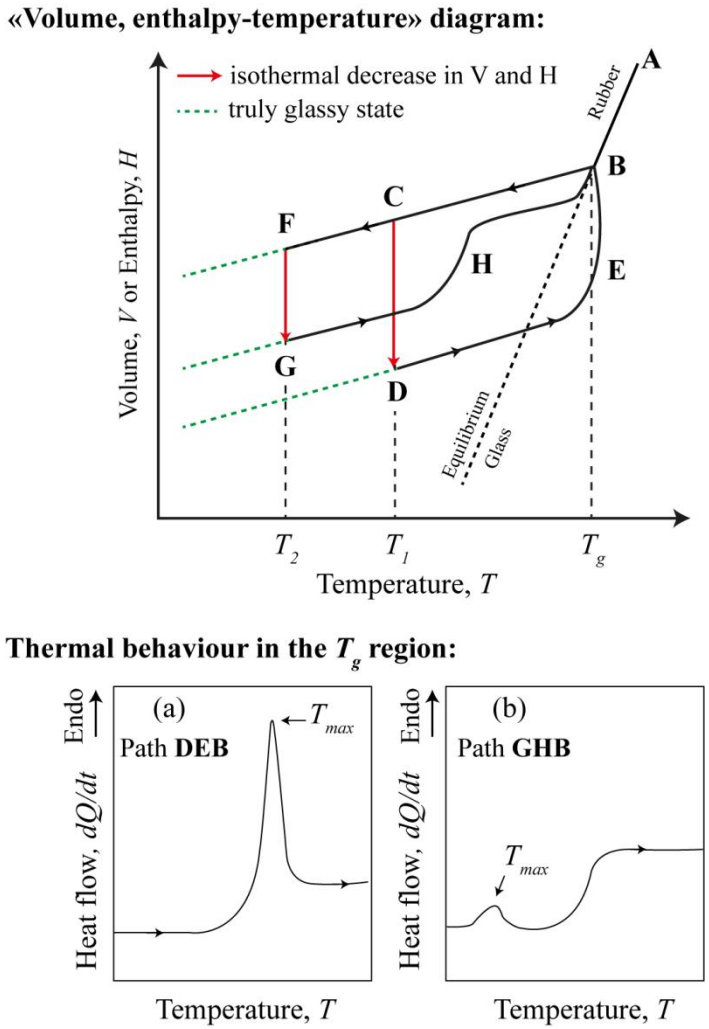

Figure 2.2. Schematic "volume, enthalpy-temperature" diagram featuring different aging temperatures and the corresponding thermal behaviour in the T_g region (Adapted from *ref.* [50, 59]).

Both T_{max} and δ_H values increase linearly with log t_a and with T_a up to a limiting value. At this point, no further increase in T_{max} and δ_H is observed as the annealed glass approaches equilibrium. Since physical aging of glasses depend on the kinetic character of the glass-transition phenomenon, a careful study of the physical aging kinetics may be useful to predict long-term material properties.

2.1.2. Physical aging kinetics

It has been reported that the enthalpy recovered during the physical aging of glasses depends on several variables. The thermal history, the cooling rate, T_a, t_a and the heating rate significantly affect the extent of configurational rearrangement that a glass experiences over time. When all of these parameters are kept constant, except for t_a, a direct measure of the overall relaxation rate of chain segments may be provided by isothermal enthalpy relaxation experiments. The physical aging kinetics (β_H) of a bulk sample may be estimated from *equation 2.1*, as already reported elsewhere [61].

$$\beta_H = d\delta_H / d(\log t_a) \qquad \textbf{(2.1)}$$

Where δ_H is the enthalpy recovered and t_a the isothermal aging time.

Since the cooperative configurational rearrangement of supercooled polymer glasses is not a Debye process, they cannot be described using a single relaxation time. Commonly, the time dependence of the segmental relaxation or the kinetics of the approach of a system to the equilibrium state is approximated using a Kohlrausch-Williams-Watts function (KWW, stretched exponential function), as given by *equation 2.2*,

$$\phi(t_a) = exp\left(-\left(\frac{t_a}{\tau_0}\right)^{\beta}\right) \qquad \textbf{(2.2)}$$

Where τ_0 is the KWW relaxation time and β a parameter that characterizes the distribution of relaxation times between molecules. A broad distribution of relaxation times is expected for a small value of β.

Based on *equation 2.2*, an another model of enthalpy relaxation has been proposed by Cowie and Fergusson as follows:

$$\delta_H(t_a) = \delta_{H_\infty} \times [1 - \phi(t_a)] \qquad \textbf{(2.3)}$$

Where $\delta_H(t_a)$ is the enthalpy change at time t_a and $\delta_{H\infty}$ the equilibrium enthalpy relaxation for t_a approaching ∞.

This empirical Cowie-Fergusson model has been successfully used to investigate structural relaxation processes in poly(vinyl methyl ether) (PVME), PVME/PS blends [62, 63], semi-crystalline PET [64], poly(ether ether ketone) (PEEK) [65], carbonate-amide copolymers [56] and Poly[(lactic acid)-co-(glycolic acid)] (PLGA) films [66]. Additionally, Know *et al.* [67] investigated the influence of the D-lactide content of various PLA grades on enthalpy relaxation using the Cowie-Fergusson model. Experimental results revealed a slight increase in the $\delta_{H\infty}$ values with decreasing the D-lactide content, while τ_0 and β values remained independent of the stereoregularity.

Authors attributed the somewhat higher $\delta_{H\infty}$ values to the fact that PLA with lower D-isomer content has higher potential to crystallize and thus can relax much efficiently at a given T_a, as compared to PLA with higher D-lactide content.

On the other hand, the extent to which the system approaches equilibrium can be characterized in terms of a limiting fictive temperature (T_f). T_f defines the temperature at which the glass would be in its equilibrium state. This parameter can be determined from standard DSC heating runs by integrating the experimental heat flow *vs* temperature trace. *Figure 2.3* illustrates a schematic determination of T_f from the enthalpy as a function of temperature data.

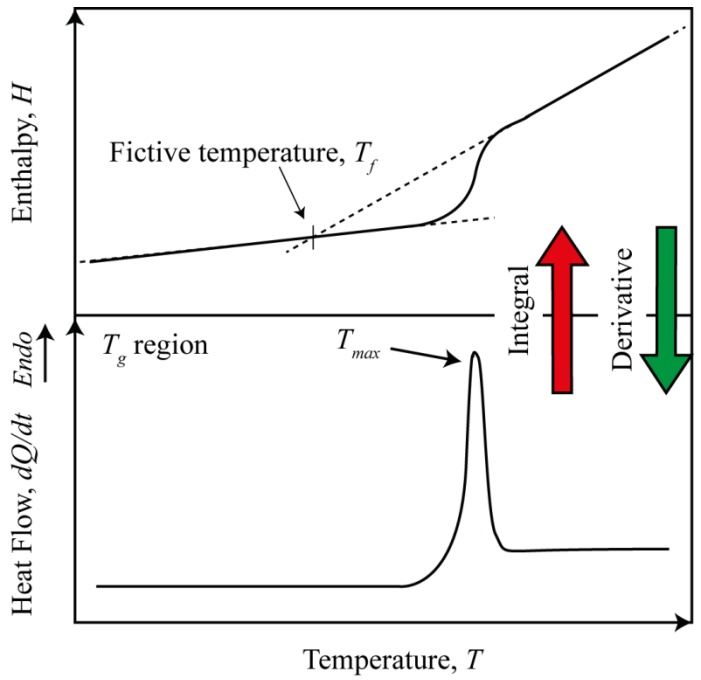

Figure 2.3. Illustration of the determination of the fictive temperature from enthalpy versus temperature plots (adapted from *ref.* [27]).

Based on the difference between T_f and T_a, Nutt and Lu [61] introduced a new overall relaxation rate (R_E) as given by:

$$R_E = -d\left(T_f - T_a\right)/d(\log t_a) \qquad \textbf{(2.4)}$$

Where T_f is the fictive temperature, T_a the aging temperature and t_a the isothermal aging time.

Numerous other models, known as multiparameter phenomenological (MP) models, have been developed to investigate the development of physical aging (*e.g.* the Moynihan and Kovacs-Aklonis-Hutchinson-Ramos (KAHR) models). These

approaches include the dependence of the relaxation time on aging history through the consideration of the fictive temperature (T_f). That is, these models are useful to compare the enthalpy relaxation behaviours between samples at different degree of subcooling ($\Delta T=T_g-T_a$).

2.2. Chain heterogeneity analysis using thermal fractionation

2.2.1. General considerations

It has been largely established that the presence of defects in semicrystalline polymer chains reduce the crystallisable sequence lengths available; leading to the crystallisation of different lamellar thicknesses. These defects may be induced by the polymerization conditions (*e.g.* tacticity, branching, cross-linking, etc.) and/or chemical modifications during processing (*e.g.* degradation reactions, reactive extrusion, etc.).

The distribution of short chain branching (SCB) may significantly influence the polymer's physical and mechanical properties, as already shown for PE synthesised from the copolymerisation of ethylene with α-olefins. Consequently, the molecular information related to the distribution of α-olefin comonomer along the chain is of great interest [68].

The *Temperature Rising Elution Fractionation* (TREF) is usually used to characterise the comonomer distribution in ethylene/α-olefin copolymers. This technique produces separation by the elution of polymer fractions at successively rising temperatures of a material that has been previously crystallised from solution on an inert support during very slow cooling or multiple steps [68]. The application of TREF has been successfully extended to PP homopolymers and copolymers [69-72] and PET [73].

TREF is frequently placed at the forefront of molecular fractionation in polymer science. However, these measurements are time intensive, expensive (use of solvents) and their implementations are not trivial. This is due to the preparative or analytical fractionation in solution. Based on these experimental limitations, this technique might not be a valuable option if a rapid characterisation of a polymer is desired.

On this basis, Monrabal [74] developed a fractionation technique, namely *Crystallisation Analysis Fractionation* (CRYSTAF) in order to shorten testing time. The main differences between CRYSTAF and TREF is that, while CRYSTAF monitors the concentration of the polymer in solution during the crystallisation step, TREF monitors the concentration of the polymer in solution during the elution step. The analysis time is slightly reduced but remains significant [68].

The above experimental limitations led to the development of new thermal fractionation techniques using standard DSC equipment. This innovative concept involves a temperature protocol that is designed to produce the crystallisation of a distribution of lamellar crystals whose size reflects the distribution of crystallisable segments along the chain. Gray and Casey [75] pioneered this methodology and reported the distribution of SCB in linear low density PEs (LLDPE) using a self-annealing thermal procedure.

The *Step Crystallisation* (SC) and *Successive Self-nucleation and Annealing* (SSA) are the two principal and well-accepted thermal fractionation techniques. The main difference between SC and SSA is that, while SC induces molecular segregation using a programmed cooling step from the melt; SSA applies a series of heating and cooling cycles to the sample. Since the polymer chains are never physically separated in thermal fractionation methods, these procedures are sensitive to both intra and intermolecular defects. Regarding TREF or CRYSTAF, the chain is detected only after the dissolution of the whole chain. Thus, they appear to be more sensitive to intermolecular than intramolecular chain heterogeneities [68, 76, 77].

The SSA protocol designed and introduced by Müller *et al.* [78] is based on the procedure reported by Fillon *et al.* [79]. In this technique, a sequential application of self-nucleation and annealing steps is applied to a polymer. After the SSA thermal conditioning, a final DSC heating run reveals a series of melting peaks that reflect the heterogeneous nature of the chain structure [80]. Each melting peak corresponds to the melting of crystallites with different average thickness which depends on the crystallisable polymer sequence lengths available. A correlation between melting temperature (T_m) and lamellar thickness (l) has been established, as given by the Thomson-Gibbs equation [68, 71]:

$$l = \frac{2\sigma T_m^0}{\Delta H_V (T_m^0 - T_m)} \qquad \textbf{(2.5)}$$

Where σ is the lamellar surface free energy, ΔH_v the enthalpy of fusion and $T_m{}^0$ the equilibrium melting temperature.

According to *equation 2.5*, the higher the melting point of the endothermic signal, the thicker the lamellar crystals (and thus the longer the crystallized polymer sequence length). It has been reported that the SSA technique yields a higher fractionation resolution in a shorter analysis time as compared to the SC protocol [68, 78].

The SSA methodology has been successfully applied to numerous PE in order to evaluate the influence of the synthesis conditions on the chain architecture, topological changes induced by functionalisation, modifications of cross-linked LDPE and the miscibility between several PE grades [68, 81-86]. Additionally, valuable results have

been reported for the characterization of the tacticity distribution of PP [71], nanocomposites of high-density PE/carbon nanotubes [87], hydrogenated polybutadiene [88] and the influence of the hydrolytic degradations on the poly(*p*-dioxanone) crystallisation behaviour (biodegradable polymer) [89].

Benefiting from convenient experimental procedure and shorter analysis time, the SSA fractionation techniques can provide valuable information on the chain structure heterogeneity. Nevertheless, while a large number of communications report the thermal fractionation of PE using the SSA protocol, the extension of this method to semi-crystalline polyesters is rare.

The chemical heterogeneities in PET and in poly(ethylene terephthalate-*co*-isophthalate) (PETI) have been investigated by Lodefier *et al.* [73]. Authors compared the results obtained by TREF and SC analysis and concluded that both techniques provide similar information regarding the irregularities in the molecular chain. On this basis, Sanchez [90] evaluated the influence of the *transesterification* reactions between PET and several concentrations of PC on the size of the lamellar crystals using the SSA concept, as shown in *figure 2.4*. Authors reported valuable results and concluded that the longest crystallisable sequences that form the thicker lamellas were the most rapidly affected with increasing PC content.

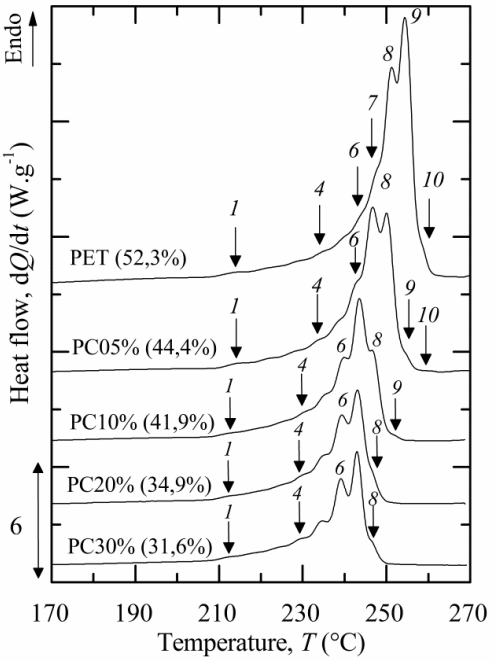

Figure 2.4. Final DSC heating scan at 10 ºC.min^{-1} of PET/PC blends with increasing PC content after applying a SSA thermal protocol. Arrows indicate different peak

positions and the degree of crystallinity is indicated in brackets (adapter from *ref.* [90]).

2.2.2. Applicability of the thermal fractionation to PLA

Under specific annealing and/or crystallisation conditions, PLA resins may exhibit a double melting peak upon heating, as already observed in numerous semicrystalline polymers (PS, PP, PET). Three main mechanisms have been proposed to justify this melting behaviour [91, 92]:

- The melt-recrystallisation mechanism: the low- and high-temperature endotherms might be attributed to the melting of original crystals and crystals formed through the melt-recrystallisation process upon heating, respectively.

- The dual (or multiple) lamellae population mechanism: the double (or multiple) melting peaks may be associated with the melting processes of two (or multiple) different morphologies (different lamellar thickness) which were crystallised prior to the heating scan.

- The dual crystal structure mechanism: usually exhibited in the case of polymorphic polymers. In the DSC curve, the double melting peaks result in the melting of two different crystal structures.

Regarding PLA, the double melting peak has been usually attributed to the melt-recrystallisation mechanism, as already reported by numerous authors [20, 91-94]. This mechanism considers that the lower temperature endotherm corresponds to the melting of crystals initially present. Upon further heating, these partially melted crystals recrystallise into thicker lamellar crystals, which melt at higher temperatures. Nevertheless, the influence of the defect distribution along the chain on the melting behaviour has not been investigated yet, to the best of the knowledge of the author.

The crystallisable regular isotactic PLLA chain segments may be disrupted by the formation of defects in two different ways: **(i)** the random introduction of small amounts of D-lactide during polymerisation and **(ii)** the reactive processing of PLA with multi-functional reactive agents and/or other reactive polymers. Consequently, it is believed that the SSA technique could be extended to PLA resins in order to evaluate these structural heterogeneities.

2.3. Rheology and molecular structure in polymers

Over the years, capillary rheometry has been widely used to characterize polymer shear flow properties. However, recent developments in dynamic rheometry make it possible to infer molecular information about a melted polymer from its viscoelastic behaviour. Benefiting from convenient experimental procedure and better efficiency with respect to rheological information, dynamic rheometry is of practical interest and has been used throughout this work. Thus, the theoretical aspects of several concepts are carefully revised in this section.

In order to relate viscoelastic properties to molecular dimensions, the characterization of the polymer flow properties over an extended range of time or frequency is required. That is, it is necessary to report data from the glassy region (short times/high frequencies) to the terminal behaviour (long times/low frequencies). The simplest deformation pattern is a step-strain (relaxation test), which yields the stress relaxation modulus ($G(t)$), as illustrated in *figure 2.5*.

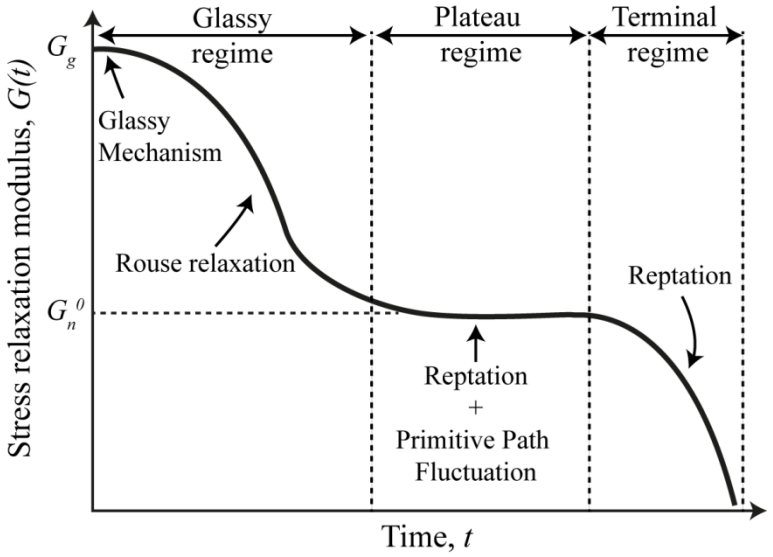

Figure 2.5. General shape of the stress relaxation modulus of a well entangled, monodisperse polymer. The different relaxation mechanism associated to their respective regime are indicated in the curve (adapted from *ref.* [95]).

At extremely short times, the only mechanism for relaxation is the stretching and bending of chemical bonds (*i.e.* glassy mechanism), as there is no time for translational Brownian motion to occur. This behaviour leads to a large glassy modulus value (G_g). Then, at longer, but still quite short times, a transition zone is observed during which the stress significantly relaxes. This behaviour is characteristic of the Rouse relaxation mode which solely involves short-range motions of the chain

(*i.e.* entanglements do not act into stress relaxation) [95]. The Rouse modes of molecular motion are to some degree analogous to the modes of vibration of a string fastened at both ends, as shown in *figure 2.6* [96].

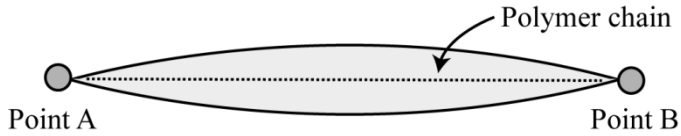

Figure 2.6. Mode of motion in a vibrating string between two points (referred to as point A and B), which are analogous to the modes of motion in a polymer molecule according to the Rouse model (adapter from *ref.* [96]).

For further time increase, $G(t)$ appears to become relatively time independent. That is, stress relaxation is significantly impeded by topological constraints which are imposed by the neighbouring chains. The $G(t)$ trace features a plateau corresponding to the *plateau modulus* G_n^0. These constraints are referred to as entanglements and confer on melted polymers long relaxation times and high viscosities.

It has been found that the ways in which entanglements slow down the relaxation of a polymer can be quantitatively predicted by the *tube model*. The tube theory replaces the topological entanglement constraints from neighbouring chains by a hypothetical tube surrounding a given chain segment, as shown in *figure 2.7*. The chain is confined in this tube, forcing it to move for the most part along the axis of the tube.

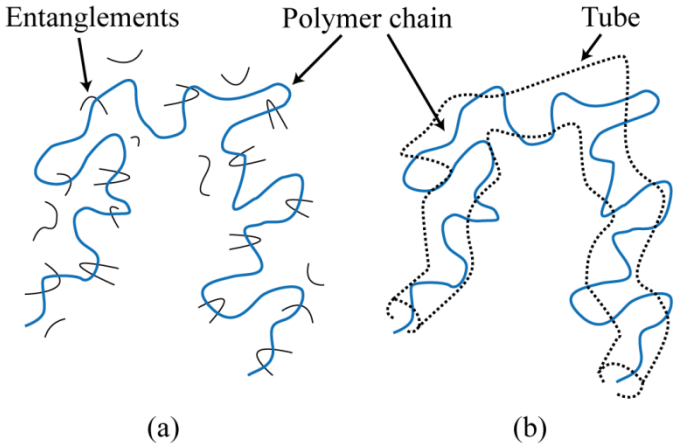

Figure 2.7. (a) Schematic representation of a polymer chain entangled with neighbouring chains. **(b)** The entanglements with surrounding chains are represented by a tube (adapted from *ref.* [96]).

In high MW melts, polymer molecules are highly entangled and a chain may escape from its entanglement through the combined effects of primitive path fluctuations (PPF) and reptation relaxation mechanisms. That is, wrinkling motions initially relax the end of the chains (*i.e.* PPF). However, this mechanism is too slow to relax chain segments near the centre and a relatively slow process of self-diffusion (*i.e.* reptation) is simultaneously involved to relax portions of the chain near the centre [95]. *Figure 2.8* illustrates the above combined relaxation process.

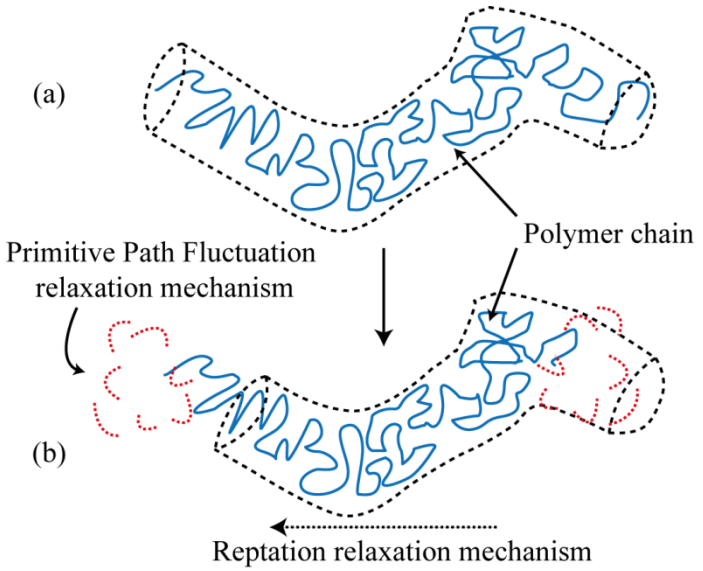

Figure 2.8. (a) Schematic representation of a polymer chain surrounded by a tube. **(b)** relaxation of the chain due to the combined effects of primitive path fluctuations and reptation relaxation mechanisms (adapted from *ref.* [96]).

Finally, a complete stress relaxation is observed at long times whereby a chain can escape from its entanglement solely by reptation [95].

However, these aspects present a practical problem in that:

- G_g cannot be measured using standard melt rheometer as existing instruments cannot achieve the very fast (or high-frequency) deformations required.
- The complete stress relaxation measurements can take very long time, thus promoting possible thermo-oxidative degradations.

To overcome these experimental limitations, oscillatory shear is the technique usually used to study the viscoelasticity of a molten polymer. This procedure yields the dynamic storage (G') and loss (G'') modulus as functions of an angular frequency (ω).

2.3.1. Melt rheology under oscillatory perturbations

Rheological oscillatory experiments may be performed under small amplitude (SAOS) or large amplitude oscillatory shear (LAOS) conditions. The following section focused on the SAOS conditions due to the interest in investigating and quantifying the linear viscoelastic behaviour of melted polymers.

Recall that if the ***deformation is small*** *or applied* ***sufficiently slowly****, the molecular arrangements are* ***never far from equilibrium****. The mechanical response is then just reflections of the dynamic processes at the molecular level which go on constantly, even for a system at equilibrium. This is the domain of* ***linear viscoelasticity (LVE)****. The magnitudes of stress and strain are related linearly, and the behaviour for any liquids is completely described by a single function of time* (Written by Bill Graessley, Princeton University) [97].

A sinusoidal shear stress perturbation, $\tau(t)$, is applied to the sample when dynamic experiments are performed using a controlled-stress rotational rheometer. This value is selected in the LVE regime and should be large enough to provide satisfactory data resolution.

$$\tau(t) = \tau_0 . \sin(\omega t) \qquad \textbf{(2.6)}$$

where τ_0 is the shear stress amplitude, ω the oscillation frequency and t the time. The applied oscillatory stress produces a time-dependent deformation, $\gamma(t)$, into the sample as given by:

$$\gamma(t) = \gamma_0 . \sin(\omega t + \delta) \qquad \textbf{(2.7)}$$

where γ_0 is the strain amplitude and δ the phase angle difference between the applied $\tau(t)$ and the resulting $\gamma(t)$ waves, as shown in *figure 2.9*.

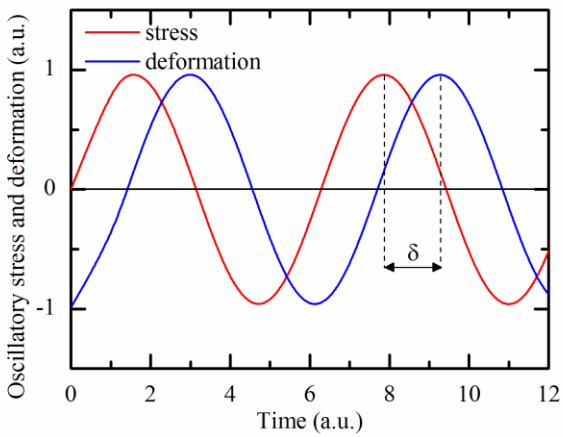

Figure 2.9. Oscillatory stress (τ) wave and the resulting strain (γ) response wave.

For purely elastic melted materials, the stress and strain are in phase (δ=0º). In contrast, the stress and the strain are out-of-phase (δ=90º) when purely viscous melted materials are considered. Polymers are considered as viscoelastic materials and present a δ ranged from 0 to 90º.

From the ratio of the applied stress to that of the resulting deformation, the magnitude of the complex shear modulus $|G^*(\omega)|$, which is the overall response of the system, is calculated as follows:

$$|G^*(\omega)| = {}^{\tau_0}/_{\gamma_0} \quad \textbf{(2.8)}$$

Using trigonometric identities, $|G^*(\omega)|$ can be separated into two components:

- An elastic component, namely the dynamic storage modulus ($G'(\omega)$) which is in phase with the strain:

$$G'(\omega) = |G^*(\omega)|.\cos\delta(\omega) \quad \textbf{(2.9)}$$

G' is the degree to which a material behaves like an elastic solid and stores energy.

- A viscous modulus, namely dynamic loss modulus ($G''(\omega)$) which is in phase with the strain rate:

$$G''(\omega) = |G^*(\omega)|.\sin\delta(\omega) \quad \textbf{(2.10)}$$

G'' is the degree to which a material behaves like an ideal liquid and dissipates energy.

Based on *equation 2.8*, the magnitude of the complex viscosity $|\eta^*(\omega)|$ is given by:

$$|\eta^*(\omega)| = {}^{|G^*(\omega)|}/_{\omega} \quad \textbf{(2.11)}$$

On the other hand, oscillatory experimental data can be analyzed using the complex compliance ($|J^*(\omega)|$) whose magnitude is established from *equation 2.8* as follows:

$$|J^*(\omega)| = {}^{\gamma_0}/_{\tau_0} = {}^{1}/_{|G^*(\omega)|} \quad \textbf{(2.12)}$$

Similar to $G'(\omega)$ and $G''(\omega)$, the calculations of the storage ($J'(\omega)$) and loss ($J''(\omega)$) compliance proceed according to:

$$J'(\omega) = |J^*(\omega)|.\cos\delta(\omega) = {}^{G'(\omega)}\Big/_{|G^*(\omega)|^2} \quad \textbf{(2.13)}$$

$$J''(\omega) = |J^*(\omega)|.\sin\delta(\omega) = {}^{G''(\omega)}\Big/_{|G^*(\omega)|^2} \quad \textbf{(2.14)}$$

When repetitive frequency sweep experiments are performed using fresh samples, experimental between-sample errors are likely to occur in the reported LVE data. On the other hand, equipment limitations also introduce within-sample experimental errors in the measured data even though a rheometer featuring a magnetic levitation thrust with an extremely low residual torque performance is used. Consequently, experimental data require correction in order to report reliable LVE data, as detailed in *appendix (c.f. chapter 9, section 9.1.1*).

Under ideal measuring conditions, an isothermal frequency sweep limits the estimation of the viscoelastic properties to a frequency range of 4 decades (0.0628-628 rad.s^{-1}). Thus, the terminal regime is likely to remain experimentally unestimated for polymers with long relaxation times (*e.g.* polyolefins). Infinitely low ω are not accessible using oscillatory shear experiments due to extensive measurement times. Frequency sweep with 10 points per decades and with a minimum measurement frequency of 0.0628 rad.s^{-1} takes about 24 min. This makes frequency sweep at very low ω a very time ineffective method whose measurements may be flawed by a possible thermal degradation of the sample.

These experimental limitations may be overcome using the Time-Temperature Superposition (TTS) principle. The measurement of standard isothermal frequency sweeps at different temperatures, which are then superimposed, enables the estimation of the LVE data over larger ranges of frequency.

2.3.2. Time-temperature superposition

The essence of the TTS concept is based on the similar modification of the time dependence of molecular motions and of relaxation times by changing the temperature of measurements. In other words, the sequence of molecular relaxation remains unchanged with changing the temperature of measurement (*i.e.* thermorheologically simple polymer).

On this basis, by considering the modulus data, a series of isothermal measurements collected at different temperatures can be shifted horizontally on the logarithmic frequency axis onto each other using a horizontal shift factor (a_T), as illustrated in *figure 2.10*. This approach allows the generation of master curves which span wider ranges of frequency than the range of the original data.

Depending on the range of temperature under study and its distance from T_g, the dependence of a_T on temperature may follow either an Arrhenius (*c.f. equation 2.15*) or a Williams, Landel, Ferry (WLF) (*c.f. equation 2.16*) function.

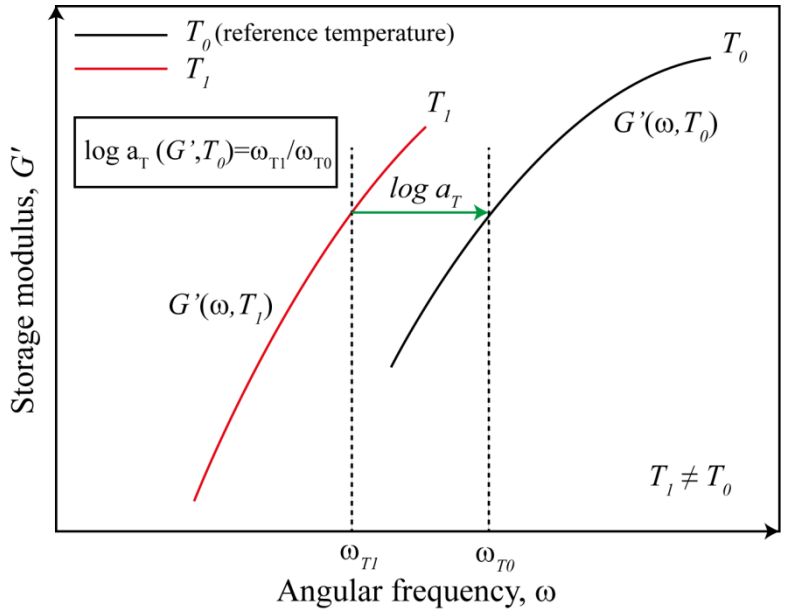

Figure 2.10. Schematic representation of the time temperature superposition principle. For illustration purposes, the dynamic storage modulus has been selected. T_o defines the reference temperature.

Regarding noncrystallisable polymers or those with an extremely slow crystallisation kinetics, the temperature dependence of the rheological data within 100 ºC of their T_g can be modelled by the WLF equation. However, if the temperature range is narrow and/or superior to 100 ºC above T_g, the Arrhenius form is preferred to describe the a_T relation with temperature [95, 98].

$$\ln(a_T(T)) = \frac{E_a}{R}\left(\frac{1}{T} - \frac{1}{T_0}\right) \quad \textbf{(2.15)}$$

$$\log(a_T(T)) = \frac{-C_1(T - T_0)}{[C_2 + (T - T_0)]} \quad \textbf{(2.16)}$$

Where E_a is the activation energy for flow and R the gas constant. C_1 and C_2 are empirical constants obtained from curve fitting. T_0 is the reference temperature and T the temperature of measurement.

A horizontal shift factor alone is often not sufficient to make the modulus data measured at T superpose onto those obtained at the reference temperature, and a vertical shift factor (b_T) may be necessary. Initially, Rouse [95] reported that b_T should be calculated from *equation 2.17.a*, even though other authors later reports that b_T could equally reflect the temperature dependence of the plateau modulus (*c.f. equation 2.17.b*) [99-101].

$$b_T = \frac{T_0 \rho_0}{T \rho} \quad \textbf{(2.17.a)}$$

$$b_T = \frac{G_N^0(T)}{G_N^0(T_0)} = \frac{\rho T M_e(T_0)}{\rho_0 T_0 M_e(T)} \quad \textbf{(2.17.b)}$$

Where ρ_0 and ρ are the polymer density at T_0 and T, respectively. M_e is the molecular between entanglements and G_n^o the plateau modulus.

To conclude, the physical meaning of b_T has not been fully established yet and further investigations are required.

Two main raisons had encouraged scientists to develop the TTS principle. From an experimental point of view, this principle allows to significantly increase the range of times or frequencies over which the linear behaviour is determined. From a polymer scientific point of view, it provides additional information about the molecular structure.

However, special care should be taken when operators are working with the TTS. This empirical principle should not be used when the rate of relaxation times and molecular motions is not equally modified by changing the temperature of measurements. The shift factors are function of both time and temperature (*i.e.* thermorheologically complex polymers). The rheological response curves at different temperatures cannot be superimposed to form a master curve by a simple transition along the frequency axis.

Within the LVE regime, the Cole-Cole representation of rheological data has been the first approach to verify the validity of the TTS. In this plot, the imaginary part (η'') is plotted against the corresponding value of the real part of $|\eta^*(\omega)|$ (η'), respectively. However, this way of plotting reveals that isothermal frequency curves do not superpose as viscosities are strong functions of temperature.

A time-independent plot may be obtained when both imaginary versus real components are normalized by the limiting value of $|\eta^*(\omega)|$ at low ω (*i.e.* the zero-shear rate viscosity, η_0). If the TTS is obeyed, experimental data of different isothermal frequency measurements merge into a common line. This is shown for PLA-4 sample (PLA 2002D), a linear poly (lactic acid) in *figure 2.11*.

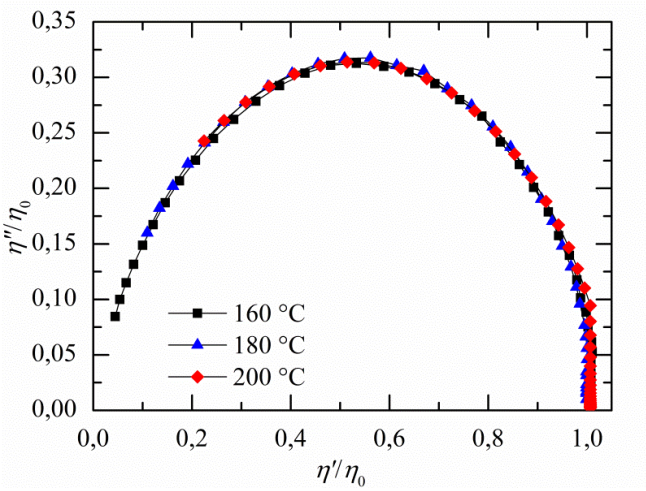

Figure 2.11. Plot of the reduced imaginary versus reduced real part of $|\eta^*(\omega)|$ to verify the validity of the TTS. Experimental data correspond to the isothermal frequency measurements (LVE) at 160, 180 and 200 °C of PLA4 samples, a linear poly(lactic acid) (PLA 2002D) that will be extensively characterized in *chapter 7*.

Based on the Cole-Cole representation, plots of $|G^*|$ versus the product of the zero-shear viscosity and frequency ($\eta_0.\omega$) are also useful for detecting thermorheologically complex behaviour [100, 102]. These plots are temperature dependent for complex material and temperature independent for simple polymers, as illustrated in *figure 2.12.*

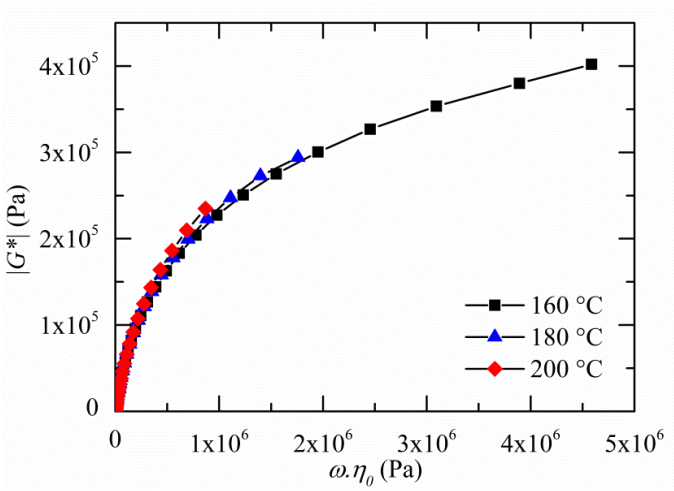

Figure 2.12. An example of simple behaviour using the plot of $|G^*|$ as functions of $\eta_0.\omega$ for PLA4 samples, a linear poly(lactic acid) (PLA 2002D). Experimental data correspond to the isothermal frequency measurements (LVE) at 160, 180 and 200 °C.

Although these plots showed encouraging results, they are likely to present significant application restrictions when isothermal frequency measurements do not reach the terminal regime. Considering that the temperature-independence of both plots is based on the consideration of η_0, data analysis may be arbitrary if η_0 is not accurately estimated for each temperature.

On this basis, Van Gurp-Palmen (vGP) reported a different approach to verify the validity of the TTS whereby the phase angle, $\delta=arctan(G''/G')$, of the frequency sweeps performed at different temperatures is plotted against the corresponding value of $|G^*|$ [103]. Since this plot are temperature and frequency independent for well entangled polymers, all isothermal frequency curves merge into a common line if the TTS holds, as shown in *figure 2.13* [104, 105].

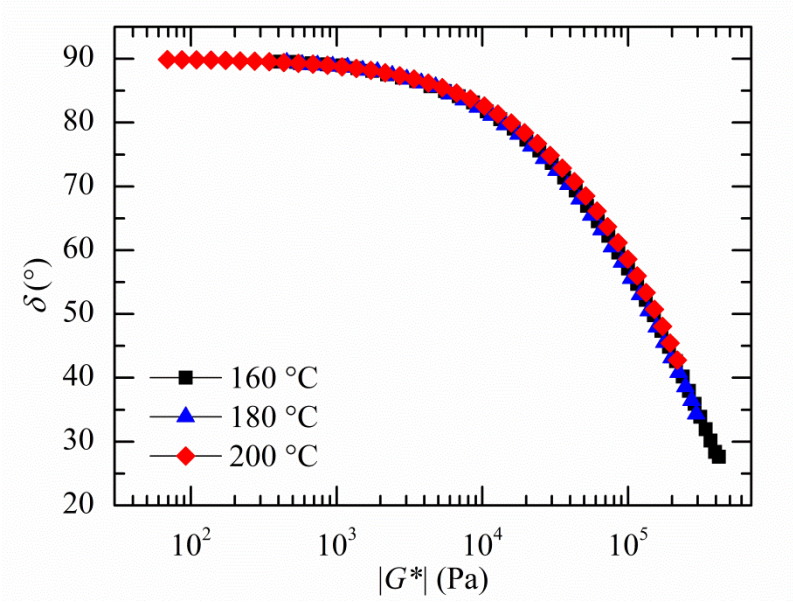

Figure 2.13. Van Gurp-Palmen plot to verify the TTS principle for PLA4 samples, a linear poly(lactic acid) (PLA 2002D). Experimental data correspond to the isothermal frequency measurements (LVE) at 160, 180 and 200 °C.

Independently of the polymer under study, the accessible range of frequencies is commonly limited due to both the usual poor thermal dependency of polymer rheological properties and the limited temperature window for rheological measurements. Even using the TTS principle, it is not always possible to collect sufficient rheological information to reach the infinitely low ω range, whereby contains information regarding molecules with the longest relaxation times (*e.g.* large polydispersity, long chain branching, etc).

To overcome these experimental issues, creep-recovery experiments have been defined as a viable solution in order to determine polymer long-time behaviour due to its faster rate to reach the steady state.

2.3.3. Melt rheology under static perturbations

In a creep-recovery experiment, a constant shear stress $\tau(t) = \tau_0$ is applied to the melted sample at a time t_0 and the resultant time-dependent shear deformation $\gamma(t)$ is measured over time, as shown in *figure 2.14*. The applied stress should be small enough to avoid $\gamma(t)$ entering the nonlinear deformation regime before reaching the steady state, but large enough to provide satisfactory resolution of data. At the time $t_1 > t_0$, the stress is instantaneously removed ($\tau(t)=0$) and the time-dependent recoverable deformation $\gamma_r(t)$ is measured. Calculations of the time-dependent creep, $J(t)$, and the time-dependent recoverable, $J_r(t)$, compliance from $\gamma(t)$ and $\gamma_r(t)$ proceed according to *equation 2.18* and *2.19*, respectively.

$$J(t) = {}^{\gamma(t)}/_{\tau_0} \tag{2.18}$$

$$J_r(t) = {}^{\gamma_r(t)}/_{\tau_0} \text{ with } \gamma_r(t) = \gamma(t_1) - \gamma(t - t_1) \tag{2.19}$$

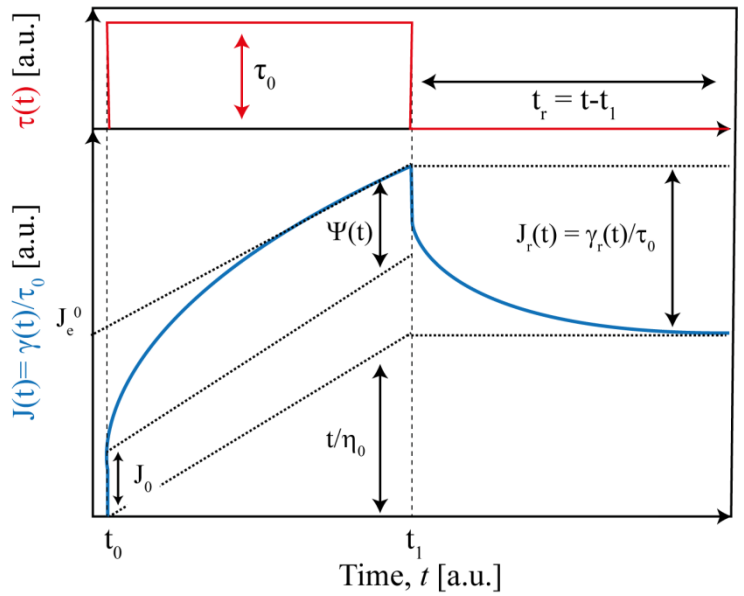

Figure 2.14. Principle of the creep-recovery experiments. The separation of the different compliances was performed according to [106, 107].

Phenomenologically, the creep compliance *J(t)* may be decomposed in three different terms according to *figure 2.14.*

$$J(t) = J_0 + J_r(t).\psi(t) + {}^{t}/_{\eta_0} \quad \textbf{(2.20)}$$

J_0 is the spontaneous elastic part of the compliance which is usually neglected for melted polymers due to its extremely low value (about 10^{-9} Pa^{-1}) [106, 107]. $\psi(t)$ is the delayed viscoelasticity function which is equal to 0 at time zero and 1 for $t \to \infty$. t / η_0 represents the irreversible viscous term. During the creep phase, when the steady state is reached, $J_r(t) << t / \eta_0$ and the zero shear-rate viscosity η_0 can be defined as [108]:

$$\lim_{t\to\infty} \frac{t}{J(t)} = \eta_0 \quad \textbf{(2.21)}$$

Similarly, η_0 can be determined from the plot of the creep time divided by the linear creep compliance (t/J) as a function of creep time (t), as shown in *figure 2.15*.

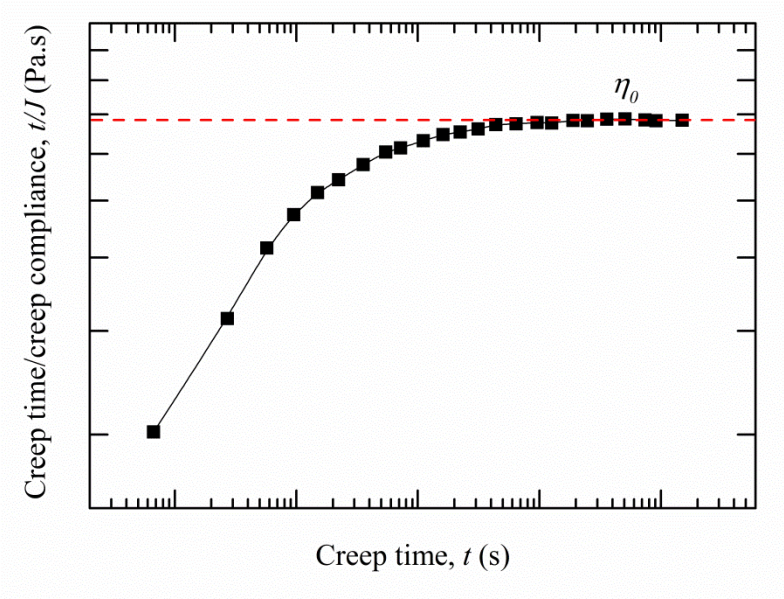

Figure 2.15. General shape of the creep time divided by the linear creep compliance versus the creep time in the linear range of deformation.

The recoverable compliance is found to be independent of the creep time t_1 if the steady state is reached during the creep phase. After a sufficiently long creep and recovery time, $J_r(t)$ tends to reach a limiting plateau value. This parameter is defined as the linear steady-state elastic compliance, J_e^0, and is a measure of the material elasticity in the melted state. It can be determined as follows:

$$\lim_{t\to\infty} J_r(t) = J_e^0 \quad \textbf{(2.22)}$$

Theoretically, the creep-recovery experiment is the most direct method to determine J_e^0. However, it is practically impossible to isolate solely the energetic mechanisms stored in the sample, which are necessary to drive the sample during the recovery phase. Although a high precision controlled stress rheometer featuring a magnetic levitation thrust is used, the bearing supporting the fixtures is not frictionless. A residual torque is generated, disturbing the recovery phase and the recoverable deformation measurements. Consequently, the recovery data requires a "*drift correction*" in order to calculate reliable J_e^0 values, as detailed in *appendix* (*c.f. chapter 9, section 9.1.2*) [106, 107, 109].

2.3.4. Correlation between melt rheology and molecular dimensions

Most polymers are viscoelastic materials. Their response to a mechanical loading ranges between that of a true solid (δ=0º) and that of a true liquid (δ=90º). Considering that the applied stress or strain is sufficiently small, the reported experimental data are within the domain of the linear viscoelasticity region (LVE). This condition greatly simplifies the complete mathematical description of the viscoelastic behaviour of a polymer.

The viscoelastic properties of a polymer may be experimentally measured using several methods (*e.g.* stress relaxation, oscillation, creep-recovery experiments), as previously reported. All of these procedures are supposed to provide similar information. However, the range of measurements and the form of the experimental data are different. Considering that the linear theory of viscoelastic functions is verified, the different stress relaxation ($G(t)$), oscillation ($G'(\omega)$, $G''(\omega)$ and/or $J'(\omega)$, $J''(\omega)$) and creep-recovery ($J(t)$, $J_r(t)$) functions may be interconverted, as shown in *figure 2.16*.

These linear viscoelastic interconvertions cannot be performed directly. Intermediate functions such as relaxation, $H(\tau)$, or retardation, $L(\lambda)$, spectrum should be initially determined. Nevertheless, they are not experimentally accessible and should be calculated from the standard viscoelastic functions. They are defined as the core functions of a material as both spectra only depend on the molecular structure and molecular relaxation processes [110, 111].

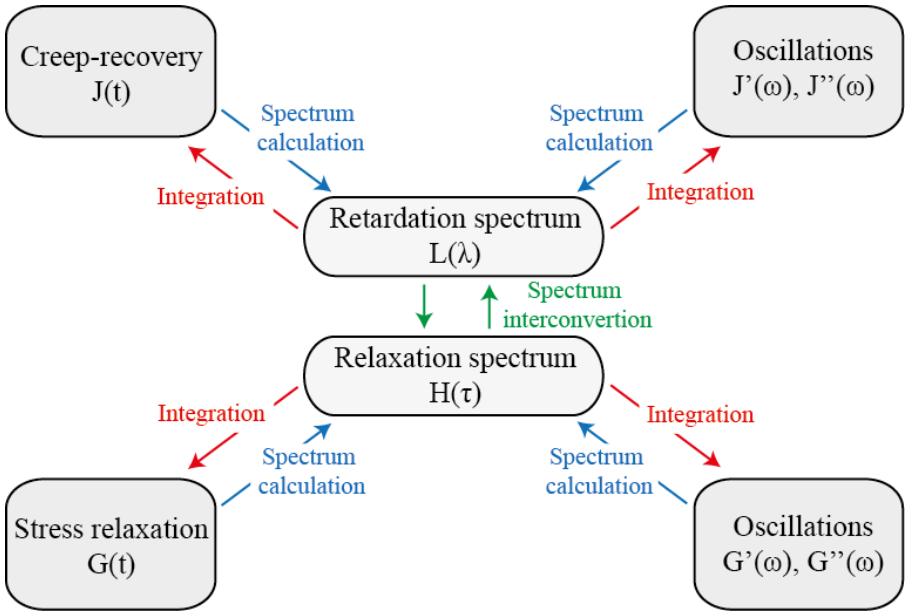

Figure 2.16. Road map showing the linear viscoelastic interconvertions.

The procedure to calculate $H(\tau)$ and/or $L(\lambda)$ from only one material function is not straightforward. However, the greater challenge is to combine data from two different functions in order to generate a continuous "*composite linear spectrum*" over extended time/frequency ranges. The main difficulty arises from the inversion of a pair of Fredholm integral equations of the first kind (*c.f. chapter 9, section 9.1.3, equations 9.4 to 9.13*) of a data set containing possible experimental errors and which is only available over a limited frequency range. The combination of these different drawbacks leads to a mathematically ill-posed problem.

To this end, Honerkamp and Weese [112] developed a reliable nonlinear method of regularization in order to counter these experimental issues. This method yields a smooth relaxation spectrum by taking into account noise in the experimental data. The resulting relaxation spectrum is reliable in the region corresponding to the experimental time window based on the Davies and Anderssen criteria (*c.f. chapter 9, section 9.1.3*) [110-112].

Both spectra may be predicted in a continuous or discrete mode. Discrete spectra are not usually recommended because information present in the original data set is likely to be lost. This is because discrete values are calculated from averages of the original data over time intervals. Continuous spectra are considered as more reliable in order to predict the viscoelastic behaviour of materials. Moreover, it is easier to combine two continuous than two discrete spectra [113].

a) Plateau modulus, MW between entanglements, characteristic relaxation times, entanglement density and characteristic ratio

According to the linear theory of viscoelastic functions, the combination of frequency sweeps and creep-recovery experiments is reliable for all data measured within the LVE regime. The combination of both tests primarily provides the advantage of enlarging the range of times or frequencies over which the linear behaviour is determined.

*Figures 2.17*and *2.18* show the usual good agreement between both procedures in order to generate a continuous "*composite linear spectrum*".

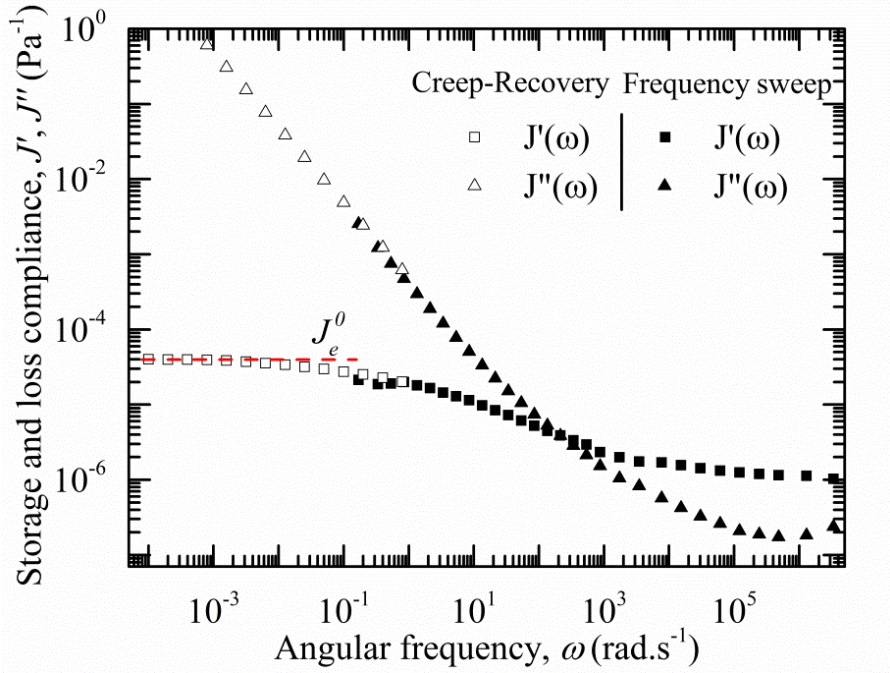

Figure 2.17. *J'(ω)* and *J''(ω)* viscoelastic functions for PLA4 samples (PLA 2002D) at 180 °C in the linear range of deformation. The open symbols represent the conversion of the creep-recovery data calculated from retardation spectrum and the filled symbols the data obtained from frequency sweep experiments.

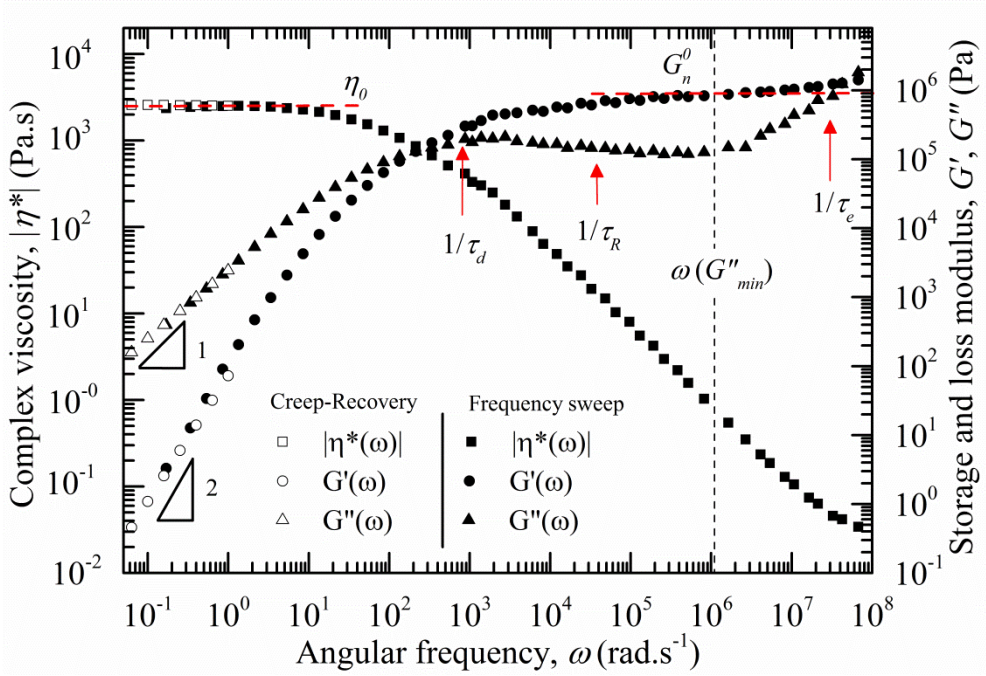

Figure 2.18. $|\eta^*(\omega)|$, $G'(\omega)$ and $G''(\omega)$ viscoelastic functions for PLA4 samples (PLA 2002D) at 180 °C in the linear range of deformation. The open symbols represent the conversion of the creep-recovery data calculated from retardation spectrum and the filled symbols the data obtained from frequency sweep experiments.

At low frequencies, the storage modulus, $G'(\omega)$, becomes proportional to the square of ω (*i.e.* $G' \propto \omega^2$) and the loss modulus, $G''(\omega)$, to ω (*i.e.* $G'' \propto \omega$). This trend is characteristic of the terminal region, also called the "*zone of terminal relaxation*". This limiting behaviour at low ω may be understood by considering *equations 9.4.* and *9.5 (c.f. chapter 9, section 9.1.3)*. As the frequency approaches zero, the denominator inside the summation approaches one, and the numerator is denominated by the term with the longest relaxation time, which is called the "*terminal relaxation time*" [105].

Calculations of η_0 and J_e^0 proceed according to *equations 2.23* and *2.24*, respectively. Both parameters are similar to those determined by creep-recovery experiments (*c.f. section 2.3.3*). However, these approximations are only true if the sample under study reveals the terminal regime (*i.e.* $G' \propto \omega^2$ and $G'' \propto \omega$) at infinitely low frequencies ($\omega \to 0$).

$$\lim_{\omega \to 0} \frac{G''(\omega)}{\omega} = \lim_{\omega \to 0} \frac{1}{\omega . J''(\omega)} = \eta_0 \qquad \textbf{(2.23)}$$

$$\lim_{\omega \to 0} \frac{G'(\omega)}{G''(\omega)^2} = \lim_{\omega \to 0} J'(\omega) = J_e^0 \qquad \textbf{(2.24)}$$

At high ω, long range motions are not fast enough to allow molecular relaxation due to the numerous topological constraints (*i.e.* entanglements) imposed by the presence of other chains. Thus, relaxation is largely prevented and the elastic component of the complex modulus, $G'(\omega)$, reaches a quasi-plateau known as the *plateau modulus*, G_n^0, as shown in *figure 2.18*. The relaxation modulus, $G(t)$, shows this same plateau over a certain range of times, as illustrated in *figure 2.5*. This behaviour is another obvious effect of entanglements on polymer rheology causing a melted polymer to act like a rubber when it is deformed more rapidly than the molecules can escape their entanglements [96].

There are various semi-empirical methods to determine G_n^0 from viscoelastic measurements. While the *G'* plateau is essentially flat for monodisperse and high MW polymers, there is no ω at which a true plateau is observed for high MW and narrow-disperse or polydisperse polymers. The slope of *G'* in the plateau region increases with increasing polydispersity. On this basis, two principal approaches have been reported in order to determine G_n^0 for polydisperse systems:

Case 1: If *G"* exhibit a minimum at the high-frequency side of the crossover modulus (where $G'(\omega)=G''(\omega)$), G_n^0 is determined from the value of *G'* at the frequency, ω_{min}, where *G"* passes through a minimum, as illustrated in *figure 2.18* [114-116].

$$G_n^0 = G'(\omega)_{\,G'' \to minimum} \qquad \textbf{(2.25)}$$

Case 2: If *G"* does not have a minimum (usually observed for polymers with a very broad MWD or low MW), G_n^0 is determined from the value of *G'* at the frequency ω_{min} where $\tan \delta = G''/G'$ passes through a minimum [104, 117]:

$$G_n^0 = G'(\omega)_{\,\tan \delta \to minimum} \qquad \textbf{(2.26)}$$

However, since both the type of molecular structure and the breath of the MWD may difficult the experimental evaluation of G_n^0, the numerical integration methodology of $G''(\omega)$ using *equation 2.27* is an another approach, as already reported elsewhere [96, 115, 118, 119].

$$G_N^0 = \frac{2}{\pi} \int_{-\infty}^{+\infty} G''(\omega) d \ln \omega \qquad \textbf{(2.27)}$$

The majority of the plateau modulus reported in the literature has been obtained by this method [115, 120, 121]. The mathematical determination of G_n^0 using *equation 2.27* has the great advantage to remain independent of the MWD [115].

According to the Ferry's definition [105, 114], the *molecular weight between entanglements* (M_e) is closely related to G_n^0, as indicated by *equation 2.28*. M_e corresponds to the MW between two topological interactions (*e.g.* entanglements) between one polymer chain and its neighbours that significantly impedes the polymer chain motion as well as its ability to relax after a deformation is imposed. This behaviour gives to polymers, high viscosities, high modulus and good mechanical properties.

$$M_e = {\rho RT}/{G_N^0} \quad \textbf{(2.28)}$$

Where ρ is the melt density at the temperature of measurement (T) and R the universal gas constant (R=8.314 J.mol^{-1}.K^{-1}).

Based on the calculation of M_e, different polymer chain parameters, namely the "*number of entanglements*" per molecule (Z), the *entanglement density* (ν_e), *characteristic relaxation times* (τ) of the chains and/or the *characteristic ratio* (C_∞) may be estimated.

Because high MW polymers are significantly entangled, the "*number of entanglements*" per molecule (Z) may be estimated on the knowledge of M_e and the weight-average molecular weight, M_w, as follows (Ferry definition) [114]:

$$Z = \frac{5}{4}\frac{M_w}{M_e} \quad \textbf{(2.29)}$$

The characteristic times of different relaxation modes (*c.f. figure 2.18*) correlate with M_e via the number of entanglements Z as follows [115]:

$$\tau_d = 3Z^2\tau_e \quad \textbf{(2.30)}$$

$$\tau_R = Z^2\tau_e \quad \textbf{(2.31)}$$

Where τ_d is the reptation disengagement time (uncorrected for contour length fluctuations), τ_e the relaxation time of a segment between entanglements and τ_R the Rouse relaxation time of a chain.

In a coil, the *entanglement density* (ν_e) is defined as the density of physical contacts between chains and can be easily calculated from M_e [118, 122]:

$$\upsilon_e = {\rho_a}/{M_e} \quad \textbf{(2.32)}$$

Where ρ_a is the amorphous density of the polymer under study. In the current study, this value was determined for each sample at room temperature according to the

immersion method in water based on the Archimedes' principle (ASTM D792-00 standard).

The characteristic ratio (C_∞) is a measure of how large the polymer coil is under unperturbed conditions relative to the freely jointed chain. That is, it is a measure of the intrinsic flexibility and rigidity of a coiled chain. Essentially, this parameter is the inherent rigidity associated with the individual chain segments (*i.e.* bond angles and lengths) of the polymer species, which determines the overall capability of the chain to rotate around its own axis, resulting in either flexible or rigid behaviour of the bulk polymer [118].

According to the topological model developed by Wu [123], C_∞ may be predicted purely from the chemical structure of the polymer using *equation 2.33*.

$$C_\infty = \sqrt{n_v M_e / 3M_r} \qquad \textbf{(2.33)}$$

Where n_v is the number of real or virtual repeating bond per monomer unit around which the polymer chain is able to rotate and M_r the MW of the repeat unit. Regarding linear PLA, n_v =3 and M_r =72.06 g.mol^{-1} [118, 124].

b) Zero shear-rate viscosity versus molecular weight

The dependency of η_0 on the weight-average molecular weight (M_w) of melted polymers is of growing interest because it allows some understanding of the network structure. Below a critical MW, M_c, polymer melts are unentangled and η_0 is proportional to M_w (*c.f. equation 2.34*), as illustrated in *figure 2.19* [105, 125].

As the MW increases above M_c, η_0 starts to increase much more rapidly with MW, often approaching a power law dependence as given by *equation 2.35*. This behaviour is one of the noteworthy effects of entanglement coupling. It occurs when the polymeric chains reach a sufficient length causing entanglement and impede the segmental motions of the neighbouring chains more strongly than simple hydrodynamic drag [105, 126]. Both tendencies have been experimentally confirmed by Berry and Fox for numerous linear polymer structures [105, 126].

$$\eta_0 = K_1 M_W \text{ for } M_w < M_c \qquad \textbf{(2.34)}$$

$$\eta_0 = K_2 {M_W}^{\alpha} \text{ for } M_w > M_c \qquad \textbf{(2.35)}$$

The exponent α is not defined as a universal constant but its value usually ranges from 3.4 to 3.6 for most entangled linear flexible polymers. K_1 and K_2 are parameters which are dependent on the chemical structure of the polymer and the temperature of the determination. M_c is the critical MW for entanglements.

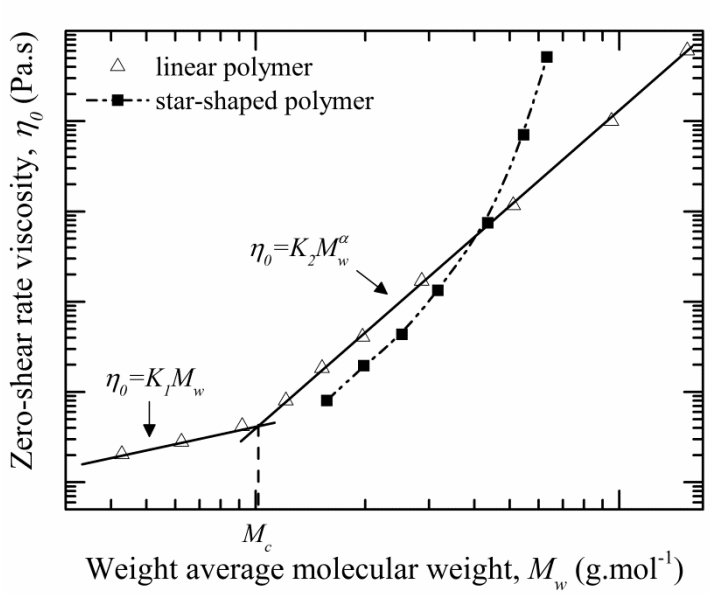

Figure 2.19. Schematic representation of the influence of entanglements and uniform star-shaped topology on the zero shear rate viscosity as a function of the weight-average molecular weight (Adapted from *ref.* [105, 125]).

Kraus and Gruver reported the first evidence concerning the failure of the η_0-M_w relation (*c.f. equation 2.35*) for star-shaped polybutadienes [127]. As illustrated in *figure 2.19*, star polymers with unentangled arms exhibit a lower viscosity than their linear homologues of similar MW. In a limited range of MW, the η_0-M_w relation roughly follows the power law dependence of linear polymers. As the branches entangle, a threshold is reached where η_0 increases, and over a fairly narrow range of MW, the slope of the log(η_0) versus log(M_w) curve exponentially increases.

Flow properties are significantly modified when branching is introduced into the initial linear matrix. It has been reported for polymers with similar MWs and MWDs that η_0 tends to decrease when short chain branching is grafted to the main backbone. This behaviour results from a poor branch entanglement due to the short length of the different branches. It is only when branch length reaches a significant size (M_b), as compared to the entanglement spacing, that branches themselves strongly entangle (referred to as long chain branching, LCB) and enhanced melt properties.

Figure 2.20 illustrates the effects of the presence of LCB on the shape of the viscosity curve. A couple of noteworthy features specific to the viscosity functions in LCB polymers are η_0 increase and the enhanced shear-thinning regime while its onset is shifted to lower frequencies [128-131].

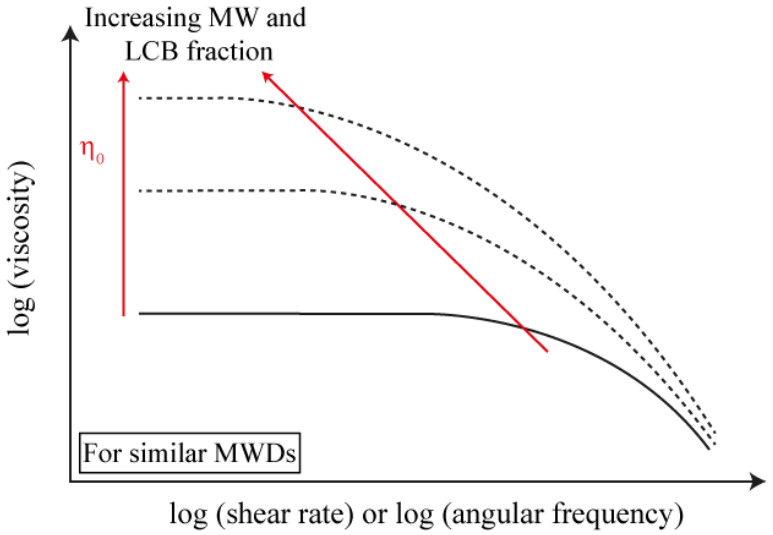

Figure 2.20. Schematic representation of a double logarithmic plot of the viscosity as a function of shear rate or angular frequency with increasing MW and LCB fraction.

There is now a deeper theoretical and experimental understanding of the uniform LCB effects on the η_0-M_w relationship. Star-shaped and LCB polymers with various numbers of arms exhibit an exponential dependence of η_0 on the number of entanglements per side branch as follows [105, 108, 132]:

$$\eta_0 = K\left(\frac{M_a}{M_e}\right)^{\alpha} exp\left(v'\frac{M_a}{M_e}\right) \qquad \textbf{(2.36)}$$

Where M_a is the MW of the long chain branch and M_e the MW between entanglements. α and v' are constants equal to approximately 1 and 0.5, respectively [108, 132]. K is defined as a factor of proportionality which is dependent on the temperature and the nature of the branch.

An exponential dependence of η_0 on M_w has also been seen for branched polymers having a more complex structure, such as H-shaped, POM-POM like structure [133-135].

c) Correlation between rheological curves and long chain branching

Melt rheological properties exhibit a high sensitivity to the presence of LCB, even at concentrations below the detection limits of classical spectroscopic or chromatographic methods. This is due to significant differences between the relaxation behaviour of linear and LCB chains. Thus, rheological measurements remain one of the most useful methods to obtain large-scale molecular information.

However, obtaining molecular information about LCB using only rheology-based methods is not trivial. Numerous studies reported that increasing the MW, broadening the MWD or increasing the content of LCB have similar effects on the shear viscosity function [99, 136-139]. That is, the distribution of relaxation times is not a unique function of chain architecture. The separation of the MW and polydispersity effects from that of LCB is an important prerequisite in order to correlate branching topology and rheological properties.

On this basis, different quantitative correlations based solely on melt measurements have been utilized to estimate the degree of LCB. Garcia-Franco *et al.* [140] and Trinkle *et al.* [141] used the so-called van Gurp-Palmen (vGP) plot to estimate low levels of LCB in various polydisperse polyolefin systems by calculating the area included between the curve corresponding to the branched polymer and its linear homologue. Another commonly-used method to relate shear rheological properties to LCB level is based on the "*Dow rheology index*" (*c.f. equation 2.37*), which was specifically designed for polyolefins with narrow and similar MWDs and hence cannot be used otherwise [142].

$$DRI = \frac{G_N^0\left(\lambda/\eta_0\right) - 1}{10} \qquad \textbf{(2.37)}$$

In contrast to other rheological properties, which are affected by both the broadening of the MWD and the presence of LCB, the dependence of η_0 on M_w (*c.f. equation 2.35*) has been reported as independent of the distribution of MW for linear PE [139, 143, 144], PS [145] and PP [146]. Consequently, the deviation from *equation 2.35*, which has been established for linear polymers, is a good indicator of the presence of LCB in polyolefins, as already reported by numerous authors [108, 119, 139, 147-150].

The estimation of the flow activation energy, E_a, is another example of LCB characterization by considering rheological measurements alone. The activation energy for viscous flow is affected by chain flexibility, intermolecular interactions, the concentration of polar groups and side-chain branches. While the presence of LCB yields an increase in both the temperature dependence and E_a, the thermorheological behaviour becomes complex [151-153]. That is, the sequence of the molecular relaxations is temperature dependent. Unfortunately, the situation is ambiguous because the absence of an enhanced E_a and/or the loss of simple thermorheological behaviour do not necessarily exclude the presence of low amounts of LCB, as already reported for sparsely branched HDPE resins [138, 154, 155] and for branched poly(butyleneisophthalate) [156]. Therefore, the flow activation energy data alone cannot always indicate the presence of LCB.

Several authors also attempted to combine shear rheology and spectroscopic or chromatographic methods. Shroff and Mavridis [138], Wang *et al.* [157] and Janzen and Colby [147] coupled SEC-viscosimetry technique with shear rheology to detect LCB. Adams *et al.* [158] reported a technique to estimate the level of LCB by comparing MWDs measured by SEC with MWDs inferred from the inversion technique of the viscosity data proposed by and Tuminello [159]. Although promising results were obtained for detecting branching down to 0.005 LCB per 1000 carbon atoms, final LCB content estimations were based on NMR experiments.

d) Estimation of the MWD from rheological measurements

SEC is frequently placed at the forefront of molecular characterization in polymer science. However, this technique is time consuming, expensive (use of solvents) and experimental data may be flawed by coelution issues. Thus, an increasing interest has grown to infer MWD from rheological measurements. This technique provides specific advantages as compared to SEC. For instance, standard rheological property measurements are less time consuming than SEC elution curves analysis. The previous dissolution of the polymer, which can be the rate-limiting step for analysis time, is not necessary to measure viscoelastic properties.

Benefiting from convenient experimental procedures and higher resolution with respect to HMW components, this technique may be used to perform high throughput process controls in industrial settings. However, it should be kept in mind that this method cannot replace SEC measurements. Both methods have to be used simultaneously in order to complete each other.

Zeichner *et al.* [105] developed the simplest procedure to estimate a measure of the breath of the MWD (*i.e.* polydispersity index, PDI) from the $G'(\omega)$ and $G''(\omega)$ curves. Experimental results indicated that the PDI was related to the crossover modulus, G_c, as follows:

$$PDI = \frac{10^6}{G_c} \qquad \textbf{(2.38)}$$

Where G_c is the value of $G'(\omega)$ and $G''(\omega)$ where the two modulus are equal ($G'(\omega) = G''(\omega)$). That is, where the curves of $G'(\omega)$ and $G''(\omega)$ cross.

Authors reported promising results for PP. However, this empirical relation has been specifically designed for a single family of polyolefins and it cannot be expected to be valid for other groups of polymers. Moreover, the estimation of the PDI using G_c is not representative of the whole MWD.

While the manipulation of the rheological data to infer complete MWDs has been of growing interest, it is not a trivial operation. Over years, different mathematical

methods, which are classified in two general categories, have been proposed. Those based on an integral approach and those based on the differential approach [160].

- Integral approach

In 1986, Tuminello [161] developed an analytical method in which the shape of the cumulative MWD was firstly assumed and then related to $G'(\omega)$ through the double reptation mixing rule. The bimodality of the predicted MWDs was maintained and Fleissner [146] reported that this technique provides qualitatively reliable results for polydisperse HDPE.

In 1991, Malkin and Teishev [162] developed a transformation procedure in which the shear-viscosity curve was transformed into the MWD using an assumed bulk mixing rule of linear architectures as follows:

$$\eta^{1/\alpha} = \sum w_i \, \eta_i^{1/\alpha} \qquad \textbf{(2.39)}$$

Where α is the exponent in the power law dependence between η_0 and M_w. w_i is the weight fraction of component i and η_i its corresponding viscosity. A feature of the above mixing rule is that the coupling effects between individual components with different chain lengths are taken into account.

While there are valid reasons to question the detailed assumptions leading to this mixing rule, Tuminello and Cudremauroux [163] reported promising results to predict MWD from complex dynamic viscosity data of PS. Based on the above mixing rule, Malkin and Teishev [162] developed an explicit differential solution (*equation 2.40*) to determine the MWD from viscosity data by fitting the raw viscosity data to simple viscosity models.

$$W(m) = 1 + \frac{1}{\nu}\left(\frac{\eta}{\eta_0}\right)^{1/\alpha}\left(\frac{\dot{\gamma}}{\dot{\gamma}_c}\right)^{\nu/\alpha}\left.\frac{d\ln\eta}{d\ln\dot{\gamma}}\right|_{\dot{\gamma}=\dot{\gamma}_c m^{-\alpha/\nu}} \qquad \textbf{(2.40)}$$

Where *W(m)* is the cumulative MWD. That is, the cumulative weight fraction of polymer up to a reduced MW, *m*, which is defined as the ratio of the MW, *M*, to that of M_w (*c.f. equation 2.41*). $-\nu$ is the slope of the power-law region. $\dot{\gamma}$ is the shear rate and $\dot{\gamma}_c$ the critical shear rate which is a horizontal scaling parameter fixing the position of the transition region between the low shear rate plateau and the power-law regime.

$$m = \frac{M}{M_w} \qquad \textbf{(2.41)}$$

Negative conclusions were reported due to the loss of important characteristic information related to the shape of the MWD (*e.g.* bimodality) during calculations.

In 1994, Mead [164] developed a new integral approach which relates the steady shear relaxation modulus (*G(t)*) to the MWD through the double reptation mixing rule coupled with a Tsengoglou single exponential relaxation function. The bimodality of the predicted MWD was maintained for PB blends. However, a significant loss of qualitative agreement (*e.g.* peak location, peak overall breath) was observed between the inferred and experimentally measured MWDs.

- Numerical approach

In 1994, Mead [165] developed a differential approach based on a similar approach than his integral method [164] but which allows the introduction of multiple relaxation times in the calculations. As compared to the experimentally determined MWDs, author reported promising results to infer the MWD shape, the peak location and the overall breaths of a series of PB blends.

In 1994, Shaw and Tuminello [159] proposed a numerical method based on *equation 2.40*. In this technique, the viscosity curve is extrapolated at both ends and the MWD spectrum is calculated numerically. Wood-Adams and Dealy [158, 160] reported promising results to estimate MWD for polydisperse linear PE. Over years, this technique has been refined by Wood-Adams and Dealy [160] and Liu *et al.* [166].

In 1995, another numerical relationship was developed by Wasserman [167] to infer MWD from the relaxation modulus function. This procedure is equivalent to the Mead's technique [165] due to the large similarity in the mixing rule and numerical solution algorithm used.

Tuminello [168] developed a numerical method based on an analogy with polymer solution in order to compute the relative MWD of linear polymers from $G'(\omega)$ functions. The dynamic data are transformed into a cumulative weight distribution which is then fitted and differentiated to a cumulative MWD. This technique was tested using both PS as well as cellulose data and deduced MWD spectra did not match experimental points. Authors concluded that further development should be considered.

Among the numerous procedures detailed above, both Shaw and Tuminello [159] and Mead [165] numerical methods appear to be the most successful ones. Although the latter features a more complex numerical algorithm than the former, the quality of the MWD prediction remains similar. Nevertheless, these protocols are limited to linear and monomodal polymers.

As compared with other robust protocols based on the inversion of the dynamic modulus [169-171], the Shaw and Tuminello technique allows the inversion of the

melt viscosity data with no *a priori* assumptions about G_n^0 values or the shape of the MWD, prior to analysis.

According to Shaw and Tuminello method [159], the Cox-Merz assumption can be assumed as valid to be used in this approach and steady-state viscosity (*i.e.* $\eta(\dot{\gamma})$) can be substituted by $|\eta^*(\omega)|$ and $\dot{\gamma}$ by ω. Similar to the procedure developed by Malkin and Teishev [162], $|\eta^*(\omega)|$ is related to the MWD using *equation 2.39* which allows the derivation of *equation 2.40* in order to correlate *W(m)* to $|\eta^*(\omega)|$. The logarithmic differential MWD (*w (log m)*) is then calculated by differentiating *equation 2.40* with respect to *log (m)*. Thus, *w*log(*m*) is the differential form of *W*(*m*) (*c.f. equation 2.40*), *w*log(*m*) = d*W*(*m*)/d log(*m*). Since *m* is related to *M* using *equation 2.41*, *w*log(*m*) = d*W*(*m*)/d log(*m*) = d*W*(M)/d log(*M*).

$$w(\log m_i) = \left[\frac{-\ln(10)}{m_i \upsilon^2}\right]\left[\frac{\eta_i^*}{\eta_0}\right]^{1/\alpha}\left[\alpha\frac{\mathrm{d}^2 \ln \eta_i^*}{\mathrm{d} \ln \omega_i^2} + \upsilon\frac{\mathrm{d} \ln \eta_i^*}{\mathrm{d} \ln \omega_i} + \left(\frac{\mathrm{d} \ln \eta_i^*}{\mathrm{d} \ln \omega_i}\right)^2\right] \qquad \textbf{(2.42)}$$

In the high frequency limit, $-\nu$ is the slope of the power-law region. For linear polymers, α represents the exponent in the power law dependence between η_0 and M_w. *m* is the reduced MW which is related to ω using *equation 2.43*.

$$m_i = \left({}^{\omega_i}/_{\omega_c}\right)^{\upsilon/\alpha} \qquad \textbf{(2.43)}$$

ω_c is the critical frequency, which is a horizontal scaling parameter fixing the position of the transition region between the Newtonian and shear-thinning regime. ω_c is determined by a linear fitting passing through the last decade of the natural log of $|\eta^*|$against the natural log of ω. The *Yintercept* is then used in *equation 2.44* to calculate ω_c [160].

$$\omega_c = \exp[(\ln \eta_0 - Yintercept)/-\upsilon] \qquad \textbf{(2.44)}$$

Shaw and Tuminello [159] stated that the polymer MWD may only be estimated from high quality and complete rheological data. The sum of the derivative terms in *equation 2.42* decreases to zero when the terminal and power law regions are reached, respectively. A proper MWD estimation requires accurate experimental data between both regimes since data have to be differentiated twice.

Independently of the polymer under study, the accessible range of ω is usually limited due to equipment limitations and/or the poor thermal dependence of polymers. It is not always possible to collect sufficient rheological information for this technique to be successful even though a *composite linear spectrum* (*i.e.* TTS coupled with the conversion of the creep-recovery data) is constructed.

Moreover, experimental both between- and within-sample errors also lower the precision of the dynamic data sets, independently of the operator's skilfulness. A viable solution in order to reduce noise issues and to extend the range of ω at both ends is to fit the set of available data using well-known viscosity models.

e) Description of the flow behaviour using well-defined viscosity models

Regarding linear polymers with narrow MWDs, the *Carreau-Yassuda* phenomenological model (referred to as CY) (*c.f.* equation 2.45) showed sufficient flexibility to fit properly $\eta(\dot{\gamma})$ functions from the terminal to the shear-thinning regime.

$$\eta(\dot{\gamma}) = \eta_0[1 + (\tau_0\dot{\gamma})^{\alpha}]^{(\nu-1)/\alpha} \qquad \textbf{(2.45)}$$

η_0 is the zero-shear viscosity which is the limiting value at low $\dot{\gamma}$ of the steady flow viscosity. τ_0 is the characteristic viscous relaxation time, fixing the position of the transition region between the Newtonian and shear-thinning regime. α is the width of this transition (*i.e.* inverse measure of the breadth of the relaxation spectrum) and (ν-1) the slope $d\,log\,\eta/d\,log\,\dot{\gamma}$ of the shear-thinning regime at high $\dot{\gamma}$. All of these parameters are indicted in *figure 2.21*.

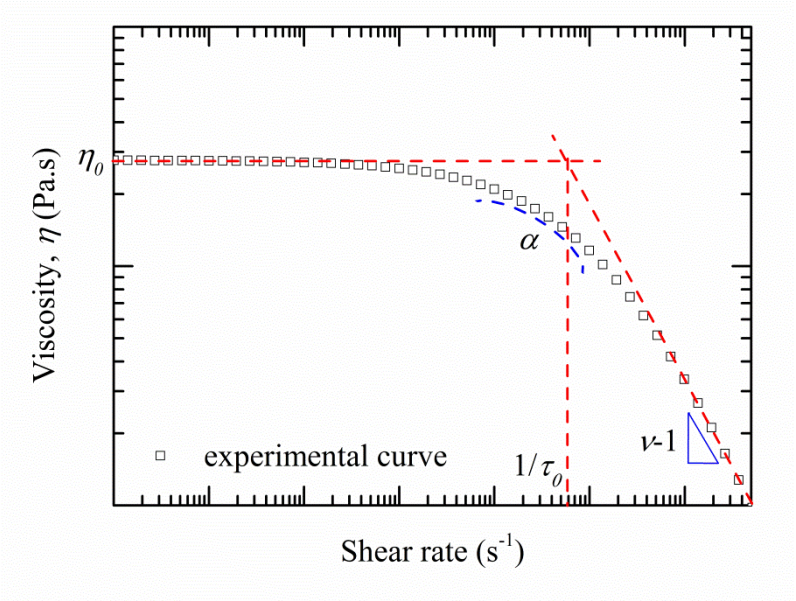

Figure 2.21. General trace of the viscosity functions of a linear polymer featuring a narrow MWD. The Carrreau-Yassuda parameters are indicated in the curve.

Within the LVE regime, the applicability of the Cox-Merz rule [172, 173] (*c.f. equation 2.46*) to linear polymers allows to relate $\eta(\dot{\gamma})$ to $|\eta^*(\omega)|$ in *equation 2.45*.

$$\eta(\dot{\gamma}) = |\eta^*(\omega)| \text{ for } \dot{\gamma} = \omega \qquad \textbf{(2.46)}$$

A specific advantage of *equation 2.45* is that the width of the transition between the terminal and the power-law regions may be adjusted independently of the high frequency asymptotic slope through the parameter α [174]. This property provides to this model a great flexibility to perform accurate numerical descriptions of viscosity functions for polydisperse polymers. It has been widely used in analyses of melt processes because of its mathematical simplicity, and this makes it possible to derive explicit equations describing many flow situations [128, 129, 131, 174, 175]. The effects of changing the adjustable parameters in the CY model on the predicted viscosity curve are illustrated in *figure 2.22*.

Nevertheless, Stadler *et al.* [107, 176] reported that the CY model does not present sufficiently flexibility to fit $|\eta^*(\omega)|$ functions of sparsely LCB high density metallocene catalyzed polyethylene (LCB-mHDPE) featuring several curvatures in the shear-thinning regime. Authors introduced *an extension of the phenomenological CY model* (referred to as CY-Ext) which features additional flexibilities in fitting the shape of the above described curves, as given by:

$$|\eta^*(\omega)| = \eta_0 \prod_{i=1}^{m} (1 + (\tau_i \omega)^{\alpha_i})^{(\upsilon_i - 1)/\alpha_i} \qquad \textbf{(2.47)}$$

Where η_0 is the zero-shear rate viscosity and *m* the number of curvatures in the shear-thinning regime. τ_i and α_i represent the characteristic viscous relaxation times and the width of each transition region between each curvature, respectively. $(\upsilon_i\text{-}1)$ is the slope $d \log|\eta^*|/d \log \omega$ of each curvature in the shear-thinning regime.

This model describes the viscosity data as a sum of several simple generalized Newtonian fluid functions, whose individual behaviours are based on species exhibiting different relaxation times (*i.e.* different molecular architectures). Although this model showed encouraging results, it is likely to present significant application restrictions when dynamic rheological analyses are considered. This extended model is based on the initial phenomenological CY model developed to describe flow curves. Regarding LCB polymers, the ability to predict non-linear flow properties from linear viscoelastic measurements is not trivial.

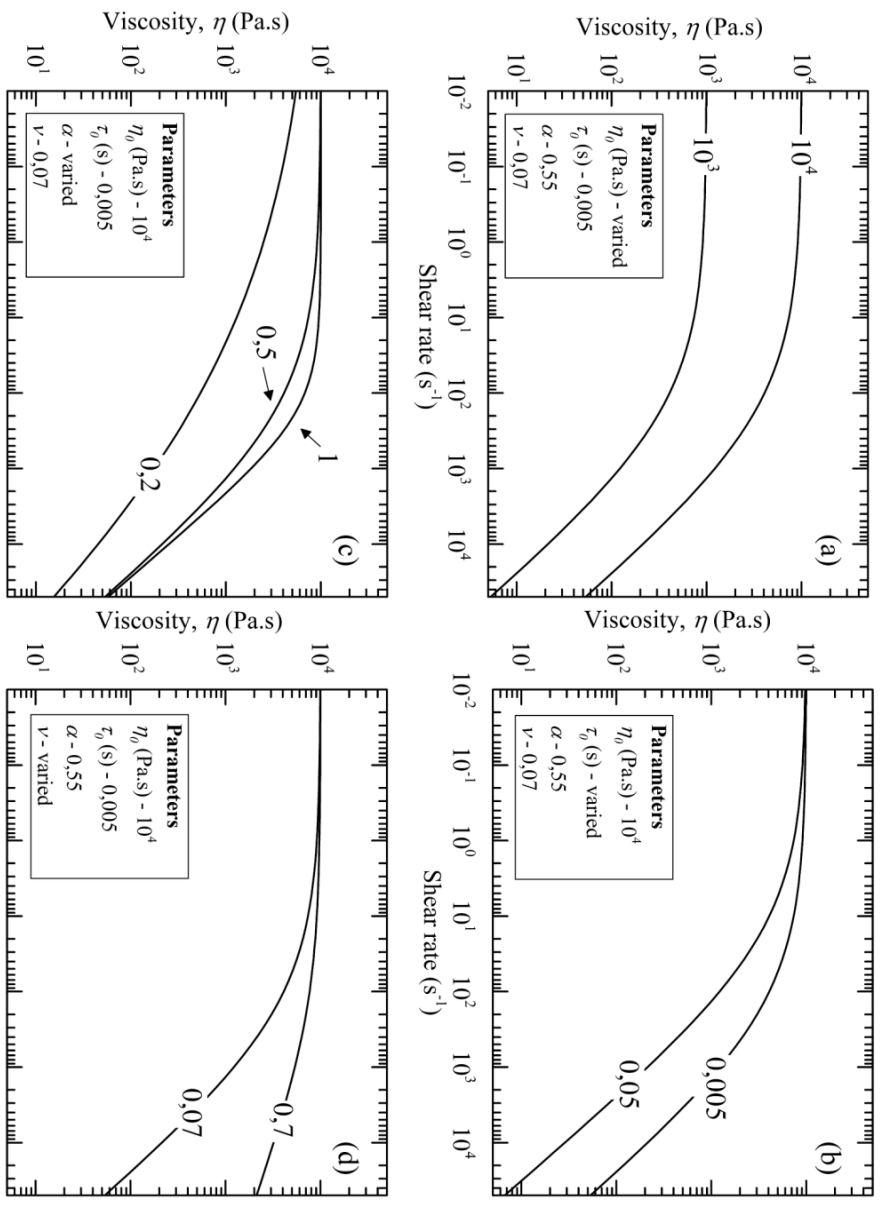

Figure 2.22. Effects of changing the **(a)** η_0, **(b)**, τ_0, **(c)** α, **(d)** ν parameters in the CY model on the predicted viscosity curve.

In the frame of the whole project MAT2010-19721-C02-01, Chatillon and Santana [177] reported a good agreement in the Cox-Merz equality for PLA-2 samples, a linear poly(lactic acid) (PLA 4032D), at 200 °C, as shown in *figure 2.23*. However, experimental results revealed a significant divergence between both shear experiments for LCB-PLA samples.

These observations are in line with the previous works of Ferri and Lomellini [178], Carreau *et al.* [179] and Corre *et al.* [47]. Authors reported significant deviations between $\eta(\dot{\gamma})$ and $|\eta^*(\omega)|$ for LCB polymers and identified a relevant failure in the Cox-Merz equality for branched architecture [180]. Therefore, linear viscoelastic data analysis may be inaccurate if the CY-Ext model is used to fit $|\eta^*(\omega)|$experimental points.

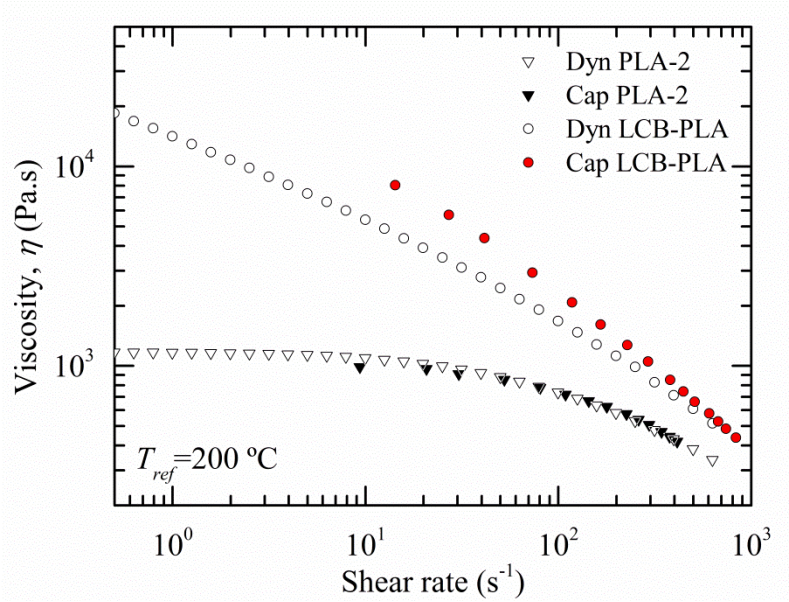

Figure 2.23. Influence of the topological modifications on the Cox-Merz validity. Open and full symbols are viscosity experimental data points from dynamic (referred to as Dyn) and steady shear experiments (referred to as Cap) at 200 ºC, respectively, in the linear range of deformation. (figure reproduced with permission from [177]).

Initially used to fit complex dielectric constant spectra, Havriliak and Negami [181] extended the empirical Cole-Cole model spectrum to linear viscoelastic behaviour of polymers melts and specifically to $|\eta^*(\omega)|$ function as follows:

$$\eta^*(\omega) = \eta_\infty + (\eta_0 - \eta_\infty)[1 + (i\tau_0\omega)^\alpha]^{(\nu-1)/\alpha} \qquad \textbf{(2.48)}$$

Where η_0 is the zero-shear rate viscosity. τ_0 is the characteristic viscous relaxation time which is a horizontal scaling parameter fixing the position of the transition region

between the Newtonian and shear-thinning regime. α is a measure of the width of the "knee" and (ν-1) is the high frequency slope $\mathrm{d}\log|\eta^*|/\mathrm{d}\log\omega$ of the shear-thinning regime. η_∞ is the high-frequency limiting value of $|\eta^*|$ which indicated the onset of the glassy behaviour. It is usually neglected due to its extremely low value, as reported by Dorgan *et al.* [174].

For negligible η_∞ value and taking the scalar magnitude of *equation 2.48* leads to the *Havriliak-Negami* model (referred to as HN):

$$|\eta^*(\omega)| = \eta_0 \left(1 + 2(\tau_0\omega)^\alpha \cos\left(\alpha\frac{\pi}{2}\right) + (\tau_0\omega)^{2\alpha}\right)^{(\nu-1)/2\alpha} \qquad \textbf{(2.49)}$$

This model has the great advantage to be exempted from the Cox-Merz rule. However, values of α other than 1 cause an incorrect low frequency scaling. That is, *G'* and *G"* do not have appropriate slopes of 2 and 1, respectively, on a logarithmic scale at low frequencies [174, 175].

Discarding the Cox-Merz rule, a mathematical model able to parameterize the $|\eta^*(\omega)|$ functions of LCB polymers, which include different relaxation times in the shear-thinning regime, has not been described in literature yet to the best of the knowledge of the author.

Recall that the numerical procedure of Shaw and Tuminello [159] (*c.f. equation 2.42*) was developed to infer MWD from viscosity functions for linear flexible polymers. Since viscosity data are differentiated twice in *equation 2.42*, well-known viscosity models are usually used to filtered raw data in order to smooth out noises. To this end, both phenomenological CY and "Vinogradov fluidity" models have been used [160, 166]. Within the LVE, the assumption of the validity of the Cox-Merz rule (*c.f. equation 2.46*) allows for an equivalent form of both viscosity models in terms of $\eta(\dot{\gamma})$ to $|\eta^*(\omega)|$.

This work aimed to extend the Shaw and Tuminello [159] method to sparsely LCB PLA resins. However, this is only possible if the linear viscoelastic model for MWD calculation is independent of any empiricism and is defined as the fingerprint of the MWD. However, discrepancies or loss of fundamental molecular structure-rheological information between calculation and experimental MWD are expected. The usefulness of the melt measurements to estimate MWDs could be therefore questioned.

Various methods based on the "double reptation" mixing rule showed promising results to predict a quantitative relationship between linear viscoelastic material functions and mono- or multimodal MWD. Mead [164] and Wasserman [167] developed analytical methods to invert the double reptation model in order to yield the

underlying MWD. This technique is largely applied to deduce MWDs from LVE data, but the calculation procedure is a mathematically ill-posed problem and time consuming. The main difficulty arises from the inversion of Fredholm integral equations of the first kind. Any noise in the experimental data affects the precision of the results and specific regularization techniques (*e.g.* Tikhonov regularization) are necessary to moderate these effects [112, 182].

Since MWD estimation procedure from rheological measurements might be used regularly in industrial settings, experimentation and interpretation should be straightforward. Therefore, a simpler mathematical model which could be used together with the inversion procedure of Shaw and Tuminello (1994) and which contains essentially equivalent molecular information than the double reptation method is required.

Considering linear flexible polymers, Garcia-Franco and Mead [183] revealed that the Cole-Cole model relaxation spectrum with appropriately chosen parameters is functionally similar to the double reptation model. Initially introduced in the context of the dielectric relaxation, the empirical Cole-Cole model spectrum was extended to the linear viscoelastic behaviour of polymer melts and specifically to $|\eta^*(\omega)|$ by Havriliak and Negami [181]. They proposed the generalization of the Cole-Cole function according to *equation 2.49*.

However, the HN model is only useful to capture the main features of $|\eta^*(\omega)|$ data featuring a unique curvature in the shear-thinning regime. *Equation 2.49* does not provide an accurate fitting in other cases. A complex viscosity model that captures the main features of $|\eta^*(\omega)|$ data showing a broad transition zone with distinct relaxation processes in the shear-thinning region has not been described yet. Based on *equation 2.47* and *equation 2.49*, an extension of the Havriliak-Negami model (referred to as HN-Ext) is suggested in the present work as follows:

$$|\eta^*(\omega)| = \eta_0 \prod_{i=1}^{n} (1 + 2(\tau_i\omega)^{\alpha_i} \cos\left(\alpha_i \frac{\pi}{2}\right) + (\tau_i\omega)^{2\alpha_i})^{(\upsilon_i - 1)/2\alpha_i} \qquad \textbf{(2.50)}$$

Where n represents the number of separated relaxation processes or curvatures in the shear-thinning regime. η_0 is the zero-shear viscosity value and τ_i the characteristic viscous relaxation times of each transition region. α_i is the respective curvature of the knee and (ν_i-1) the slope $\mathrm{d}\log|\eta^*|/\mathrm{d}\log\omega$ of each curvature in the shear-thinning regime.

Equation 2.50 aims to fit available sets of $|\eta^*(\omega)|$ data corresponding to LCB polymers featuring the above LCB polymer characteristics. That is, the double logarithmic slope $\mathrm{d}\log|\eta^*|/\mathrm{d}\log\omega$ has to monotocally increase with decreasing ω

(without local minimum in the investigated ω range), or *equation 2.50* cannot be used otherwise [176].

Turning the high sensitivity of rheology into a quantitative technique, to show LCB and to infer MWD, has been useful in the characterization of polyolefins. However, in today's world of awareness of the environmental situation and of "green" chemistry, bio-polyesters (*e.g.* PLA) have gained much attention as a replacement for conventional polymers obtained from petrochemical feed stocks. For the purpose of providing specific processing behaviour, their rheological properties may be tailored through the modification of the chain architecture. However, communications which report the molecular characterization and the MW determination of structurally modified PLA from rheological measurements are rare. Dorgan *et al.* [174] provided some insight into the molecular dimensions using the packing model for linear PLA featuring different D-lactide contents.

2.4. Micromechanisms of deformation in polymers

Under loading, the mechanical behaviour of polymers is defined by distinctive features as compared to other materials (*i.e.* metal, ceramic, etc). When polymers are subjected to an applied stress or strain, their mechanical properties are highly dependent on the testing conditions, such as temperature (T) and strain rate ($\dot{\varepsilon}$). While at low T and/or high $\dot{\varepsilon}$, a polymer may be glass-like, at high T and/or low $\dot{\varepsilon}$, the same polymer may be rubber-like. Polymers are classified as viscoelastic solids due to the competition between both elastic and viscous components. Thus, for the realization and interpretation of a mechanical test at T and $\dot{\varepsilon}$ fixed, the deformation should be considered as the sum of these three following mechanisms [184, 185]:

- **Instantaneous elastic deformation**: at low stresses or within the material elastic limit, an applied stress induces an instantaneous elastic strain, which is self-reversing when the load (F) is removed (governed by the Hooke law: $\sigma=E\varepsilon$). At the molecular level, this deformation solely involves a stretching of the bonding lengths and a modification of the bonding angles.

- **Anelasticity or viscoelastic deformation**: an applied stress produces a deformation which depends on the time rate. This type of deformation is recoverable in the time and no definite relation has been established between stress and strain yet. At a molecular level, this deformation involves segmental motions of the polymeric chains under loading. The intensity of this component mostly depends on the chain rigidity of the polymer.

- **Plastic deformation**: this type of deformation is commonly observed after the yield point. It is permanent and non reversible. Under loading, molecular chains slip past

each other with a high viscous component (governed by the Newton's law: $\sigma = \eta d\varepsilon/dt$). Plastic deformations usually precede fracture.

While instantaneous elastic deformations are exhibited in most of the mechanical solicitations, anelastic and plastic deformations are achieved at higher strain levels. In order to design a plastic part, the stress at yield, σ_y, is defined as an important parameter. Upon unloading, it separates self-reversible to permanent deformations. Yielding process is usually associated with an enough high stress level able to induce an initial plastic deformation. From a micro-structural point of view, two main micro-mechanisms based on the molecular chain slippage are identified to describe polymer yielding process [184-187]:

- **Craze yielding** yields a brittle fracture. It takes place in brittle materials. It is a cavitation process, modifying the matrix density. Crazes lead to a catastrophic failure under constant loading.

- **Shear yielding** yields a ductile fracture. It takes place in ductile materials. Above σ_y, a stable neck is formed and samples undertake plastic deformation. It involves the shear flow of the matrix at a constant volume and takes place uniformly throughout the sample. The material density remains roughly unchanged.

2.4.1. Craze yielding

Although craze yielding is a highly localized plastic deformation process, which usually appears in amorphous polymers, semycristalline thermoplastics may also feature this micromechanism of deformation [188-190]. Above a critical stress value, crazes grow along a plane normal to the major tensile stress. Due to their lower density as compared to the undeformed polymer matrix, they are optically detectable and may be used to prevent early failure or crack propagation. A stressed transparent polymer, which contains a high density of crazes, is defined as "stress-whitened" [184, 191, 192].

The idea of the craze interfaces spanned by fibrils was pioneered by Bessonov *et al.* [193], even though Kambourg [194] was the first to observe the internal morphology of a PC craze. A craze consists in a dense array of fibrils which are separated by voids, as illustrated in *figure 2.24*. Fibrils lie perpendicular to the craze-bulk interface and are aligned with the major tensile stress. They allow for the load bearing between two free surfaces and lead to a stabilization of the craze formation in order to avoid a fast coalescence of several voids. The presence of voids, which gives rise to a substantial dilatational component, separates strictly craze deformation from shear deformation.

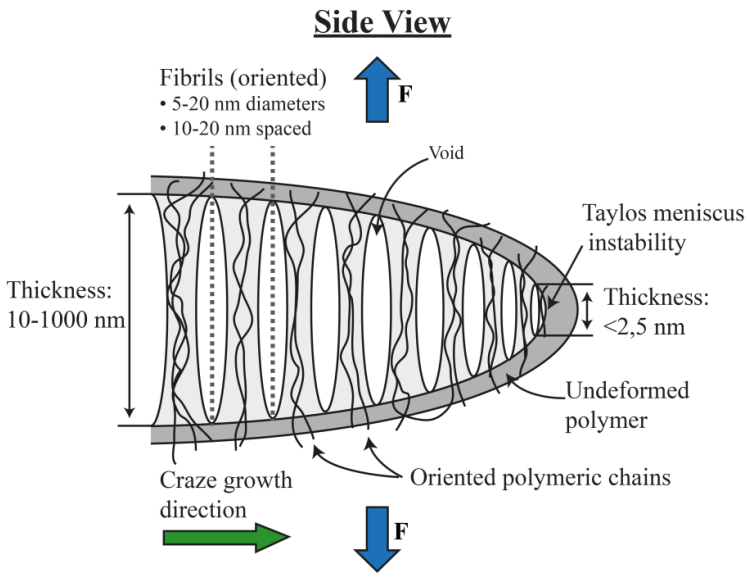

Figure 2.24. Schematic representation of a craze structure (Adapted from *ref.* [90]).

The nucleation of a craze may be promoted by the presence of an initial craze, defects in the matrix, heterogeneities in the molecular network and/or the high triaxial stress state exhibited by thick samples. Regardless of polymer intrinsic factors, high $\dot{\varepsilon}$, low T, aggressive environments (environmental stress-cracking or solvent crazing) and internal or external stresses promote craze nucleation [195, 196]. The identification of the mechanisms and processes, which control the nucleation, the growth and the stabilization of a craze, has been mainly discussed due to the difficulty to characterize the stress state sufficiently locally at the initiation site. Finally, a three steps mechanism has been reported by Kramer [196] to describe craze nucleation.

Step 1: Generation of a local plastic deformation by shear in the vicinity of a defect leading to significant lateral stresses.

Step 2: Void nucleation in order to release the triaxial constraints. The overall hydrostatic tension must be positive in order to allow cavitation formation.

Step 3: Void growth and strain hardening of the intervening polymer ligaments as molecular orientation proceeds. This leads to the stabilization of the craze structure.

If the stress increase, which occurs in step 1, promotes further shear deformation, the deformation will occur via shear banding and a craze nucleus will clearly not be formed. Step 2 is therefore considered as the critical step of the process [191, 197, 198].

Under constant loading, when a craze is nucleated and stabilized, later it has to grow both in width and length. Based on Taylor's ideas [199] and later refined by

Fields *et al.* [200] and Argon *et al.* [201], the craze grows following an interface convolution mechanism which is reported as the meniscus instability. The physical basis underlying this instability lies in the difference in hydrostatic pressure across an interface between two different surfaces [191]. *Figure 2.25* illustrates the interface convolution mechanism at a crack tip, which give rise to the void-fibril structure of a craze [191, 196, 202]. Steps "**a**" to "**c**" show the successive stage in the growth of the crack dimensions, leaving behind isolated fibrils.

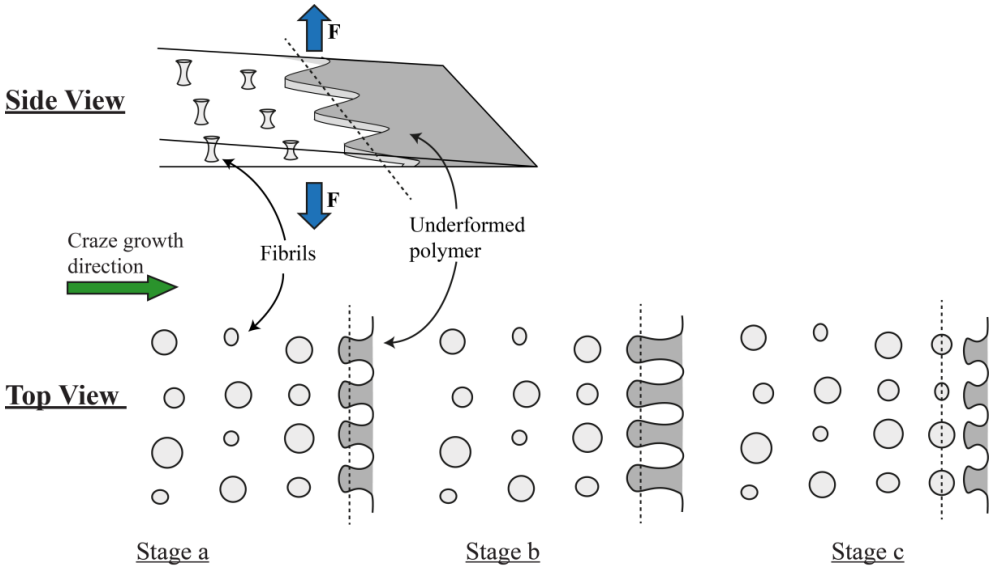

Figure 2.25. Schematic representation of the meniscus instability at the crack tip. This interface convolution mechanism gives rise to the void-fibril structure of a craze (adapted from *ref.* [90, 191]).

Regarding well entangled polymers, entanglement points included in both undeformed polymer layers close to the fibrils should be disentangled to allow the formation of the void-fibril structure. *Figure 2.26* illustrates two entangled chains passing through two different fibrils separated by a void. Under loading, two mechanisms have been suggested in order to remove the entangled point:

- **Chain scission**: the polymer chain is suddenly broken. Similar to PS, the crazing stress is MW independent at room temperature [203].
- **Chain disentanglement**: the entanglement point is lost by the relative motion of the two chains involved. Similar to PC, the crazing stress is MW dependent [204, 205].

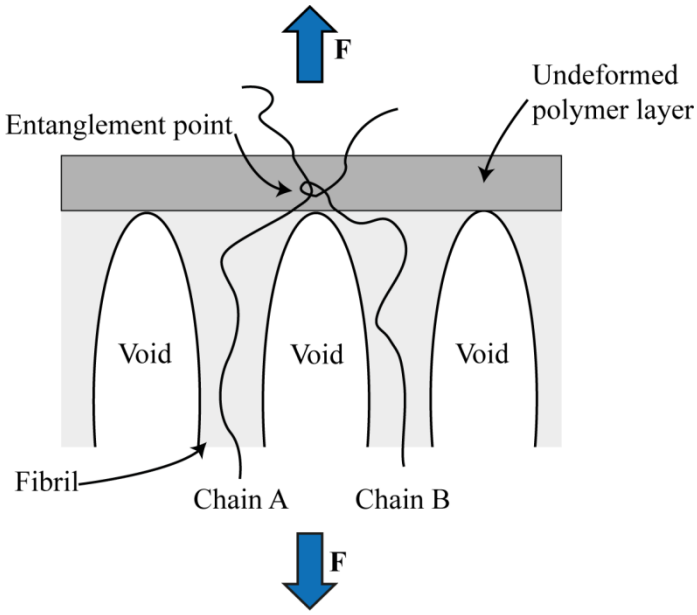

Figure 2.26. Schematic representation of the stretching mechanism during the craze growth. Chains A and B are entangled in the undeformed polymer layer (adapted from *ref.* [90, 191]).

The progressive increase in the local stress induces the failure of the highly stretched fibrils spanning the craze leading to void coalescence and crack propagation.

2.4.2. Shear Yielding

Under loading, a polymer yields when it starts to deform plastically. The yield point corresponds to the initiation of permanent plastic deformations. Yielding is of tremendous technological importance if brittle fracture would be suppressed. It defines the maximum limit of the polymer strength related to the service stress in load-bearing applications. Moreover, it could be associated to the required conditions for shaping parts during manufacturing process. Shear deformation leads to a permanent change in the dimensions and in the shape of the body but without significant change in volume. Regarding specimens, for which the width is much larger than the thickness, yielding process is classified as localized or diffuse. This depends on the volume of polymer affected, as illustrated in *figure 2.27*.

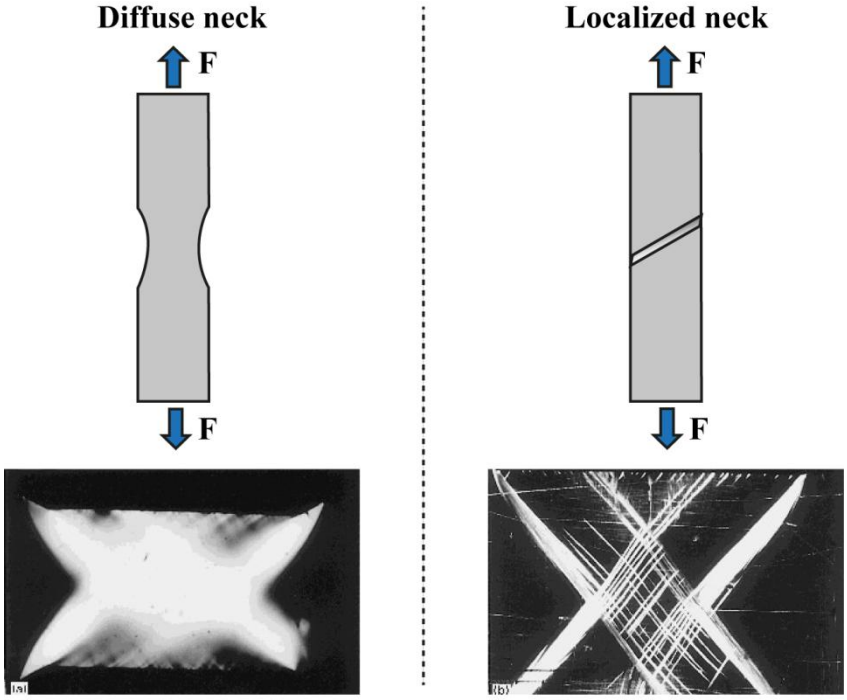

Figure 2.27. Differentiation between localized and diffuse neck during yielding process. Under compression loading, **(a)** diffuse necking in PMMA and **(b)** localized necking in PS at 20 ºC (adapted from *ref.* [206]).

Under tensile loading, amorphous polymers usually feature diffuse necking, which extend could be much larger than the sample thickness. Both effects are due to the large scale cooperative intersegmental displacements during yielding. For semi-crystalline polymers, necking process is classified as localized because yielding occurs in the material surrounding the crystalline regions trough processes such as slip (the planes of atoms slide over one another to new equilibrium position) or twinning. The neck is a narrow band inclined to an angle to the main load direction [187, 206-208].

In numerous materials, localized necking arises from an inhomogeneous and instable flow. This is due to the faster increase in the plastic strain in some local regions as compared to the overall body. This localisation of plastic strain is generally related to geometrical considerations and/or material intrinsic properties. The neck formation coupled with a reduction in the cross-sectional area is a common example of geometry instability. The necking process theory is based upon Considère´s construction and has been considered and refined by several authors [207, 209]. This flow instability involves a strain softening process beyond the yield point, which enables the neck to stabilise and extent throughout the specimen at a lower stress level. For isotropic materials, Bowden [210] identified a criterion relating the

characteristics of the deformed region to the dependence of the constraint (deformation restrictions) imposed by the surrounding material. It was applied to three different sample geometries (*c.f. figure 2.28*) loaded in tension in order to illustrate three types of inhomogeneous deformation [187].

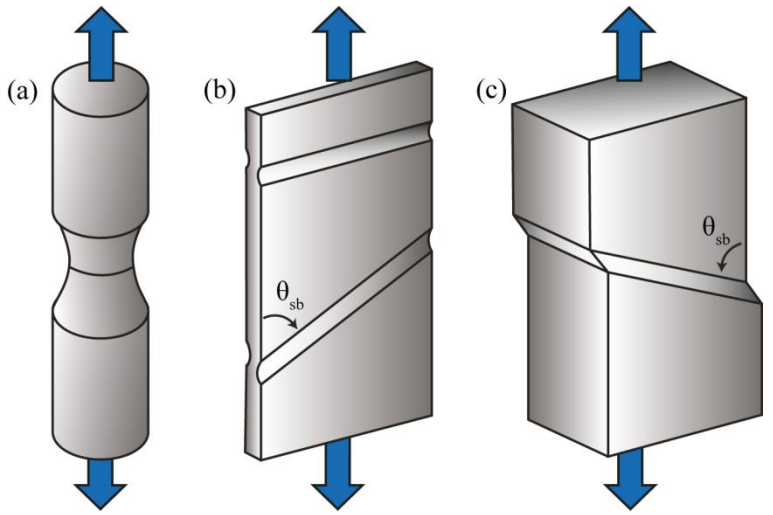

Figure 2.28. Three different types of localized necking under tensile loading. **(a)** symmetric neck in cylindrical samples, **(b)** inclined neck in flat sheet samples, **(c)** shear band in tick samples (plane strain) (adapted from *ref.* [187]).

(a) **Symmetrically necked region**: Commonly observed in cylindrical tensile sample due to the lack of external restraints.

(b) **Inclined neck:** Usually displayed by flat specimens tested in uniaxial tension which feature restraints along the length direction. In the necked region, the material relaxes inward if the width is similar or larger than the thickness of the strip. If the triaxial constraints are released by a physical mechanism (*e.g.* cavitation) this deformation process may also be displayed by tick samples.

(c) **Shear band:** Displayed by tick specimens under plane strain-state conditions. This deformation occurs at constant volume and is associated with a large stress concentration which promotes strain softening.

Regarding isotropic materials, yielding initially produces shear bands at an angle, θ_{sb}, equal to 54.7º angle with the long axis of the specimen, as illustrated in *figure 2.28*. However, if the material under deformation dilates and allows volume expansion, θ_{sb} increases and may reach its limiting value of 90º [187, 207].

Regarding glassy polymers, the nucleation of intense shear and microshear bands tends to be promoted by [187, 207, 211, 212]:

- Low T and high $\dot{\varepsilon}$
- A poor sensitivity of σ_y with $\dot{\varepsilon}$
- High content of local inhomogeneities
- A pronounced strain softening
- High $\dot{\varepsilon}$ when the sample is slowly cooled from the melt

A large level of plastic deformation is expected if amorphous polymers yield homogeneously (diffuse shear zones). This yielding process promotes ductile behaviour and a high toughness of the material. In contrasts to metals, shear banding (localized shear zones) does not lead to brittle fracture. Shear bands may be stabilized (strain softening) and extent throughout the specimen, leading to a ductile behaviour.

2.4.3. Crazing versus shear yielding in amorphous polymers

In practice, tensile deformations observed in many glassy polymer systems are subjected to a competition between crazing and shear yielding mechanisms. While numerous glassy polymers (*e.g.* PC, PET, etc.) are prone to ductile behaviour, others (*e.g.* PS, PMMA) usually behave in a brittle manner [213-215].

It has been established that entanglements is an essential parameter for the propagation and stabilisation of crazes and/or shear yielding micromechanisms in glassy polymers. They could define the type of deformation encountered in a particular polymer. Regarding PS, entanglements are essential for stable craze nucleation and stabilization. If the MW is below a critical value (M_0), only few fibrils bridge the craze and fracture is rapidly observed. However, when $MW>M_0$, crazes have a denser fibril structure and can reach larger extensional ratio before failure [185, 216].

For several different amorphous polymers, it has been reported that the entanglement density, ν_e, and C_∞ (a measure of the chain stiffness) controlled the mode of deformation. Whereas, shear yielding is promoted in polymers with a high entangled molecular network, crazing tends to be favoured in polymers featuring a low entanglement density. This molecular dimension may be estimated from the chemical structures which lead to a possible control of the brittle/ductile transition by chemical group addition in polymers [217-219].

Several glassy polymers present a brittle behaviour under certain testing conditions. However, they exhibit a ductile behaviour when these conditions are changed. $\dot{\varepsilon}$ and T are two factors which affect principally the micromechanisms of deformations of amorphous polymers. The temperature at which crazing is suppressed

to promote shear yielding is usually indentified as the brittle/ductile transition temperature (T_b). The determination of this parameter can be carried out following the *Ludwig-Davidenkov-Orowan hypothesis*. At a constant $\dot{\varepsilon}$, by considering that both the stress promoting brittle fracture (σ_b) and the stress promoting plastic deformation (σ_y) are two independent parameters, the fracture type is dictated by such process which requires less energy as illustrated in *figure 2.29*,. The intersection between σ_b and σ_y defines T_b. An increase in $\dot{\varepsilon}$ shifts T_b to higher temperatures [184, 220].

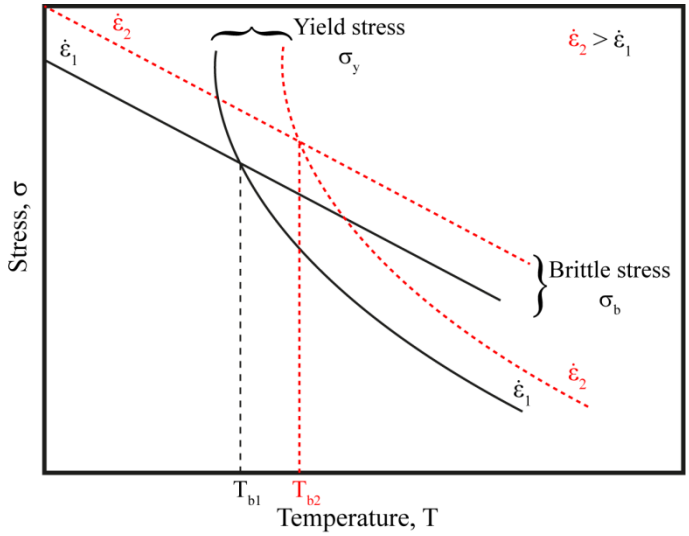

Figure 2.29. Schematic representation of the *Ludwig-Davidenkov-Orowan hypothesis* correlated with the effect of strain rate upon T_b (Adapted from *ref.* [90, 220]).

2.5 Fracture mechanics

In engineering applications, one of the most important properties of materials is fracture toughness. The term *fracture mechanics* refers to a vital specialization within solid mechanics in which the presence of a crack is assumed. Quantitative relations between the crack length, the material inherent resistance to crack growth, and the stress at which the crack propagates at high speed to cause structural failure is therefore looked for [221].

The difference between a brittle and ductile fracture is investigated from two different aspects of great technical interest: (1) the energy dissipated in fracture and (2) the nature of the fractured surface. The use of the *fracture mechanics* has been reported as a valuable tool in order to study the above described aspects and their implications in the selection of a material.

Ductile fracture involves a large amount of plastic deformation and can be detected beforehand. However, brittle fracture is more catastrophic. The brittle behaviour in polymers may be investigated on the basis of the *Griffith theory*. *Griffith proposed that a brittle material contains a population of inherent defects which produce a stress concentration of sufficient magnitude so that the theoretical cohesive strength is reached in localized regions at a nominal stress which is well below the theoretical value* [222].

Inglis [223] provided the first quantitative evidence for the stress concentration effect of defects (referred to as crack) by analyzing elliptical holes in flat plates, as shown in *figure 2.30*.

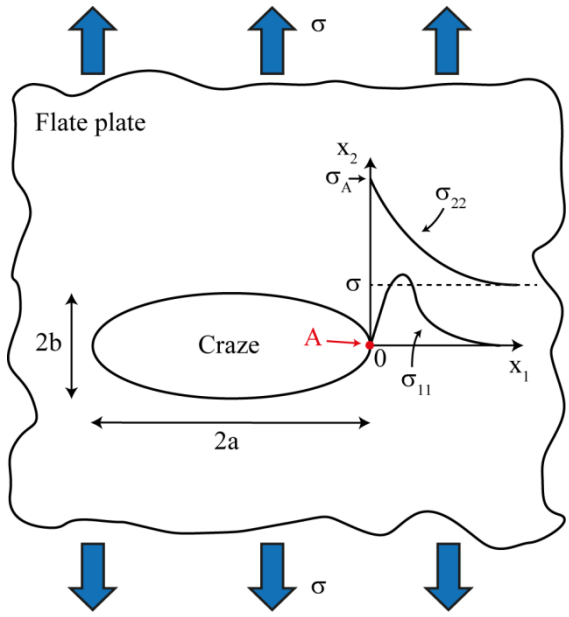

Figure 2.30. Under uniform tensile stress, an elliptical hole in infinitely flat plate produces stress intensification, as shown in σ_{22} which is amplified from σ to σ_a (adapter from *ref.* [90, 224, 225]).

For a plate with a thickness, *B*, a width, *W*, which features an elliptical hole *2a* long by *2b* wide subjected to a uniform tensile stress (σ) perpendicular to the major axis of the ellipse, the maximum stress at the crack tip, σ_A, (*c.f. figure 2.30*, point A) is given by *equation 2.51*. This analysis assumed that the crack is not influenced by the plate boundary (*i.e. W*>> *2a* and plate height>> *2b*) [224, 226].

$$\sigma_A = \sigma(1 + \frac{2a}{b}) \qquad \textbf{(2.51)}$$

Where the ratio σ_A/σ is defined as the stress concentration factor k_t. As the defect (*e.g.* crack) is sharpened ($a/b>>1$), the stress intensification of the applied tensile stress (σ) at the crack tip is likely to exceed three orders of magnitude ($k_t>>3$); thus overcoming the theoretical cohesive strength of the material. In the limit of an infinitely sharp crack (*i.e.* $a/b\rightarrow\infty$), e*quation 2.51* predicts an infinite stress at the crack tip. This is obviously nonphysical because no material is able to withstand infinite stress. This result foresees that a material featuring a sharp crack should theoretically fail upon the application of an infinitesimal load [224, 226].

Consequently, a fracture criterion cannot be solely based on the local stress. Moreover, the micromechanisms of deformation in polymers may prevent and/or inhibit stress intensification.

Rather than focusing on the crack-tip stresses, that is not relevant for real materials, the above mathematical paradox may be resolved using the *Griffith energy-balance approach*. This concept states that crack propagation occurs when the released elastic strain energy is at least equal to the energy required to generate new crack surface. In other works, a crack can form (or an existing crack can grow) only if such a process causes the total energy to decrease or remain constant [224, 226].

On the other hand, the high stress concentration at the crack tip before crack propagation may exceed the elastic limit of the material; leading to the formation of a certain amount of plastic deformation at the crack tip. The relation between the size of the crack and the plastic zone at the crack tip may influence the fracture mode.

Based on all the above described features, the fracture mechanics has been divided in three main approaches, namely, the *Linear-Elastic Fracture Mechanics* (LEFM), the *Elastic-Plastic Fracture Mechanics* (EPFM) and the *Post-Yielding Fracture Mechanics* (PYFM). Whereas the LEFM concept is restricted to materials whose global behaviour is linear elastic (obeying Hooke's law) with limited plastic deformation at the crack tip, the EPFM and PYFM concepts are applicable to structures which exhibit time-independent, nonlinear behaviour (*e.g.* plastic deformation) [221, 224].

Additionally, the crack loading mode, which enable a crack to propagate, is another important parameter to consider. The literature treats three different types of cracks, termed mode I, II and III, as illustrated in *figure 2.31*. Mode I is a normal-opening type of crack. Modes II and III are sliding and tearing shear modes, respectively. Mode I is technically the most important but also the most critical. This is due to the lowest energy level, which is required to reach material failure, as compared to modes II and III.

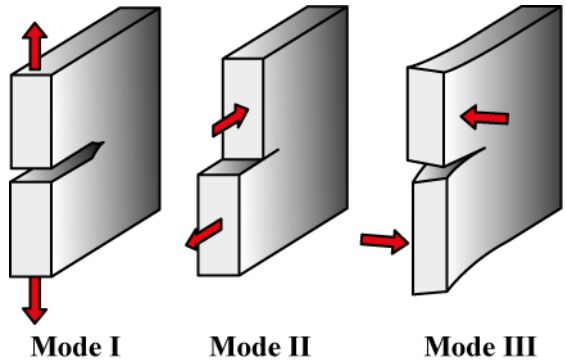

Figure 2.31. Three standard loading modes of crack. Mode I: Opening or tensile mode. Mode II: Sliding or in-plane shear mode. Mode III: Tearing or antiplane shear mode (Adapted from *ref.* [90, 221]).

2.5.1. Linear-Elastic Fracture Mechanics (LEFM)

This concept is strictly reserved to those materials which obey the Hooke's law. That is, the stress (σ) is linearly related to infinitesimal deformation (ε). As it will be described in this section, two different approaches are commonly used to provide insight to the fracture behaviour of a considered material.

a) The energy-balance approach (Griffith's theory)

As previously described, the Inglis solution (*c.f. equation 2.51*) poses a mathematical difficulty to define a fracture criterion in the limit of a perfectly sharp crack. On this basis, Griffith employed an *energy-balance approach* in order to investigate the change in the total internal energy of a material as the crack begins to propagate. This concept postulates that the **total energy of the system** (U_T) may be partitioned into two additive terms: **the elastic strain energy** (U_e) and **the work of crack formation** (W_c) [225, 227, 228].

$$U_T = U_e + W_c \tag{2.52}$$

Regarding a flat plate (*c.f. figure 2.30*) with a volume, *V*, a thickness, *t*, and which is subjected to a uniform tensile stress (σ) perpendicular to the major axis, U_e is given by:

$$U_e = +\frac{V\sigma^2}{2E} \tag{2.53}$$

Where *E* is the Young's modulus. By introducing a defect *2a* long by *2b* wide into the plate, a region of material adjacent to the free surfaces is unloaded; thus leading to a decrease in U_e, as follows:

$$U_e = -\frac{\sigma^2}{E}\pi a^2 t \tag{2.54}$$

Under loading, U_e is released by crack growth, whose propagation involves the rupture of atomic bonds at the crack tip and yields the generation of two new surfaces. According to Griffith, the work of crack formation done per unit area of crack surface (G_c), is mainly used to form two new crack surfaces and the remainder is dissipated as heat. Accordingly, W_c is given by:

$$W_C = +2atG_c \tag{2.55}$$

The introduction of crack leads *equation 2.52* to be rewritten into the respective specific terms:

$$U_T = -\frac{\sigma^2}{E}\pi a^2 t + 2atG_c \tag{2.56}$$

According to *equation 2.54* and *2.55*, it is obvious that the dependence on the crack length (a) of each of this contribution is opposite, as illustrated in *figure 2.32*.

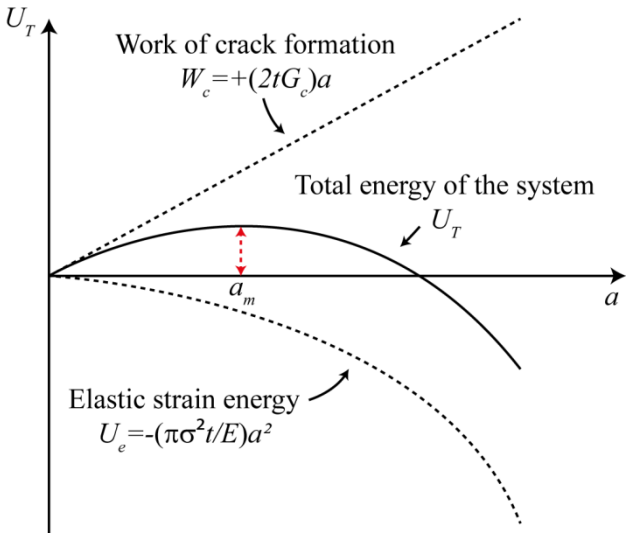

Figure 2.32. Dependence of the total energy of a infinite flat plate, U_T, on the crack length, *a*, subjected to a uniform tensile stress (σ) perpendicular to the major axis and which features a crack with a length of 2*a* (adapted from *ref.* [90, 225, 228]).

Under uniform tensile loading, just before crack propagation, the work of crack propagation balances the decrease in elastic strain energy as given by:

$$\frac{d}{da}\left(\frac{\sigma^2}{E}\pi a^2 t\right) = \frac{d}{da}(2atG_c) \tag{2.57}$$

Or equivalently

$$\sigma^2 \pi a = G_c E \tag{2.58}$$

Under a given stress, U_T reaches a maximum for a determined a, which may be defined as a **critical crack length**, a_m, as shown in figure 2.32. For values of a below a_m, dU_T/da is positive. That is, U_T increases with the crack size. Consequently, cracks of this size will not propagate and this is the region in which fracture is inhibited. By contrast, when the threshold a_m is exceeded, dU_T/da is negative. The total energy of the system decreases with increasing a, thus leading to a catastrophic crack propagation [225, 227].

On this basis, it is assumed that the fracture occurs when G_c exceeds a critical value, as given by:

$$\frac{1}{t}\frac{\partial U_T}{\partial a} = \frac{1}{t}\frac{\partial}{\partial a}(W_c - U_e) \geq G_c \tag{2.59}$$

Where dW_c-dU_e is the energy available for the formation of the new surface. G_c is the energy required to extend a crack over unit area, which is also called **the critical strain energy release rate** [225, 227].

b) Stress intensity criterion (Irwin's approach)

Regarding linear elastic materials, Irwin reported that the stress field around a sharp crack could be defined by a unique parameter named the **stress-intensity factor**, K. Fracture occurs when the value of K exceeds a critical value, K_c, which is defined as the **fracture toughness** of the material. By introducing a defect (*e.g.* crack) $2a$ long into an infinite flat plate, which is subjected to a uniform tensile stress (σ) perpendicular to the major axis, the stress actuating at a point with polar coordinates r, θ relative to the crack tip is given by (*c.f. figure 2.33*) [225, 227]:

$$\sigma_{ij} = \frac{K}{\sqrt{2\pi r}} f_{ij}(\theta) \quad \text{with} \quad K = \sigma\sqrt{\pi a} \tag{2.60}$$

Where σ_{ij} are the components of the stress tensor at a point whose polar coordinates are r and θ.

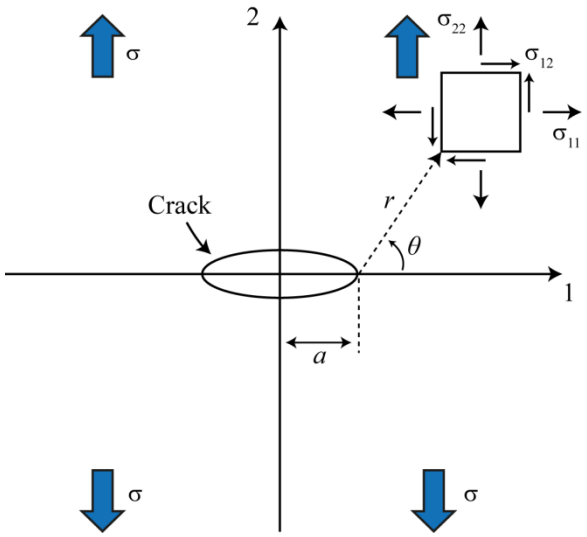

Figure 2.33. Stress field around a sharp crack *2a* long into an infinite flat plate, which is subjected to a uniform tensile stress (σ) perpendicular to the major axis (adapted from *ref.* [225, 227]).

The interesting feature of *equation 2.60* is that it applies not only in the case considered here (uniaxial tensile loading of an infinite plate), but it may be applied to a wide variety of geometry containing a sharp crack. In order to take into account the sample geometry and the effect of finite size of the sample, *K* has been rewritten as follows [225, 227]:

$$K = \phi\sigma\sqrt{\pi a} \qquad \textbf{(2.61.a)}$$

$$K = f\left(\frac{a}{W}\right)\frac{P}{B\sqrt{W}} \qquad \textbf{(2.61.b)}$$

Where ϕ and *f(a/W)* are dimensionless functions which depend on the ratio of the crack length to that of the width (*a*/*W*) of the respective sample geometry. *P* is the load, *W* the sample width and *B* the specimen thickness.

When the crack is on the point to spread at a defined stress, σ_F, *K* is defined as K_c. Experimentally, K_c is easily obtained by measuring the stress, σ, at which a crack starts to grow. K_c is then determined using *equation 2.61*.

c) Relation between G_c and *K*

By considering a thin body subjected to a uniaxial tensile loading, the thickness of the sample at the tip of a stressed crack decreases due to the Poisson contraction (ν). This tensional state defines the **plane-stress condition**. As the thickness increase, the normal and orthogonal stresses increase ($\sigma_{33}=\nu(\sigma_{11}+\sigma_{22}) \neq 0$); thus enhancing the

triaxial stress field at the crack tip. Under uniaxial tensile loading, the thickness of the specimen does not decrease by Poisson contraction because plastic constraint and **plane-strain conditions** occur at the crack tip [224, 225, 227].

The fracture toughness of a material depends on the volume of material which can be plastically deformed prior to crack propagation. According to the state of stress near the crack tip, this volume will depend on the sample thickness. *Figure 2.34* illustrate the general trend of K_c as a function of the sample thickness.

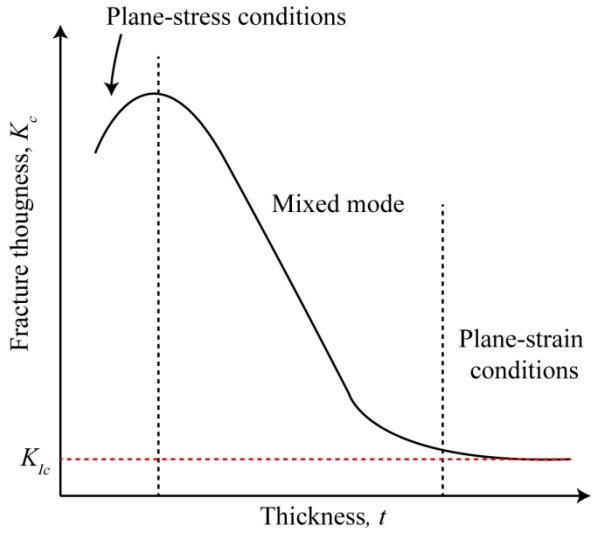

Figure 2.34. General shape of the variation of the stress-intensity factor as a function of the sample thickness (adapted from *ref.* [90, 226, 227]).

In plane-stress conditions, the material exhibits the maximum fracture toughness because a significant volume of the specimen at the crack tip is available for plastic deformation energy absorption (biaxial stress field). In plane-strain conditions, K_c significantly drops to a level that may be one-third than the plane-stress value. The high degree of plastic constraint reduces the extent of yielding at the crack tip because when all three principal stresses are tensile the shear stresses generated are lower. Since yielding is driven by shear components of stress, the crack will propagate under lowered stress values and without significant variation in the sample thickness [225-227].

This lower level of toughness, K_{IC} (the subscript I refers to the mode I), is defined as the most critical and is defined as the lowest limit of material toughness in any given engineering application. Substituting *equation 2.61* into *equation 2.58* yields a simple relationship between G_{IC} and K_{IC} [224-227]:

$$G_{IC} = \frac{K_{IC}^2}{E^*} \quad \textbf{(2.62)}$$

Where $E^*=E$ under plane-stress conditions and $E^*=E/(1-\nu^2)$ under plane-strain conditions.

In order to ensure pure plane-strain conditions, the specimen thickness, *t*, and crack length, *a*, are both to be greater than a certain value. Specifically:

$$t \text{ and } a \geq 2.5\left(\frac{K_{IC}}{\sigma_y}\right)^2 \quad \textbf{(2.63)}$$

Stress intensification of the applied tensile stress at the crack tip is likely to induce a region of plasticity near the crack tip; thus leading to further relaxation of crack-tip stresses. The elastic stress analysis becomes increasingly inaccurate as the LEFM are available when moderate crack-tip yielding occurs. An estimation of the size of the crack-tip plastic-zone may be obtained considering the Irwin approach, where the elastic stress analysis is used to estimate the elastic-plastic boundary [224, 226].

For plane-stress conditions, yielding occurs when $\sigma_{yy}=\sigma_{YS}$, the uniaxial yield strength of the material. Substituting yield strength into the left side of *equation 2.52* (for cracks on the crack plane, *i.e.* $\theta=0$) and solving for *r* gives a first-order estimate of the plastic zone size [224, 226]:

$$r_y = \frac{1}{2\pi}\left(\frac{K_I}{\sigma_{YS}}\right)^2 \quad \textbf{(2.64)}$$

If strain hardening is neglected, the stress distribution for $r = r_y$ can be represented by a horizontal line at $\sigma_{yy}=\sigma_{YS}$ as illustrated in *figure 2.35*.

According to *figure 2.35*, the material in the plastic zone carries less stress than it would otherwise carry if the material remained elastic. Irwin accounted for the softer material in the plastic zone by defining an effective crack length, a_{eff}, that is slightly longer than the initial crack size. a_{eff} is defined as the sum of the initial crack length, *a*, and a plastic zone correction, r_y, as illustrated in *figure 2.35* [224, 226].

$$a_{eff} = a + r_y \quad \textbf{(2.65)}$$

On this basis, the effective stress intensity is obtained by inserting a_{eff} into the *K* expression (*c.f. equation 2.61*) [224, 226].

$$K_{eff} = \phi\sigma\sqrt{\pi a_{eff}} \quad \textbf{(2.66)}$$

Where ϕ is a dimensionless parameter which is dependent on the ratio of the effective crack length to that of the width (a_{eff}/W) for the geometry of interest.

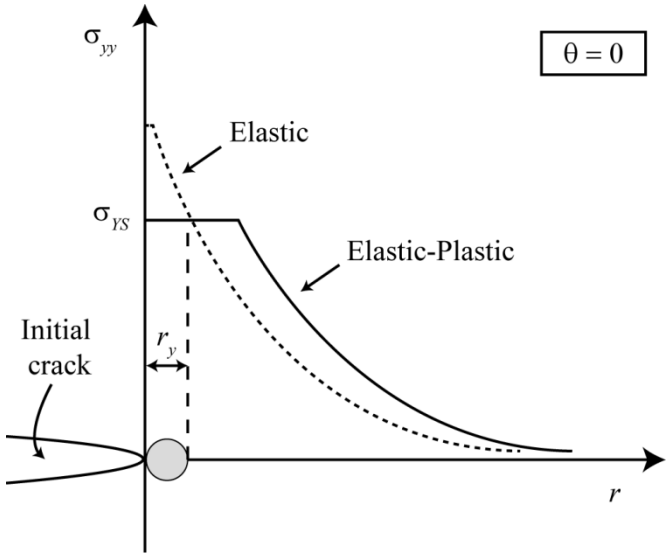

Figure 2.35. Onset of plastic deformation at the crack tip. The initial crack length plus the plastic zone radius, r_y, defines the "effective" crack length (based on *ref.* [224, 226]).

Since the effective crack size is taken into account in the geometry correction factor, ϕ, an iterative solution is usually required to solve for K_{eff}. That is, K is first determined in the absence of a plasticity correction; a first order estimate of a_{eff} is then obtained from *equation 2.64*, which in turn is used to estimate K_{eff}. A new a_{eff} is computed from the K_{eff} estimate, and the process is repeated until successive K_{eff} estimates converge [224].

Another model of the crack-tip plastic zone has been proposed by ***Dugdale*** for the case of plane stress. Dugdale considered the plastic regions to take the form of narrow strips extending a distance R from each crack tip, as shown in *figure 2.36* [224, 226].

For purposes of the mathematical analysis, the internal crack length $2c$ is allowed to extend elastically to a length $2a$; however, an internal stress is applied in the region $|c|<|x|<|a|$ to reclose the crack. It may be shown that this internal stress must be equal to the yield strength of the material such that $|c|<|x|<|a|$ represents local regions of plasticity. By combining the internal stress field surrounding the plastic enclaves with the external stress field associated with a stress σ acting on the crack, Dugdale demonstrated that [226]

$$\frac{c}{a} = cos\left(\frac{\pi}{2}\frac{\sigma}{\sigma_{ys}}\right) \quad \textbf{(2.67)}$$

Or since $a = c + R$

$$\frac{R}{c} = sec\left(\frac{\pi}{2}\frac{\sigma}{\sigma_{ys}}\right) - 1 \quad \textbf{(2.68)}$$

When the applied stress $\sigma << \sigma_{ys}$, *equation 2.68* leads to

$$\frac{R}{c} \approx \frac{\pi^2}{8}\left(\frac{\sigma}{\sigma_{YS}}\right)^2 \quad \textbf{(2.69)}$$

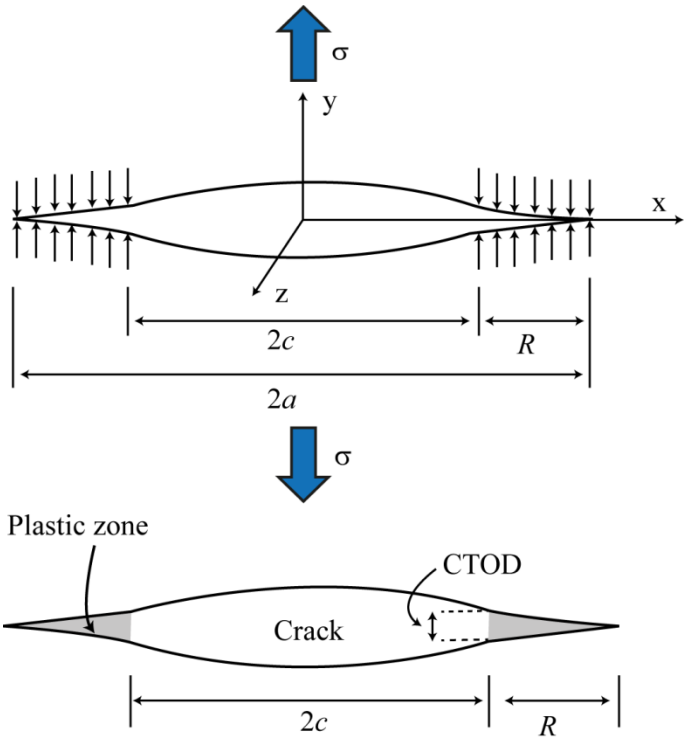

Figure 2.36. Dugdale plastic zone strip model for non-hardening solids. Plastic zones *R* extend as thin strips from each end of the crack (based on *ref.* [226]).

2.5.2. Elastic-Plastic Fracture mechanics (EPFM)

The LEFM is a powerful approach in order to quantitatively evaluate the fracture behaviour of materials whose global behaviour is linear elastic (*e.g.* PS, PMMA). However, this concept is no longer valid for materials that exhibit large-scale yielding at the crack tip or in the body of the specimen prior to failure (*e.g.* PE, PP, nylon).

On this basis, an alternative fracture mechanics, namely *Elastic-Plastic Fracture Mechanics* (EPFM) have been developed. This concept may be used as a fracture criterion for elastic-plastic materials that exhibit time-independent, non-linear behaviour (*i.e.* plastic deformation). Two elastic-plastic parameters, termed the *J contour integral* and the *crack-tip-opening displacement* (*CTOD*) are briefly introduced in this section.

a) The *J* contour integral

This *J-integral* concept has been developed by Rice and yields the fracture characterization of bodies which exhibit non-linear elastic behaviour due to an extensive crack tip plasticity. Rice demonstrated that the path-independent contour integral (referred to as *J contour integral, Γ)*, which surround the crack tip, may describe **the flow of energy** into the crack tip region during crack propagation. In other words, the difference between the external work and the internal potential energy within the *J* contour integral may be calculated as follows [224, 226]:

$$J = \int_{\Gamma} \left(W dy - T_i . \frac{\partial u_i}{\partial x} ds \right) \qquad \textbf{(2.70)}$$

Where $W = \int \sigma_{ij} d\varepsilon_{ij}$ is the strain energy density related to the stress and strain components σ_{ij} and ε_{ij} in the crack tip region. T_i is the stress vector acting at a given point on the contour Γ and u_i the displacement vector. *ds* is the increment along the contour Γ, as illustrated in *figure 2.37.*

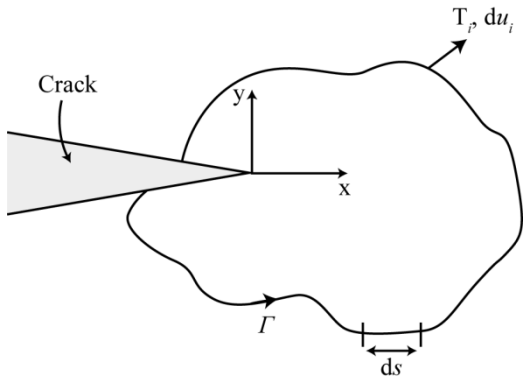

Figure 2.37. Arbitrary contour, Γ, surrounded the tip of a crack (adapted from *ref.* [224, 226]).

The interesting feature of *J* values is that they remain independent of the path chosen for integration around the crack. *J* values equate zero in the absence of released energy within the *J* contour integral and the external work is elastically stored in the material. When the *J* contour integral encloses a crack propagation, *J-integral*

quantifies the work realized per unit crack extension, d*a*. On this basis, *J* is currently defined as **the nonlinear energy release rate per unit area** in nonlinear materials [224, 226].

Physically, *J* can be interpreted as the variation of the strain energy, Δ*U*, between two identically loaded bodies possessing slightly different crack lengths (*e.g. a* and *a*+Δ*a*). In each case, the strain energy corresponds to the area below the load-displacement curve; suggesting that the differences between both curves corresponds to the change in strain energy, Δ*U*, associated with an incremental crack advance Δ*a* (*J*=d*U*/d*a*), as shown in *figure 2.38* [224, 226].

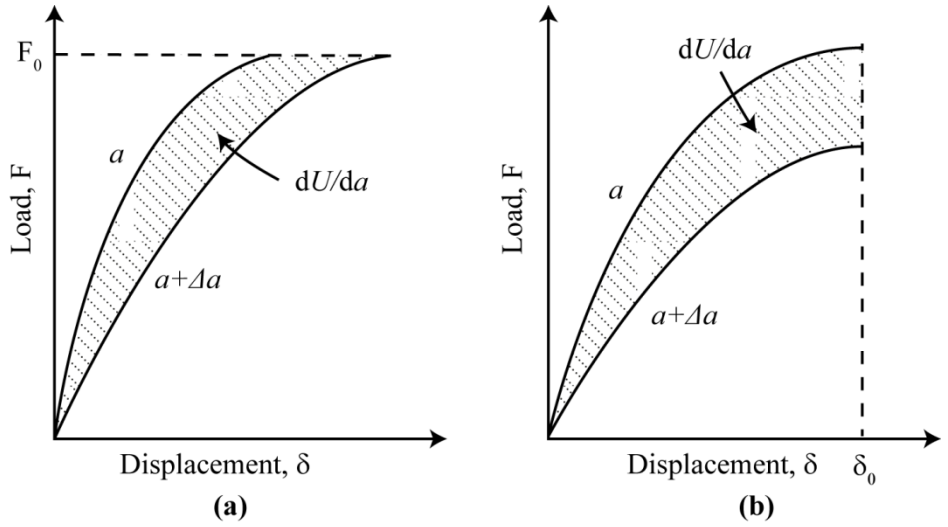

Figure 2.38. Schematic determination of the *J-integral* **(a)** in load control or **(b)** at a fixed displacement. The hatched area represents the strain energy variation d*U*/d*a* between two identically loaded bodies possessing slightly different crack lengths, *a* and *a*+ Δ*a* (adapted from *ref.* [224, 226]).

Thus if the body is in load control (*F*), calculation of *J* proceeds according to:

$$J = \int_0^F \left(\frac{\partial \delta}{\partial a}\right)_F dF \qquad \textbf{(2.71)}$$

If the crack advances at a fixed displacement (δ), *F*=0, and *J* is given by:

$$J = -\int_0^\delta \left(\frac{\partial F}{\partial a}\right)_\delta d\delta \qquad \textbf{(2.72)}$$

Since, for elastic conditions, *G*=d*U*/d*a*, the relation between *J* and *G* is apparent. *J* is a more general version of the energy release rate. Regarding linear elastic materials, *J* equates the strain energy release rate *G* (*c.f. section 2.5.1 a*) [224, 226].

$$J = G \tag{2.73}$$

Analogous to G_{IC}, which represent the critical strain energy release rate during crack extension, one may define the value J_{IC} which characterizes the toughness of a material near the outset of crack extension. It has been reported that J_{IC} equates G_{IC} values determined from valid plane-strain fracture-toughness specimens which exhibit a predominantly elastic conditions associated with sudden failure without prior crack propagation [224, 225].

$$J_{IC} = G_{IC} = \frac{K_{IC}^2}{E}(1 - \upsilon^2) \tag{2.74}$$

b) Crack-tip-opening displacement

First proposed by Wells [229], an elastic-plastic parameter termed *the crack-tip-opening displacement* (CTOD, δ) is introduced in this section. It describes crack-tip conditions in elastic-plastic materials and can be used as a fracture criterion when the LEFM concept is no longer valid. Initially, the CTOD concept was developed in order to extend the elastic stress intensity factor (K_I) approach into elastic-plastic yielding conditions. Critical value of CTOD (δ_c), which is determined at the unstable crack propagation onset, gives nearly geometry-independent measures of fracture toughness, even for relatively large amounts of crack-tip plasticity [224, 230].

Under uniaxial tensile loading, an initially sharp crack blunts with plastic deformation; resulting in a finite displacement (δ) at the crack tip. Several definitions of CTOD can be found in the literature. The two most common definitions are the opening displacement at the original crack tip and the displacement at the intersection of a 90° vertex with the crack flanks, as illustrated in *figure 2.39*.

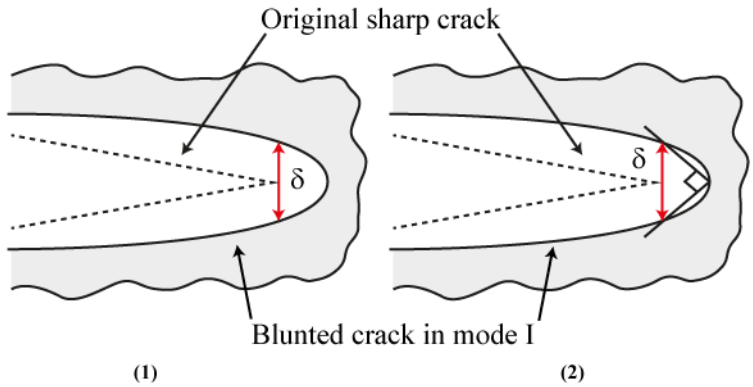

Figure 2.39. Common definitions of the CTOD: **(1)** opening displacement at the original crack tip and **(2)** displacement at the intersection of a 90° vertex with the crack flanks (Adapted from *ref.* [224]).

A direct equivalence is observed between both definitions if the crack blunts in a semicircle. Two CTOD test standards have been published by ASTM with designation E1290-89 and E1820-96. [224, 230].

Initially proposed by Dugdale [231] for perfectly plastic materials, the strip-yield model assumes plane-stress conditions and a nonhardening material. Regarding an infinite plate featuring a centre cracked loaded in mode I, calculation of the CTOD proceeds according to [230, 232]:

$$CTOD = \delta = \frac{8a\sigma_y}{\pi E}\ ln\left(sec\left(\frac{\pi\sigma}{2\sigma_y}\right)\right) \approx \frac{\pi\sigma^2 a}{\sigma_y E} = \frac{K_{IC}^2}{\sigma_y E} \qquad \textbf{(2.75)}$$

Where a is the crack length, σ_y the yield stress, σ the applied stress and E the Young's modulus.

The strip-yield model assumes plane-stress conditions and a non-hardening material. The actual relation between CTOD and K_I depends on stress state and strain hardening. The more general form of this relationship can be expressed as follows [224, 230]:

$$CTOD = \frac{K_{Ic}^2}{m * E^* * \sigma_y} \qquad \textbf{(2.76)}$$

Where m=1 and E^*=E under plane-stress conditions and m=2 and E^*=$E/(1-\nu^2)$ under plane-strain conditions.

Finally, the CTOD may related to the J-Integral according to the following expression [233]:

$$CTOD = m\frac{J}{\sigma_y} \qquad \textbf{(2.77)}$$

Where m is a dimensionless constant which depends on the stress state and strain hardening. Usually, m equals 1 for plane-stress and 2 for plane-strain conditions [224, 230].

2.5.3. Post-Yielding Fracture mechanics: Essential Work of Fracture

Under small-scale yielding conditions, a single parameter (*e.g. K, G, J, CTOD*) may be considered to characterize the stress state at the crack tip; resulting in a geometry-independent fracture criterion. However, large-scale yielding ahead of the crack tip (*e.g.* extensive plasticity) is sometimes observed before crack propagation. In this specific case, a single parameter can no longer be used to characterize the crack-

tip conditions because fracture toughness depends on the size and geometry of the considered sample.

On this basis, the *Essential Work of Fracture* (EWF), which belongs to the *post-yielding fracture mechanics* (PYFM), has been developed. This approach was originally proposed by Broberg [234, 235] in order to determine fracture toughness of metallic sheets under plane stress conditions. Later, this methodology has been refined by Cotterell and Reddel [236], Mai and Cotterell [237] and applied to ductile polymers under plane-strain and plane-stress conditions [238, 239].

According to Broberg, when a ductile body, which exhibits a central crack, is subjected to a uniform tensile stress, the plastic zone ahead of the crack tip may be divided in two regions: an **inner fracture process zone** (IFPZ) and an **outer process deformation zone** (OPDZ) which includes the different plastic deformations induced by the plastic flow. Thus, the work dissipated in the IFPZ is expected to be intrinsic to the tested material, while the work associated to the OPDZ should be dependent on both the sample geometry and the ligament length (l).

Accordingly, when a crack propagates after the generation of an extensive plastic damage zone, the work required for the whole fracture process (W_f) may be partitioned into two additives work terms, considering the zone of the process where it is involved.

$$W_f = W_e + W_p \qquad \textbf{(2.78)}$$

W_e is the **essential work of fracture**. It takes place in the IFPZ and it is the work necessary for the generation of a new surface. W_p is the **nonessential work of fracture**. It takes place in the OPDZ and corresponds to the work which is consumed by several deformation mechanisms (*e.g.* crazing, micro-voiding, shear yielding) [240-242].

Although, W_e is considered as a surface-related energy whose value is proportional to the fracture area (lt), W_p is a volume-related energy whose value is proportional to the volume of the deformed zone ($\beta l^2 t$), as illustrated in *figure 2.40*. l is the ligament length and t the sample thickness. β corresponds to the shape factor of the necked zone related to the volume of deformed material surrounding the ligament length, which value depends on the OPDZ geometry.

Considering the surface- and volume-dependence of the constituent terms, *equation 2.78* can be rewritten into the respective specific terms [242, 243]

$$W_f = w_e l t + \beta w_p l^2 t \qquad \textbf{(2.79)}$$

$$\frac{W_f}{lt} = w_f = w_e + \beta w_p l \qquad \textbf{(2.80)}$$

Where w_f is the **specific total work of fracture**, w_e the **specific essential work of fracture** (per ligament area unit) and w_p the **specific non-essential work of fracture** (per volume unit).

w_f is the total work of fracture and is experimentally determined by integration of the area below the load-displacement curve for each ligament length. w_e is an intrinsic material parameter under plane-stress conditions and β as well as w_p are independent on l. w_e and the plastic term (βw_p) are easily obtained from the best linear regression of a set of values represented in a graph plotting w_f versus l as illustrated in *figure 2.41* [243-245].

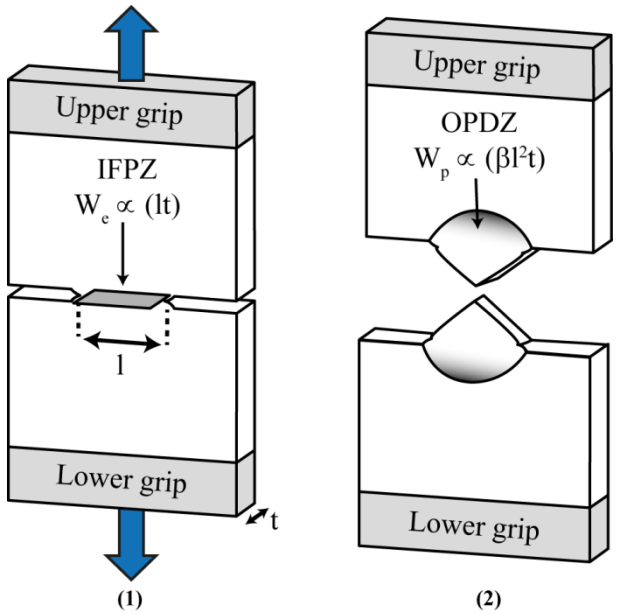

Figure 2.40. Geometry of the deeply double-edge notched test (DDENT) specimen together with the inner fracture process zone (IFPZ) and outer process deformation zone (OPDZ) concepts **(1)** before and **(2)** after fracture (mode I) (Adapted from *ref.* [246]).

However, *equation 2.80* is valid only if the prerequisites listed below are fully satisfied [245, 246]:

- The load-displacement traces at different l should be geometrically similar to one another.
- The ligament should be fully yielded before the crack propagation onset.
- The fracture should take place under the same stress state.

The EWF concept provides specific advantages as compared to the different methodologies available to evaluate G_{IC}, K_{IC} and/or J_{IC}. For instance, the EWF experimental protocol is much more straightforward in order to evaluate the fracture behaviour of ductile polymers. Moreover, raw data analysis is less time consuming than those required for determining G_{IC}, K_{IC} and/or J_{IC}. Benefiting from convenient experimental procedure and faster analysis time, the EWF concept has been extensively used to evaluate the fracture behaviour of ductile and modified polymeric systems featuring large-scale yielding ahead of the crack tip [34, 238, 239, 242-244, 246-252]. In 1995, the European Structural Integrity Society-Technical Committee 4 (ESIS-TC4) proposed a protocol specifying testing conditions [245].

a) Specimen size criteria

Some restrictions on specimen dimensions have been imposed by the ESIS-TC4 in order to ensure the validity of the EWF approach. Regarding DDENT specimens under plane-stress condition, l should be in the following range [239, 242, 243, 245, 246]:

$$\max(3t, 5mm) \leq l \leq \min\left(\frac{W}{3}, 2r_p\right) \quad \textbf{(2.81)}$$

Where t and W are the specimen thickness and width, respectively. r_p is the size of the plastic zone at the crack tip.

The minimum condition established by the protocol is to ensure that the whole ligament of a pre-notched specimen is fractured under a pure plane-stress condition. As shown in *figure 2.41*, a plane strain/plane stress mixed mode is likely to occur for smaller l; thus leading to the failure of *equation 2.80.*

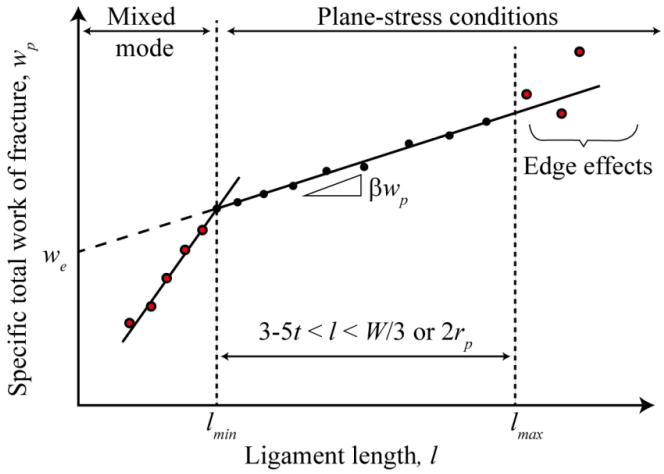

Figure 2.41. Schematic representation of the specific total work of fracture versus ligament length. Black points correspond to the validity range of the EWF technique (adapted from *ref.* [90, 224]).

The maximum condition established by the ESIS is to avoid edge effects during the fracture process, which may affect the OPDZ, and to ensure that the ligament is fully yielded before the onset of crack propagation. *l* should be smaller than 2 folds the plastic zone radius, r_p, at the crack tip. This parameter may be estimated as follows:

$$2r_p = \frac{1}{\pi}\frac{Ew_e}{\sigma_y^2} \qquad \text{Circular plastic zone} \qquad (\mathbf{2.82})$$

$$2r_p = \frac{\pi}{8}\frac{Ew_e}{\sigma_y^2} \qquad \text{Linear plastic zone} \qquad (\mathbf{2.83})$$

Where *E* is to the Young's modulus and σ_y the yield stress of a material subjected to an uniaxial tensile test.

Another verification in order to evaluate the stress state along the ligament during fracture is based on the Hill's plasticity theory [253]. This concept established that if a pre-notched DDENT specimen is fractured under pure plane-stress conditions, the maximum stress (σ_{max}) should be equal to 1.15 times its respective yield stress (σ_y) determined by a conventional uniaxial tensile test at the same crosshead (*c.f. equation 2.84*).

$$\sigma_{\max} = 1.15\ \sigma_{\mathrm{y}} \qquad (\mathbf{2.84})$$

This condition has been extensively used by numerous laboratories and all of them found discrepancies. A gradual increase in σ_{max} was usually observed with decreasing *l*, until reaching a critical value (l_{min}) where a steeper increase was measured. This threshold defines the transition from plane stress to a mixed stress state.

On this basis, due to the difficulties in defining l_{min} according to the Hill's theory, it was proposed to use an average value of maximum stresses (σ_m). This concept excludes any experimental EWF data for which σ_{max} is not include in the following range:

$$0.9\sigma_{\mathrm{m}} \leq\ \sigma_{\max}\ \leq 1.1\sigma_{\mathrm{m}} \qquad (\mathbf{2.85})$$

These limits are rather arbitrary, but have been useful to determine the transition from a pure plane-stress to a mixed-mode stress state [239, 245, 246].

b) Specific non-essential work of fracture and shape factor

w_p is not an intrinsic material parameter. However, its evaluation allows to take into account the effects of several deformation mechanisms which contribute to energy dissipation (*e.g.* crazing, micro-voiding, shear yielding) during large-scale yielding and which are not quantified by w_e. Thus, w_p may be used as a comparative

parameter between different materials for both similar specimen geometries and experimental conditions.

w_p cannot be directly calculated from *equation 2.80* due to its combination with β. An estimation of the shape of the necked zone (*i.e.* OPDZ) surrounding the fractured ligament is previously required in order to derive a w_p value. A special care should be taken during this operation as it is important to properly define the boundaries of the fully yielded zone without including a diffuse area, as already reported by Ferrer-Balas *et al.* [247]. This latter zone corresponds to a diffuse outer plastic zone (DOPZ) (*c.f. figure 2.41*), which appears during the initial loading, at the end of the elastic regime when crack does not start to propagate yet.

According to the first ESIS protocol, for a DDENT specimen geometry, the OPDZ tends to be circular, elliptical or diamond-shaped as illustrated in *figure 2.42*. Additionally, Ferrer-Balas *et al.* [248] proposed a new OPDZ geometry, which results from the intersection between two parabolas, giving an "eye"-shaped region (*c.f. figure 2.42*(d)). β is easily obtained from the best linear regression of a set of values represented in a graph plotting the height of the OPDZ (h) versus l according to the following equations:

Circular: (**2.86**) $\beta = \frac{\pi}{4}$ **Diamond:** (**2.87**) $\beta = \frac{h}{2l}$ **Elliptical:** (**2.88**) $\beta = \frac{\pi h}{4l}$ **Parabolic:** (**2.89**) $\beta = \frac{2h}{3l}$

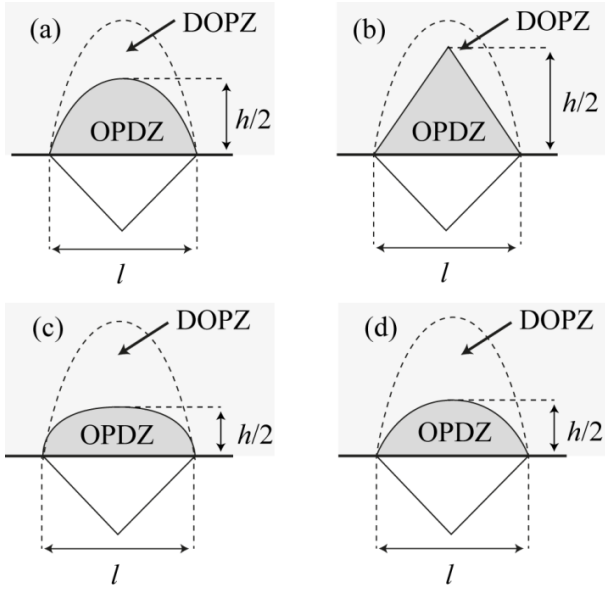

Figure 2.42. Schematic drawing of the OPDZ geometries together with the diffuse outer plastic zone (DOPZ) found in DDENT specimen: **(a)** circular, **(b)** diamond, **(c)** elliptical and **(d)** parabolic. (Adapted from *ref.* [90, 248]).

c) Correlation between the EWF methodology and the *J-Integral*

According to Mai and Cotterell [237], w_e is defined in mode I as follows:

$$w_e = d_i \int_0^{\varepsilon_{n,v}} \sigma_v d\varepsilon_v + \int_{\varepsilon_n}^{\delta_c} \sigma_{FPZ}(\delta_{FPZ}) d\delta_{FPZ} \qquad (\mathbf{2.90})$$

Where d_i is the thickness of the IFPZ which is of the order of the sample thickness. σ_v and ε_v is the true stress and true strain, respectively. $\varepsilon_{n,v}$ and ε_n is the true and engineering strain, respectively, at the onset of the yielding process ahead of the crack tip. σ_{FPZ} and δ_{PFZ} are the stress and the CTOD values within the FPZ, respectively. δ_c is a critical value of the CTOD in mode I.

By comparing *equations 2.70*and *2.90*, it is apparent that the first term of both equations is equivalent. They are related to the work needed to neck the process zone. Similarly, both second terms are equally equivalent and defined the work needed to reach the fracture of the process zone.

Under stable crack propagation condition, *J* values follow approximately a linear relationship for small crack lengths, Δa. Thus, this condition can be expressed as follows [237]:

$$J = J_{IC} + (\frac{dJ}{da})\Delta a \qquad (\mathbf{2.91})$$

By comparing *equations 2.80* with *2.91*, it can be deduced that

$$J = w_f \qquad w_e = J_{IC} \qquad \beta w_p = \alpha(dJ/da) \qquad (\mathbf{2.92})$$

Where α is a dimensionless parameter which is dependent on the sample geometry. Usually, α =0.25 for DDENT geometry and α =0.5 for Deeply-Single-Edge-Notched Tensile (DSENT) geometry.

As above described, it has been demonstrated theoretically that w_e is equivalent to J_c (and thus to G_c) in mode I, which has also been supported experimentally by different authors investigating the fracture behaviour of PET [90], PLA [252], ABS [254] and Ethylene-Propylene Bock Copolymer (EPBC) [255]. The advantage of the EWF method as compared to the *J-Integral* is, in many cases, its experimental simplicity.

Chapter 3: Materials

3.1. Poly (Lactic Acid)

Poly(lactic acid) (PLA) cannot be considered as a "modern" thermoplastic polymer. In the early 1780s, it structural basis, lactic acid (LA) (2-hydroxypropanoic acid) was first refined by the Swedish chemist Carl Wilhelm Scheele, who isolated LA from sour milk. In 1873, the German chemist Johannes Wislicenus established its chemical structure. Ten years later, Charles E. Avery was the first to produce it commercially at Littleton, in Massachusetts (USA).

The introduction of the lactic acid production in Europe was pioneered by the German pharmacy Boehringer Ingelheim in 1895 [256]. Although LA existed for two centuries, in 1932 the American chemist Wallace Hume Carothers and co-workers were the pioneers to develop a method to polymerize lactic acid in order to produce aliphatic polyesters (*e.g.* PLA). However, the resulting polymer had poor mechanical properties due to its low molecular weight (MW). An optimization of both the polymerization process and the lactide purification techniques led to the production of a higher MW polymer, which was patented in 1954 by the American chemical company DuPont® [15, 18, 35, 257].

Until the late 1980s, the high cost of PLA production limited its applications to the biomedical field, including implants, controlled drug release and biocompatible sutures. However, recent advances in the bacterial fermentation and the development of new processing techniques allow the production of cheaper PLA with higher MW. The breakthrough occurred in the beginning of the 1990s. The American Cargill Inc. company based in Minneapolis managed to produce a HMW PLA. A commercially viable lactide ring opening reaction was established from renewable feed-stocks which can compete with traditional resins [14, 258, 259].

Currently, at least six companies are contributing to the commercial PLA resin production around the globe: Cargill (United States of America), Mitsui Chemicals, Inc. (Japan), Purac (Netherland), Teijin Limited (Japan), Solanyl Biopolymers Inc. (Holland) and Futerro (Belgium). Since 2002, the joint venture of "Cargill Inc." and "The Dow Chemical Company" resulted in the Cargill Dow LLC. The operation of this manufacturing plant produces a 136 000 tones/year NatureWorks PLA [18, 260]. In 2010, NatureWorks PLA production costs were established around 1.4 to 5 €/kg and will continue to decrease over the following years [261].

In today's world of awareness of the environmental situation and of "green" chemistry, PLA has been viewed as a promising material as compared to several biopolymers. Its compostability under industrial composting conditions and its production from renewable resources have been its main attractive features. Other interesting properties such as it low toxicity, its negative carbon footprint, its tailored properties and its remaining transparency after processing have placed this biopolymer in the forefront of the plastic industry, specifically in the food packaging and other consumer product fields.

Currently, PLA is widely used in short-life eco-friendly applications such as rigid and flexible film packaging, cold drink cups, bottles, cutlery, etc. Finally, in the environmental conditions, PLA has a degradation time ranging from 6 months to two years as compared to the 500 or 1000 years for conventional plastics [11, 262, 263].

3.1.1. Polymerization processes of high molecular weight PLA

2-hydroxypropanoic acid ($C_3H_6O_3$) or more commonly called lactic acid is the simplest 2-hydroxycarboxylic acid containing a chiral carbon atom in its molecular structure. It exists in two different enantiomeric forms as shown in *figure 3.1*. Whereas, the (R)-lactic acid or L-(+)-lactic acid rotates the plane of polarized light clockwise, the (S)-lactic acid or D-(-)-lactic acid rotates the plane in a counterclockwise direction.

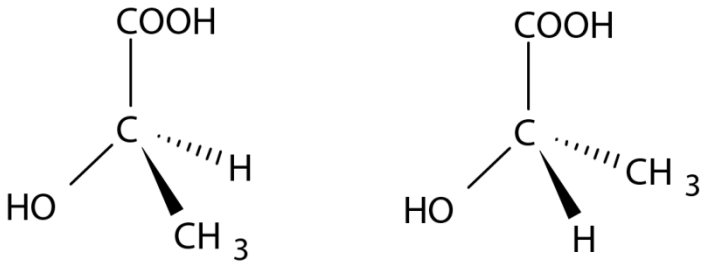

(R)-Lactic acid
L-(+)-Lactic acid

(S)-Lactic acid
D-(-)-Lactic acid

Figure 3.1. The two different enantiomeric forms of lactic acid (Adapted from *ref.* [13, 35]).

Lactic acid can be synthesized by either chemical synthesis or microbial fermentation. Since 1990, the latter process is the commercially viable mechanism to produce almost all lactic acid available on the market (70-90% of LA worldwide demand). It is considered as an eco-friendly solvents free process. It allows essentially the formation of the L-lactic acid (99.5 %) in high purity with a residual content of D-lactic acid (0.5 %) by bacterial fermentation of carbohydrates using an optimized

strain of Lactobacillus or even fungi [264, 265]. In this solvent free process, different kinds of carbohydrates obtained from agricultural byproducts can be used, such as sucrose (from cane or beet sugar), glucose, maltose and dextrose (from corn or potato starch) or even lactose (from cheese whey). The ability to control the L/D ratio in the final batch process introduces the potential to tailor the process-structure property relationships of the resulting synthesized polymer [12, 35].

The US Food and Drug Administration (US FDA) classifies lactic acid as generally recognized as safe (GRAS) for its use as a food additive. It is used in a wide range of applications such as cosmetic, beverage, food, medical and pharmaceutical industries. However, the major demand in lactic acid is still in food packaging applications (85%) [256, 266].

Three different polymerization routes are available in order to manufacture HMW PLA (greater than 100 000 $g.mol^{-1}$) from lactic acid:

- **The direct condensation polymerization process** is a solvent based synthesis. It has been reported as the cheapest way to synthesize PLA. However, the complexity to yield a final solvent-free HMW PLA led to its unsuccessful establishment [11, 12, 267].

- **The azeotropic dehydrative condensation polymerization process** is a organic solvent based process patented by Mitsui Toatsu Chemicals in 1995 [268]. Since 2003, it seems that this polymerization route is not used anymore due to its unfriendly impact on the environment (generation of toxic residues) [5, 267, 269, 270].

- **The ring opening polymerization (ROP) process of the cyclic lactide dimer** is a solvent free process developed and patented by Cargill Incorporated in 1992 [271]. This technique was pioneered by Carothers in 1932; however the synthesis of HMW PLA remained unavailable until the optimization of the purification techniques developed by DuPont in 1954. Nowadays, it is the current route used by Cargill Dow LLC to manufacture almost all HMW PLA available for commodity applications in a commercially viable continuous process. *Figure 3.2* illustrates a brief description of the ROP process.

As shown in *figure 3.2*, a low MW PLA prepolymer (DP_n=30-70, M_n<5 000 $g.mol^{-1}$) is initially produced by a continuous polycondensation of an aqueous lactic acid solution. Then, under reduced pressures and high temperatures, the resulting product is catalytically depolymerized into a melted mixture of lactides (cyclic dimer of lactic acid) which is continuously purified by vacuum distillation (dashed green box). L-Lactide, D-Lactide and meso-Lactide (with high L content) are thereby

synthesized due to the previous lactic acid's enantiomeric configuration. Their concentrations depend on the temperature, catalyst type and lactic acid feed stocks.

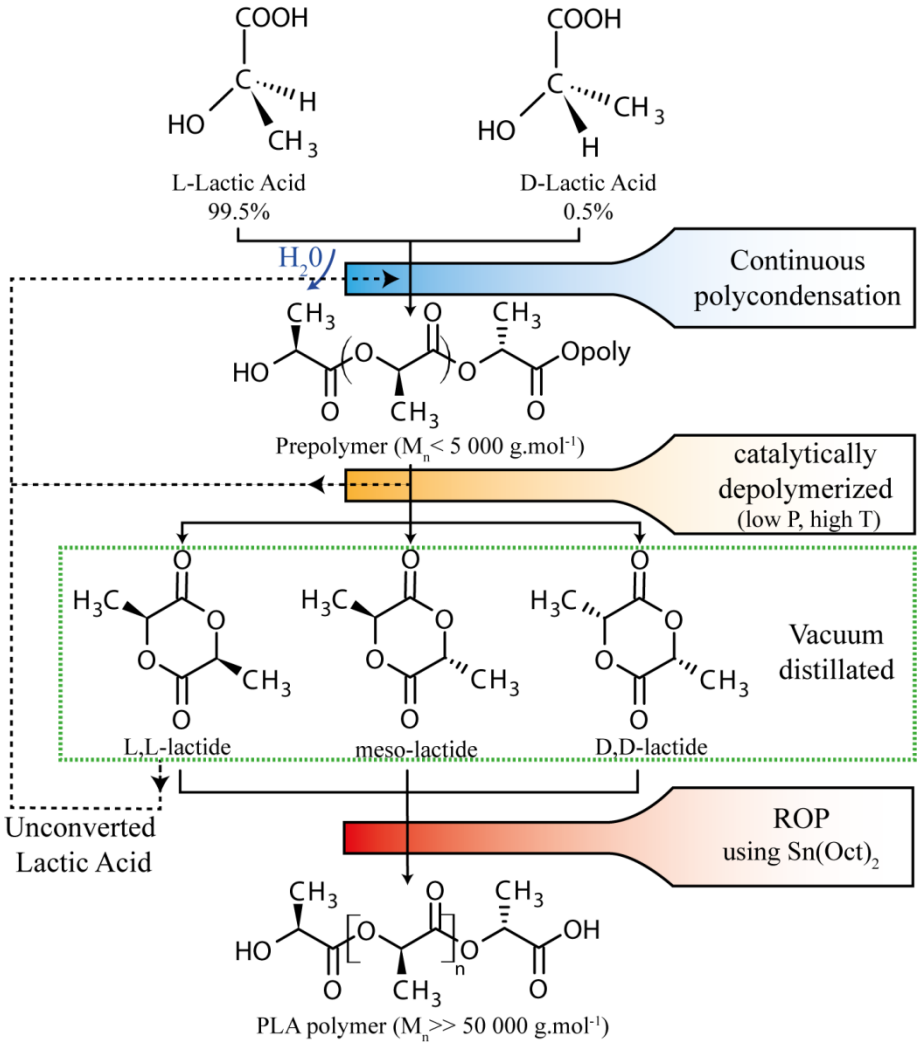

Figure 3.2. Schematic representation of the ROP manufacturing route (Adapted from *ref.* [11, 35]).

Finally, HMW PLA (DP_n =700-15 000, M_n>>50 000 g.mol^{-1}) with a controlled optical purity is manufactured by controlled ROP via a coordination-insertion mechanism of the lactides using an organometallic catalyze such as tin octoate ($Sn(Oct)_2$), in the melted state. The key to such a process is based on the continuous removal of non-polymerized monomers and water by vacuum distillation. Consequently, side reactions are avoided and the MWs achievable are better controlled [263, 267, 270, 272].

Recently, it has been established that catalysts based on tin (Sn) compounds showed cytotoxic effects in both humans as well as animals and neurotoxic effects in animals. Therefore, new catalysts showing less toxicity are under development [273-275]. This production of HMW PLA is based on a two step process coupled with additional purification stages which lead to an increase of the final production costs. In order to find better economically viable processes, several researchers are looking for alternative routes to produce HMW PLA in a continuous solvent free process. Such new solutions include reactive extrusion of lactides [42, 276, 277], melt polycondensation and/or sequential melt-solid polycondensation mechanisms [278].

By controlling temperatures, residence time, catalyst type and the concentration of the three lactide stereosiomers, ROP mechanism presents a novel aspect to control the sequencing and proportions of the L- and D-lactide units in the final polymer [279]. *Table 3.1* summarizes the different PLA grades which may be manufactured by the ROP process. Due to the larger production of L-lactic acid from bacterial fermentation, most commercial PLA grades are optical copolymers of L-lactide with small amounts of D-lactide or meso-lactide. Therefore, the control of the optical purity (OP) introduced the potential to tailor the final properties of the polymer [11, 35, 280].

Table 3.1. Principal PLA molecular structures derived from ROP route using different catalyst [11, 263, 273, 279].

Polymerized monomer	Tacticity	Material identification
L,L-lactide D,D-lactide	Isotactic	Poly (L-lactide) (**PLLA**) Poly (D-lactide) (**PDLA**)
Meso-lactide	Atactic No stereocontrol	Poly (meso-lactide)
	Predominantly Isotactic -(LD)$_n$-	
	Syndiotactic in dimers -(LD)-(DL)-(LD)-	
Equimolar amounts of L,L-lactide and D,D-lactide	Predominantly Atactic -(LD/DL)$_n$-	Poly (rac-lactide) (**PDLLA**)
	Heterotactic -(LDDL)$_n$-	
	Stereoblock Isotactic -(LD)$_m$-(DL)$_n$-	
Predominantly L-lactide with small amounts of D- or meso-lactide (*commercial grades*)	Atactic Random optical copolymers	Poly (LD-lactide) (**PD,L-LA** or **P(L-LA-*co*-*meso*-LA)**)

3.1.2. Industrial processing by extrusion

Processing and manufacturing of PLA end products employ similar technologies as for conventional thermoplastic polymers (PE, PP, PET, etc). Extrusion is by far the most widely adopted technique for continuously melt processing PLA. Commercial PLA grades maybe processed using conventional extruder devices combined with general purpose screws with L/D ratios ranging from 24:1 to 30:1. When single screw extruders are used, the compression ratio defined as the ratio of the flight depth in the feed section to that of the metering section is another important screw parameter. Screws with large compression ratios may provide excessive shear heating imparted to the polymer; thus leading to inadequate melting performances and possible thermal degradations. NatureWorks recommends screw compression ratios between 2.5:1 and 3.1:1 in order to optimize PLA melt properties during processing [281, 282]. Extruder screws used to process PET polymers are appropriated to process commercial PLA resins [15, 283, 284].

Special care should be taken when extruders principally designed for processing polyolefins are used for transforming PLA. Commercial PLA resins have a higher density ($\approx$ 1.24 $g.cm^{-3}$) than most polyolefins (0.91-0.96 $g.cm^{-3}$). Therefore, if a production line transforming polyolefins (*i.e.* LLDPE) is already operating close to its maximum available power to drive, the same line may be limited by excessive power consumption if PLA resins are introduced [285].

On the market, many extrusion processing methods with their respective variations are available to process PLA polymers. The most used of them are the following: palletising extrusion, co-extrusion, film blowing, melt spinning and the conventional extrusion film/sheet casting process. Regarding the latter, the resulting manufactured films/sheets may be thereafter transformed to packaging containers or cups using thermoforming processes. No significant changes in equipments or tooling have been highlighted when thermoformers switch from PET or PS to PLA. In contrast, due to a shrinkage effect more pronounced in PP as compared to PLA resins, moulds and trim tools designed for the former should be optimized before switching to the latter [286, 287].

PLA resins have an inherently poor melt strength as compared to conventional thermoplastic polymers. This is partially due to its highly linear chain architecture and poor entanglement density [35]. This feature leads to several drawbacks during large-scale production causing sagging of melts, necking and may lead to a possible reduction of the processing throughputs. Consequently, film/sheet casting extrusion, blown film extrusion and foaming processes are subjected to different issues briefly listed below [35, 283, 285]:

- Film/sheet casting extrusion: limitation of both the extrusion rates and the film/sheet thickness.
- Blown film extrusion: difficulties in the formation of the bubble and poor bubble stability.
- Foaming processes: collapse of the foam structure during the stabilization phase of the cell growth.

3.1.3. Degradation mechanisms during melt processing

Similar to several polar polymers (*e.g.* PA, ABS, PET, etc), additional complications are highlighted due to the poor thermal stability of PLA resins at high temperatures. The transparent visual aspect of amorphous PLA end products may be greatly altered by colour formation due to numerous thermal degradations; thus representing a considerable issue in the packaging sector [288]. Nowadays, thermal degradation of PLA polymers in the range of conventional processing temperatures has been extensively studied and the degradation mechanisms are well established.

Moisture, processing temperatures, residence times, reactive end groups, residual catalyst, oligomers, unreacted monomers and MW are factors which affect the thermal stability of PLA [289-292]. The degradation by-products are water, cyclic oligomers, lactic monomers, lactides, and polymerization catalysts [278]. The resulting loss of MW is due to various degradation reactions occurring simultaneously by random main-chain scissions in the melted state, as already reported by several authors [292-295].

The principal degradation mechanisms include thermohydrolysis [296], cyclic oligomerisation, depolymerisation [294, 297], intra and intermolecular transesterification reactions by cleaving ester bonds [298, 299]. For much higher temperatures (>300 ºC), pyrolysis might also be considered as a depolymerisation mechanism [291].

Thermohydrolytic degradation

Thermohydrolysis is a water-based degradation mechanism which leads to a significant decrease in the MW of the initial polymer during melt processing. Due to the random main-chain scission nature of the reaction, three different scenarios are expected if the terminal –OH and –COOH groups are not end capped, as shown in *figure 3.3*.

- **Case "a"**: thermohydrolysis of an ester linkage may take place at the end of the chain; suggesting the formation of a sub-linear chain with a lower MW and a monomer lactic unit.

- **Case "b"**: thermohydrolysis of an ester linkage takes place at exactly two repeated units from the end of the chain; giving rise to the formation of a sub-linear chain with a lower MW and a lactide. In the present instance, H_2O is considered as a catalyser of degradation and does not attack the main polymer backbone. Further thermohydrolysis of the lactide possibly leads to the formation of two monomeric lactic units.
- **Case "c"**: thermohydrolysis of an ester linkage randomly occurs in the intra chain of the polymer; leading to the formation of two sub-linear chains with lower MWs.

Several authors reported that the rate of thermohydrolysis is catalyzed by residual moisture, water concentration and processing temperatures [263, 292, 300]. This degradation mechanism is classified as autocatalytic since its rate increases with increasing the concentration of hydrophilic impurities (*i.e.* functional ends groups and lactides).

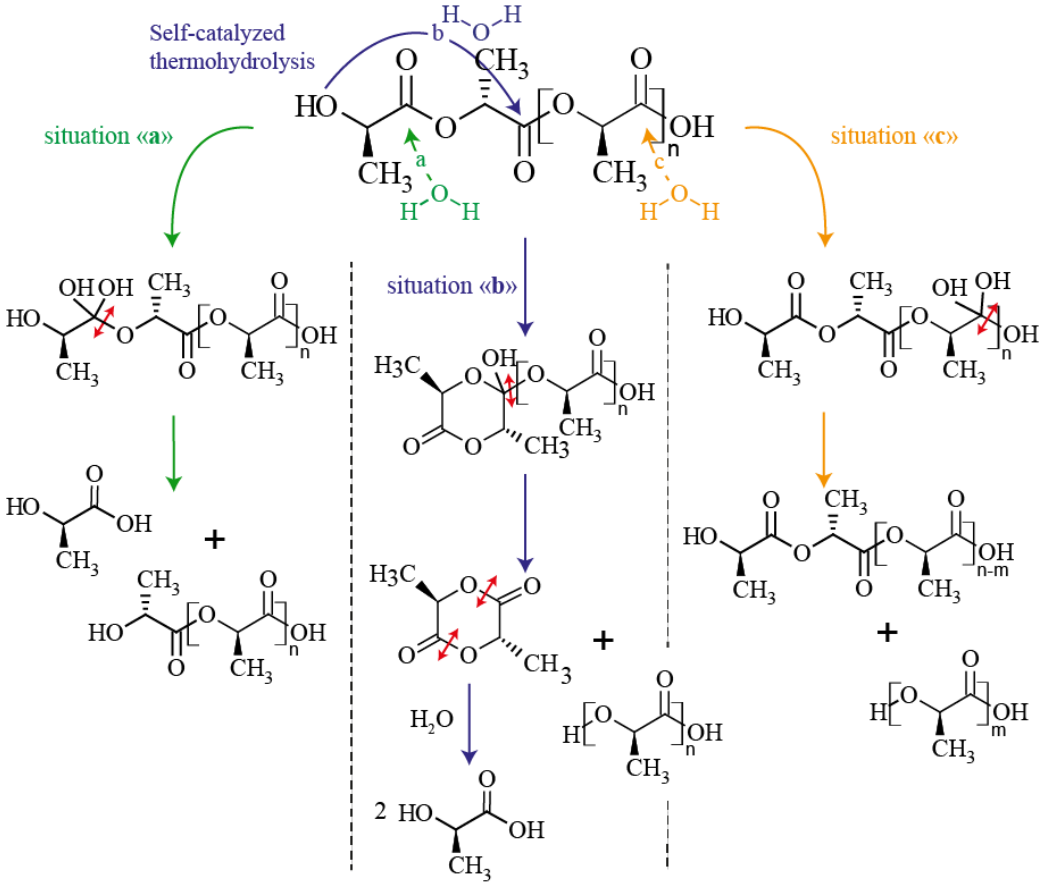

Figure 3.3. Depolymerisation resulting from the thermohydrolysis sensitivity of PLA (Adapted from *ref.* [11, 301]).

Transesterification mechanisms

As reported in a large number of communications, there are two types of transesterification mechanisms: intramolecular and intermolecular. Regarding the former, it is usually associated to a thermal-based degradation mechanism which leads to a reduction of the MW of the initial polymer, as shown in *figure 3.4*. [296, 302].

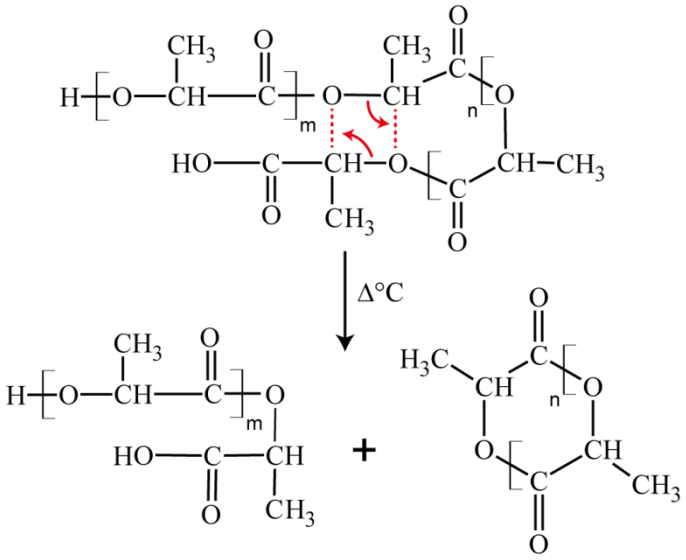

Figure 3.4. Depolymerisation due to intramolecular transesterification of PLA during melt processing (Adapted from *ref.* [298, 299]).

Wachsen and coworkers [296, 303] reported that intramolecular transesterification reactions are principally responsible of the degradation of PLLA during melt processing between 180 and 230ºC. Yu *et al.* [293] proposed a mathematical model in order to predict the variations in the molecular properties of PLLA polymers during melt processing.

As can be seen in *figure 3.4*, the formation of a sub-linear chain with a lower MW and a lactide if n=1 (referred to as backbiting or zip-like depolymerization) or cyclic oligomer if n≥ 2 may be expected by intramolecular transesterification during melt processing. Remaining concentration of polymerization catalyst, lactic monomers, cyclic oligomers and hydroxyl end groups enhance the rate of intramolecular transesterification [299, 302, 304].

On the other hand, intermolecular transesterification affects principally the sequence of different polymeric segments. It is a reaction between two ester linkages of two different chains which exchange their radicals during melt processing. As a result, the PDI of the initial polymer is possibly increased and the MW undertakes variations [296, 302]. Publications reporting this mechanism as a degradation reaction

in the melt are rare [305, 306]. The general mechanism of this reaction is shown in *figure 3.5*.

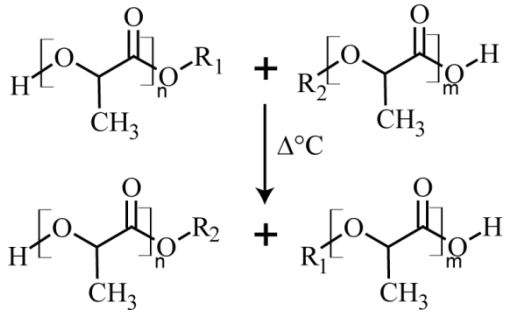

Figure 3.5. Intermolecular transesterification of PLA at high temperatures (Adapted from *ref.* [296, 307]).

Pyrolytic Cis eliminations

This reaction should be taken into account only at high temperatures (>300ºC) and usually does not take place using conventional melt process conditions. The pyrolitic elimination of an ester linkage leads to the generation of a sub-chain containing a new carboxylic acid end group and another sub-chain containing an acryloyl group. Both of them have a lowered MW as compared to the initial polymeric chain [300]. *Figure 3.6* shows the general mechanism of this reaction.

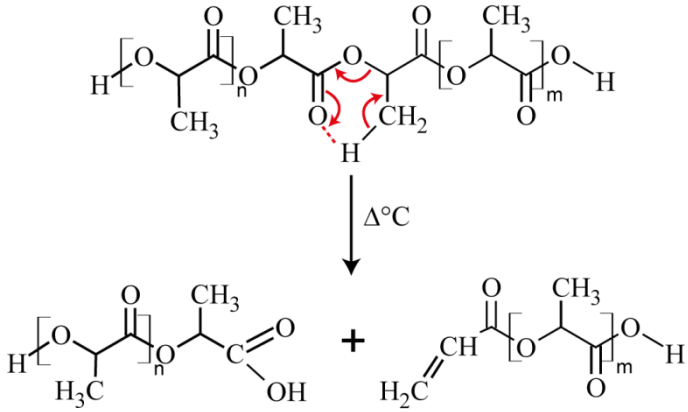

Figure 3.6. Pyrolitic Cis elimination of PLA (Adapted from *ref.* [300]).

3.1.4. Enhancement of PLA melt properties

The use of PLA in some specific processing techniques (*i.e.* sheet casting extrusion, blown film extrusion, foaming) is complicated due to the material limited melt strength and elasticity. Its insufficient thermal stability during melt processing is another shortcoming of PLA. Carlon *et al.* [46] and Gogolewski *et al.* [308] showed that the degradation of PLA already occurred at 160 ºC under extrusion and injection molding processes, respectively. Therefore, large-scale commercial applications using PLA could result expensive and time intensive in order to manufacture end products with the required quality.

In the past decades, similar issues and processing limitations have been reported in numerous studies dealing with PET [40, 41, 45]. Several methods based on chain extension/branching have been reported as efficient to overcome these limitations and to enhance melt properties [309]. Among these different techniques, solid-state polycondensation is a process used to manufacture HMW PET. It is performed in the solid state, thus avoiding melt degradations. However, the diffusion rate of small molecule by-products, which control the final rate of the reaction, is significantly reduced. Consequently, the production costs are significantly increased [40, 310].

An alternative method to overcome these shortcomings is to perform chain extension/branching reactions in melted bulk using reactive processing. Regarding PET, reactive extrusion process has shown encouraging results [40, 43, 44, 311]. When this conversion technique is combined with a multifunctional reactive agent, it takes advantages of the melt degradation by-products to enhance the melt strength, the MW and to stabilize the melt properties of the polymer. This is achieved by reconnecting the polymer chains and creating a branched structure. This technique can be considered as more cost-effective and more convenient than solid state processing. In fact, no particular changes in equipments are necessary when extruders switch from conventional extrusion to reactive extrusion processes. The absence of diluents places this reactive technique in the forefront of the eco-friendly processes and can lead to larger volume of production.

On this basis, numerous authors reported that reactive extrusion is also an attractive way to minimize PLA melt degradations and to enhance its melt properties [42, 312]. The creation of an extended and/or branched architecture is achieved through functional group reactions using reactive agents. Among the large number of reactive agent available on the market, the different functional groups able to react with each other are -COOH/epoxy, -OH/epoxy [47, 94, 313, 314], -COOH/isocyanate [315], -OH/dianhydride [316] and -OH/isocyanurate [316, 317].

Free radical reactions using peroxide [46, 131, 316-319] have also been reported as a possible solution to carry out branching reactions. This mechanism is

straightforward to carry out using reactive extrusion when free radical initiators are present in the melted bulk.

The reactive agent concentration, the working temperatures and the extrusion residence time are three important parameters in order to optimize the end-product properties when reactive extrusion is used. A literature survey of the main processing conditions and results to modify PLA matrix is given in *table 3.2*.

Table 3.2. Summary of the main processing conditions to modify PLA together with the corresponding results.

Authors (Year) [ref.]	Main objective	PLA grades (L/D ratio) Type of chain extender *[supplier]*	Processing conditions	Observations*
Carlson *et al.* (1998) [46]	Effect of the processing temperatures and initiator concentrations on the MW increase of extruded PLA.	Poly (lactic acid) (96/4) *[Cargill Central Research]* Difunctional di-tertiary alkyl peroxide (Lupersol 101) Concentration: 0.1 to 0.5 wt.% *[Elf Atochem]*	Reactive Extrusion - co-rotating intermeshing twin-screw extruder (L/D: 14:1) (4 barrel zones) - temperature: ranged from 160 to 200 ºC - screw rotation speed: 100 rpm - residence time: n.s.	- Significant degradation of the PLA for samples without initiator. - Branching reactions were operative at processing temperatures around 170-180 ºC and initiator concentration ranged from 0.1 to 0.25 wt.%. - Similar processing temperatures combined with higher initiator contents (0.5 wt.%) favored highly branched systems with the possible formation of microgels (radical coupling reactions). - Regarding highly branched samples, an additional peak appeared in the HMW tail of the monomodal PLA MWD. - T_g remained similar for all the samples
Di *et al.* (2005) [315]	Processing of HMW PLAs for specific processes.	Poly (lactic acid) (92/8) *[NatureWorks]* 1,4-butanediol (BD) Concentration: COOH/1,4-butanediol ratio: 1.1 to 2:1 *[Aldrich-Sigma]* 1,4-butane diisocyanate (BDI) Concentration: OH/1,4-butane diisocyanate ratio: 1.1 to 2:1 *[Aldrich-Sigma]*	Haake melt mixer - mixing volume: n.s. - N_2 atmosphere - temperature: 170 ºC - screw rotation speed: 60 rpm - blending time: n.s.	- The use of BDI as CE with PLA is complicated. In order to observe reactivity between both materials, PLA -COOH end groups have to be initially reduced using a different chain extender. BD was initially used to fix PLA -COOH end groups. Then, the resulting free -OH end groups may react with BDI in order to achieve chain-extension and MW enhancement. - MWs were increased at BD and BDI concentrations equal to -COOH and -OH contents in PLA, respectively. Excessive BD content induced degradation and excessive BDI concentration induced crosslinking. - T_g increased and T_m decreased with increasing MW. - The melt strength and melt viscosity were enhanced for modified PLA samples. However, a significant transition in G' and $\|\eta^*\|$ in the low frequency region might indicate the presence of microgels.

* CE: chain extender, MA: masterbatch, *PDI*: polydispersity index, X_c: degree of crystallinity, T_g: glass transition, T_m: melting temperature, E': storage modulus (DMTA), E: Young's Modulus, ε_b: strain at break, SEM: scanning electron microscopy, G': storage modulus (Rheology), $|\eta^*|$: complex viscosity, E_a: flow activation energy, n.s.: not specified

Table 3.2. Summary of the main processing conditions to modify PLA together with the corresponding results.

Authors (Year) [ref.]	Main objective	PLA grades (L/D ratio) Type of chain extender *[supplier]*	Processing conditions	Observations*
Pilla *et al.* (2008) [94]	Effect of epoxy-based chain-extender addition on the cell morphology and mechanical properties of bulk and microcellular PLA.	PLA 3001D (92/8) *[NatureWorks]* Multifunctional epoxy-styrene-acrylic oligomer CESA-Extend OMAN 698502 Concentration: 8 wt.% of MA *[Clariant Additive Masterbaches]*	Reactive Extrusion - co-rotating twin-screw extruder 32 mm (L/D: 36:1) (7 barrel zones) - temperature: 157 to 168 ºC (feeding zone to die) - screw rotation speed: 200 rpm Tensile bars (ASTM D638-03, Type I) were injection-molded with the pelletized material - Arburg Allrounder 320S (screw ø: 25 mm), equipped with MuCell® technology - Nozzle temperature: 165-170 ºC - Mold temperature: 15 ºC - Injection speed: 40 $mm.s^{-1}$	- A significant enhancement of the molecular parameters was observed with the addition of the MA. - Decrease in X_c with the formation of branching. - The fracture surface of all the branched injection-molded PLA samples exhibited a higher density of craze random nucleation as compared to their neat counterparts. - A DMA study did not show any significant changes in E' and T_g between PLA and branched PLA samples. In contrast, the damping properties ($tan\ \delta$) of the branched PLA samples seemed to be slightly enhanced. - Besides a slight decrease in E, both σ_y and ε_b values were slightly increased with the introduction of branches.
Yang *et al.* (2008) [317]	Improvement of the thermal stability of PLA by chemical crosslinking.	PLA 3001D (92/8) *[NatureWorks]* Triallyl isocyanurate Concentration: 0.15 to 3 wt.% *[Chen Guan Co.]* Dicumyl peroxide Concentration: 0.2 to 1.5 wt.% *[Chen Guan Co.]*	Internal mixer - mixing volume: n.s. - temperature: 180 ºC - screw rotation speed: 50 rpm - blending time: 10 min Compression molding - temperature: 190 ºC - time: 3 min - cooled to 20 ºC for 3 min	- Under melt processing, an increase in the gel fraction was measured with increasing both reactive agent concentrations. - T_g and T_m were shifted to lower temperatures due to an increase in the gel fraction and crosslinking density. - Enhancement of the thermal stability of all crosslinked samples. - Besides an increase in E, crosslinked PLA samples were more brittle as compared to neat PLA samples under uniaxial tensile loading.

* CE: chain extender, MA: masterbatch, *PDI*: polydispersity index, X_c: degree of crystallinity, T_g: glass transition, T_m: melting temperature, E': storage modulus (DMTA), E: Young's Modulus, ε_b: strain at break, SEM: scanning electron microscopy, G': storage modulus (Rheology), $|\eta^*|$: complex viscosity, E_a: flow activation energy, n.s.: not specified

Table 3.2. Summary of the main processing conditions to modify PLA together with the corresponding results.

Authors (Year) [ref.]	Main objective	PLA grades (L/D ratio) Type of chain extender *[supplier]*	Processing conditions	Observations*
Pilla *et al.* (2009) [313]	Effect of the epoxy-functionalized CE addition on the foaming ability of PLA processed via microcellular extrusion process.	PLA 3001D (92/8) *[NatureWorks]* Multifunctional epoxy-styrene-acrylic oligomer CESA-Extend OMAN 698493 Concentration: 0.7 to 1.3 wt.% of MA *[Clariant Additive Masterbaches]*	<u>Internal Mixer</u> - single screw with a mixing screw ratio of 30:1 (L/D) and ¾'' diameter - mixing volume: n.s. - temperature: samples were collected between 130 and 160 ºC at 10 ºC of interval - screw rotation speed: n.s. - foaming agent: 4%-CO_2 - nucleating agent: talc-0.5%	- Slight decrease in the MW of neat PLA after processing. - In contract, the MW of the initial PLA increased up to 100% with the addition of 1.3 wt.% of MA. - The addition of talc and MA (0.7-1 wt.%) gave rise to a denser and more uniform cell structure. 1% was considered as the optimum MA content to foam PLA in presence of talc. - The cell density was reduced with the addition of 1.3 wt.% of MA. The melt strength was supposed too high to allow cell nucleation. - X_c decreased with increasing MA contents.
Sungsanit *et al.* (2010) [131]	Rheological, thermal and mechanical characterization of linear and branched PLA melt compounded with PEG.	PLA 4032D (98/2) *[NatureWorks]* Difunctional di-tertiary alkyl peroxide (Lupersol 101) Concentration: 0.25 wt.% *[Sigma-Aldrich]*	<u>Reactive Extrusion</u> - co-rotating twin screws extruder 30 mm (L/D: 42:1) - temperature: 160 to 190 ºC (feeding zone to die) (11 zones) - screw rotation speed: 100 rpm - residence time: n.s. - peroxide was introduced in zone 7 under a pressure of 2.12 MPa - vacuum was applied in the metering zone	- Increase in the melt strength and melt viscosity of branched PLA samples - The thermal properties remained unchanged between lineal and branched PLA samples - Branched samples exhibited a slight increase in the impact strength due to a larger nucleation of highly localized plastic deformations (rougher fracture surface observed using SEM)

* CE: chain extender, MA: masterbatch, *PDI*: polydispersity index, X_c: degree of crystallinity, T_g: glass transition, T_m: melting temperature, *E'*: storage modulus (DMTA), *E*: Young's Modulus, ε_b: strain at break, SEM: scanning electron microscopy, *G'*: storage modulus (Rheology), $|\eta^*|$: complex viscosity, E_a: flow activation energy, n.s.: not specified

Table 3.2. Summary of the main processing conditions to modify PLA together with the corresponding results.

Authors (Year) [ref.]	Main objective	PLA grades (L/D ratio) Type of chain extender *[supplier]*	Processing conditions	Observations*
Liu *et al.* (2010) [316]	Processing of highly branched PLAs with a relative control on the generated structures via functional group reactions.	PLA 2002D (96/4) *[NatureWorks]* Pyromellitic dianhydride (PMDA) Concentration: 0.31 to 0.61 wt.% *[Sinopharm Chemical Reagent]* Phthalic anhydride (PA) Concentration: 0.65 wt.% *[Sinopharm Chemical Reagent]* Triglycidyl isocyanurate (TGIC) Concentration: 0.61 wt.% *[Huangshan Taida Chem. Comp.]* Dicumyl peroxide (DCP) Concentration: 0.2 wt.% *[Shanghai Chemicals Factory]*	Internal mixer - mixing volume: n.s. - temperature: 190 and 200 ºC - screw rotation speed: 60 rpm - blending time: up to 35 min	- PLA did not show reactivity with PMDA and TGIC agent alone. In contrast, a significant increase in MW and the formation of a branching structure was revealed when PLA was melt blended with these two reactive agents together. - Regardless of the peroxide based samples, all other samples presented an incomplete reaction after processing (35 min). An annealing treatment was therefore applied in order to complete the reactions. - As compared to peroxide based samples, linear and non-linear rheological results showed a drastic increase in the chain relaxation times for all annealed samples. - Linear, star-like chains with 3 arms and three-like chains with two generation topologies were predicted by the branch-on-branch dynamic model. - Regarding peroxide based samples, linear chains and small amount of comb-like chains with 3-arms was predicted. The melt strength and chain relaxation times were increased but at a lower extent as compared to other samples. - As compared to lineal PLA samples, the melt flow index of all LCB PLA samples decreased.

* CE: chain extender, MA: masterbatch, *PDI*: polydispersity index, X_c: degree of crystallinity, T_g: glass transition, T_m: melting temperature, *E'*: storage modulus (DMTA), *E*: Young's Modulus, ε_b: strain at break, SEM: scanning electron microscopy, *G'*: storage modulus (Rheology), $|\eta^*|$: complex viscosity, E_a: flow activation energy, n.s.: not specified

Table 3.2. Summary of the main processing conditions to modify PLA together with the corresponding results.

Authors (Year) [ref.]	Main objective	Type of chain extender	Processing conditions	Observations*
Mihai *et al.* (2010) [314]	Investigation of the rheological and extrusion foaming behaviour of chain-branched PLA.	PLA 4032D (98/2) PLA 8302D (90/10) *[NatureWorks]* Multifunctional epoxy-styrene-acrylic oligomer CESAExtend OMAN 698493 Concentration: 0.2 to 2 wt.% of MA *[Clariant Additive]*	Internal Mixer - mixing volume: 60 cm^3 - N_2 atmosphere - temperature: 200 ºC - screw rotation speed: 80 rpm - blending time: 20 min Reactive Extrusion Foaming - co-rotating twin-screw extruder 34 mm (12 barrel zones) - temperature: 190 ºC - screw rotation speed: 150 rpm - flow rate: 10 $kg.h^{-1}$	- The shear viscosity, the melt strength and melt elasticity increased with the increasing MA content. - The elongational viscosity and the magnitude of the strain-hardening was enhanced with the MA amount. - Regarding amorphous PLA 8302D, foam morphologies and densities remained independent on the MA content. - Regarding semi-crystalline PLA 4032D, the foam density was reduced with the increasing MA content. For larger foaming agent contents, similar foam morphologies were obtained regardless of the MA content.
Corre *et al.* (2011) [47]	Melt strengthening of PLA through reactive extrusion: rheological and physicochemical characterization	PLA 3051D (96/4) *[NatureWorks]* Multifunctional epoxy-styrene-acrylic oligomer CESAExtend OMAN 698493 Concentration: 1 to 3 wt.% *[Clariant Additive Masterbaches]*	Internal Mixer - conical co-rotating twin screws with a recirculating channel - temperature: 210 ºC - screw rotation speed: 50 rpm - blending time: up to 12 min Reactive Extrusion - twin-screw extr. 25 mm (L/D: 36) - temperature: 210 ºC in all zones (feeding zone: 75ºC) - screw rotation speed: 20 to 45 rpm -residence time: 3 to 12 min -flow rate: 3.5 $kg.h^{-1}$	- Regarding chain extended PLA samples, a high MW shoulder was added to the monomodal PLA MWD. - Over shearing and stretching, the thermal stability, the melt strength and the melt viscosity were enhanced - Topological changes increase the melt response time - By comparing dynamic and steady-shear rheological experiments, authors reported an increasing discrepancy in the Cox-Merz relation with increasing CE content. - E_a decreased for all chain extended PLA samples due to a reduced polarity (decrease in COOH end groups concentration). - The elongational viscosity and the magnitude of the strain-hardening were enhanced with increasing CE.

* CE: chain extender, MA: masterbatch, *PDI*: polydispersity index, X_c: degree of crystallinity, T_g: glass transition, T_m: melting temperature, *E'*: storage modulus (DMTA), *E*: Young's Modulus, ε_b: strain at break, SEM: scanning electron microscopy, *G'*: storage modulus (Rheology), $|\eta^*|$: complex viscosity, E_a: flow activation energy, n.s.: not specified

3.1.5. Thermal and mechanical performances of HMW PLA

Since the current demand for PLA commercial grades is increasing for engineering/packaging applications, a perfect knowledge of their properties is required. However, the constant increase in the demand reveals sometimes several lacks of specific characteristics data, which may be critical in order to optimize processes and part qualities. The state of the art and the presentation of the most relevant properties of processed PLA are not trivial. Their properties strongly depend on the MW, the optical stereoregularity and the manufacturing process coupled with its respective parameters. In this section, an intent to provide qualitative information on the current knowledge of the thermal, mechanical and fracture behaviour is achieved.

a) Thermal properties

As a result of a high dependence of the solid-state morphology and crystallinity on the physical and mechanical performances, numerous studies report PLA crystallization behaviour [12, 15, 20, 263, 320, 321]. Initially, this section focuses on the description of the polymorphism and crystallization behaviour of PLLA and PDLA homopolymers due to their higher sensitivity to crystallize as compared to commercial PLA grades. Similar crystallization and polymorphic behaviour are expected for PLLA and PDLA resins. However, the crystallization behaviour of PDLA has been hardly investigated due to the predominantly L-lactic acid commercial production.

Regarding PLLA, the MW, the processing conditions and thermal and/or mechanical treatments influence the crystallization of different helical chain conformation and cell symmetries. Using diffraction techniques (*e.g.* X-ray, electron diffraction), three different "ordered" crystalline forms (α-, β- and γ-) and one "disordered" crystal modification (α'-) have been identified:

- **The α-crystalline structure** is considered as the most common polymorph and the most stable crystal phase due to its highest melting temperature (T_m ≈180-185 °C). It may crystallize from the melt when the crystallization temperature (T_c) is higher than 120 ºC [322] and/or from solution-spinning processes at low drawing temperatures and/or low hot-draw ratios [323, 324]. This crystal form is characterized by an orthorhombic (or pseudo-orthorhombic) unit cell which contains two antiparallel chains in a left-handed 10_3 helical chain conformation (10 Å rise/ 3 monomeric units). The unit cell dimensions are a=10.66 Å, b=6.16 Å, c=28.88 Å, as already reported elsewhere [12, 324-327].

- The **α'-disordered structure** has been introduced as a new crystalline form by Zhang et *al.* [328, 329] in 2005 and has already been observed by numerous authors [92, 322, 328, 330]. It is defined as a limiting disordered modification of the α-forms and may crystallize when T_c is lower than 120 ºC, regardless of the polymer MW [322, 323, 330]. Commonly, a mixture between α'- and α-forms crystallizes around 100-120 °C due to the discontinuousness of the crystallization kinetics (polymorphism) in this temperature region [330, 331]. IR spectra analysis suggests that the α'-form is defined as it α-homologue. It is characterized by a 10_3 helix chain conformation packed in an orthorhombic (or pseudo-orthorhombic) unit cell. However, the lattice dimensions are slightly increased (*a*=10.72 Å, *b*=5.94 Å, *c*=28.88 Å) because the backbone side group packing (including C=O, CH_3 and C-CH_3) is looser and disordered within the α' unit-cell [328, 330].
  The solid-solid α' to α transition mechanism is observed upon heating to 150-160 ºC [92, 322, 331]. In a DSC heating scan, an exotherm appears prior to the dominant melting peak. This solid phase transition may be also achieved by an annealing process at elevated temperatures (120-160 ºC) [332]. It results in a rearrangement of the PLLA backbone side group packing within the unit cell to a more energy-favourable state. Thus, the lattice dimensions are reduced and a stronger interaction between the neighbouring chains is achieved [333].

- **The β–crystalline structure** was observed for the first time by Eling *et al.* [334] in 1982 and exhibits a T_m around 170-175 °C. This crystal form is considered as thermally less stable than its α-homologue due to its lower T_m. β crystals can grow upon mechanical stretching (molecular orientation) of their stable α-counterparts. This crystal-crystal transformation takes place at high temperatures and high hot-draw ratios [321, 323, 326]. According to Hoogsten *et al.* [324], this crystal form is characterized by an orthorhombic unit cell (*a*=10.31 Å, *b*=18.21 Å, *c*=9.00 Å) containing six chains in a left-handed 3_1 helical chain conformation even though Brizzolara *et al.* [335] suggested an orthorhombic unit cell with only two parallel chains. Recent studies of Puiggalí and co-workers [336] stated that the β-form exhibits a frustrated structure which contains only three 3_1 helix chains in a trigonal unit cell with the following dimensions: *a*=*b*=10.52 Å, *c*=8.80 Å. This structure is formed to accommodate the random up-down orientation of neighbour chains, which is associated with rapid crystallization conditions [333, 336]. To conclude, the crystal structure of the β form has not been resolved yet and further investigations are required.

- **The γ-crystalline structure** has been recently introduced by Cartier *et al.* [337] through epitaxial crystallization on a hexamethylbenzene substrate (low MW organic solvent). This crystal structure is characterized by two antiparallel helices with 3_1 helical conformation, packed in an orthorhombic unit-cell (*a*=9.95 Å, *b*=6.25 Å, *c*=8.80 Å). This crystalline form has only been induced by epitaxial crystallization [93, 333], to the best of the knowledge of the author.

The effects of the copolymer ratio (L- to D,L-) on both the glass transition temperature (T_g) and the melting temperature (T_m) have been extensively investigated [15, 263, 321, 338]. At a given MW, a roughly linear T_m depression, from 180 ºC for PLLA to 115 ºC and a T_g decrease from 63 ºC to about 55 ºC has been reported with increasing the D-lactide content, as shown in *figure 3.7*.

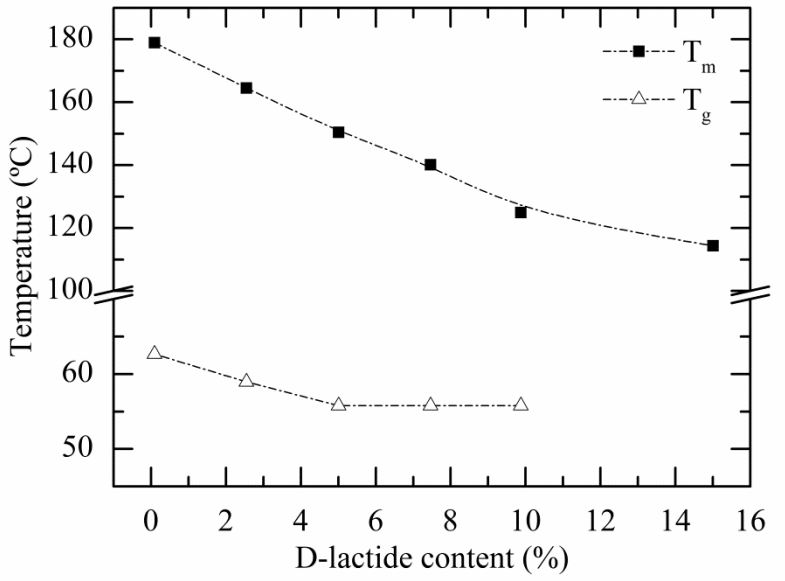

Figure 3.7. Effect of an increasing D-lactide content on the glass transition (T_g) and melting (T_m) temperatures, respectively (Adapted from *ref.* [321]).

An increase in the copolymer ratio equally decreases the rate and the degree of crystallisation (X_c), respectively [15, 263, 288, 320, 338, 339]. This trend is due to the formation of stereochemical "defects" in the PLLA's natural helical chain conformation. Above a D-lactide content of 7%, the crystallisation rate is extremely lengthy and the resulting polymer is no longer crystallisable (*i.e.* amorphous) [11].

Regardless of the D-lactide content, manufactured PLA parts are amorphous if no further treatments are applied after processing. This is due to the slow crystallization rate of PLA as compared to the cooling rates of high-throughput thermoplastic

processes. Consequently, T_g determines the upper use temperature for most commercial applications; restricting considerably the application fields of PLA products. Among the numerous procedures used to enhance X_c from the melt, the addition of low contents of isotactic PDLA (up to 15 wt.%) into isotactic PLLA has been reported as the most effective method [340, 341]. Stereocomplex crystallites are formed in PLLA/PDLA blends which acts as heterogeneous nucleation sites for subsequent PLLA crystallization.

b) Mechanical properties

Mechanical properties of PLA are usually comparable to those of PS or PET depending on the MW, the stereoregularity, X_c, the processing conditions and the degree of orientation [11, 278, 342, 343]. Similar to PS, amorphous PLA is defined as a stiff and brittle polymer with low strain at break (ε_b) which fractures through crazing mechanism under uniaxial tensile loading. Numerous authors reported a Young's modulus (E) ranged from 1 to 4 GPa, a tensile strength (σ_y) between 50 and 90 MPa and ε_b ranging from 2 to 8% [215, 317, 344, 345]. Its inherent brittleness does not only affect the end-use behaviour but also the handling and processing behaviours; thus leading to important drawbacks in large-scale productions [15, 346]. In the literature, two main reasons have been suggested in order to explain this behaviour:

- The characteristic ratio (C_∞) and the entanglement density (ν_e) parameters have been established as two important contributors to the deformation mechanisms for polymer glasses [27, 124, 217]. High C_∞ values correspond to stiff polymer chains, loosely entangled and which exhibit a brittle behaviour due to the crazing mechanism as mode of deformation. Regarding HMW PLA, C_∞ has been established from 9.1 to 11.7 and ν_e around 0.14 mmol.cm^{-3} [124, 217]. As compared to the characteristics network parameters of brittle isotactic PS (C_∞= 13.9, ν_e= 0.036 mmol.cm^{-3} (25°C)) [118] and ductile PE (C_∞= 5.7, ν_e= 0.615 mmol.cm^{-3} (25°C)), the reported C_∞ and ν_e values are in good agreement with the brittle behaviour experimentally observed.

- The high physical aging kinetics exhibited by amorphous PLA parts has drastic effect on their mechanical properties. While E and σ_y increase with aging, ε_b is strongly reduced leading to the "ductile-brittle" transition [27, 66, 345].

c) Fracture behaviour

Besides a large number of communications dealing with mechanical properties, only few studies report the fracture behaviour of PLA [241, 252, 316, 347-351].

Perego and coworkers [349] reported impact resistance values using Izod impact tests for amorphous PLA samples with viscosity average MW (M_v) ranging from 47 to 114 $kg.mol^{-1}$. Fairly similar impact strength values were found due to the complete glassy state of all the samples.

Grijpma and coworkers [350] investigated the impact resistance of oriented amorphous PLA samples using Charpy and Izod impact tests. For informational purposes, the different samples were obtained using a non-conventional injection moulding process in which the melt was cooled under oscillating shear conditions. Authors reported an enhancement of the impact behaviour with significant molecular orientations as compared to the non-oriented polymer.

Applying the *linear-elastic fracture mechanics* (LEFM) on single edge notched bend (SENB) samples, Park *et al.* [347, 351] and Nascimento *et al.* [348] studied the effect of loading rates and crystal fractions on the PLA fracture toughness (K_{IC}). Under plane strain conditions, higher K_{IC} values were found for samples loaded at low rates as compared to impact rates, regardless of X_c. For samples tested at low strain rates, the measured differences were attributed to an additional dissipation of energy due to the formation of multiple crazes in the vicinity of the crack tip. In contrast, this dilatational mechanism was suppressed at impact rates; giving rise to a lower relaxation of the stress concentrations and therefore to a depression in K_{IC} values.

Park and coworkers [347, 351] reported a decrease in the fracture toughness with increasing the crystallinity at low strain rates. This trend was attributed to a slight suppression of the multiple crazes formation in the crack tip region. In contrast, Nascimento and coworkers reported a reversed trend. A significant increase in K_{IC} values was found for semi-crystalline PLA samples (similar X_c) loaded at low strain rates. Differences of behaviour between both communications were attributed to different thermal histories and different processing conditions/methods.

Additional results of Park and coworkers [351] showed an enhancement of the PLA fracture toughness under impact rates with increasing the degree of crystallinity. This behaviour was attributed to an increase in the fibril formation process under impact rate.

Whereas only few communications report PLA fracture behaviour under plane-strain conditions, fracture properties of thin PLA films, which take place under plane-stress conditions, are rare. Recently, our research group [241] investigated the effect of a “de-aging” thermal treatment at T_g on the fracture toughness of amorphous

extruded-calendered PLA sheets with different optical purities using the concept of the *post-yield fracture mechanics* (PYFM).

Under plane-stress conditions, the EWF method was applied on de-aged and aged DDENT PLA specimens. Experimental results combined with digital image correlation (DIC) analysis showed that aged samples did not fully satisfy the EWF preconditions. Under tensile loading, this trend was attributed to the brittle behaviour of aged samples. Fracture parameters were compared to the G_{IC} values estimated by Park *et al.* [347] and Nascimento *et al.* [348] using the LEFM under plain-strain conditions. Significant differences were observed between both fracture mechanics values. The lower values reported by Gámez-Pérez *et al.* [241] were attributed to the difference in state of tensions between both analyses.

The de-aging thermal treatment significantly enhanced the fracture toughness of PLA samples and allows a proper analysis using the EWF concept. An increase in the essential work of fracture (w_e) and a decrease in the plastic term (βw_p) was found with increasing the D-lactide content. According to the authors, these tendencies are likely to be attributed to the dependence of the chain stiffness parameters on the D-la ctide content.

3.2. Materials selected for the study

3.2.1. Poly(lactic acid) grades

Two different commercial PLA extrusion grades, named PLA 4032D® and PLA 2002D®, were purchased from NatureWorks (Arendonk, Belgium) in pellets form. Their technical characteristics are compiled in *table 3.3*. During the course of this work, both PLA grades were distinguished by their respective D-lactide content.

NatureWorks recommends to dry PLA resins in-line to less than 250 parts per million (ppm) (<0.025 wt.%) moisture and to keep resins at this moisture level during the whole melt processing. A significantly reduced moisture content (<50 ppm) is highly recommended for melt processes with significant residence times and/or high processing temperatures (>240 ºC) [284, 352].

According to the technical data sheets, PLA-4 resin (*i.e.* PLA 2002D) is reserved for extrusion/thermoforming applications, including dairy, transparent food containers, blister packaging or even cold drink cups [282]. On the other hand, PLA-2 resin (*i.e.* PLA 4032D) is recommended for biaxially oriented sheet/film production with potential applications in laminations, printed films with higher curing temperatures or even other packaging applications [281].

Table 3.3. Technical specifications for both PLA grades used [281, 282].

Properties	ASTM method	Ingeo 2002D®	Ingeo 4032D®
Sample nomenclature	-	PLA-4	PLA-2
Tacticity	-	Random optical copolymers	
D-lactide content (%)	-	4.25	2
Relative viscosity	-	3.96	4.01
Density, ρ (g.cm^{-3})	D1505-03	1.24	1.24
Number-average molecular weight, M_n (kg.mol^{-1}) [a]	D5296-97	99	90
Weight-average molecular weight, M_w (kg.mol^{-1}) [a]	D5296-97	187	181
z-Average molecular weight (kg.mol^{-1}) [a]	D5296-97	337	351
Polydispersity index, *PDI* [a]	D5296-97	1.9	2.0
Melt Flow Index (g/10 min) (210ºC/2.16kg) [b]	D1238-04	5.8 ± 0.2	6.4 ± 0.3
Melting peak temperature, T_{mp} (ºC) [c]	D3418-03	152 ±1	167 ±1
End melting peak temperature, T_{me} (ºC) [c]	D3418-03	158 ±1	173 ±1
Degree of crystallinity, X_c (%) [c]	D3418-03	35 ±1	39 ±1

[a] Relative values determined for raw materials using SEC-DRI experiments (*c.f. chapter 5, section 5.1.4*).
[b] Determined for raw materials using MFI experiments (*c.f. chapter 5, section 5.1.3*).
[c] Determined for raw materials using DSC experiments, from the first heating cycle at 10 ºC.min^{-1} (*c.f. chapter 5, section 5.1.5. a*).

3.2.2. Styrene-acrylic multi-functional-epoxide oligomeric agent

Although diisocyanate compound was the first reactive agent used to achieve chain extension with PLA, the bifunctional molecules have a narrow processing window. Additionally, the interest in using this reactive agent is limited due to its high toxicity and its high volatility. Dianhydride and isocyanurate-based compounds presented an inefficient time reaction with PLA which initially leads to a degradation of the polymeric matrix. The liquid state of peroxide compounds makes their handling difficult when extruders are used.

On this basis, a styrene-acrylic multi-functional-epoxide oligomeric agent (referred to as SAmfE) has been selected for the present study to overcome the above limitations. It allows MW enhancement at a much broader range of processing temperatures. The improvement of shear and elongational properties of modified PLA with SAmfE have been already highlighted in deep-draw thermoforming and orientation processes [353]. Moreover, it is accepted by the Food & Drug Administration (FDA) to be used in food-contact packaging.

BASF (Ludwigshafen, Germany) kindly supplied a SAmfE grade in flake form under the commercial name Joncryl ADR-4300F®. Its semi-developed formula is shown in *figure 3.8* and its technical specifications are listed in *table 3.4* [354].

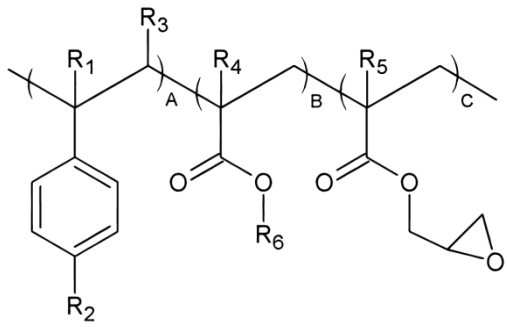

Figure 3.8. Semi-developed formula of the SAmfE agent (based on [354]).

Where R_1 to R_5 groups are hydrogen atoms (H), methyl groups (CH_3), higher alkyl groups or a combination of them and R_6 an alkyl group. Its molecular chain is composed of three classes of solid or liquid monomers: styrenics (referred to as repeat unit A), methacrylates (referred to as repeat unit B) and glycidyl acrylates (an epoxy-functional acrylate) (referred to as repeat unit C) and are each between 1 and 20.

Table 3.4. Technical characteristics for the SAmfE agent [354].

Properties	**Joncryl ADR-4300F®**
Material nomenclature	SAmfE/ reactive agent
Particle size (mm)	2.5 - 4.0
Specific gravity	1.08
Weight-average molecular weight, M_w (g.mol^{-1})	5500
Epoxy equivalent weight (g.mol^{-1})	433
Functionality	≈12
Glass transition, T_g (ºC)	56
Typical dosage (%)	0.1-1.0
Processing temperature range (ºC)	170-330
Glassy state	amorphous

Chapter 4: Processing methods

4.1. Laboratory-scale: Internal mixer

Both PLA grades were blended with different concentrations of reactive agent at a laboratory scale using an internal mixer (Brabender Plastic-Corder W50EHT, Brabender GmbH & Co., Duisburg, Germany), equipped with a torque measuring system. Torque data acquisition was performed using a commercial WinMix Brabender Mixer software version 3.2.31. The mixing chamber had a volume of 55 cm^3 and was equipped with two counter-rotating mixing screws (roller blade type "W"). Three different electrical heating elements and a compressed air cooling system allowed temperature conditioning in the mixing chamber. The bulk temperature of the processed material was measured using a separate thermocouple situated in the mixing chamber.

Prior to processing, both PLA grades were vacuum-dried overnight at 55 °C over silica gel in order to remove any excess moisture. SAmfE was dried overnight under vacuum at room temperature (23 ºC ±2) over silica gel. The mixing chamber was preheated at a nominal temperature of 180 ºC and the screw rotation speed was set to 50 rpm. Initially, the mixing chamber was purged with nitrogen (N_2, 3 bars) for 2 min in order to remove the ambient atmosphere. Once all the setting conditions were optimized, 50 g of pre-dried PLA was introduced into the mixing chamber and the N_2 blanket was established. Due to the solid state of both PLA grades, the initial torque value increased considerably. Afterward, the high torque peak rapidly decreased due to the melting of the polymer. A completely melted state was observed within 4 minutes. The corresponding amount of SAmfE, as detailed in table *4.3*, was introduced into the mixing chamber at this time. This was considered as the starting point of all the experiments.

In a first step, for each preparation, torque (Γ) vs. mixing time (t) was monitored for a prolonged time in order to follow the evolution of the reaction. An optimum reaction time of 13 min was deduced from these mixing experiments, as it will be explained in *section 6.2* (*c.f. chapter 6*). Fresh blends were equally processed applying this optimum reaction time of 13 min. The internal mixer was stopped and the material was discharged and cooled to room temperature.

The obtained material was ground into pellets using a cutting mill (Pulverisette 15, Fritsch GmbH, Idar-Oberstein, Germany) and vacuum-dried overnight at 55°C

over silica gel. Plates with a nominal thickness of 1 mm were prepared by compression moulding at 200 ºC for 7 minutes (40 bars) in an IQAP LAP PL-15 hot plate press (IQAP Masterbatch SL, Barcelona, Spain), equipped with temperature and pressure regulating systems. Then, the sample was transferred to the cold part of the press (equipped with an attached water-cooling system) for 3 min and quickly cooled to room temperature at approximately -50 ºC.min^{-1}. Laboratory-scale processing conditions are summarized in *table 4.1*.

Table 4.1. Laboratory scale processing conditions.

Processing parameters	Conditions	Observations
Drying stage		
PLA		
Temperature (ºC)	55	-
Time (h)	overnight	over silica gel
SAmfE		
Temperature (ºC)	23 ±2	Room temperature
Time (h)	overnight	over silica gel
Melt processing stage		
Screw speed (rpm)	50	-
Residence time (min)	13	Nitrogen blanket
Set point temperature (ºC)	180	-
SAmfE nominal concentration (wt.%)	0.5 and 1	-
Compression moulding stage		
Heating		
Temperature (ºC)	200	-
Time (min)	7	-
Pressure (bars)	40	-
Cooling		
Temperature (ºC)	23	Room temperature
Time (min)	3	-
Cooling rate	≈ -50 ºC.min^{-1}	-

4.2. Pilot-plan scale: One-step reactive extrusion-calendering

In this section, the main emphasis is on a continuous process, which can be commercially viable or used as a model for commercial processes. The scaling up of the laboratory-scale conditions was performed using a co-rotating twin screw extruder with a screw diameter of 25 mm (L/D=36) (KNETER 25X24D, Collin GmbH, Ebersberg, Germany).

Prior to processing, raw PLA pellets were dried at 80ºC for 3 hours in a PIOVAN (DSN506HE, Venice, Italy) hopper-dryer (dew point = -40ºC) and kept under the

same drying temperature over the whole processing time. The reactive agent was powdered using a mortar and pestle and stored overnight under vacuum at room temperature over silica gel. It is well established that the reaction kinetics between hydroxyl groups and epoxy ring is notoriously slow [355]. Consequently, a maximum screw speed of 40 rpm was chosen in order to maximize the residence time. It was eventually established to 4.33 min.

Intermeshing co-rotating twin screws featuring three kneading blocks, each 100 mm in length, equally distributed along the screw length were used, as schematically illustrated in *figure 4.1*. The extruder features seven heating zones set at 150, 160, 160, 160, 170, 175 and 175 °C from the feeding zone to the die, respectively.The extruder was operated by starve feeding at a constant rate of 2.54 $kg.h^{-1}$. Both polymer and SAmfE were simultaneously introduced in the hopper of the feeding zone under a nitrogen blanket (2,5 bars) after that the extrusion line was started and stabilized with raw PLA. The feeding rate of the SAmfE was adjusted to the polymer feeding rate in order to process each formulation described in *table 4.3*. Vacuum was applied in the metering zone to remove volatiles created during the reactive stage.

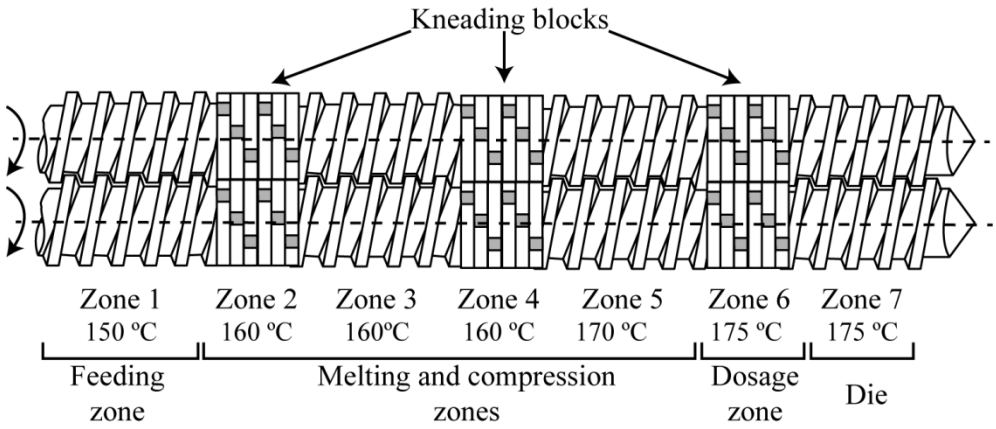

Figure 4.1. Schematic representation of the intermeshing co-rotating twin screws with a 25 mm diameter.

The melted materials were extruded through a sheet die and calendered on a vertical three-polished chrome roller stack (Techline CR72T, Collin GmbH, Ebersberg, Germany), equipped with a water-cooling system. The chill roll (D=72 mm) temperature was set to 50 ºC with a rotation speed of 1.25 rpm. Calendered sheets with a nominal thickness of 1 mm and a nominal width of 100 mm were manufactured. The processing conditions of the one-step reactive extrusion calendering process are summarized in *table 4.2*. This allows for the production of 25 $m.h^{-1}$ of calendered sheets which affords a sufficient quantity of materials to perform a complete thermal, rheological, mechanical and fracture characterization.

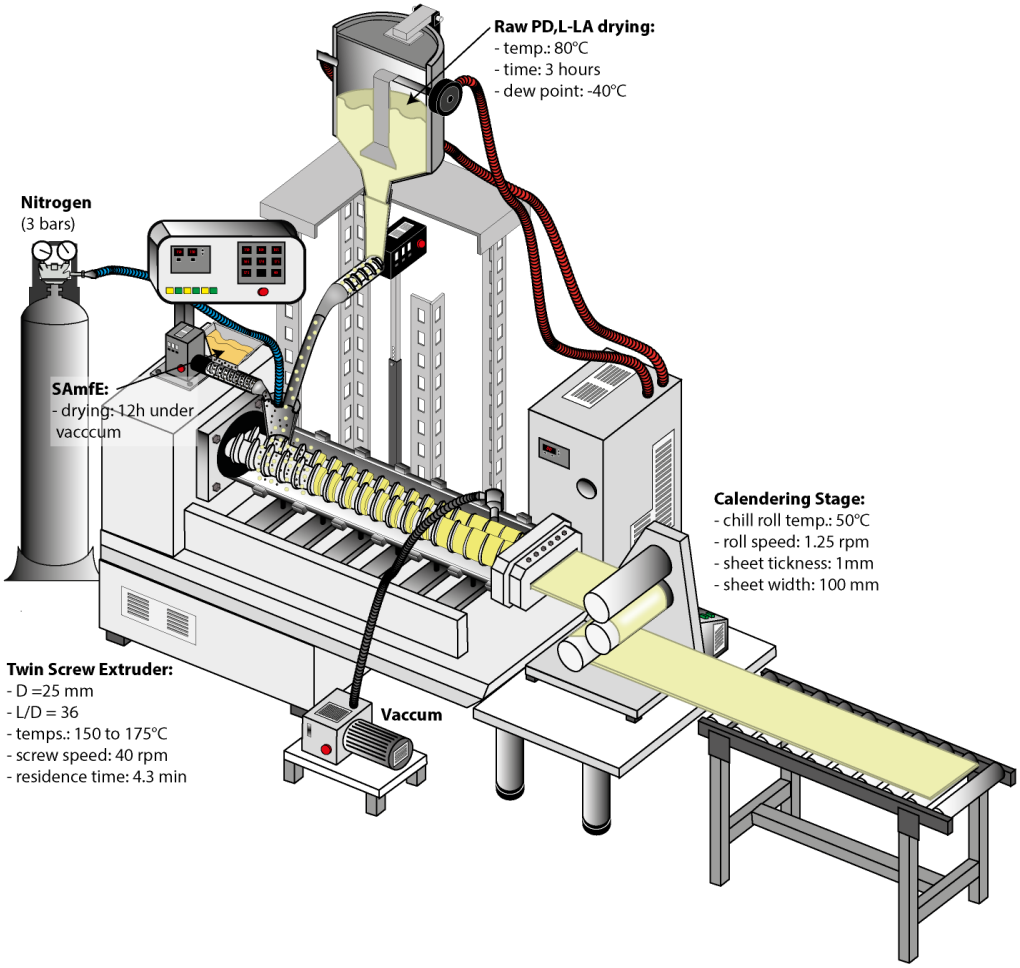

Figure 4.2. Schematic representation of the one-step reactive extrusion-calendering process.

The complex viscosity at 0.08 rad.s^{-1} was used as a monitoring parameter over extrusion time, as it will be explained in *section 7.1.1* (*c.f. chapter 7*). It was observed that the viscosity monotonously increased with the extrusion time up to reach a constant value. At this point (≈ 20 min), no further increase in the viscosity values was observed with the extrusion time, suggesting a similar degree of structural modifications.

Accordingly, samples prior to the SAmfE addition (referred to as PLA4 and PLA2) and from the stabilized viscosity regime were analyzed (referred to as PLA4-REX0.5, PLA2-REX0.5 and PLA2-REX0.6). All prepared samples are summarized in *table 4.3*.; samples were distinguished by their different D-lactide content and the nominal amount of added SAmfE.

Table 4.2. Pilot plant scale processing conditions.

Processing parameters	Conditions	Observations
Drying stage		
PLA		
Temperature (ºC)	80	Dew point (-40ºC)
Time (h)	3	-
SAmfE		
Temperature (ºC)	23	Room temperature
Time (h)	overnight	over silica gel
Reactive extrusion stage		
Screw speed (rpm)	40	-
Residence time (min)	4.33	-
Temperature profile		
Zone 1 (ºC) (Feeding zone)	150	Nitrogen blanket SAmfE addition
Zone 2 (ºC)	160	-
Zone 3 (ºC) (melting and	160	-
Zone 4 (ºC) compression zones)	160	-
Zone 5 (ºC)	170	-
Zone 6 (ºC) (Dosage zone)	175	Vacuum applied
Zone 7 (ºC) (die)	175	-
Calendering stage		
Chill roll temperature (ºC)	50	-
Chill roll speed (rpm)	1.25	-

4.3. Sample nomenclature and de-aging thermal treatment

In the current study, all prepared samples are specified in *table 4.3*; the samples were distinguished by their different D-lactide content, the amount of added SAmfE and the type of melt processing.

After processing, the inherent brittleness of PLA does not only affect the end-use behaviour of PLA parts reserved for commercial applications but also the material handling at laboratory scale. This brittle behaviour usually leads to important drawbacks during sample preparation. Takahashi *et al.* [356] and Gámez-Pérez *et al.* [241] reported that these issues may be minimized by applying a "de-aging" thermal treatment at T_g or slightly above T_g to PLA.

On this basis, a thermal treatment, as illustrated in *figure 4.3*, was applied to extruded sheets in order to avoid excessive edge defects during cutting samples for mechanical characterizations. In a typical procedure, sheets were heated to 60 ± 1 ºC for 40 min in a convection oven (J.P. Selecta, s.a., Barcelona, Spain) and subsequently quenched in an ice water bath (2 ± 2 ºC) for 15 min. After drying, the different

samples were immediately extracted from the center of the sheet, parallel to the main axis of the machine direction (MD) and/or to the transversal direction (TD).

Table 4.3. Formulation and nomenclature of all investigated samples.

Melt processing	PLA grade	Sample nomenclature	Nominal amount of SAmfE (wt.%)	Mesured SAmfE content (wt.%) [a]
Internal mixer	Ingeo 2002D®	PLA-4 "neat"	0	-
		PLA-4+0.5J	0.5	-
		PLA-4+1J	1	-
	Ingeo 4032D®	PLA-2 "neat"	0	-
		PLA-2+0.5J	0.5	-
		PLA-2+1J	1	-
One-step reactive extrusion-calendering	Ingeo 2002D®	PLA4	0	-
		PLA4-REX0.5	0.5	0.5 ±0.1
	Ingeo 4032D®	PLA2	0	-
		PLA2-REX0.5	0.5	0.5 ±0.1
		PLA2-REX0.6	0.6	0.6 ±0.1

[a] Determined using FT-IR experiments (*c.f. chapter 5, section 5.1.1*). Values determined only for extruded samples due to possible loss of SAmfE content induced by the dynamic nature of the process.

As it will detailed in *section 7.5* (*c.f. chapter 7*), the influence of the thermal history on the dynamic mechanical thermal, mechanical and fracture behaviour is investigated. That is, de-aged samples (referred to as Da) were tested immediately after the end of the "de-aging" thermal treatment. On the other hand, physical aged samples were stored at room temperature for one week prior to testing in order to simulate industrial storage conditions.

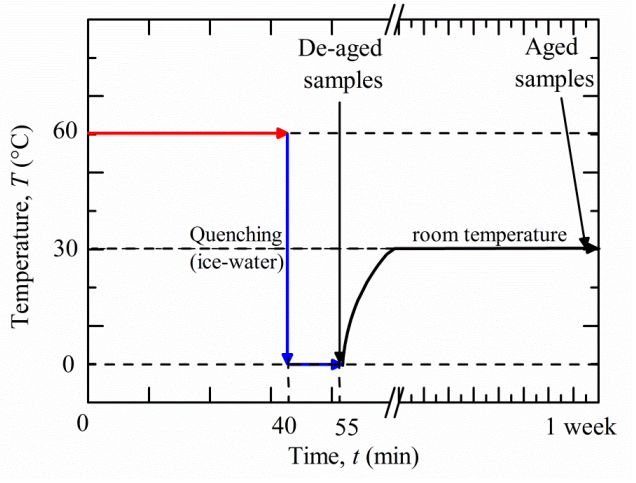

Figure 4.3. Plot illustrating the thermal treatment applied to the extruded sheets after processing.

Chapter 5: Experimental methods

5.1. Physico-chemical characterization

5.1.1. Fourier Transform-Infrared Spectroscopy (FT-IR)

Infrared spectra were recorded on a Nicolet 6700 FT-IR spectrometer (Thermo Fisher Scientific, Waltham, MA, USA) using the transmission sampling technique. Spectra were obtained in the wavenumber interval ranging from 400 to 4000 cm^{-1} with a total of 32 scans and a resolution of 4 cm^{-1}. Data were acquired and analyzed using a commercial OMNIC software version 7.3 Service Pack 1.

- **Spectral analysis**

Prior to analyzing, amorphous thin films with a thickness lower than 25 μm were cast from tetrahydrofuran (THF) solutions onto glass plates. In a typical procedure, a 150 mL beaker equipped with a magnetic stirrer was charged with 75 mL of THF and pre-heated at 60 °C for 10 min. At a stirring speed of 300 min^{-1}, one gram of each compression moulded plate and extruded sheet was dissolved for 40 min.

Then, 5 to 6 drops of each sample solution were deposited on a glass plate and quickly transferred to a convection oven (J.P. Selecta s.a., Barcelona, Spain) at 50 °C for 5 min in order to avoid crystallization and to completely remove the THF.

- **Quantitative determination of the SAmfE content**

Based on the Beer-Lambert law (*c.f. equation 5.1*), an internal standard FT-IR method was used to estimate the SAmfE content. This analysis was only performed on extruded sheets due to possible loss of reactive agent induced by the dynamic nature of the process.

$$A = \varepsilon . C . l \qquad \textbf{(5.1)}$$

Where A is the absorbance, ε the molar attenuation coefficient, C the molar concentration of the attenuating species and l the path length.

Based on the above experimental conditions, 10 different solutions were prepared by dissolving a total amount of one gram of PLA together with several concentrations of reactive agent (ranging from 0 to 50 wt.%). Then, each sample solution was cast onto glass plates. The peak areas corresponding to the vibration of the SAmfE aromatic ring (1601 and 1493 cm^{-1}) were measured and normalized to the peak area corresponding to the stretching vibrations of the PLA C-OO groups (870 cm^{-1}) defined as the internal standard, respectively, according to *equation 5.2*.

$$\frac{A_{SAmfE}}{A_{PLA}} = k\frac{C_{SAmfE}}{C_{PLA}} \qquad \textbf{(5.2)}$$

Where A_{SAmfE} is the absorbance peak area of a characteristic SAmfE group and C_{SAmfE} the percentage of reactive agent into the solution. A_{PLA} is the absorbance peak area of a characteristic PLA group and C_{PLA} the percentage of PLA into the solution. k is the relative response factor.

The resulting calibration curves are plotted in *figure 5.1*. k was determined from the measured slope as indicated in each curve. Analysis of the two independent sets of calibration revealed good linear relations between the relative peak areas and relative concentrations of the compounds of interest. As expected, a clear deviation of this linearity was observed for high C_{SAmfE}/C_{PLA} ratios. Therefore, these experimental points were discarded from the linear fitting analysis.

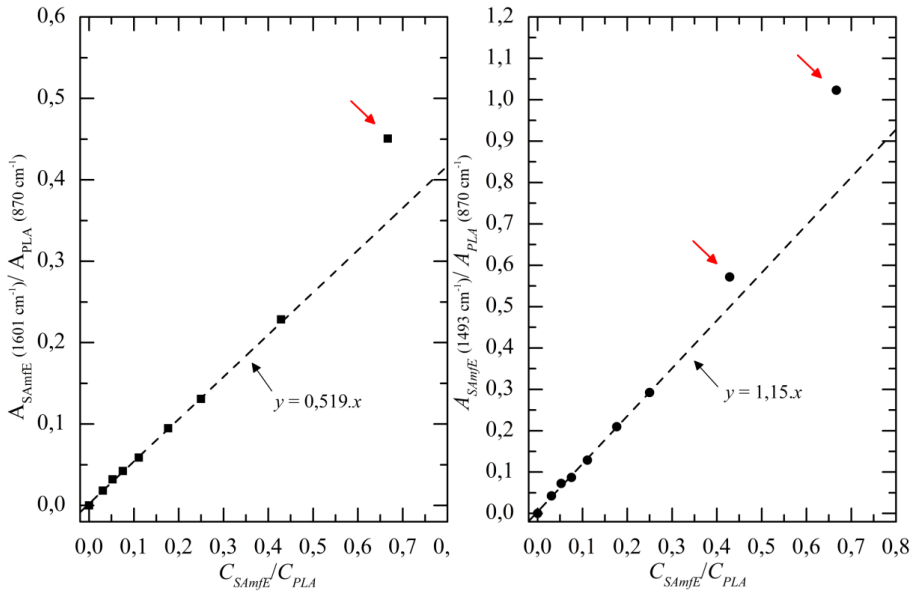

Figure 5.1. FT-IR calibration curves. Experimental points indicated by a red arrow were omitted from the linear fitting analysis. The relative response k is indicated for each curve.

5.1.2. Nuclear Magnetic Resonance (NMR)

^{1}H NMR spectra were obtained using a Bruker AMX spectrometer (Bruker Corporation, Billerica, MA, USA) operating at 300 MHz for proton investigation with tetramethylsilane (TMS) as internal standard. Data were acquired and analyzed using a commercial Bruker WinNMR software version 4.0. Prior to testing, all samples were dissolved in a deuterochloroform solution ($CDCl_3$) with a concentration of 30 mg.mL^{-1}. A total of 64 scans with 32k data points were recorded with a relaxation delay of 1s.

5.1.3. Melt Flow Index (MFI) and melt density determination

The melt flow index of PLA raw materials was measured using a CEAST MELTVIS 6542/002 apparatus (CEAST, Pianezza, TO, Italy) according to the ASTM 1238-04c standard. The temperature was set to 210 °C and the weight used was equal to 2.16 kg. Prior to testing, pellets were vacuum-dried overnight at 55 °C over silica gel in order to remove any excess moisture.

The melt density of all extruded sheets was experimentally determined using a flow test apparatus 4106 (Zwick Roell, Ulm, Germany) at 180 ºC. PLA sheets were ground into pellets using a cutting mill (Pulverisette 15, Fritsch GmbH, Idar-Oberstein, Germany) and vacuum-dried overnight at 55°C over silica gel. 5 grams were charged into the device cylinder, preheated for 35 s and subsequently loaded with a weight of 12.5 kg. The portion of the cylinder between 110 and 140 mm above the bottom of the piston was used to determine the melt flow-volume rate (MVR). In this same interval range, cuts of the extrudate were taken at uniform time intervals of 10 s in order to determine the MFI value. Calculation of the melt density (ρ) at 180 ºC proceeds according to *equation 5.3*.

$$\rho = \frac{MFI}{MVR} \qquad \textbf{(5.3)}$$

5.1.4. Size Exclusion Chromatography (SEC)

MWDs were measured on an Agilent HPLC model Infinity 1260 SEC system (Agilent Technologies, Santa Clara, CA, USA) with differential refractive index detection (SEC-DRI) at room temperature. An Agilent PL HFIPgel (300 x 7.5 mm) specialist column with a separation range from 200 to 800 kg.mol^{-1} was used at a flow rate of 1mL.min^{-1}. Hexafluoroisopropanol (1,1,1,3,3,3-hexafluoro-2-propanol, HFIP) containing 0,02 mol.L^{-1} of sodium trifluoroacetate to prevent polyelectrolyte effect was used as eluent. Filtered samples were injected at a volume of 100 µL. Measurements were repeated three times using fresh samples in order to improve accuracy. A total of 7 narrow poly(methyl methacrylate) standards with MWs

covering the entire MW range of the investigated samples (from 2 to 900 kg.mol^{-1}) were injected to perform the log M_w versus retention time calibration via the peak position method [357]. Data were acquired and analyzed using a commercial Agilent Chemstation software version B.04.03.

In order to perform a reliable molecular analysis, some important prerequisites were taken into account prior to testing. The **full dissolution** of the sample was assured by dissolving a predetermined amount of each material for 20 minutes at room temperature. The stationary phase (Polystyrene/Divinylbenzene) was selected in order to **avoid absorption issues**. An **appropriate injection concentration** was calculated in order to **avoid shear degradation** in the injector due to viscous fingering according to *equation 5.4* [358].

$$[\eta] * C * 0.1 * V_{inj} < 0.5 \; to \; 1 \qquad (\mathbf{5.4})$$

Where $[\eta]$ corresponds to the intrinsic viscosity (dL.g^{-1}), C is the injection concentration (g.L^{-1}) and V_{inj} is the injection volume (mL)

Figure 5.2 illustrates the characteristic molecular weight averages on a MWD spectrum. Calculations of the **number-average molecular weight** ($\boldsymbol{M_n}$), **the weight-average molecular weight** ($\boldsymbol{M_w}$) and **z-average molecular weight** ($\boldsymbol{M_z}$) proceed according to [359, 360]:

Discrete spectrum	Continuous spectrum	
$M_n = \frac{\sum_i w_i}{\sum_i w_i/M_i} = \frac{\sum_i n_i M_i}{\sum_i n_i}$	$M_n = \frac{\int_0^\infty w(M)dM}{\int_0^\infty w(M)/MdM}$	(**5.5**)
$M_w = \frac{\sum_i w_i M_i}{\sum_i w_i} = \frac{\sum_i n_i {M_i}^2}{\sum_i n_i M_i}$	$M_w = \frac{\int_0^\infty M.w(M)dM}{\int_0^\infty w(M)dM}$	(**5.6**)
$M_z = \frac{\sum_i w_i {M_i}^2}{\sum_i w_i M_i} = \frac{\sum_i n_i {M_i}^3}{\sum_i n_i {M_i}^2}$	$M_w = \frac{\int_0^\infty M^2.w(M)dM}{\int_0^\infty M.w(M)dM}$	(**5.7**)

Where w_i is the weight-fraction of the component molecules i, M_i the molar mass of the component molecules of type i and n_i the number fraction of the component molecules i.

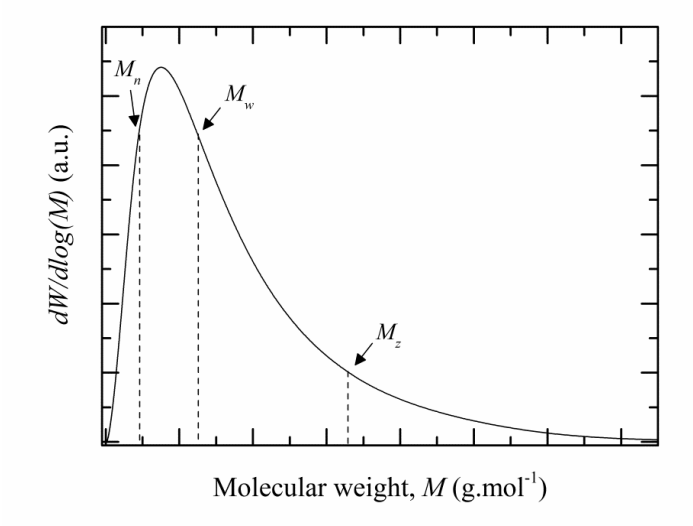

Figure 5.2. Molecular weight spectrum with a Schultz-Flory distribution. Dashed lines indicate the position of M_n, M_w and M_z values (Adapted from *ref.* [359, 360]).

The width of the MWD is often defined as the **polydispersity index** (***PDI***). Regarding samples featuring a Schultz-Flory-type MWD, the *PDI* is defined as follows [107, 359]:

$$PDI = \frac{M_w}{M_n} \qquad (\mathbf{5.8})$$

5.1.5. Differential Scanning Calorimetry (DSC)

DSC experiments were performed on a MDSC Q2000 instrument (TA Instrument, New Castle, DE, USA) coupled to a refrigerated cooling system. Temperatures and the heat of fusion were calibrated with indium at 10 ºC.min^{-1}. The heat capacity constant was calibrated with sapphire. All experiments were conducted under dry nitrogen atmosphere. The sample weight was 5-6 mg and Tzero DSC aluminium pans were used. A commercial TRIOS software version 3.0.1.3156 (TA Instruments) was used for data analysis. DSC experiments were divided into four different groups:

a) Standard thermal analysis

Experiments were conducted at a heating/cooling rate of 10 ºC.min^{-1} using the following protocol:

- **First heating scan (H1)** from 30 °C to 200 °C and isothermally held at 200 °C for t_{eq}=2 min in order to reveal the thermal transitions and to erase the previous thermal history, respectively.

- **Cooling scan (C)** from 200 °C to 30 °C in order to induce a controlled or "standard" thermal history and isothermally held at 30 °C for t_{eq}=1 min.
- **Second heating scan (H2)** from 30 °C to 200 °C in order to determine the thermal properties.

It is noteworthy to mention that each of the DSC measurements was repeated three times using fresh samples in order to improve accuracy.

From the above steps, the following characteristic parameters were determined:

- **The midpoint glass transition temperature** ($\boldsymbol{T_{g,m}}$). It was reported as the temperature at the half-height of the heat capacity increase ($1/2\Delta C_p$) which is also called the "temperature of half-unfreezing". The midpoint was preferred for the determination of T_g, as this method has been established more reliable than the method using the "onset" temperature [56].
- The cold crystallization transition was defined by two parameters: **The cold crystallization temperature** ($\boldsymbol{T_{cc}}$) was determined as the point where the exotherm reached a minimum and **the cold crystallization enthalpy** ($\boldsymbol{\Delta H_{cc}}$) by integrating the corresponding area underneath the cold crystallization peak.
- The melting transition was defined by three parameters: **The melting peak temperature** ($\boldsymbol{T_{mp}}$) was determined as the point where the endotherm reached a maximum and **the end melting temperature** ($\boldsymbol{T_{me}}$) as the high temperature end peak of the melting endotherm. **The melting enthalpy** ($\boldsymbol{\Delta H_m}$) was determined by integrating the corresponding area underneath the melting peak.
- The crystallization transition during the cooling run was defined by two parameters: **The crystallization temperature** ($\boldsymbol{T_c}$) was determined as the point where the exotherm reached a minimum and **the crystallization enthalpy** ($\boldsymbol{\Delta H_c}$) by integrating the corresponding area underneath the cold crystallization peak.
- **The degree of crystallinity** ($\boldsymbol{X_c}$) was calculated from the first and second heating scans according to *equation 5.9*:

$$\chi_c(\%\, Crystallinity) = \frac{\Delta H_m - \Delta H_{cc}}{\Delta H_m^0}.100 \qquad \textbf{(5.9)}$$

Where ΔH_m is the melting enthalpy and ΔH_{cc} the cold-crystallization enthalpy. ΔH_m^0 is the melting enthalpy for a 100 % crystalline PLA specimen (*i.e.* ΔH_m^0=93.6 J.g^{-1}, [215]).

b) Thermal fractionation: chain structural heterogeneity distribution

✓ **Self-nucleation procedure (SN)**

According to the methodology developed by Fillon *et al.*[79] and later refined by other authors [68, 81, 361], self-nucleation (SN) experiments were carried out using the following thermal protocol (see *figure 5.3* for a schematic representation of the SN procedure):

- **(a) Erasure** of the previous thermal history by heating the sample to 200 ºC for t_{eq}=2 min.
- **(b) Cooling scan** from 200 °C to 30 °C at 10 °C.min^{-1} in order to induce a controlled or "standard" thermal history and isothermally held at 30 °C for t_{eq}=1 min.
- **(c) Heating scan** from 30 °C to a selected self-seeding temperature (T_s) at 10 °C.min^{-1} located in the final melting temperature range.
- **(d) Isothermal step** at T_s for t_{eq}=5 min.
- **(e) Cooling scan** from T_s to 30 °C at 10 °C.min^{-1} and isothermally held at 30 °C for t_{eq}=1 min.
- **(f) Heating scan** from 30 °C to 200 °C at 10 °C.min^{-1}.

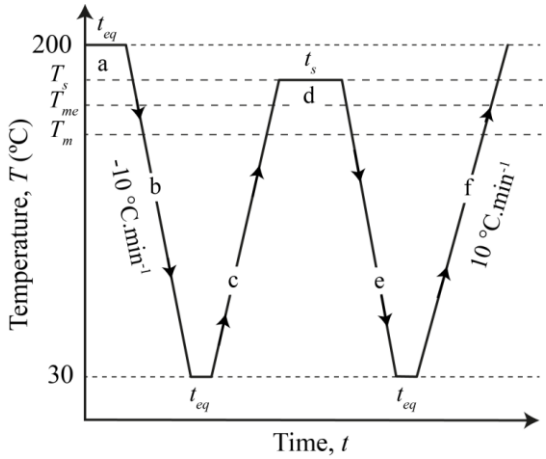

Figure 5.3. Schematic representation of the self-nucleation procedure. The letters indicate the running step.

Steps **a** to **f** were repeated at different T_s in order to cover the final melting temperature range of the sample considered. Depending on the T_s selected, the polymer displays three different behaviours due to the so-called self-nucleation domains as defined by Fillon *et al.* [79]. A schematic representation of the three domains is illustrated in *figure 5.4*.

Domain I (or complete melting domain): sample is heated to a high T_s temperature which is usually located well above T_{mp}. On subsequent cooling (step **e**), no change in the crystallization temperature is observed as compared to the standard T_c recorded in step **b**. This trend indicates that the number of nuclei remains constant and minimal.

Domain II (or exclusive self-nucleation domain): sample is heated to a T_s temperature which should be high enough to melt almost all of the polymer crystals, but low enough to leave "small" crystal fragments that can later self-seed the polymer during cooling [361]. This temperature is usually located in the upper part of the melting range. On subsequent cooling step (step **e**), T_c shifts to higher temperatures as compared to the standard T_c recorded in step **b**.

Domain III (or self-nucleation and annealing domain): In this range, partial melting takes place. The unmelted and annealed crystals at T_s modify the subsequent DSC trace in four different points: (a) in step **e**, recrystallization appears just below T_s, and/or (b) the crystallization exotherm may exhibit two peaks, (c) in step **f**, the shape of the melting transition is significantly modified and/or (d) an extra endothermic peak possibly appears at higher temperatures due to the melting of the annealed crystals at T_s.

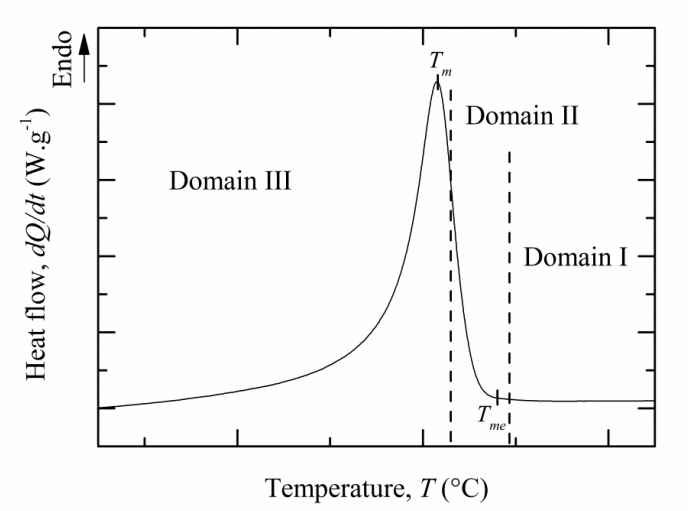

Figure 5.4. Melting endotherm in the "standard" state and indication of the different domains. Domains I, II and III correspond to complete melting, self-nucleation and incomplete melting domains, respectively (Adapted from *ref.* [79, 90]).

✓ Successive self-nucleation and annealing procedure (SSA)

The Successive self-nucleation and annealing procedure (SSA) is based on the accumulation of self-nucleation and annealing steps which promotes the potential molecular fractionation during crystallization. This thermal fractionation procedure

has been designed and first reported by Müller *et al.* [78] dealing with various PE systems. As schematically illustrated in *figure 5.5*, the SSA methodology was applied to samples using the following protocol:

- **(a) Erasure** of the previous thermal history by heating the sample to 200 ºC for 2 min.
- **(b) Cooling scan** from 200 °C to 30 °C at 10 °C.min^{-1} in order to create a controlled or "standard" thermal history and isothermally held at 30 °C for t_{eq}=1 min.
- **(c) Heating scan** at 10 °C.min^{-1} from 30 °C to a selected self-seeding temperature which corresponds to the lowest T_s temperature within *Domain II*. This first T_s (referred to as T_{s1}) must be determined previously by performing separated SN experiments.
- **(d) Isothermal step** at T_{s1} for t_{eq}=5 min.
- **(e) Cooling scan** from T_s to 30 °C at 10 °C.min^{-1} and isothermally held at 30 °C for t_{eq}=1 min.
- **(f) Steps c to e were repeated** at increasingly lower T_s and the difference in T_s were kept constant at 5°C. The number of repetition was set to 5 and 6 for PLA-4 and PLA-2 based materials (*c.f. table 5.1*), respectively, in order to cover the entire melting range of the sample featuring a standard thermal history.
- **(g) Heating scan** from 30 °C to 200 °C at 10°C.min^{-1} to reveal the multiple melting endotherms.

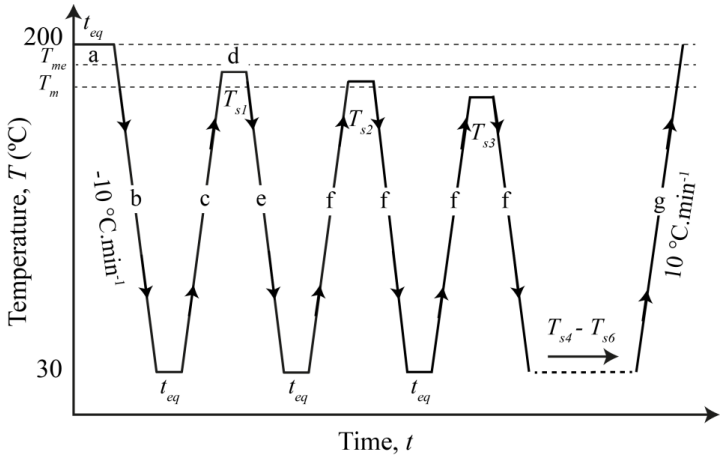

Figure 5.5. Schematic representation of the SSA technique steps (Adapted from *ref.* [68, 362]).

An optimum self-nucleation T_{s1} was defined for all unmodified samples, as it will be explained in *sections 6.6.1*(*c.f. chapter 6*) and *7.6.2.a* (*c.f. chapter 7*), respectively. For

each PLA type, the initial T_{s1} was kept constant for unmodified and reactively modified samples in order to study the effect of the structural modifications on the molecular fractionation. *Table 5.1* summarizes the different T_s used to perform thermal fractionation according to the type of melt processing.

Table 5.1. Self-seeding temperatures pattern for PLA-2 and PLA-4 based samples.

Melt processing	Sample nomenclature	T_{s1} (°C)	T_{s2} (°C)	T_{s3} (°C)	T_{s4} (°C)	T_{s5} (°C)	T_{s6} (°C)
Internal mixer	PLA-2 "neat"	169	164	159	154	149	144
	PLA-4 "neat"	154	149	144	139	134	-
One-step reactive Extrusion-calendering	PLA2	171	166	161	156	151	146
	PLA4	156	151	146	141	136	-

c) Physical aging analysis

This section presents the experimental procedure to evaluate the physical aging kinetics based on enthalpy relaxation measurements. These measurements were carried out on a PerkinElmer Pyris 1 device (Perkin Elmer, Waltham, MA, USA) coupled to a 2P intracooler. Experiments were conducted under dry nitrogen atmosphere. Temperature and heat of fusion were calibrated with lead and indium at 10 ºC.min^{-1}. The instrumental baseline was run from time to time, and the baseline was subtracted from the sample run. The sample weight was 5-6 mg and standard DSC aluminium pans were used. A commercial TRIOS software version 3.0.1.3156 (TA Instruments) was used for data analysis.

Since the enthalpy recovered (δ_H) during physical aging is dependent on both the thermal history that a glass experiences and the experimental variables (*e.g.* cooling and heating rates, annealing time and temperature), all of these parameters were fixed between samples. As schematically illustrated in *figure 5.6*, samples were aged at T_a = 30 ºC ($T_a \approx T_g$ -30 °C) for different aging times (t_a) using the following thermal protocol:

- **(a) Erasure** of the previous thermal history by heating the sample to 200 ºC for t_{eq}=2 min.
- **(b) Quenching** from 200 °C to -10 °C at 100 °C.min^{-1} (maximum cooling rate of the device) and isothermally held at -10 °C for t_{eq}=2 min. Samples were quenched into the glassy state at a high rate in order to create poorly stabilized glasses with large values of excess enthalpy. Thus, enthalpy relaxations are enhanced during annealing.
- **(c) Heating scan** from -10 °C to 10 °C at 50 °C.min^{-1} in order to bring samples quickly to the starting temperature.

- **(d) Heating scan** from 10 °C to 80 °C at 10 °C.min^{-1} in order to record the de-aged state of the sample (referred to as "*quenched reference sample*" for further analysis).
- **(e) Erasure** of the previous thermal history by heating the sample to 200 ºC for t_{eq}=2 min.
- **(f) Quenching** similar to step **(b)**
- **(g) Heating scan** from -10 °C to T_a =30 °C at 50 °C.min^{-1} in order to bring samples quickly to the physical aging temperature ($T_a \approx T_g$ - 30 °C).
- **(h) Isothermal step** at 30 °C for t_a=10 min in order to induce an aged state.
- **(i) Quenching** from 30 °C to -10 °C at 100 °C.min^{-1} and isothermally held at -10 °C for t_{eq}=2 min.
- **(j) Heating scan** similar to step (c).
- **(k) Heating scan** from 10 °C to 80 °C at 10 °C.min^{-1} in order to reveal the aged state of the sample
- **(l) Steps (e) to (k) are repeated** at increasingly higher t_a in order to generate different aged states. The number of repetition was set to 6 using the following t_a: 30, 70, 100, 300, 700 and 1000 min.

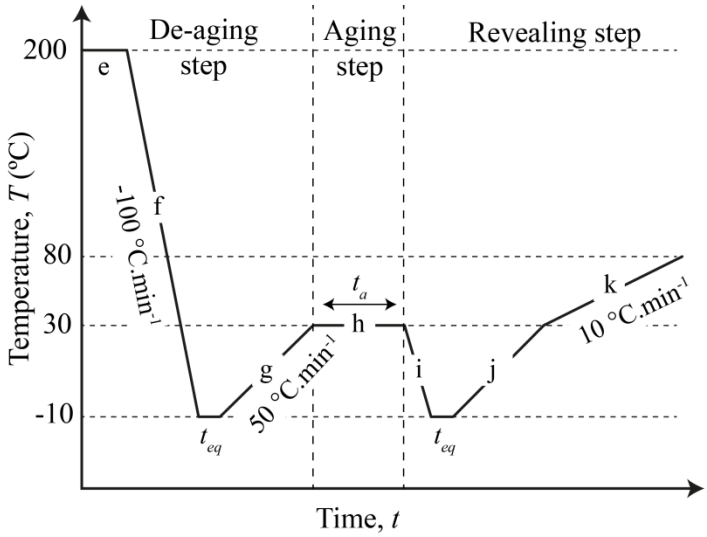

Figure 5.6. Schematic representation of the physical aging and annealing procedure.

As a result of the current aging temperature (30 ºC), a significant annealing time is required to reach a complete material structural equilibrium. Therefore, three freshly de-aged samples were aged for 1 week and another three for 6 months at room temperature and thereafter heated from 30 °C to 80 °C at 10 °C.min^{-1} in order to reveal their aged state.

Each of the DSC measurements was repeated three times using fresh samples in order to improve accuracy and to minimize the errors brought by baseline fluctuations and calibrations.

δ_H was calculated after a defined t_a as the difference in area between the DSC trace of an isothermally aged and the quenched reference sample, as illustrated in *figure 5.7*.

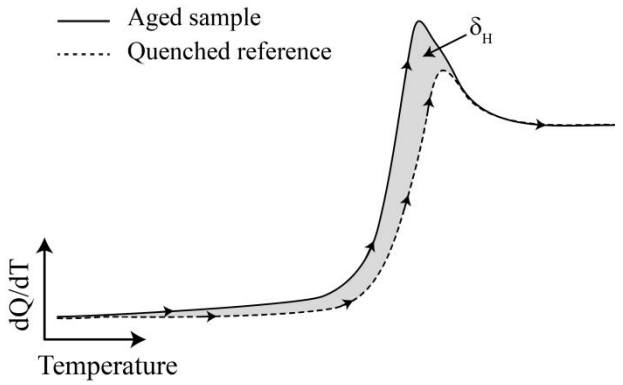

Figure 5.7. Schematic representation of the DSC trace for a quenched reference (dashed line) and an aged sample (full line) in the glass transition region. The area enclosed by both curves represents the recovered enthalpy (δ_H).

5.1.6. Dynamical Mechanical Thermal Analysis (DMTA)

DTMA experiments were performed on a DTMA Q800 instrument (TA Instrument, New Castle, DE, USA). A commercial Universal Analysis 2000 software version 4.5A (TA Instruments) was used for data analysis.

The dynamical mechanical thermal properties of the extruded sheets were investigated using a single cantilever bending mode at a frequency of 1 Hz and a deformation of 0.02% (LVE). The temperature range was set from 30 ºC to 150 ºC at a heating rate of 2 ºC.min^{-1}. Samples with nominal dimensions of 17.5 x 12 x 1 mm^3 were extracted from the centre of the extruded sheets in the MD direction as described in *section 4.3* (*c.f. chapter 4*). The storage modulus (*E'*), the loss modulus (*E''*) and the loss factor (*tan δ*) were determined according to the standard procedure.

The evaluation of the mechanical anisotropy degree (*R*) of the extruded sheets was investigated in tensile mode at 30°C. Experiments were carried out using the multi-frequency mode (1, 5, 10, 15, 20, 30 Hz). The oscillation strain was set to 0.05% (LVE), the static force to 0.5 N and the force track to 150%. Samples with nominal dimensions of 20 x 6 x 1 mm^3 were extracted from the centre of the extruded sheets in the MD and TD direction as detailed in *section 4.3* (*c.f. chapter 4*). Calculation of *R* proceeds according to *equation 5.10*.

$$R = \frac{E'_{MD}}{E'_{TD}} \; at \; 30\,°C \qquad (\mathbf{5.10})$$

Where E'_{MD} and E'_{TD} is the storage modulus at 30 °C in the machine and in the transversal direction, respectively.

Each of the DMTA measurements was repeated three times using fresh samples in order to improve accuracy.

5.2. Rheological Dynamic Analysis (RDA)

5.2.1. Sample conditioning

The initial X_c exhibited by a polymer may significantly affect its viscoelastic behaviour when rheological experiments are performed in its rubbery state above T_g ($T_g < T < T_m$). Thus, the temperature dependence over a large range of temperatures could be meaningless if this crystalline phase is not previously removed.

Prior to testing, amorphous samples were prepared in order to enlarge the temperature window for dynamic measurements. In a typical procedure, sheet parts were vacuum-dried over silica gel at 55°C overnight and subsequently melted at 5 °C above their respective melting temperature for 2 min between two steel plates in a hot plate press. Then, they were quickly quenched in an ice water bath (2 ± 2°C) for 5 min in order to avoid crystallization. After drying, disks with 25 mm in diameter were extracted from the centre of the sheet and vacuum-dried overnight at room temperature over silica gel. The amorphous state of the samples was investigated using DSC experiments, from the first heating run (30-200°C) at 10 °C.min^{-1}. As will be explained in *section 7.2.2 (c.f. chapter 7)*, solely unmodified PLA samples (*i.e.* PLA4 and PLA2) were stabilized with an antioxidative stabilizer Irganox 1010 (1 wt.%) in order to avoid excessive thermal degradation throughout rheological measurements at 170, 180 and 200 ºC. For testing temperatures below 170 ºC, unmodified PLA samples were not stabilized because chemical degradations were not an issue.

5.2.2. Testing conditions

Measurements were performed on an AR-G2 magnetic bearing rheometer (TA Instruments, New Castle, DE, USA) in parallel plate (25 mm) configuration with a constant gap of 1 mm. Tests were conducted in dry nitrogen atmosphere in order to minimize the thermo-oxidative degradations of the resin

The melt thermal stability throughout rheological measurements was verified through dynamic time sweep experiments at 50 rad.s^{-1} with 0.2 % strain amplitude.

The limits of the LVE region were determined for each material by performing dynamic strain sweep experiments. In these tests, $G'(\omega)$ remained constant at low strains but decreased at larger values, indicating a nonlinear response. The limit of the LVE was taken as the point at which $G'(\omega)$ decreased by 5% from its low strain plateau value. Relaxation of the sample is also checked before each test by measuring normal force decay.

As will be explained in *section 7.2.3 (c.f. chapter 7)*, dynamic frequency sweeps were carried out in the temperature ranges of 70-85 ºC and 150-200 ºC in 10 °C intervals for PLA-4 based samples, while PLA-2 based samples were only tested in the temperature range of 150-200 °C. In the present study, 200 ºC was established as the maximum testing temperature to avoid pronounced thermo-oxidative degradations throughout rheological testing. ω were swept from 628 to 0.0628 rad.s^{-1} at fixed strain amplitude in the LVE. Each frequency sweep was repeated three times using fresh samples. The technique developed by Tchir and Saucier [363] (*c.f. chapter 9, section 9.1.1*) was used to minimize the between-sample error.

The viscoelastic functions measured at different temperatures were reduced to master curves at 180 ºC using the TTS principle for samples which relaxation processes are not time-dependent with temperature (thermorheologically simple). This temperature (180 ºC) was chosen due to the better compromise between flow properties and thermal stability throughout rheological testing. A commercial TRIOS software version 3.0.1.3156 (TA Instruments) was used for data acquisition and analysis.

In order to ensure sufficient data at low ω, creep-recovery tests were conducted at 180 ºC. Within the LVE, the creep time was set to be sufficiently long to reach the steady-state according to the methodology of Gabriel and Münstedt [364]. The recovery experiments were started from the steady-state of the creep phase and were conducted until reaching a steady value of recoverable compliance. The average of three fresh samples was determined. Creep-recovery data were converted to retardation spectra $L(\lambda)$ using the commercial Rheology Advantage software version 5.4.0 (TA Instruments) based on the NLREG method developed by Honerkamp and Weese [112]. Then the complex shear compliance $J^*(\omega)$ was calculated from $L(\lambda)$ and $|\eta^*(\omega)|$ from $J^*(\omega)$. The interested reader can found more information about viscoelastic transformations in *section 9.1.3* (*c.f. chapter 9*).

Since significant errors are likely to occur during the calculation of the retardation spectrum from experimental data, the predicted terminal region (referred to as $G' \propto \omega^2$ and $G'' \propto \omega$) was verified using *equations 5.11*and *5.12* and data obtained from the creep-recovery experiments.

$$G'(\omega) = {\omega^2.\eta_0^2.J_e^0}/{1 + (\omega.\eta_0.J_e^0)^2} \quad \textbf{(5.11)}$$

$$G''(\omega) = {\omega.\eta_0}/{1 + (\omega.\eta_0.J_e^0)^2} \quad \textbf{(5.12)}$$

5.3. Mechanical Characterization

The mechanical characterization was carried out using uniaxial tensile tests according to the ASTM D638 standard. Specimens of type I (*c.f. figure 5.8*) were extracted from the centre of the sheet, parallel to the MD direction and following the protocol described in *section 4.3* (*c.f. chapter 4*). Tests were performed at room temperature (23 ± 3°C) using a universal testing machine (SUN 2500, GALDABINI, Cardano al Campo, Italy) equipped with a 5 kN load cell at a constant crosshead speed of 10 mm.min^{-1}. The actual displacement of the calibrated zone (ΔL_x) were measured with a video extensometer (OS-65D CCD, Minstron, Taipei, Taiwan) coupled to a Windows based software (Messphysik, Fürstenfeld, Austria).

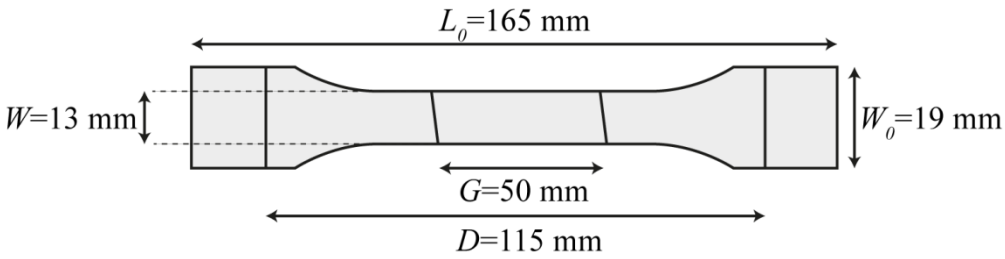

Figure 5.8. Tensile specimen of Type I with sample dimensions. L_o: length overall, D: distance between grips, G: gage length, W_o: width overall, W: width of the narrow section (based on ASTM D638 standard).

From the load-deformation curves the engineering stress-strain curves were calculated according to:

$$\sigma_i = {F_i}/{A_0} \quad \textbf{(5.13)}$$

$$\varepsilon_x = \frac{\Delta L_x}{L_0}.100 = \frac{L_x - L_0}{L_0}.100 \quad \textbf{(5.14)}$$

Where σ_i is the engineering stress and F_i is the load at a given deformation. A_0 defines the transversal section of a sample. ε_x is the engineering strain, L_0 is the gauge length of the initial specimen (50 mm) and ΔL_x is the increase in the specimen length between gauge marks during the test.

From the engineering stress-strain curves the following parameters were calculated. Reported values correspond to the average of five valid tests.

- **The Elastic or Young's modulus, *E*.** It is the ratio of stress to strain in the linear region of the stress-strain curves.
- **The yield strength, σ_y.** According to the curves obtained in the present study, it is defined as the point where the stress reaches a maximum after exceeding the limit of proportionality.
- **The yield strain, ε_y.** Engineering strain at the yield point.
- **The strain at break, ε_b.** Engineering strain where the failure is observed

5.4. Fracture Characterization

5.4.1. De-aged samples

Identical devices as described in the mechanical characterization section (*c.f. section 5.3*) were used to perform uniaxial fracture tests and to measure displacement of the process zone. Tests were performed with a crosshead speed of 1 mm.min^{-1} at room temperature (23 ± 3 ºC). DDENT samples were mechanized from the centre of the sheet, parallel to the MD direction as described in *section 4.3* (*c.f. chapter 4*), with the following dimensions: Length L=105 mm, width W=65 mm, thickness t=1 mm and distance between grips ZG=65 mm (*c.f. figure 5.9*). Ten ligament lengths, ranging from 6 to 24 mm, were tested. Each of them was repeated three times using fresh samples. Prior to testing, initial cracks were sharpened using a fresh razor blade with an edge radius of 0.13 μm. The work required for the whole fracture process (W_f) was measured by integrating the corresponding area underneath the load-displacement curve for each ligament length.

After testing, the accurate ligament length (l) and the height (h) of the OPDZ or "plastic" zone, surrounding the ligament length, were measured using a binocular lens microscope (Carton, Pathumthani, Thailand). This allowed for the determination of the shape factor (β), calculated from the slope of h versus l using a linear regression analysis. In addition, a video monitoring system (two digital cameras Xenoplan 1.4/23-0.902, Schneider Kreuznach, Bad Kreuznach, Germany) coupled to a optical strain measurement system (ARAMIS®, GOM GmbH, Braunschweig, Germany) was employed for an advanced strain analysis using digital image correlation (DIC).

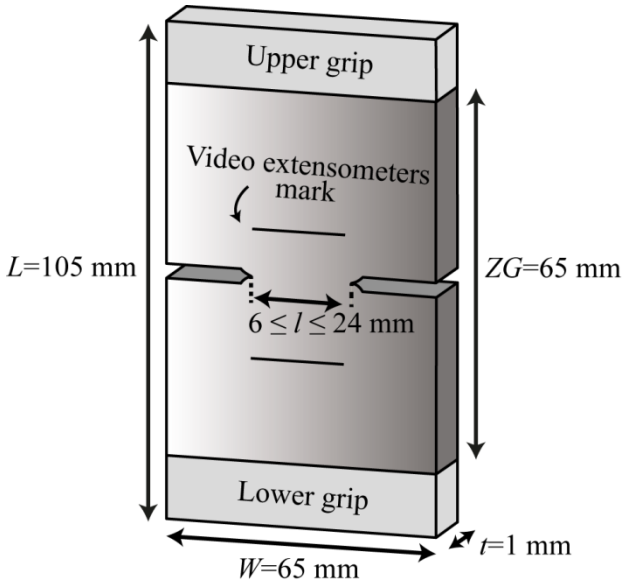

Figure 5.9. Schematic representation of the DDENT geometry with sample dimensions.

5.4.2. Aged samples

Single-Edge-Notched Tension (SENT) test geometry was used to perform these tests. They were mechanized from the centre of the sheet, parallel to the MD direction (*c.f. chapter 4*, *section 4.3*), with the following dimensions: Length L=140 mm, width W=50 mm, thickness t=1 mm and distance between grips ZG=100 mm (*c.f. figure 5.10*). According to a previous dimensional analysis, these dimensions ensured similar crack tip constraints ahead of the crack tip between DDENT and SENT samples. In order to perform a preliminary inspection of the possible change in the fracture toughness of aged samples, a unique ligament length (l) equal to 20 mm was tested. 5 samples were evaluated for each material. The initial crack was sharpened using a fresh razor blade with an edge radius of 0.13µm, directly after the thermal treatment applied. Prior to testing, polarized light microscopy (Nikon, Optiphot-Pol XTP-11, Japan) was used to verify the pre-crack quality. No damage at the crack tip and an extremely sharp crack tip was observed.

Uniaxial tests were performed on a servo-hydraulic testing system (Amsler HC25, Zwick Roell, Ulm, Germany), equipped with a 2 kN load cell, in tensile configuration. Tests were conducted with a crosshead speed of 10 $mm.min^{-1}$ at room temperature (23 ± 3 ºC). A similar video monitoring system as described in *section 5.3.a* was used for advanced strain analysis using DIC analysis.

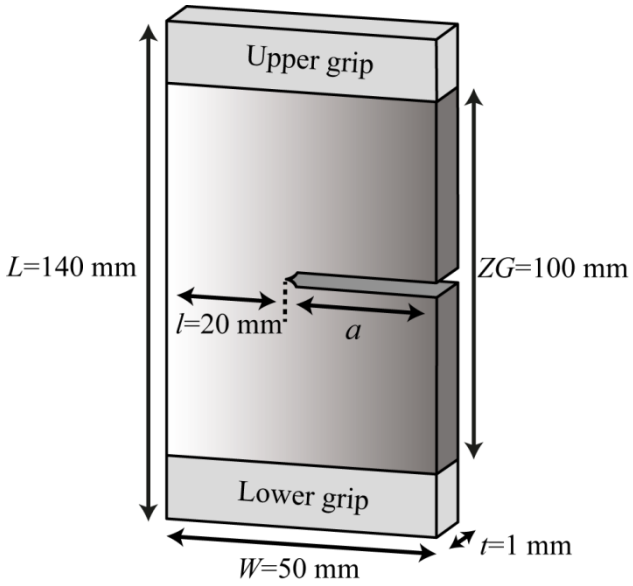

Figure 5.10. Schematic representation of the SENT geometry with sample dimensions.

Prior to testing, samples were "speckle coated" with white and black aerosol paints in order to create an optically active random structure. During the tests, displacements of this non-uniform surface pattern were recorded by a series of digital images (1600x1200 pixels) at a frame rate of 10 Hz. After testing, the DIC post-test analysis was performed using a commercial DIC software, Aramis® (GOM GmbH, Germany). The displacement field ahead of the crack tip was analyzed by viewing a rectangular field of 15.2 mm x 0.46 mm, meshed by square facets (9x9 pixels) with a 3 pixels overlapping area. A full-field three-dimensional measurement of the specimen shape and strain field was thus calculated by deriving these discrete displacements. Using the strain field measurement, the CTOD, δ, may therefore be determined just before the crack propagation onset. It was measured between two fixed nodes ahead of the initial crack tip, following the procedure described in *section 2.5.2.b* (*c.f. chapter 2*).

5.5. Fractography characterization

5.5.1. Optical Microscopy (MO)

The morphology of the surface normal to the fracture plane of the tensile samples was inspected using optical microscopy. Observations were performed using a polarized light microscopy (Nikon, Optiphot-Pol XTP-11, Japan) coupled to both a ProgRes® CT3 Camera (JENOPTIK Optical Systems GmbH, Jena, Germany) and a commercial ProgRes CapturePro version 2.5 software.

5.5.2. Scanning Electron Microscopy (SEM)

The fractured surfaces of all aged (SENT geometry) and de-aged (DDENT geometry) fracture samples were inspected using scanning electron microscopy (JEOL, JSM-7001F, Tokyo, Japan). Experiments were performed under vacuum with an accelerating voltage of 2 kV. Samples were previously coated with platinum vapour in order to increase the conductivity and to ensure good observations.

Results and Discussions

Chapter 6:

Laboratory scale: Internal mixer

6.1. Expected chain topologies

Reactive extrusion of polyesters and epoxies as reactive agent has been extensively studied and the reactions are well established [41, 45, 47, 314, 365]. Both polyester functional end groups (*i.e.* carboxyl, -COOH, and hydroxyl, -OH, groups) can react with epoxy groups via ring-opening reactions, creating covalent bonds with hydroxyl groups. However, a higher reactivity of epoxy towards the -COOH groups as compared to -OH groups was reported in the literature. This is due to the stronger polarization of the hydroxyl groups of carboxylic acid [40, 355, 366].

Since a multi-functional-epoxide reactive agent was used (functionality $f_n \approx 12$), several PLA chains might be chemically bonded to one SAmfE molecule, as shown in *figure 6.1*. Initially, little reaction reactivity of terminal -COOH groups towards SAmfE is expected, as most terminal -COOH groups on PLA chains might be end-capped to be –OH groups. This is commonly achieved in the production of commercial PLA grades in order to prevent excessive moisture absorption during storage [288, 316]. Consequently, the low remaining concentration of uncapped -COOH end groups and/or the new functional end groups on PLA chains induced by the thermo-oxidative degradations during processing open SAmfE epoxy rings which results in (a) grafting reactions and/or (b) chain extension reactions and/or (c) *n* arms star formation.

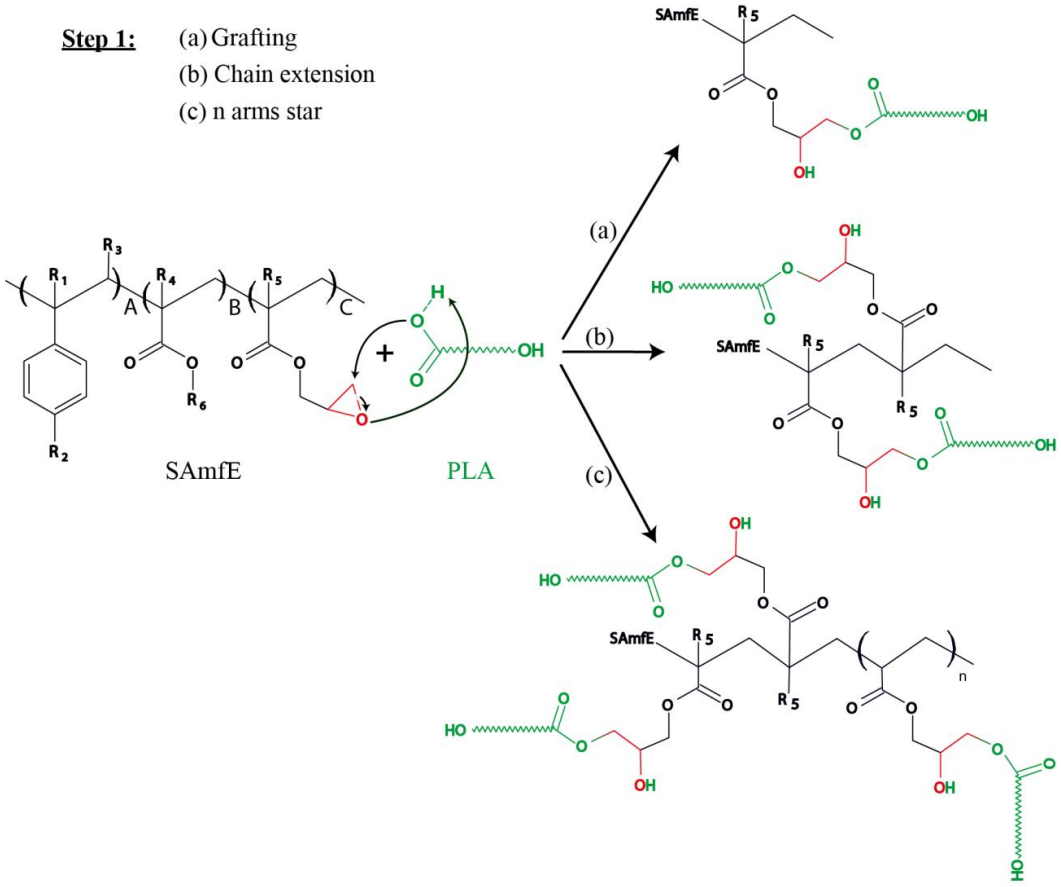

Figure 6.1. Proposed reaction mechanisms of PLA chains and SAmfE molecule.

For long reaction times, the formation of new terminal -OH and -COOH groups is expected due to the action of different degradation mechanisms at high temperatures. In a second step, the remaining free epoxy groups may further react with the new terminal -COOH groups which probably lead to (d) stretched H, (e) pom-pom, (f) comb or (g) tree type structures. An excess of SAmfE may eventually generate a (h) network structure.

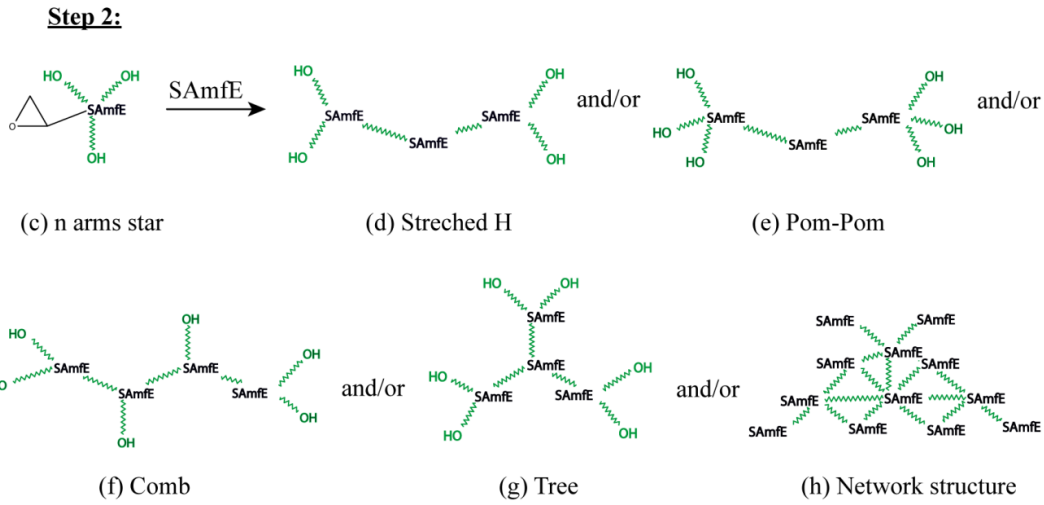

Figure 6.2. Expected chain structures for longer reaction times.

6.2. Effect of the SAmfE content on the reaction profile

The effect of SAmfE addition on both PLA viscosities was evaluated in an internal mixer in order to follow the evolution of the chain extension/branching reactions. The torque trace (Γ) and the bulk temperature (T_b) were recorded over prolonged mixing time (t=35 min), as shown in *figure 6.3.a* and *6.3.b*, respectively. Torque measurements were used to calculate the specific mechanical energy (SME) according to *equation 6.1* [367]. The SME defines the mechanical energy transferred to the melted polymer by the rotor shaft. In other words, the cumulative energy requires for mixing the melted polymer up to a specific time. Results are given in *table 6.1*.

$$SME = \frac{\omega}{m}\int_{4}^{t_{max}} \Gamma(t)d(t) \qquad \textbf{(6.1)}$$

Where ω is the screw speed (rad.s^{-1}) and m the sample weight (g). $\Gamma(t)$ is the torque at a time t (Nm) and t_{max} the mixing time (s). In the current study, $\Gamma(t)$ was integrated from 4 min (corresponding to the complete melted state of the samples, *c.f. chapter 4, section 4.1*) to 35 min.

The torque of both PLA "neat" samples decreased monotonously over mixing time, as shown in *figure 6.3.a*. This behaviour indicated the occurrence of several thermo-oxidative degradation reactions during melt processing. In addition, results suggest that PLA-2 "neat" samples exhibited a more pronounced decrease in $\Gamma(t)$ than its PLA-4 homologue over time, which behaviour was reflected in the lowered SME values.

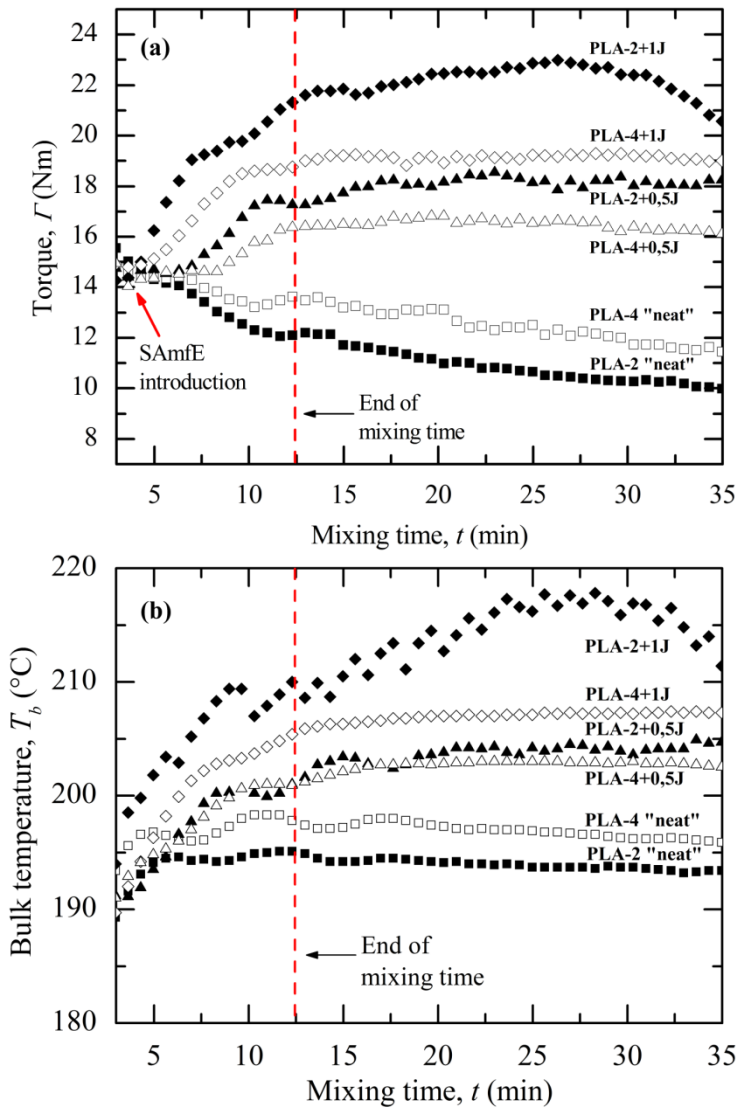

Figure 6.3. Influence of the SAmfE amount on the (**a**) torque trace and on the (**b**) bulk temperature as a function of the mixing time.

Table 6.1. Specific mechanical energy for "neat" and modified PLA samples.

Sample nomenclature	Nominal amount of SAmfE (wt.%)	Filling mass (g)	SME ($J.g^{-1}$)
PLA-2 "neat"	0	50	374
PLA-4 "neat"	0	50	413
PLA-4+0.5J	0.5	50.25	513
PLA-2+0.5J	0.5	50.25	556
PLA-4+1J	1	50.5	594
PLA-2+1J	1	50.5	674

The observed difference in thermal stability between both "neat" samples may result from:

- The higher content of terminal functional groups (*i.e.* lower M_n values) exhibited by PLA-2 raw material as compared to PLA-4 (*c.f. chapter 3, section 3.2.1, table 3.3*), which probably catalyses hydrolysis reactions [289-292]. Besides intermolecular transesterification, terminal -OH groups also enhance backbiting reactions via intramolecular transesterification, as already reported by Korhonen *et al.* [304].

- The width of the processing window, which may affect the melt stability for semicrystalline polyesters, as already reported by Lim *et al.* [15] and Bigg [288]. PLA-4 presents a wider processing window (200-T_{me} = 42 ºC) than PLA-2 (= 27 ºC) according to their respective T_{me} (*c.f. chapter 3, section 3.2.1, table 3.3*). Since PLA-4 exhibited a lower melting temperature, the local shear field applied to the material up to its complete melted state was probably lowered as compared to PLA-2. This trend might have minimized the effects of the thermo-mechanical degradations, increasing further thermal stability during mixing.

Besides a possible decrease in the MW, the random main-chain scission nature of the melt degradation mechanisms led to the generation of new terminal -OH and -COOH functional groups [292-295]. The generation of a higher concentration of functional end groups may be expected for PLA-2 due to its lower thermal stability over time.

Regarding "neat" samples, the bulk temperature increased up to 195 °C even though the set temperature was 180 °C. This increase in temperature is frequently attributed to the bulk self-heating which results from the mechanical shearing effects imparted to the polymer by the rotation of the screw relative to the mixing chamber wall. Since PLA-2 "neat" samples exhibited a smaller SME, less viscous dissipations occurred and the bulk temperature was slightly lower.

A strong torque increase was observed when both PLA types were mixed with SAmfE. This increase was in all cases higher for PLA-2 than PLA-4 based samples. Both observations were reflected in the calculated SME values. The observed trend may be attributed to the higher amount of functional end groups exhibited by PLA-2 (initially displayed by raw material and generated during processing) which results in a higher reactivity towards SAmfE. Regarding PLA-2+0,5J and PLA-4+1J samples, some torque fluctuations were observed between 10 and 15 minutes. This might be a consequence of the stick and split behaviour on the wall of the mixing chamber due to a possible increase in the melt elasticity. The bulk temperature increased up to 205 °C

with increasing SAmfE content due to both the mechanical shearing and the effect of the exothermal nature of the chemical reaction.

It is well known that the viscosity is proportional to the torque value, which depends on the MW and on the chain structure. Thus, the observed torque behaviour is likely to be due to an increase in the polymer MW (chain extension/branching) and/or to the possible creation of non-uniform branched structure in MW, in architectures and in the number of branch points per macromolecules which might hold LCB.

The torque of PLA-2+1J sample did not reach stabilization over time but increased continuously, reached a maximum around 28 minutes and then decreased. Due to the high content of SAmfE and the apparent higher reactivity of PLA-2, a significant increase in torque was observed. Crosslinking reactions might have taken place besides branching reactions, giving rise to network structure formation (*c.f. figure 6.2* (*h*)). At some point (28 min) the combination of high bulk temperature (≈ 220 ºC) and a high local shear field could initiate some degradation processes, resulting in a torque decrease as the network structure (gel molecules) may be broken.

As shown in *figure 6.3.b*, significant temperature fluctuations were observed in the bulk. This could be a consequence of the stick and split behaviour of an inhomogeneous melt on the wall of the mixing chamber.

Under these processing conditions, an optimum reaction time was considered as the point when the torque stabilized, avoiding an excessive reaction time to prevent the aforementioned secondary reactions. Considering these results, an optimum mixing time of 13 min was chosen which corresponds to the first torque stabilization (plateau on torque trace, *c.f. figure 6.3.a*). Fresh blends using this chosen processing time of 13 min were thereafter produced and used to perform the following molecular, physico-chemical, thermal and rheological characterizations.

6.3. Molecular characterization: SEC-DRI analysis

A preliminary study to determine the molecular modifications of PLA, resulting from the coupling reactions, was performed using SEC-DRI. *Figure 6.4* shows the MWD of raw (*i.e.* PLA-4 and PLA-2 pellets), unmodified (*i.e.* PLA-4 and PLA-2 "neat") and modified (*i.e.* PLA-4+0.5J, PLA-2+0.5J, PLA-4+1J and PLA-2+1J) PLA samples.

Both PLA "neat" samples displayed a monomodal distribution which changed to a bi- and three-modal one with increasing SAmfE content, as shown in *figure 6.4*. This was associated to the presence of two or three different hydrodynamic volumes, respectively, which could be a consequence of significantly different chain topologies.

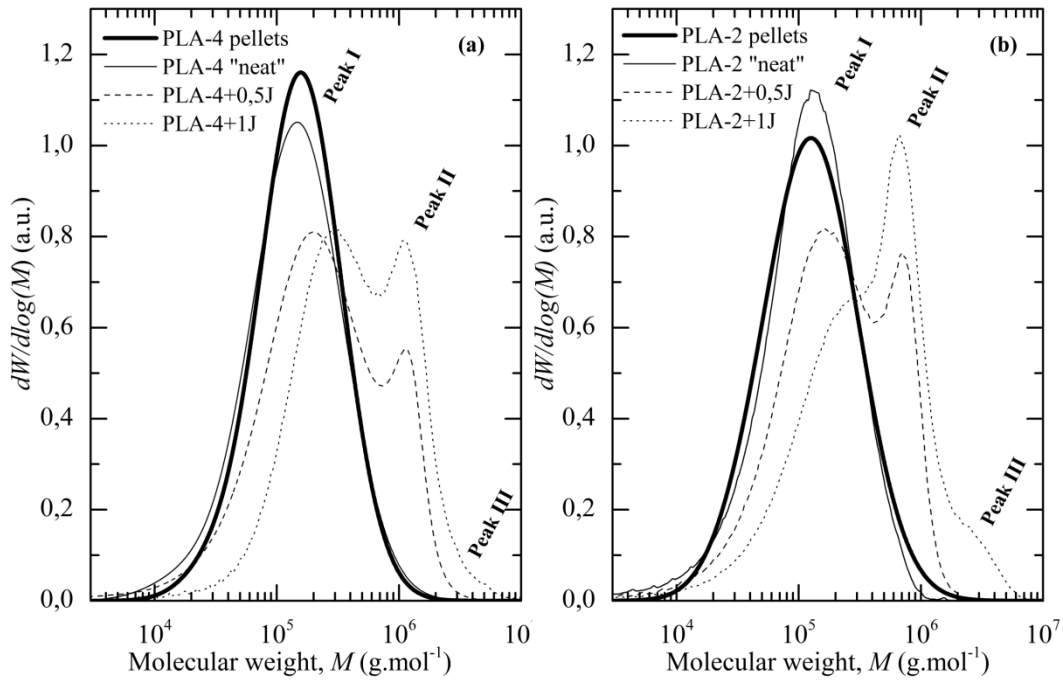

Figure 6.4. Influence of the reactive process on the MWD for (**a**) PLA-4 and (**b**) PLA-2 based samples.

Due to the linear topology of both PLA "neat" samples, the first peak at low MWs for all modified samples may be attributed to a linear population and the second peak (at higher MWs) to an increase in the population of high MW linear chains and/or the presence of branched structures. Special attention should be paid to PLA-2+1J and PLA-4+1J samples. These samples displayed a shoulder (referred to as Peak III) in the HMW tail of the second peak, which might be attributed to the presence of highly branched populations.

Since SEC column separates the polymer molecules on the basis of their size in solution, classical SEC technique (employing a single concentration detector, *i.e.* UV and/or DRI) is not a suitable method to accurately determine the MW of branched samples. This is because branched chains exhibit smaller hydrodynamic volumes than their linear homologues of equivalent MW. Preparative SEC experiments [24] and/or multi-detector technique may be a more appropriate technique to study modified samples but this analysis was beyond the scope of this preliminary study.

On the other hand, qualitative information about complex MWDs can be extracted from classical SEC data by performing a deconvolution of the MWD spectrum into elementary curves. The condition is to find true peaks centred at the same maxima as exhibited by experimental data. In the current study, the

deconvolution procedure proceeds according to log-normal (area) functions as given by *equation 6.2*.

$$\frac{dW}{dlog(M)} = \frac{a_0}{\sqrt{2\pi} * a_1 * a_2 * \sqrt{\exp(a_2^2)}} * \exp\left(-\frac{1}{2}\left(\frac{\ln M}{\frac{a_1}{a_2}}\right)^2\right) \quad \textbf{(6.2)}$$

Where a_0, a_1 and a_2 are related to the area, the centre and the width of the log-normal (area) function, respectively.

Table 6.2 summarizes the relative MW values as determined using SEC-DRI together with the partial areas corresponding to each of the deconvoluted peaks coupled with the relative MW averages calculated.

Table 6.2. Numerical analysis of the MWD depicted in *figure 6.4.*

Sample nomenclature		M_n [a] (kg.mol^{-1})	M_w [a] (kg.mol^{-1})	M_z [a] (kg.mol^{-1})	***PDI***	**Area (%)**
PLA-4 pellets	**global**	**99.9**	**186.5**	**336.6**	**1.9**	**100**
PLA-4 "neat"	**global**	**82.3**	**182.6**	**370.8**	**2,2**	**100**
PLA-4+0,5J	**global**	**104.4**	**348.5**	**848.1**	**3.3**	**100**
	Peak I [b]	95.0	254.0	598.0	2,7	60
	Peak II [b]	1 123.4	1 221.5	1 328.3	1.1	40
PLA-4+1J	**global**	**100.7**	**331.5**	**696.2**	**3.3**	**100**
	Peak I [b]	87.4	242.9	517.5	2.8	58
	Peak II [b]	709.0	782.73	864.2	1.1	36
	Peak III [b]	1 806.5	1 923.4	2 047.8	1.1	6
PLA-2 pellets	**global**	**90.3**	**181.4**	**355.7**	**2.1**	**100**
PLA-2 "neat"	**global**	**71.2**	**154.7**	**282.1**	**2.2**	**100**
PLA-2+0,5J	**global**	**101.7**	**282.5**	**565.7**	**2.8**	**100**
	Peak I [b]	88.2	196.8	386.0	2.2	57
	Peak II [b]	706.2	763.6	825.7	1.1	43
PLA-2+1J	**global**	**116.3**	**513.2**	**1 358.2**	**4.4**	**100**
	Peak I [b]	86.1	283.2	603.1	3.3	41
	Peak II [b]	663.1	743.8	834.3	1.1	35
	Peak III [b]	1 735.2	2 351.1	3 099.3	1.4	25

[a] Relative MW values based on PMMA standards in HFIP.
[b] Results obtained from the deconvolution analysis using log-normal functions.

According to *table 6.2*, a decrease in relative MW averages was detected for PLA-2 and PLA-4 "neat" samples as compared to raw materials. This is due to the action of different degradation mechanisms during processing. PLA-2 samples exhibited a more pronounced decrease in M_w than PLA-4 samples which probably resulted from the higher thermo-mechanical degradations over mixing time (*c.f. section 6.2*).

When 0,5 wt.% of SAmfE was added, M_w and the PDI of peak I increased, remaining the dominant fraction in all cases (higher relative area of the deconvolution). This could be a consequence of possible chain extensions coupled with co-elution problems of different chain topology structures.

Slight differences between both PLA types may be observed when comparing the relative areas of peaks I and II. As can be seen in *table 6.2*, for PLA-2 based samples, the relative area proportion attributed to Peak II was always higher as compared to PLA-4 based samples. This may be expected if the higher degree of degradation over mixing time is considered. The formation of a higher concentration of -COOH end groups, enhanced coupling reactions and led to a larger degree of structural modifications.

When the SAmfE content was doubled (from 0,5 to 1 wt.%), the respective areas of peak II and III increased at the expense of peak I. This indicates an increase of this "new" chain topology content which could be attributed to LCB and/or more complex topological structures (*e.g.* comb, tree or network structure). For PLA-2+1J sample, the summation of peak II and III relative areas exceeded the peak I area. Possibly a network structure coupled with LCB was generated due to the pronounced modification degree reached in this system. During sample conditioning, evidence of this last assumption was obtained by visual inspection and solubility tests which showed the existence of gel structures.

6.4. Physico-chemical characterization of the coupling reactions

Since spectroscopic methods are sensitive to conformation and local molecular environment, several data sets of FT-IR and ^{1}H NMR measurements were analyzed in this section as part of an ongoing effort to detect and identify the molecular changes in modified PLA samples, respectively.

6.4.1. FT-IR analysis

A preliminary trial was performed in an intent to identify the possible coupling reactions between PLA functional end groups (*i.e.* –OH and –COOH) and the epoxy groups of the reactive agent using FT-IR spectroscopy. IR spectra, which were obtained from samples casted onto glass plates after dissolving 1 g of the corresponding material into THF (*c.f. chapter 5, section 5.1.1*), are shown in *figure 6.5*. PLA-2+1J samples were discarded from this analysis, as untrustworthy peaks are likely to be observed due to gel or crosslinked particles.

The characteristic peak band assignments for SAmfE raw material and PLA based material IR spectra are summarized in *table 6.3* and *6.4*, respectively.

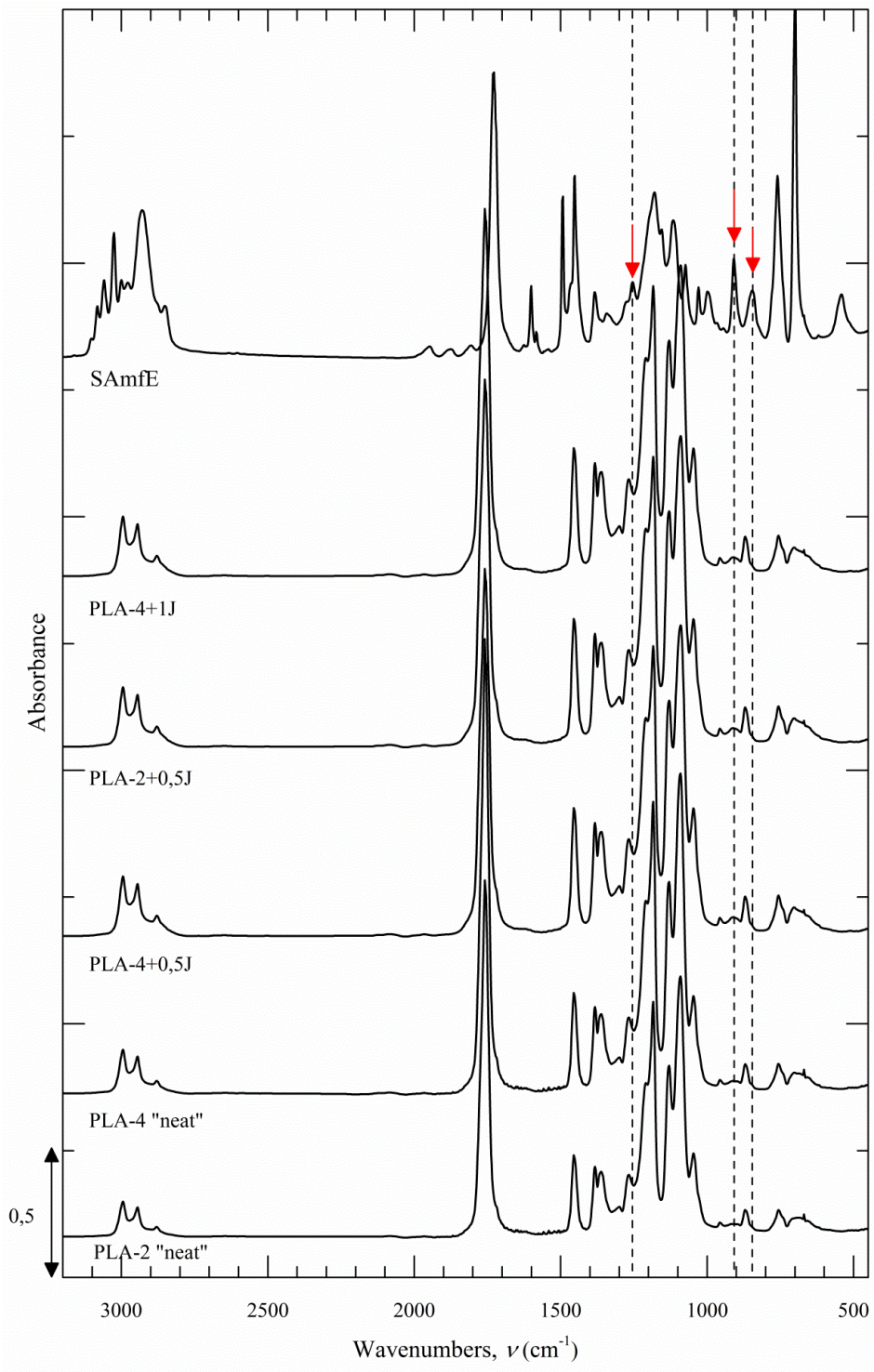

Figure 6.5. Infrared spectra of PLA-2 “neat”, PLA-4 “neat”, PLA-4+0.5J, PLA-2+0.5J, PLA-4+1J samples and SAmfE raw material. The red arrows indicate the

absorbance peaks characteristic of the epoxy groups and the dashed lines the band sensitive to remaining epoxy groups.

Table 6.3. Wavenumbers and their corresponding vibrational assignments for SAmfE IR spectrum [365, 368].

Wavenumbers, ν (cm^{-1})	Assignments	Nature of vibration *
700	ar C=C	δ
762	ar C-H	δ oop
847	epoxy ring	δ
909	epoxy ring	st s
1256	epoxy ring	st as
1453	CH_3	δ as
1468, 1492	ar C-C	-
1583, 1600	ar skeletal vibration, C=C	st
1727	C=O	st
1807, 1877, 1948	ar overtone bands	-
3000-2850	C-H	st
3025, 3058, 3084	ar C-H	st

* st: stretching (ν), δ: bending, s: symmetrical, as: asymmetrical, oop: out-of-plane, ar: aromatic

Table 6.4. Wavenumbers and their corresponding vibrational assignments for PLA based samples IR spectra [12, 368-370].

Wavenumbers, ν (cm^{-1})	Assignments	Nature of vibration *
756	Crystalline phase	-
871	Amorphous phase	-
868	C-C	st
1045	$C\text{-}CH_3$	st
1093, 1130, 1184	C-O-C	st as
1268	C=O	δ
1360, 1382	CH	δ (s and as)
1453	CH_3	δ as
1757	C=O	st
2880	C-H	st s
2945, 2994	$C\text{-}CH_3$	st (s and as)

* st: stretching (ν), δ: bending, s: symmetrical, as: asymmetrical

While Kister *et al.* [369] identified that the vibrational position of the δCH (1360 and 1382 cm^{-1}) and symmetric δCH_3 (1453 cm^{-1}) bending modes are sensitive to the polymer tacticity, both PLA "neat" samples exhibited similar IR spectra, as shown in *figure 6.5*. Under these testing conditions, these results suggest that IR spectra remained independent on the modest variations in the D-lactide content between both PLA types used in the present study.

The absorbance peak shifted at 847, 909 and 1256 cm^{-1} (indicated by red arrows) in the SAmfE IR spectrum are characteristic to the vibrational position of the epoxy ring bending and stretching modes, as reported in *table 6.3*. Although "neat" samples were compared to modified samples with an increasing content of SAmfE agent, PLA-4+0.5J, PLA-2+0.5J and PLA-4+1J IR spectra exhibited neither the absorbance peaks belonging to the epoxy functional groups nor new characteristic signal bands. Since the peak absorbance intensity is proportional to the concentration of absorbing species, this trend is probably due to:

- A total consumption of the available epoxy functional groups during processing.
- A remaining concentration of epoxy groups below the detection limits of the FT-IR analysis.
- A content of topological modifications below the detection limits of this technique.

6.4.2. ^{1}H NMR analysis

Since FT-IR analysis failed to identify possible coupling reactions between PLA and SAmfE, a preliminary trial was performed to characterize the molecular structure using ^{1}H NMR spectroscopy. ^{1}H NMR spectra, which were obtained for both PLA "neat" and PLA-4+1J samples, are compared in *figure 6.6*. Excluding samples with gel structures (*i.e.* PLA-2+1J materials), PLA-4+1J material was selected due to its largest degree of structural modifications; thus, minimizing issues of detection limits. Similarly, SAmfE agent was analyzed using ^{1}H NMR. However, the corresponding ^{1}H NMR spectrum is not showed in *figure 6.6* but in *appendix* (*c.f. chapter 9, section 9.2, figure 9.3*) because the characteristics peaks could not be resolved well.

In the polymerization of the lactide, often a starter molecule such as isopropanol is used, leading to a final polymer with few –COOH groups. Moreover, most terminal –COOH groups on commercial PLA types are end-capped, as already reported in *section 6.1*. On this basis, while the carboxyl content may be negligible in the as-received materials, its presence was considered in the following analysis. This is due to the actions of the several thermo-mechanical degradations during mixing; giving rise to the formation of new functional end groups (*i.e.* –OH and/or –COOH end groups).

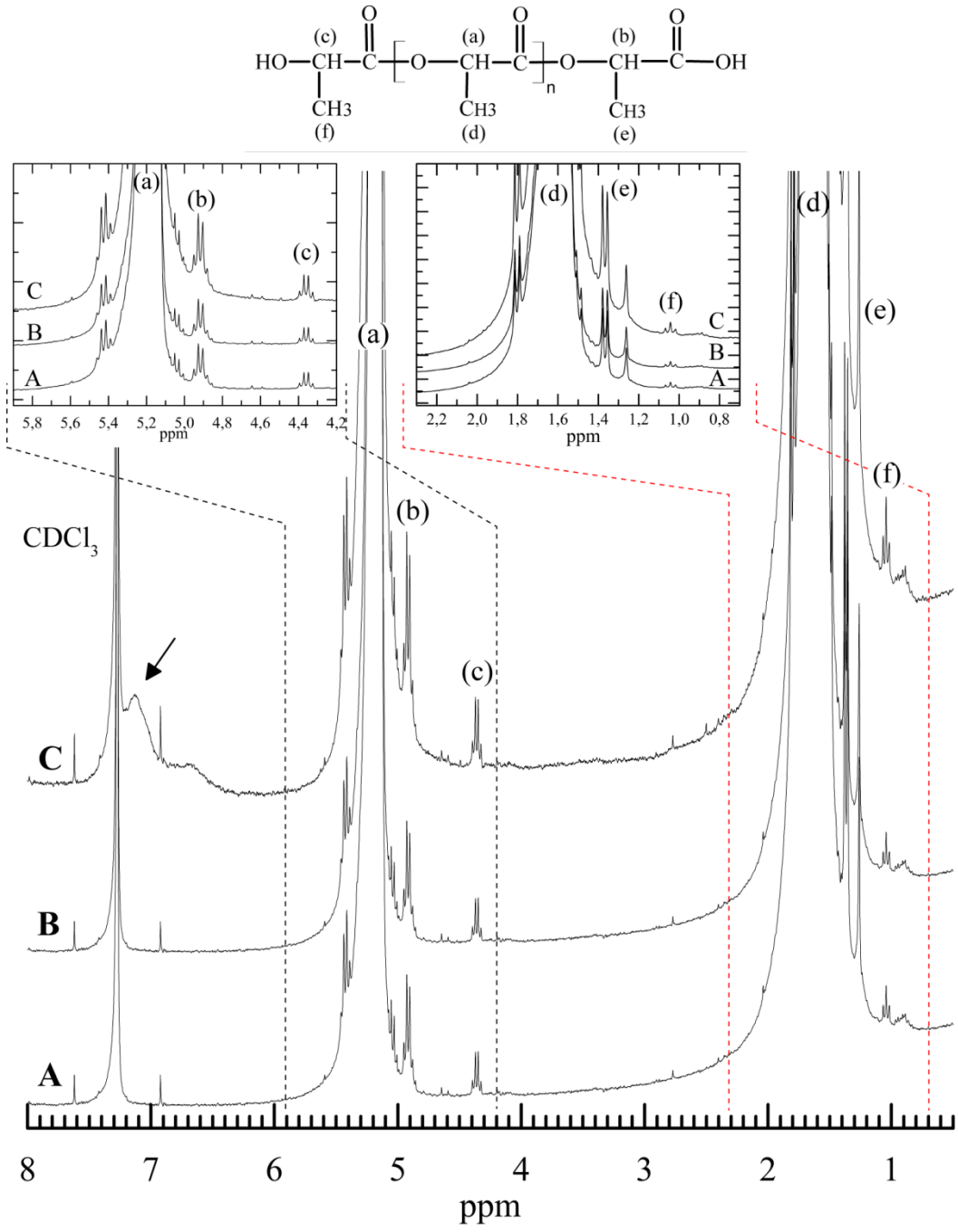

Figure 6.6. ^{1}H NMR spectra of (**A**) PLA-2 "neat", (**B**) PLA-4 "neat" and (**C**) PLA-4+1J samples with peak assignments. The arrow indicates the signal which probably belongs to the protons in the aromatic rings of the SAmfE molecules.

In all spectra, the most intense signals at 1.8 and 5.2 ppm correspond to methine (-CH) and methyl ($-CH_3$) protons at the (a) and (d) positions, respectively. The resonance peaks at 4.4 ppm is thought to belong to the methine protons next to the terminal -OH groups. Other respective peak assignments are compiled in *table 6.5*. The sharp peak at 7.29 ppm is due to the deuterated chloroform $CDCL_3$ [371, 372].

Table 6.5. ^{1}H NMR chemical shifts [371, 372].

ppm	Multiplicity	Molecular position	protons
5.2	quartet	a	Methine
5.0	quartet	b	Methine
4.4	quartet	c	Methine
1.8	quartet	d	Methyl
1.4	quartet	e	Methyl
1.04	quartet	f	Methyl

In previous studies, peak assignments in NMR spectra to particular stereosequences in PLA was achieved using statistical methods [370, 372, 373]. However, ^{1}H NMR spectra were found to be roughly similar between both PLA "neat" samples in the present study. It should be noted that the repeatability of the measurements was in the order of ± 10%. Therefore, results suggest that the modest variations in the D-lactide content between both PLA types were not large enough to influence the resonance properties under the testing condition used.

Using ^{1}H NMR measurements, Meng *et al.* [371] identified the coupling reactions between PLA and a multi-epoxy reactive agent (*i.e.* Joncryl-4368). In comparison with the spectrum of neat PLA, authors reported two additional sharp peaks at 1.28 and 0.9 ppm for PLA compounded with 0.5 wt.% of Joncryl-4368. The much sharper peak at 1.28 ppm was attributed to the resonance of methyl protons at (m_1) and (m_3) positions, and the new peak at 0.90 ppm to methyl protons at the (i) position, as shown in *figure 6.7*.

While a broad peak overlapped the signal of the solvent (indicated by an arrow) for PLA-4+1J samples (which probably belongs to the protons in the aromatic ring of SAmfE [371]), all ^{1}H NMR spectra were found to be similar as shown in *figure 6.6*. Similar observations were highlighted for PLA-4+0.5J and PLA-2+0.5J samples; suggesting the absence of structural changes. Nevertheless, as it will be shown in *section 6.7*, the significant differences in the rheological properties suggest topological modifications.

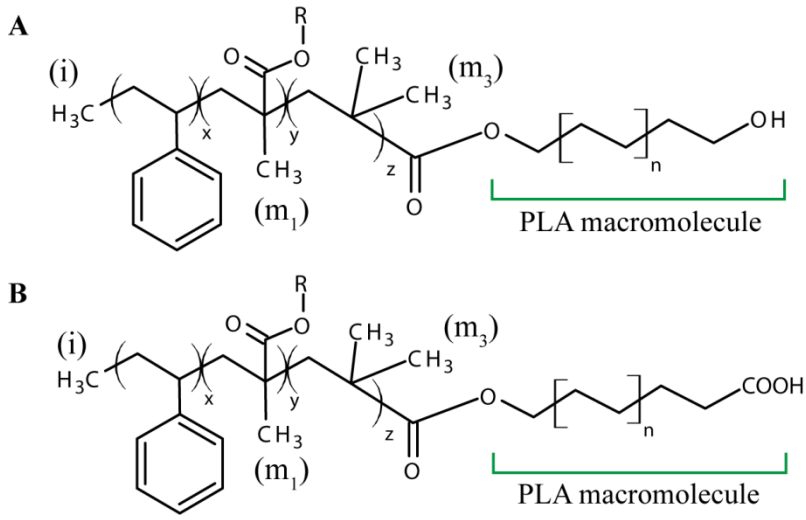

Figure 6.7. Chemical structure of PLA reacted with Joncryl-4368 as reported by Meng *et al.* [371] **A**: carboxyl groups with epoxy groups and **B**: hydroxyl groups with epoxy groups.

Since complementary information about the number of branches are usually obtained using NMR, it is surprising that ^{1}H NMR measurements had not displayed new characteristic peaks belonging to the chemical coupling of PLA end groups with the SAmfE agent.

Recall that characteristic SAmfE peaks are not resolved well under the testing conditions used. Consequently new characteristic peaks belonging to the coupling reaction between PLA end groups and the epoxy ring will not be identified straightforwardly. On the other hand, it should be kept in mind that the SAmfE agent has a functionality of 12. Thus, one SAmfE molecule might chemically bond several PLA chains during mixing. Given the HWM of the initial linear PLA coupled with the minimized thermo-oxidative degradations during processing, the MW of the probably grafted chains is likely to exceed the MW for entanglements, M_c.

Modified PLA samples are not carefully prepared model polymer based on specific polymerization technologies. The topological modifications achieved during mixing are not trivial and would be a mixture of several types of non-uniform structures in MW, in architectures and in the number of branch points per macromolecules. Unfortunately, NMR exhibits a limited sensitivity to sparsely and/or non-uniform branched macromolecules. The number of branch points cannot be counted below the usual detection limit of about 1 branch per 10^4 carbon atoms, as already reported by numerous authors in transition metal-catalyzed HDPE [119, 138, 147, 151].

Moreover, this technique cannot distinguish branches of six carbon atoms length and longer, even though this length has been increased to at least 10 carbon atoms under specific testing conditions [374]. The source of trouble is the physical reality that NMR cannot differentiate between the magnetic resonance properties of long branches and the polymer backbone because they give rise to the same spectral pattern irrespective of chain length [147, 155, 375]. On this basis, ^{1}H NMR characterization apparently failed to characterize modified PLA samples due to the non-uniform and/or over-sized macromolecules probably created during processing.

6.5. Thermal behaviour: DSC analysis

6.5.1. PLA raw materials

For the purpose of investigating the thermal behaviour of both PLA raw materials, the thermal protocol described in section *5.1.5.a* (*c.f. chapter 5*) was used. The first heating (**H1**), the cooling (**C**) and the second heating (**H2**) steps of PLA-4 and PLA-2 materials as-received are shown in *figure 6.8*. The corresponding thermal properties obtained from the heating and cooling ramps are compiled in *table 6.6*.

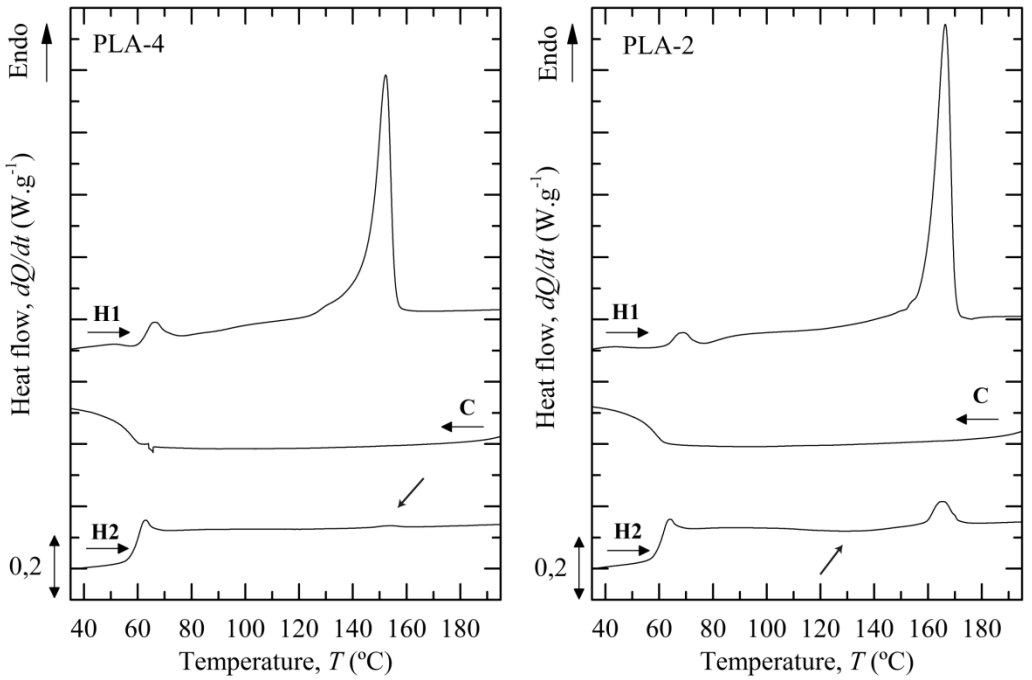

Figure 6.8. Thermal behaviour at 10 ºC.min^{-1} of PLA-4 and PLA-2 raw materials. **H1**: first heating scan; **C**: cooling and **H2**: second heating scan.

Table 6.6. Thermal properties of PLA-2 and PLA-4 raw materials.

	Parameters	PLA-4	PLA-2
First heating (H1)	$T_{g,m}$ (°C)	62.3 ±0.6	64.0 ±0.8
	T_{cc} (°C)	-	75 ±2
	ΔH_{cc} (J.g^{-1})	-	1 ±1
	$X_{c,cc}$ (%)	-	1 ±1
	T_{mp} (°C)	152.2 ±0.1	166.8 ±0.6
	T_{me} (°C)	159 ±1	174 ±1
	ΔH_m (J.g^{-1})	38 ±4	43 ±4
	$X_{c,m}$ (%)	40 ±4	46 ±5
	X_c (%)	40 ±4	45 ±4
Cooling (C)	$T_{g,m}$ (°C)	56.4 ±0.3	56.9 ±0.3
	T_c (°C)	-	-
	$\Delta H_{c,c}$ (J.g^{-1})	-	-
	$X_{c,c}$ (%)	-	-
Second heating (H2)	$T_{g,m}$ (°C)	61 ±1	61 ±2
	T_{cc} (°C)	-	131 ±3
	ΔH_{cc} (J.g^{-1})	-	4 ±1
	$X_{c,cc}$ (%)	-	4 ±1
	T_{mp} (°C)	-	166.0 ±0.6
	ΔH_m (J.g^{-1})	153.1 ±0.3	3.6 ±0.4
	$X_{c,m}$ (%)	0.2 ±0.2	3.8 ±0.4
	X_c (%)	0	1 ±1

Regarding the first heating step (**H1**), both materials did not cold-crystallized during heating because they were supplied in crystallized form. This observation corroborates the calculated degree of crystallinity, X_C. After industrial manufacturing, a post-crystallization step is usually added to the process in order to stabilize pellets against increased moisture absorption. The chemical stability of the polymer is therefore increased due to a rate of water absorption, a swelling behaviour and a biological degradation, which is minimized, as compared to amorphous PLA [272].

Moreover, recall that PLA raw materials must be dried before melt processing in order to minimize an excessive material degradation at high temperatures. In commercially relevant scale, most PLA grades are supplied in a crystallized state which enable drying pellets at higher temperatures. This characteristic allows for shorter drying times and is therefore a cost-effective technique for production [15, 283, 352].

The glass transition temperatures were found to be slightly higher in the first heating step as compared to their corresponding temperatures in the second heating run. This trend could be attributed to the effect of the enthalpic relaxations at T_g (*i.e.* overshoot superimposed in the T_g transition) and the high degree of crystallinity exhibited by the materials as-received.

According to the cooling conditions used in the present study, both materials did not crystallize during the controlled cooling run (**C**). This behaviour could be attributed to the slow kinetics of crystallization exhibited by PLA resins, as already reported elsewhere [11, 19, 92].

In the subsequent heating scan (**H2**), PLA-4 showed no cold-crystallization and an extremely weak melting endotherm (indicated by an arrow), while PLA-2 exhibited an undefined cold-crystallization peak (indicated by an arrow) and a weak melting peak. These tendencies confirm that PLA thermal properties are mainly dependent on the D-lactide content.

Under controlled heating rate, PLA-4 showed a much lower T_{mp} than PLA-2 irrespective of the heating run considered. This observation is in line with the study of Saeidlou *et al.* [338] who reported a linear decrease of approximately 5 °C in T_{mp} for every 1 mol.% increase in *meso*-lactide. The presence of both meso- and D-lactide units in a L-lactide matrix induces imperfections in the crystalline structure which leads to a depression of T_{mp} [11].

6.5.2. Processed PLA samples

The effects of the reactive process (and thus those of the topological changes) on the PLA thermal behaviour were investigated using DSC measurements. Since compression moulded samples were subjected to a final cooling stage with an uncontrolled cooling rate, the thermal transitions revealed in **H1** may be meaningless if samples are compared to one another. Consequently, corresponding DSC traces and thermal properties are reported in *figure 9.4* and *table 9.1*, respectively (*c.f. chapter 9, section 9.3.1*). The controlled cooling (**C**) and second heating (**H2**) scans are shown in *figure 6.9* and *figure 6.10*, respectively. *Table 6.7* summarizes the detailed thermal properties recorded in **C** and **H2** steps, for all samples processed at laboratory scale.

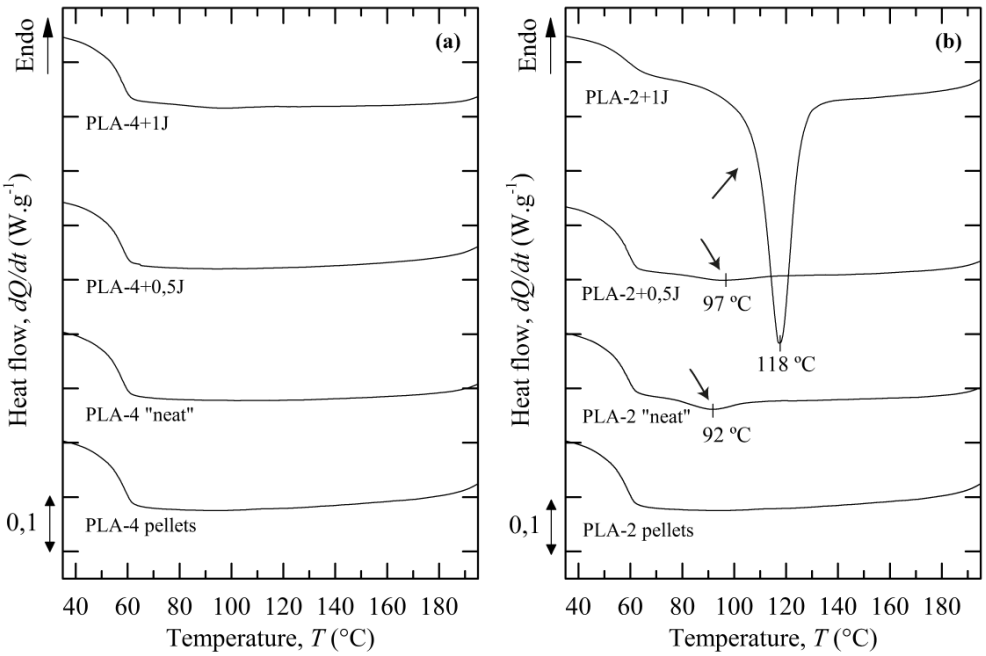

Figure 6.9. Controlled cooling scan (**C**) at 10 ºC.min^{-1} of **(a)** PLA-4 and **(b)** PLA-2 based materials processed at laboratory scale.

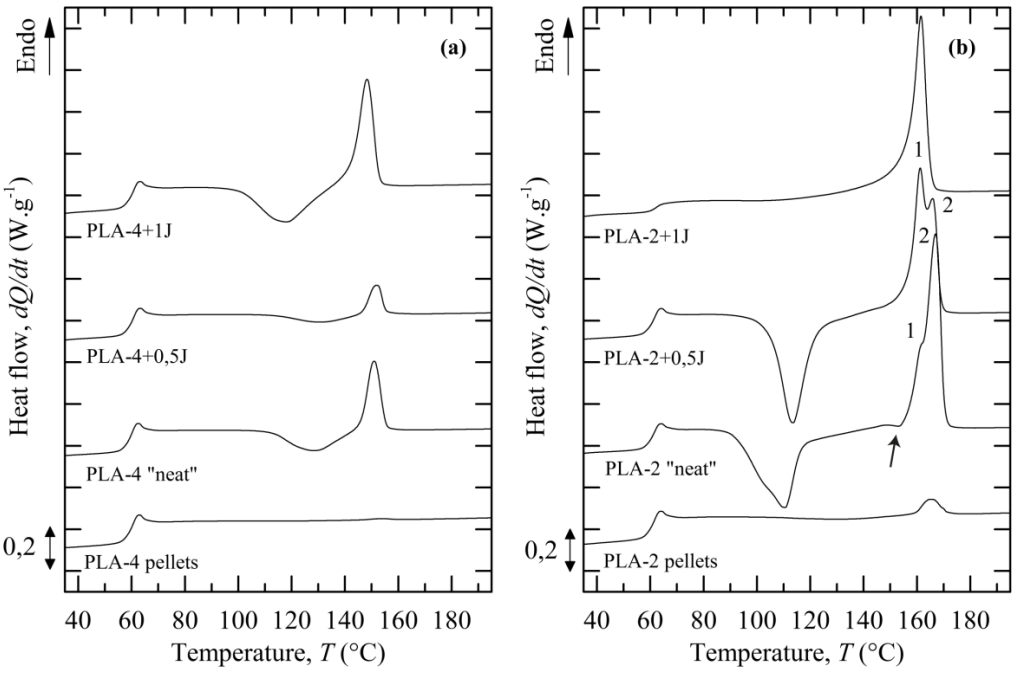

Figure 6.10. Second heating scan (**H2**) at 10 ºC.min^{-1} of **(a)** PLA-4 and **(b)** PLA-2 based materials processed at laboratory scale.

Table 6.7. Thermal properties of PLA-2 and PLA-4 based materials processed at laboratory scale.

	Parameters	PLA-2 "neat"	PLA-4 "neat"	PLA-2 +0.5J	PLA-4 +0.5J	PLA-2 +1J	PLA-4 +1J
Cooling (C)	T_c (°C)	91.7 ±0.1	-	97 ±1	-	117.0 ±0.5	-
	$\Delta H_{c,c}$ (J.g^{-1})	3 ±2	-	1.8 ±0.2	-	37 ±1	-
	$X_{c,c}$ (%)	3 ±2	-	1.9 ±0.2	-	39 ±1	-
Second heating (H2)	$T_{g,m}$ (°C)	59.7 ±0.6	58.8 ±0.2	60.1 ±0.1	59.6 ±0.3	61 ±2	59.7 ±0.3
	T_{cc} (°C)	110.5 ±0.4	127.6 ±0.8	113.3 ±0.1	128.4 ±0.5	-	116 ±2
	ΔH_{cc} (J.g^{-1})	35 ±4	9 ±4	34 ±8	4 ±1	-	19 ±3
	$X_{c,cc}$ (%)	37 ±5	9 ±4	36 ±8	4 ±1	-	21 ±3
	T_{mp1} (°C)	161.4 ±0.5	150.8 ±0.5	161.3 ±0.1	152.1 ±0.2	161.5 ±0.2	148.4 ±0.1
	T_{mp2} (°C)	166.6 ±0.4	-	165.7 ±0.3	-	-	
	T_{me} (°C)	172.7 ±0.5	158.2 ±0.6	171.4 ±0.7	159.6 ±0.3	167.5 ±0.1	155.1 ±0.5
	ΔH_m (J.g^{-1})	39 ±3	10 ±3	35 ±8	4 ±1	39 ±3	20 ±3
	$X_{c,m}$ (%)	42 ±3	10 ±3	37 ±8	4 ±1	42 ±3	22 ±3
	X_c (%)	5 ±3	1 ±1	1 ±1	0 ±0	42 ±3	1 ±1

According to the cooling conditions used in the present study, PLA-4 based materials did not crystallize during the controlled cooling run (**C**), as shown in *figure 6.9.a*. By contrast, processed PLA-2 "neat" exhibited a weak crystallization exotherm (indicated by an arrow) which decreased in magnitude and shifted to slightly higher temperatures for PLA-2+0.5J. Special attention should be paid to PLA-2+1J material. These samples revealed a well defined crystallization transition upon cooling from the melt which shifted to much higher temperatures as compared to PLA-2 "neat" samples. This behaviour might be induced by remaining infusible particles (*e.g.* gels), acting as self-seeding nuclei.

Upon reheating, both PLA "neat" samples exhibited a higher tendency to crystallize as compared to raw materials. This behaviour could be attributed to an enhancement of the medium-range translation processes on the chain folding needed for crystallization due to the slight decrease in MW after processing. The thermal behaviour of both PLA "neat" samples clearly depends on the stereochemical purity, as shown in *figure 6.10*. By increasing the D-lactide content, besides a decrease in the tendency to crystallize upon heating, T_{cc} shifted to higher temperatures. This behaviour can be explained by the introduction of microstructural defects in the PLLA's natural helical chain conformation. The D-lactide units induce "defects" or "disruption" in the crystal arrangement leading to a decrease in the rate of crystallization and in X_c [263, 288, 338]. These results are in line with those reported by Kolstad [339]. Authors reported an increase in the crystallization half-time of 40% for every 1 wt.% increase in meso-lactide.

T_{cc} shifted to higher temperatures and the tendency to crystallize upon heating appeared to decrease with adding 0.5 wt.% of SAmfE, for each PLA type. The observed raise in MW coupled with the topological restrictions caused by the possible modifications in the chain architecture may difficult the macromolecular chain short-range transport movements needed for the crystallization process. Consequently, both the rate of crystallization and X_c decreased, as already reported elsewhere [15, 92, 263, 288, 320, 338]. Melt compounded PLA-4 with 1 wt.% of SAmfE yielded a decrease in T_{cc}. This behaviour might be induced by the presence of possible gels (*c.f.* presence of a population of very HMW as shown in *figure 6.4.a*), actuating as self-seeding nuclei throughout heating. Note that PLA-2+1J samples did not follow the above described trends due to its crystallization upon cooling from the melt.

Regarding the melting transition, PLA-2 "neat" samples exhibited a small exotherm (around 152 ºC, indicated by an arrow) prior to the two overlapped endotherms (marked as 1 and 2). Numerous authors attributed this exothermic peak before the dominant melting transition to the α'-to-α transition of the α'-crystals generated during the cold-crystallization process. Then, the double melting-peak is possibly due to the melt-recrystallization mechanism. The low-temperature shoulder

may be attributed to the melting of the original crystals, while the high-temperature endotherm may be attributed to the melting of crystals generated through the melt-recrystallization mechanism upon heating [20, 91-94].

With the addition of 0.5 wt.% of SAmfE, results suggest that the intensity of the low temperature shoulder (marked as 1) grew at the expense of the principal endotherm (marked as 2) and the latter eventually disappeared in PLA-2+1J. This behaviour might be attributed to the melting of two different crystalline populations with different lamellar thicknesses and degrees of perfection according to the Thomson-Gibbs equation (*c.f. chapter 2, section 2.2.1, equation 2.5*). The chain architecture modifications possibly achieved in the initial linear PLA may enhance the crystallization of less perfect crystals (lower lamellar thickness) due to an increasing content of end groups and/or branching points which in turn exhibit a lower T_{mp} [94, 313, 376]. While the lower T_{mp} exhibited by PLA-4+1J sample probably agreed with the above described explanation, this trend was not observed for PLA-4 "neat" and PLA-4+0.5J samples due to their lower ability to crystallize upon heating, under these testing conditions.

6.6 Thermal fractionation: chain heterogeneity distributions

Using DSC analysis, the investigation performed in this section summarized the following aspects:

- Evaluation of the self nucleation methodology on two unmodified PLA samples which exhibit an increasing D-lactide content.
- Preliminary evaluation of the changes in the molecular structures of reactively modified samples using the *Successive Self-Nucleation and Annealing* fractionation concept.

6.6.1. Self nucleation experiments

The main goal of these experiments was to determine the first T_s temperature (T_{s1}) used in the SSA protocol according to the thermal protocol described in *section 5.1.5.b* (*c.f. chapter 5*). This temperature should correspond to the lowest T_s within domain II, which causes the maximum self-nucleation without annealing, in order to improve the fractionation resolution [68, 361]. Since this work aimed to study the effect of the structural modifications on the chain heterogeneity of each PLA type; the initial T_{s1}, of modified samples, should be similar to the T_{s1} of "neat" samples.

The cooling and heating scans after thermal conditioning at the indicated T_s are shown in *figure 6.11* and *6.12* for PLA-4 and PLA-2 "neat" samples, respectively.

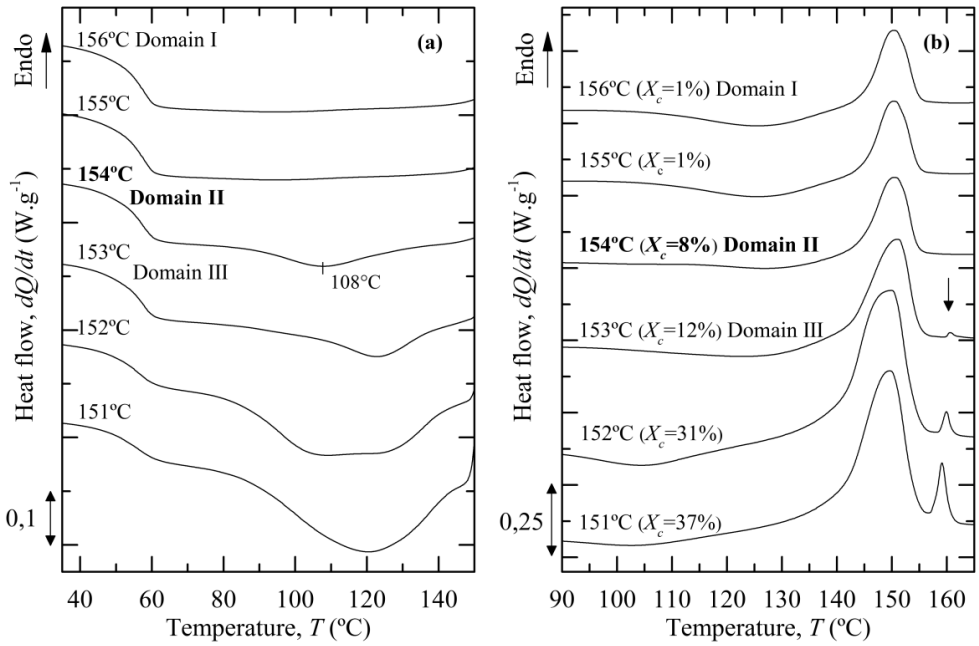

Figure 6.11. (**a**) cooling and (**b**) heating scans at 10 °C.min^{-1} after SN at the indicated T_s temperatures for PLA-4 "neat" samples. The degree of crystallinity developed during the corresponding thermal cycle is indicated in brackets.

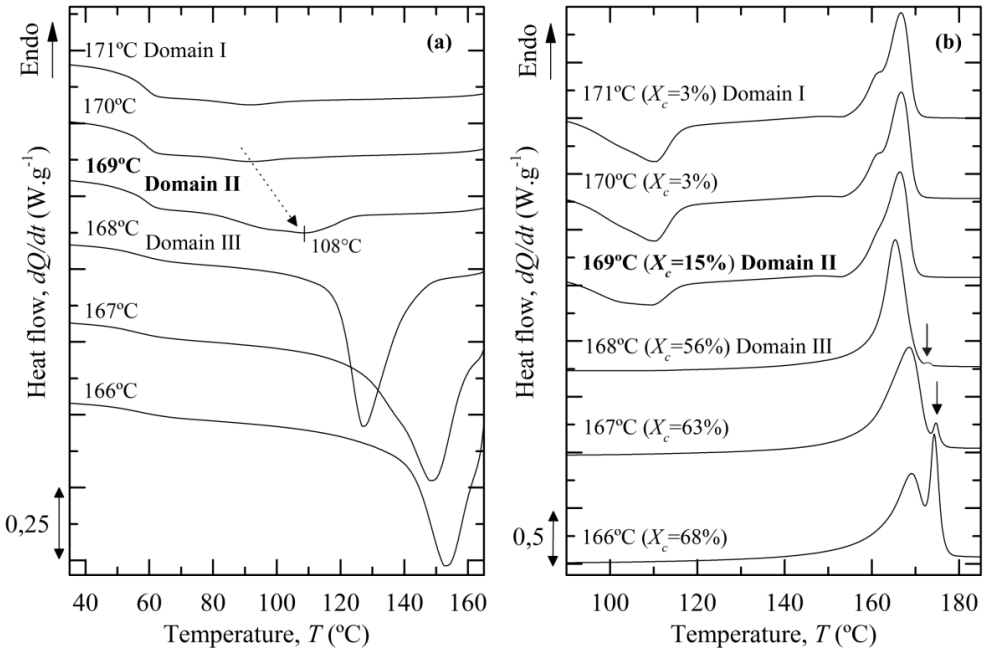

Figure 6.12. (**a**) cooling and (**b**) heating scans at 10 °C.min^{-1} after SN at the indicated T_s temperatures for PLA-2 "neat" samples. The degree of crystallinity developed during the corresponding thermal cycle is indicated in brackets.

When PLA-4 and PLA-2 were thermally conditioned for 5 min above 154 and 169 °C, respectively, both samples presented similar thermal behaviour in both the subsequent cooling (step **e**) and heating (step **f**) runs of the protocol showed in *figure 5.3* (*c.f. chapter 5, section 5.1.5.b*). This behaviour suggests that all crystalline memory was erased at these T_s temperatures; indicating the characteristic behaviour of domain I.

After being thermally conditioned at 154 and 169 °C, a crystallization shoulder centered in 108 ºC was exhibited by both "neat" samples in the subsequent cooling scans, respectively. On the other hand, the shape of their respective melting endotherms remained fairly unaffected in step **f** as compared to those obtained in step **c**. That is, the melting endotherm of PLA-4 appeared to be slightly narrower and the extend of the low-temperature shoulder seemed to be slightly reduced at the expense of the high-temperature endotherm for PLA-2 "neat" samples. This thermal behaviour suggests that the T_s temperature was high enough to melt almost all of the polymer crystals, but low enough to leave "small" crystal fragments that can act as self-nuclei. Upon cooling, they recrystallized but due do to their infinitely small sizes they cannot be annealed [68, 81]. This behaviour is characteristic of domain II.

Temperatures below 154 and 169 °C produced self-nucleation and annealing which revealed the typical behaviour of polymers in domain III. While crystallization took place almost immediately on cooling, both materials exhibited large crystallization exotherms with decreasing the T_s temperature. On reheating, an additional endothermic peak at high temperatures was observed (around 159 and 173 ºC for PLA-4 and PLA-2, respectively. Indicated by an arrow) and both T_{mp} and X_c increased with decreasing T_s.

On this basis, the optimum self-nucleation temperature which induced self-nucleation without annealing are T_{s1}= 154 and 169 °C for PLA-4 and PLA-2 "neat" samples, respectively.

6.6.2. Preliminary application of the SSA methodology to PLA polymers

A preliminary application of the *Successive Self-nucleation and Annealing* (SSA) fractionation technique was used in order to evaluate chain heterogeneities in all investigated samples. Although this technique has been extensively used to provide information on the distribution of SCB in polyolefins [68, 81, 88], it is believed that this fractionation method could be extended to PLA in order to investigate the molecular changes induced by the reactive process. Results obtained by the SSA technique usually are similar to those obtained by *Temperature Rising Fractionation* (TREF) or by *Crystallization Analysis Fractionation* (CRYSTAF). However, the previous dissolution of the polymers is not necessary using the SSA technique and fractionation during crystallization may be therefore extended to partially crosslinked

polymers (*e.g.* PLA-2+1J samples) [68, 362]. *Figure 6.13* compares the final melting runs after unmodified and modified PLA samples were fractionated using the SSA protocol, as described in *section 5.1.5.b* (*c.f. chapter 5*).

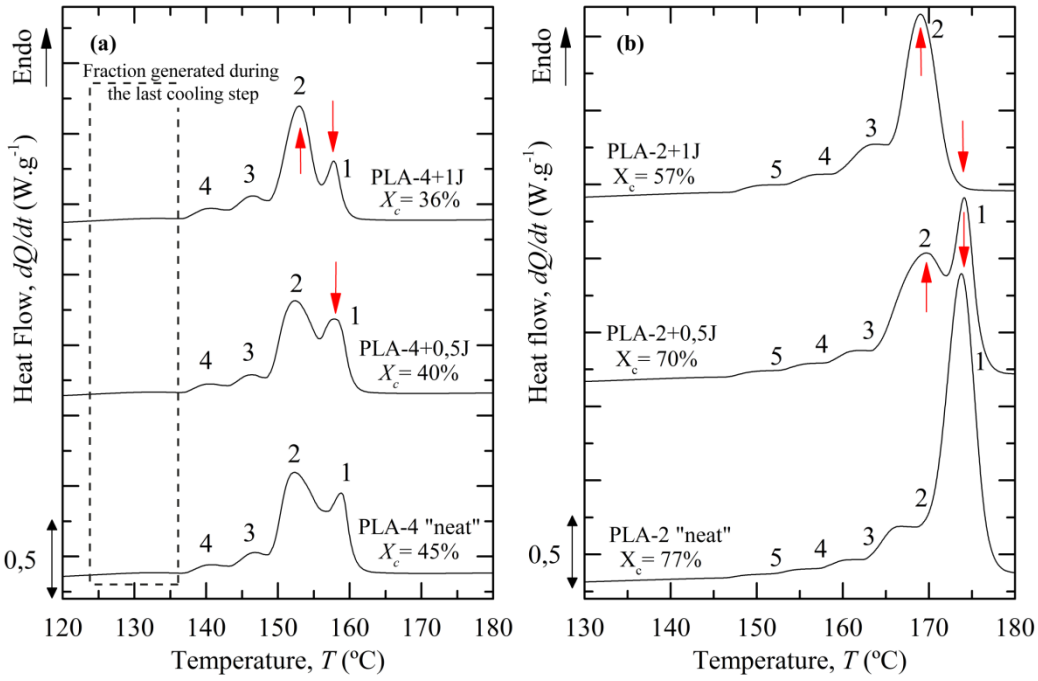

Figure 6.13. Final DSC heating scan (step **g**) at 10 ºC.min^{-1} of (**a**) PLA-4 and (**b**) PLA-2 based samples after applying the SSA thermal protocol.

The different heating scans show the effects of the accumulation of "*n*" self-nucleation and annealing steps using T_s temperatures ranging from 154 to 134 °C and from 169 to 144 °C for PLA-4 and PLA-2 based samples, respectively, with a fractionation window of 5 °C. They reflect the material that has crystallized in successive steps of SSA. Recall that 154 and 169 °C did not cause annealing because they are temperatures within domain II of PLA-4 and PLA-2 "neat" materials, respectively. Therefore, only 4 and 5 steps were able to produce annealing for PLA-4 and PLA-2 based materials, respectively (*c.f. chapter 5, section 5.1.5.b, table 5.1*). The final melting traces show 4 and 5 melting peaks in *figure 6.13. a* and *b*, respectively; thus illustrating the capability of the technique to induce thermal fractionation in PLA.

Regarding PLA-4 based samples, an additional fraction at low temperatures (*i.e.* around 130 ºC, indicated in the dashed rectangle) was revealed after thermal fractionation. This last fraction was likely to be crystallized during the last cooling run (step **f**). Even though a self-seeding temperature is probably missing in the thermal

protocol of PLA-4 based samples (*i.e.* T_s =129ºC), the fractionated populations exhibited in *figure 6.13.a* remained unaffected.

It is well known that the SSA-DSC endotherm areas are proportional to the mass fraction of crystalline phase that are formed at each T_s [362]. Thus, the DSC curves of *figure 6.13* were integrated and the partial degree of crystallinity (referred to as partial X_c) corresponding to each peak was calculated. *Figure 6.14* shows the evolution of the magnitude of the partial X_c for each endotherm that are formed at each T_s with an increase in the SAmfE concentration for both PLA types.

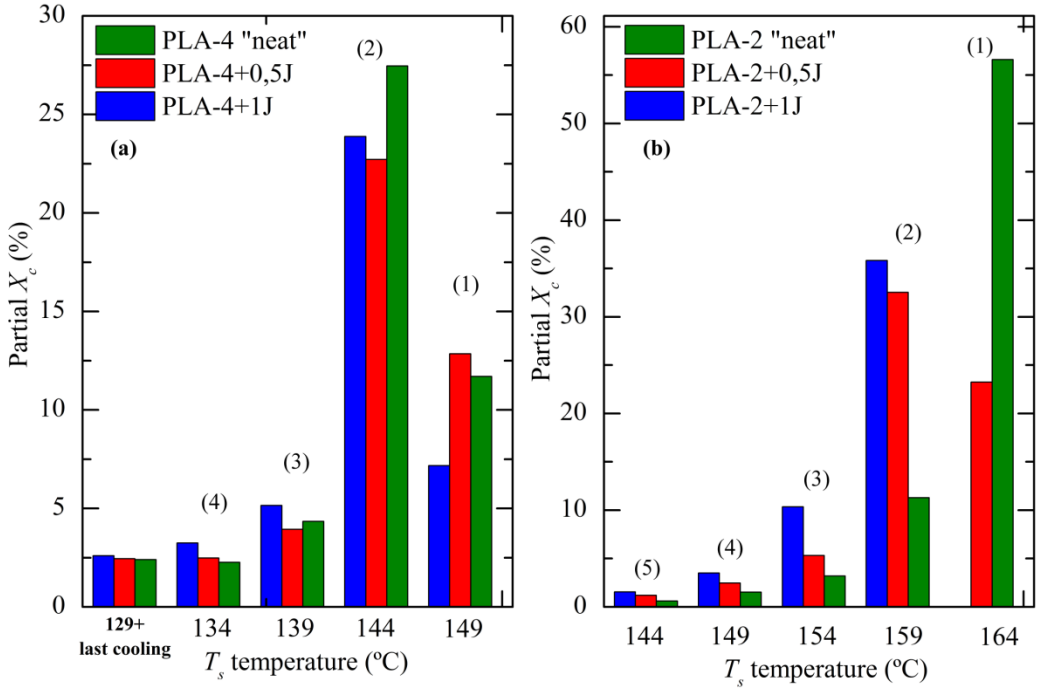

Figure 6.14. Partial degree of crystallinity developed at each T_s temperature for **(a)** PLA-4 and **(b)** PLA-2 based samples. The corresponding melting endotherm according to *figure 6.13* is indicated in brackets.

Based on the melting temperature of each endotherm shown in *figure 6.13*, results suggest that PLA-4 "neat" samples developed thinner lamellas (lower melting temperatures) than PLA-2 "neat" samples after thermal fractionation according to the Thomson-Gibbs equation (*c.f. chapter 2, section 2.2.1, equation 2.5*).On the other hand, while the thickest lamellas (marked as 1) remain the dominant crystallized fraction for PLA-2 "neat" samples, the development of thinner lamellar crystals (marked as 2) seemed to be promoted at the expense of the thicker ones for PLA-4 "neat" samples. Moreover, a decrease in the final X_c was apparent.

These observations point towards the influence of the stereoregularity on the chain folding needed for the crystallization process. It should be kept in mind that the SSA protocol has been designed to fractionate chains according to their crystallisable sequence lengths which are usually separated by irregularities. Regarding both PLA "neat" samples, the random sequencing of low amounts of D-lactide units in the main polymeric chain during the ROP process changes the length distribution of the crystallisable regular isotactic PLLA chain segments by introducing "defects" or "disruptions" in the chemical group stereo-arrangement that cannot enter in the lamellar structure. Higher the concentration of D-lactide units, shorter the crystallisable regular isotactic PLLA sequences as illustrated in *figure 6.15*. On this basis, the resulting shorter uninterrupted sequences promote the development of thinner lamellas, which would melt at lower temperatures, and alter the final X_c during thermal fractionation. Similar effects of the tacticity distribution on the lamellar thickness distribution have already been reported by Virkkunen *et al.* [71, 72] for isotactic PP.

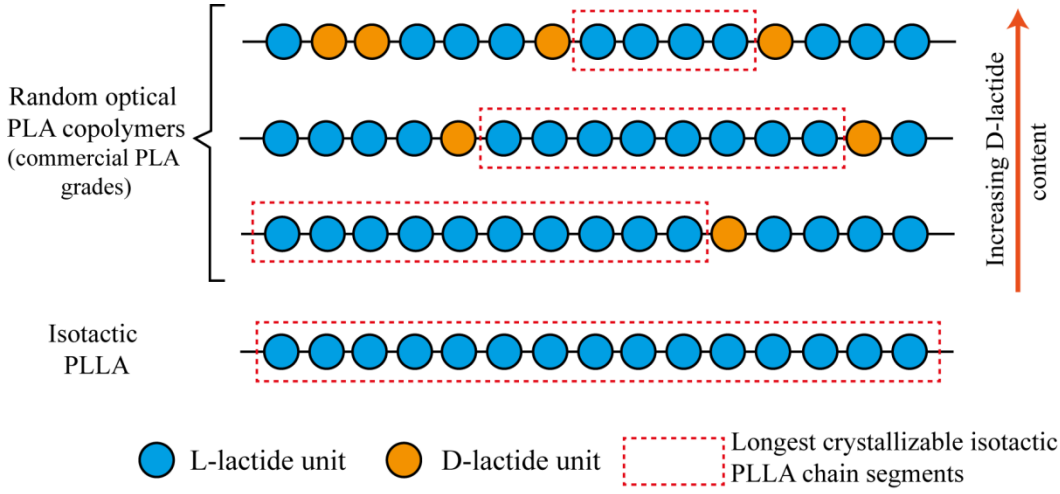

Figure 6.15. Illustration of the effect of an increasing D-lactide content on the length of the crystallisable regular isotactic PLLA chain segments for commercial PLA grades.

Melt compounding PLA with 0.5 wt.% of SAmfE led to a progressive decrease in the peak height of the highest temperature endotherms (marked as 1, indicated by a red arrow) coupled with a simultaneous increase in the peak height and a broadening of the lower temperature neighbouring endotherms (marked as 2), as shown in *figure 6.13*. The calculated partial X_c corroborates the previous observations and evidences an increase in the partial areas corresponding to thinner lamellar crystals at the expense of the dominant crystallized fraction (marked as 2 for PLA-4 and as 1 for PLA-2 "neat" samples) with the addition of SAmfE, as shown in *figure 6.14*. For both

PLA+1J samples, the endotherm marked as 2 was narrowed as compared to other samples which could reflect the development of a more uniform distribution of lamella thickness in this dimension range. Regarding, PLA-2+1J samples, the highest melting point fraction presented by PLA-2 "neat" samples was suppressed. The final X_c declined with increasing SAmfE content.

Based on the assumption that both the crystallization occurred in the α form (*c.f. chapter 5, section 3.1.5*) and that each endothermic peak corresponds to the melting of crystallites with different average thickness, coupling reactions play two important roles on the final SSA results.

- Branching points of the possible non-uniform branched structured generated during the mixing process could act as microstructural defects in the linear polymer chain which further limits the length of the crystallisable sequences. The remaining regular PLLA linear chain sequences (between two D-lactic units) are probably further shortened and thinner crystals are produced at the expense of thicker ones. These changes imply a decrease in the final X_c [68, 362].

- The significant increase in MW as measured using SEC-DRI (*c.f. table 6.2*) coupled with the topological restrictions caused by possible branched structures reduced the mobility of the polymer chains. The reptation-like mobility of chains to crystallization sites is probably slowed down and a depression in the crystallisable lamella thickness and X_c was observed [68, 362].

For PLA-2+1J samples, the HMW coupled with the presence of gels probably further reduced the chain mobility which inhibits the crystallization of the thickest lamella population. This observation is in line with the conclusion of Pérez *et al.* [362] dealing with ethylene-butene copolymers modified by peroxide crosslinking. On this basis, the SSA results indicate that both the random sequencing of low amounts of D-lactide units in regular isotactic PLLA chains and/or chain architecture modifications (and thus higher MW values) deplete the longest crystallisable sequences that form the thicker lamellas, as shown in *figure 6.13* and *6.14*.

As compared with the final heating scan after thermal fractionation of several short chain branched polymers (VLDPE, LLDPE, HPB) [68, 81, 88, 361], sharp and well-defined melting peaks were not observed in *figure 6.13*. Similar limitations have been observed for HDPE materials [68, 87] and PET/PC blends [90] after thermal fractionation. According to Trujillo *et al*. [87], results suggest that thermal fractionation proceeds solely by differences in MW of the crystallisable sequences and is not as efficient as in the case of polyolefins featuring short chain branching.

6.7. Consequences of the topological changes on the melt rheology

A preliminary trial was performed to evaluate the effects of the addition of SAmfE on the rheological behaviour of PLA materials using dynamic rheological measurements at 180 °C. This temperature was chosen as the better compromise between flow properties and thermal stability throughout rheological testing. *Figure 6.16* and *6.17* report the $|\eta^*(\omega)|$ and $G'(\omega)$ functions, respectively, for "neat" and modified PLA samples.

The linear terminal regime was rapidly reached (around 10^0 rad.s^{-1}) for "neat" samples, but the lowest ω accessible (0.0628 rad.s^{-1}) using a frequency sweep experiment was still far from the terminal zone for modified samples. This is because neither $|\eta^*(\omega)|$ reached a plateau nor $G'(\omega)$ reached the terminal double logarithmic slopes of 2, as shown in *figure 6.16* and *6.17*, respectively. Since branched polymers are usually defined as thermorheologically complex materials, the applicability of the TTS principle is restricted [103, 377]. In order to prevent the violation of this principle, the combination of a frequency sweep and the conversion of the creep-recovery data at 180 °C was a viable strategy in order to extent rheological measurements towards lower ω, as shown in both figures.

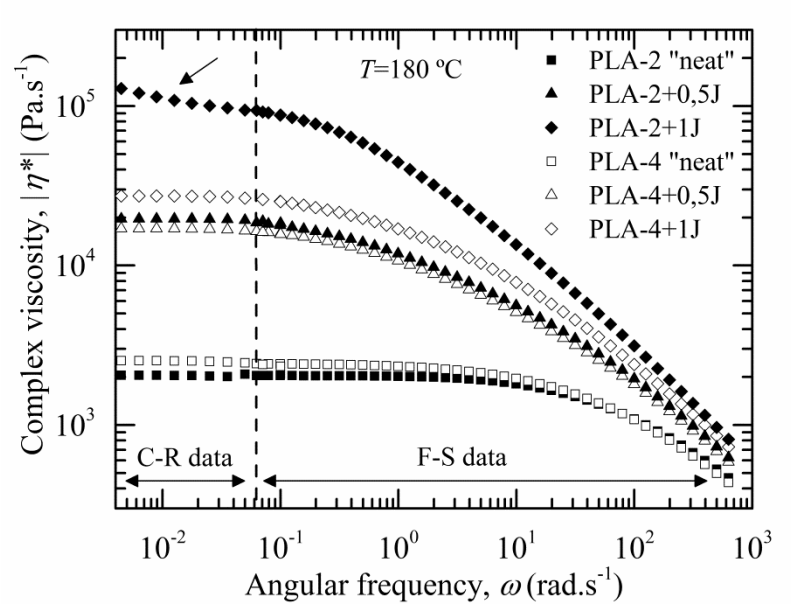

Figure 6.16. Effects of the SAmfE addition on the complex viscosity functions at 180 °C. F-S data: frequency sweep data, C-R data: conversion of the creep-recovery data calculated from retardation spectrum.

At first glance, both experiments (*i.e.* frequency sweep and the conversion of the creep-recovery data) connected well with each other. Both "neat" samples exhibited the typical behaviour of linear flexible polymers, as shown in *figure 6.16*. The terminal (Newtonian) region was shown over a wide range of ω and was followed by the pseudo-plastic regime with increasing ω. This behaviour is due to a relative fast relaxation process of the different linear chains by self-diffusion which is also termed reptation [96] (*c.f. chapter 2, section 2.3*). PLA-2 "neat" samples exhibited a slightly lower η_0 value as compared to PLA-4 "neat". This trend could be attributed to the slight difference of MW observed between both samples (*c.f. table 6.2*).

In contrast, besides a significant increase in η_0, the onset of the terminal region shifted to lower ω and the transition zone between the terminal and power-law region was enlarged for modified samples. Although these trends could be attributed to the alteration of the molecular mobility due to the increasing number of interactions and entanglements per chains (*i.e.* higher relative M_n values for modified samples, *c.f. table 6.2*), both the increase in MW and the architectural modifications have similar effects on the viscosity function. One of the most prominent differences was the increase in MW according to SEC-DRI measurements (*c.f. table 6.2*).

For a given SAmfE content, differences between both PLA types may be observed when comparing η_0 values. PLA-2 samples always exhibited an higher η_0 as compared to PLA-4 samples. This may be expected if the higher degree of degradation over mixing time is considered. The formation of a higher concentration of terminal functional groups enhanced coupling and/or branching reactions and led to both a larger increase in MW and a possibly larger degree of structural modifications.

Special attention should be paid to PLA-2+1J. A clear shoulder was observed at low ω (indicated by an arrow), which is a common behaviour for heterogeneous systems (*e.g.* gel particles) with different relaxation times in the low ω range.

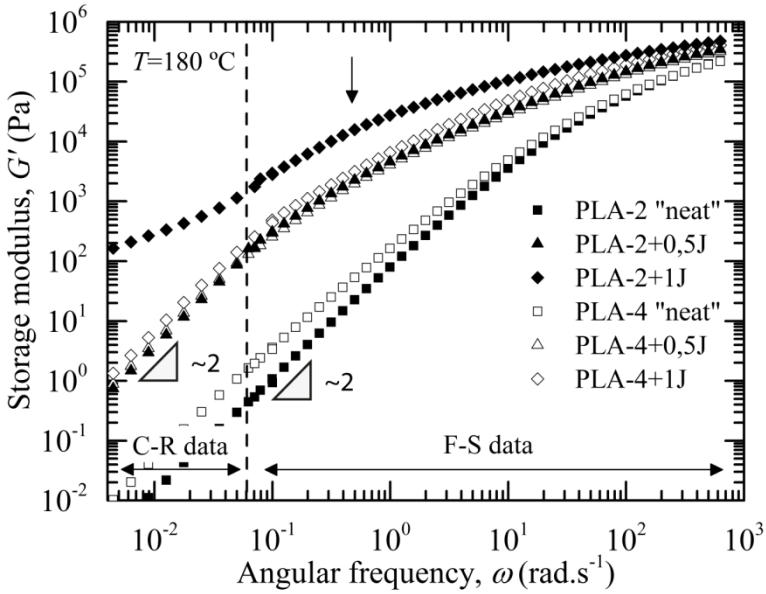

Figure 6.17. Variation of the storage modulus with angular frequency for "neat" and modified PLA samples at 180°C. F-S data: frequency sweep data, C-R data: conversion of the creep-recovery data calculated from retardation spectrum.

In the high ω range (10^2-10^3 rad.s^{-1}), all $G'(\omega)$ functions tend to converge towards a roughly similar plateau value. This trend suggests that the molecular motions, which govern the high ω range, remained roughly independent of the molecular structure, as already reported by different authors [98, 378].

In contrast, significant differences in $G'(\omega)$ were observed at low ω (5.10^{-3}-10^2 rad.s^{-1}). As compared to "neat" samples, an additional intermediate relaxation regime (indicated by an arrow) was observed between the terminal (*i.e.* $G' \propto \omega^2$) and plateau region for modified samples. PLA-2+1J samples even displayed a significant transition in $G'(\omega)$ at low ω. While these behaviours are characteristic of branched polymers and complex branch-on-branch topological structure, respectively [152, 178, 316, 376, 378], definitive conclusions about the presence of these structures cannot be drawn from *figure 6.17*. This is because both the increase in MW as measured using SEC-DRI (*c.f. table 6.2*) and the topological modifications have convoluted effects on the dependence of G' on ω. However, these phenomena are usually attributed to a significant increase in the chain relaxation times due to the formation of a better cohesive molecular network.

In addition, $G'(\omega)$ exhibited higher values for modified samples as compared to "neat" ones in the low ω range (5.10^{-3}-10^2 rad.s^{-1}). This tendency indicates an enhancement of the melt elasticity according to Corre *et al.* [47] and Liu *et al.* [316].

It is known that the melt elasticity has a direct relationship with the melt strength which is an indication of the resistance for a melt to extension. Since the melt strength is highly dependent on the amount of the longest chains present in the system, the above observation is in line with the increasing relative M_z values (*c.f. table 6.2*) when PLA is melt compounded with the SAmfE agent.

6.8. Summary

Under the processing conditions used in the lab-scale mixing process, results suggest a competition between polymer chain degradations and coupling reactions during processing. The higher melting temperature exhibited by PLA-2 material has drastic effects on the melt stability. The possible higher local shear field applied to the material up to its complete melted state is likely to enhance thermo-mechanical degradations; thus lowering further thermal stability over mixing time. The resulting larger concentration of terminal groups leads to a higher reactivity of PLA-2 material towards SAmfE. Consequently, the higher the stereoregularity of the PLA type, the lower the critical SAmfE concentration to generate crosslinking.

After processing, a significant increase in MW was measured using SEC-DRI measurements. By increasing the SAmfE content (from 0.5 to 1 wt.%), the monomodal MWD observed for "neat" PLA changed and a second and third MW peak appeared at high MWs, respectively.

Since modified PLA samples are not carefully prepared model polymer based on specific polymerization technologies, the topological modifications achieved are not trivial and would be a mixture of several types of non-uniform structures in MW, in architectures and in the number of branch points per macromolecules. Classical spectroscopic techniques, such as FT-IR and ^{1}H NMR, exhibited limited sensitivity to detect and identify the topological changes due to this complex molecular environment and a concentration of structural modifications probably below the detection limits of these techniques.

Upon heating from the glassy to the melting state, a decrease in the D-lactide content enhanced the cold-crystallization process, while a reverse trend was observed with increasing SAmfE content. That is, the enhancement of both the MW and the possible topological restrictions inhibit chain mobility and therefore decrease X_c. On the other hand, the amount of D-lactide content, the increase in MW and the possible formation of branching points alter the length distribution of the regular crystallisable PLLA chain segments. With increasing both the D-lactide and the SAmfE content, the increasing concentration of irregular molecular structures change the final crystal perfection distribution during crystallization; thus promoting the development of thinner lamellas and a depression of the final X_c.

Definite conclusions about the presence of branched structures cannot be drawn from rheological measurements because the significant enhancement of the MW and the possible formation of non-uniform branched structures have convoluted effects on the rheological properties. However, while the complex viscosity was significantly increased at low ω, this difference was not as pronounced for values near the usual extrusion ω (between 100 and 1000 rad.s^{-1}) when PLA was melt compounded with SAmfE. This behaviour could lead to a desirable benefit on the industrial level as PLA and reactively modified PLA can be similarly processed without relevant changes in extrusion processing conditions.

Regarding modified samples, $G'(\omega)$ was less shear sensitive over the investigated ω range and higher values were apparent in the low ω range. These trends indicate an increase in the melt elasticity which can minimize several drawbacks (*i.e.* sagging of melts, necking, etc) during film/sheet casting, film blowing and/or foaming processes.

Results and Discussions

Chapter 7:

Pre-industrial scale: One-Step Reactive Extrusion-Calendering process

This chapter presents the results which are obtained from the scaling up of the processing conditions used in *chapter 6.* Sample formulations and identifications are given in *table 4.3* (*c.f. chapter 4, section 4.3*). These compositions were selected in order to prevent crosslinking reactions and to maintain a proper melt homogeneity during continuous processing in pilot plan.

Based on the higher reactivity exhibited by PLA-2 type towards SAmfE, these sample formulations were selected to generate three degrees of structural modifications. Initially, the rheological properties of the modified materials were correlated to both the more reactive PLA type and the increasing SAmfE amount. Then, the effect of the topological modifications on the thermal, mechanical and fracture behaviours were investigated.

7.1. Scaling up and process monitoring

As a result of the inability to monitor on-line the reaction profile during the scaling up, the rheological response of the materials to chain extension/branching reactions was evaluated using dynamical rheological measurements. Frequency sweeps experiments at 190 °C (temperature of the sheet at the die exit) were carried out in different points along the calendered sheet length in order to determine the sheet part that showed a similar degree of structural modifications. The complex viscosity close to 0,08 $rad.s^{-1}$ was used as monitoring parameter. On this basis, a profile of modification along the extruded sheet, expressed as extrusion time was plotted and represented in *figure 7.1*.

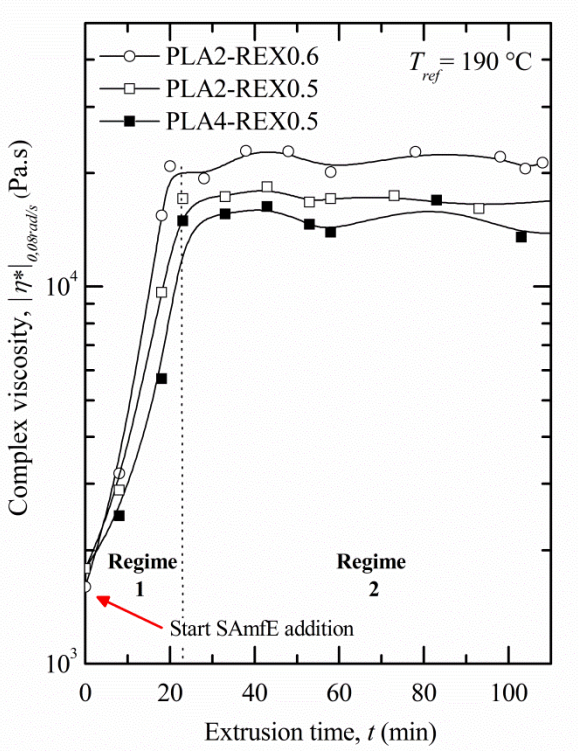

Figure 7.1. Complex viscosity closed to 0.08 rad.s^{-1} as a function of extrusion time for PLA-REX samples.

Throughout extrusion time, two different regimes were observed as shown in *figure 7.1*. The first regime (referred to as regime 1) corresponds to the time needed to reach the saturation of the reactive entities in the dosage zone of the extruder. In all cases this time was longer than in the previous internal mixer preparation (20 versus 13 min). This situation could be expected if the dynamic nature (continuous flow) of the extrusion process is considered.

From an industrial point of view, the stabilization of a production line requires a specific time in order to reach a stable regime. In the present study, this specific time was needed to reach the saturation of the reactive species involved such as PLA functional end groups and epoxies. Regarding the study performed in the internal mixer, it must be remembered that the mixing process works by batch in which no continuous “discharge” of the bulk mixed was performed contrary to the extrusion process.

In the second regime (referred to as regime 2), this saturation condition appeared to be reached and all specimens exhibited a similar viscosity for a given sample composition. This trend suggests a similar degree of modification (chain extension and/or branching) over extrusion time. The increasing viscosity values with both the

more reactive PLA type (*i.e.* PLA-2) and the concentration of SAmfE agreed well with the previous rheological measurements, as shown in *section 6.7* (*c.f. chapter 6*).

7.2. Chain structure analysis

As concluded in *chapter 6*, classical spectroscopic methods (*i.e.* FT-IR, ^{1}H NMR) exhibit limited sensitivity to the presence of the topological changes under investigation. Nevertheless, a significant modification of the complex viscosity and storage modulus functions against the angular frequency was observed with an increase in the SAmfE concentration. Since rheological properties react very sensitively on molecular changes, rheology and especially linear viscoelasticity could be a valuable tool to gain further understanding of the molecular structure. In this section, the chain architecture modifications achieved in PLA-REX samples are discussed using both SEC analysis as well as rheological properties and are finally estimated on the basis of the so-called van Gurp-Palmen plots.

7.2.1. Molecular characterization

The multifunctional epoxy-functionalized reactive agent, used in manufacturing PLA-REX samples, is likely to promote the formation of LCB and/or complex topological structures, as already reported by numerous authors [47, 102, 371, 379]. In solution, LCB polymers exhibit a more compact configuration than their linear homologues for a given MW. An underestimation of the MW of LCB polymers by SEC is likely to occur due to coelution issues of different molecular topologies. For the purpose to provide the closest approximation to the real MWD for branched polymers, SEC coupled with multiple detectors should be used.

A preliminary trial was performed to evaluate the MW of PLA-REX samples using SEC with in line differential refractive index, viscometry and multi angle light scattering (MALLS) detectors. Before testing, samples were carefully dissolved in tetrahydrofuran (THF, used as eluting phase) and filtered. After filtering, the filters were dried under vacuum, in order to remove the remaining THF, and subsequently weighted to contribute to a quantitative detection of possible gel structures. The weight of the filters before and after filtration was found to be roughly similar; confirming the total dissolution of all the samples in THF. Nevertheless, the radius of gyration (as measured by MALLS) as well as the intrinsic viscosity (as measured by viscometer) was found to be roughly similar for all samples, indicating the absence of structural changes. As will be shown in *section 7.2.3*, significant differences in rheological behaviour of the different samples were found. Therefore, it can be assumed that the aforementioned SEC-multiple detectors results are not trustworthy.

It is surprising that SEC-MALLS measurements have not displayed such a HMW components even at a low concentration, because the scattering signal from MALLS

depends on concentration c multiplied by the molecular weight M. Consequently, the sensitivity of the SEC-MALLS towards HMW macromolecules is greater than that of the conventional SEC-DRI measurements.

Recall that conventional light-scattering measurements provide accurate results for strictly uniform HMW macromolecules with respect to MW and structure. This limitation arises from a similar angular dependence of the scattering intensity by the shape of the macromolecules and their non-uniformity in MW. Unfortunately, there is no reliable way of separating these two effects from each others.

Recall that the commercial multifunctional epoxy-functionalized reactive agent, which is used in manufacturing PLA-REX samples, is able to promote the formation of long chain branching and/or complex topological structures, as shown elsewhere [47, 102, 371, 379]. Nevertheless, since PLA-REX samples are not a carefully prepared model polymer based on specific polymerization technologies, the topological modifications achieved are not trivial. They would be a mixture of several types of non-uniform structures in MW, in architectures and in the number of branch points per macromolecules.

Therefore, the well defined ratio of the radii of gyration of a branched, $R_{G,b}$, and a linear, $R_{G,l}$, macromolecule with the same MW, which enables the determination of the degree of branching of a uniform branched polymer, cannot be used in the current study. This is because light scattering yields different averages for MW and radius of gyration namely the weight-average molecular weight (M_w) and the z-average radius of gyration ($R_{G,z}$) [132, 380].

By definition, $R_{G,z}$ is more sensitive to M_z than M_w for a non-uniform branched polymer. That is, $R_{G,z}$ values are usually larger than the radius of gyration, which corresponds to a macromolecule with MW equal to M_w, for a non-uniform branched polymers [132, 380].

In solution, LCB polymers exhibit a more compact configuration than their linear homologues for a given M_w. In other words, branched macromolecules feature a lower radius of gyration as compared to their linear counterpart of similar MW. On the other hand, branching broadens the MWD; thus enhancing discrepancies between $R_{G,Z}$ and M_w [132, 380].

Consequently, both the effects of branching and non-uniformity on $R_{G,z}$ are compensating for each others, thus hiding specific information on the type of structural modifications. In other words, the dependence of $R_{G,Z}$ on M_W of a randomly modified polymer with a non-uniform structure will be similar to that of its linear counterpart (*e.g.* PLA-REX and PLA samples).

Similar experimental limitations have been already reported for investigating sparsely LCB-PE [157], PP featuring low amounts of LCB [108, 381] and LCB metalocene catalyzed PE (which is a blend of linear and branched chains) [149]. Authors concluded that this technique is not enough sensitive to estimate slight changes in molecular dimensions between the very low amount of non-uniform branched structures and the dominant linear fraction. While we could expect that SEC-DRI data may be flawed due to coelution issues, van Ruymbeke *et al.* [99] reported that the error on the MWD may be considered to be negligible for low levels of structural modifications. On this basis, standard SEC-DRI equipment was preferred to investigate the molecular modifications of PLA induced by reactive extrusion. *Figure 7.2* shows the MWD for PLA and PLA-REX samples and the corresponding relative MW averages are compiled in *table 7.1*.

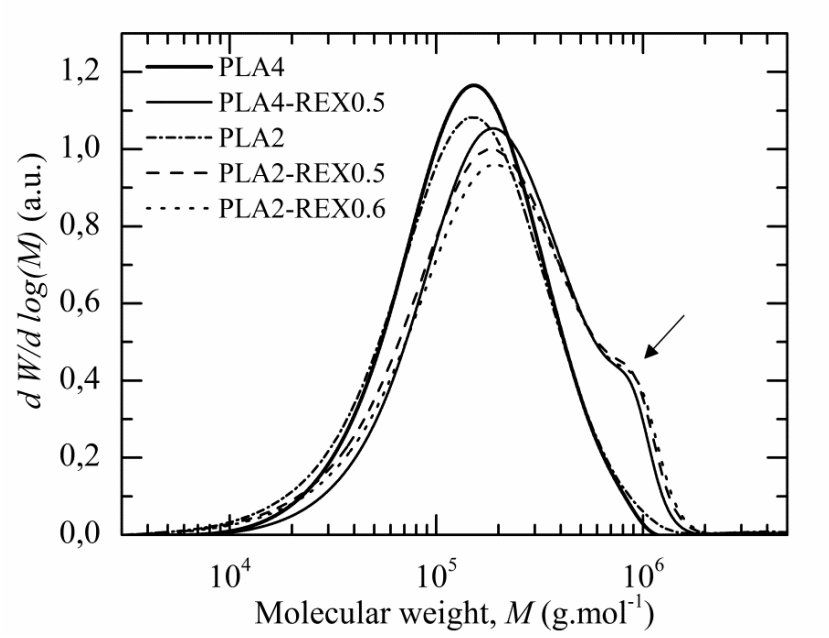

Figure 7.2. Effect of the REX processing on the shape of the MWD. The arrow indicates the shoulder which appeared in the HMW tail of the MWD corresponding to PLA-REX samples.

Both PLA samples displayed a narrow monomodal MWD as shown in *figure 7.2*. While a slight decrease in MWs was observed for unmodified PLA samples as compared to PLA raw materials, this decrease lied within chromatographic error normally associated with a SEC separation (about 3% for M_w measurements) [382]. In the present study, this trend could be attributed to a minimized effect of the different thermo-oxidative degradation mechanisms on the PLA matrix due to a satisfactory optimisation of the processing conditions (*i.e.* nitrogen blanket, relative short

residence time, vacuum, etc). When the above values are compared with the relative MW values reported in *chapter 6* (*c.f. section 6.3, table 6.2*), results suggest that the mixing conditions used in the continuous extrusion process generated less degradations than in internal mixer process.

Table 7.1. Numerical analysis of the molecular weight distributions. For comparison purposes, relative MW values of raw materials were included.

Sample nomenclature		M_n [a] (kg.mol^{-1})	M_w [a] (kg.mol^{-1})	M_z [a] (kg.mol^{-1})	*PDI*	Area (%)
PLA-4 pellets	**global**	100 ±2	187 ±4	337 ±2	1.9 ±0.1	100
PLA4	**global**	92 ±6	185 ±3	329 ±30	2.0 ±0.2	100
PLA4-REX0.5	**global**	119 ±1	246 ±2	475 ±7	2.08 ±0.03	100
	Peak I [b]	112	205	347	1.8	78
	Peak II [b]	795	843	894	1.1	22
PLA-2 pellets	**global**	90 ±1	181 ±1	356 ±5	2.1 ±0.1	100
PLA2	**global**	85 ±1	179 ±1	345 ±4	2.13 ±0.04	100
PLA2-REX0.5	**global**	106 ±2	272 ±3	545 ±10	2.57 ±0.08	100
	Peak I [b]	105	241	415	2.3	75
	Peak II [b]	865	952	1 010	1.1	25
PLA2-REX0.6	**global**	120 ±1	292 ±1	604 ±83	2.44 ±0.03	100
	Peak I [b]	113	246	471	2.2	71
	Peak II [b]	990	1 058	1 130	1.1	29

[a] Relative MW values based on PMMA standards in HFIP. They were calculated from the average of three experiments based on fresh samples.
[b] Results obtained from the deconvolution analysis using log-normal functions.

The MWD of PLA-REX samples significantly differed from those of PLA samples, as shown in *figure 7.2*. The MWD spectra were broadened and a shoulder appeared in the HMW tail (around 800 kg.mol^{-1}, indicated by an arrow). Results suggest that the two principal hydrodynamic volumes, which controlled the elution time, were roughly similar between PLA-REX samples as all three spectra were approximately centred on the same MW peak values. Under the current processing conditions, this trend might be a consequence of the formation of similar architectural topologies. The displacement of the original PLA peak to higher MWs suggests that weight fractions with higher MWs were generated at the expense of the low MW populations.

Since SAmfE is a multi-functional-epoxide reactive agent, the observed trend could be attributed to the chemical bonding of several PLA chains to one SAmfE molecule. However, the topological modifications achieved are not trivial and would be a mixture of several types of non-uniform structures in MW, in architectures and in the number of branch per macromolecules. During sample conditioning, the total dissolution of the samples in HFIP confirmed that no gels were generated. In this way, differences in the MWD shape may indicate an increase in the population of high MW

linear chains and/or the presence of branched structures. This hypothesis is in line with the significant enhancement of MWs between PLA and all PLA-REX samples and with the study of Corre *et al.* [47].

It is well known that the inverse of the number-average molecular weight (M_n) is related to the number of functional terminal groups and M_n to the number of entanglements per chains. As can be seen in *table 7.1*, M_n increased with the addition of SAmfE, suggesting both the consumption of terminal end groups during chain extension and/or chain branching reactions and an increase in the number of entanglements per chains.

PLA2-REX0.5 samples exhibited higher MW values than PLA4-REX0.5 samples for equivalent amount of SAmfE agent. This trend may be due to the combination of two different effects. On one hand, PLA-2 raw material (*i.e.* PLA-2 pellets) shows a higher amount of functional end groups than PLA-4 one (*c.f. table 7.1*), which could result in a higher reactivity towards SAmfE during processing. On the other hand, the degree of thermal degradation during processing should be considered, as terminal end groups for commercial PLA are usually end-capped [288, 316]. Bigg [288] suggests that the thermal stability during processing depend on the width of the processing windows. PLA-2 raw material exhibits a narrower processing window than PLA-4 (according to their respective end melting temperatures, *c.f. chapter 3, section 3.2.1, table 3.3*). This aspect will increase the local shear field applied to the material up to its complete melting state during mixing which could enhance thermo-mechanical degradations, lowering further thermal stability during mixing. Therefore, a higher amount of reactive functional end groups may be created and the reactivity towards SAmfE is probably enhanced.

As compared to internal mixer samples (*c.f.* PLA+0.5J, *chapter 6, section 6.3*), a less evident bimodal distribution in all PLA-REX samples was observed. Possibly, lower degrees of structural modifications were generated due to the shorter reaction time (13 *vs.* 4.33 min) during REX processing. Therefore the differences in hydrodynamic volume were less pronounced in PLA-REX samples.

Possible errors in the determination of the relative average MWs are expected for PLA-REX materials as samples did not feature a Shultz-flory type MWD. On this basis, the peak deconvolution technique can be a valuable solution in order to quantitatively resolve these experimental issues. By using log-normal (area) functions (*c.f. chapter 6, section 6.3, equation 6.2*) and similar deconvolution conditions as describe in *section 6.3*, each MWD spectrum was deconvoluted. Partial areas and relative MW averages calculated are given in *table 7.1*.

7.2.2. Melt stability throughout rheological testing

Dynamic time sweep experiments were conducted during 1450 s (≈ 24 min) in order to ensure the melt stability throughout rheological measurements. This experimental time allows to complete both frequency sweeps over an angular frequency ranged from 628 to 0.0628 rad.s^{-1} with 10 points per decade and creep-recovery experiments (using fresh samples). Although the melt stability was evaluated for each testing temperature, only results corresponding to the measurements at 200 ºC are plotted in *figure 7.3*. This temperature was chosen due to the usual poor thermal stability of PLA at high temperature over prolonged time (see *figure 7.3*, unstabilized PLA4 sample).

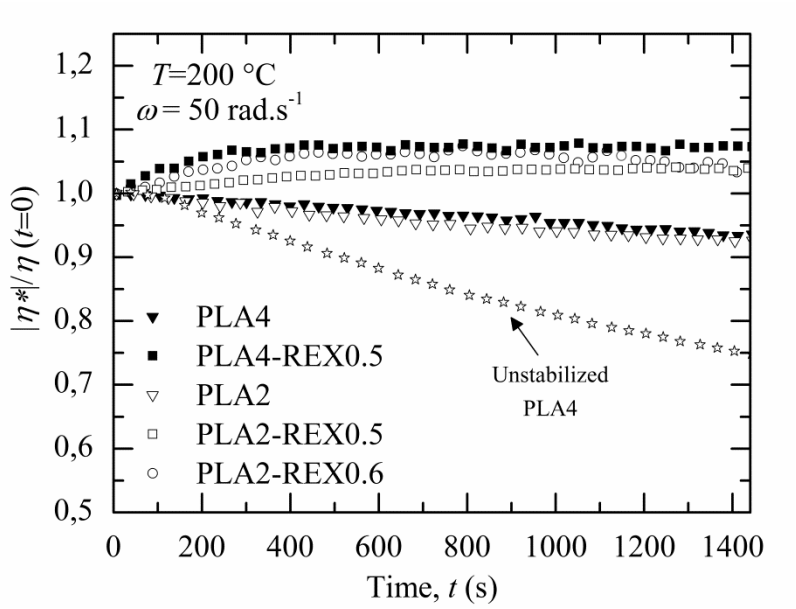

Figure 7.3. Thermal stability of PLA and PLA-REX samples at 200 ºC under a nitrogen atmosphere at 50 rad.s^{-1}.

The addition of either 1 wt.% of Irganox 1010 or the addition of SAmfE significantly increased the melt stability of both PLA types. Al-Itry *et al.* [102] suggested that thermal degradation of PLA can be assumed as negligible if the complex viscosity, normalized by its initial values at t=0 ($|\eta^*|/|\eta^*(t=0)|$) does not decrease by more than 10% within the total testing time. As shown in *figure 7.3*, the $|\eta^*|/|\eta^*(t=0)|$ traces slightly decreased and increased (± 8%) over testing time for PLA and PLA-REX samples, respectively.

The thermal stability was also checked by comparing the MW parameters and MWD of the processed materials before and after rheological testing. Thus, the MW

was evaluated on the recovered samples using SEC-DRI measurements. The total dissolution of the samples in HFIP suggested that no gels were generated during rheological measurements. *Figure 7.4* shows the MWD for the recovered PLA and PLA-REX samples and the corresponding relative MW averages are compiled in *table 7.2*.

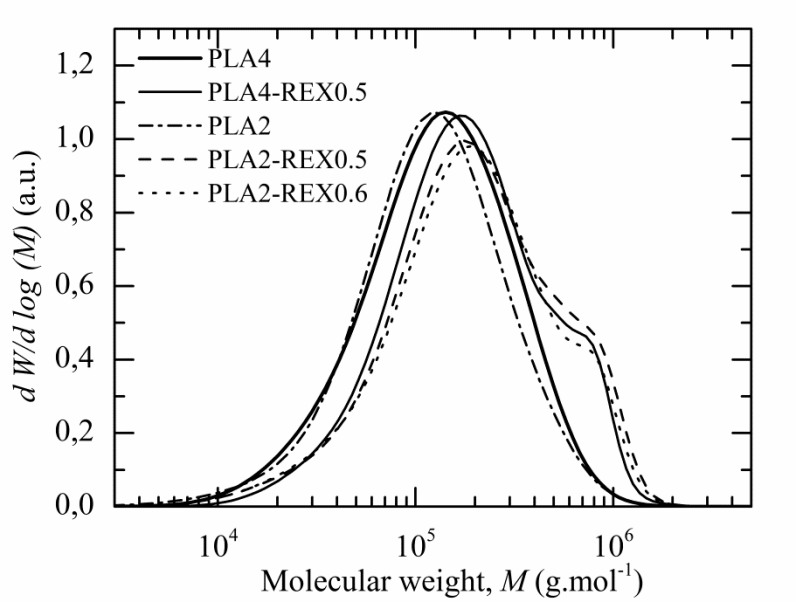

Figure 7.4. MWD for recovered PLA and PLA-REX samples after rheological testing at 200 °C during 1450 s (≈24 min).

Table 7.2. Corresponding relative MW values for the recovered samples after rheological testing.

Sample nomenclature	M_n (kg.mol^{-1})	M_w (kg.mol^{-1})	M_z (kg.mol^{-1})	***PDI***
PLA4	84	180	322	2.2
Error (%)*	9	3	2	2
PLA4-REX0.5	116	267	500	2.2
Error (%)*	1	8	5	8
PLA2	76	167	312	2.2
Error (%)*	10	6	9	3
PLA2-REX0.5	113	284	563	2.5
Error (%)*	7	8	3	3
PLA2-REX0.6	110	282	536	2.6
Error (%)*	4	4	2	1

* The error percentages arise from the difference between the measured MW values after and before (*c.f. table 7.1*) rheological testing, respectively.

The MWD traces were found to be roughly similar to that shown in *figure 7.2* and the relative MW averages and PDI values agreed with previous MW values (see *table 7.1*) within 10 %. Consequently, these trends suggest that further rheological properties remained roughly unaffected by thermal degradations and/or MW changes throughout rheological testing.

7.2.3. Thermorheological behaviour and temperature dependence

For non-crystallisable polymers or those with a very slow crystallization kinetics (*e.g.* PLA), the rheological response could be characterized in the four regions. That is, in the terminal, plateau, transition and glassy zones. This is due to the possibility to perform dynamic measurements in a large temperature window (from T_g to above T_m). While high temperatures predict the terminal region (*i.e.* $G' \propto \omega^2$ and $G'' \propto \omega$), low temperatures govern the glassy behaviour. A previous thermal characterization is necessary to determine the thermal transitions of interest (*i.e.* T_g, T_{cc}, T_m and T_{me}) as the experimental conditions (*i.e.* amplitude strain, dynamic window) should be adjusted as a function of the testing temperature. At the lower temperatures, it is necessary to use very small deformation amplitudes in order to remain within the limits of the LVE and to avoid overloading the instrument.

On this basis, the thermal behaviour of PLA and PLA-REX samples was investigated using DSC experiments, from the first heating run (**H1**) at 10 °C.min^{-1} (*c.f. chapter 5, section 5.1.5.a*). Those relevant thermal properties for rheological measurements are compiled in *table 7.3*.

Table 7.3. Thermal properties determined from the first heating scan (**H1**) for PLA and PLA-REX samples.

Sample nomenclature	$T_{g,m}$ (ºC)	T_{cc} (ºC)	T_{mp} (ºC)	T_{me} (ºC)
PLA4	60.7 ±0.3	121 ±4	152 ±2	158 ±1
PLA4-REX0.5	61.8 ±0.7	116 ±2	149 ±1	156 ±1
PLA2	61.1 ±0.6	107.0 ±0.2	168.3 ±0.4	172.0 ±0.5
PLA2-REX0.5	62.4 ±0.8	109 ±2	166.6 ±0.1	173 ±2
PLA2-REX0.6	62.5 ±0.7	111 ±2	166.1 ±0.2	171 ±2

Since PLA-4 and PLA-2 polymers are prone to crystallize under specific conditions, it is important to ensure that crystallization did not occur during rheological experiments which are conducted between T_g and T_{me}. DSC experiments were carried out to evaluate the evolution of X_c throughout rheological testing at different temperatures below T_{me}, as detailed in *section 9.4 (c.f. chapter 9)*. *Figures 9.10* and *9.11* (*c.f. chapter 9, section 9.4*) present the final heating scans (**H3**) together

with X_c after simulating the testing time required to perform a complete or partial frequency sweep.

In the absence of self-seeding nuclei, the poor sensitivity to crystallize of PLA-4 based samples allowed experimentations at temperatures where the effects of the degradation are negligible (*i.e.* 150 °C) and in the glassy region (*i.e.* 70 and 80, 85 °C). Below their respective T_{me}, PLA-2 based samples can only be tested for prolonged time (≈25 min) at 170 °C. Below 170 ºC, the higher sensibility of PLA-2 based samples to crystallize implied a reduction of the testing time (and thus of the experimental frequency range). That is, viscoelastic measurements were only collected from 628.3 to 12.5 rad.s^{-1} at T_a= 160 and 150 °C.

Special care should be taken when operator are working with the TTS principle. In order to generate the final master curve over an extended ω range, the considered material has to present a thermorheologically simple behaviour. The essence of this concept is based on the similar modification of the time dependence of molecular motions and of relaxation times by changing the temperature of measurements.

Within the LVE regime, the van Gurp-Palmen plot (vGP-plot) is a powerful tool for detecting thermorheological simplicity or complexity behaviour, as already discussed in *section 2.3.2* (*c.f. chapter 2*). Moreover, it provides specific advantages as compared to both the normalized Cole-Cole and |G*($\eta_0.\omega$)| plots. The construction of the vGP plot remains independent on the determination of η_0 for each testing temperature, which can be the rate-limiting step for analyze time at low testing temperatures. On this basis, the phase angle, δ, is plotted against the corresponding |*G**| values for PLA-4 and PLA-2 based materials in *figure 7.5* and *7.6*, respectively. Regardless of the polymer tacticity or chemical nature, all data should merge into the same curve if the empirical TTS principle holds.

According to the above vGP criterion, PLA4 samples could be considered as thermorheologically simple over a certain range of time or frequencies. That is, this material presented a minor deviation from the time temperature superposability for dynamic measurements conducted just above T_g (specifically at T_a=70ºC, red curve). This type of deviation is probably due to short-time viscoelastic relaxation mechanisms (*i.e.* side-group motions) other than configurational changes of the polymer backbone, especially occurring near T_g, and which feature different relaxation sequences [383-385].

Regarding PLA4-REX0.5 samples, this lack of thermorheological simplicity seemed to be enhanced as the measured viscoelastic responses at 70, 80 and 85 ºC shifted differently with temperature. The higher number of entanglement per chains (*c.f.* M_n values in *table 7.1*) coupled with the increase in MW probably increase the

intermolecular interactions between polymeric chains, leading to a stronger coupling between chains. This effect might induce a greater sensitivity of segmental relaxations with temperature, as already suggested in the framework of Ngai's coupling model; thus enhancing deviations at testing temperatures close to T_g [178, 383-385].

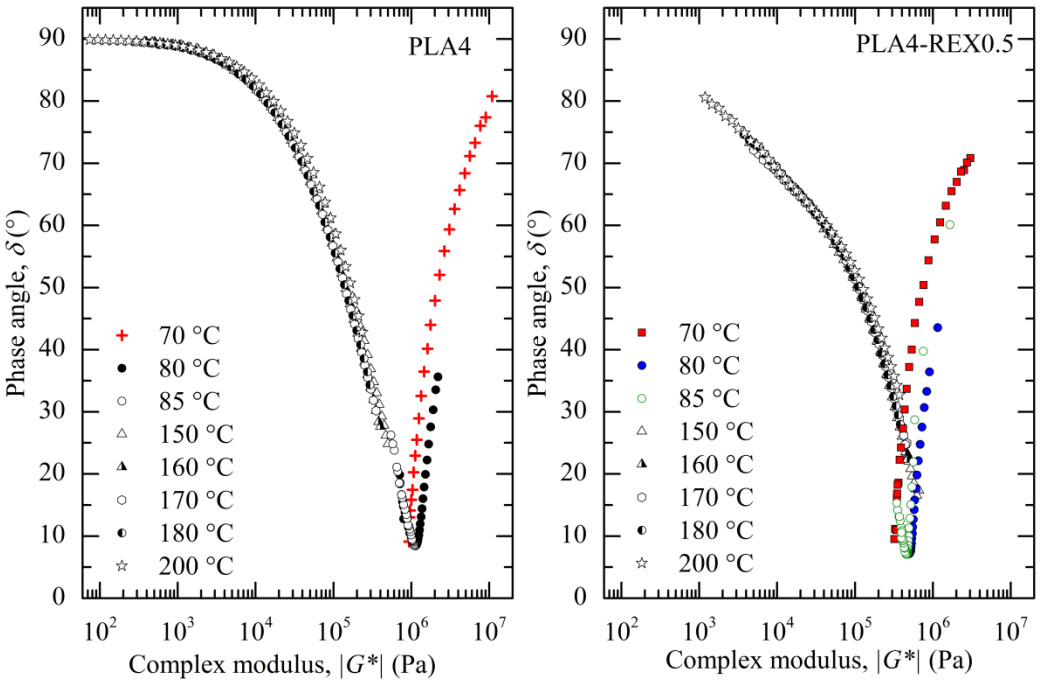

Figure 7.5. Verification of the TTS principle for PLA-4 based sample. Colours indicate rheological measurements which do not verify the TTS principle.

While PLA2 and PLA2-REX0.5 samples showed a thermorheologically simple behaviour, a modification of the dependence of δ on $|G^*|$ values was apparent for the latter as compared to the former. This trend could be attributed to both the increase in MW and a possible modification of the molecular architecture (chain extension/branching) through reactive extrusion.

On the other hand, PLA2-REX0.6 samples were thermorheologically complex. This loss of thermorheological simple behaviour suggests the formation of topological modifications, which probably hold LCB, as already reported by Al-Itry *et al.* [102] for PLA and Wood-Adams and Costeux [100], Lohse *et al.* [152] and van Ruymbeke *et al.* [99] for LCB polyolefins. That is, the presence of long chain branches significantly increases the melt response time and commonly yields a modification of the sequence of the molecular relaxations as a function of the testing temperature. In the present work, the architectural changes achieved are probably not well defined as

PLA2-REX0.6 samples are not a carefully prepared model polymer based on specific polymerization technologies.

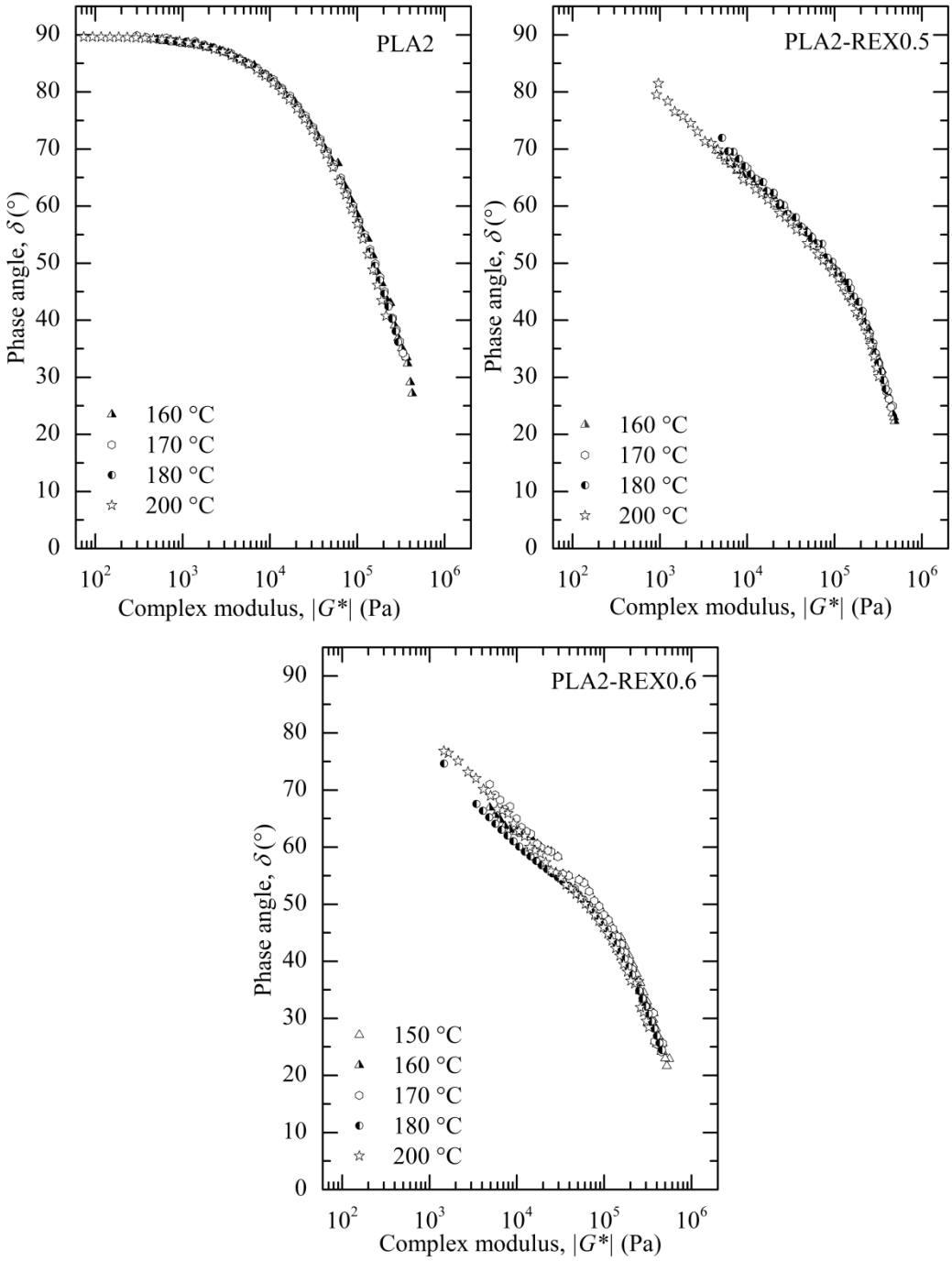

Figure 7.6. Verification of the TTS principle for PLA-2 based sample.

By comparing *figure 7.5* to *figure 7.6*, it is apparent that the phase angle, δ, passed through a minimum and rose again with increasing $|G^*|$ values solely for PLA-4 based samples. This is because dynamical measurements were performed in both the glassy and rubbery regions. By contrast, PLA-2 based samples only exhibited data on the left side of the minimum (*c.f. figure 7.6*) due to the narrower testing temperature range evaluated (*i.e.* solely high temperature range).

For the purpose to evaluate the effects of the topological modifications on the temperature dependence of the viscoelastic functions, the Williams-Landel-Ferry dependence (*c.f. chapter 2, section 2.3.2, equation 2.16*) was first evaluated for PLA-4 based samples. This is due to the fact that rheological measurements were available from T_g to temperatures which exceed the T_g of PLA by more than 100 ºC. In both the frequency range and/or the temperature experimental windows evaluated, η_0 was not straightforwardly observed for PLA4 and PLA4-REX0.5 samples. Thus, $G'(\omega)$ and tan δ (raw data of the equipment) were considered better candidates for the shifting process. The G' and tan δ curves, measured at 70, 80, 85, 150, 160, 170 and 200 °C, were shifted along the frequency axis to 180 °C using the TTS principle.

The thermorheological complex behaviour observed in the low temperature range (*i.e.* just above T_g) implied the use of a vertical shift factor, b_T. The vertical shifting is commonly determined from both the temperature dependence of the relaxation modulus (as defined by Rouse, *c.f. chapter 2, section 2.3.2, equation 2.17.a*) and/or the temperature dependence of the plateau modulus, G_n^o (*c.f. chapter 2, section 2.3.2, equation 2.17.b*). Unfortunately, the situation is confusing. Several authors reported that the use of both definitions does not superpose well data for linear polybutadiene [101] and poly(vinyl acetate) [105, 386] and a more generally applicable shift factor definition is not presently available. In the present study, the assignment of the b_T values did not follow the above described temperature dependences and was somewhat arbitrary in the high frequency range. However, results provide a good general picture of the linear response for both materials over a very broad range of frequency, as shown in *figure 7.7*.

On this basis, the good superposition between all the measurements enables the construction of the temperature dependence of a_T over 14 decades of temperatures for PLA4 and PLA4-REX0.5 samples, as shown in *figure 7.8*.

Similar average WLF parameters were obtained between both materials within the experimental error, as reported in *figure 7.8*. These values agree with the study of Dorgan *et al.* [174] who reported C_1=3.24 1/K and C_2 = 164.9 K for HMW linear PLA. Results suggest that the temperature dependence of a_T did not show a clear dependence on the chain architecture modifications in the whole temperature range under study. However, it is rather unlikely that this analysis would display a

modification of the temperature dependence for PLA4-REX0.5 due to both the arbitrary b_T values for the high frequency range and/or the few points covering the whole temperature range (*i.e.* 8 experimental points for 14 decades of temperature).

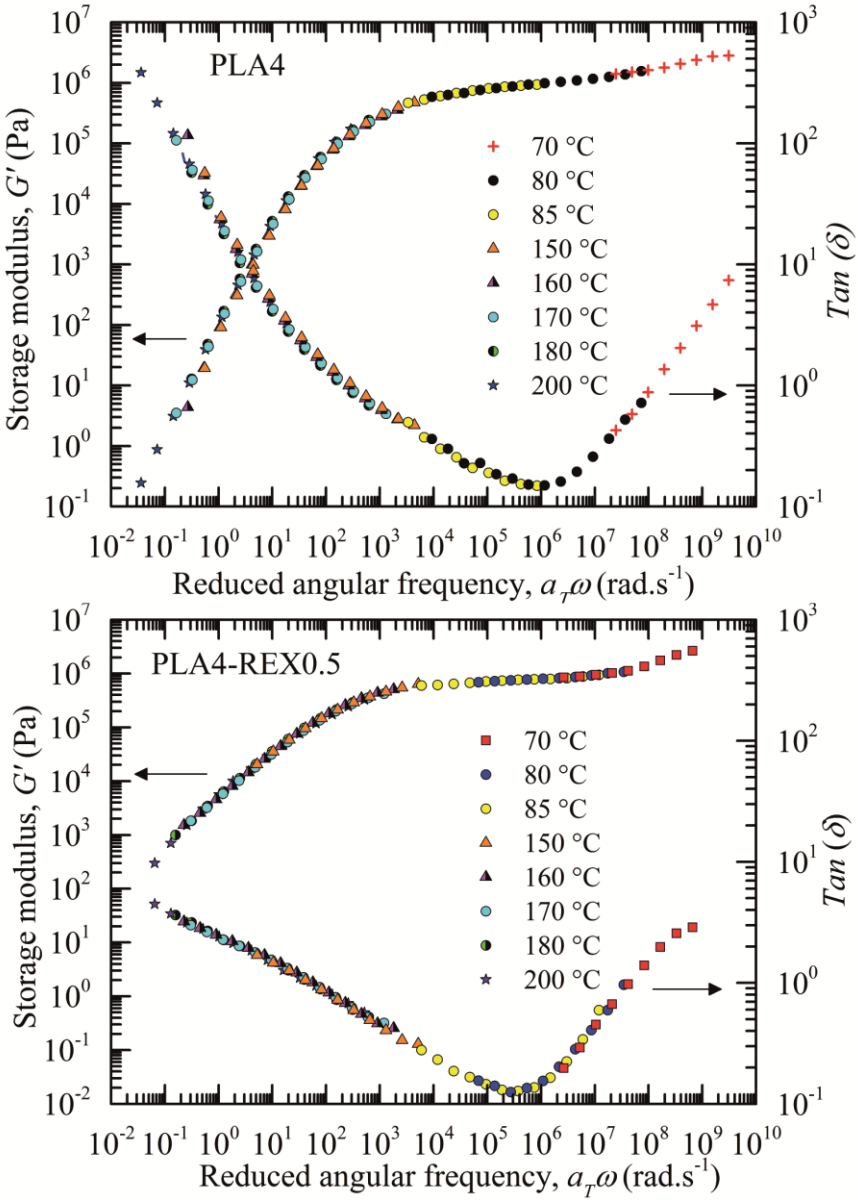

Figure 7.7. Storage modulus and *tan (δ)* functions versus reduced frequency for PLA4 and PLA4-REX0.5 samples. The reference temperature is 180 ºC. Only three points/decade are reported for each temperature measurements so that the reader can appreciate the TTS validity better.

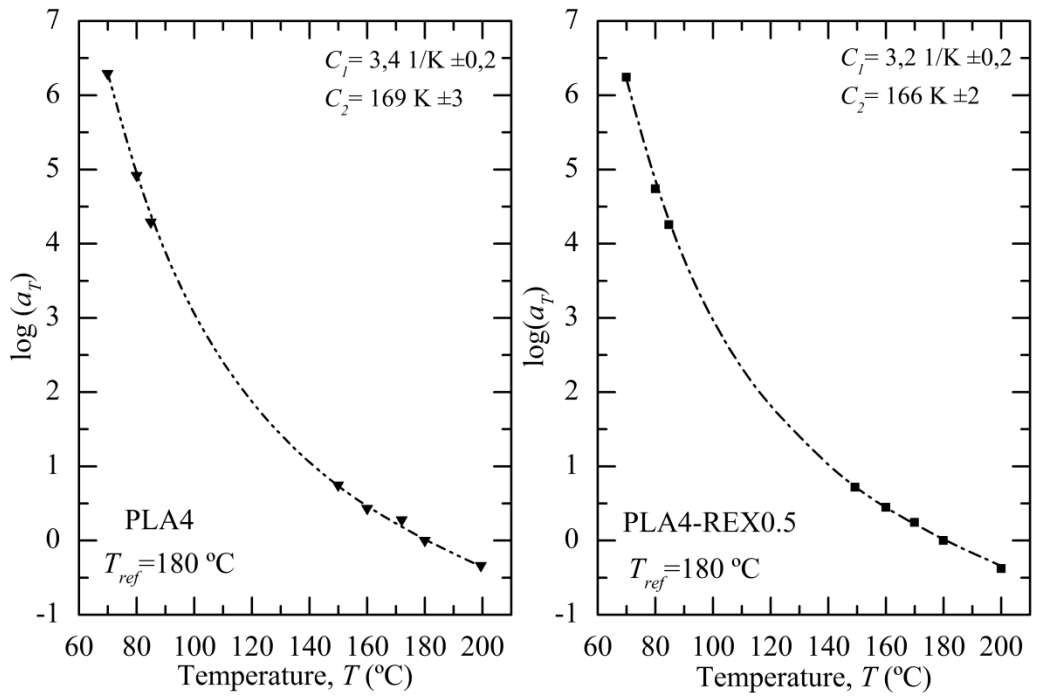

Figure 7.8. Horizontal shift factor (a_T) versus temperature for PLA4 and PLA4-REX0.5 samples with 180 ºC as reference temperature. The statistical errors derived from the master curve construction are not shown as they were smaller than the symbol size. The dashed lines represent the WLF experimental data fits according to *equation 2.16* (*c.f. chapter 2, section 2.3.2*). The corresponding WLF parameters are indicated in the upper right hand corner of each figure.

Consequently, the effects of both the stereoregularity and the topological modifications on the temperature dependence of the viscoelastic functions were investigated over a narrower temperature range, using the activation energy, E_a. That is from now on only testing temperatures, which exceed T_g (≈ 61 ºC) by more than 100 ºC, were considered (*i.e.* 160, 170, 180 and 200 ºC).

Recall that the concept of a single activation energy is meaningless if the temperature sensitivity is time-dependent. Consequently, E_a was solely calculated for samples, which exhibit a thermorheologically simple behaviour, over the temperature range considered. That is PLA4, PLA2, PLA4-REX0.5 and PLA2-REX0.5 samples.

In both the frequency range and the temperature experimental windows evaluated, η_0 was not straightforwardly observed for PLA4-REX0.5 and PLA2-REX0.5 samples. Thus, $G'(\omega)$ and *tan* δ were considered better candidates for the shifting process. The G' and *tan* δ curves, measured at 160, 170 and 200 °C, were shifted along the

frequency axis to 180 °C using the TTS principle, as shown in *figure 7.7* and *figure 7.9* for PLA-4 and PLA-2 based samples, respectively.

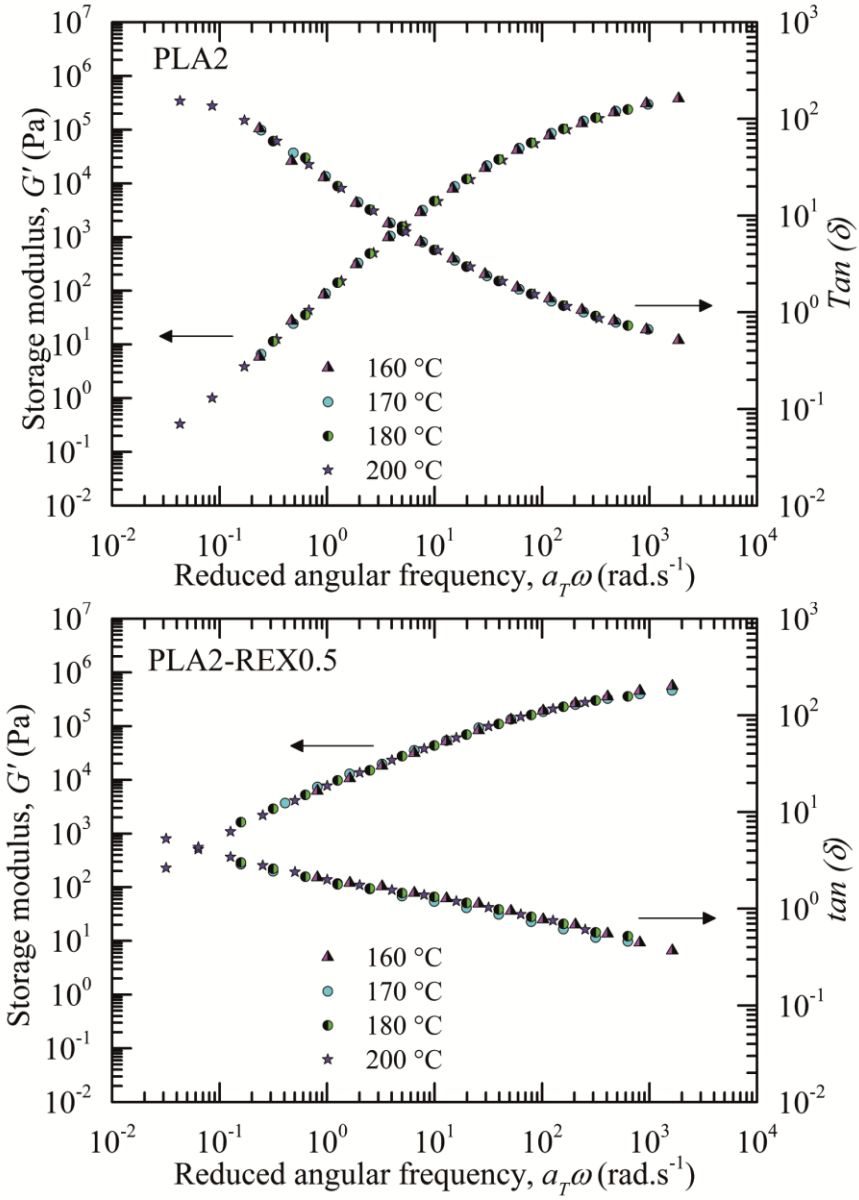

Figure 7.9. Storage modulus and *tan (δ)* functions versus reduced frequency for PLA2 and PLA2-REX0.5 samples. The reference temperature is 180 ºC. Only three points/decade are reported for each temperature measurements so that the reader can appreciate the TTS validity better.

Good superposition between all the measurements is apparent. Since the viscoelastic measurements were available only far above the glass transition temperature of all sample and over a relatively narrow temperature range, the

horizontal shift factor, a_T, follows an Arrhenius relation with temperature, as given by *equation 2.15* (*c.f. chapter 2, section 2.3.2*). E_a was obtained from the best linear regression of a set of values represented in a graph plotting the natural logarithmic values of a_T versus $1/T$, as shown in *figure 7.10*. Results are given in *table 7.4*.

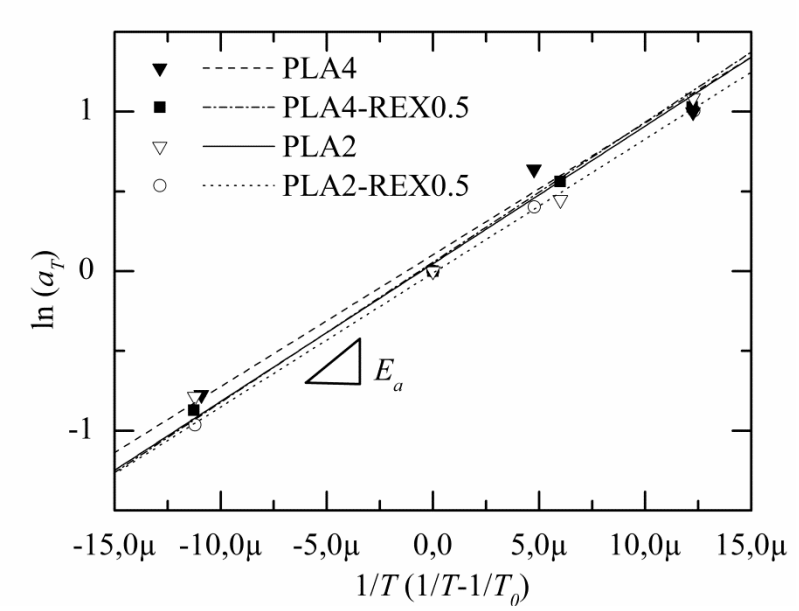

Figure 7.10. Horizontal shift factor (a_T) versus $1/T$ ($1/T$-$1/T_0$) for all thermorheological simple samples with 180 °C as reference temperatures. The statistical errors derived from the master curve construction are not shown as they were smaller than the symbol size. The different lines represent the Arrhenius experimental data fits according to *equation 2.15* (*c.f. chapter 2, section 2.3.2*).

Table 7.4. Activation energy for thermorheologically simple samples. The reference temperature is 180 °C.

Sample identification	**PLA4**	**PLA4-REX0.5**	**PLA2**	**PLA2-REX0.5**
$\boldsymbol{E_a}$ (kJ.mol^{-1})	85 ±6	86 ±3	88 ±3	87 ±3
$\boldsymbol{R^2}$	0.9901	0.9961	0.9910	0.9995

Over the range of data considered, E_a did not show a clear dependence neither on the stereoregularity between both linear PLA samples nor on the architectural modifications between PLA4-REX0.5, PLA2-REX0.5 samples and their linear homologues. Close examination of the E_a measurements revealed that all values ranged from 85 to 88 kJ.mol^{-1} within the statistical error of the experiments.

These results are consistent with the modest effects of the chain architectures on the flow activation values (ranged between 79 and 116 $kJ.mol^{-1}$) reported by Dorgan *et al.* [130] for linear and branched (*i.e.* star-shaped) PLA polymers. Authors stated that differences in the PLA molecular architecture cannot be distinguished using the calculation of E_a. This is because the temperature dependency of the viscoelastic functions is independent of the MW but mainly depends on local segmental relaxations rather than large-scale relaxation mechanisms (*e.g.* reptation, constraint release, etc).

Independently of the chain architectures, the similarity between E_a values suggests that this technique is not enough sensitive to distinguish subtle differences in the PLA molecular architecture. However, the absence of an enhanced E_a and/or the loss of thermorheological simple behaviour does not necessarily exclude the presence of topological changes in PLA-REX samples, which possibly hold low levels of LCB, as already reported in Wasserman and Graessley [154], Vega *et al.* [155] and Shroff and Mavridis [138] for sparsely LCB HDPE resins, Munari *et al.* [156] for branched poly(butyleneisophthalate) and Ferri and Lomellini [178] and Hepperle *et al.* [387] for LCB PS.

7.2.4. Influence of the topological changes on the viscoelastic properties

a) Complex viscosity functions

In order to determine if PLA4-REX0.5 and PLA2-REX0.5 samples showed any behaviour consistence with the presence of topological modifications, which might hold low amounts of LCB, the viscoelastic functions were investigated. Regarding the TTS principle, recall that if spectra of two sets of data overlap (*e.g.* $G'(\omega)$ and $tan(\delta)$ as shown in *figures 7.7* and *7.9*), all other materials functions (*e.g.* $|\eta^*(\omega)|$) will also overlap. Thus, *figure 7.11* shows the $|\eta^*(\omega)|$ master curve for PLA2, PLA4, PLA4-REX0.5, PLA2-REX0.5 samples.

These dynamic mechanical spectra, which cover seven magnitudes of angular frequency, are the combination of two types of experiments: (a) data in the range 10^{-1}-10^{4} $rad.s^{-1}$ obtained from the TTS and (b) data in the range 5.10^{-4}- 10^{-1} $rad.s^{-1}$ obtained from the conversion of the creep-recovery data calculated from retardation spectrum. Additionally, $|\eta^*(\omega)|$ of PLA2-REX0.6 was added to *figure 7.11*. It was solely constructed from the combination of the frequency sweep performed at 180 °C and the conversion of the creep-recovery data, as this sample exhibited a thermorheologically complex behaviour.

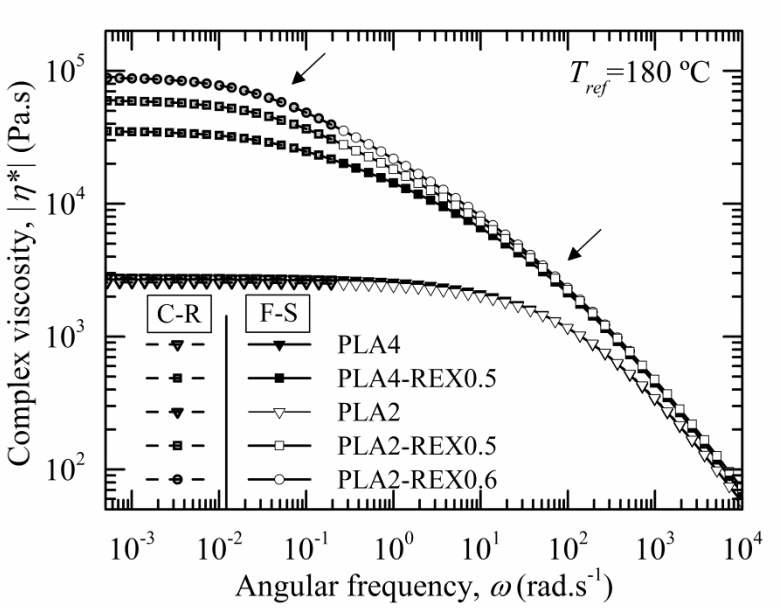

Figure 7.11. Effect of the addition of the SAmfE agent on the absolute magnitude of the complex viscosity versus angular frequencies at a reference temperature of 180 ºC. C-R: conversion of the creep-recovery data calculated from retardation spectrum. F-S: frequency sweep data reduced to master curve using the TTS principle. The arrows indicate the two different curvatures in the transition zone between the terminal and power-law region.

Both parts connected well with each other and showed different relaxation information between PLA-REX samples and their linear homologues, as shown in *figure 7.11*. Both PLA samples (*i.e.* PLA4 and PLA2) exhibited the typical behaviour of linear polymers. The terminal (Newtonian) region was observed over a wide range of ω, suggesting a relatively fast relaxation process of the chains. In contrast, besides a significant increase in η_0, the onset of the terminal region was shifted to lower ω for PLA-REX samples. The transition zone between the terminal and power-law region was enlarged and two different curvatures were observed (indicated by arrows). However, these differences were not as pronounced at low ω and all $|\eta^*(\omega)|$ functions converged to roughly similar values, as already observed for internal mixer samples (*c.f. chapter 6, section 6.7, figure 6.16*).

Both linear PLA samples (*i.e.* PLA4 and PLA2) present somewhat higher η_0 values as compared to "neat" internal mixer samples (*c.f. chapter 6, section 6.7, figure 6.16*). These results are in line with the previous SEC-DRI discussion (*c.f. section 7.2.1*) and suggest that a higher level of degradation was developed during internal mixing preparation due to the higher thermo-mechanical exposition time (13 min) as compared to the REX-calendered samples (4.33 min). Additionally, PLA4-REX0.5

and PLA2-REX0.5 exhibited higher η_0 values than their modified homologues reported in *section 6.7* (*c.f. chapter 6*, PLA-4+0.5J and PLA-2+0.5J samples). This is possibly due to a higher local shear field during REX-calendering processing; thus leading to a larger degree of reaction (and thus of structural modifications).

The CY (*c.f. chapter 2, section 2.3.4 (e), equation 2.45*) and HN (*c.f. chapter 2, section 2.3.4 (e), equation 2.49*) models were used to fit $|\eta^*(\omega)|$ experimental data of PLA4 and PLA2 samples. Both functions were fitted to the entire set of available data using the least square method in order to capture the salient feature of $|\eta^*(\omega)|$ in an efficient and accurate numeric way. The resulting parameters are given in *table 7.5*. For the purpose to determine if both the CY-Ext and the H-N-Ext models can be used to describe $|\eta^*(\omega)|$ functions of PLA-REX samples, the double logarithmic slope d log$|\eta^*|$/d log ω was calculated in the investigated ω range and results are shown in *figure 7.12*.

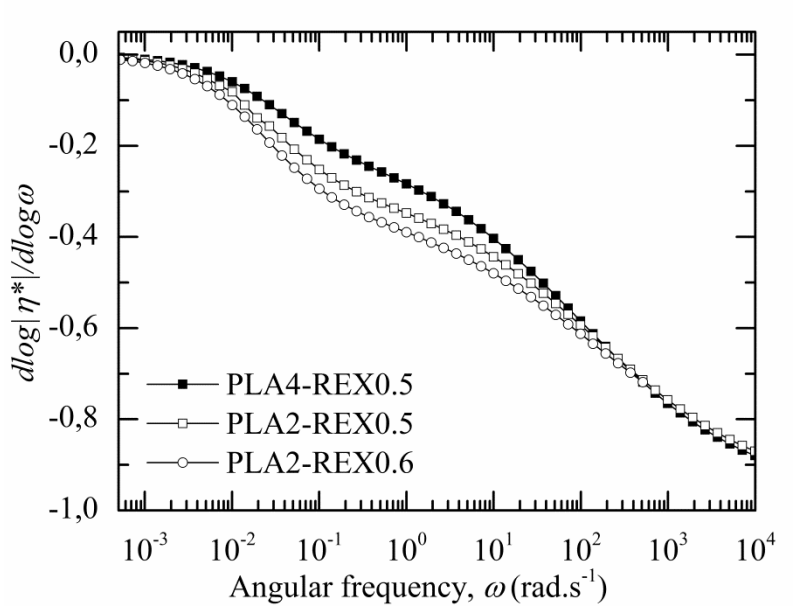

Figure 7.12. Double logarithmic derivative of the viscosity functions of PLA-REX samples.

Since d log$|\eta^*|$/d log ω monotonously increases with decreasing ω, both the CY-Ext and the HN-Ext models were used to fit $|\eta^*(\omega)|$ data. The double curvature exhibited in the transition region between the terminal and pseudo-plastic region suggested that m=n=2. Accordingly, *equation 2.47* and *2.50* were rewritten as *equation 7.1* and *7.2*, respectively. *Table 7.5* summarizes the results of the different fits.

$$|\eta^*(\omega)| = \frac{\eta_0}{[(1+(\tau_1\omega)^{2\alpha_1})^{(1-\nu_1)/2\alpha_1}][(1+(\tau_2\omega)^{2\alpha_2})^{(1-\nu_2)/2\alpha_2}]} \quad \textbf{(7.1)}$$

$$|\eta^*(\omega)| = \frac{\eta_0}{\left[\left(1+2(\tau_1\omega)^{\alpha_1}\cos\left(\alpha_1\frac{\pi}{2}\right)+(\tau_1\omega)^{2\alpha_1}\right)^{(1-\nu_1)/2\alpha_1}\right]\left[\left(1+2(\tau_2\omega)^{\alpha_2}\cos\left(\alpha_2\frac{\pi}{2}\right)+(\tau_2\omega)^{2\alpha_2}\right)^{(1-\nu_2)/2\alpha_2}\right]} \quad \textbf{(7.2)}$$

Figure 7.13 shows the general trace of $|\eta^*(\omega)|$ functions exhibiting two separated relaxation processes in the transition region with the different parameters of *equations 7.1* and *7.2*.

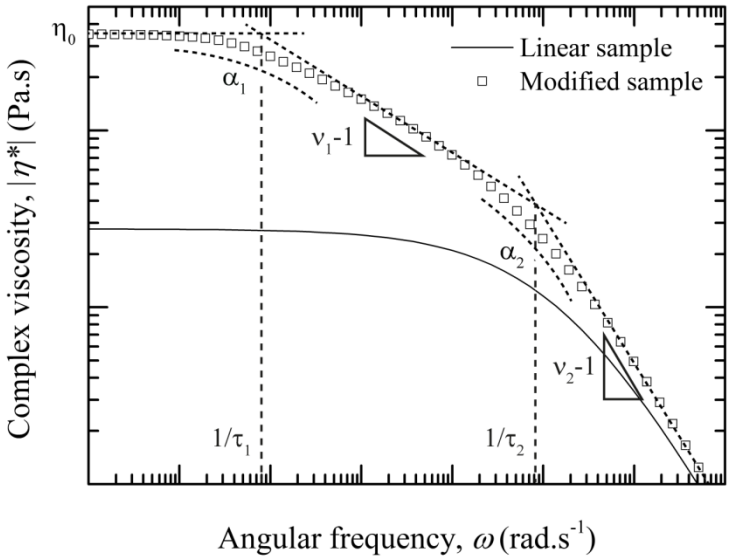

Figure 7.13. General trace of $|\eta^*(\omega)|$ functions exhibiting two separated relaxation regimes in the transition zone. Parameters included in both extended viscosity models (*i.e. equations 7.1 and 7.2*) are reported in the corresponding curve.

Table 7.5. Numerical results of the different fitting models at 180 ºC.

	Fitting models [a]	η_0 (kPa.s)	τ_1 (s)	α_1	ν_1	τ_2 (s)	α_2	ν_2
PLA4	CY	2.8	$5.19.10^{-3}$	0.548	0.0726	-	-	-
	HN	2.8	$5.19.10^{-3}$	0.498	0.0726	-	-	-
PLA4-REX0.5	CY-Ext	35.4	29.85	1	0.795	0.01	0.45	0.240
	HN-Ext	35.4	29.85	1	0.795	0.01	0.381	0.240
PLA2	CY	2.7	$4.50.10^{-3}$	0.591	0.0381	-	-	-
	HN	2.7	$4.50.10^{-3}$	0.531	0.0383	-	-	-
PLA2-REX0.5	CY-Ext	60.1	35.60	1	0.703	0.0065	0.45	0.332
	HN-Ext	60.1	35.60	1	0.703	0.0065	0.38	0.332
PLA2-REX0.6	CY-Ext	90	42.85	1	0.673	0.006	0.41	0.362
	HN-Ext	90	42.85	1	0.673	0.006	0.36	0.362

[a] CY: Carreau-Yassuda, HN: Havriliak-Negami, CY-Ext: extended Carreau-Yassuda, HN-Ext: extended Havriliak-Negami.

As shown in *table 7.5*, the first characteristic relaxation time (τ_1) increased with both the more reactive PLA type (*i.e.* PLA2) and the SAmfE content. These results suggest that the transition zone between the Newtonian and the power-law region was broadened with an increase in M_w (*c.f. table 7.1*). In addition, the increasing values of ν_2 imply that $|\eta^*(\omega)|$ was more shear-sensitive with increasing M_w.

Although these trends could be attributed to the alteration of the molecular mobility due to the increasing number of interactions and entanglements per chains (*i.e.* higher relative M_n values for PLA-REX samples, *c.f. table 7.1*), conclusions about the presence of LCB cannot be drawn from *figure 7.11*. This is because both the increase in MW as measured by SEC-DRI (*c.f. table 7.1*) and the topological modifications have convoluted effects on the dependence of $|\eta^*|$ on ω. One of the most prominent differences was the increase in MW according to SEC-DRI measurements (*c.f. table 7.1*).

Therefore, an appropriate method to remove the MW dependence on the $|\eta^*(\omega)|$ behaviour is looked for. One of the most useful methods is the time-molecular weight (TMW) superposition principle, which is fulfilled for polymer exhibiting similar and narrow MWD (*e.g.* PLA and PLA-REX samples, *c.f. table 7.1*) [137]. Initially, this concept assumes that the dependence of η_0 on M_w follows *equation 2.35* (*c.f. chapter 2, section 2.3.4.b*) for linear polymer well above M_c. Then, Ferry [388] reported that the longest relaxation time, τ_1, was proportional to the product of the steady-state compliance, J_e^0 and η_0, as given by:

$$\tau_1 \propto J_e^0 \eta_0 \qquad \textbf{(7.3)}$$

Since Ferry [388] reported that J_e^0 is commonly found to be independent of M_w above $2M_c$, the resulting relationship for the longest relaxation time yields the same M_w dependence as η_0. Consequently, when these concepts are combined, an equivalent shifting along the time, or rate, axis and the viscosity axis is achieved. On this basis, the TMW superposition is applied using the shift factor, a_M, as follows [137]:

$$a_M = \eta_0(M_w) \Big/ \eta_0(M_w)_L \qquad \textbf{(7.4)}$$

Where $\eta_0(M_w)$ is the zero-shear rate viscosity of the modified samples (*e.g.* PLA-REX) and $\eta_0(M_w)_L$ the zero-shear rate viscosity of its corresponding linear samples of equivalent MW. In principle, the application of the shift factor, a_M, should reveal the individual contribution of the topological modifications on the $|\eta^*(\omega)|$ function [137].

For the purpose to remove the MW effects of the viscosity functions of PLA-REX samples, the established dependence of η_0 on M_w for linear polydisperse PLA at 180

°C (*i.e.* $\eta_0 = 5.5.10^{-15} M_w^{3.4}$, [174]) is used to estimate η_0 of their corresponding linear sample of equivalent MW. The shifted viscosity curves are shown in *figure 7.14* together with both linear PLA samples.

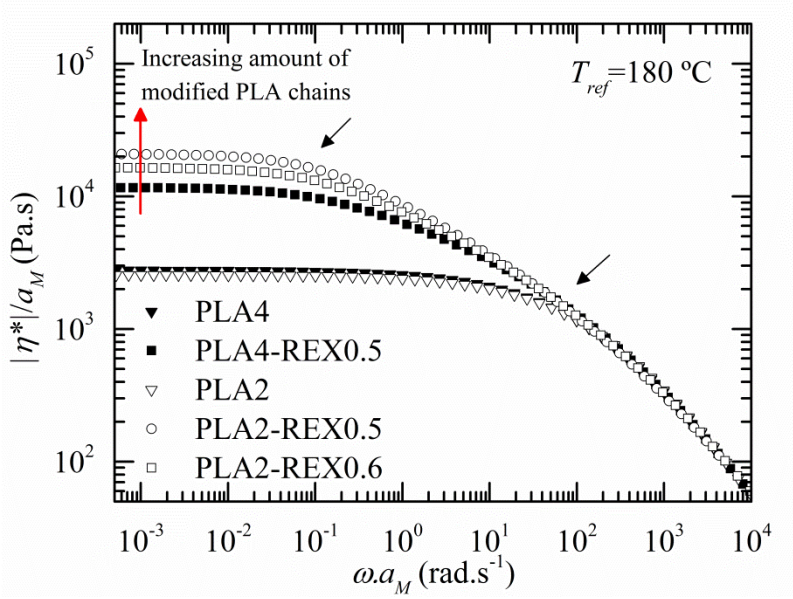

Figure 7.14. Shifted complex viscosity functions for PLA-REX samples together with both linear PLA samples at 180 °C.

A difference in the dependence of $|\eta^*|$ on ω between PLA and PLA-REX samples is apparent in *figure 7.14*. While η_0 increased, the onset of the terminal region was shifted to lower ω and the transition zone between the Newtonian and the power-law region was enhanced for the latter. Moreover, the additional curvature between both regions was still exhibited by PLA-REX samples (indicated by black arrows). These trends are one of the noteworthy effects of the alteration of the molecular mobility due to the increasing number of interactions and entanglements per chains (*i.e.* higher relative M_n values for PLA-REX samples, *c.f. table 7.1*), which led to a decreasing rate of molecular relaxation. It could occur when the polymeric chains, belonging to the architecturally modified macromolecules, become sufficiently long to entangle and impede the segmental motions of the neighbouring chains more strongly than simple hydrodynamic drag.

Since the TMW principle shifts rheological data to a single master curve if all the considered samples are linear, the above results suggest the presence of macromolecules featuring longer relaxation times. In other words, these differences in the trend of $|\eta^*(\omega)|$ must be primarily attributed to the presence of different branched structures which possibly hold low levels of long chain branches rather than the minor

variations in the PDI values (*c.f. table 7.1*) [152, 176]. On the other hand, η_0 gradually shifted to higher values for both the more reactive PLA type (*i.e.* PLA2) and the increasing SAmfE content, which behaviour might be correlated with an increasing amount of modified PLA chains. This is further supported by the fact that the trend of temperature dependence of the viscoelastic functions changed from a thermorheological simple to a complex behaviour with increasing the SAmfE content (*c.f. figure 7.6*, PLA2-REX0.5 and PLA2-REX0.6 samples).

b) Storage and loss modulus functions

Similarly to $|\eta^*(\omega)|$, $G'(\omega)$ and $G''(\omega)$ master curves, which were constructed from the combination of the TTS and the conversion of creep-recovery data for PLA2, PLA4, PLA4-REX0.5, PLA2-REX0.5 samples, are shown in *figure 7.15*. $G'(\omega)$ and $G''(\omega)$ of PLA2-REX0.6 was also added to *figure 7.15*, but it was derived solely from the combination of the frequency sweep performed at 180 °C and the conversion of the creep-recovery data (thermorheologically complex behaviour).

As shown in *figure 7.15*, both parts connected well with each other and showed different relaxation information between PLA-REX samples and their linear homologues. Unlike PLA "neat" internal mixer samples (*c.f. chapter 6, section 6.7, figure 6.17*), PLA2 and PLA4 samples exhibited a similar frequency dependence over the ω range investigated. This tendency is in line with the lower degree of degradation exhibited by these latter.

In the high ω range (10^3-10^5 rad.s^{-1}), G' and G'' values converged towards a roughly similar value, respectively. A similar trend was already observed for $|\eta^*(\omega)|$ functions as shown in *figure 7.11*. This behaviour suggests that the molecular motions, which govern the high ω range, remained independent of the molecular structure, as already reported by Kasehagen *et al.* [378] and Dealy *et al.* [98].

In contrast, significant differences in $G'(\omega)$ and $G''(\omega)$ were observed in the low frequency range (5.10^{-4}-10^2 rad.s^{-1}). An additional intermediate relaxation regime (indicated by an arrow) was observed between the terminal (*i.e.* $G' \propto \omega^2$ and $G'' \propto \omega$) and plateau region for PLA-REX samples. Moreover, higher and increasing G' and G'' values were found in the low ω range for both the more reactive PLA type (*i.e.* PLA2) and the increasing SAmfE content. These observations are consistent with numerous works [47, 152, 178, 316, 376] and with the increasing M_z values as reported in *table 7.1*. Results suggest the formation of a network having a higher melt strength and which is less shear sensitive with decreasing ω [47, 316].

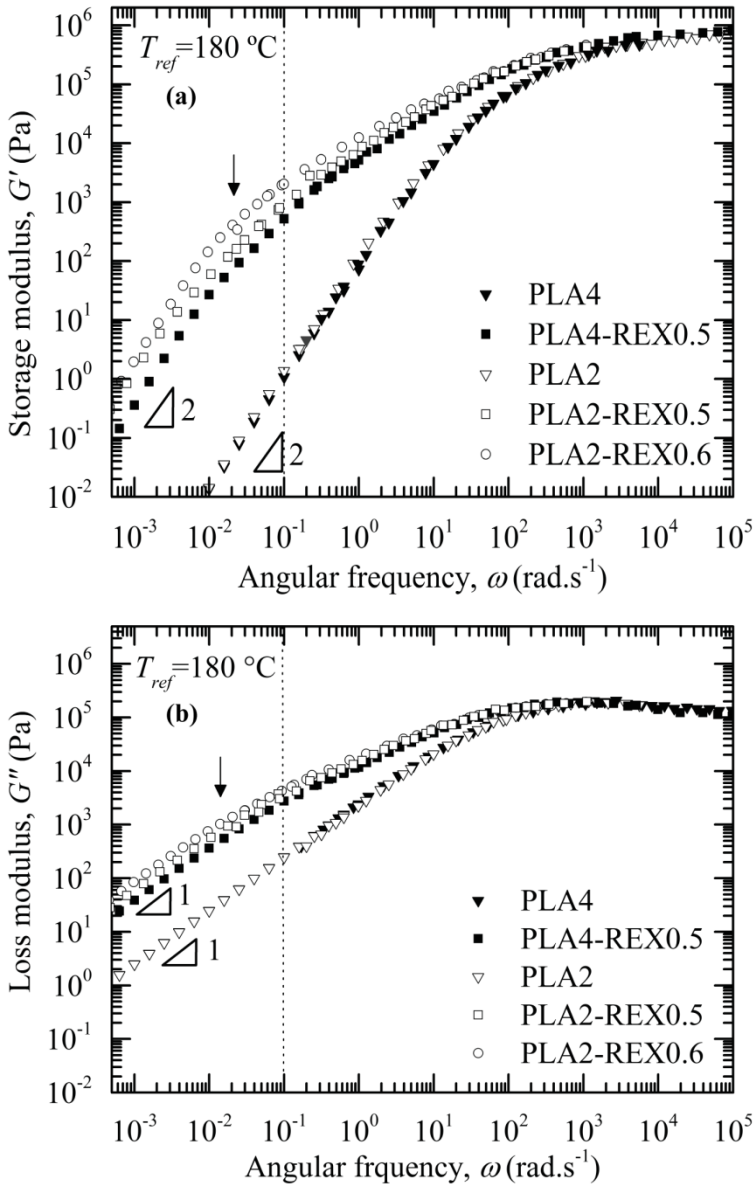

Figure 7.15. Influence of the reactive process on the **(a)** storage and **(b)** loss modulus functions. The reference temperature is 180 °C. Arrows indicate an additional curvature in the transition zone between the terminal and the plateau region. Dotted lines roughly indicate the transition between the conversion of the creep-recovery data calculated from retardation spectrum and the frequency sweep data reduced to master curve using the TTS principle.

While definitive conclusions about the presence of LCB in PLA-REX samples cannot be drawn from *figure 7.15* (convoluted effects between the increase in MW and

the topological changes), the determination of molecular dimensions is feasible from the plateau modulus, G_n^0. Since viscoelastic measurements were performed in both the glassy and rubbery regions for PLA4 and PL4-REX0.5 samples (*c.f. figure 7.7*), G_n^0 is experimentally determinable (referred to as $G_{n\,exp}^0$). *Figures 7.16* and *7.17*show the master curves of $G'(\omega)$ and $G''(\omega)$ over an extended ω range for PLA4 and PL4-REX0.5 samples, respectively, so that the reader can appreciate the G_n^0 determination better.

The determination of the plateau modulus is somewhat ambiguous from the $G'(\omega)$ curves which are plotted in *figure 7.16* and *7.17*. This is because $G'(\omega)$ did not exhibit a true plateau but increased monotonously with ω. This behaviour is usually observed for polydisperse systems due to the overlapping of multiple relaxation processes in the high ω range. Since G'' exhibit a minimum at the high-frequency side of the crossover modulus (where $G'(\omega)=G''(\omega)$), $G_{n\,exp}^0$ was determined from the value of G' at the frequency ω_{min} where G'' passes through a minimum, as illustrated in *figure 7.16* and *7.17* (*c.f. chapter 2, section 2.3.4.a, equation 2.25*). $G_{n\,exp}^0$ values are compiled in *table 7.6*.

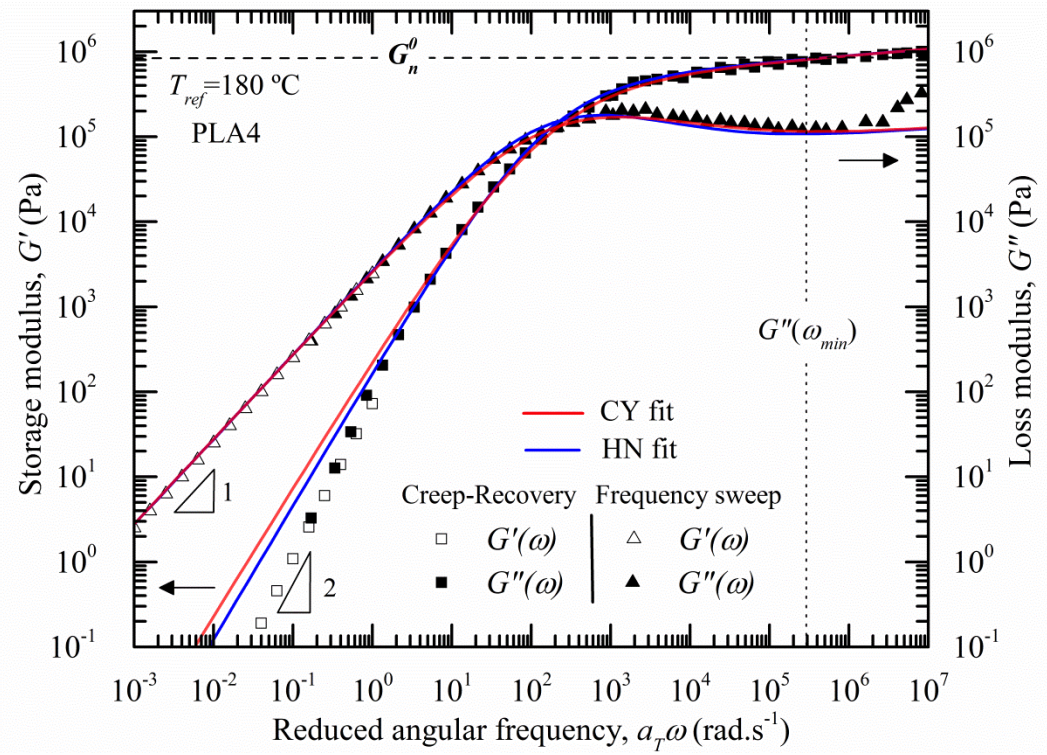

Figure 7.16. Master curve of storage and loss modulus functions for PLA4 samples at a reference temperature of 180 ºC. Solid lines are model predictions according to *equations 9.14* and *9.15* (*c.f. chapter 9, section 9.4.2*). CY: Carreau-Yassuda model, HN: Havriliak-Negami model. The vertical dotted line indicates the frequency where

experimental *G"* values pass through a minimum. The horizontal dashed line indicates the plateau modulus value.

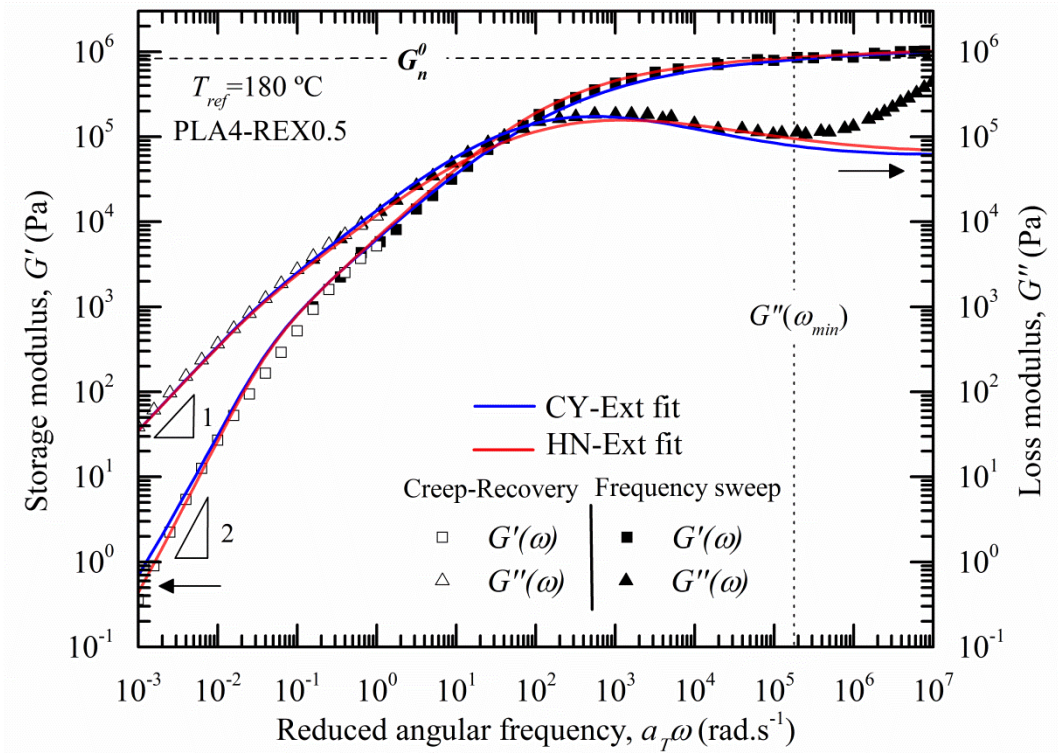

Figure 7.17. Master curve of storage and loss modulus functions for PLA4-REX0.5 samples at a reference temperature of 180 ºC. Solid lines are model predictions according to *equations 9.19* and *9.20* (*c.f. chapter 9, section 9.4.2*). CY-Ext: extended Carreau-Yassuda model, HN-Ext: extended Havriliak-Negami model. The vertical dotted line indicates the frequency where experimental *G"* values pass through a minimum. The horizontal dashed line indicates the plateau modulus value.

A slight increase in the $G_n^{0}{}_{exp}$ value was apparent for PLA4-REX samples as compared to its linear homologue (*i.e.* PLA4). This trend agrees with the higher relative M_n values as measured using SEC-DRI measurements (*c.f. table 7.1*) and suggests that PLA4-REX0.5 samples possibly featured a higher number of entanglements per chains.

The second strategy in order to determine G_n^o is to considerate the integration method of $G''(\omega)$ using *equation 2.27* (*c.f. chapter 2, section 2.3.4.a*). Nevertheless, the integral method is meaningful only if the high-frequency (or extremely short times) relaxation mechanisms (*i.e.* glassy and Rouse modes), which are not sensitive to MW, are excluded. That is, the integral is to be taken only over contributions to the

integrand from the relaxations related to entanglements (*i.e.* terminal and plateau regimes, *c.f. chapter 2, section 2.3, figure 2.5*).

Table 7.6. Molecular dimensions deduced from melt measurements at 180 ºC.

	PLA4	PLA4-REX0.5	PLA2	PLA2-REX0.5	PLA2-REX0.6
$G_{n\ exp}^{0}$ [a] (10^5 Pa)	8.15	8.79	n/a	n/a	n/a
G_n^{0} [b] (10^5 Pa)	8.40	8.70	7.69	8.92	10.1
ρ [c] ($g.cm^{-3}$)	1.15 ±0.02	1.15 ±0.01	1.11 ±0.01	1.12 ±0.01	1.125 ±0.004
M_e [d] ($kg.mol^{-1}$)	5.16	4.98	5.44	4.72	4.18
Z [e]	45	62	41	72	87
ν_e [f] ($mmol.cm^{-3}$)	0.25	0.26	0.23	0.24	0.30
C_∞ [g]	8.5	8.3	8.7	8.1	7.6
J_e^{0} [h] (10^{-5} Pa^{-1})	2.4 ±0.4	40 ±5	3 ±1	49 ±10	55 ±7

[a] **Plateau modulus**: experimentally determined (*c.f. equation 2.25, chapter 2, section 2.3.4.a*).
[b] **Plateau modulus**: analytically estimated (*c.f. equation 2.27, chapter 2, section 2.3.4.a*).
[c] **Melt density**: estimated as defined in *section 5.1.3* at 180 °C (*c.f. chapter 5*).
[d] **Molecular weight between entanglements**: estimated using *equation 2.28* (*c.f. chapter 2, section 2.3.4.a*).
[e] **Number of entanglements per chain**: estimated using *equation 2.29* (*c.f. chapter 2, section 2.3.4.a*).
[f] **Entanglement density**: estimated using *equation 2.32* (*c.f. chapter 2, section 2.3.4.a*).
[g] **Characteristic ratio**: estimated using *equation 2.33* (*c.f. chapter 2, section 2.3.4.a*).
[h] **Linear steady-state elastic compliance**: experimentally estimated using creep-recovery experiments.
n/a: not available.

To this end, Ferry proposed a method to remove Rouse modes when the curve of log (G'') versus log (ω) exhibits a well defined maximum. This involves that the linear portion of experimental data on the right-hand side of the peak is linearly extrapolated to G''=0. However, this approach of eliminating Rouse modes is arbitrarily since the extrapolation is based on few data just past the peak. Errors in G_n^o prediction are therefore expected [105].

In the current work, an intent to remove the Rouse modes from $G'(\omega)$ and $G''(\omega)$ functions was performed for PLA4 and PLA4-REX0.5 samples using a numerical approach. To this end, the CY, the HN, the CY-Ext and the HN-Ext models were rationalized into the real (G') and imaginary (G'') components of $|G^*|$ (*c.f. chapter 9, section 9.4.2*). Then, $G'(\omega)$ and $G''(\omega)$ functions were predicted using the corresponding numerical parameters as reported in *table 7.5* and the resulting viscoelastic properties were overlaid with experimental data points as shown in *figures 7.16* and *7.17*.

Regarding PLA4 samples, while predicted *G''(ω)* curve superimposed well with experimental data points on the left side of the crossover modulus, discrepancies appeared at low ω for *G'(ω)* (from 10^{-2} to 10^{1} rad.s^{-1}). This behaviour is due to the fact that values of α other than 1 (*c.f table 7.5*) cause an incorrect low frequency scaling of *G'(ω)*, as already reported by Dorgan *et al.* [174, 175]. By contrast, these fitting issues appeared to be minimized for PLA4-REX0.5 samples, suggesting a higher flexibility of the extended viscosity models (*i.e.* CY-Ext and HN-Ext) to predict viscoelastic measurements.

On the right side of the crossover modulus, estimated *G'*(ω) traces fit well experimental data over the whole ω range, while increasing discrepancies between predicted and experimentally measured *G''* traces were apparent in the highest ω range (from 10^{5} to 10^{7} rad.s^{-1}). The significant increase of experimental *G''* data (from 10^{6} to 10^{7} rad.s^{-1}) is possibly due to the actions of the high-frequency Rouse modes [96]. The original tube model assumes that relaxation of linear polymeric chains occurs by reptation alone [96]. The usual fast decrease in *G''* after passing the *G''* maximum, which is predicted by pure reptation alone, was not observed for predicted *G''* traces neither in *figure 7.16* nor in *figure 7.17*.

Estimated *G''* traces fit well experimental data up to the point where experimental *G''* data pass through a minimum (indicated by a vertical dotted line). This tendency might be attributed to the consideration of both reptation and primitive path fluctuation relaxation processes in the viscoelastic predictions, as already reported by Dealy and Larson [96]. This trend suggests that predicted *G''* functions are possibly exempted from the high-frequency Rouse modes.

On this basis, a preliminary trial to estimate G_n^o was performed using the integration method (*c.f. chapter 2, section 2.3.4.a, equation 2.27)*. The integration limits were defined from 1.10^{-12} to 2.10^{15} rad.s^{-1} as it was the maximum range which can be integrated by the numerical analysis software used.

Numerical integration of each predicted *G''* function yielded G_n^o values at 180 °C. For each samples, similar G_n^o values were obtained using either the CY-based or HN-based model. Consequently, only one value was reported for each sample in *table 7.6* for the sake of clarity. G_n^o values estimated using the integration method match those experimentally deduced within an uncertainty of about 3%.

Based on the previous reliable data, the integration method was extended to PLA-2 based samples as G_n^o remained experimentally undeterminable. Then, G_n^o were used to estimate several molecular dimensions (*i.e.* M_e, Z, ν_e and C_∞) of PLA and PLA-REX samples whose values are compiled in *table 7.6*.

Regarding both PLA samples, results suggest a high sensitivity of the D-lactide content on the molecular dimensions. Chain stiffness (C_∞) slightly declined with decreasing stereoregularity. Although a similar trend has been reported by Joziasse *et al.* [124] and Kang *et al.* [389], the effects of the stereoregularity on the natural PLLA chain stiffness has not been resolved yet from a micro-structural point of view. A possible explanation might be that the introduction of D-lactide units changes the length distribution of the regular isotactic PLLA chain segments by introducing "disruptions" in the chemical group stereo-arrangement. These microstructural defects probably act as flexibilisation centres; thus lowering the chain stiffness. In the absence of external stress, a more randomly coiled structure might be expected since the polymer chain flexibility is enhanced. The density of coils in the space possibly increased; promoting a higher number of entanglements.

This assumption was supported by the larger ν_e and Z values exhibited by PLA4 as compared to PLA2 material which yielded lower M_e and higher G_n^o values, respectively.

The differences observed between both PLA materials must be viewed with a degree of scepticism given the modest variations in the stereosequence distribution and the degree of incertitude provided by the *G"* integration method. Nonetheless, the estimated values match those reported by numerous authors [118, 130, 217, 390]. Regarding linear PLLA and PLA samples with MWs ranging from 100 to 1000 kg.mol^{-1} (*PDI* from 1 to 2), G_n^o has been established between 0.5 to 1 MPa, M_e between 4-10 kg.mol^{-1} and ν_e between 0.14-0.16 mmol.cm^{-3} (25 ºC). Differences between data provided by the different authors could be attributed to slight variation in both the experimental determination of G_n^o and/or the estimation of the amorphous and melt density values.

Regarding PLA-REX samples, G_n^o, ν_e and Z values raised while M_e declined with both the more reactive PLA type (*i.e.* PLA2) and the increasing SAmfE content. These trends are the noteworthy effects of an increasing number of interactions and entanglements per chains, which is in line with the higher relative M_n values (*c.f. table 7.1*) as measured using SEC-DRI experiments. It could occur when the polymeric chains, belonging to the architecturally modified macromolecules, become sufficiently long to entangle with the neighbouring chains. Additionally, a decrease in C_∞ values was apparent with an increase in the amount of modified PLA chains (*c.f. figure 7.14*). Therefore, these results could be primarily attributed to the presence of branched structures, which possibly hold LCB, than the increase in MW as reported in *table 7.1*.

The effects of the structural modifications on the melt elastic properties were investigated using creep-recovery experiments. The linear steady-state elastic compliance J_e^0 (related to the melt elasticity) was determined for PLA and PLA-REX samples according to the methodology reported by Gabriel and Münstedt [364].

Similar J_e^0 values were found for PLA2 and PLA4 samples within the experimental error, as shown in *table 7.6*. Recall that the measurements of J_e^0 above 10^{-4} Pa^{-1} are possible with an error of about ±10%, while the uncertainty of elastic compliance below that limit is around 20% [139].

The elasticity of PLA-REX samples was higher by an order of magnitude as compared to their linear homologues, which value further rose with increasing the content of modified PLA chains.

The differences in the J_e^0 values between PLA and PLA-REX samples can mainly be attributed to the effect of the branched structures created during processing (decreasing rate of molecular relaxations), because the breath of the MWD (*c.f. table 7.1*) was found to be roughly similar between all samples. The observed tendency matches previous rheological measurements (*i.e.* higher *G'* values at low ω, *c.f. figure 7.15.a*), those reported by Gabriel and Münstedt [132, 148, 364] for mLLDPE and those reported by Graessley and Rouvers [391] for four and six-arm PS stars.

7.2.5. Branch-on-Branch model

To further strengthen the assumption that PLA-REX samples possibly hold LCB, experimental *G'* and $|\eta^*|$ data points were compared with theoretical dynamic mechanical spectrum predicted by the branch-on-branch (BOB) model [392] from the experimental MWDs. This model is based on the basic idea of the hierarchical relaxation of branched structures and yields linear viscoelastic properties by calculating stress relaxation modulus [393]. By using this general BoB model, linear viscoelasticity of branched polymers with different chain architectures can be predicted, including symmetric and asymmetric-stars, H-type, comb and Cayley tree-like chains. The predictions assessed using the BOB model for branched polymers matched quite satisfactorily the corresponding experimental data points, as already reported by Das *et al.* [393] for numerous branched mPE and Liu *et al.* [316] for LCB PLA.

In the present work, the BoB model was tried to find out the existence of LCB in PLA-REX samples, which can be done by fitting the experimental data (*i.e.* $|\eta^*(\omega)|$, $G'(\omega)$) with the model predictions. Recall that PLA-REX samples are not model polymers. That is, the topological modifications achieved during processing are not trivial and would be a mixture of several types of non-uniform structures in MW, in architectures and in the number of branch points per macromolecules. Therefore, this study did not aim to establish the exact compositions and chain structures of PLA-REX samples, but solely to qualitatively evaluate the existence of branched structures.

The first try was performed for both linear PLA samples (*i.e.* PLA4 and PLA2), as shown in *figure 7.18*, because their MW and MWD can be accurately determined

using SEC-DRI measurements. The MWD was assumed to follow a log-normal distribution and the entire distribution of MW was assumed linear for further calculations. *Table 7.7* summarizes the different fitting parameters used for the simulation process of PLA4 and PLA2 samples. The number of monomers in an entanglement length, *N*, is defined as the ratio of M_e (*c.f. table 7.6*) to that of the MW of the monomer. The Rouse entanglement time, τ_e, was previously defined according to *equation 2.30* (*c.f. chapter 2, section 2.3.4.a*).

Table 7.7. Fitting parameters for PLA4 and PLA2 samples.

Parameters	PLA4/PLA2
Dilation exponent α	0.5
Mass of monomer (g.mol^{-1})	72
Number of monomer in an entanglement length	60
Mass density of the polymer (g/cc)	1.2 ±0.1
Entanglement time, τ_e (s)	5e-8
Temperature (K)	453.15
M_w (kg.mol^{-1})	185 ±3
Polydispersity index	1.8 ±0.1

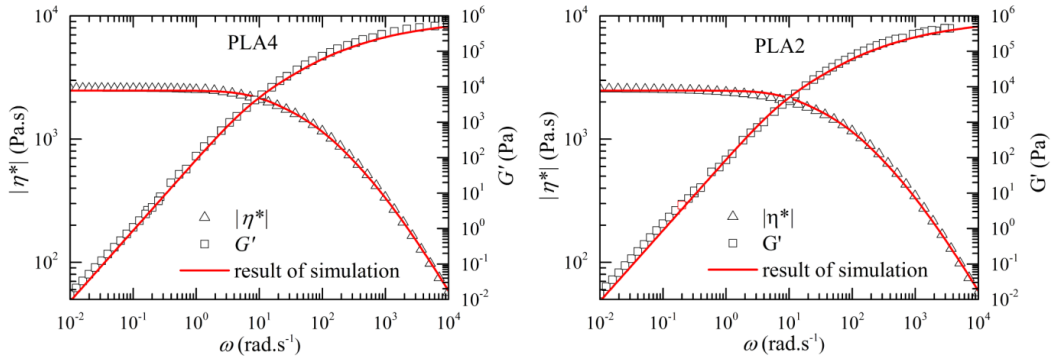

Figure 7.18. Experimental (open symbols) and predicted (solid line) linear viscoelastic properties using the BOB model (assuming that the entire distribution of MW was linear) for linear PLA4 and PLA2 samples at 180 °C.

The linear viscoelastic predictions for linear PLA4 and PLA2 samples fit well the experimental data points as shown in *figure 7.18*; thus indicating that PLA4 and PLA2 samples do not hold branches.

A similar procedure was used to fit oscillatory shear data for PLA-REX samples assuming the entire MWD was made up of linear chains. Since both the density and the Rouse entanglement time values used for linear PLA samples are parameters which are characteristic of PLA resins, similar values were used to estimate the viscoelastic properties of PLA and PLA-REX samples. *Table 7.8* compiles the fitting

parameters. Experimental data points and viscoelastic properties simulations are plotted in *figure 7.19*.

Table 7.8. Fitting parameters for PLA-REX samples.

Parameters	PLA4-REX0.5	PLA2-REX0.5	PLA2-REX0.6
Dilation exponent α	0.5	0.7	0.7
Mass of monomer (g.mol^{-1})	72	72	72
Number of monomer in an entanglement length	54	53	52
Mass density of the polymer (g/cc)	1.2 ±0.1	1.2 ±0.1	1.2 ±0.1
Entanglement time, τ_e (s)	5e-8	5e-8	5e-8
Temperature (K)	453.15	453.15	453.15
M_w (kg.mol^{-1})	246 ±2	272 ±3	292 ±1
Polydispersity index	2.1 ±0.1	2.2 ±0.1	2.4 ±0.1

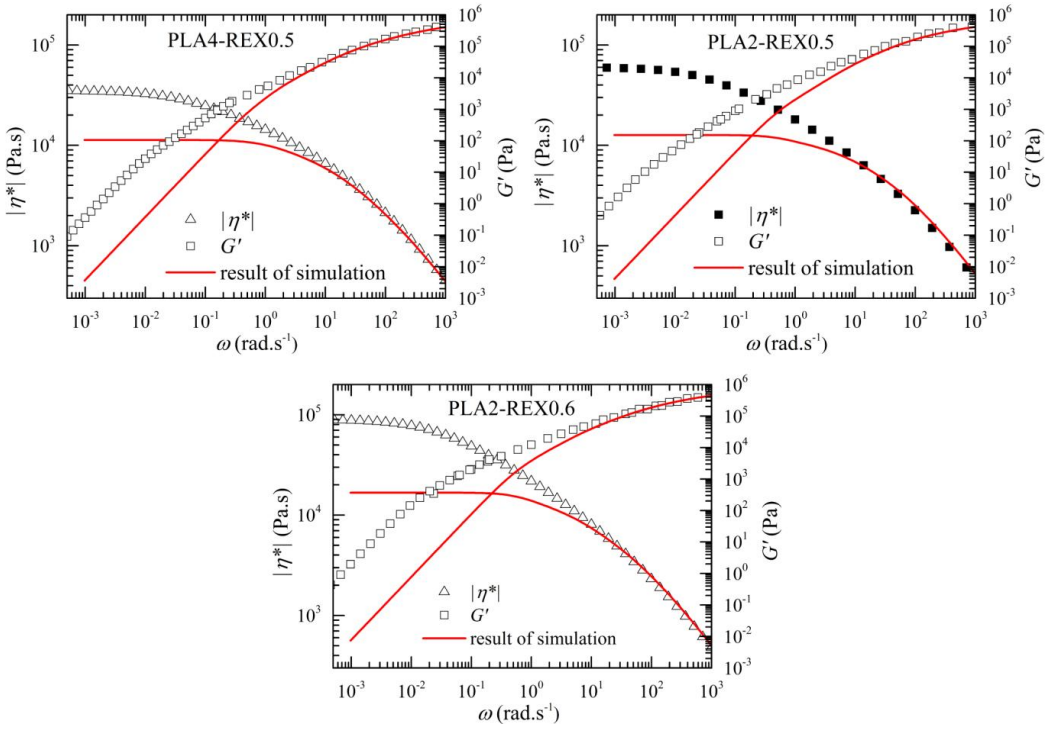

Figure 7.19. Experimental (open symbols) and predicted (solid line) linear viscoelastic properties using the BOB model (assuming that the entire distribution of MW was linear) for PLA-REX samples at 180 °C.

While the linear viscoelastic predictions for both linear PLA samples fit well the experimental data points, significant discrepancies between the predicted curves and the experimental data points were observed for PLA-REX samples in the low ω region

when the entire distribution of MW was assumed to be linear. Experimental points shift to higher values as compared to the simulation traces. Since predictions were entirely based on linear chains, results suggest the presence of macromolecules featuring still longer relaxation times and which lead to a completely different spectrum of relaxation times. In other words, this trend implied that PLA-REX samples include some LCB macromolecules.

7.2.6. Proposed chain architecture

The Cole-Cole and vGP-plots are considered as valuable tools to get an insight into molecular structures. Obviously, the Cole-Cole plot might reveal similar information as compared to vGP-plots. However, a higher sensitivity to polymer chain structures has been reported for the latter due to the consideration of the phase angle δ parameter instead of the viscosity [377].

In this section, solely temperatures far away from T_g were considered for PLA-4 based samples as molecular information related to the chain structure are exhibited from the medium to low ω range (*i.e.* transition and terminal regions). Similarly to $G'(\omega)$ and/or $|\eta^*(\omega)|$ master curves, the vGP plots were predicted from the combination of the TTS master curve data referenced at 180 ºC and the conversion of creep-recovery data for PLA4, PLA2, PLA4-REX0.5, PLA2-REX0.5 samples, as shown in *figure 7.20*. Regarding PLA2-REX0.6 samples, it was obtained from the combination of the viscoelastic measurements at 180 ºC and the conversion of the corresponding creep-recovery data.

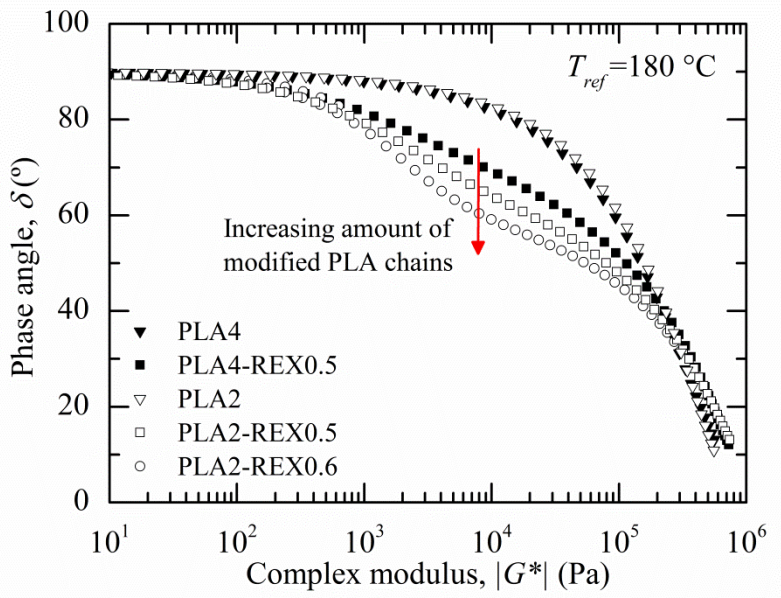

Figure 7.20. Effects of the chain architecture modifications on the van Gurp-Palmen plot.

The results obtained from the vGP plot appear to agree with the previous results. That is, both PLA samples exhibited the classical behaviour of a well entangled linear polymer. The δ curvature exhibits a limiting plateau value at 90º for low $|G^*|$ values (viscous behaviour) which decreases monotonically up to 0º for further $|G^*|$ increase (elastic behaviour).

In contrast, a completely different scenario was observed for PLA-REX samples. Moving from low to high $|G^*|$ values, δ decreased from the flow plateau (90º) to its minimum value at lower $|G^*|$ values as compared to PLA samples, but not strictly monotonically. The curves were flattened and δ values were lowered. Based on the conclusions derived from *figure 7.14* and *figure 7.19*, these changes in the vGP plot must be attributed to the presence of topological changes, which hold sparsely LCB, rather than the presence of two fractions of linear chain architectures with different MWs [140, 141]. This is supported by the fact that PLA-REX samples showed an enhancement of both the η_0 and the transition zone between the terminal and power-law region when the MW effects were removed (*c.f. figure 7.14*) and that the BOB model did not predict accurate viscoelastic properties when the assumed distribution of MW was linear. The gradual shift of δ towards lower values for both the more reactive PLA type and the increasing SAmfE content match well the above trend (*c.f. figure 7.14*), indicating an increasing content of modified PLA chains. According to *figure 7.20*, PLA2-REX0.5 showed a higher degree of structural modifications than PLA4-REX0.5 samples for equivalent SAmfE amount, which tendency agrees well with the previous SEC-DRI results (*c.f. table 7.1*).

Although topological modifications were developed in PLA-REX samples, the exact chain topology remained unidentified. Based on the detailed classification of LCB polymers by their topology developed by Trinkle *et al.* [141], PLA-REX samples did not seem to exhibit a well-defined chain architecture. Due to the statistical nature of the chemical bonding coupled with a possible competition between random chain degradation, chain extension and chain branching, the determination of the branch MW and the branching degree is not trivial. It would be a mixture of several types of non-uniform structures in MW, in architectures and in the number of branch per macromolecules.

Recall that SAmfE agent has a functionality of 12 (*c.f. chapter 3, section 3.2.2, table 3.4*). Thus, several PLA chains were possibly grafted to one SAmfE molecule during processing. In contrast to LCB PEs, PLA chains themselves do not acquire branches. The structure of the resulting modified PLA might be closer to a star-like macromolecule with SAmfE backbone actuating as the branch point. The MW of each arm is supposed to be different due to both the polydispersity of the neat polymer and the effects of the different random degradation mechanisms during processing [39].

The failure of the TTS principle coupled with the usual increase in E_a values that would be expected for PLA suspected of containing LCB was not observed for PLA4-REX0.5 and PLA2-REX0.5 samples but do not leave out this possibility since these materials show an enhancement of both the η_0 and the transition zone between the terminal and power-law region when the MW effects were removed (*c.f. figure 7.14*). Similarly to sparsely LCB HDPE (which is a blend of linear and low levels of branched structures) [138, 154, 155], this behaviour may be attributed to polymers with extremely low fractions of LCB for which the main fraction of remaining linear chains dominates the thermorheological behaviour and attenuates the effect of the structural modifications. Regarding PLA2-REX0.6 samples, this behaviour changed when the degree of topological changes exceeded a critical value. Accordingly, rheological results suggest that the different REX systems could be considered as a mixture between a high fraction of linear chains and a low but increasing amount of non-uniform branched structures, which include sparsely LCB, with both the more reactive PLA type (*i.e.* PLA2) and the increasing SAmfE content.

7.2.7. Influence of the topological changes on the relaxation spectrum

The relaxation spectrum was calculated using the commercial Rheology Advantage software (TA Instruments) according to *equations 9.4* and *9.5*. To gain further understanding of the time distribution of chain relaxations with the presence of sparsely non-uniform branched structures, the weighted relaxation spectrum ($\lambda H(\lambda)$) was estimated for each sample, as shown in *figure 7.21*.

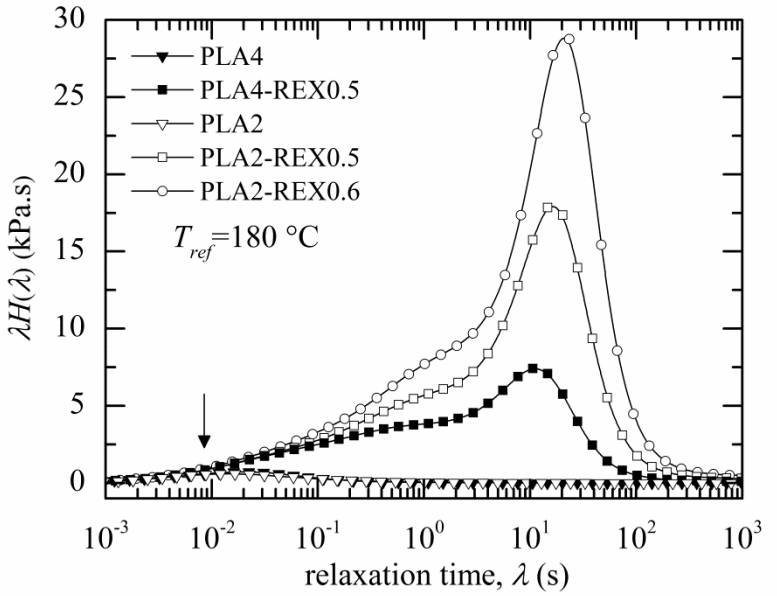

Figure 7.21. Effect of the molecular structure on the time-weighted relaxation spectrum.

Both PLA samples exhibited a unique peak at low relaxation times (around 10^{-2} s, indicated by an arrow) which could be attributed to the fast relaxation process of the linear chains by reptation [96] (*c.f. chapter 2, section 2.3*).

By contrast, broader and more complex spectra were observed for PLA-REX samples. The main relaxation peak was shifted to longer relaxation times and a shoulder appeared in the low relaxation time tails. Results suggest that the response time of the melt was significantly enlarged even though PLA-REX samples contain a low amount of modified PLA chains. This tendency corroborates the previous rheological measurements and agrees with the works of Wood-Adams *et al.* [100] for LCB PEs and Corre et *al.* [47] for architecurally modified PLA.

The enhancement of the relaxation times, even at very low concentrations of LCB, can be visualized by looking at *figure 7.22*. The "slip links" along the polymer backbone represent entanglement with other chains. While a linear polymer (*i.e.* PLA4, PLA2) is free to relax by relatively fast self-diffusion processes along a hypothetical tube surrounding a given chain segment, it is obvious from *figure 7.22.b* that the mobility of the LCB polymer is restricted and must relax through some other longer mechanisms.

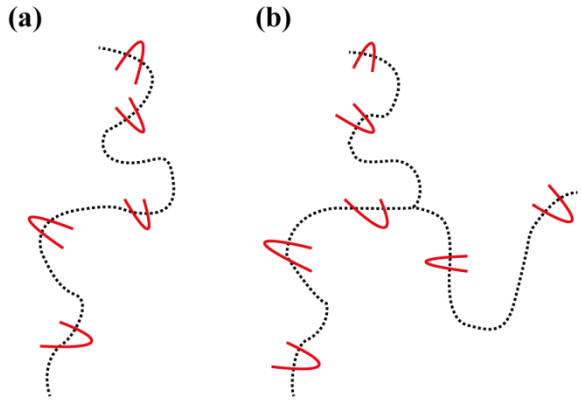

Figure 7.22. Illustration representing **(a)** a well entangled linear chain and **(b)** a LCB macromolecules. The "slip links" indicates entanglements due to the neighbouring chains (adapted from *ref.* [309]).

In star-like topology, the diffusion of the arm back towards the main backbone allows only thereafter the relaxation of this latter by "snake-like" motions along a tube [47, 152, 179]. Regarding PLA-REX samples, the reptation mechanism is possibly not inhibited due to the fraction of remaining linear chains, but it is superseded by slower relaxation mechanisms (*i.e.* primitive path fluctuations, constraint release), as already reported by Corre *et al.* [47] and Al-Itry *et al.* [102].

7.3. MWD determination from melt rheology

Since branching significantly affects both the polymer flow properties and its processing behaviour, the characterization of the polymer architecture on a molecular level is of significant importance. PLA-REX matrix may be assumed as randomly and sparsely modified since the content of modified chains, the length of the arms and their stereo localization are controlled by the statistical nature of the reaction. A rigorous quantitative characterization is therefore not trivial.

A preliminary trial was performed to evaluate the MW of PLA-REX samples using SEC with in line multiple detectors, as reported in *section 7.2.1*. Nevertheless, untrustworthy results were obtained due to both a degree of structural modifications probably below the limits of detection of this technique and the non uniformity in MW and in architecture of the branched macromolecules.

On this basis, SEC-DRI measurements were preferred to enhance the contrast between PLA and PLA-REX samples. A significant increase in the MW coupled with a slight broadening of the MWD was associated to the structural modifications. However, this technique is time consuming, expensive (use of solvents) and experimental data may be flawed by coelution issues as linear and branched chains might possess similar hydrodynamic volume but different MWs [309, 358, 380].

A preceding experiment was conducted to fractionate the different molecular entities in order to minimize coelution issues. PLA-REX was dissolved in chloroform ($CHCl_3$) and then heptane (C_7H_{16}) was progressively added to the solution in order to promote the crystallization of the species of highest MW. The resulting SEC-DRI measurements were found to be fairly similar to the unfractionated polymer, indicating the crystallization of all MW species with the formation of self-seeding nuclei. This tendency was attributed to the fast crystallization kinetics of PLA in solution.

Since molecular characterization of PLA-REX samples remained complicated using chromatographic techniques, an increasing interest has grown to deduce molecular properties from shear rheology. Based on the changes observed in the $|\eta^*(\omega)|$ behaviour with the presence of topological modifications, it is reasonable to expect some modifications in the shape of the deduced MWD spectrum from integral and/or numerical methods. The Shaw and Tuminello methodology (*c.f. chapter 2, section 2.3.4.d*) was used to infer MWD from $|\eta^*(\omega)|$ functions. This approach was selected because no previous assumptions of G_n^0 or MWD parameters are necessary to invert viscosity data. Since $|\eta^*(\omega)|$ data must be differentiated twice in *equation 2.42* (*c.f. chapter 2, section 2.3.4.d*), raw data were filtered using values given in *table 7.5* in order to smooth out noises. In addition, all $|\eta^*(\omega)|$ traces were extrapolated at both ends to ensure the prediction of complete MWDs.

7.3.1. Scaling up of the deduced MWD toward relative MWD

According to the numerical approach developed by Shaw and Tuminello [159], the MWDs deduced from rheological measurements are plotted against the reduced MW, *m* (*c.f. chapter 2, section 2.3.4.d, equation 2.41*). Scaling *w log (m)* toward the relative MWD is the key point for the robustness of the determination of relative value of MWs and MWD. In order to remove the dependence of the deduced results on M_w, a relationship relating *M* to *m* is suggested (*c.f. equation 7.5*) from the combination of *equations 2.35, 2.41 and 2.43* (*c.f. chapter 2, section 2.3*).

$$M = m.(\eta_0/K)^{1/\alpha} \qquad \textbf{(7.5)}$$

Where η_0, *M* and *m* are the zero-shear rate viscosity, the MW and the reduced MW as defined in *equation 2.23* and *equation 2.41*, respectively (*c.f. chapter 2, section 2.3*). α and *K* are the exponent and the coefficient of the power law dependence of η_0 on M_w according to *equation 2.35*. The use of *equation 7.5* with accurate α and *K* values removes the scaling up and the calibration of the relative MWD on chromatographic data.

For the purpose to investigate how structural modifications affect the η_0 - M_w correlation, η_0 values at 180 ºC as a function of the relative M_w, as determined using SEC-DRI (*c.f. table 7.1*), are plotted in *figure 7.23*. Experimental data points from Dorgan *et al.* [174] were also added in order to enlarge the span of MWs considered. The dashed line represents the relation found for linear HMW PLA with an exponent α of 3.4 ± 0.1 and a coefficient *K* of 5.5. 10^{-15} (R^2=0.9991) [174].

It is apparent that the data corresponding to both linear PLA samples matched well the previous relation. Moreover, this finding suggests that "*a priori*" the dependence of η_0 on M_w remained unaffected by the stereoregularity for HWM polydisperse linear PLA polymers.

However, a clear deviation of $\eta_0(M_w)$ from $\eta_0 \approx M_w^{3.4}$ towards higher viscosity values was found for PLA-REX samples. Since the power law dependence of η_0 on M_w is one of the relationships which remains independent of sample polydispersity [132, 144, 146, 174, 390], the minor variations in the breath of the MWD between PLA and PLA-REX samples (*c.f. table 7.1*) cannot account for this deviation from the dashed line.

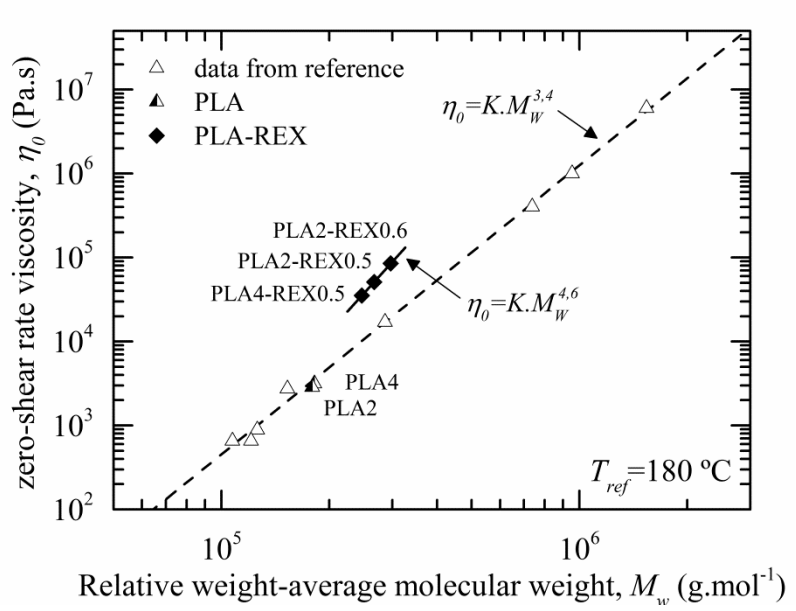

Figure 7.23. Plot of the zero-shear rate viscosity at 180 ºC with the relative weight-average MW as determined using SEC-DRI. The dashed line indicates the correlation between η_0 and M_w established by Dorgan *et al.* [174] with the corresponding data points (open triangles).

For the purpose to scale *w log*(*m*) towards the MWD without resorting of chromatographic data (*i.e. equation 7.5*) for PLA-REX samples, a power-law dependence could be considered as reliable in order to plot η_0 with M_w. This is due to the narrow span of MWs covered by REX samples (246-292 kg.mol^{-1}). Over the MW covered, an exponent α of 4.6 ± 0.1 and a coefficient K of 1.3.10^{-21} were measured for PLA-REX samples. Dorgan *et al.* [130] reported an even stronger scaling factor for 4 and 6 arms star-like PLA polymers.

7.3.2. Linear PLA polymers

For both PLA samples, the viscosity MWDs deduced from rheological measurements were calculated and results were compared to the SEC-DRI MWDs as shown in *figure 7.24*. *m* was scaled up with MW using *equation 7.5* and the corresponding data obtained from *figure 7.23* (*i.e.* α=3.4 and K=5.5.10^{-15}). Relative MW values with respect to the fitting model considered are compiled in *table 7.9*. Calculations of the error percentages proceed according to the differences between the deduced relative MWs and the corresponding values as measured using SEC-DRI (*c.f. table 7.1*).

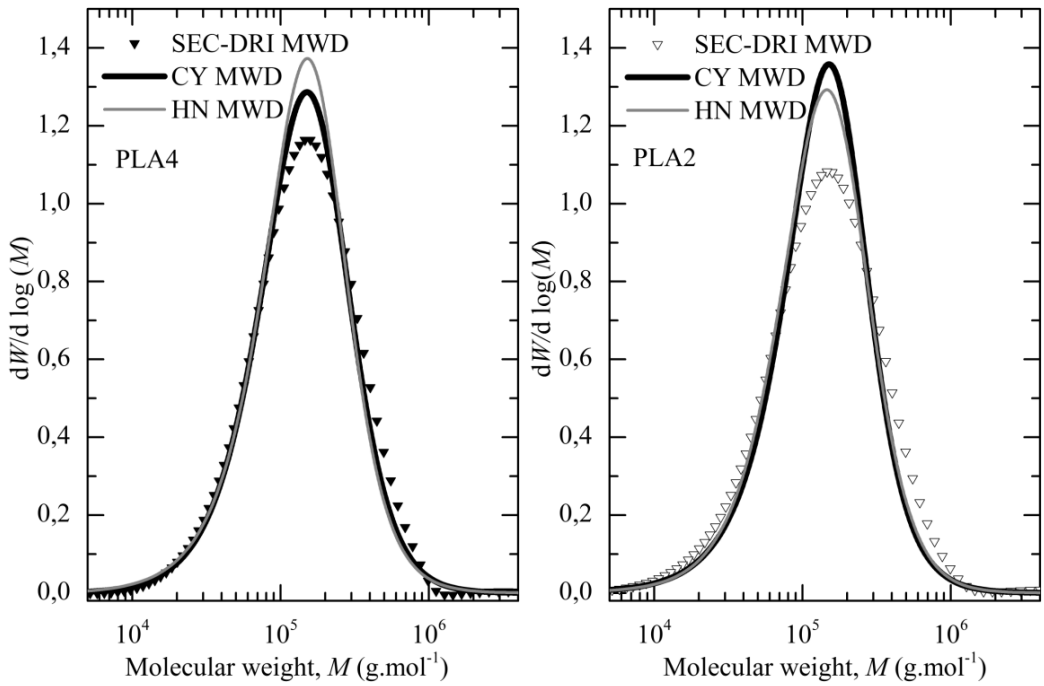

Figure 7.24. Comparison between SEC-DRI MWD data and MWD inferred from viscosity measurements for PLA4 and PLA2 samples.

Table 7.9. Effect of the viscosity fitting model on the relative MW averages.

Sample	Fitting model	M_n (kg.mol^{-1})	M_w (kg.mol^{-1})	M_z (kg.mol^{-1})	M_n/M_w
PLA4	CY	97	185	357	1.90
	Error (%)[a]	*5.5*	*0.1*	*8.2*	*5.9*
	HN	93	181	350	1.93
	Error (%)[a]	*2.0*	*2.6*	*6.2*	*4.7*
PLA2	CY	89	178	347	2.00
	Error (%)[a]	*4.6*	*0.6*	*0.6*	*5.5*
	HN	89	178	347	2.00
	Error (%)[a]	*4.6*	*0.7*	*0.8*	*5.2*

CY: Carreau-Yassuda, HN: Havriliak-Negami

[a] The error percentages arise from the difference between the deduced values from rheological measurements and the corresponding SEC-DRI values (*c.f. table 7.1*).

Regarding both PLA samples, viscosity MWDs fit well experimental SEC-DRI data. A good agreement was observed on the location of the main peak and on the breath of the MWD. Discrepancies in the HMW tail between the inversion technique predictions and the SEC data is probably a consequence of the assumed log-normal distribution for the calculated MWDs. Similar quantitative accuracy between both inferred and SEC MWDs have been already reported by Wood-Adams and Dealy for

linear PEs [158]. The principal point here is that the CY and HN viscosity models appear to provide approximately equivalent molecular information for a well entangled linear polymer with a PDI of about two.

The robustness of the HN model to capture the fundamental molecular information resides in its mathematical structure. Gross [394] stated that the shape of the relaxation spectrum ($H(\lambda)$) was accurately described by an analytical expression derived from *equation 2.48* (*c.f. chapter 2, section 2.3.4.e*). When the Cox-Merz rule holds, a direct correlation may be established between the CY parameters and the $H(\lambda)$ parameters. In this manner, the phenomenological model initially developed to describe non-linear steady flow properties may contain similar molecular information as the HN model.

7.3.3. PLA-REX samples

Figure 7.25 shows the comparison of MWD spectra deduced from melt and SEC-DRI measurements for PLA-REX samples. *m* was scaled up with MW using *equation 7.5* and the corresponding data obtained from *figure 7.23* (*i.e.* α=4.6 and K=1.3.10^{-21}). Relative MW averages with respect to the fitting model considered are compiled in *table 7.10*. Calculations of the error percentages proceed according to the differences between the deduced relative MWs and the corresponding values as measured using SEC-DRI (*c.f. table 7.1*).

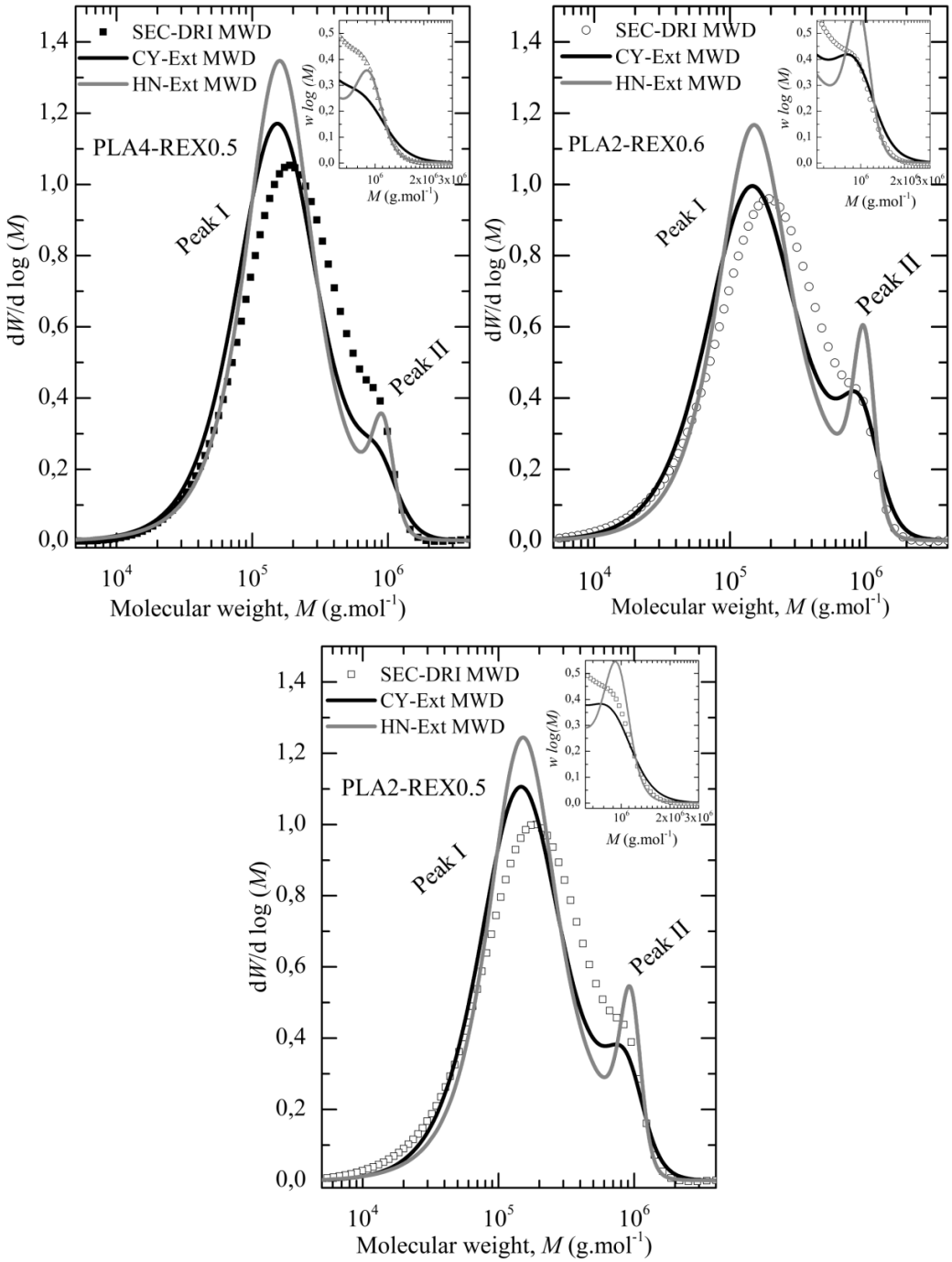

Figure 7.25. Effect of the viscosity fitting model on the MWD deduced from rheological measurements for PLA-REX samples. Inserts show a detailed view of the HMW tails.

Table 7.10. Effect of the viscosity fitting model on the relative MW averages.

Sample	Fitting model	M_n (kg.mol^{-1})	M_w (kg.mol^{-1})	M_z (kg.mol^{-1})	M_n/M_w
PLA4-REX0.5	CY-Ext	110	245	530	2.24
	Error (%)[a]	*8.3*	*0.1*	*10.5*	*8.2*
	HN-Ext	118	245	493	2.08
	Error (%)[a]	*0.6*	*0.1*	*3.7*	*0.4*
PLA2-REX0.5	CY-Ext	114	272	595	2.39
	Error (%)[a]	*7.2*	*0.1*	*8.4*	*7.0*
	HN-Ext	115	278	572	2.28
	Error (%)[a]	*7.8*	*2.1*	*4.8*	*11*
PLA2-REX0.6	CY-Ext	107	292	666	2.73
	Error (%)[a]	*11.8*	*0.1*	*9.3*	*10.5*
	HN-Ext	121	294	618	2.44
	Error (%)[a]	*0.8*	*0.6*	*2.2*	*0.2*

CY-Ext: extended Carreau-Yassuda, HN-Ext: extended Havriliak-Negami

[a] The error percentages arise from the difference between the deduced values from rheological measurements and the corresponding SEC-DRI values (*c.f. table 7.1*).

The two different relaxation regimes observed in the trace of $|\eta^*(\omega)|$ between the Newtonian and shear-thinning regimes (*c.f. figure 7.11*) for PLA-REX samples is here reflected in terms of bi-modal distribution of MW. Regardless of the fitting model considered, the MW averages and PDI values agreed within 10% between rheological and SEC-DRI measurements. However, the peak positions and the shape of the MWDs between both measurements did not match. The position of the second peak (marked as Peak II) was fairly constant between all measurements. Nevertheless, the peak MW (M_p) of the first peak (marked as Peak I), which is inferred by rheological measurements, shifted to lower MWs as compared to SEC data. Although similar differences have been already reported by Wood-Adams and Dealy [158] for LCB PEs, authors have not resolved yet the main reason of these descrepencies.

Figure 7.26 reports the M_p values of the first peak obtained from SEC-DRI and rheological measurements, respectively. While SEC data depicts a constant increase in M_p with the amount of topological modifications, M_p values estimated from rheological measurements, were roughly centred in similar MW values between PLA and PLA-REX samples.

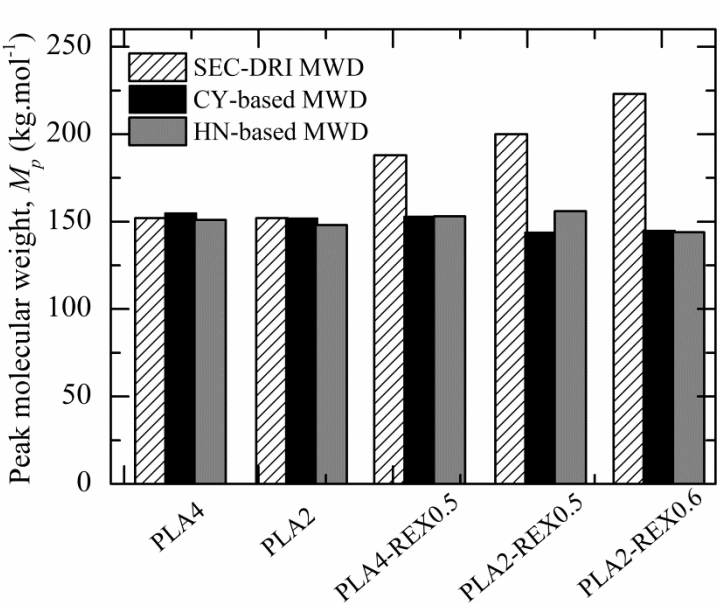

Figure 7.26. Comparison of M_p for the first peak deduced from SEC-DRI and rheological measurements. CY-based MWD: MWD inferred from viscosity functions fitted using the CY model for PLA samples and using the CY-Ext model for PLA-REX samples. HN-based MWD: MWD inferred from viscosity functions fitted using the HN model for PLA samples and using the HN-Ext model for PLA-REX samples.

Since $|\eta^*(\omega)|$ is related to the MWD using the mixing rule developed by Malkin and Teishev [162] (*c.f. chapter 2, section 2.3.4.d, equation 2.42*), the bimodal viscosity MWDs should be interpreted as the summation of two distinct and narrow distributions of MW that would correspond to two distinct types of macromolecules in architecture and in MW. Both of them are correlated with each separated relaxation process exhibited in the $|\eta^*(\omega)|$ trace as illustrated in *figure 7.27*.

Peak I was related to the linear chain fraction in all spectra due to the linear architecture of PLA samples. This signal is governed by the second transition region in $|\eta^*(\omega)|$ (i=2 in *equations 7.1 and 7.2*) as the MW is inversely related to ω by combining *equation 2.41* and *equation 2.42* (*c.f. chapter 2, section 2.3.4.d*). It remained centred in roughly similar MW values due to a possible similar time-dependence of the relaxation processes governing the linear population in PLA and PLA-REX samples. The second peak at high MW is ruled by the intermediate relaxation regime in the $|\eta^*(\omega)|$ trace (i=1 in *equations 7.1 and 7.2*), resulting from the longer relaxation times induced by the topological changes.

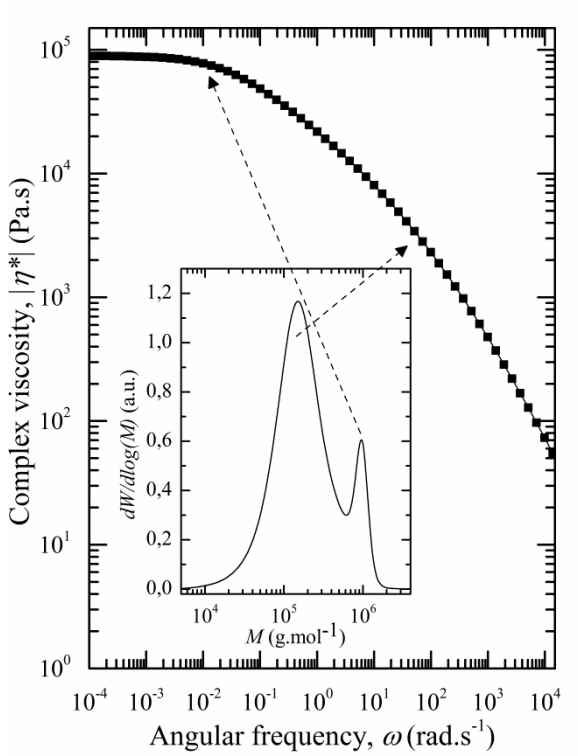

Figure 7.27. Inverse transform of the complex viscosity function to MWD spectrum with peak indication. PLA2-REX0.6 samples were chosen for illustration purposes.

Despite the fact that the second peak position appeared to be located in good agreement between all measurements, its resolution was greatly affected by the viscosity model used to fit $|\eta^*(\omega)|$ data. The bimodality appeared to be better resolved when the HN-Ext model was used. This enhanced resolution might be a consequence of the incorporation of the complex time dependence of the viscoelastic response into the characterization.

As the Cox-Merz assumption does not hold for LCB polymers, a direct correlation between the CY-Ext parameters and the $H(\lambda)$ parameters cannot be established. A loss of subtle information about molecular and relaxation processes possibly occur when the CY-Ext model is used to fit $|\eta^*(\omega)|$ data. The flattening of the HMW peak might be a consequence of this fitting issue.

Figure 7.28 depicts the effects of the increasing content of modified PLA chains on the viscosity MWDs with respect to the viscosity model used to fit $|\eta^*(\omega)|$ raw data.

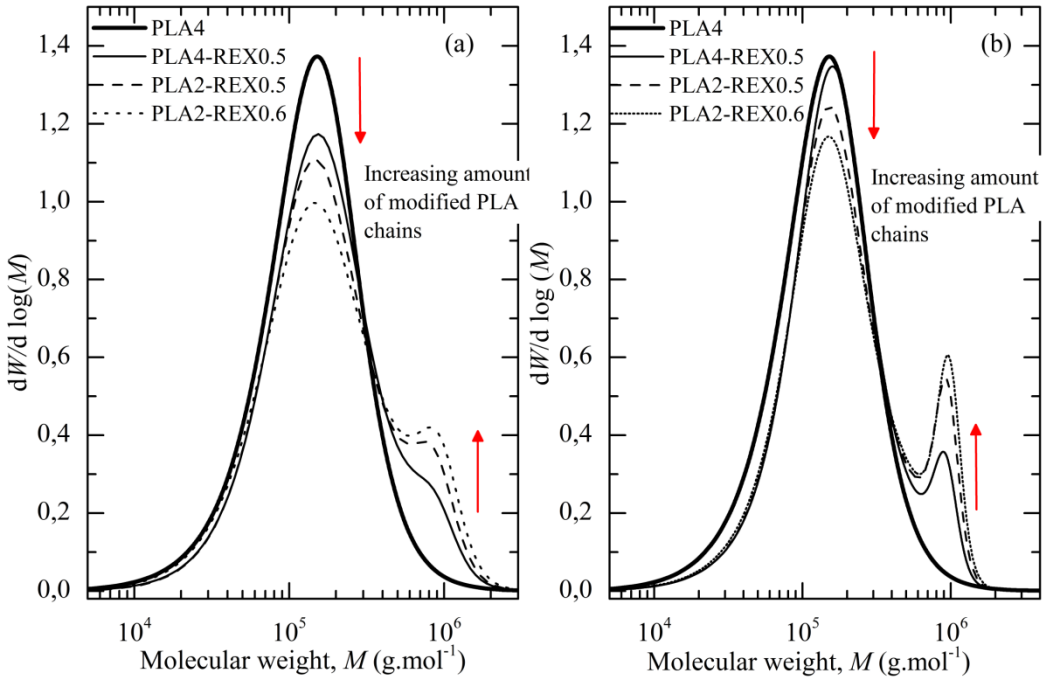

Figure 7.28. Effect of an increasing content of modified PLA chains on the MWD inferred from rheological measurements. The corresponding MWD were deduced from $|\eta^*(\omega)|$ fitted with **(a)** the extended Carreau-Yassuda and **(b)** the extended Havriliak-Negami model.

During processing, several PLA chains are possible grafted to one SAmfE molecule. As shown in *figures 7.14 and 7.20*, the content of modified PLA chains increased at the expense of the linear chain fraction for both the more reactive PLA type (*i.e.* PLA-2) and the increasing SAmfE content. In *figure 7.28*, the evolution of the height of both peaks suggests that the extent of the relaxation processes related to the modified chain fraction grows at the expense of those related to the linear chain fraction. The observed trend could be assumed as characteristic of an increasing content of modified PLA chains. This tendency was found to be better discretized when the HN-Ext model was used to fit raw $|\eta^*(\omega)|$ data, as previously mentioned.

7.4. Quantitative estimation of the amount of modified PLA chains

Since one of the primary objectives of this work was to evaluate the effects of structural modifications on the linear viscoelastic behaviour of PLA, a quantitative estimation of the amount of modified PLA chains is of great interest. The degree of branching for polyolefins is usually reported as the number of LCB's per 10 000 carbon atoms. However, this definition is inapplicable to characterize PLA-REX

samples. This is due to a probable mixture of various sparsely non-uniform branched structures generated through reactive extrusion.

Numerous intents to evaluate the structural modifications have been performed using SEC-multiple detectors experiments (as detailed in *section 7.2.1*). Nevertheless, unreliable results were obtained due to an architecturally modified chain content possibly below the detection limit of these techniques and to the non-uniformity of the different branched macromolecules. In the present work, the contrast between the eluted linear and modified chain fractions was enhanced using SEC-DRI measurements, as shown in *figure 7.2*. While the shoulder in the HMW tail of SEC data may indicate an increase in the population of high MW linear chains and/or the presence of branching, its position (along the MW axis) and its magnitude are likely to be flawed due to coelution issues.

Nevertheless, since PLA-REX samples feature a low content of sparsely and non-uniform branched structures, the error on the MWD may be considered to be negligible, as already reported by van Ruymbeke *et al.* [99] for HDPE featuring low levels of LCB. Thus, the partial area below the shoulder (indicated by an arrow in *figure 7.2*) could be related to a quantitative amount of modified PLA chains which extend may be estimated using a deconvolution analysis. All MWD spectra were analyzed using log-normal functions (*c.f. chapter 6, section 6.3, equation 6.2*) with the condition of finding two peaks centred at the same maxima as exhibited by experimental data. This concept has been illustrated for PLA4-REX0.5 samples in *figure 7.29*. The partial areas corresponding to the content of modified PLA chains (referred to as peak 2 in *figure 7.29*) are compiled in *table 7.11*.

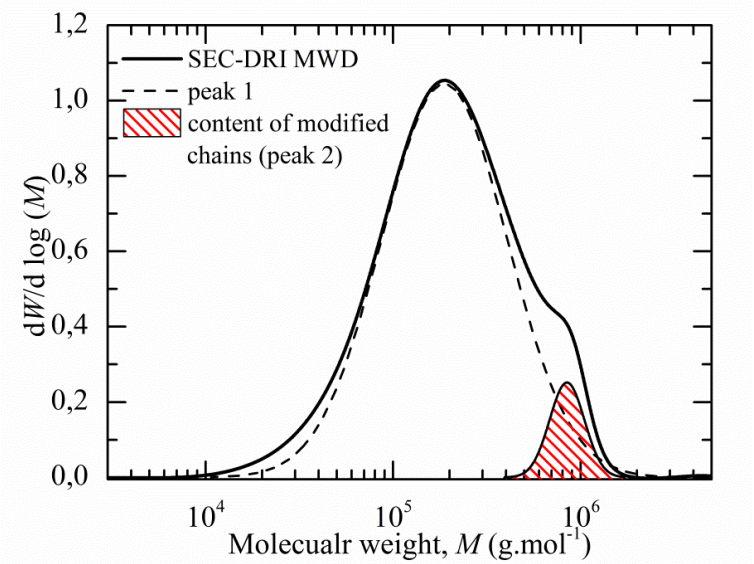

Figure 7.29. Illustration of the deconvolution analysis for MWD as determined using SEC-DRI analysis for PLA-REX0.5 samples.

Commonly, complementary information about the number of branches can be obtained using NMR measurements. A preliminary trial was performed to characterize the molecular structure of PLA-REX samples using ^{1}H NMR experiments. ^{1}H NMR spectra of both PLA2 and PLA-REX samples with the highest amount of structural modifications (*i.e.* PLA2-REX0.6) are shown in *figure 7.30* together with peak assignments.

In the polymerization of the lactide, often a starter molecule such as isopropanol is used, leading to a final polymer with few –COOH groups, as already reported in *chapter 6* (*c.f. section 6.4.2*). Moreover, most terminal –COOH groups on commercial PLA types are end-capped. On this basis, while the carboxyl content may be negligible in the as-received materials, its presence was considered in the following analysis. This is due to the actions of the several thermo-mechanical degradations during processing; leading to the formation of new functional end groups (*i.e.* –OH and/or –COOH end groups).

In both spectra, the most intense signals at 1.8 and 5.2 ppm correspond to methyl (-CH_3) and methine (-CH) protons at the (c) and (b) positions, respectively, which belong to the main PLA chain. The resonance peaks at 1.04 and 4.4 ppm are thought to belong to the -CH_3 and -CH protons next to the terminal -OH groups (*i.e.* (d) and (a) positions, respectively). Note that the sharp peak at 7.29 ppm is due to the deuterated chloroform $CDCL_3$ [371, 372].

The broad peak, which overlaps the signal of the solvent (indicated by an arrow) for PLA2-REX0.6 samples, probably belongs to the protons in the aromatic rings of SAmfE molecules. While the coupling reactions between PLA and a multi-epoxy reactive agent have been identified by Meng *et al.* [371] (*c.f. chapter 6, section 6.4.2*), both spectra remained similar in the present work. Similar observations were highlighted for PLA4-REX0.5 and PLA2-REX0.5 samples; suggesting the absence of branched structures. Recall that NMR cannot detect sparsely and/or non-uniform branched macromolecules and cannot distinguish LCB to the main polymer backbone. This is because both give rise to the same spectral pattern irrespective of the chain length. However, the rheologically relevant branches are those long enough to entangle, as it was shown in *section 7.2*.

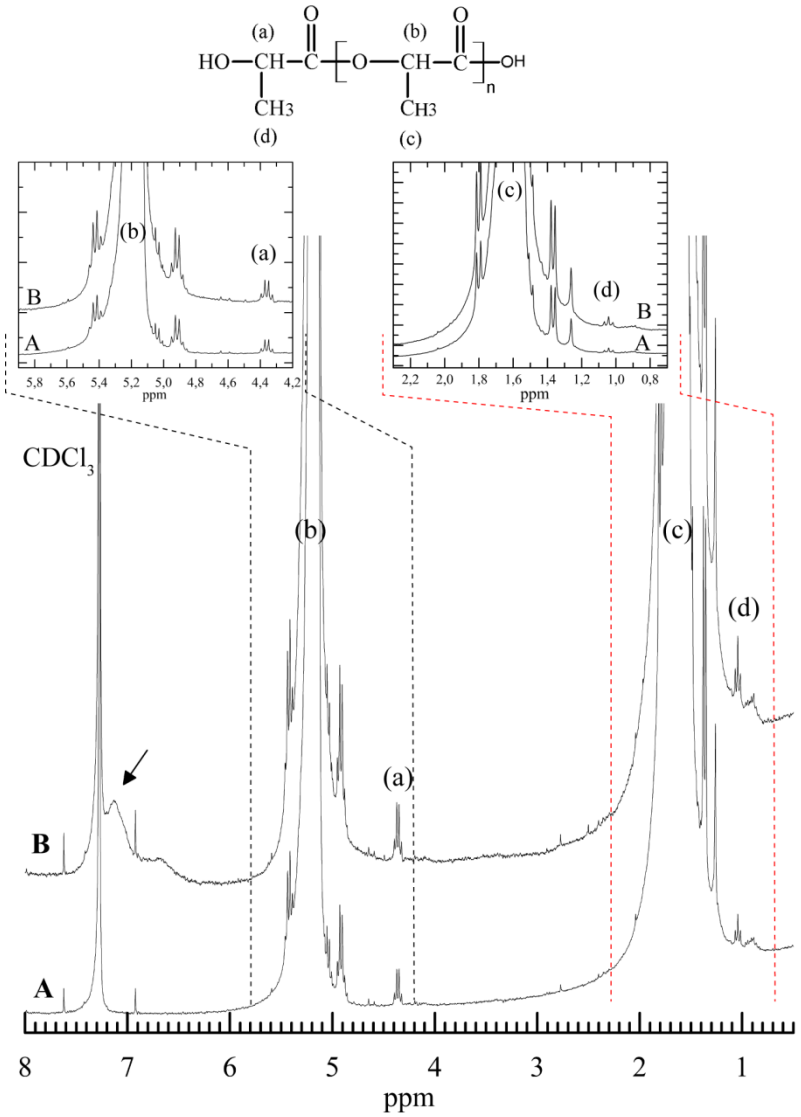

Figure 7.30. ^{1}H NMR spectra of (**A**) PLA2 and (**B**) PLA2-REX0.6 with peak assignments. The arrow indicates the signal which probably belongs to the protons in the aromatic rings of the SAmfE molecules.

On the other hand, ^{1}H NMR data permitted to estimate an increase in the number of terminal groups between PLA and PLA-REX samples. Similar magnetic resonance properties between both the linear PLA chains and the PLA chains grafted to SAmfE molecules were assumed in this approach, as schematically illustrated in *figure 7.31*.

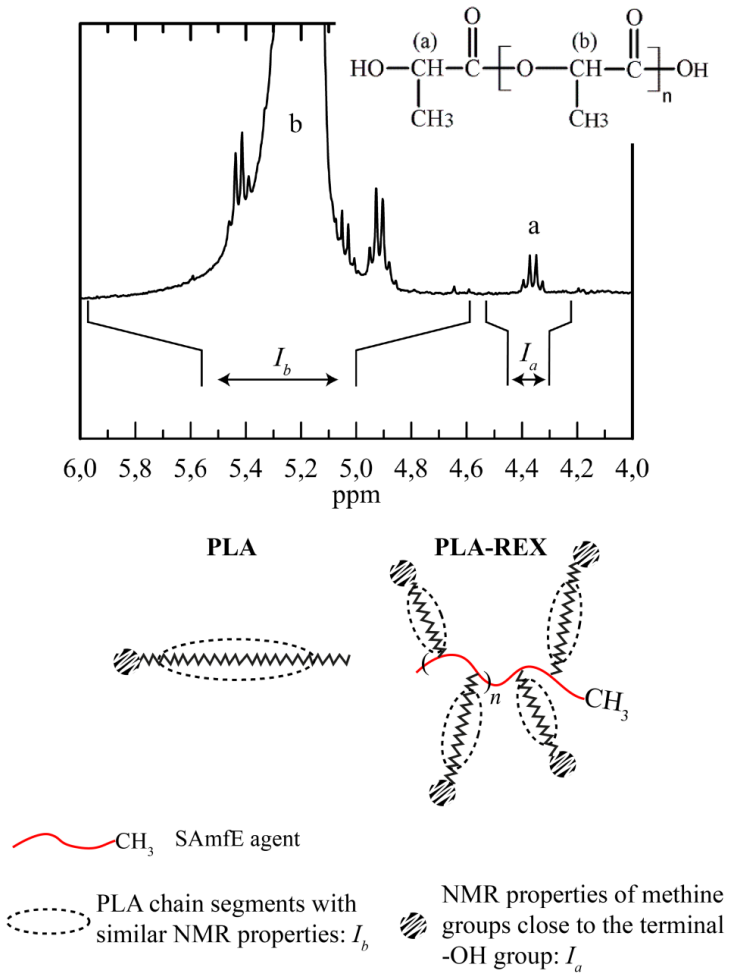

Figure 7.31. Illustration of the integral analysis for ^{1}H NMR measurements.

It is well know that the relative number of resonance protons in a polymeric chain is related to the integration of the corresponding resonance peak intensities (*I*). For linear PLA, the analysis of the integration ratio between the (a) and (b) peaks leads to an absolute value of the "*degree of polymerization*" ($DP_n = I_b/I_a$). This procedure solely remains valid for linear PLA chains as they bear only one hydroxyl end group close to the (a) position. For PLA-REX samples, the number of hydroxyl groups per macromolecule, close to the (a) position, possibly increased because branched polymers are characterized by the presence of branch points and the presence of more than two end groups. Therefore, the DP_n of PLA-REX sample ($(DP_n)_{PLA\text{-}REX}$) is possibly underestimated as compared to its linear homologue ($(DP_n)_{PLA}$). For a given MW, $(DP_n)_{PLA}$ was related to $(DP_n)_{PLA\text{-}REX}$ using a correlation factor *K*, which was defined as an average of terminal groups, according to:

$$(DP_n)_{PLA} = K * (DP_n)_{PLA-REX} \quad \textbf{(7.6)}$$

However, the increasing MW values upon SAmfE addition suggest that *equation 7.6* required MW correction using SEC-DRI experiments. Thus, the DP_n ratio between PLA-REX and PLA samples measured by NMR was related to those obtained from the ratio of molar masses measured by SEC as follows:

$$\left[\frac{(DP_n)_{PLA-REX}}{(DP_n)_{PLA}}\right]_{NMR} * K = \left[\frac{(DP_n)_{PLA-REX}}{(DP_n)_{PLA}}\right]_{SEC} \quad \textbf{(7.7)}$$

Where $[(DP_n)]_{NMR}=I_b/I_a$. I_a and I_b are the integral areas of the methine proton at the (a) and (b) position, respectively. $[(DP_n)]_{SEC}=M_n/M_0$. M_n is the relative number-average MW and M_o the MW of the repeat unit. In the current study, the integration ratio between both resonance peaks was normalized with respect to one methine proton at the (a) position (I_a=1) for all samples.

An increasing number of terminal groups was related to the amount of modified PLA chains (ΔK) which can be calculated from *equation 7.8*. Numerical values are summarized in *table 7.11*.

$$\Delta K\ (\%) = \left(\frac{(I_b)_{PLA}}{(I_b)_{PLA-REX}} * \frac{M_{n\ PLA-REX}}{M_{n\ PLA}} - 1\right) * 100 \quad \textbf{(7.8)}$$

Where $(I_b)_{PLA}$ and $(I_b)_{PLA\text{-}REX}$ are the integral areas of the methine proton at the (b) position of the PLA and PLA-REX samples, respectively. $M_{n\ PLA\text{-}REX}$ and $M_{n\ PLA}$ are the relative number-average MWs of PLA-REX and of the PLA sample type as determined using SEC-DRI (*c.f. table 7.1*). It should be noted that the repeatability of the measurements was in the order of ±10%.

Based on the rheological data reported in *section 7.2*, viscoelastic measurements in the melted state appeared to react very sensitively on molecular changes, even at very low contents. Thus, the following aims to quantify the content of modified PLA chains solely based on rheological measurements.

In a first intent, the *Dow Rheology Index* (DRI, *c.f. chapter 2, section 2.3.4.c, equation 2.37*) was used to estimate an amount of modified PLA chains. Nevertheless, this index has been designed for polyolefins featuring a unique curvature in the shear-thinning regime (and thus an unique characteristic relaxation time, λ) and hence cannot be used for PLA-REX samples even though both characteristic times exhibited in the transition region are considered separately.

On the other hand, the patterns observed in *figure 7.28* could be used to estimate a content of modified chains simply from knowledge of viscosity MWD alone. The

evolution of the peaks corresponding to the modified chain topology was followed using a deconvolution analysis. All MWD spectra were analyzed using log-normal functions (*c.f. chapter 6, section 6.3, equation 6.2*) with the condition of finding two peaks centred at the same maxima as exhibited by experimental data, as shown in *figure 7.32*. The partial area below the second peak was related to a quantitative amount of modified PLA chains. Results are given in *table 7.11*.

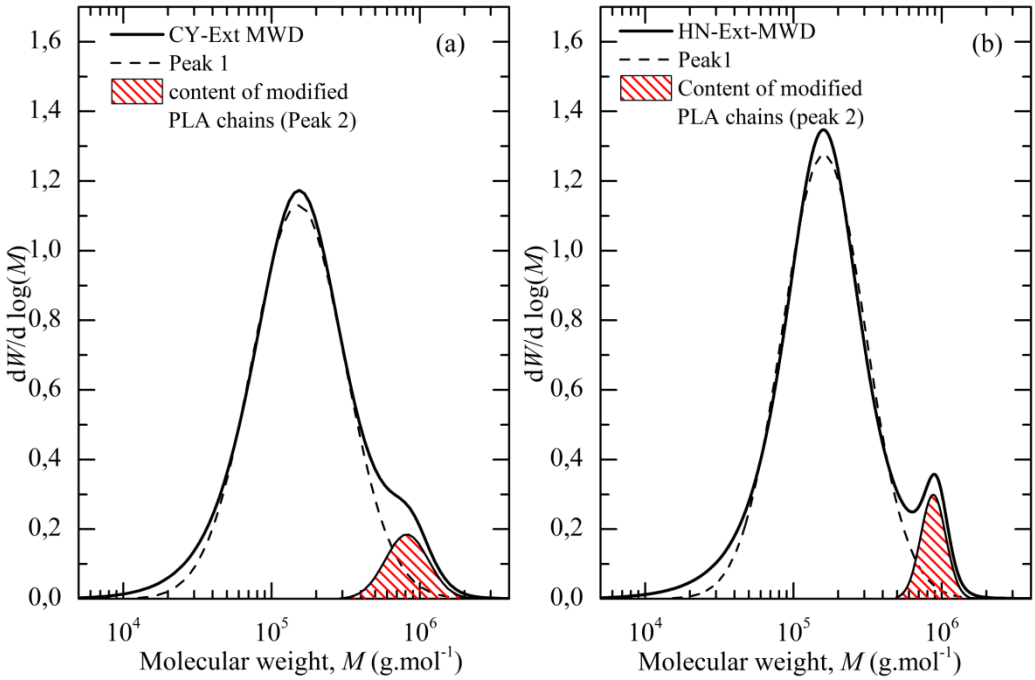

Figure 7.32. Illustration of the deconvolution analysis for MWDs inferred from rheological measurements of PLA4-REX0.5 samples. Raw $|\eta^*(\omega)|$ were filtered using the **(a)** CY-Ext and **(b)** HN-Ext model, respectively.

Table 7.11. Quantitative estimation of the amount of modified PLA chains.

Sample	**Amount of modified PLA chains (%)**			
	SEC-DRI [a]	NMR	Rheological MWD [b]	
			CY-Ext	HN-Ext
PLA4-REX0.5	22	19	21	22
PLA2-REX0.5	25	24	23	24
PLA2-REX0.6	29	29	30	32

CY-Ext: extended Carreau-Yassuda model, HN-Ext: extended Havriliak-Negami model

[a] Partial area below the shoulder in the HMW tail in MWD spectrum from SEC-DRI measurements.

[b] Partial area below the second peak exhibited in the MWD inferred from melt measurements.

By examining the obtained data, an apparent increase in the amount of modified chains was observed for the more reactive PLA type (*i.e.* PLA2) and the increasing SAmfE content. For each sample, all measurements were largely similar as shown in *table 7.11*. Consequently, the methodology developed from solely rheological measurement can be considered as reliable to quantitatively estimate the amount of modified PLA chains.

Although the deconvolution of the MWDs inferred from the inversion of the CY-Ext and/or the HN-Ext models provided similar information regarding the content of modified PLA chains, MWDs inferred from the inversion of the HN-Ext viscosity model can be considered as more reliable. That is, the larger discretization between the molecular information related to the linear and modified PLA fractions in the predicted bimodal MWDs allowed to adjust with higher accuracy the deconvoluted peaks to the MWD (*i.e.* position of the peak maxima along the MW axis, peak width, etc).

7.5. Thermal properties

The results obtained up to that point suggest an enhancement of the rheological properties (*i.e.* melt elasticity) due to an increasing content of structural modifications with both the more reactive PLA type and the SAmfE content. Since the effects of the topological modifications on the thermal, mechanical and fracture behaviours are of interest, from now on only PLA-REX samples featuring the lowest and highest content of modified PLA chains will be considered for the sake of clarity. That is, only PLA4-REX0.5 samples and PLA2-REX0.6 samples will be investigated and then compared to their PLA4 and PLA2 homologues, respectively.

Using DSC analysis, the investigations performed in this section summarized the following aspects:

- Evaluation of the thermal behaviour of PLA and PLA-REX samples.
- Evaluation of the changes in the molecular fractionation between PLA and PLA-REX samples using the *Successive Self-Nucleation and Annealing methodology*.
- Evaluation of the effects of topological changes on the kinetics of enthalpy relaxation for samples aged at T_a=30 °C.

Using DMTA analysis, the effects of the structural modifications on the de-aged and aged PLA dynamic mechanical thermal properties were studied.

7.5.1. Thermal behaviour

a) Extruded sheets: "As received analysis"

To contribute to the investigation of the thermal behaviour of PLA and PLA-REX samples using DSC, the thermal protocol described in *section 5.1.5.a* (*c.f. chapter 5*) was used. The first DSC heating scans (**H1**) at 10 ºC.min^{-1} of PLA-4 and PLA-2 based materials aged for 1 week (*c.f. chapter 4, section 3.3*) are shown in *figure 7.33*. Thermal properties obtained from the corresponding heating scans are summarized in *table 7.12*.

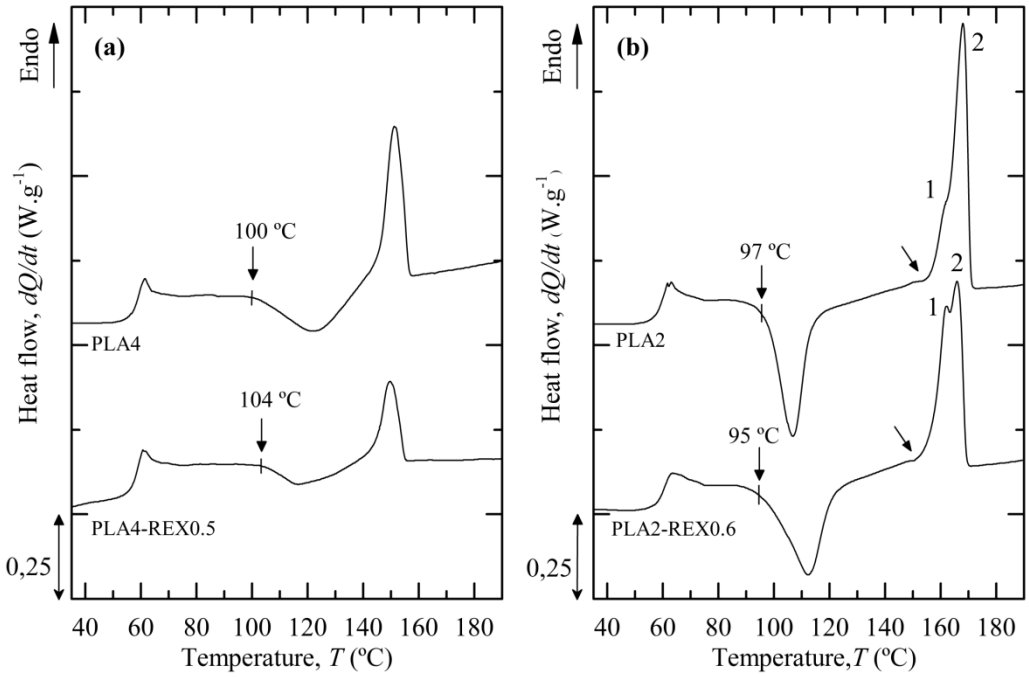

Figure 7.33. First DSC heating scan (**H1**) at 10 ºC.min^{-1} for **(a)** PLA-4 and **(b)** PLA-2 based materials aged for 1 week. The onset of the cold-crystallization process is indicated by an arrow together with the corresponding temperature.

Table 7.12. Thermal properties of PLA-4 and PLA-2 based samples aged for 1 week.

	Parameters	**PLA4**	**PLA4-REX0.5**	**PLA2**	**PLA2-REX0.6**
First heating **(H1)**	$T_{g,m}$ (°C)	57.3 ±0.5	57.4 ±0.3	58.7 ±0.4	58.8 ±0.4
	T_{cc} (°C)	123 ±2	117 ±2	107 ±1	112 ±1
	ΔH_{cc} (J.g^{-1})	19 ±2	8 ±3	31 ±2	28 ±3
	$X_{c,cc}$ (%)	20 ±1	9 ±2	33 ±3	30 ±2
	T_{mp1} (°C)	151 ±1	150 ±2	161.3 ±0.8	162 ±1
	T_{mp2} (°C)	n/a	n/a	168 ±2	165 ±1
	T_{me} (°C)	157.4 ±0.3	155.8 ±0.6	172.7 ±0.6	170.9 ±0.4
	ΔH_m (J.g^{-1})	21 ±2	10 ±4	34 ±3	32 ±1
	$X_{c,m}$ (%)	22 ±2	11 ±1	36 ±4	34 ±3
	X_c (%)	2 ±1	2 ±2	3 ±2	4 ±3

n/a: not available

The midpoint T_g appeared to remain unaffected by the modification of the chain architecture through reactive extrusion, as shown in *table 7.12*. Similar results have been already reported by Pilla *et al.* [94] for PLA architecturally modified with an epoxy-based chain-extender. However, the glass transition appeared to be overlapped with enthalpy relaxation in the T_g region. This phenomenon has been extensively studied and the effects are well established [52]. Upon heating, the large change in the potential energy was attributed to the alteration of locally ordered domains to a more disordered conformational state.

Regarding PLA-4 based samples, while the onset of the cold-crystallization process shifted to slightly higher temperatures for PLA-REX samples (indicated by an arrow in *figure 7.33.a*), the maximum rate of conversion decreased with the addition of SAmfE, as indicated in *figure 7.34.a* (51.1 *vs* 46.1 %.min^{-1} for PLA4 and PLA4-REX0.5, respectively). Upon constant heating, this behaviour led to a depression (-45%) in the maximum degree of cold-crystallization achievable as shown in *figure 7.35.a*. The unusual decrease in T_{cc} with structural modifications, which is exhibited by PLA4-REX0.5 samples, is probably due to the overlapping of the cold-crystallization and melting processes, respectively.

By contrast, while the onset of the cold-crystallization process was roughly similar for PLA-2 based samples, T_{cc} shifted to higher temperatures for PLA2-REX0.6 materials. A depression in the ability to crystallize upon constant heating is apparent, as shown in *figure 7.34.b,* which tendency led to a slight decrease (-7%) in the maximum degree of cold-crystallization (*c.f. figure 7.35.b*). All above trends were mainly attributed to the increase in MW (*c.f. table 7.1*) and to the introduction of microstructural defects (*e.g.* branch points) which possibly difficult the reptation-like mobility of chains to crystallization sites [15, 92, 263, 288, 320, 338, 395].

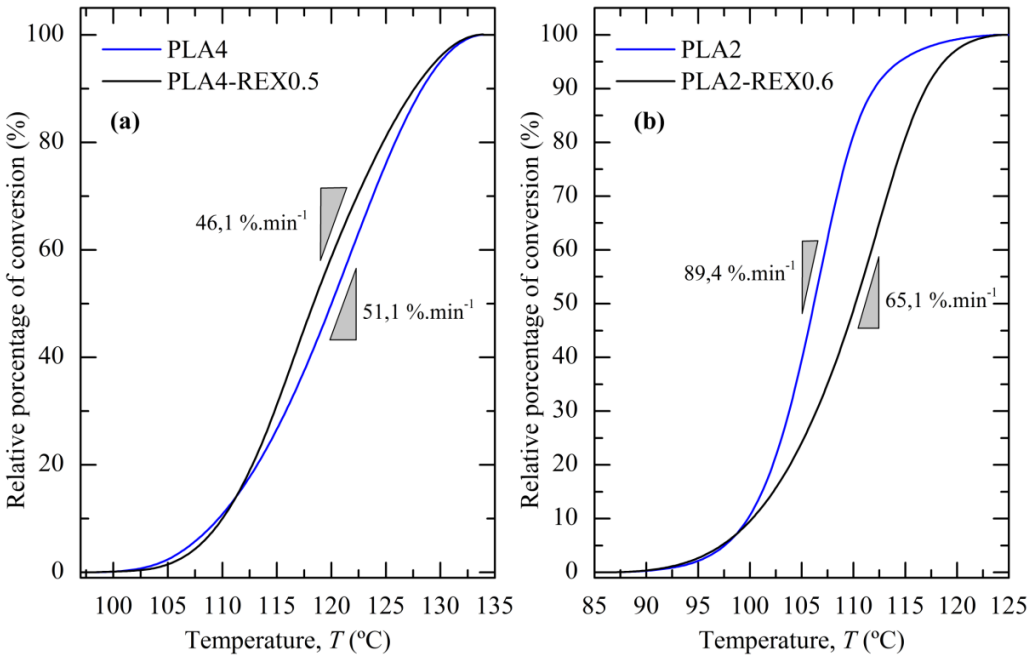

Figure 7.34. Relative percentage of conversion as a function of the temperature for **(a)** PLA-4 and **(b)** PLA-2 based samples upon heating at 10 ºC.min^{-1}. The maximum rate of conversion is indicated for each sample.

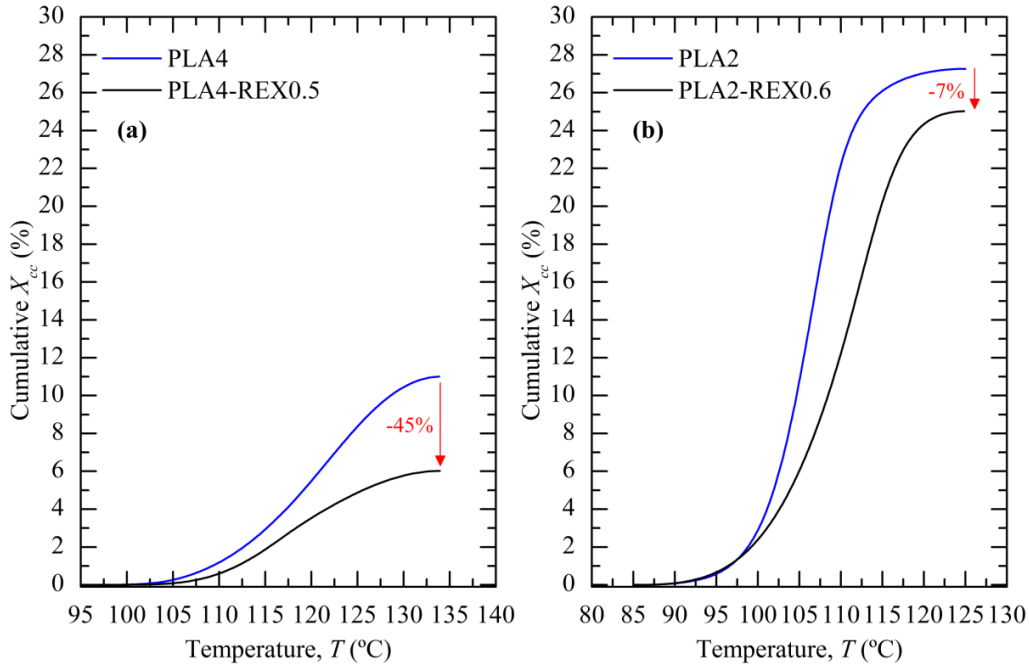

Figure 7.35. Cumulative degree of cold-crystallization as a function of the temperature for **(a)** PLA-4 and **(b)** PLA-2 based samples upon heating at 10 ºC.min^{-1}.

PLA2 samples exhibited a small exotherm (indicated by an arrow in *figure 7.33.b*) prior to the dominant melting peak, which apparently features two overlapped endotherms. With the addition of SAmfE, two peculiarities were observed in the melting transition of PLA2-REX0.6 samples. One is the remaining small exothermic peak just before the melting peak and the other is the separation of the shoulder from the dominant endotherm into two separated peaks. These changes were not observed in PLA-4 based samples due to their poor ability to crystallize upon constant heating.

Regardless of the PLA type considered, the melting temperature remained fairly insensitive to the addition of SAmfE, as shown in *table 7.12*. This tendency matches those reported by numerous authors [14, 396] who stated that T_m increases with the MW up to a critical value (M_n ≈80-100 kg.mol^{-1}) and thereafter reaches a constant value upon further increase. According to X_c values, all the samples can be considered to be amorphous due to the low crystalline fraction developed during processing. This behaviour was attributed to the slow crystallization kinetics of PLA as compared to the relative fast cooling rate applied to the melted material at the die exit [19].

According to the above, the melting transitions observed in *figure 7.33* were induced by the melting of crystals, which were crystallized during the cold-crystallization process, upon heating. However, results suggest that topological modifications reduce the maximum rate of conversions upon heating (*c.f. figure 7.34*); thus lowering the degree of cold-crystallization (*c.f. figure 7.35*). Unfortunately, this behaviour is likely to complicate the attainable maximum service range temperatures which may be achieved during secondary crystallization processes (*i.e.* thermoforming processes, annealing thermal treatments, etc) of the considered materials.

For the purpose of providing an illustrative data set to identify the origin of the double melting peaks in PLA-2 based samples, a preliminary MDSC trial was performed. To meet the heat only requirements, the heating rate was set to 2.5 ºC.min^{-1}, the period to 200 s and the amplitude to 0.8 ºC from 30 to 220 ºC. Both the reversible heat flow (Rev HF, $\Delta H_{Rev\ HF}$) and the nonreversible heat flow (Nonrev HF, $\Delta H_{norev\ HF}$) were recorded along the melting transitions (*i.e.* from 125 to 190 ºC). Recall that a step change in the reversing heat flow is related to an increase in the molecular mobility, while crystallization processes (kinetic component) appear on the non-reversing heat-flow traces, as already reported elsewhere [397, 398].

Numerous authors reported the double melting phenomenon for various polyesters (*c.f.* PET, PBT, PA, etc) [20, 92, 399]. This melting behaviour has been frequently attributed to three main mechanisms, namely, melt-recrystallization, dual lamellae population or dual crystal structure mechanism [91, 92].

The melt-recrystallization mechanism considers that the lower temperature endotherm corresponds to the melting of crystals initially present. Upon further heating, these partially melted crystals recrystallize into thicker lamellar crystals, which melt at higher temperature. The dual lamellae population mechanism considers that the double melting peaks are associated to the melting of two different lamellar perfections according to the Thomson-Gibbs equation (*c.f. chapter 2, section 2.2.1, equation 2.5*) but without recrystallization upon heating [68, 71]. Finally, the dual crystal structure mechanism results from the melting of two different crystal structures in polymorphic polymers [20, 91-94].

The modulated melting transitions of PLA2 and PLA2-REX0.6 are shown in *figure 7.36* and *7.37*. The slower heating rate enhanced the cold-crystallization of more uniform crystals upon heating; changing the double melt peak observed in *figure 7.33.b* to a monomodal melting transition (see heat flow (HF) traces). It is interesting to note that the enthalpy calculated below the melting transition recorded in the HF curve (ΔH_{HF}) equals the sum of the enthalpy calculated in the Rev HF ($\Delta H_{Rev\ HF}$) and in the Nonrev HF ($\Delta H_{norev\ HF}$), as shown in *figures 7.36* and *7.37*. That is, $\Delta H_{HF} = \Delta H_{Rev\ HF} + \Delta H_{norev\ HF}$. This result suggests that the crystallization components were properly separated from the melting processes in the range of temperature under investigation; indicating reliable results.

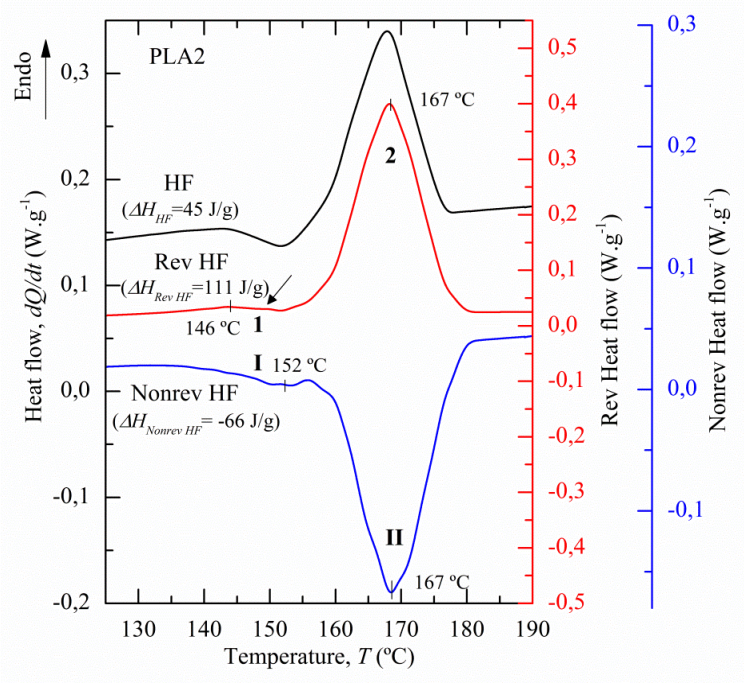

Figure 7.36. Heat flow (HF), reversing heat flow (Rev HF) and nonreversing heat flow (Nonrev HF) obtained from the first heating scan at 2.5 ºC.min^{-1}, a period of 200 s and an amplitude of 0.8 ºC for PLA2 samples.

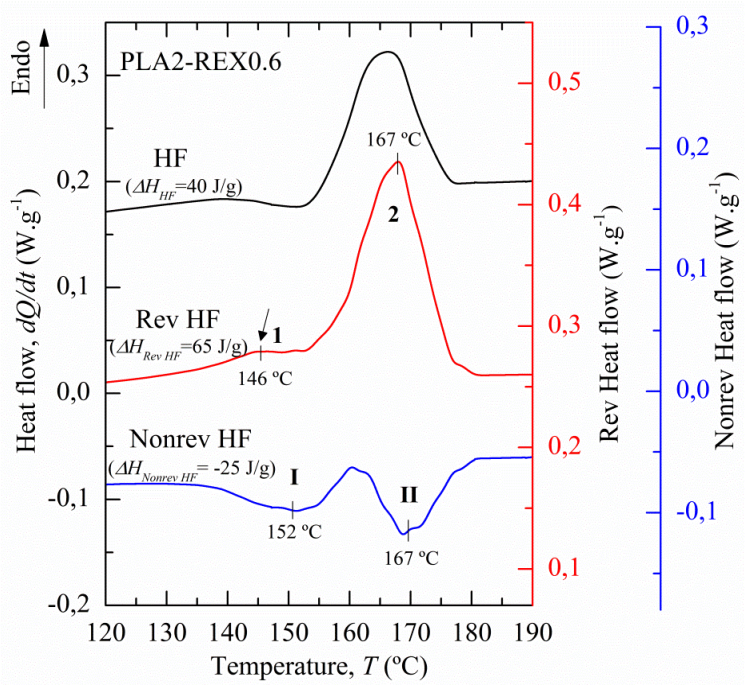

Figure 7.37. Heat flow (HF), reversing heat flow (Rev HF) and nonreversing heat flow (Nonrev HF) obtained from the first heating scan at 2.5 ºC.min^{-1}, a period of 200 s and an amplitude of 0.8 ºC for PLA2-REX0.6 samples.

On the reversing heat flow signal, two endotherms were observed around 146 ºC (marked as 1, indicated by an arrow) and 167 ºC (marked as 2), respectively, as shown in *figure 7.36* and *7.37*. On the other hand, two exothermic peaks which are centred on 152 ºC (marked as I) and 167ºC (marked as II), respectively were observed on the non reversing heat flow traces. On this basis, results suggest that the existence of two exotherms at practically the same temperature than the endotherms is an indication of two simultaneous melt-crystallization processes.

The endotherm centred on 146ºC coupled with the exotherm centred on 152 ºC indicated the fusion and the further recrystallization at slightly higher temperatures of the α'-crystals (crystallized during the cold-crystallization process upon heating) into α-crystals upon heating [332, 400]. This transition is commonly named α'-to-α transition and induced the exothermic peak prior to the main melting peak in the *HF* trace, as shown in *figure 7.33.b* (indicated by an arrow). Recall that α'-crystals are defined as a limiting disordered modification of the α form which lattice dimensions are slightly larger than α–crystals (*c.f. chapter 3, section 3.1.5.a*).

Finally, the endotherm centred on 167ºC coupled with the exotherm centred on 167 ºC indicated the simultaneous fusion and recrystallization upon heating of the α-

crystals crystallized during both the cold-crystallization process and the α'-to-α transition as reported above.

b) Thermal transitions under controlled cooling/heating ramps

Using DSC analysis, the following discussion summarized the evaluation of the effects of the topological changes on the thermal behaviour without considering the previous thermo-mechanical aspects induced by the REX-calendering stage. *Figure 7.38* and *7.39* show the controlled cooling (**C**) and second heating (**H2**) scans, respectively, for PLA-4 and PLA-2 based materials. *Table 7.13* summarizes the thermal properties determined from **C** and **H2** cycles.

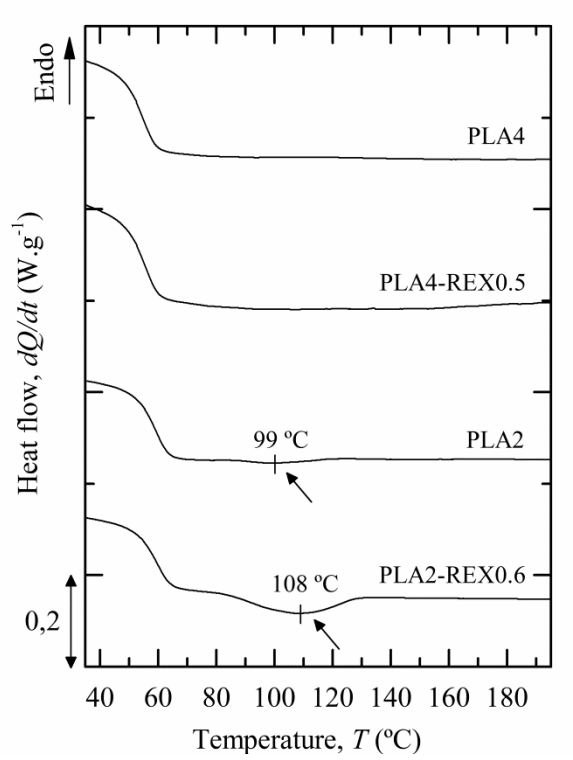

Figure 7.38. Controlled cooling scans (**C**) at 10 ºC.min^{-1} for PLA-2 and PLA-4 based samples. Arrows indicate the crystallization exotherms for PLA-2 based samples.

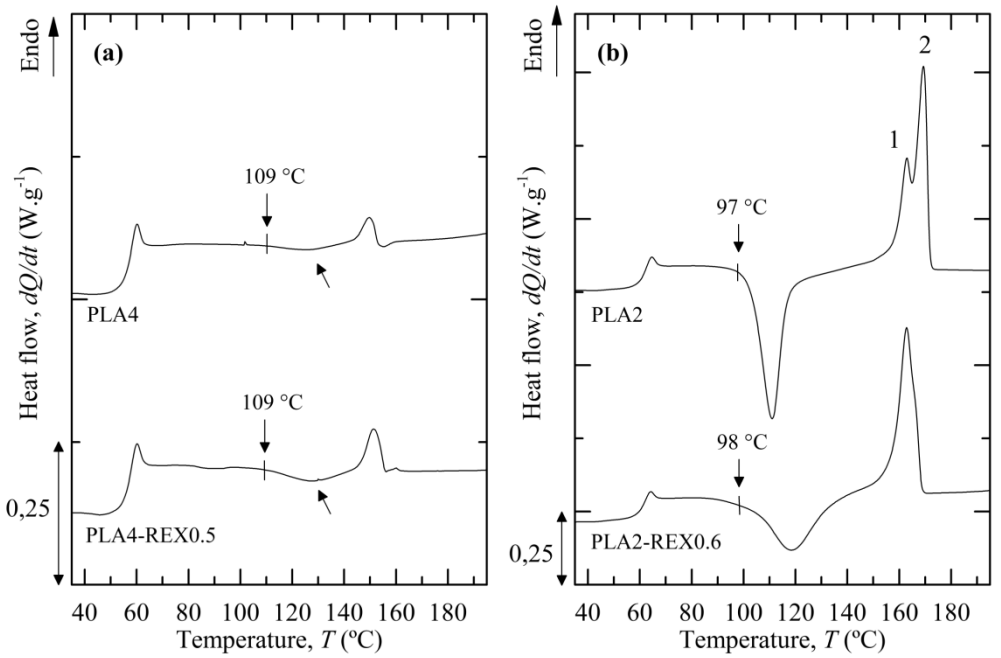

Figure 7.39. Second DSC heating scan (**H2**) at 10 ºC.min^{-1} for **(a)** PLA-4 and **(b)** PLA-2 based materials. The onset of the cold-crystallization process is indicated by an arrow together with the corresponding temperature for each sample.

Table 7.13. Thermal properties determined from the **C** and **H2** runs.

	Parameters	**PLA4**	**PLA4-REX0.5**	**PLA2**	**PLA2-REX0.6**
Cooling (C)	T_c (°C)	n/a	n/a	99.4 ±0.5	108.2 ± 0.4
	$\Delta H_{c,c}$ (J.g^{-1})	n/a	n/a	0.4 ±0.4	4 ±3
	$X_{c,c}$ (%)	n/a	n/a	0	0
Second heating (H2)	$T_{g,m}$ (°C)	56.1 ±0.5	56.3 ±0.3	60.8 ±0.5	60.6 ±0.4
	T_{cc} (°C)	126.5 ±0.3	125.3 ±0.7	111.1 ±0.5	118.5 ±0.6
	ΔH_{cc} (J.g^{-1})	2 ±1	2 ±1	33 ±3	24 ±2
	$X_{c,cc}$ (%)	2 ±1	2 ±2	35 ±3	26 ±5
	T_{mp1} (°C)	151.3 ±0.3	149.7 ±0.5	163.1 ±0.4	162.9 ±0.8
	T_{mp2} (°C)	n/a	n/a	169.4 ±2	n/a
	T_{me} (°C)	155 ±1	156.5 ±0.3	173.8 ±0.4	170.2 ±0.5
	ΔH_m (J.g^{-1})	3 ±2	2 ±1	33 ±2	27 ±4
	$X_{c,m}$ (%)	3 ±2	2 ±1	35 ±4	29 ±3
	X_c (%)	1 ±1	0	0	3 ±2

n/a: not available

According to the cooling conditions used in the present study, PLA-4 based materials did not crystallize during the controlled cooling run (**C**) (*c.f. figure 7.38*). By contrast, PLA2 samples exhibited a weak crystallization peak around 99 °C (indicated by an arrow). This difference in behaviour may be attributed to the higher stereochemical purity exhibited by PLA-2 based materials. The crystallization transition appeared to be broadened and shifted to higher temperatures (around 108 °C) for PLA2-REX0.6 samples. This behaviour can be explained by the observed raised in MW (*c.f. table 7.1*) coupled with the introduction of microstructural defects (*e.g.* branch points) which can difficult the macromolecular chain short-range transport movements needed for the crystallization process.

Upon reheating, the midpoint T_g remained insensitive to structural changes for each PLA type, as shown in *table 7.13*. This tendency matches those reported by Dorgan *et al.* [129], Korhonen *et al.* [304] and Nofar *et al.* [401] regarding LCB, star- and comb-like (4-9 arms) PLA architectures.

By considering the cold-crystallization process, similar behaviours were found as previously reported in *section 7.5.1.a*. That is, PLA4-REX0.5 samples showed an unusual decrease in T_{cc} as compared to PLA4 samples even though the onset temperature of the corresponding process was similar between both samples. This trend is probably due to the overlapping of the cold-crystallization and melting processes, respectively.

By contrast, while the onset of the cold-crystallization process was roughly similar for PLA-2 based samples, T_{cc} shifted to higher temperatures for PLA2-REX0.6 materials. A depression in the ability to cold-crystallize upon constant reheating is apparent as shown in *table 7.13*.This tendency was more pronounced for PLA-2 than PLA-4 based samples due to their larger sensitivity to crystallize upon heating. All above trends were mainly attributed to the increase in MW (*c.f. table 7.1*) and to the introduction of microstructural defects (*e.g.* branch points) which possibly difficult the reptation-like mobility of chains to crystallization sites [15, 92, 263, 288, 320, 338, 395].

PLA2 samples exhibited a well-defined double melting peak (marked as 1 and 2). By contrast, the well-defined high temperature endotherm (marked as 2 for PLA2 samples) disappeared and overlapped the high temperature tail of the low temperature endotherm (marked as 1 for PLA2 samples) for PLA2-REX0.6 samples. Consequently, T_{mp} declined with the introduction of SAmfE. This depression in T_{mp} agreed with the higher T_{cc} values found for PLA2-REX0.6 and was probably due to the increase in microstructural defects (*e.g.* branch points) which promoted the crystallization of thinner and inhomogeneous lamellar crystals according to the Thomson-Gibbs equation (*c.f. chapter 2, section 2.2.1, equation 2.5*) [68, 362].

By comparing internal mixer and REX-calendered samples, slight differences in the thermal behaviour were found. That is, REX-calendered samples exhibited slightly higher T_{cc} temperatures and a lower extend to crystallize upon reheating as compared to internal mixer samples. In addition, results suggest that REX-calendered samples exhibited slightly higher T_{mp} than their compression-moulded homologues. In the specific case of PLA2-REX0.6 sample, the melting process followed the trend as previously described in *section 6.5.2* (*c.f. chapter 6*). That is, the intensity of the low temperature shoulder (marked as 1) grew at the expense of the principal endotherm (marked as 2) and eventually overlapped the high temperature tail of the low temperature endotherm before probably disappearing for larger degrees of structural modifications (*c.f.* PLA-2+1J samples).

All above described results are in line with the previous SEC-DRI and rheological discussions (*c.f. section 7.2*). They suggest that a larger degree of degradation was developed during internal mixing preparation due to the higher thermo-mechanical exposition time (13 min) as compared to the REX-calendered samples (4.33 min). Based on the slight variations in the thermal behaviour of REX-calendered samples, it is reasonable to expect some modifications in the thermal fractionation.

7.5.2. Thermal fractionation

Following the thermal protocol described in *section 5.1.5.b* (*c.f. chapter 5*), the determination of the temperature that causes the maximum self-nucleation without annealing (T_{s1}) was carried out. Recall that since this work aimed to study the effect of the structural modifications on the chain heterogeneity of each PLA type using the SSA protocol, the initial T_{s1} of PLA-REX samples, should be similar to the T_{s1} of its linear homologues. Based on the results reported in *section 9.3.2.a* (*c.f. chapter 9*), 156 and 171 ºC were found to be the optimum self-nucleation temperatures for PLA4 and PLA2 samples, respectively.

Both extruded PLA samples exhibited slightly higher T_{s1} temperatures (> 2ºC) than internal mixer PLA "neat" samples (*c.f. chapter 6, section 6.6.1*). This observation is in line with the slight increase in T_m exhibited by these former (*c.f. section 7.5.1.b*) which results from the lower degree of degradations induced during REX-calendering processing.

Figure 7.40 compares the final melting runs after applying the SSA protocol to REX-calendered samples.

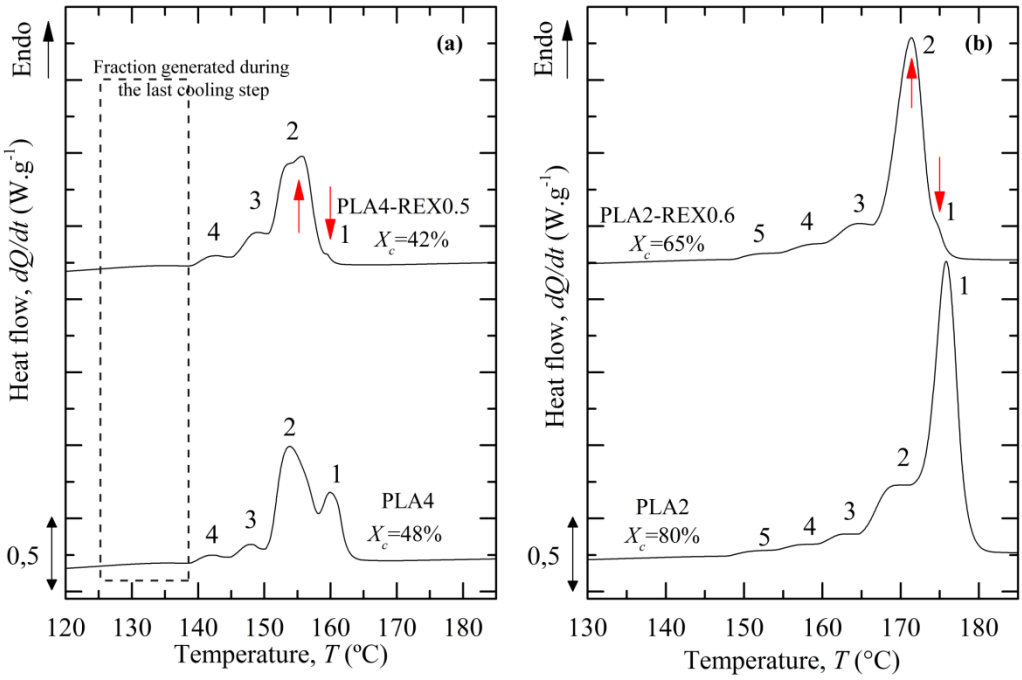

Figure 7.40. Final DSC heating scan (step **g**) at 10 ºC.min^{-1} of **(a)** PLA-4 and **(b)** PLA-2 based materials after applying the SSA thermal protocol.

The different heating scans show the effects of the accumulation of "*n*" self-nucleation and annealing steps using T_s temperatures ranging from 156 to 136 °C and from 171 to 146 °C for PLA-4 and PLA-2 based samples, respectively, with a fractionation window of 5 °C. They reflect the material that has crystallized in successive steps of SSA. Recall that 156 and 171 °C did not cause annealing because they are temperatures within domain II of PLA4 and PLA2 materials, respectively. Therefore, only 4 and 5 steps were able to produce annealing for PLA-4 and PLA-2 based materials, respectively (*c.f. chapter 5, section 5.1.5.b, table 5.1*). The final melting traces show 4 and 5 melting peaks in *figure 7.40. a* and *b*, respectively. These results corroborate those reported in *section 6.6.2* (*c.f. chapter 6*) and illustrate the capability of the SSA technique to induce thermal fractionation in PLA.

Regarding PLA-4 based samples, an additional fraction at low temperatures (*i.e.* around 132 ºC, indicated in the dashed rectangle) was revealed after thermal fractionation. This last fraction was likely to be crystallized during the last cooling run (step **f**). Even though a self-seeding temperature is probably missing in the thermal fraction of PLA-4 based samples (T_s =131 ºC), the fractionated populations exhibited in *figure 7.40.a* remained unaffected.

After thermal conditioning, the X_c depression observed for PLA-REX samples was more pronounced for PLA2-REX0.6 (-19%) than PLA4-REX0.5 (-12%) samples. Since microstructural defects (*e.g.* branch points) and MW increase inhibit crystallization process [68, 362], this trend may be attributed to the larger content of structural modifications exhibited by PLA2-REX0.6 as compared to PLA4-REX0.5 samples (*c.f. section 7.2*).

It has been well established that the SSA-DSC endotherm areas are proportional to the mass fraction of crystalline phase that are formed at each T_s [362]. Thus, all the DSC curves were integrated and the partial degree of crystallinity (referred to as partial X_c) corresponding to each melting peak was calculated. *Figure 7.41* shows the influence of the structural modifications on the evolution of the magnitude of the partial X_c for each endotherm.

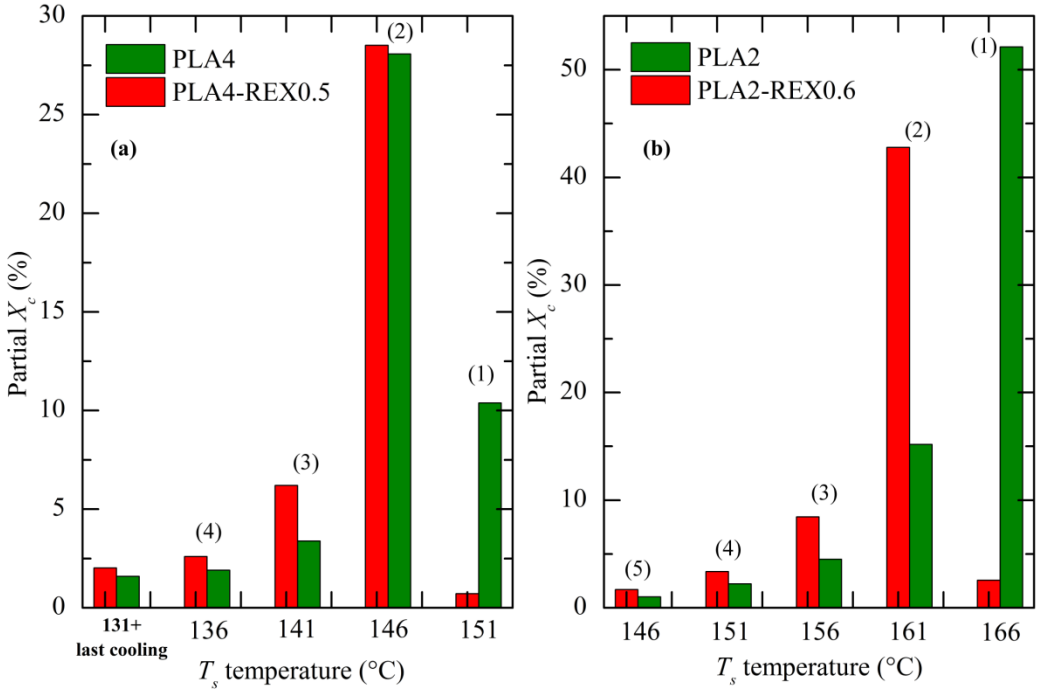

Figure 7.41. Partial degree of crystallinity developed at each T_s temperature for (**a**) PLA-4 and (**b**) PLA-2 based samples. The corresponding melting endotherm according to *figure 7.40* is indicated in brackets.

The observed differences in the distribution of chain heterogeneities between both linear PLA samples have been attributed to the influence of the random sequencing of low amounts of D-lactide unit on the crystallisable size of uninterrupted isotactic PLLA chain segments. The interested reader is referred to *section 6.6.2* (*c.f. chapter 6*) for further details.

Regarding both PLA-REX samples, similar tendencies were observed as compared to the results reported in *section 6.6.2*. That is, the development of thinner and more imperfect lamellar crystals was promoted at the expense of the thicker and more perfect fraction (marked as 1) with the addition of SAmfE, as shown in *figure 7.41*.

On the basis of the results obtained up to this point, PLA-REX samples seemed to exhibit a higher degree of structural modifications than internal mixer samples. Even though significant differences in reaction times are apparent between both processes ($t_{brabender}$=13 min, $t_{REX\text{-}calendering}$=4.33 min), this trend could be attributed to the higher local shear field coupled with the minimized thermo-oxidative degradations induced during REX-calendering processing.

7.5.3. Enthalpy relaxation kinetics

The changes in calorimetric enthalpy in the T_g region (*i.e.* enthalpy relaxation), which occur during physical aging experiments, were used to evaluate the effects of the topological modifications on the segmental relaxation behaviour of PLA-REX samples. In the current study, PLA-2 and PLA-4 based samples were aged at 30°C (T_a= T_g-30 ºC) for various aging times (from 0 min to 1 week), according to the procedure described in *section 5.1.5.c* (*c.f. chapter 5*).

Since samples are subjected to repeated aging and de-aging steps, the influence of a de-aging thermal treatment on the thermal properties is of great interest. Thus, the first heating runs (**H1**) at 10 ºC.min^{-1} for de-aged PLA and PLA-REX samples (*c.f.* thermal treatment details in *chapter 4, section 4.3*) were recorded and compared to the H1 scans of samples aged for 1 week, as shown in *figure 7.42*. Corresponding thermal properties are given in *table 7.14*.

As already reported by numerous authors [56, 241, 402], results suggest that the extent of the endothermic peak at T_g (indicated by an arrow) became less obvious for de-aged as compared to aged samples. This trend is due to a decrease in the excess enthalpy of relaxation in the T_g region. For further temperature increase, the thermal behaviour of PLA and PLA-REX samples appeared to remain fairly insensitive to the de-aging thermal treatment, as shown in *figure 7.42* and *table 7.14*.

Accordingly, this trend suggests that possible changes in the rate of segmental relaxation must be primarily attributed to the presence of the structural modifications rather than the minor variations in the thermal properties.

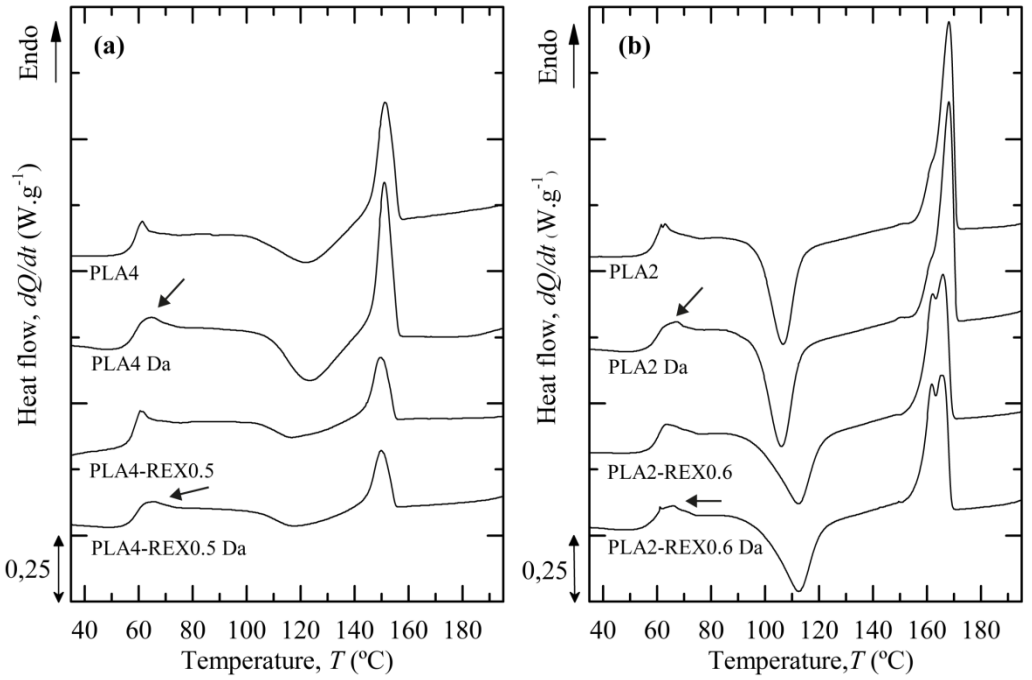

Figure 7.42. First DSC heating scan (**H1**) at 10 ºC.min^{-1} for aged and de-aged (Da) **(a)** PLA-4 and **(b)** PLA-2 based samples. Arrows indicate the absence of the typical T_g overshoot for de-aged samples.

Table 7.14. Thermal properties of de-aged and aged PLA-4 and PLA-2 based samples

Sample nomenclature	$T_{g,m}$ (ºC)	T_{cc} (ºC)	ΔH_{cc} (J.g^{-1})	T_{mp1} (ºC)	T_{mp2} (ºC)	ΔH_m (J.g^{-1})	X_c (%)
			De-aged				
PLA4 Da	57.2 ±0.4	123 ±2	21 ±3	151 ±1	n/a	22 ±2	1 ±1
PLA4-REX0.5 Da	58.1 ±0.3	117 ±1	9 ±2	150 ±2	n/a	10 ±1	1 ±1
PLA2 Da	58.8 ±0.5	106 ±1	31 ±2	161.3 ±0.8	168 ±2	34 ±3	3 ±2
PLA2-REX0.6 Da	57.9 ±0.6	112 ±2	28 ±1	162 ±1	165 ±1	32 ±3	3 ±3
			Physical aged				
PLA4	57.3 ±0.5	123 ±2	19 ±2	151 ±1	n/a	21 ±2	2 ±1
PLA4-REX0.5	57.4 ±0.3	117 ±2	8 ±3	150 ±2	n/a	10 ±4	2 ±2
PLA2	58.7 ±0.4	107 ±1	31 ±2	161 ±1	168 ±2	34 ±3	3 ±2
PLA2-REX0.6	58.8 ±0.4	112 ±1	28 ±3	162 ±2	165 ±1	32 ±1	4 ±3

n/a: not available

Figure 7.43 shows the heating scans after isothermal aging at 30°C (T_a= T_g-30 ºC) and at the indicated t_a for PLA-4 and PLA-2 based samples.

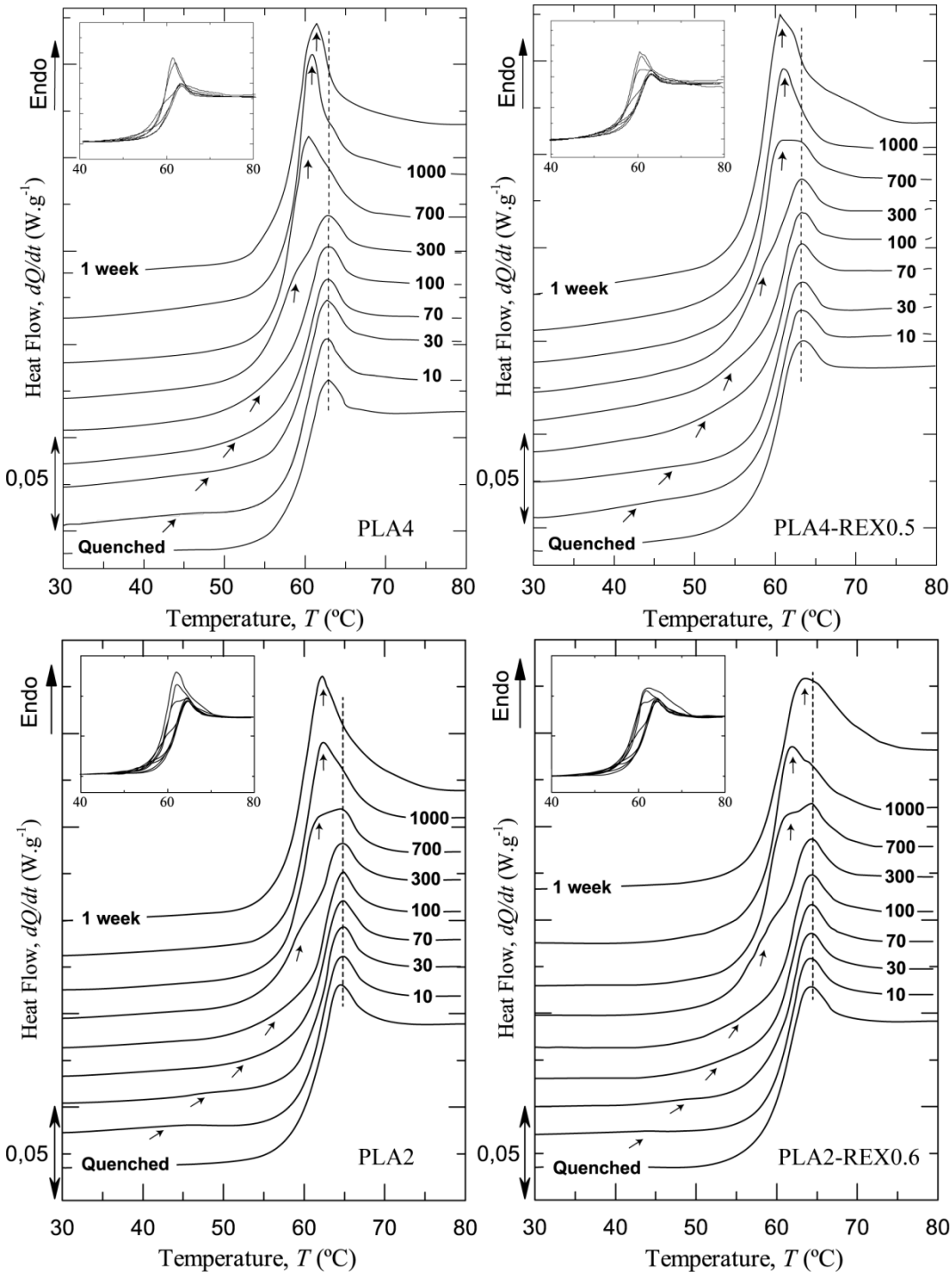

Figure 7.43. DSC heating scans at 10 ºC.min^{-1} of aged PLA-4 and PLA-2 based samples at T_a= T_g-30 ºC in the T_g region at the indicated aging times, t_a (in minutes). Inserts display an overlay of the same curves to justify the correct superimposition of

the individual heating runs below and above T_g. Arrows indicate the evolution of the sub-T_g endothermic maxima.

Initially, samples were analyzed for a possible thermal degradation by carefully studying the DSC trace in the glass transition region (from 40 to 80 ºC) due to the repeated isothermal steps (*c.f. chapter 5, section 5.1.5.c*). All DSC heating scans were well superimposed in the glassy and in the rubbery regions as shown in the inserts of *figure 7.43*. This tendency suggests that samples remained unaffected by degradation or irreversible changes and that they attained a reproducible state each time they were heated above T_g.

Although no isothermal aging step was performed on quenched samples, the glass transition appeared to be overlapped with enthalpy relaxation (overshoot). Similar behaviour has been observed by Pan *et al.* [27] for PLLA and PDLA samples. This is possibly due to the physical aging of the amorphous phase upon heating to T_g. Besides the constant overshoot above T_g, an additional endothermic signal (indicated by an arrow) was revealed below T_g for isothermally aged samples. The intensity of this additional endotherm increased and shifted to higher temperature with increasing t_a. For samples aged up to 700 minutes, an overlapped shoulder in the T_g transition appeared which merged with the constant overshoot above T_g when t_a further increased.

It is well known that a non-equilibrium amorphous state is generated when samples are quenched from the melt. As a result of the annealing temperature below but close to T_g, these thermodynamically unstable glassy polymers tend towards an equilibrium state through slow segmental rearrangements over time. These molecular motions lead to volume relaxation and to a decrease in v_f , as experimentally verified by Cowie and coworkers [51]. On this basis, the above behaviour was associated with the loss of free volume which led to a decrease in segmental mobility of PLA chains in the glassy state during physical aging, as already reported by Kwon *et al.* [67] for PLA films with various D-lactide contents. While Pan *et al.* [27] and Kwon *et al.* [67] report an endothermic peak of enthalpy relaxation at the high-temperature side of T_g, de-aging process occurred below T_g in the present study. This trend is in line with the theory proposed by Struik [403] stating that when an amorphous polymer phase is aged at a *sub-*T_g temperature (T_a<<T_g-20 ºC), de-aging process occurs below T_g (*c.f. chapter 2, section 2.1.1*)

Based on the DSC heating runs reported in *figure 7.43*, δ_H was determined for each sample (*as detailed in chapter 5, section 5.1.5.c, figure 5.7*) and plotted as a function of t_a, as shown in *figure 7.44*. The insert includes also the measurements of samples which were aged for 6 months. Since all samples were subjected to a similar thermal protocol before revealing the aging state (*c.f. chapter 5, section 5.1.5.c*), the

dependence of the relaxation time on the previous history was removed. Consequently, the consideration of the fictive temperature was not necessary and the Cowie-Fergusson model (referred to as CF, *c.f. chapter 2, section 2.1.2, equation 2.3*) was considered sufficiently flexible to study the isothermal enthalpy relaxation behaviours as a function of t_a. The three adjustable parameters (*i.e.* $\delta_{H\infty}, \tau_0$ and β) were determined by using a non-linear least-squares curve-fitting algorithm and results are compiled in *table 7.15*.

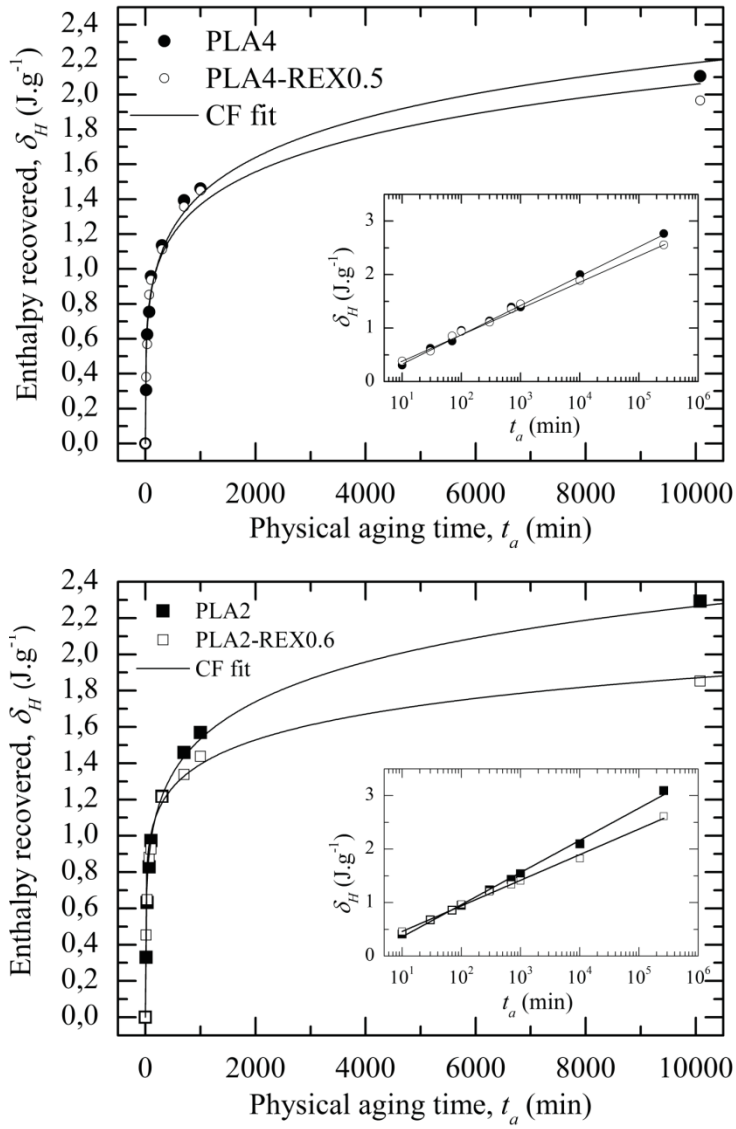

Figure 7.44. δ_H at 30 ºC as a function of t_a for PLA-4 and PLA-2 based samples. The Cowie-Ferguson (CF) model is fitted for each sample (solid line) and the insert shows the linear correlation between δ_H and log (t_a). Inserts include also the measurements of samples aged for 6 months.

Table 7.15. Cowie-Ferguson model parameters and enthalpy relation kinetics.

Sample nomenclature	PLA-4	PLA4-REX0.5	PLA-2	PLA2-REX0.6
$\delta_{H\infty}$ ($J.g^{-1}$)*	2.8 ±0.3	2.6 ±0.4	3.1 ±0.2	2.6 ±0.1
τ_0 (10^3) (min)	14 ±4	107 ±30	18 ±3	110 ±20
β	0.26 ±0.02	0.22 ±0.02	0.26 ±0.01	0.17 ±0.01
β_H ($J.g^{-1}$ per decade)	0.55 ±0.02	0.51 ±0.02	0.56 ±0.01	0.47 ±0.01
R^2 (δ_H *vs.* log(t_a))	0.993	0.993	0.999	0.995

* $\delta_{H\infty}$ was determined by DSC tests of samples aged for 6 months at room temperature

A linear relationship was established for the enthalpy recovered as a function of log (t_a). This observation indicates a proper fitting of the experimental data, as already reported elsewhere [5, 13, 32]. Based on this result, the rate of physical aging, β_H, (*c.f. chapter 2, section 2.1.2, equation 2.1*) was estimated and results are summarized in *table 7.15*.

The effects of the chain architecture modifications on δ_H over t_a can be seen best when comparing PLA2 and PLA2-REX0.6 samples as shown in *figure 7.44*. In the case of PLA-4 based material, these effects were very small since difference between both materials was minimal.

δ_H increased rapidly when t_a increased to 700-1000 minutes as shown in *figure 7.44*. As t_a further increased, δ_H tended to reach a plateau which value was lowered for PLA-REX samples as compared to their linear homologues.

According to *table 7.15*, both linear PLA samples exhibited a similar rate of enthalpy relaxation, β_H. This rate appeared to decrease with increasing the content of modified PLA chains ($\beta_{H\ PLA4} > \beta_{H\ PLA4\text{-}REX0.5} > \beta_{H\ PLA2\text{-}REX0.6}$). Since the experimental parameters were fixed between samples, the lower β_H could be attributed to a slower relaxation rate of PLA chains which mainly arise from both the increase in MW (*c.f. table 7.1*) and the presence of branch points. PLA-REX samples exhibited a higher entanglement density than PLA samples according to *table 7.6*. In the timeframe of the experiments, the increasing number of entanglement points, which act as "*cross link points*", may slow down disentanglement and unknotting process rates of the chains. The short-range molecular motions, which drive the thermodynamic variables closer to their equilibrium values, are likely to be inhibited; thus decreasing the rate of enthalpy relaxation, β_H. This β_H slow-down broadened the distribution of relaxation time (lower β) and increased τ_0 with increasing the content of modified PLA chains.

7.5.4. DMTA analysis

For the purpose to evaluate the effects of the topological modifications on the dynamic mechanical properties of PLA and PLA-REX samples, a DMTA analysis was carried out using a single cantilever bending mode. Both de-aged and aged samples (*c.f. chapter 4, section 4.3*) were investigated in order to determine if aging affects the temperature dependence of the thermo-mechanical viscoelastic functions. This information is helpful in order to evaluate the material handling possibilities immediately after extrusion and/or after being stored for 1 week at room temperature. The storage modulus, *E'*, and the damping or loss factor, tan δ=*E''/E',* traces of de-aged and aged samples, which were recorded from 30 to 120 ºC in the machine direction (MD), are shown in *figure 7.45*. On the other hand, loss modulus (*E''*) traces are shown in appendix (*c.f. chapter 9, section 9.3.2.b*). *Table 7.16* summarized the following results:

- The storage modulus at 30 ºC, $E'_{(30ºC)}$, and at 60 ºC, $E'_{(60ºC)}$, respectively
- The glass transition temperature, T_g. It was determined as the point where tan δ (referred to as T_g (tan δ)) and *E''* (referred to as T_g (*E''*)) reached a maximum, respectively.
- The drop percentage in *E'* between 30 and 60 ºC. It was calculated according to *equation 7.9*

$$Drop\ (\%) = \frac{E'_{(30°C)} - E'_{(60°C)}}{E'_{(30°C)}} * 100 \qquad \textbf{(7.9)}$$

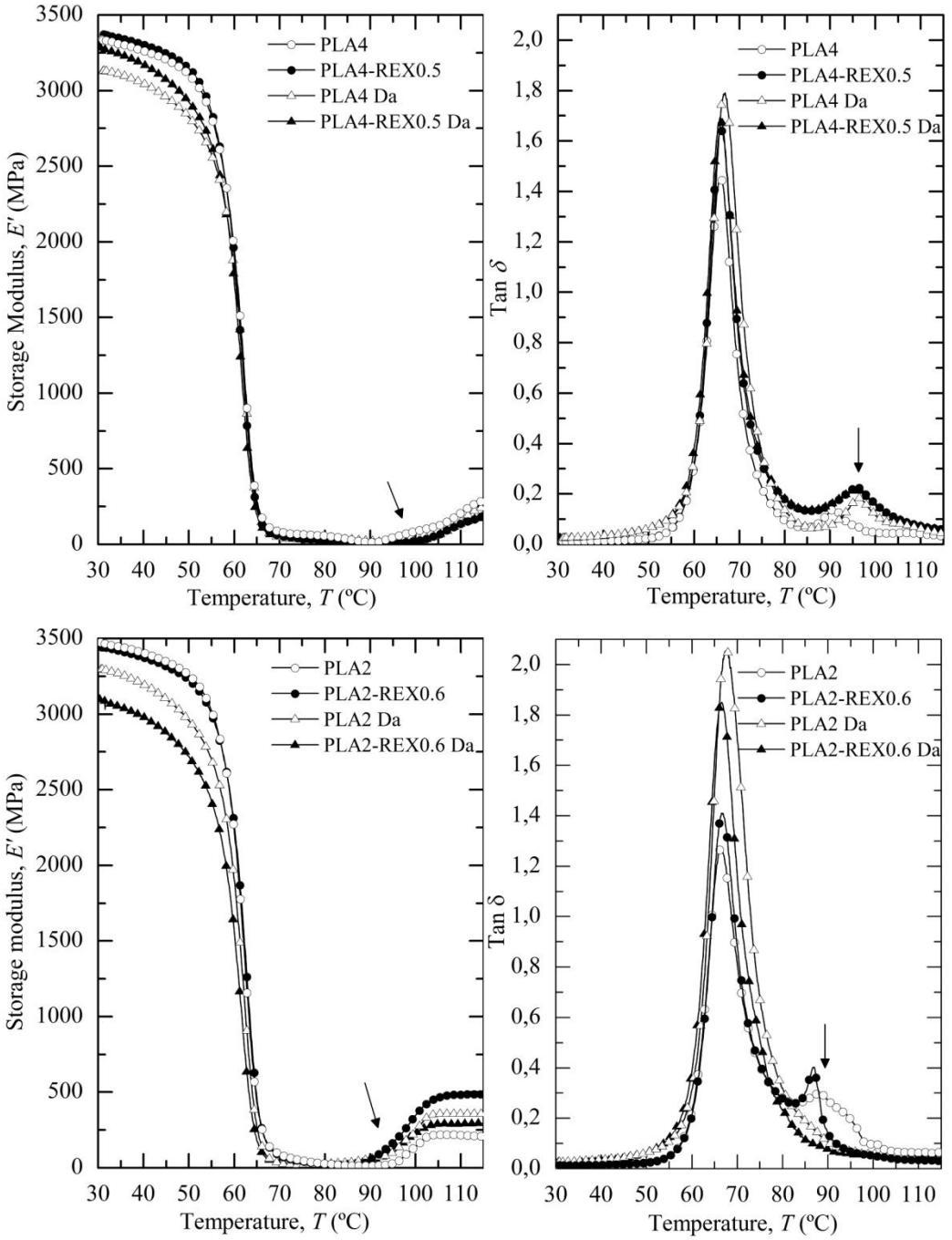

Figure 7.45. Storage modulus and tan δ traces for de-aged and aged PLA-4 and PLA-2 based materials tested in MD at 2 °C.min^{-1}.

Table 7.16. DMTA parameters for de-aged and aged materials tested in MD at 2°C.min^{-1}.

Sample nomenclature	$E'_{(30°C)}$ (GPa)	$E'_{(60°C)}$ (GPa)	***Drop*** (%)	T_g ***(E'')*** (°C)	T_g ***(tan δ)*** (°C)
		De-aged			
PLA4 Da	3.3 ±0.2	1.7 ±0.1	47.3 ±0.2	63 ±4	65 ±2
PLA4-REX0.5 Da	3.1 ±0.3	1.6 ±0.3	48.7 ±0.2	60.9 ±0.8	65.5 ±0.3
PLA2 Da	3.1 ±0.3	1.6 ±0.4	47.2 ±0.3	61.6 ±0.7	67.2 ±0.5
PLA2-REX0.6 Da	3.2 ±0.1	1.8 ±0.3	44.8 ±0.2	61.9 ±0.7	66.8 ±0.4
		Physical aged			
PLA4	3.4 ±0.1	1.8 ±0.2	47.1 ±0.1	61.3 ±0.9	65 ±2
PLA4-REX0.5	3.4 ±0.1	2.0 ±0.1	41.3 ±0.1	61.8 ±0.2	65 ±1
PLA2	3.4 ±0.2	2.3 ±0.1	30.5 ±0.1	62.1 ±0.8	66 ±1
PLA2-REX0.6	3.5 ±0.1	2.3 ±0.1	34.7 ±0.1	62.4 ±0.4	66 ±1

In the glassy range, results suggest that *E'* values slightly increased with aging. These tendencies could be attributed to a decrease in the ability to dissipate energy through molecular motions due to the decreasing amount of free volume as aging proceeds. However, the differences in *E'* values between samples for a given thermal history must be viewed with a degree of scepticism given the degree of incertitude provided by the algorithm that is used in order to calculate the elastic modulus, *E* (*c.f. equation 7.10*) [404].

$$E = \frac{K_s}{F}\frac{L^3}{24I}\left[1 + \frac{24}{5}.(1+\nu).\left(\frac{t}{L}\right)^2\right] \quad \textbf{(7.10)}$$

With

$$I = \frac{wt^3}{12} \quad \textbf{(7.11)}$$

Where K_s is the measured stiffness, *F* the load, *L* the sample length (fixed to 17.5 mm in single cantilever flexure mode), *I* the sample moment of inertia, ν the Poisson's ratio, *w* the sample width and *t* the sample thickness.

Experimental both between- and within-sample errors are unavoidable, independently of the operator's skilfulness. The main source of experimental within-sample errors results from slight variations in the determination of the sample dimensions. Thus, a statistical analysis was performed to evaluate the propagation of the error measurements in the calculated *E* values.

By considering the general function $q = k.x^{\alpha}.y^{\beta}$ with an error of $x \pm \delta x$ and $y \pm \delta y$, the propagation of the error is calculated using the following expression:

$$\frac{\delta q}{|z|} \approx \alpha \frac{\delta x}{|x|} + \beta \frac{\delta y}{|y|} \qquad \textbf{(7.12)}$$

In the current study, x equals w and $\alpha = -1$. Correspondingly, y equals t and $\beta = -3$. Therefore, the propagation of the error measurements in the calculated E values can be estimated using *equation 7.13*.

$$\left|\frac{\delta E}{E}\right| \approx \left|-\frac{\delta w}{w}\right| + \left|-3\frac{\delta t}{t}\right| \qquad \textbf{(7.13)}$$

Results suggest the following:

- A relative error of **1%** in the determination of the **sample width, *w*,** causes a percentage of error of **1%** in the final calculated E values.
- A relative error of **1%** in the determination of the **sample thickness, *t*,** causes a percentage of error of **3%** in the final calculated E values.
- A relative error of **1%** in the determination of both the **sample thickness** and **sample thickness** causes a percentage of error of **4%** in the final calculated E values.

According to the above results, small variations in the sample thickness, which can be the limiting factor for calendered films featuring low thickness, could significantly influence the calculated E values. In the current study, the largest relative error in the determination of the sample width and thickness was established to 3 and 1%, respectively. Consequently, it can be assumed that E' values at 30 ºC remained insensitive to both the formation of non-uniform branched structures for a given thermal history.

In the glassy region (between 30 and 55 ºC), de-aged samples seemed to exhibit a more pronounced decrease in E' with increasing the temperature as compared to aged samples. This tendency could be attributed to the increased chain mobility which results from the enhancement of the amount of free volume.

In the T_g region, samples experienced a drastic decrease in E' values which drop between 30 and 60 ºC appeared to be slightly reduced for aged samples. The temperatures, which correspond to the tan δ and/or E'' peaks (referred to as T_g), remained fairly insensitive to both the topological changes and the thermal history, according to *table 7.16*. These results agree well with the previous DSC data (*c.f. table 7.14*).

Nevertheless, the full width at half maximum of both tan δ and E'' peaks decreased with aging as an effect of the narrower distribution of relaxation times as aging proceeds. These tendencies could be attributed to a decrease in the ability to dissipate energy through molecular motions due to the decreasing amount of free volume with aging. In addition, a decrease in the molecular mobility is reflected in the decreasing height of the tan δ peak; suggesting a depression of the damping properties. Regardless of the PLA type, results suggest that de-aged linear PLA samples exhibited slightly larger damping properties than de-aged PLA-REX samples. By contrast, a reversed trend was observed for samples aged for 1 week. The slight decrease in the rate of physical aging exhibited by PLA-REX samples (*c.f. section 7.5.3*) might be a possible explanation. That is, the increase in MW (*c.f. table 7.1*) coupled with the formation of non-uniform branched structures decrease the rate of segmental relaxation over time, thus leading to a remaining larger molecular mobility after being aged for 1 week (and thus larger damping properties).

No significant differences were apparent between de-aged and aged PLA and PLA-REX samples above 65 ºC, as shown in *figure 7.45*. An increase in E' values (indicated by an arrow) and an additional peak in the tan δ curves (indicated by an arrow) were observed with further temperature increase. While the former was attributed to the cold-crystallization process occurring during heating, the latter might be attributed to an increase in the molecular mobility due to the short-range transport movements of chains needed for the crystallization process. In addition, results suggest that both processes shifted to higher temperatures for PLA-4 based samples as compared to PLA-2 ones. This behaviour can be explained by the amount of D-lactide units (actuating as microstructural defects) which were randomly sequenced in the main polymeric chain during the ROP process. Higher the D-lactide content, larger is the concentration of "defects" or "disruption" in the PLLA crystal arrangement; thus decreasing the rate of crystallization. All above observations are in line with those reported by Pan *et al.* [27] for de-aged and aged PLLA samples.

To conclude, caution must be exercised in interpreting DMTA results above T_g. In the current study, the drastic loss of structural rigidity above T_g of all the samples (resulting from their amorphous state) induced slight variations in the sample width throughout testing. Since the calculated parameters (*i.e.* E', E'') assume that the sample behaves in a linearly elastic manner, these changes are likely to yield discrepancies in the observed trends at high temperatures.

7.6. Mechanical characterization: tensile properties

The direction of the molecular orientation is of particular importance when the mechanical properties are evaluated. According to the processing conditions detailed in *section 4.2* (*c.f. chapter 4*), the calendering stage might have induced polymer chain orientation during sheet manufacturing. Consequently, a preliminary evaluation of the mechanical anisotropy degree, *R*, in MD and TD was conducted using DMTA analysis in tensile mode at 30 °C and at multiple frequencies of 1, 5, 10, 15, 20 and 30 Hz (*c.f. chapter 5, section 5.1.6*). For the purpose to correlate the dynamic mechanical properties with the tensile behaviour in the low strain region, *equation 7.14* was used to convert the frequency of the DMTA measurements to an apparent strain rate, $\dot{\varepsilon}^{0\,UT}$. The founding principles of *equation 7.12* have been reported by Xiao *et al.* [405] and subsequently used by Al-Jabareen [208]. *Table 7.17* summarizes the *R*-ratios results calculated using *equation 5.10* (*c.f. chapter 5, section 5.1.6*).

$$\dot{\varepsilon}^{0\,UT} \approx 4.f^{DMTA}.\varepsilon^{DMTA}_{peak-to-peak} \quad \textbf{(7.14)}$$

Where f^{DMTA} is the frequency of the DMTA measurements and $\varepsilon^{DMTA}_{peak-to-peak}$ is the peak-to-peak amplitude of the oscillation strain (fixed to 0.1% in the current study).

Table 7.17. Anisotropy degree (*R*) at 30 °C for different strain rates.

Frequency DMTA (Hz)	**strain rate** (s^{-1})	**PLA4**	**PLA4-REX0.5**	**PLA2**	**PLA2-REX0.6**
1	0.004	1.01 ±0.02	1.0 ±0.2	1.01 ±0.01	1.04 ±0.08
5	0.02	1.01 ±0.02	1.0 ±0.2	1.01 ±0.01	1.04 ±0.08
10	0.04	1.01 ±0.02	1.0 ±0.2	1.01 ±0.01	1.04 ±0.08
15	0.06	1.01 ±0.02	1.0 ±0.2	1.02 ±0.01	1.04 ±0.08
20	0.08	1.01 ±0.02	1.0 ±0.2	1.01 ±0.01	1.04 ±0.08
30	0.12	1.0 ±0.1	1.0 ±0.2	1.0 ±0.2	1.0 ±0.2

Results suggest that PLA and PLA-REX samples featured an isotropic behaviour, which one remained independent on the deformation rate. During processing, the calendering stage did not induce polymer chain orientation probably due to the low rotation speed of the chill roll (1.25 rpm, *c.f. chapter 4, section 4.2*). Consequently, the following tensile and fracture characterizations were only performed in MD.

Figure 7.46 shows the typical tensile engineering stress-strain curves of de-aged and aged PLA and PLA-REX samples tested in MD at 10 $mm.min^{-1}$. At first glance, results suggest that the mechanical behaviour of both PLA and PLA-REX samples were significantly dependent on the previous thermal history. De-aged samples behaved in a ductile manner while aged samples featured a brittle behaviour.

Regarding aged samples, it should be noted that both materials presented a local maximum in the engineering stress which may be associated to a yield point. However, the formation of crazes prevented the propagation of a stable neck, giving rise to a premature brittle fracture. *Table 7.18* summarizes the mechanical parameters of de-aged and aged PLA and PLA-REX samples.

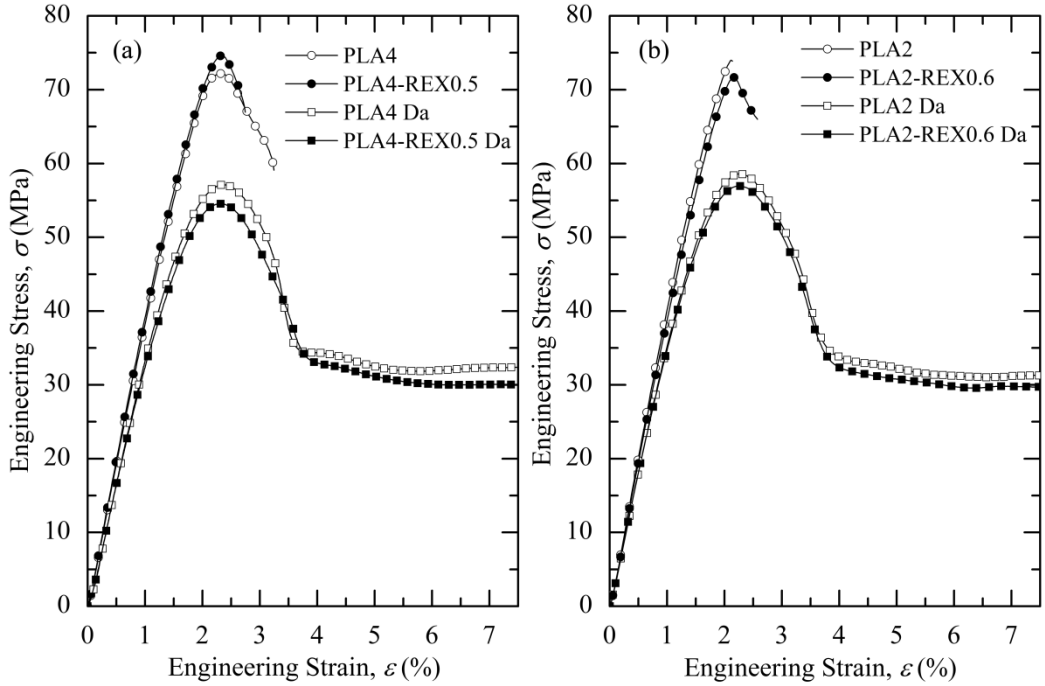

Figure 7.46. Typical tensile engineering stress-strain curves for (**a**) PLA-4 and (**b**) PLA-2 based materials at 10 mm.min^{-1}.

Table 7.18. Uniaxial tensile parameters at 10 mm.min^{-1}.

Sample nomenclature	E (GPa)	σ_y (MPa)	ε_y (%)	ε_b (%)	X_c [a] (%)
		De-aged			
PLA4 Da	3.4 ±0.1	57 ±2	2.44 ±0.09	147 ±15	2 ±1
PLA4-REX0.5 Da	3.5 ±0.1	54.4 ±0.8	2.29 ±0.05	139 ±7	3 ±3
PLA2 Da	3.2 ±0.2	58.7 ±0.5	2.29 ±0.02	165 ±10	16 ±2
PLA2-REX0.6 Da	3.3 ±0.1	57.6 ±0.8	2.26 ±0.04	165 ±5	12 ±1
		Physical aged			
PLA4	3.4 ±0.1	72 ±1	2.30 ±0.02	2.9 ±0.3	n/a
PLA4-REX0.5	3.4 ±0.1	73 ±3	2.2 ±0.2	2.78 ±0.04	n/a
PLA2	3.5 ±0.1	74 ±2	2.2 ±0.1	2.2 ±0.1	n/a
PLA2-REX0.6	3.3 ±0.1	73 ±1	2.18 ±0.03	2.5 ±0.1	n/a

[a] The tested specimens were cut from the necked zone of tensile samples stretched at 100 % of their initial length. X_c values were determined from the first DSC heating runs at 10 ºC.min^{-1} and repeated three times for each material. Corresponding plots are shown in appendix (*c.f. chapter 9, section 9.3.2.c*).
n/a: not available

De-aged samples showed the typical behaviour of ductile polymers with stable neck propagation up to < 100 % of their initial length owing to the cold drawing process. Results suggest that neither the stereochemical purity nor the topological changes appeared to affect the tensile behaviour within the experimental error. These tendencies match well those reported by numerous authors [94, 128, 316, 317, 406]. A possible explanation might be that the larger v_f amount, which is induced by the thermal treatment, promote more irregular and more free polymer chain conformations. These higher disordered chain arrangements might have induced a larger proportion of twisted chains possibly leading to a similar average dynamic environment of the entangled polymer coils between de-aged PLA and PLA-REX materials. Similar polymer coils and segment mobility may have been present, leading to analogous mechanical properties for both materials upon loading.

Nevertheless, significant differences may be appreciated if the stretched region of each sample was considered. After loading, although stretched PLA-4 based samples remained transparent, the whitening of the stretched region was less pronounced for PLA2-REX0.6 than PLA2 samples, as shown in *figure 7.47*. Similar to PET polymer, this whitening is usually attributed to the strain-induced crystallization effect. However, stretching of the PLA polymer does not induce a stable crystal formation, as already reported by Stoclet *et al.* [407] and Velazquez-Infante *et al.* [408]. Upon loading, a mesomorphic phase is generated whose conformation and dimensional parameters are close to those of stable crystals but without regular spacing.

An additional heating step is necessary to bring enough energy to this metastable crystal form to transform into a stable crystal one with a lowered energetical conformation as shown elsewhere [345]. According to the degree of crystallinity obtained after heating the stretched samples up to 200 ºC (*c.f. table 7.18*), results suggest that the ability to generate a crystalline state was reduced for PLA2-REX0.6 samples. This decrease in the ability to "crystallize" upon stretching could be attributed to the formation of microstructural defects (*e.g.* branch points) with the addition of SAmfE.

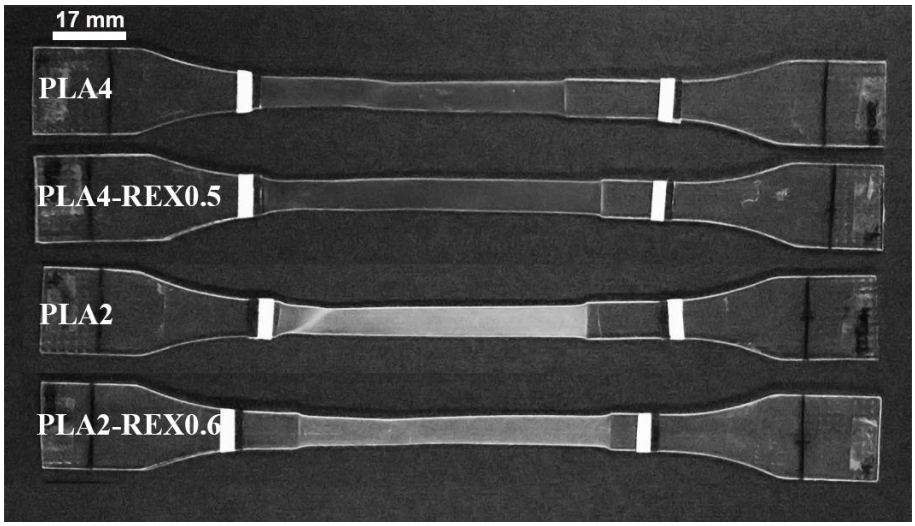

Figure 7.47. Visual aspect of the necked region of all de-aged samples stretched at 100 % of their initial length.

As expected, the above behaviour changed significantly when aged samples were considered. After testing, a visual inspection of aged samples (*c.f. figures 7.48* and *7.49*) revealed that both PLA samples exhibited long crazes. This scenario changed substantially when PLA-REX samples were considered. The stress-whitened zone was confined in the region surrounding only the fractured zone. A more detailed inspection of the fractured region revealed a larger proportion of shorter crazes, which became thinner and better defined. The irregularities present in the molecular pattern (*e.g.* branch points) coupled with a higher entangling knots density (*c.f. table 7.6*) might have stopped the growth of long crazing planes and promoted the formation of various shorter ones under tensile loading [192, 195].

With aging, changes, which have been observed in the mechanical behaviour, can be attributed to a significant reduction of the ability to dissipate energy through molecular motions. Since the molecular mobility was reduced, E and σ_y values increased and ε_y drastically decreased (ductile-brittle transition) under tensile loading [66, 241]. Similar behaviour has been reported regarding numerous glassy polymers (PC, PET, etc) which were aged below their respective T_g [56, 66, 409].

Results suggest that neither the stereochemical purity nor the topological changes appears to affect the tensile behaviour of aged samples within the experimental error, as shown in *table 7.18*.

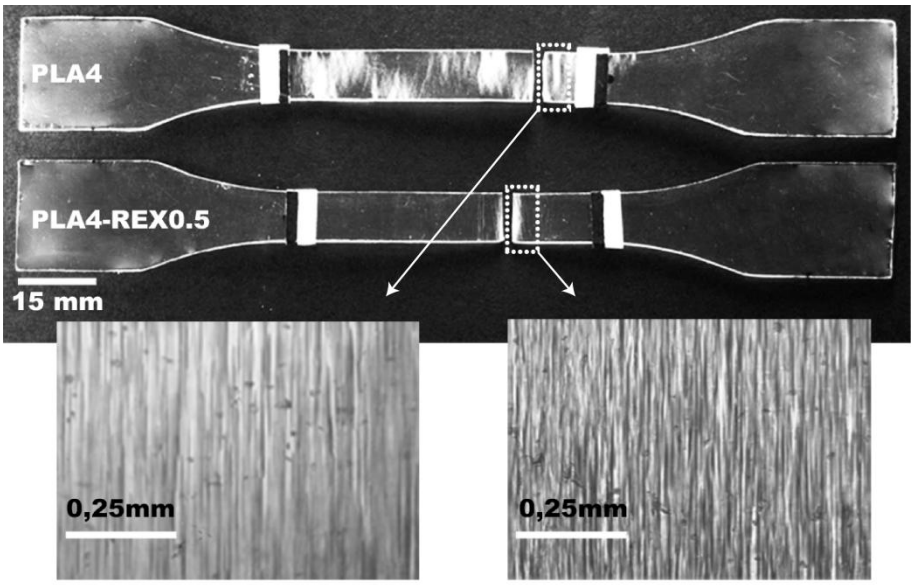

Figure 7.48. Light macrophotographs of aged PLA4 and PLA4-REX0.5 samples after testing at 10 mm.min^{-1}. Micrographs were taken from the surrounding fractured part of each sample.

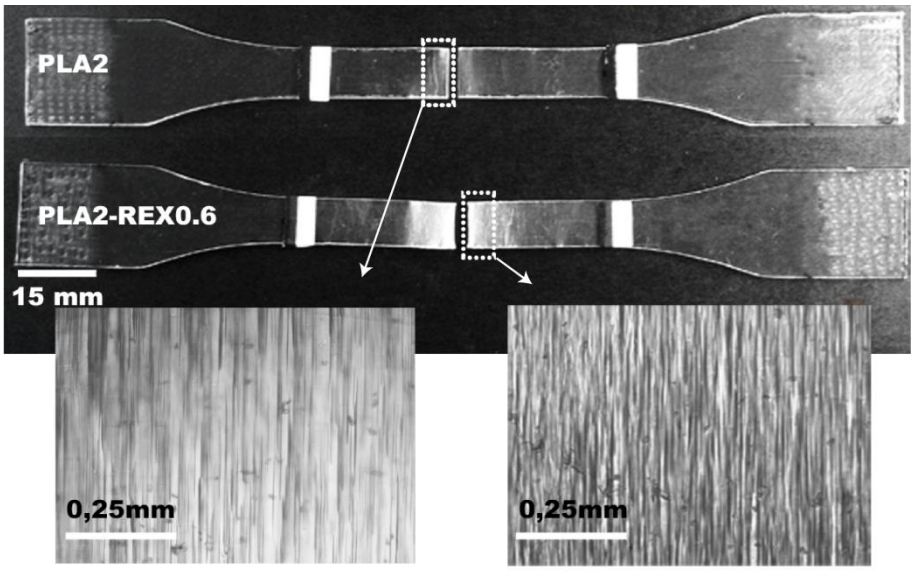

Figure 7.49. Light macrophotographs of aged PLA2 and PLA2-REX0.6 samples after testing at 10 mm.min^{-1}. Micrographs were taken from the surrounding fractured part of each sample.

According to Grijpma *et al.* [217] and Penning *et al.* [124] , C_∞ and ν_e parameters are important contributors to the mode of fracture for amorphous polymers. While high C_∞ values correspond to stiff polymer chains, loosely entangled and which exhibit a brittle behaviour, lower C_∞ values promote ductile behaviours. Under tensile stress, this statement agrees well with the characteristics network parameters of brittle isotactic PS (C_∞= 13.9, ν_e= 0.036 mmol.cm^{-3} (25°C)) and those of ductile PE (C_∞= 5.7, ν_e= 0.615 mmol.cm^{-3} (25°C)) [118].

In the present study, although C_∞ and ν_e decreased and increased, respectively, with the content of modified PLA chains (*c.f. table 7.6*), the mechanical behaviour of aged PLA-REX samples remained brittle. Accordingly, the brittle behaviour of PLA and PLA-REX samples must be primarily attributed to the fast physical aging kinetics exhibited by the polymeric matrix rather than its characteristics network parameters.

7.7. Fracture behaviour

This section presents the influence of the architectural modifications on both de-aged and aged fracture behaviours which were investigated using the *Post-Yielding Fracture* and the *Elastic-Plastic Fracture Mechanics*, respectively. An evaluation of the possible changes in the micromechanisms of deformation between unmodified and modified samples was performed using *Scanning Electron Microscopy* (SEM).

7.7.1. De-aged samples

The fracture behaviour of de-aged samples was evaluated using Deeply Double Edge-Notched Tension (DDENT) specimens. Under uniaxial loading, a large plastic deformation was observed at both crack tips; suggesting the applicability of the *post-yielding fracture mechanisms* through the *Essential Work of Fracture* (EWF) concept, as justified below. These observations are in good agreement with those already published by Gámez-Pérez *et al.* [241]. Following the recommendations of the European Structural Integrity Society-Technical Committee 4 (ESIS-TC4) [245], the DDENT sample geometry was preferred due to:

- The facility to satisfy the full ligament yielding preconditions before the onset of crack propagation [90, 410].
- The insurance of a low constraint level under fully plastic conditions.

The presentation of the EWF results is divided in two subsections:

- Validation of the EWF experiment prerequisites.
- Influence of the chain architectural modifications on the fracture behaviour.

a) Validation of the Essential Work of Fracture methodology

Figure 7.50 shows the load-displacement curves for PLA-4 and PLA-2 based materials, respectively. It was found that the load-displacement traces were geometrically similar to one another in the range of l under study. Consequently, this finding fulfils one of the main prerequisite for the validity of the EWF methodology, as already reported elsewhere [246, 250, 410]. The self-similarity trend ensures that cracks propagate under similar conditions, which remains independent of l. After the maximum load point, a significant load drop was observed in all traces which trend is probably due to the full ligament yielding.

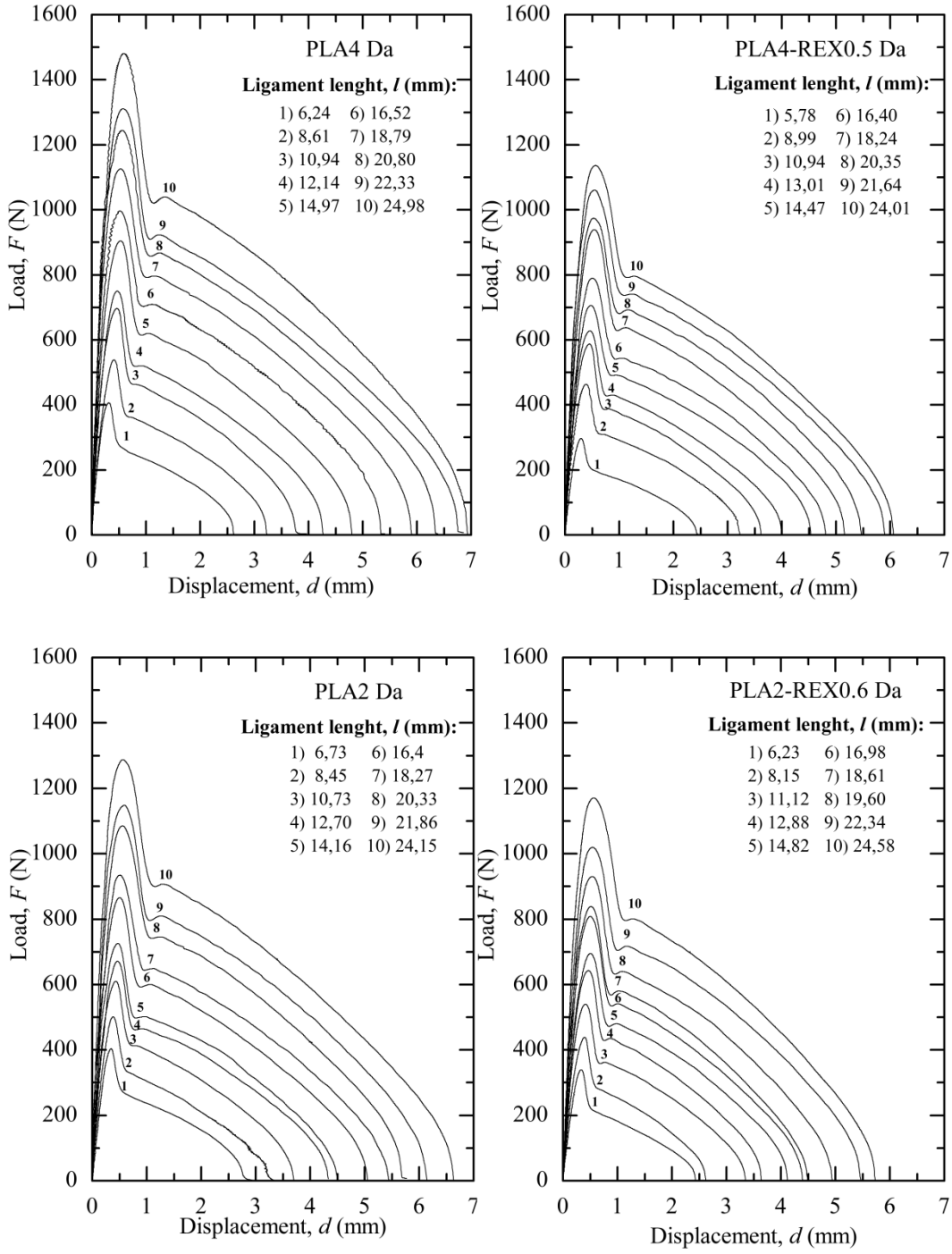

Figure 7.50. Comparison of the load *vs.* displacement curves at different ligament length for de-aged PLA-4 and PLA-2 based materials tested at 1 mm.min^{-1}.

A further validity check is linked to the full ligament yielding prior to final fracture. *Figure 7.51* displays the engineering stress as a function of the normalized displacement curves for de-aged PLA and PLA-REX samples. The strain field surrounding the ligament length was determined by DIC analysis. Results suggest that the onset of yield appeared in point "**b**". Yielding process was initiated well before the maximum stress and from both sharpened cracks due to the high stress concentration ahead of notches. At point "**e**", the ligament was fully yielded and the crack propagation was simultaneously initiated from both sides of the specimen. This finding fulfilled the crucial precondition of total plastic collapse of the ligament prior to crack initiation [246, 250, 410].

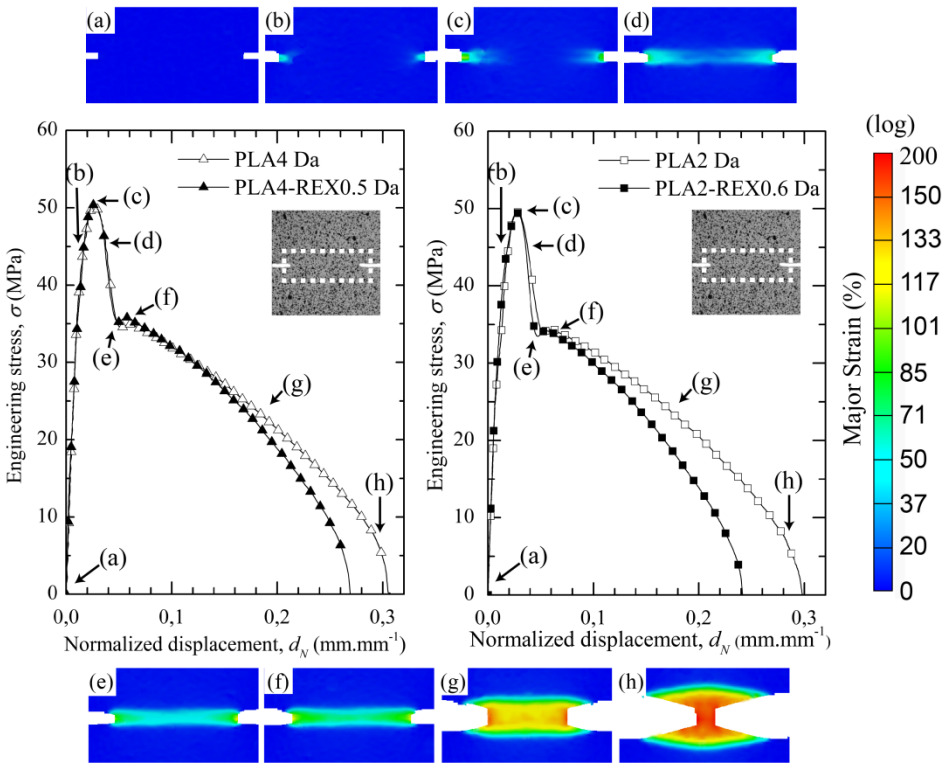

Figure 7.51. Engineering stress versus normalized displacement (by a *l* of 18 mm) curves for de-aged PLA-2 and PLA-4 based samples tested at 1mm.min^{-1}. The strain field surrounding the ligament length was determined in some characteristic points by DIC analysis in the rectangular field (white dashed line, insert).

To ensure that the EWF measurements were conducted under uniform stress state, the results were checked according to *equation 2.85* (*c.f. chapter 2, section 2.5.3.a*) [245]. *Figure 7.52* represents the maximum stress as a function of *l* for all de-aged samples. Although σ_{max} monotonously decreased between the 1.1-0.9σ_m limits with

increasing *l*, results suggest that all the EWF experiments were conducted under uniform stress state (pure plane stress in this case).

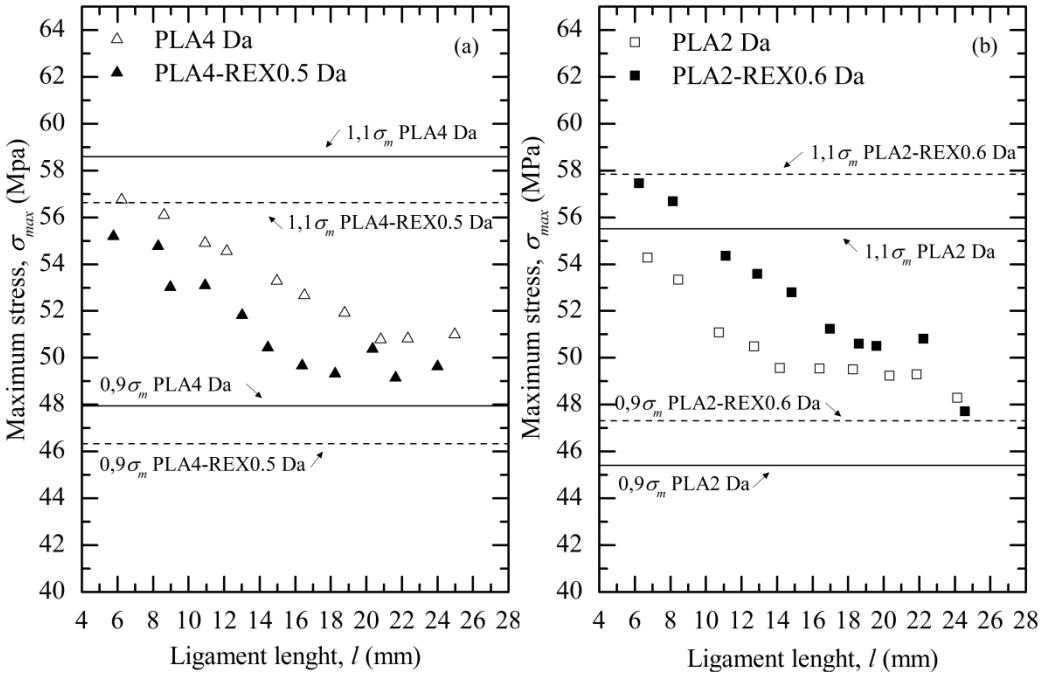

Figure 7.52. Maximum stress vs. ligament length for de-aged (**a**) PLA-4 and (**b**) PLA-2 based samples tested at 1 mm.min^{-1}.

Figure 7.53 shows the specific total work of fracture, w_f, versus ligament length, *l*. The linear dependence of w_f on *l* is another evidence to confirm that all the EWF experiments were conducted under uniform stress state, as already reported elsewhere [244, 411].

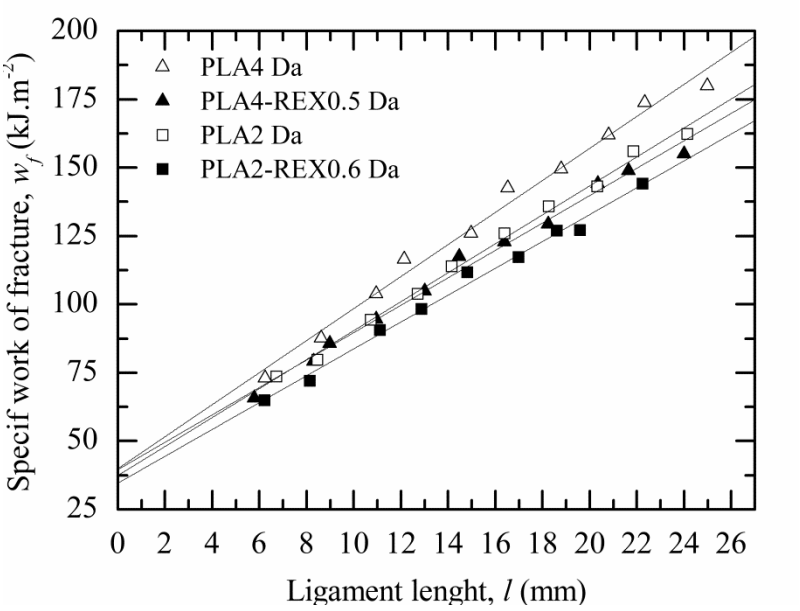

Figure 7.53. Specific work of fracture as a function of the ligament length for de-aged PLA-4 and PLA-2 based samples. The points are experimental data, and the line represents experimental data fits according to *equation 2.80* (*c.f. chapter 2, section 2.5.3*).

b) Fracture parameters

Considering that all prerequisites were largely verified, *equation 2.80* was used for the analysis. Based on *figure 7.53*, characteristic EWF parameters were calculated and results are compiled in *table 7.19*.

Table 7.19. Influence of the structural modifications on the EWF parameters.

Sample nomenclature	w_e (kJ.m^{-2})	βw_p (MJ.m^{-3})	β (10^{-2})	w_p (MJ.m^{-3})	R^2 (w_f *vs.* l)
PLA4 Da	39 ±3	5.8 ±0.2	8.3 ±0.5	69.9 ±0.2	0.994
PLA4-REX0.5 Da	39 ±2	5.0 ±0.2	6.3 ±0.6	79.4 ±0.2	0.995
PLA2 Da	37 ±2	5.3 ±0.1	8.3 ±0.6	63.9 ±0.1	0.998
PLA2-REX0.6 Da	34 ±2	4.9 ±0.2	6.1 ±0.5	80.3 ±0.2	0.996

Although a slight decrease in w_e was observed between PLA2 and PLA2-REX0.6 samples, results suggest that structural modifications did not significantly affect the work required for the onset of crack propagation; associated to the essential term (w_e). Similar w_e values were determined by Gámez-Pérez *et al.* [241] for de-aged PLA films with a nominal thickness of 0.3 mm. This observation is in line with previous communications stating that for amorphous polymers, w_e is a material constant,

independent of the specimen geometry and MW under plane-stress condition [239, 246, 251, 412].

By considering each PLA type, βw_p values appeared to slightly decrease with chain architecture modifications. This decrease can be seen best when comparing PLA-4 and PLA4-REX0.5 samples as shown in *table 7.19*. This trend matches the different post yielding behaviours observed for PLA-REX samples in *figure 7.51*. Nevertheless, the differences in βw_p values observed between both unmodified PLA samples (*i.e.* PLA4 and PLA2) must be viewed with a degree of scepticism. The slightly higher thickness exhibited by PLA4 samples ($t_{PLA4}\approx$1.2mm *vs.* $t_{PLA2}\approx$1mm) might have induced a larger work consumption to induce plastic deformations, thus leading to higher βw_p values.

Since w_p cannot be directly calculated from *equation 2.80* due to its combination with the shape factor, β, a detailed analysis of the βw_p term was necessary to elucidate the effects of the chain architecture modifications on the non-essential term. After testing, the height of the OPDZ, *h*, surrounding the ligament length, *l*, was measured and a visual inspection suggests that the plastic zone featured a parabolic geometry (*c.f. chapter 3, section 2.5.3.b, figure 2.42*). β was obtained from the best linear regression of a set of values represented in a graph plotting *h* versus *l* values and using *equation 2.89* (*c.f. chapter 3, section 2.5.3.b*).

Over the range of data considered, results suggest that β decreased with structural modifications; thus indicating a significant decrease in the volume of deformed material surrounding the ligament length. On the other hand, a significant rise in w_p was obtained, indicating an increase in the energy density dissipated in the deformation process surrounding the plane of crack propagation.

The deformation processes should be considered in order to physically interpret the trends provide by the above parameters. Shear banding *via* network stretching appears to be the dominant deformation mechanism in the whole process zone (IPFZ and OPDZ) of amorphous thermoplastic polyesters, as already reported by Karger-Kocsis *et al.* [250]. For ductile amorphous polymers, this deformation process (network stretching) matches well the physical interpretation of the EWF parameters presented by Chen *et al.* [37].

Recall that at the testing temperature, samples presented a significant molecular relaxation time, suggesting that entangling knots may have acted as “chemical” cross-linking points [413]. In a typical procedure, the network stretches until a “locked” point under loading which is governed by the entangled knots. Once this “locked” point is reached, the covalent bonds of the entangled chains ahead of the crack tip are stretched to a critical value and eventually break, leading to crack propagation. Thus,

the content and the degree of viscoelastic and viscoplastic flow that may undergo the molecular network prior to reach the "locked" point governs the size and energy density surrounding the crack propagation plane.

In the present study, the network stretching mechanism was evidenced by the full recovery of the stretched zone when broken specimens were kept at T_g for a short period of time, as shown in *figure 7.54*. Similar features have been already reported by Karger-Kocsis and coworkers regarding amorphous polymers, which were not subjected to strain induced crystallization under tensile loading [244, 251, 414, 415]. This behaviour is frequently correlated to the memory effect.

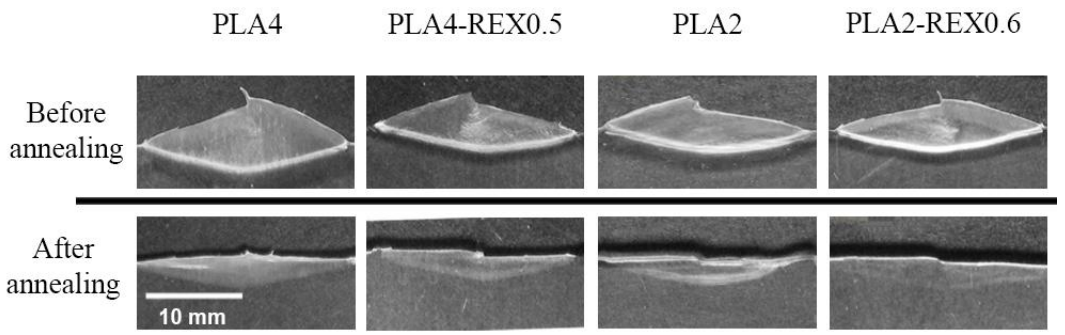

Figure 7.54. Macrophotographs taken from the stretched zone of broken DDENT samples before and after annealing (10 min at T_g). For demonstration purposes, DDENT specimens of unusual fracture behaviour (different planes of propagation) were selected.

After loading, since the initial entanglement network structure remained unchanged, it acted as the driving force for network retraction. This behaviour is related to the cold drawing process, which is a thermodynamically reversible process in glassy polymers. It has been attributed to the fact that deformation enhanced anisotropy in the loading direction by changing the chain conformation. Regarding low deformation rates, the entangled network is stretched but remains undisrupted and the coils containing the polymer chains are deformed from isotropic spheres to anisotropic ellipsoids, as shown in *figure 7.55* [250, 251, 416-419].

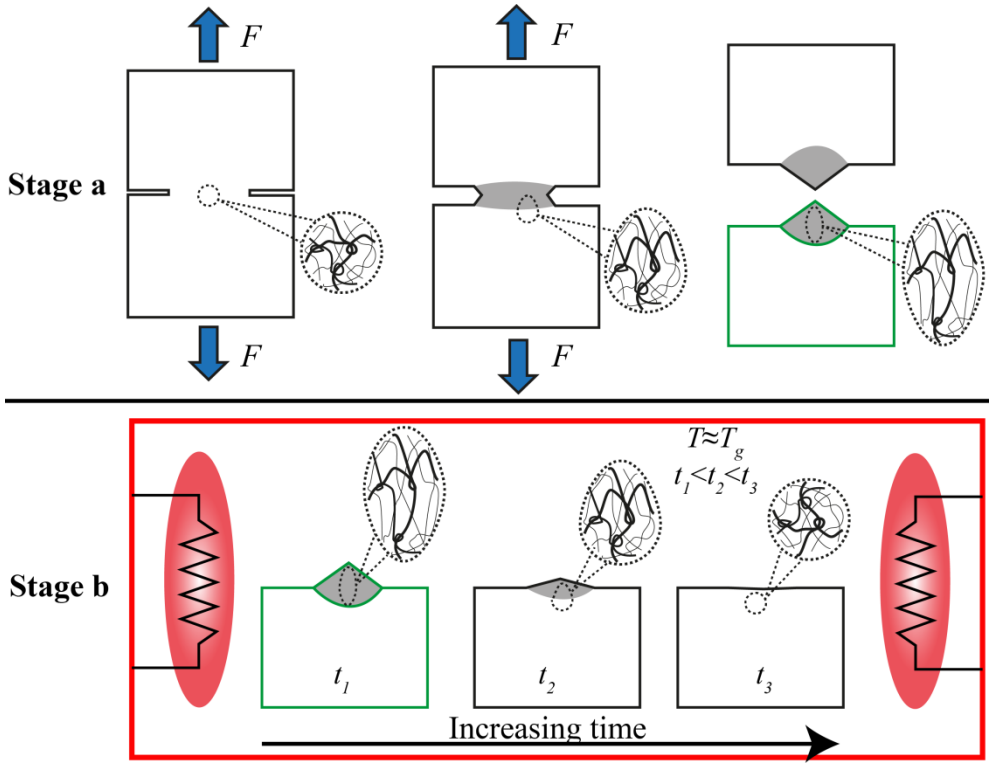

Figure 7.55. Cold drawing process: **(a)** stretching of the polymer network, **(b)** shape-recovery at T_g.

Thus, under uniaxial loading, as long as disentanglements did not take place, the deformation mechanism governing the network stretching was principally dependent of the entangled network. Beyond the yield point, a more entangled network (*e.g.* PLA-REX samples) may accommodate lower network extension as compared to a less entangled structure. This was attributed to the fact that M_e decreased and the entanglement density increased (*c.f. table 7.6*), which trend possibly gave rise to a lowered backbone stretching level.

Therefore, the molecular network was able to distribute and relieve the stress in a smaller volume element (*i.e.* lower β value). In a highly entangled network, the mechanical work content, which is necessary to generate the plastic flow, is supposed to increase, leading to a higher w_p value. This is due to a decrease in the ability to orientate the molecular chains under uniaxial loading [416, 420].

The morphology of the fractured surfaces was evaluated using SEM after fracture experiments. *Figure 7.56* shows the macrophotographs taken from the usual plastic zone of the broken DDENT specimens and the SEM images of the corresponding fractured surfaces ahead of the crack tip. An obvious decrease in the size of the OPDZ

was observed for both PLA-REX samples. This decrease can be seen best when comparing PLA2 and PLA2-REX0.6 samples. These observations agree well with the decrease in β values due to the formation of a more entangled molecular network (*c.f. table 7.19*).

Ahead of the crack tip, both PLA samples showed the topographical features of river line patterns which are probably due to the high constraint level before crack propagation. These river lines merge progressively to form long ridges parallel to the crack propagation direction. The SEM micrographs showed intense flow on the fracture surfaces coupled with a significant decrease in the sample thickness. By contrast, both PLA-REX samples exhibited a fractured surface relatively more regular and smoother. Under loading, these observations math well the aforementioned discussion which reports a decrease in the degree of viscoplastic flow that may undertake the molecular network with the modification of the molecular architecture.

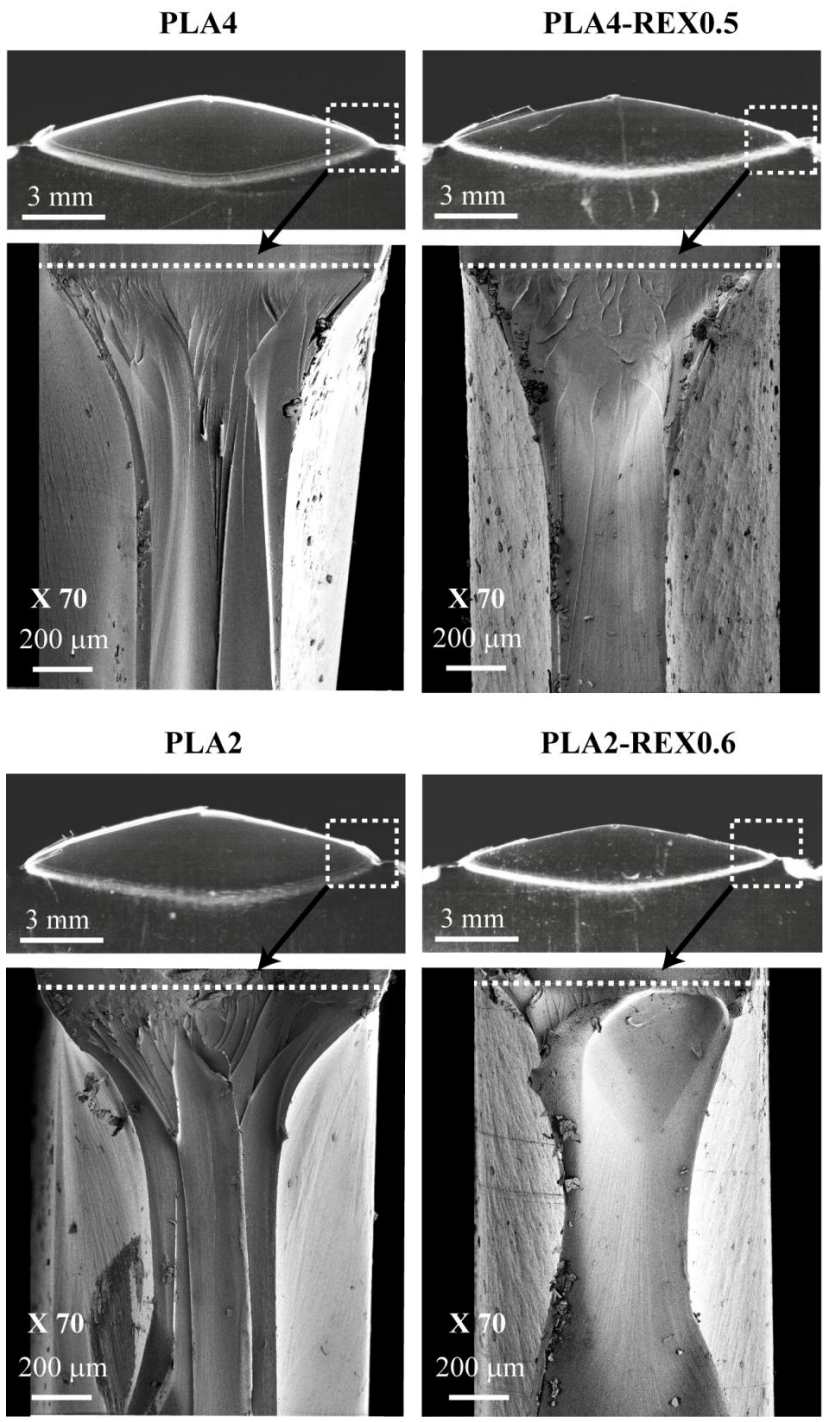

Figure 7.56. taken from the plastic zone of the broken DDENT samples tested at 1 $mm.min^{-1}$. The fractured surface ahead of the crack tip (white dashed rectangle) was observed by SEM. The white dashed line indicates the initial crack tip.

7.7.2. Aged samples

Aged PLA and PLA-REX samples feature an inherent brittle behaviour under uniaxial tensile loading, as previously reported in *section 7.6*. Unlike DDENT samples, Single-Edge-Notched Tension (SENT) geometry was preferred to evaluate the fracture behaviour of aged samples in order to avoid issues of crack propagation outside of the ligament plane. Moreover, probabilities of damages at the crack tip, which extend can flaw experimental data using DDENT samples, are minimized using SENT geometry.

A preliminary intent was performed to evaluate the fracture behaviour of aged PLA and PLA-REX samples using the *linear-elastic fracture mechanics*. The stress-intensity factor, K_{app} at the crack tip just before the crack propagation onset was determined using *equation 2.61.b* (*c.f. chapter 2, section 2.5.1.b*). The dimensionless function *f(a/W)* was selected according to the model reported by Tada *et al.* [224] for SENT geometry (*c.f. equation 7.15*). Results are given in *table 7.20*. The load at the crack propagation onset, *P*, is equally reported.

$$f\left(\frac{a}{W}\right) = \frac{\sqrt{2tan\left(\pi a/2W\right)}}{cos\left(\pi a/2W\right)}\left[0.752 + 2.02\left(\frac{a}{W}\right) + 0.37\left(1 - sin\left(\frac{\pi a}{2W}\right)\right)^3\right] \qquad \textbf{(7.15)}$$

Where *a* is the crack length and *W* the specimen width.

Table 7.20. Influence of the structural modifications on the fracture parameters for a unique crack length (*i.e. a*=30mm).

		PLA4	PLA4-REX0.5	PLA2	PLA2-REX0.6
$\boldsymbol{P}$ [a] (N)		635 ±23	467 ±28	615 ±49	393 ±40
$\boldsymbol{K_{app}}$ [b] (MPa.m$^{1/2}$)		14.7 ±0.4	13.0 ±0.7	13 ±1	11.4 ±0.4
CTOD [c] (mm)	Plane-stress	0.88 ±0.06	0.68 ±0.08	0.65 ±0.09	0.54 ±0.01
	Plane-strain	0.50 ±0.04	0.38 ±0.05	0.37 ±0.05	0.30 ±0.01
$\boldsymbol{\delta_c}$ [d] (mm)		0.45 ±0.08	0.24 ±0.04	0.31 ±0.02	0.18 ±0.05
$\boldsymbol{J_0}$ [e] (kJ.m^{-2})		32 ±6	18 ±4	23 ±2	13 ±1

[a] **Load at the crack propagation onset**: experimentally determined.

[b] **Stress-intensity factor**: estimated using *equation 2.61.b* (*c.f. chapter 2, section 2.5.1.b*).

[c] **Crack-tip-opening displacement**: estimated using *equation 2.76* (*c.f. chapter 2, section 2.5.2.b*).

[d] **Crack-tip-opening displacement**: experimentally determined.

[e] **Nonlinear energy release rate per unit area**: estimated using *equation 2.77* (*c.f. chapter 2, section 2.5.2.b*).

Recall that a unique crack length (*i.e.* a=30mm) was evaluated and therefore the obtained results are solely comparative. Results suggest that a decrease in K_{app} was apparent for PLA-REX samples as compared to their linear homologues. This trend was attributed to the decrease in the load required to reach the crack propagation onset for PLA-REX samples. In the current study, K values are much higher as compared to the results reported by Nascimento *et al.* [348] and/or Park *et al.* [351] for PLA resins under plane-strain conditions. These results are consistent with the influence of the stress state on the variation of the stress intensity factor, as shown in *figure 2.34* (*c.f. chapter 2, section 2.5.1.c*). In the current study, it should be kept in mind that the specimen dimensions were selected in order to approach the same constraint level as compared to DDENT samples. It is well known that in mixed mode and/or under plane-stress conditions, the fracture toughness of the sample increases because a significant volume of the specimen at the crack tip is available for plastic deformation energy absorption. Consequently, K increases [90, 226, 227].

During testing, a visual inspection of the process zone suggested the formation of an extensive blunting ahead of the crack tip before crack propagation (*i.e.* large-scale yielding at the crack tip). However, it is well known that the elastic stress analysis is increasingly inaccurate as the LEFM are available when crack-tip yielding is confined to the immediate vicinity of the tip. On this basis, an intent to perform the plastic-zone correction to the stress-intensity factor was performed using the Dugdale's strip-model, as detailed in *section 2.5.1.c* (*c.f. chapter 2*). Nevertheless, an increasing effective stress-intensity factor was found with performing the iteration process. Similar trend have been already reported by Hertzberg [226]. Authors concluded that the entire procedure of applying the plasticity correction become increasingly suspect when the computed plastic zone becomes an appreciable fraction of the initial crack length.

Consequently, the *elastic-plastic fracture mechanics* was preferred to evaluate the fracture behaviour of aged samples. The determination of the J_{ic} involves the testing of numerous specimens, which makes the procedure both tedious and time intensive. Since this study aimed to compare quantitatively the fracture behaviour of aged samples, the CTOD, δ_c, at the onset of crack propagation was determined for these testing conditions, as detailed in *section 5.4.2* (*c.f. chapter 5*). Based on the δ_c values, calculation of the nonlinear energy release rate per unit area, J_0, proceeds according to *equation 2.77* (*c.f. chapter 2, section 2.5.2.b*) with m=1. Mechanical parameters for aged samples, which are compiled in *table 7.18*, were used for the above calculations. Results are reported in *table 7.20*. In addition, the resulting strain field at the onset of crack propagation, which was determined using DIC analysis for each sample, is shown in *figure 7.57*.

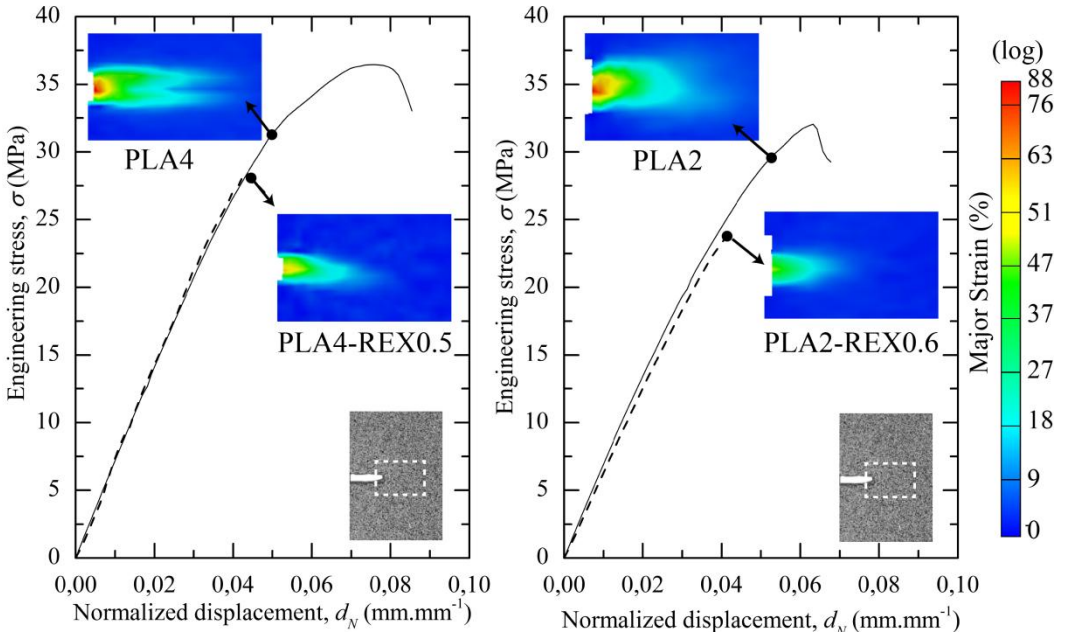

Figure 7.57. Engineering stress vs. normalized displacement (by *l* of 20 mm) for aged PLA-2 and PLA-4 based samples. The strain field ahead of the crack tip was determined by DIC analysis in the rectangular field (white dashed line, insert) at the onset of crack propagation.

Results suggest that both PLA samples exhibited a larger blunting ahead of the crack tip as compared to PLA-REX ones, leading to a wider δ_c before the catastrophic crack propagation. As a result of this larger strain and considering that all of the samples have a similar σ_y (*c.f. table 7.18*), PLA samples presented a higher energy consumption up to the crack propagation onset as compared to PLA-REX samples

For comparison purposes, CTOD values in plane-stress and plane-strain conditions were equally calculated from K_{app} using *equation 2.76* (*c.f. chapter 2, section 2.5.2.b*). Under plane-stress conditions, calculated CTOD values did not match experimental ones, as shown in *table 7.20*. Under plane-strain conditions, the CTOD values calculated from K_{app} agreed quantitatively with δ_c within the experimental error for PLA samples. However, discrepancies were observed between both values for PLA-REX samples. A possible explanation might be that either the dimensionless function *f(a/W) (i.e. equation 7.15)* is not accurately defined for this sample geometry or an alternative procedure is needed to perform the plastic-zone correction to the stress-intensity factor, K_{app}.

In order to obtain more information about the fracture process, SEM analysis was performed on the fractured surfaces of all aged samples. *Figure 7.58* and *figure 7.59*

show an overview of the fractured ligament length together with two detailed regions for aged PLA-4 and PLA-2 based samples, respectively.

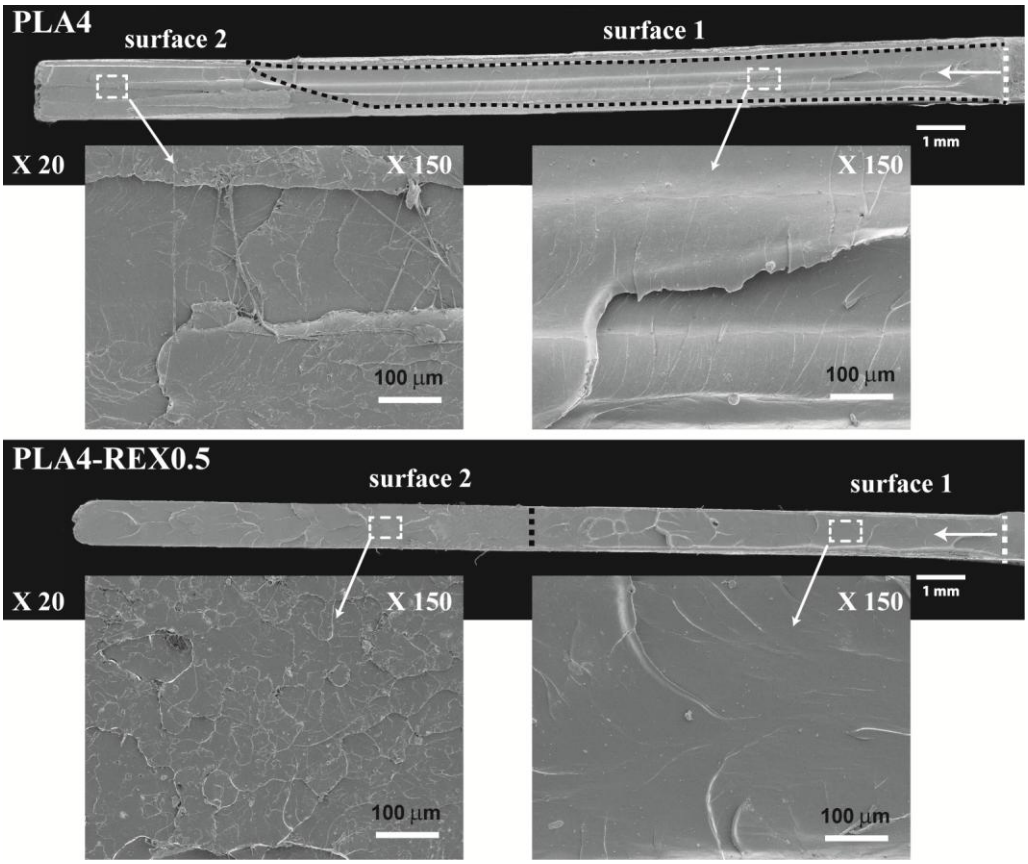

Figure 7.58. SEM micrographs of the total fractured ligament length and of two characteristic fractured surfaces for PLA4 and PLA4-REX0.5 samples. The white arrow indicates the crack propagation direction ahead of the crack tip.

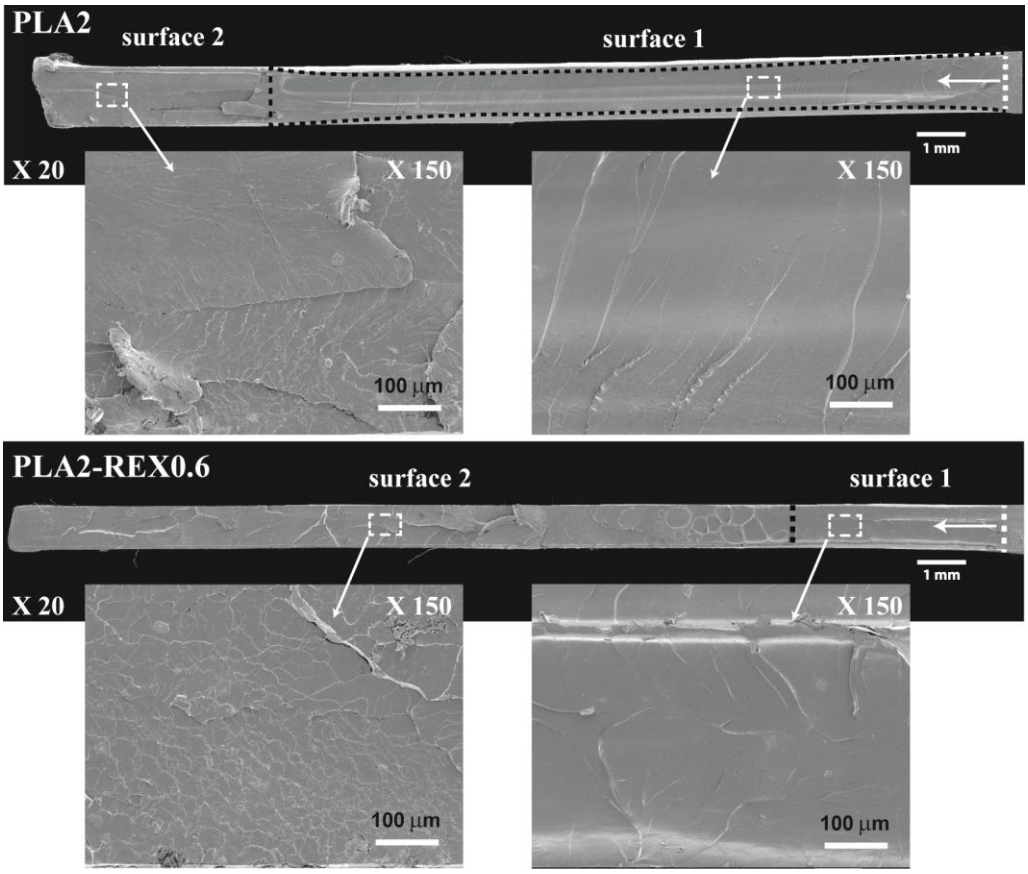

Figure 7.59. SEM micrographs of the total fractured ligament length and of two characteristic fractured surfaces for PLA2 and PLA2-REX0.6 samples. The white arrow indicates the crack propagation direction ahead of the crack tip.

All samples exhibited two different regions with different fracture surface features, as shown in *figure 7.58* and *figure 7.59*. Ahead of the crack tip, the first zone (referred to as surface 1) showed a smooth topography with only few cuts running perpendicular to the propagation direction. As a result of the smooth feature of this surface coupled with the absence of plastic tearing, this region may characterize the controlled propagation step of the crack propagation. Thus, the crack propagation onset was preceded by a long craze growth whose growth rate ($V_{craze\text{-}growth}$) was faster than the crack propagation rate (V_{crack}).

The second zone (referred to as surface 2) showed evidences of random nucleation, orientation and size of crazes in which thin fibrils may be observed. This surface topography is usually called “hackled” pattern and is characteristic of a brittle behaviour. Regarding polymeric materials, this situation is expected when V_{crack} exceeds $V_{craze\text{-}growth}$. In this region, craze nucleation and craze growth processes were

uncontrolled and erratic under uniaxial loading which means that the unstable regime of crack propagation was reached.

Surface 1 recovered two thirds of both PLA ligament length samples with a slight reduction of its initial thickness (delimited by the black dashed line). However, this length was reduced to less than half of the fractured ligament length for PLA-REX samples with no evidences of substantial thickness reduction. These observations indicated that PLA-REX samples achieved less craze thickening prior to the craze-crack transition as compared to PLA samples. This may be due to the lower molecular mobility under loading as a result of the higher entangling knots density. Therefore the mechanical work underwent by the matrix at the onset of crack propagation was lowered, giving rise to lowered *J* values. Regarding PLA samples, this "delayed" craze-crack transition was highlighted in *figure 7.57* by the further increase in the engineering stress up to a local maximum after the onset of crack propagation.

As showed in *figure 7.58* and *figure 7.59* for both PLA-REX samples, surface 2 presented a larger surface together with a higher number of craze random nucleation. This observation is in line with the behaviour previously observed in tensile tests where a larger content of short and thin crazes was generated when PLA-REX samples were loaded in mode I (*c.f. figures 7.48 and 7.49*). While no differences were observed in the uniaxial tensile parameters (*c.f. table 7.18*), in this section the CTOD analysis revealed a significant difference in the fracture properties between PLA and PLA-REX materials. Consequently, results suggest that in presence of a stress intensifier (*i.e.* notch), the modification of the chain architecture may lead to a loss of stability in the crack propagation process.

Under pure plane-stress state condition, Wu *et al.* [412] stated that w_e obtained by the EWF methodology is equivalent to J_0. Since both parameters are geometrically independent, a comparison between the EWF parameters determined in *section 7.7.1* and the J_0 parameter was possible [239, 246, 412]. As compared to de-aged samples, aged samples showed a decrease in the energy consumed by the material in order to initiate the crack propagation. Under loading, this behaviour was attributed to the significant decrease in the ability to dissipate energy through molecular motion. As shown in *tables 7.19* and *7.20*, results suggest that changes in the fracture toughness between PLA and PLA-REX samples were enhanced with aging.

Chapter 8: Conclusions

8.1. Conclusions

Under the processing conditions used in this thesis, the obtained results lead to the following conclusions. For the sake of clarity, the general conclusions have been divided in five parts.

Physico-chemical characterisations

The lower the D-lactide content, the higher is the reactivity of the PLA type towards the multi-epoxy reactive agent.

Conventional chromatographic SEC-DRI analysis revealed a significant increase in the molecular weight of PLA-REX samples as compared to their linear homologues. The molecular weight spectra changed significantly and a shoulder appeared in the high molecular weight tails.

FT-IR and ^{1}H NMR measurements remained similar between PLA and PLA-REX samples; suggesting that both techniques failed to characterize topological changes under study.

Rheological behaviour

Rheological measurements showed differences between PLA and PLA-REX samples that cannot be evidenced by conventional spectroscopic (^{1}H NMR, FT-IR) or chromatographic (SEC-multiple detectors) methods. Rheological measurements turn out to be a sensitive analytical tool to detect the presence of very small amounts of non-uniform structural modifications in PLA.

The response time of the melt was broadened and the melt elasticity of PLA-REX samples was increased. These changes can minimize numerous issues (*i.e.* sagging of melts, necking, etc) during film/sheet casting, film blowing and/or foaming.

The complex viscosity was significantly increased in the low frequency range for PLA-REX samples. However, this difference was not as pronounced for values near the usual extrusion frequency range (between 100 and 1000 rad.s^{-1}) between unmodified and reactively modified materials. This behaviour leads to a desirable

benefit on the industrial level as PLA and PLA-REX samples can be similarly processed without relevant changes in extrusion processing conditions and/or equipments.

Complex viscosity functions were successfully inverted to molecular weight distribution spectra for PLA-REX samples. Regardless of the viscosity fitting model used to both smooth out and extrapolate raw data, predicted molecular weight averages and PDI values agreed with SEC-DRI results within 10%. A larger quantification between the molecular information related to the linear and the chain modified fractions was observed with the introduction of the complex time dependence into the prediction.

Thermal behaviour

The results of this study showed that the thermal properties were slightly modified with the modification of the chain architecture. Upon constant heating, the maximum degree of cold-crystallization decreased due to an apparent drop in the relative percentage of conversion for PLA-REX materials.

Thermal fractionation using the *successive self-nucleation and annealing* procedure showed that the length distribution of crystallisable PLLA chain segments was reduced with topological changes; thus promoting the development of thinner and more irregular lamellar crystals.

Under controlled aging periods at 30 ºC, the rate of enthalpy relaxation exhibited by PLA-REX samples was slowed down. An increase in the entanglement network density is therefore a good solution to reduce the ability of reorganization towards a more ordered conformational state of PLA over time.

For a given thermal history, the thermo-dynamical properties of PLA-REX samples matched those of their linear homologues within the statistical error of the measurements.

Mechanical behaviour

The tensile properties of PLA and PLA-REX samples were not statistically different from each other for a given thermal history. This is an important finding, because it allows the viscosity or the melt strength to be tailored to the desired level without affecting mechanical properties.

The chain stiffness was decreased and the entanglement network density was enhanced with chain structure modifications, but PLA-REX samples remained brittle under tensile loading after being stored 1 week at room temperature. This suggested that the brittle behaviour of PLA must be primarily attributed to the fast physical aging

kinetics exhibited by the polymeric matrix rather than its characteristic network parameters.

Fracture behaviour

Regarding de-aged specimens, the *essential work of fracture* analysis revealed that both the work required for the onset of crack propagation and the work associated with the resistance to crack propagation remained insensitive to topological changes.

Regarding aged specimens, structural modifications induced a decrease in the energy consumed up to the onset of crack propagation due to an apparent decrease in the network extensibility; thus promoting a premature craze-crack transition.

8.2. Outlook

Based on the results of this work, the following is suggested for future investigation:

Experimental field:

- The correlation between η_0 and M_w for PLA-REX samples was only established for a limited range of M_w. For this reason it would be desirable to extend this range to lower and higher M_w.
- Further investigations of the physical aging kinetics using the *Modulated Differential Scanning Calorimetry* (MDSC) concept. The proper separation of the effects related to the enthalpy relaxations to those of the glass transition is of interest.
- The melt transition of PLA is subjected to the melt-crystallization process. A more detailed study of the SSA results obtained in this study, through the MDSC technique, should be reasonable in order to corroborate the reported data.
- The strain field ahead of the crack tip was only evaluated for a unique ligament length for aged samples. The main interest is to investigate the strain field head of the crack tip for various ligament lengths.
- The melt strength of PLA-REX has been enhanced as compared to PLA material. The main interest is to foam PLA-REX through the Mucell® microcellular foam injection molding process.

Global field :

- **Control of the thermal degradation of PLA/o-MMT nanocomposites using the addition of multi-functional epoxy chain extender/branching agent through reactive extrusion.**

  Melt compounding PLA with organically modified clays intensified the degradation of the PLA matrix, as reported in Velazquez Infante [345] through

the project MAT2007-62450. The addition of a multi-functional chain extender/branching agent could minimize the thermal degradations of the polymeric matrix during processing; thus promoting the shear field on the clay layers. A higher degree of clay dispersion and/or the formation of a strong chemical bonding between the clay organo-modifier, the reactive agent and the polymer chains might be expected. Those activities are framed in the whole project entitled "*Architectural modifications of a PLA matrix through a one-step reactive extrusion-calendering process to enhance the processability, the fracture behaviour and the preparation of biodegradable nanocomposites*" (*ref*: MAT2010-19721-C02-01) currently ongoing in the CCP.

- **Improvement of the fracture behaviour of PLA-REX/reactive fillers nanocomposites processed through reactive extrusion.**

  In this field, fumed silicate treated with epoxy and/or amino groups have been selected in order to improve the reactivity and the dispersion of the fillers into the PLA-REX matrix. The overall objective is to characterize the fracture behaviour of these new nanocomposites processed through reactive extrusion. Those activities are carried out in association with the Laboratory of Polymeric and Composite Materials, University of Mons, Belgium and are framed in the whole project entitled "*REXBIOBLEND: PLA bioblends prepared by reactive extrusion*" (*ref*: MAT2013-40730-P) that is currently undertake in the CCP.

- **Bioblends processed through reactive extrusion and injection processes.**

  In this field, PLA-REX is melt blended with technical commercial polymers (*i.e.* ABS, PA) in order to explore new fields of "long term" applications for PLA polymer (*e.g.* automotive and/or electrodomestic fields). The main attention is focused on the content of renewable raw materials in order to reduce the carbon footprint. Those activities are framed in the current project entitled "*REXBIOBLEND: PLA bioblends prepared by reactive extrusion*" (*ref*: MAT2013-40730-P).

Chapter 9: Appendix

9.1. Detailed information about rheological procedures

9.1.1. Oscillatory shear experiments – "*Optimization of LVE data sets*"

Dynamic LVE data sets are usually measured with high precision. However, experimental both between- and within-sample errors are unavoidable, independently of the operator's skilfulness. The main source of experimental between-sample errors results from the variations in sample loading and trimming. The viscoelastic data are vertically shifted due to these variations from one sample to another; thus lowering the precision of the measurements.

On the other hand, the primary source of experimental within-sample errors is attributed to equipment limitations. Modern rheometers, which feature a magnetic levitation thrust, are commonly characterized by their unprecedented low residual torque performance [421]. However, residual torque-transducer noises are usually observed at the low frequency end, leading to discrepancies in the dynamic function data. Tchir and Saucier [363] reported an increasing effect of the transducer noise on experimental data with decreasing ω. The "*critical*" frequency at which the transducer noise starts to affect data is highly dependent on both the temperature and the viscosity of the material under study.

Accordingly, Tchir and Saucier [363] suggested a procedure to identify and to correct a set of flawed data in order to estimate reliable $|\eta^*(\omega)|$ curves. The identification of the between-sample variations is carried out using the shift function, as given by:

$$\delta\eta_i(\omega) = \frac{\eta_i^*(\omega) - \eta_{\text{avg}}^*(\omega)}{\eta_{\text{avg}}^*(\omega)} \qquad \textbf{(9.1)}$$

Where $\delta\eta_i(\omega)$ is the shift function of the $|\eta^*(\omega)|$ curve *i*, $\eta_i^*(\omega)$ the $|\eta^*(\omega)|$ data of the curve under consideration and $\eta_{avg}^*(\omega)$ the average $|\eta^*(\omega)|$ curve calculated from all the curves in the data set.

For illustration purposes, the shift functions were calculated for three fresh PLA2 samples, as shown in *figure 9.1*.

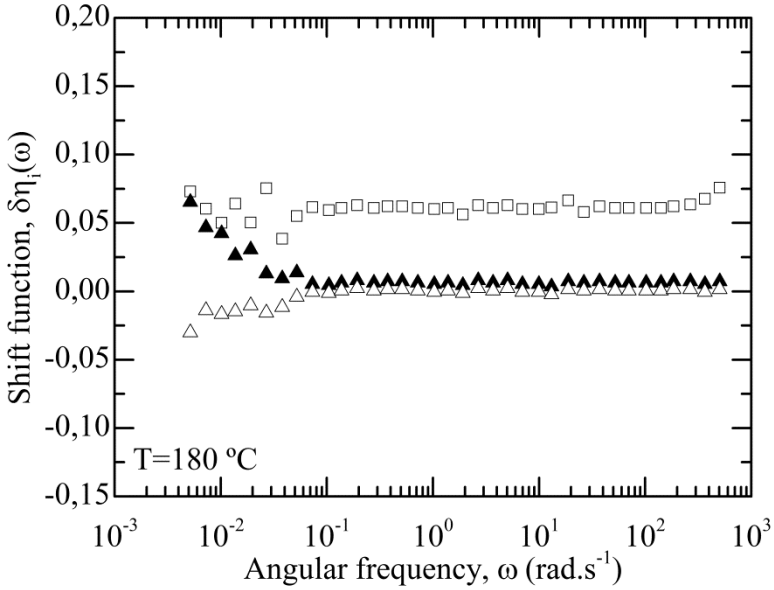

Figure 9.1. Example of shift functions calculated from three fresh PLA2 samples at 180ºC.

While noise issues were observed in the lowest ω range (from 10^{-3} to 10^{-1} rad.s^{-1}), all of the shift functions reach a constant value with increasing ω. This trend suggests the negligible effect of the residual torque-transducer noise on raw data with increasing ω. The absolute value of the average plateau values was considered as the between-sample error for a particular data set. Thus, a shift factor ($\delta\eta_i$), which is defined as the average of the shift function values in the plateau region, was calculated for each $|\eta^*(\omega)|$ function. Finally, the corrected $|\eta^*(\omega)|$ functions were calculated according to:

$$\eta^*_{i\,corrected}(\omega) = \frac{\eta^*_i(\omega)}{1+\delta\eta_i} \qquad \textbf{(9.2)}$$

where $\eta^*_{i\,corrected}(\omega)$ is the complex viscosity values corrected by the between-sample error, $\eta_i^*(\omega)$ the raw complex viscosity data and $\delta\eta_i$ the shift factor.

By applying this correction procedure, the low frequency range of all the $|\eta^*(\omega)|$ functions is corrected; removing transducer noises and allowing a proper estimation of η_0. In the present study, this methodology was equally extended to both $G'(\omega)$ and $G''(\omega)$ functions in order to identify and then to remove between and within-samples errors.

9.1.2. Creep-recovery experiments – "*Drift correction*"

A proper determination of the linear steady-state elastic compliance, J_e^0, is achieved if the bearing is free of any parasitic frictions during the recovery phase. Regarding modern rheometers, a sophisticated correction, called "*rotational-mapping*", is applied prior to testing in order to counter the effects of the air bearing drift on $J_r(t)$. This is achieved by applying counter torque values; thus minimizing the residual torque values. Nevertheless, a low residual torque always remains present even after performing this calibration [106, 109].

$J_r(t)$ requires a "*drift correction*" in order to remove the effect of the remaining parasitic residual torque on the recoverable compliance measurement, as already reported by Gabriel *et al.* [422] and Stadler [107].

In this approach, it is assumed that the drift caused by the residual torque is time-dependent. Thus, depending on the direction of the parasitic residual torque (clockwise or anticlockwise), $J_r(t)$ is corrected by adding or subtracting a correction constant (K) as given by *equation 9.3*:

$$J_r^{corrected}(t) = J_r^{uncorrected}(t) \pm K.t \qquad \textbf{(9.3)}$$

Where $J_r^{corrected}(t)$ is the recoverable compliance corrected by the "*drift correction*", $J_r^{uncorrected}(t)$ the experimental raw data and t the time of the recovery phase. K is defined as the slope of the linear regression performed at long recovery times of $J_r(t)$ in linear scale [107]. This concept is illustrated in *figure 9.2* for PLA4 samples.

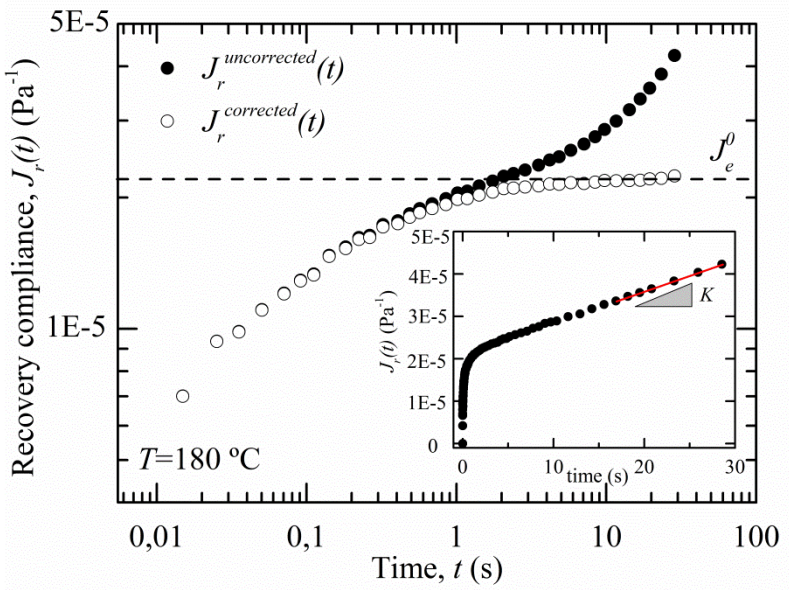

Figure 9.2. Example of the "*drift correction*" on the $J_r(t)$ data for PLA4 samples at 180 °C. The filled and opened symbols represents the experimental raw and the

corrected $J_r(t)$ data, respectively. The insert shows the linear plot of the uncorrected $J_r(t)$ *vs. t*, necessary to determine the drift correction constant *K*.

9.1.3. The linear viscoelastic regime – "*viscoelastic transformations*"

Below are briefly described the different equations used to convert standard viscoelastic functions into both relaxation, $H(\tau)$, and retardation, $L(\lambda)$, spectra, respectively.

Relaxation spectra

From oscillatory shear experiments

Frequency sweeps are the only experimental mode which can be described by both $H(\tau)$, and $L(\lambda)$, spectra, as shown in *figure 2.16* (*chapter 2, section 2.3.4*). From the dynamic storage, $G'(\omega)$, and loss, $G''(\omega)$, modulus, calculations of discrete and continuous $H(\tau)$ proceed according to *equations 9.4* and *9.5*, respectively [110, 112].

Discrete spectrum

$$G'(\omega) = G_e + \sum_{i=1}^{n} g_i(\tau_i) \frac{\omega^2 \tau_i^2}{1 + \omega^2 \tau_i^2} \qquad \textbf{(9.4.a)}$$

$$G''(\omega) = \sum_{i=1}^{n} g_i(\tau_i) \frac{\omega \tau_i}{1 + \omega^2 \tau_i^2} \qquad \textbf{(9.4.b)}$$

Continuous spectrum

$$G'(\omega) = G_e + \int_0^{+\infty} H(\tau) \frac{\omega^2 \tau^2}{1 + \omega^2 \tau^2} \, d\tau \qquad \textbf{(9.5.a)}$$

$$G''(\omega) = \int_0^{+\infty} H(\tau) \frac{\omega \tau}{1 + \omega^2 \tau^2} \, d\tau \qquad \textbf{(9.5.b)}$$

Where $g_i(\tau_i)$ are the individual modes of the discrete spectrum, τ_i their corresponding relaxation times and *n* the number of modes. $H(\tau)$ is the continuous relaxation time spectrum, τ the relaxation time and G_e the modulus at infinite times. Regarding melted polymers without a yield point, G_e is negligible due to its extremely low value [107].

Since the range of accessible experimental frequencies is limited, the range of time over which $H(\tau)$ and/or $L(\lambda)$ spectra are inferred should be delimited in order to avoid meaningless extrapolations. It has been widely believed that relaxation times corresponding to the reciprocal of the minimum and maximum experimentally available frequencies may be considered as reliable values to estimate spectrum limits. Nevertheless, Davies and Anderssen [423] reported that the interval to predict

spectrum is shorter than this range of reciprocal frequency by 1.36 decades. Authors established the following limits:

$$\frac{e^{\pi/2}}{\omega_{max}} < \tau < \frac{e^{-\pi/2}}{\omega_{min}} \qquad \textbf{(9.6)}$$

The nonlinear method of regularization developed by Honerkamp and Weese [112], which is used to convert creep-recovery data into $L(\lambda)$ in the current study (*c.f. chapter 5, section 5.2.2*), is based on the Davies and Anderssen criteria.

From relaxation experiments (step-strain)

Calculations of the relaxation spectrum, $H(\tau)$, from the relaxation modulus, $G(t)$, proceed according to *equation 9.7*.

Discrete spectrum $$G(t) = G_e + \sum_{i=1}^{N} g_i(\tau_i) \exp\left(\frac{-t}{\tau_i}\right) \qquad \textbf{(9.7.a)}$$

Continuous spectrum $$G(t) = G_e + \int_0^{\infty} H(\tau) \exp\left(\frac{-t}{\tau}\right) d\tau \qquad \textbf{(9.7.b)}$$

Commonly, the shape of $G(t)$ is similar to $H(\lambda)$ as the designation of the relaxation spectrum is derived from the relaxation test.

<u>Retardation spectra</u>

From creep-recovery experiments

From the compliance, $J(t)$, and the recoverable compliance, $J_r(t)$,calculations of the discrete and continuous retardation spectrum, $L(\lambda)$, proceed according to *equation 9.8* and *9.9*, respectively.

Discrete spectrum

$$J(t) = J_0 + \sum_{i=1}^{n} l_i(\lambda_i)\left[1 - \exp\left(-\frac{t}{\lambda_i}\right)\right] + \frac{t}{\eta_0} \qquad \textbf{(9.8.a)}$$

$$J_r(t_r) = J_0 + \sum_{i=1}^{n} l_i(\lambda_i)\left[1 - \exp\left(-\frac{t_r}{\lambda_i}\right)\right] \qquad \textbf{(9.8.b)}$$

Continuous spectrum

$$J(t) = J_0 + \int_0^{+\infty} L(\lambda)\left[1 - \exp\left(-\frac{t}{\lambda}\right)\right] d\lambda + \frac{t}{\eta_0} \qquad \textbf{(9.9.a)}$$

$$J_r(t_r) = J_0 + \int_0^{+\infty} L(\lambda)\left[1 - \exp\left(-\frac{t_r}{\lambda}\right)\right] d\lambda \qquad \textbf{(9.9.b)}$$

Where $l_i(\lambda_i)$ are the individual modes of the discrete spectrum, λ_i their corresponding retardation times and n the number of modes. t and t_r is the experimental time of the creep and recovery phase, respectively. $L(\lambda)$ is the continuous retardation spectrum, λ the retardation time and J_0 the spontaneous elastic part of the compliance. J_0 is usually negligible for melted polymers due to its low value (usually around 10^{-9} Pa^{-1}) [110, 113].

The accurate determination of the retardation spectrum from only creep experiments is not trivial. This is due to the relatively small amount of the term $\psi(t)$, which is described by the retardation spectrum, as compared to the term t / η_0 when the steady state is reached (*c.f. chapter 2, section 2.3.3, figure 2.14*). This fact may account for significant errors of prediction toward long measurement times [107].

From oscillatory shear experiments

While $H(\tau)$ spectrum may be determined from the dynamic complex modulus, the discrete and continuous $L(\lambda)$ spectrum can be calculated from the complex compliance using e*quation 9.10* and *9.11*, respectively.

Discrete spectrum

$$J'(\omega) = J_0 + \sum_{i=1}^{n} l_i(\lambda_i)\left[\frac{1}{1+\omega^2\lambda_i^2}\right] \qquad \textbf{(9.10.a)}$$

$$J''(\omega) = \sum_{i=1}^{n} l_i(\lambda_i)\left[\frac{\omega\lambda_i}{1+\omega^2\lambda_i^2}\right] + \frac{t}{\eta_0} \qquad \textbf{(9.10.b)}$$

Continuous spectrum

$$J'(\omega) = J_0 + \int_0^{+\infty} L(\lambda)\left[\frac{1}{1+\omega^2\lambda^2}\right] d\lambda + \frac{t}{\eta_0} \qquad \textbf{(9.11.a)}$$

$$J''(\omega) = \int_0^{+\infty} L(\lambda)\left[\frac{\omega\lambda}{1+\omega^2\lambda^2}\right] d\lambda + \frac{t}{\eta_0} \qquad \textbf{(9.11.b)}$$

Interconvertion between continuous relaxation and retardation spectra

The interconvertion of the continuous retardation spectrum to continuous relaxation spectrum and *vice versa* is expressed as follows [110].

$$L(\ln\lambda) = \frac{H(\ln\tau)}{\left(G_e - \int_{-\infty}^{+\infty} \frac{H(\ln\tau)}{\tau/(t-1)} d\ln t\right)^2 + \pi^2 H(\ln\tau)^2} \text{ for } \lambda = \tau \qquad \textbf{(9.12)}$$

$$H(\ln\tau) = \frac{L(\ln\lambda)}{\left(J_0 + \int_{-\infty}^{+\infty} \frac{L(\ln\lambda)}{1 - t/\lambda} d\ln t - \frac{\lambda}{\eta}\right)^2 + \pi^2 L(\ln\lambda)^2} \quad \text{for } \tau = \lambda \qquad \textbf{(9.13)}$$

Commonly, if spectra predicted from two sets of experimental data are in good agreement, the material functions (*e.g.* $G'(\omega)$, $G''(\omega)$) which are calculated by integration of both spectra will also superpose. By contrast, the inverse scenario is not necessarily verified. He *et al.* [113] showed that two set of dynamic modulus may superpose but fail to yield the same continuous spectrum using rheological data of PP. This is due to the ill-posed problem, which result from the deconvolution of flawed experimental data sets using a pair of Fredholm integral equations (*c.f. equations 9.12* and *9.13*), in order to infer a continuous spectrum.

9.2. Physico-chemical characterization "*^{1}H NMR spectrum of SAmfE*"

No clear information is revealed in *figure 9.3* because the chemical structure of SAmfE is complex and several peaks probably overlap.

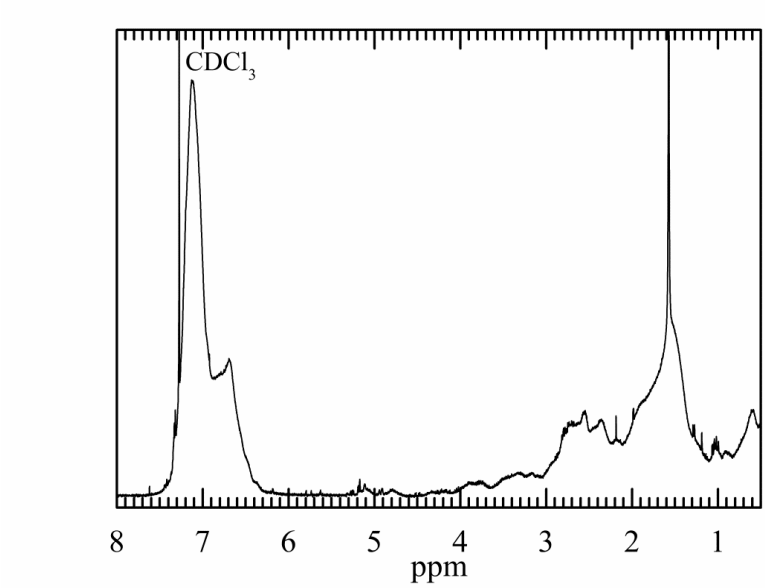

Figure 9.3. ^{1}H NMR spectrum of SAmfE raw material.

9.3. Thermal behaviour

9.3.1. Compression moulded plates – "*First DSC heating scans*"

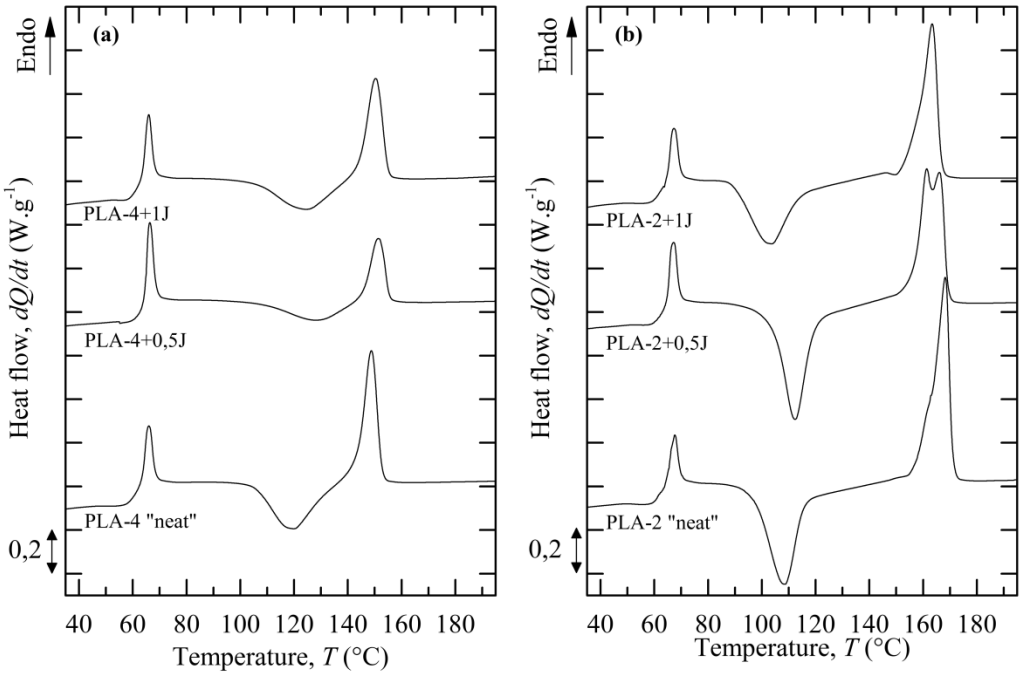

Figure 9.4. First heating scan (**H1**) at 10 ºC.min^{-1} for **(a)** PLA-4 and **(b)** PLA-2 based materials processed in an internal mixer. The corresponding thermal properties are compiled in *table 9.1*.

Table 9.1. Thermal properties during the first heating run of PLA-2 and PLA-4 based materials processed at laboratory scale.

	Parameters	PLA-2 "neat"	PLA-4 "neat"	PLA-2 +0.5J	PLA-4 +0.5J	PLA-2 +1J	PLA-4 +1J
First heating **(H1)**	$T_{g,m}$ (°C)	61 ±2	60 ±3	61 ±4	61 ±3	61 ±2	60 ±4
	T_{cc} (°C)	108.3 ±0.2	124 ±1	111.9 ±0.8	126 ±1	102.9 ±0.8	118 ±2
	ΔH_{cc} (J.g^{-1})	37 ±4	14 ±6	35 ±8	11 ±1	31 ±3	22 ±2
	$X_{c,cc}$ (%)	40 ±5	15 ±6	37 ±8	11 ±1	33 ±3	23 ±3
	T_{mp1} (°C)	167 ±1	150.0 ±0.8	161.3 ±0.3	151.4 ±0.4	163.2 ±0.2	148.5 ±0.5
	T_{mp2} (°C)	-	-	165.7 ±0.6	-	-	
	T_{me} (°C)	173.8 ±0.3	158.4 ±0.5	172.4 ±0.6	158.3 ±0.3	169.2 ±0.3	155.2 ±0.8
	ΔH_m (J.g^{-1})	39 ±3	16 ±4	34 ±7	10.7 ±0.7	32 ±2	22 ±2
	$X_{c,m}$ (%)	42 ±3	17 ±5	37 ±8	11 ±1	34 ±3	23 ±3
	X_c (%)	2±2	1 ±1	1 ±1	1 ±1	1 ±1	0 ±0

9.3.2. Extruded sheets

a) Self nucleation experiments

SN experiments (*c.f.* thermal protocol described in *chapter 5, section 5.1.5.b*) were performed in order to determine the temperature that yields the maximum self-nucleation without annealing (T_{s1}). This temperature will be used in the SSA protocol designed for REX-calendered samples. The cooling and heating scans after thermal conditioning at the indicated T_s are shown in *figure 9.5* and *9.6* for PLA4 and PLA2 samples, respectively.

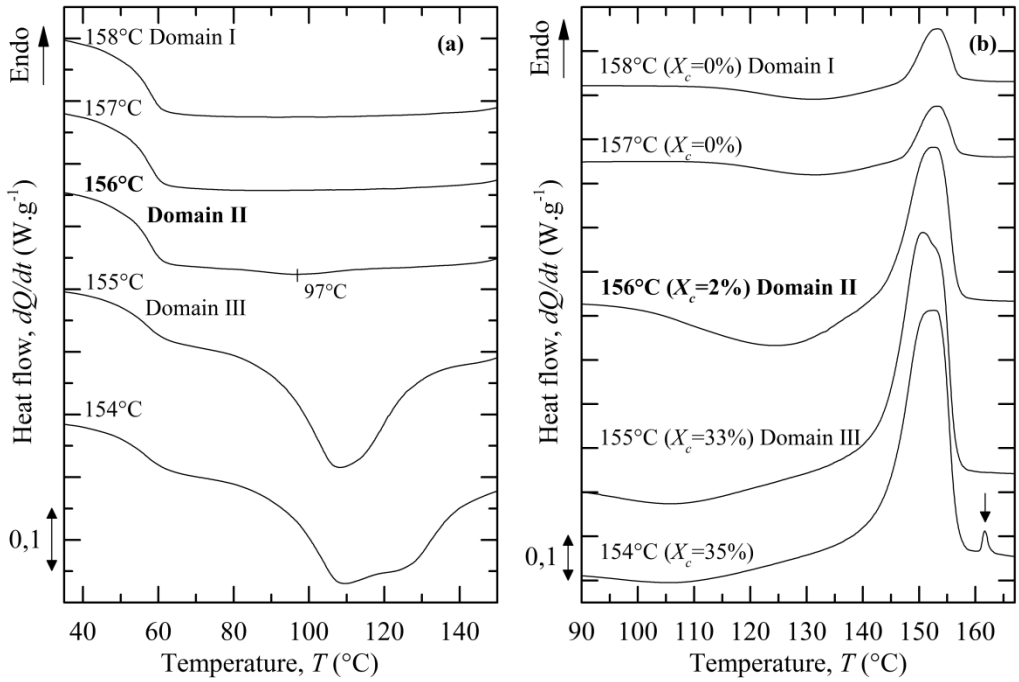

Figure 9.5. (a) cooling and **(b)** heating scans at 10 ºC.min^{-1} after SN at the indicated T_s temperatures for PLA4 samples. The degree of crystallinity developed during the thermal cycle is indicated in brackets.

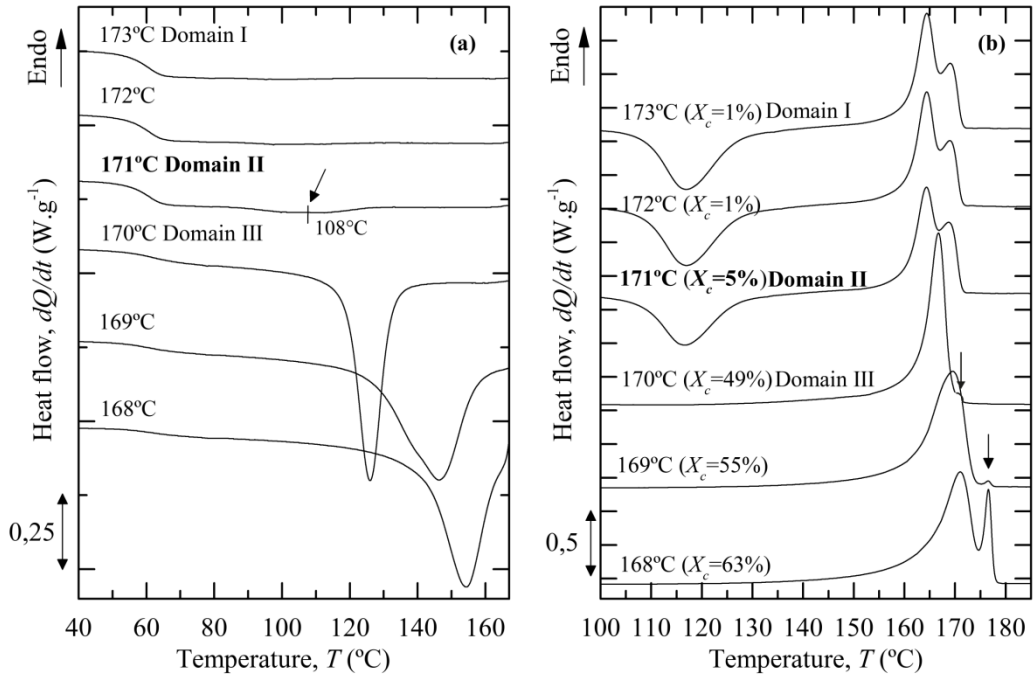

Figure 9.6. (a) cooling and **(b)** heating scans at 10 ºC.min^{-1} after SN at the indicated T_s temperatures for PLA2 samples. The degree of crystallinity developed during the thermal cycle is indicated in brackets.

When PLA4 and PLA2 were thermally conditioned for 5 min above 156 and 171 °C, respectively, both samples presented similar thermal behaviour in both the subsequent cooling (step **e**) and heating (step **f**) runs of the protocol showed in *figure 5.3* (*c.f. chapter 5, section 5.1.5.b*). This behaviour suggests that all crystalline memory was erased at these T_s temperatures; indicating the characteristic behaviour of domain I.

After being thermally conditioned at 156 and 171 °C, a crystallization shoulder centered in 97 and 108 ºC was exhibited by PLA4 and PLA2 samples in the subsequent cooling scans, respectively. On the other hand, PLA4 samples exhibited a higher melting endotherm (but the shape remained similar), while the melting endotherm of PLA2 samples remained fairly unaffected in step **f** as compared to those obtained in step **c**. This thermal behaviour suggests that the T_s temperature was high enough to melt almost all of the polymer crystals, but low enough to leave "small" crystal fragments that can act as self-nuclei. Upon cooling, they recrystallized but due do to their infinitely small sizes they cannot be annealed [68, 81]. This behaviour is characteristic of domain II.

Temperatures below 156 and 171 °C produced self-nucleation and annealing which revealed the typical behaviour of polymers in domain III. While crystallization took place almost immediately on cooling, both materials exhibited large crystallization exotherms with decreasing the T_s temperature. On reheating, an additional endothermic peak at high temperatures was observed (around 162 and 176 ºC for PLA4 and PLA2, respectively. Indicated by an arrow) and both T_{mp} and X_c increased with decreasing T_s.

An optimum self-nucleation temperature was found at 156 and 171 ºC for PLA4 and PLA2 samples, respectively.

b) DMTA analysis: *"Loss modulus"*

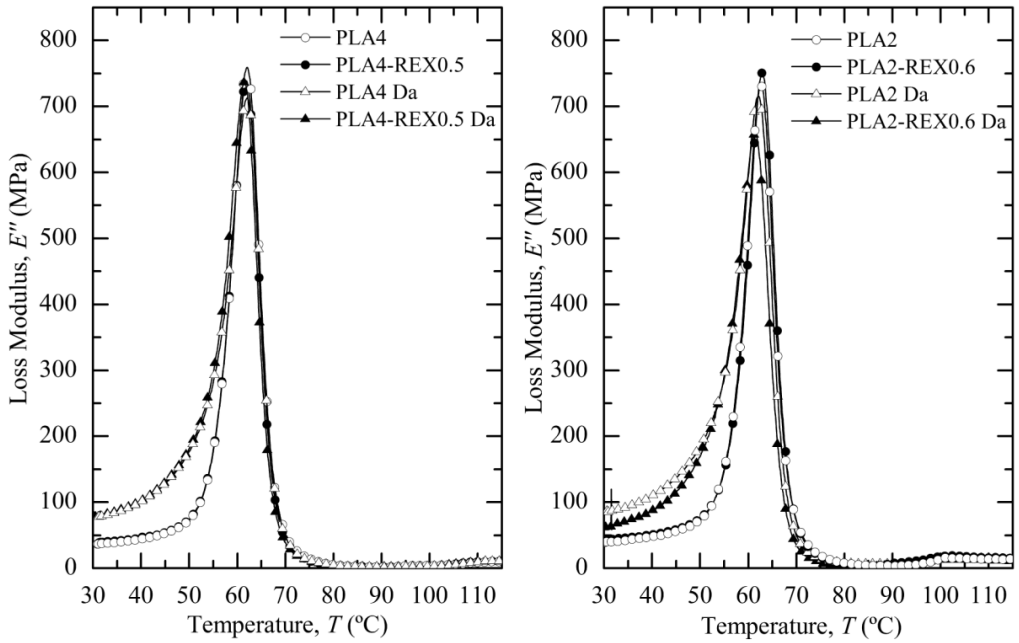

Figure 9.7. Loss modulus traces for de-aged and aged PLA-4 and PLA-2 based materials tested in MD at 2°C.min^{-1}.

c) First DSC heating scans for de-aged stretched tensile samples

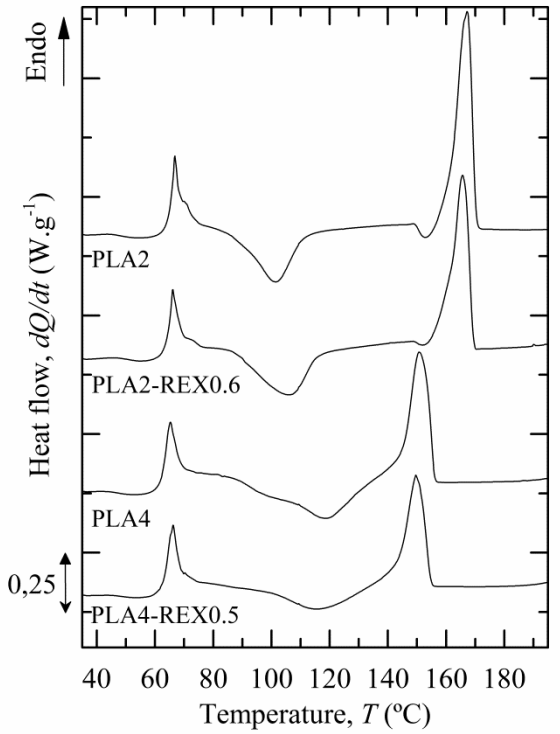

Figure 9.8. First heating scan (**H1)** at 10 ºC.min^{-1} for samples extracted from the necked zone of de-aged tensile samples stretched at 100% of their initial length.

Table 9.2. Thermal parameters obtained from the first heating scans (**H1)** depicted in *figure 9.8*.

Parameters	**PLA4**	**PLA4-REX0.5**	**PLA2**	**PLA2-REX0.6**
$T_{g,m}$ (°C)	61.2 ±0.3	61.4 ±0.2	61.9 ±0.6	63 ±1
T_{cc} (°C)	119.1 ±0.7	118 ±2	101.6 ±0.4	105.6 ±0.8
ΔH_{cc} (J.g^{-1})	25 ±1	17 ±2	21 ±2	22 ±1
$X_{c,cc}$ (%)	27 ±1	18 ±2	22 ±2	23 ±1
T_{mp} (°C)	149 ±4	150.0 ±0.4	167.1 ±0.1	165 ±2
ΔH_m (J.g^{-1})	26 ±1	21 ±1	35 ±2	32.7 ±0.6
$X_{c,m}$ (%)	28 ±1	22 ±2	38 ±2	34.7 ±0.6
X_c (%)	2 ±1	3 ±3	16 ±2	12 ±1

Results suggest that the cold-crystallization temperature shifted to lower temperatures for stretched samples as compared to unstretched ones (*c.f.* de-aged samples, *chapter 7, section 7.5.3, table 7.14*). This behaviour was attributed to the

molecular orientation which promotes cold crystallization, as already reported Karger-Kocsis [415] for stretched PET resins.

9.4. Rheological methods "*Evolution of the degree of crystallinity throughout rheological testing performed between T_g and T_{me}*"

9.4.1. Thermal protocol

Similar devices as described in *section 5.1.5* (*c.f chapter 5*) were used to investigate the evolution of the degree of crystallinity of PLA and PLA-REX samples throughout rheological testing which were conducted between T_g and T_{me}. In a typical procedure, 5-6 mg of each sample were hermetically encapsulated in Tzero DSC aluminium pans and were subjected to the following thermal protocol (see *figure 9.9* for a schematic representation of the procedure):

- **Erasure** of the previous thermal history by heating the sample to 200 ºC for t_{eq}=2 min.
- **Quenching** (**Q1**) from 200 °C to -10 °C at 100 °C.min^{-1} (maximum cooling rate) and isothermally held at -10 °C for t_{eq}=2 min. Samples were quenched into the glassy state at a high cooling rate in order to avoid crystallization.
- **Heating scan** (**H1**) from -10 °C to the "rheological testing" temperature (T_a) at 100 °C.min^{-1} to simulate sample loading and trimming before rheological testing.
- **Isothermal step** (**I**) at T_a for an annealing time (t_a) =24 min to simulate the testing time required to complete a frequency sweep (628.3 to 0.0623 rad.s^{-1}) with 10 points per decade.
- **Quenching** (**Q2**) from T_a to -10 °C at 100 °C.min^{-1} and isothermally held at -10 °C for t_{eq}=2 min.
- **Heating scan** (**H2**) from -10 °C to 30 °C at 50 °C.min^{-1} to quickly bring samples to room temperature.
- **Heating scan** (**H3**) from 30 °C to 200 °C at 10 °C.min^{-1} to reveal the degree of crystallinity developed throughout the simulated "frequency sweep".

Samples were subjected to isothermals step at T_a= 70, 80 and 85 ºC with the aim to ensure rheological data in the glassy region. For higher testing temperatures, PLA-4 based samples were subjected to annealing step at 150 ºC, while PLA-2 based samples at 150, 160 and 170 ºC. These temperatures were selected according to the available temperature range between the end of the cold-crystallization transition and T_{me}. Each of the DSC measurement was repeated three times using fresh samples in order to improve accuracy.

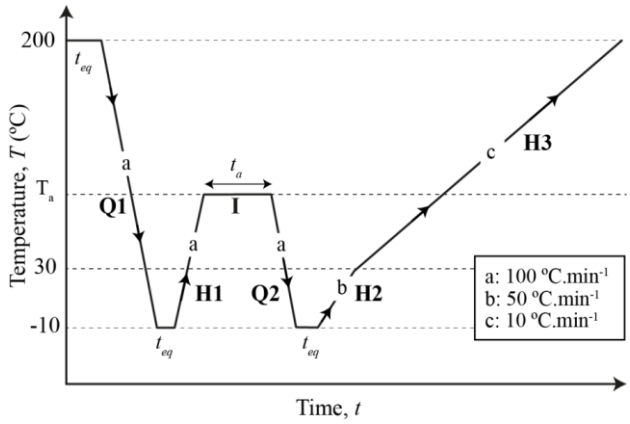

Figure 9.9. Schematic representation of the procedure used to investigate the remaining amorphous character throughout rheological testing.

9.4.2. DSC heating scan

Figures 9.10 and *9.11* present the final heating scans of PLA and PLA-REX samples after being annealed at different T_a. For the sake of clarity, solely T_a temperatures that yielded a subsequent amorphous state were represented.

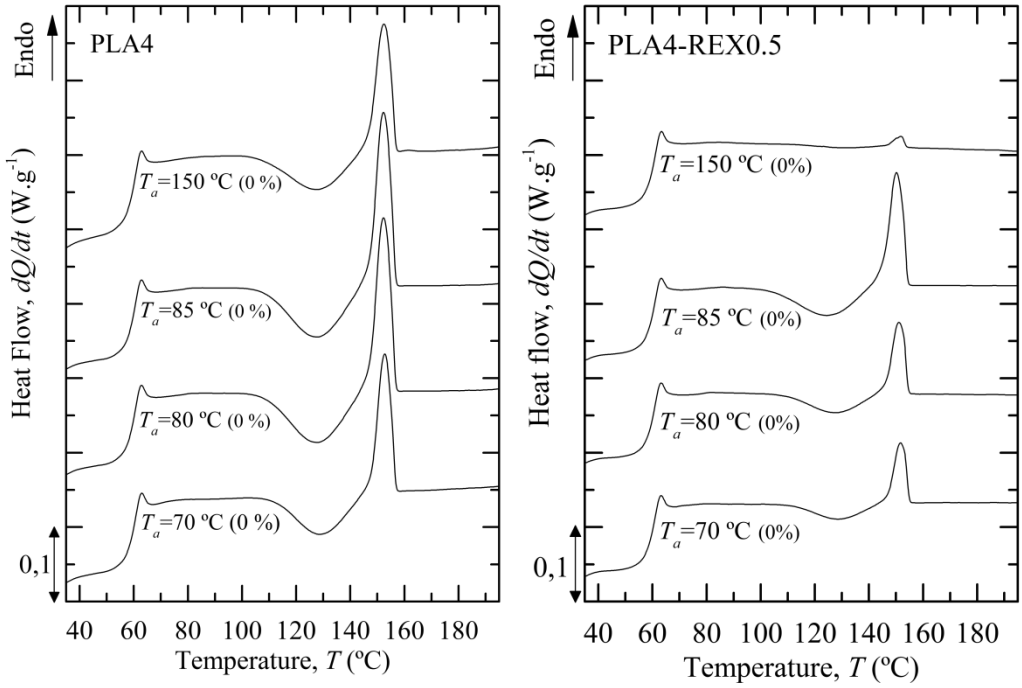

Figure 9.10. Final DSC heating scans (**H3**) for PLA4 and PLA4-REX0.5 samples annealed at different T_a for $\boldsymbol{t_a}$**=24 min**. The degree of crystallinity developed at each T_a is indicated in brackets.

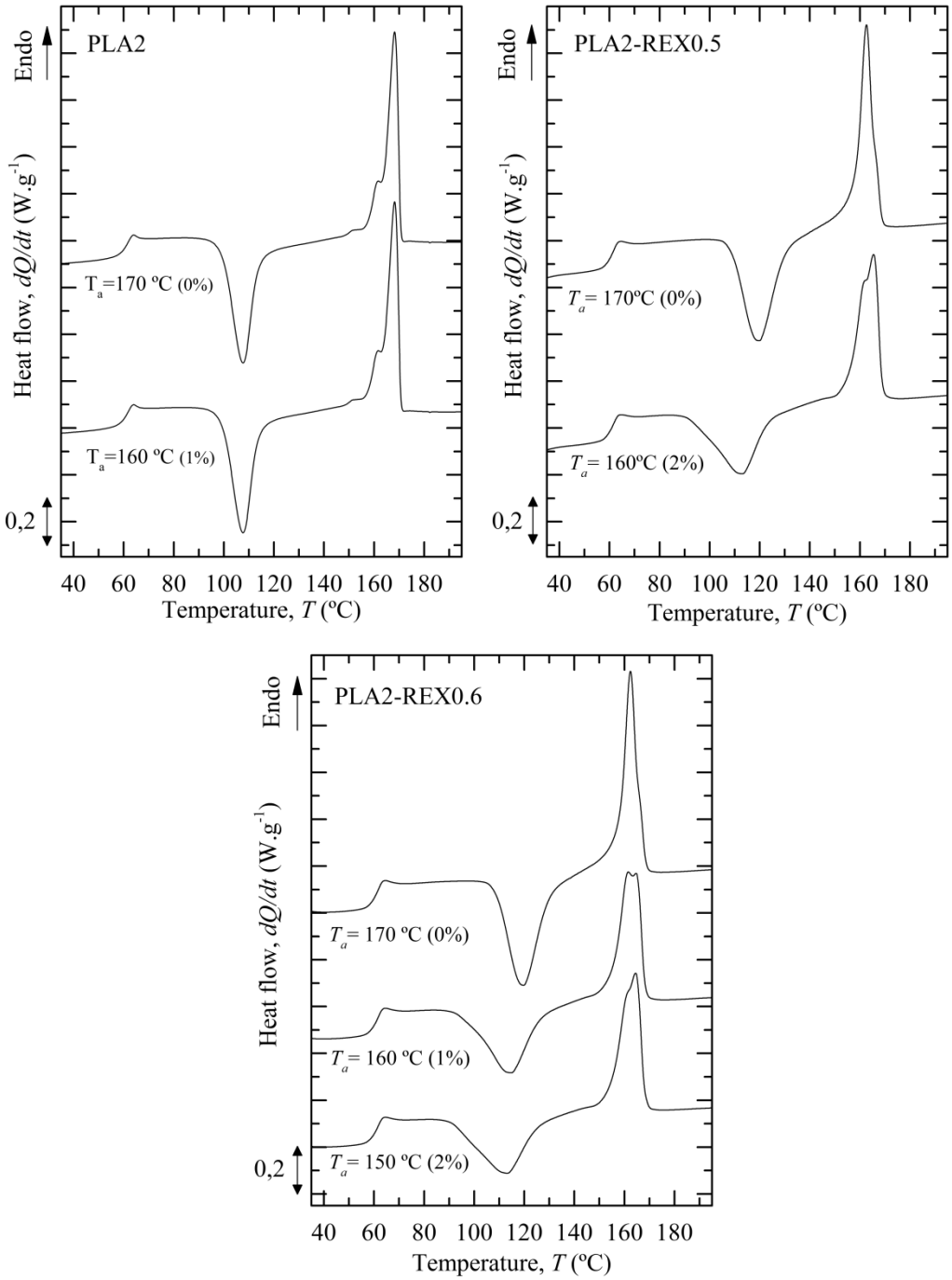

Figure 9.11. Final DSC heating scans (**H3**) for PLA2, PLA2-REX0.5 and PLA2-REX0.6 samples annealed at T_a=170 °C for $\boldsymbol{t_a}$**=25 min** and T_a=160-150 °C for $\boldsymbol{t_a}$**=2 min** (partial frequency sweep). The degree of crystallinity developed at each T_a is indicated in brackets.

Under the above described annealing conditions, PLA-4 based samples did not crystallized in the absence of self-seeding nucleus. These results suggest that complete frequency sweeps can be carried out over all the T_a temperatures considered below T_{me} (*i.e.* 70, 80, 85 and 150 °C).

After being annealed for 25 min, results suggest that PLA-2 based samples did not crystallized solely at T_a=170 ºC. This trend was attributed to their larger sensitivity to crystallize as compared to PLA-4 based materials. Since this analysis aimed to enlarge the temperature window for rheological measurements, similar experiments were repeated at T_a=160 and 150 °C but with a lowered t_a. That is, a maximum testing time of t_a = 2 min at T_a=160 °C was established in order to maintain a molecular arrangement totally disordered for all three samples. At T_a=150 °C, only PLA2-REX0.6 did not crystallize after being annealed for 2 min. This behaviour was attributed to its higher degree of structural modifications which possibly inhibits crystallization process. Based on this reduced testing time, the experimental frequency range should be equally reduced and viscoelastic measurements could be only collected from 628.3 to 12.5 rad.s^{-1} at T_a= 160 and 150 °C.

9.4.2. Storage and loss modulus calculations

The rationalization of the Havriliak-Negami model (*c.f. chapter 2, section 2.3.4.e, equation 2.48*) into the real (η') and imaginary (η'') components of $|\eta^*|$ enable the prediction of the viscoelastic modulus functions (G' and G'') as follows:

$$G'(\omega) = -\eta_0 Z \sin[\beta\phi]\,\omega \tag{9.14}$$

$$G''(\omega) = \eta_0 Z \cos[\beta\phi]\,\omega \tag{9.15}$$

Where

$$Z = \left[1 + 2(\tau_0\omega)^{\alpha}\cos\left(\alpha\frac{\pi}{2}\right) + (\tau_0\omega)^{2\alpha}\right]^{\beta/2} \tag{9.16}$$

$$\beta = \frac{(\nu - 1)}{\alpha} \tag{9.17}$$

And

$$\phi = \operatorname{atan}\left[\frac{(\tau_0\omega)^{\alpha}\sin\left(\alpha\frac{\pi}{2}\right)}{1 + (\tau_0\omega)^{\alpha}\cos\left(\alpha\frac{\pi}{2}\right)}\right] \tag{9.18}$$

By using a similar mathematical procedure, the rationalization of the extended Havriliak-Negami model (*c.f. chapter 2, section 2.3.4.e, equation 2.50*) with *n*=2 leads to:

$$G'(\omega) = -\eta_0[Z_1 \sin(\beta_1\phi_1) + Z_2 \sin(\beta_2\phi_2)]\omega \quad \textbf{(9.19)}$$

$$G''(\omega) = \eta_0[Z_1 \cos(\beta_1\phi_1) + Z_2 \cos(\beta_2\phi_2)]\omega \quad \textbf{(9.20)}$$

Where

$$Z_1 = \left[1 + 2(\tau_1\omega)^{\alpha_1}\cos\left(\alpha_1\frac{\pi}{2}\right) + (\tau_1\omega)^{2\alpha_1}\right]^{\beta_1/2} \quad \textbf{(9.21)}$$

$$Z_2 = \left[1 + 2(\tau_2\omega)^{\alpha_2}\cos\left(\alpha_2\frac{\pi}{2}\right) + (\tau_2\omega)^{2\alpha_2}\right]^{\beta_2/2} \quad \textbf{(9.22)}$$

$$\beta_1 = \frac{(\nu_1 - 1)}{\alpha_1} \quad \textbf{(9.23)}$$

$$\beta_2 = \frac{(\nu_2 - 1)}{\alpha_2} \quad \textbf{(9.24)}$$

And

$$\phi_1 = \operatorname{atan}\left[\frac{(\tau_1\omega)^{\alpha_1}\sin\left(\alpha_1\frac{\pi}{2}\right)}{1 + (\tau_1\omega)^{\alpha_1}\cos\left(\alpha_1\frac{\pi}{2}\right)}\right] \quad \textbf{(9.25)}$$

$$\phi_2 = \operatorname{atan}\left[\frac{(\tau_2\omega)^{\alpha_2}\sin\left(\alpha_2\frac{\pi}{2}\right)}{1 + (\tau_2\omega)^{\alpha_2}\cos\left(\alpha_2\frac{\pi}{2}\right)}\right] \quad \textbf{(9.26)}$$

All parameters are similarly defined as in *equations 2.48* and *2.50*.

References

Paper resulting from this PhD. thesis

[*i*] **Cailloux J.**, Santana O. O., Franco-Urquiza E., Bou J. J., Carrasco F.,. Gamez-Perez J, Maspoch M. Ll. *Sheets of branched poly(lactic acid) obtained by one step reactive extrusion calendering process: Melt rheology analysis*. eXPRESS Polymer Letters, 2013; 7(3): 304-318 (DOI: 10.3144/expresspolymlett.2013.27).

[*ii*] **Cailloux J.**, Santana O. O., Franco-Urquiza E., Bou J. J., Carrasco F., Maspoch M. Ll. *Sheets of branched poly(lactic acid) obtained by one step reactive extrusion calendering process: Physical Aging and Fracture Behaviour*, Journal of Materials Science. 2014; 49(11): 4093-4107 (DOI: 10.1007/s10853-014-8101-y).

[*iii*] Maspoch M. Ll, Santana O. O., **Cailloux J.**, Rodriguez C., Franco-Urquiza E., Belzunce J., Martinez A. B. *Ductile-brittle transition behavior of PLA/o-MMT films during the physical aging process*, eXPRESS Polymer Letters, 2015; 9(3): 185-195 (DOI: 10.3144/expresspolymlett.2015.20).

[*iv*] **Cailloux J.**, Santana O. O., Bou J. J., Carrasco F., Maspoch M. Ll. *Using Viscoelastic Properties to Quantitatively Estimate the Amount of Modified Poly(Lactic Acid) Chains through Reactive Extrusion*, Journal of Rheology. 2015; 59(5): 1191-1227 (DOI: 10.1122/1.4928071).

Other references

[1] *Bioplastics packaging-combining performance with sustainability*. www.european-bioplastics.org (Accessed Date: 22/11/2013).
[2] Endres H.J., Siebert-Raths A., *Engineering Biopolymers: Markets, Manufacturing, Properties ans Applications*. Hanser, Munich; 2011.
[3] Endres H.J., Siebert A., Kaneva Y., *Overview of the current biopolymers market situation*. Bioplastics Magazine. 2007; 2.
[4] *What are bioplastics? Material types, terminology and labels-an introduction*. www.european-bioplastics.org (Accessed Date: 22/11/2013).
[5] Burgos Bolufer N., *Desarrollo de bionanocompuestos en base a poli(acido lactico) y plastificantes de alta compatibilidad par el envasado de alimentos.* Ph.D. Thesis, Universidad de Alicante; Alicante (2013).
[6] Shen L., Worrell E., Patel M., *Present and future development in plastics from biomass*. Biofuel Bioprod Bior. 2010; 4(1): 25-40.
[7] Iida K., Harada M., Okamoto K., Hayashi H., Hirano K., *Reactive compatibilization of biodegradable poly(lactic acid)/poly(epsilon-caprolactone) blends with reactive processing agents*. Polym Eng Sci. 2008; 48(7): 1359-1368.

[8] Hu Y., Rogunova M., Topolkaraev V., Hiltner A., Baer E., *Aging of poly(lactide)/poly(ethylene glycol) blends. Part 1. Poly(lactide) with low stereoregularity*. Polymer. 2003; 44(19): 5701-5710.
[9] Yuan H., Liu Z.Y., Ren J., *Preparation, Characterization, and Foaming Behavior of Poly(lactic acid)/Poly(butylene adipate-co-butylene terephthalate) Blend*. Polym Eng Sci. 2009; 49(5): 1004-1012.
[10] Siracusa V., Rocculi P., Romani S., Dalla Rosa M., *Biodegradable polymers for food packaging: a review*. Trends Food Sci Tech. 2008; 19(12): 634-643.
[11] Auras R., Harte B., Selke S., *An overview of polylactides as packaging materials*. Macromol Biosci. 2004; 4(9): 835-864.
[12] Garlotta D., *A literature review of poly(lactic acid)*. J Polym Environ. 2001; 9(2): 63-84.
[13] Groot W., Krieken J.V., Sliekersl O., Vos S.d., Production and Purification of Lactic Acid and Lactide in: Auras R, Lim LT, Selke SEM, Tsuji H, (Eds.), *Poly(Lactic Acid): Synthesis, Structures, Properties, Processing and Applications*, Wiley, Hoboken (USA); 2010. p. 3-18.
[14] Auras R., Lim L.T., Selke S.E.M., Tsuji H., *Poly(Lactic Acid): Synthesis, Structures, Properties, Processing and Applications*. Wiley, Hoboken (USA); 2010.
[15] Lim L.T., Auras R., Rubino M., *Processing technologies for poly(lactic acid)*. Prog Polym Sci. 2008; 33(8): 820-852.
[16] Bogaert J.C., Coszach P., *Poly(lactic acids): A potential solution to plastic waste dilemma*. Macromol Symp. 2000; 153: 287-303.
[17] Dorgan J.R., Lehermeier H.J., Palade L.I., Cicero J., *Polylactides: Properties and prospects of an environmentally benign plastic from renewable resources*. Macromol Symp. 2001; 175: 55-66.
[18] Gruber P.R., *Cargill Dow LLC*. Journal of Industrial Ecology. 2004; 7(3-4): 209-213.
[19] Miyata T., Masuko T., *Crystallization behaviour of poly(L-lactide)*. Polymer. 1998; 39(22): 5515-5521.
[20] Sarasua J.R., Prud'homme R.E., Wisniewski M., Le Borgne A., Spassky N., *Crystallization and melting behavior of polylactides*. Macromolecules. 1998; 31(12): 3895-3905.
[21] Tsuji H., Ikada Y., *Crystallization from the melt of poly(lactide)s with different optical purities and their blends*. Macromol Chem Physic. 1996; 197(10): 3483-3499.
[22] Conn R.E., Kolstad J.J., Borzelleca J.F., Dixler D.S., Filer L.J., Ladu B.N., et al., *Safety Assessment of Polylactide (Pla) for Use as a Food-Contact Polymer*. Food Chem Toxicol. 1995; 33(4): 273-283.
[23] Datta R., Tsai S.P., Bonsignore P., Moon S.H., Frank J.R., *Technological and Economic-Potential of Poly(Lactic Acid) and Lactic-Acid Derivatives*. Fems Microbiol Rev. 1995; 16(2-3): 221-231.
[24] Najafi N., Heuzey M.C., Carreau P.J., *Polylactide (PLA)-clay nanocomposites prepared by melt compounding in the presence of a chain extender*. Compos Sci Technol. 2012; 72(5): 608-615.
[25] Urayama H., Moon S.I., Kimura Y., *Microstructure and thermal properties of polylactides with different L- and D-unit sequences: Importance of the helical nature of the L-sequenced segments*. Macromol Mater Eng. 2003; 288(2): 137-143.

[26] Qin L.J., Qiu J.H., Liu M.Z., Ding S.L., Shao L.A., Lu S.Y., et al., *Mechanical and thermal properties of poly(lactic acid) composites with rice straw fiber modified by poly(butyl acrylate)*. Chem Eng J. 2011; 166(2): 772-778.
[27] Pan P.J., Zhu B., Inoue Y., *Enthalpy relaxation and embrittlement of Poly(L-lactide) during physical aging*. Macromolecules. 2007; 40(26): 9664-9671.
[28] Byrne F., Ward P.G., Kennedy J., Imaz N., Hughes D., Dowling D.P., *The Effect of Masterbatch Addition on the Mechanical, Thermal, Optical and Surface Properties of Poly(lactic acid)*. J Polym Environ. 2009; 17(1): 28-33.
[29] Gupta A.P., Kumar V., *New emerging trends in synthetic biodegradable polymers - Polylactide: A critique*. Eur Polym J. 2007; 43(10): 4053-4074.
[30] Carrasco F., Pages P., Gamez-Perez J., Santana O.O., Maspoch M.L., *Processing of poly(lactic acid): Characterization of chemical structure, thermal stability and mechanical properties*. Polym Degrad Stabil. 2010; 95(2): 116-125.
[31] Badia J.D., Stromberg E., Karlsson S., Ribes-Greus A., *Material valorisation of amorphous polylactide. Influence of thermo-mechanical degradation on the morphology, segmental dynamics, thermal and mechanical performance*. Polym Degrad Stabil. 2012; 97(4): 670-678.
[32] Sanchez M.S., Mathot V.B.F., Poel G.V., Ribelles J.L.G., *Effect of the cooling rate on the nucleation kinetics of poly(L-lactic acid) and its influence on morphology*. Macromolecules. 2007; 40(22): 7989-7997.
[33] Perego G., Cella G.D., Bastioli C., *Effect of molecular weight and crystallinity on poly(lactic acid) mechanical properties*. J Appl Polym Sci. 1996; 59(1): 37-43.
[34] Gamez-Perez J., Velazquez J., Franco Urquiza E.A., Velasco J.L., Maspoch M.L., *Comportamiento a fractura de dos grados comerciales de PLA: influencia de la estructura cristalina*. XXVII Encuentro del Grupo Español de Fractura. 2010; 12: 647-652.
[35] Lunt J., *Large-scale production, properties and commercial applications of polylactic acid polymers*. Polym Degrad Stabil. 1998; 59(1-3): 145-152.
[36] Tabi T., Sajo I.E., Szabo F., Luyt A.S., Kovacs J.G., *Crystalline structure of annealed polylactic acid and its relation to processing*. Express Polym Lett. 2010; 4(10): 659-668.
[37] Carrasco F., Gamez-Perez J., Santana O.O., Maspoch M.L., *Processing of poly(lactic acid)/organomontmorillonite nanocomposites: Microstructure, thermal stability and kinetics of the thermal decomposition*. Chem Eng J. 2011; 178: 451-460.
[38] Gamez-Perez J., Nascimento L., Bou J.J., Franco-Urquiza E., Santana O.O., Carrasco F., et al., *Influence of Crystallinity on the Fracture Toughness of Poly(lactic acid)/Montmorillonite Nanocomposites Prepared by Twin-Screw Extrusion*. J Appl Polym Sci. 2011; 120(2): 896-905.
[39] Carrasco F., Pages P., Gamez-Perez J., Santana O.O., Maspoch M.L., *Kinetics of the thermal decomposition of processed poly(lactic acid)*. Polym Degrad Stabil. 2010; 95(12): 2508-2514.
[40] Japon S., Luciani A., Nguyen Q.T., Leterrier Y., Manson J.A.E., *Molecular characterization and rheological properties of modified poly(ethylene terephthalate) obtained by reactive extrusion*. Polym Eng Sci. 2001; 41(8): 1299-1309.
[41] Japon S., Boogh L., Leterrier Y., Manson J.A.E., *Reactive processing of poly(ethylene terephthalate) modified with multifunctional epoxy-based additives*. Polymer. 2000; 41(15): 5809-5818.

[42] Raquez J.M., Narayan R., Dubois P., *Recent advances in reactive extrusion processing of biodegradable polymer-based compositions*. Macromol Mater Eng. 2008; 293(6): 447-470.
[43] Incarnato L., Scarfato P., Di Maio L., Acierno D., *Structure and rheology of recycled PET modified by reactive extrusion*. Polymer. 2000; 41(18): 6825-6831.
[44] Awaja F., Daver F., Kosior E., *Recycled poly(ethylene terephthalate) chain extension by a reactive extrusion process*. Polym Eng Sci. 2004; 44(8): 1579-1587.
[45] Haralabakopoulos A.A., Tsiourvas D., Paleos C.M., *Chain extension of poly(ethylene terephthalate) by reactive blending using diepoxides*. J Appl Polym Sci. 1999; 71(13): 2121-2127.
[46] Carlson D., Dubois P., Nie L., Narayan R., *Free radical branching of polylactide by reactive extrusion*. Polym Eng Sci. 1998; 38(2): 311-321.
[47] Corre Y.M., Duchet J., Reignier J., Maazouz A., *Melt strengthening of poly (lactic acid) through reactive extrusion with epoxy-functionalized chains*. Rheol Acta. 2011; 50(7-8): 613-629.
[48] Kowalski R.C., Xanthos M., Gaylord N.G., Brown S.B., Todd D.B., Biesenberger J.A., et al., *Reactive Extrusion: Principles and Practice*. Hanser, Hoboken (USA); 1992.
[49] Brinson H.F., Catherine Brinson L., Time and Temperature Behavior of Polymers, in: Brinson HF, Catherine Brinson L, (Eds.), *Polymer Engineering Science and Viscoelasticity: An Introduction*, 2 ed, Springer, New-York; 2015. p. 231-285.
[50] Chartoff R.P., Thermoplastic polymers, in: Turi E, editor, *Thermal Analysis of Polymers*, 2nd ed, Academic Press, 1997. p. 483-743.
[51] Cowie J.M.G., Harris S., Ewen I.J., *Physical Aging in Poly(vinyl acetate). 2. Relative Rates of Volume and Enthalpy Relaxation*. Macromolecules. 1998; 31(8): 2611-2615.
[52] Pan P., Zhu B., Dong T., Yazawa K., Shimizu T., Tansho M., et al., *Conformational and microstructural characteristics of poly(L-lactide) during glass transition and physical aging*. J Chem Phys. 2008; 129(18): 184902.
[53] Struik L.C.E., *Physical Aging in Amorphous Polymers and Other Materials*. Elsevier, Amsterdam; 1978.
[54] Foltz C.R., McKinney P.V., *Quantitative study of the annealing of poly(vinyl chloride) near the glass transition*. J Appl Polym Sci. 1969; 13(10): 2235-2245.
[55] Petrie S.E.B., *Thermal behavior of annealed organic glasses*. Journal of polymer Science Part B: Polymer Physics. 1972; 10(7): 1255-1272.
[56] Tangpasuthadol V., Shefer A., Hooper K.A., Kohn J., *Thermal properties and physical ageing behaviour of tyrosine-derived polycarbonates*. Biomaterials. 1996; 17(4): 463-468.
[57] Hodge I.M., Berens A.R., *Effects of Annealing and Prior History on Enthalpy Relaxation in Glassy Polymers. 2 . Mathematical Modeling*. Macromolecules. 1982; 15(3): 762-770.
[58] Hodge I.M., Huvard G.S., *Effects of Annealing and Prior History on Enthalpy Relaxation in Glassy Polymers. 3. Experimental and Modelling Studies of Polystyrene*. Macromolecules. 1983; 16(3): 371-375.
[59] Berens A.R., Hodge I.M., *Effects of Annealing and Prior History on Enthalpy Relaxation in Glassy polymers. 1. Experimental Study on Poly(vinyl chloride)*. Macromolecules. 1982; 15(3): 756-761.

[60] Hutchinson J.M., Smith S., Horne B., Gourlay G.M., *Physical aging of polycarbonate: Enthalpy relaxation, creep response, and yielding behavior*. Macromolecules. 1999; 32(15): 5046-5061.
[61] Lu H.B., Nutt S., *Restricted relaxation in polymer nanocomposites near the glass transition*. Macromolecules. 2003; 36(11): 4010-4016.
[62] Cowie J.M.G., Ferguson R., *Physical Aging Studies in Polyvinyl Methyl-Ether) .1. Enthalpy Relaxation as a Function of Aging Temperature*. Macromolecules. 1989; 22(5): 2307-2312.
[63] Cowie J.M.G., Ferguson R., *Physical Aging Studies in Polymer Blends .2. Enthalpy Relaxation as a Function of Aging Temperature in a Polyvinyl Methyl Ether Polystyrene Blend*. Macromolecules. 1989; 22(5): 2312-2317.
[64] ArefAzar A., Arnoux F., Biddlestone F., Hay J.N., *Physical ageing in amorphous and crystalline polymers .2. Polyethylene terephthalate*. Thermochim Acta. 1996; 273: 217-229.
[65] Atkinson J.R., Hay J.N., Jenkins M.J., *Enthalpic relaxation in semi-crystalline PEEK*. Polymer. 2002; 43(3): 731-735.
[66] Yoshioka T., Kawazoe N., Tateishi T., Chen G.P., *Effects of Structural Change Induced by Physical Aging on the Biodegradation Behavior of PLGA Films at Physiological Temperature*. Macromol Mater Eng. 2011; 296(11): 1028-1034.
[67] Kwon M., Lee S.C., Jeong Y.G., *Influences of Physical Aging on Enthalpy Relaxation Behavior, Gas Permeability, and Dynamic Mechanical Property of Polylactide Films with Various D-isomer Contents*. Macromol Res. 2010; 18(4): 346-351.
[68] Müller A.J., Arnal M.L., *Thermal fractionation of polymers*. Prog Polym Sci. 2005; 30(5): 559-603.
[69] Soares J.B.P., Hamielec A.E., *Temperature Rising Elution Fractionation of Linear Polyolefins*. Polymer. 1995; 36(8): 1639-1654.
[70] Xu J.T., Feng L.X., *Application of temperature rising elution fractionation in polyolefins*. Eur Polym J. 2000; 36(5): 867-878.
[71] Virkkunen V., Laari P., Pitkanen P., Sundholm F., *Tacticity distribution of isotactic polypropylene prepared with heterogeneous Ziegler-Natta catalyst. 2. Application and analysis of SSA data for polypropylene*. Polymer. 2004; 45(14): 4623-4631.
[72] Virkkunen V., Laari P., Pitkanen P., Sundholm F., *Tacticity distribution of isotactic polypropylene prepared with heterogeneous Ziegler-Natta catalyst. 1. Fractionation of polypropylene*. Polymer. 2004; 45(9): 3091-3098.
[73] Lodefier P., Jonas A.M., Legras R., *Chemical heterogeneity of poly(ethylene terephthalate) as revealed by temperature rising elution fractionation and its influence on polymer thermal behavior: A comparison with poly(ethylene terephthalate-co-isophthalate)*. Macromolecules. 1999; 32(21): 7135-7139.
[74] Monrabal B., *Crystallization Analysis Fractionation - a New Technique for the Analysis of Branching Distribution in Polyolefins*. J Appl Polym Sci. 1994; 52(4): 491-499.
[75] Gray A.P., Casey K., *Thermal Analysis + Influence of Thermal History on Polymer Fusion Curves*. Journal of Polymer Science Part B-Polymer Letters. 1964; 2(4pb): 381-&.

[76] Zhang M., Lynch D.T., Wanke S.E., *Effect of molecular structure distribution on melting and crystallization behavior of 1-butene/ethylene copolymers*. Polymer. 2001; 42(7): 3067-3075.
[77] Zhang M.Q., Lynch D.T., Wanke S.E., *Characterization of commercial linear low-density polyethylene by TREF-DSC and TREF-SEC cross-fractionation*. J Appl Polym Sci. 2000; 75(7): 960-967.
[78] Müller A.J., Hernandez Z.H., Arnal M.L., Sanchez J.J., *Successive self-nucleation/annealing (SSA): A novel technique to study molecular segregation during crystallization*. Polym Bull. 1997; 39(4): 465-472.
[79] Fillon B., Wittmann J.C., Lotz B., Thierry A., *Self-Nucleation and Recrystallization of Isotactic Polypropylene (Alpha-Phase) Investigated by Differential Scanning Calorimetry*. J Polym Sci Pol Phys. 1993; 31(10): 1383-1393.
[80] Arnal M.L., Sanchez J.J., Muller A.J., *Miscibility of linear and branched polyethylene blends by thermal fractionation: use of the successive self-nucleation and annealing (SSA) technique*. Polymer. 2001; 42(16): 6877-6890.
[81] Arnal M.L., Balsamo V., Ronca G., Sanchez A., Muller A.J., Canizales E., et al., *Applications of successive self-nucleation and annealing (SSA) to polymer characterization*. J Therm Anal Calorim. 2000; 59(1-2): 451-470.
[82] Marquez L., Rivero I., Muller A.J., *Application of the SSA calorimetric technique to characterize LLDPE grafted with diethyl maleate*. Macromol Chem Physic. 1999; 200(2): 330-337.
[83] Arnal M.L., Sanchez J.J., Muller A.J., *Applications of successive self-nucleation and annealing (SSA) in polyolefin blends characterization*. Antec '99: Plastics Bridging the Millennia, Conference Proceedings, Vols I-Iii. 1999: 2329-2333
[84] de Gascue B.R., Mendez B., Manosalva J.L., Lopez L., Quiteria V.R.S., Muller A.J., *Experimental analysis of the grafting products of diethyl maleate onto linear and branched polyethylenes*. Polymer. 2002; 43(8): 2151-2159.
[85] Tanem B.S., Stori A., *Blends of single-site linear and branched polyethylene. I. Thermal characterisation*. Polymer. 2001; 42(12): 5389-5399.
[86] Paolini Y., Ronca G.S., Feijoo J.L., Da Silva E., Ramirez J., Muller A.J., *Application of the SSA calorimetric technique to characterise an XLPE insulator aged under multiple stresses*. Macromol Chem Physic. 2001; 202(9): 1539-1547.
[87] Trujillo M., Arnal M.L., Mueller A.J., Bredeau S., Bonduel D., Dubois P., et al., *Thermal Fractionation and isothermal crystallization of polyethylene nanocomposites prepared by in situ polymerization*. Macromolecules. 2008; 41(6): 2087-2095.
[88] Lorenzo A.T., Arnal M.L., Muller A.J., de Fierro A.B., Abetz V., *High speed SSA thermal fractionation and limitations to the determination of lamellar sizes and their distributions*. Macromol Chem Physic. 2006; 207(1): 39-49.
[89] Sabino M.A., Feijoo J.L., Muller A.J., *Crystallisation and morphology of poly(p-dioxanone)*. Macromol Chem Physic. 2000; 201(18): 2687-2698.
[90] Sánchez Mora J.J., *Comportamiento Térmico y Mecánico del Poli(Etilén Tereftalato) (PET) Modificado con Resinas Polimericas Basadas en Bisfenol-A.* Ph.D. Thesis, Universidad Politechnica de Cataluña; Barcelona (2003).
[91] Ling X., Spruiell J.E., *Analysis of the Complex Thermal Behavior of Poly(L-lactic acid) Film. I. Samples Crystallized from the Glassy State*. J Polym Sci Pol Phys. 2006; 44(22): 3185-3303.

[92] Pan P., Kai W., Zhu B., Dong T., Inoue Y., *Polymorphous crystallization and multiple melting behavior of Poly(L-lactide): Molecular weight dependence*. Macromolecules. 2007; 40(19): 6898-6905.
[93] Di Lorenzo M.L., *Calorimetric analysis of the multiple melting behavior of poly(L-lactic acid)*. J Appl Polym Sci. 2006; 100(4): 3145-3151.
[94] Pilla S., Kramschuster A., Yang L.Q., Lee J., Gong S.Q., Turng L.S., *Microcellular injection-molding of polylactide with chain-extender*. Materials Science & Engineering: C. 2009; 29(4): 1258-1265.
[95] Dealy J.M., Larson R.G., Linear Viscoelasticity-Fundamentals, in: Dealy JM, Larson RG, (Eds.), *Structure and Rheology of Molten Polymers: From Structure to Flow Behavior and Back Again*, Hanser Publisher, Munich; 2006. p. 91-130.
[96] Dealy J.M., Larson R.G., Tube Models for Linear Polymers-Fundamentals, in: Dealy JM, Larson RG, (Eds.), *Structure and Rheology of Molten Polymers: From Structure to Flow Behavior and Back Again*, Hanser Publisher, Munich; 2006. p. 193-231.
[97] Mark J., Ngai K., Graessley W., Mandelkern L., Samulski E., Koenig J., et al., *Physical properties of Polymers*. American Chemical Society; 1984.
[98] Dealy J., Park H.E., Munstedt H., *Influence of long-chain branching on time-pressure and time-temperature shift factors for polystyrene and polyethylene*. Rheol Acta. 2006; 46(1): 153-159.
[99] van Ruymbeke E., Stephenne V., Daoust D., Godard R., Keunings R., Bailly C., *A sensitive method to detect very low levels of long chain branching from the molar mass distribution and linear viscoelastic response*. J Rheol. 2005; 49(6): 1503-1520.
[100] Wood-Adams P., Costeux S., *Thermorheological behavior of polyethylene: Effects of microstructure and long chain branching*. Macromolecules. 2001; 34(18): 6281-6290.
[101] Carella J.M., Graessley W.W., Fetters L.J., *Effects of Chain Microstructure on the Viscoelastic Properties of Linear Polymer Melts - Polybutadienes and Hydrogenated Polybutadienes*. Macromolecules. 1984; 17(12): 2775-2786.
[102] Al-Itry R., Lamnawar K., Maazouz A., *Reactive extrusion of PLA, PBAT with a multi-functional epoxide: Physico-chemical and rheological properties*. Eur Polym J. 2014; 58: 90-102.
[103] Van Gurp M., Palmen J., *Time-temperature superposition for polymeric blends*. XII th International Congress on Rheology, Proceedings. 1996: 134-135.
[104] Trinkle S., Friedrich C., *Van Gurp-Palmen-plot: a way to characterize polydispersity of linear polymers*. Rheol Acta. 2001; 40(4): 322-328.
[105] Dealy J.M., Larson R.G., Linear Viscoelasticity- Behavior of Molten Polymers, in: Dealy JM, Larson RG, (Eds.), *Structure and Rheology of Molten Polymers: From Structure to Flow Behavior and Back Again*, Hanser Publisher, Munich; 2006. p. 131-191.
[106] Franck A., *Creep Recovery Measurements of Polymers*. 77th Annual Meeting of the American Society of Rheology, TA Instrument (2005).
[107] Stadler F.J., *Molecular Structure and Rheological Properties of linear and Long-Chain Branched Ethene-/α-Olefin Copolymers*. Ph.D. Thesis, Friedlish-Alexander-University Erlangen-Nürnberg; Erlangen (2007).

[108] Auhl D., Stange J., Munstedt H., Krause B., Voigt D., Lederer A., et al., *Long-chain branched polypropylenes by electron beam irradiation and their rheological properties*. Macromolecules. 2004; 37(25): 9465-9472.
[109] Barnes H.A., Bell D., *Controlled-stress rotational rheometry: An historical review*. Korea-Aust Rheol J. 2003; 15(4): 187-196.
[110] TA_Instrument, *Spectral Analysis and the Interconversion of Linear Viscoelastic Functions*. Application Library, TA Instrument, (2005).
[111] TA_Instrument, *Application of Viscoelastic Transformations to Rheological Analysis of Human Biological Fluids*. Application Library, TA Instrument, (2005).
[112] Honerkamp J., Weese J., *A Nonlinear Regularization Method for the Calculation of Relaxation Spectra*. Rheol Acta. 1993; 32(1): 65-73.
[113] He C.X., Wood-Adams P., Dealy J.M., *Broad frequency range characterization of molten polymers*. J Rheol. 2004; 48(4): 711-724.
[114] Larson R.G., Sridhar T., Leal L.G., McKinley G.H., Likhtman A.E., McLeish T.C.B., *Definitions of entanglement spacing and time constants in the tube model*. J Rheol. 2003; 47(3): 809-818.
[115] Liu C.Y., He J.S., van Ruymbeke E., Keunings R., Bailly C., *Evaluation of different methods for the determination of the plateau modulus and the entanglement molecular weight*. Polymer. 2006; 47(13): 4461-4479.
[116] Dealy J.M., Larson R.G., Entanglements and the tube model, in: Dealy JM, Larson RG, (Eds.), *Structure and Rheology of Molten Polymers: From Structure to Flow Behavior and Back Again*, Hanser Publisher, Munich; 2006. p. 193-231.
[117] Wu S.H., Beckerbauer R., *Chain Entanglement in Homopolymers, Copolymers and Terpolymers of Methyl-Methacrylate, Styrene and N-Phenylmaleimide*. Polymer. 1992; 33(3): 509-515.
[118] Cooper-White J.J., Mackay M.E., *Rheological properties of poly(lactides). Effect of molecular weight and temperature on the viscoelasticity of poly(l-lactic acid)*. J Polym Sci Pol Phys. 1999; 37(15): 1803-1814.
[119] Wood-Adams P.M., Dealy J.M., deGroot A.W., Redwine O.D., *Effect of molecular structure on the linear viscoelastic behavior of polyethylene*. Macromolecules. 2000; 33(20): 7489-7499.
[120] Fetters L.J., Lohse D.J., Richter D., Witten T.A., Zirkel A., *Connection between Polymer Molecular-Weight, Density, Chain Dimensions, and Melt Viscoelastic Properties*. Macromolecules. 1994; 27(17): 4639-4647.
[121] Fetters L.J., Lohse D.J., Garcia-Franco C.A., Brant P., Richter D., *Prediction of melt state poly(alpha-olefin) rheological properties: The unsuspected role of the average molecular weight per backbone bond*. Macromolecules. 2002; 35(27): 10096-10101.
[122] Fetters L.J., Lohse D.J., Graessley W.W., *Chain dimensions and entanglement spacings in dense macromolecular systems*. J Polym Sci Pol Phys. 1999; 37(10): 1023-1033.
[123] Wu S., *Chain Structure and Entanglement*. J Polym Sci Pol Phys. 1989; 27(4): 723-741.
[124] Joziasse C.A.P., Veenstra H., Grijpma D.W., Pennings A.J., *On the chain stiffness of poly(lactide)s*. Macromol Chem Physic. 1996; 197(7): 2219-2229.
[125] Dealy J.M., Wissbrun K.F., *Melt Rheology and Its Role in Plastics Processing*. Klumer Academic Publishers, Dordrecht; 1999.

[126] Van Krevelen D.W., Te Nijenhuis K., Rheological properties of polymer melts, in: Van Krevelen DW, Te Nijenhuis K, (Eds.), *Poperties of Polymers: Their Correlation with Chemical Structure; their Numerical Estimation and Prediction from Additive Group Contributions*, Elsevier, Amsterdam; 2009. p. 525-599.
[127] Kraus G., Gruver J.T., *Rheological Properties of Multichain Polybutadienes*. J Polym Sci Part A. 1965; 3(1): 105-122.
[128] Lehermeier H.J., Dorgan J.R., *Melt rheology of poly(lactic acid): Consequences of blending chain architectures*. Polym Eng Sci. 2001; 41(12): 2172-2184.
[129] Dorgan J.R., Lehermeier H., Mang M., *Thermal and rheological properties of commercial-grade poly(lactic acid)s*. J Polym Environ. 2000; 8(1): 1-9.
[130] Dorgan J.R., Williams J.S., Lewis D.N., *Melt rheology of poly(lactic acid): Entanglement and chain architecture effects*. J Rheol. 1999; 43(5): 1141-1155.
[131] Sungsanit K., Kao N., Bhattacharya S.N., Pivsaart S., *Physical and rheological properties of plasticized linear and branched PLA*. Korea-Aust Rheol J. 2010; 22(3): 187-195.
[132] Gabriel C., Munstedt H., *Influence of long-chain branches in polyethylenes on linear viscoelastic flow properties in shear*. Rheol Acta. 2002; 41(3): 232-244.
[133] Archer L.A., Varshney S.K., *Synthesis and relaxation dynamics of multiarm polybutadiene melts*. Macromolecules. 1998; 31(18): 6348-6355.
[134] McLeish T.C.B., Milner S.T., *Entangled dynamics and melt flow of branched polymers*. Branched Polymers Ii. 1999; 143: 195-256.
[135] McLeish T.C.B., Allgaier J., Bick D.K., Bishko G., Biswas P., Blackwell R., et al., *Dynamics of entangled H-polymers: Theory, rheology, and neutron-scattering*. Macromolecules. 1999; 32(20): 6734-6758.
[136] Vega J., Aguilar M., Peón J., Pastor D., Martínez-Salazar J. Effect of long chain branching on linear-viscoelastic melt properties of polyolefins. e-Polymers; 2002. p. 1-35.
[137] Doerpinghaus P.J., Baird D.G., *Separating the effects of sparse long-chain branching on rheology from those due to molecular weight in polyethylenes*. J Rheol. 2003; 47(3): 717-736.
[138] Shroff R.N., Mavridis H., *Long-chain-branching index for essentially linear polyethylenes*. Macromolecules. 1999; 32(25): 8454-8464.
[139] Stadler F.J., Munstedt H., *Terminal viscous and elastic properties of linear ethene/alpha-olefin copolymers*. J Rheol. 2008; 52(3): 697-712.
[140] Garcia-Franco C.A., Lohse D.J., Robertson C.G., Georjon O., *Relative quantification of long chain branching in essentially linear polyethylenes*. Eur Polym J. 2008; 44(2): 376-391.
[141] Trinkle S., Walter P., Friedrich C., *Van Gurp-Palmen Plot II - Classification of long chain branched polymers by their topology*. Rheol Acta. 2002; 41(1-2): 103-113.
[142] Lai S., Plumley T.A., Butler T.I., Knight G.W., Kao C.I., *Dow Rheology Index (DRI) For Insite Technology Polyolefins (ITP): Unique Structure-Processing Relationships* Annual Technical Conference-Society of Plastics Engineers. 1994; 40: 1814-1815.
[143] Munstedt H., Auhl D., *Rheological measuring techniques and their relevance for the molecular characterization of polymers*. J Non-Newton Fluid. 2005; 128(1): 62-69.

[144] Stadler F.J., Piel C., Kaschta J., Rulhoff S., Kaminsky W., Munstedt H., *Dependence of the zero shear-rate viscosity and the viscosity function of linear high-density polyethylenes on the mass-average molar mass and polydispersity*. Rheol Acta. 2006; 45(5): 755-764.
[145] Munstedt H., *Dependence of the Elongational Behavior of Polystyrene Melts on Molecular-Weight and Molecular-Weight Distribution*. J Rheol. 1980; 24(6): 847-867.
[146] Fleissner M., *Characterization of Polymer Molecular Mass-Distribution from Rheological Measurements*. Makromol Chem-M Symp. 1992; 61: 324-341.
[147] Janzen J., Colby R.H., *Diagnosing long-chain branching in polyethylenes*. J Mol Struct. 1999; 485: 569-584.
[148] Gabriel C., Kokko E., Lofgren B., Seppala J., Munstedt H., *Analytical and rheological characterization of long-chain branched metallocene-catalyzed ethylene homopolymers*. Polymer. 2002; 43(24): 6383-6390.
[149] Stadler F.J., Piel C., Kaminsky W., Munstedt H., *Rheological characterization of long-chain branched polyethylenes and comparison with classical analytical methods*. Macromol Symp. 2006; 236: 209-218.
[150] Piel C., Stadler F.J., Kaschta J., Rulhoff S., Munstedt H., Kaminsky W., *Structure-property relationships of linear and long-chain branched metallocene high-density polyethylenes and SEC-MALLS*. Macromol Chem Physic. 2006; 207(1): 26-38.
[151] Malmberg A., Gabriel C., Steffl T., Munstedt H., Lofgren B., *Long-chain branching in metallocene-catalyzed polyethylenes investigated by low oscillatory shear and uniaxial extensional rheometry*. Macromolecules. 2002; 35(3): 1038-1048.
[152] Lohse D.J., Milner S.T., Fetters L.J., Xenidou M., Hadjichristidis N., Mendelson R.A., et al., *Well-defined, model long chain branched polyethylene. 2. Melt rheological behavior*. Macromolecules. 2002; 35(8): 3066-3075.
[153] Gotsis A.D., Zeevenhoven B.L.F., Tsenoglou C.J., *Effect of long branches on the rheology of polypropylene*. J Rheol. 2004; 48(4): 895-914.
[154] Wasserman S.H., Graessley W.W., *Prediction of linear viscoelastic response for entangled polyolefin melts from molecular weight distribution*. Polym Eng Sci. 1996; 36(6): 852-861.
[155] Vega J.F., Santamaria A., Munoz-Escalona A., Lafuente P., *Small-amplitude oscillatory shear flow measurements as a tool to detect very low amounts of long chain branching in polyethylenes*. Macromolecules. 1998; 31(11): 3639-3647.
[156] Munari A., Pezzin G., Pilati F., *Linear and Branched Poly(Butyleneisophthalate) - Activation-Energy for Melt Flow*. Rheol Acta. 1990; 29(5): 469-474.
[157] Wang W.J., Kharchenko S., Migler K., Zhu S.P., *Triple-detector GPC characterization and processing behavior of long-chain-branched polyethylene prepared by solution polymerization with constrained geometry catalyst*. Polymer. 2004; 45(19): 6495-6505.
[158] Wood-Adams P.M., Dealy J.M., *Using rheological data to determine the branching level in metallocene polyethylenes*. Macromolecules. 2000; 33(20): 7481-7488.
[159] Shaw M.T., Tuminello W.H., *A Closer Look at the Mwd-Viscosity Transform*. Polym Eng Sci. 1994; 34(2): 159-165.

[160] Wood-Adams P.M., Dealy J.M., *Use of rheological measurements to estimate the molecular weight distribution of linear polyethylene*. J Rheol. 1996; 40(5): 761-778.
[161] Tuminello W.H., *Molecular-Weight and Molecular-Weight Distribution from Dynamic Measurements of Polymer Melts*. Polym Eng Sci. 1986; 26(19): 1339-1347.
[162] Malkin A.Y., Teishev A.E., *Flow Curve Molecular-Weight Distribution - Is the Solution of the Inverse Problem Possible*. Polym Eng Sci. 1991; 31(22): 1590-1596.
[163] Tuminello W.H., Cudremauroux N., *Determining Molecular-Weight Distributions from Viscosity Versus Shear Rate Flow Curves*. Polym Eng Sci. 1991; 31(20): 1496-1507.
[164] Mead D.W., *Determination of Molecular-Weight Distributions of Linear Flexible Polymers from Linear Viscoelastic Material Functions*. J Rheol. 1994; 38(6): 1797-1827.
[165] Mead D.W., *Numerical Interconversion of Linear Viscoelastic Material Functions*. J Rheol. 1994; 38(6): 1769-1795.
[166] Liu Y.M., Shaw M.T., Tuminello W.H., *Optimized data collection for determination of the MWD from the viscosity data of polymer melts*. Polym Eng Sci. 1998; 38(1): 169-176.
[167] Wasserman S.H., *Calculating the Molecular-Weight Distribution from Linear Viscoelastic Response of Polymer Melts*. J Rheol. 1995; 39(3): 601-625.
[168] Tuminello W.H., Buck W.H., Kerbow D.L., *Rheological Molecular-Weight Distribution Determinations of Ethylene Tetrafluoroethylene Copolymers - Implications for Long-Chain Branching*. Macromolecules. 1993; 26(3): 499-503.
[169] Nobile M.R., Cocchini F., *Evaluation of molecular weight distribution from dynamic moduli*. Rheol Acta. 2001; 40(2): 111-119.
[170] Cocchini F., Nobile M.R., *Constrained inversion of rheological data to molecular weight distribution for polymer melts*. Rheol Acta. 2003; 42(3): 232-242.
[171] Chen X.Y., Zhang Y.M., *Determining molecular weight scale and molecular weight distribution of ethylene-tetrafluoroethylene alternating copolymer via a rheological technique*. J Appl Polym Sci. 2012; 125(3): 2442-2448.
[172] Cox W.P., Merz E.H., *Correlation of Dynamic and Steady Flow Viscosities*. J Polym Sci. 1958; 28(118): 619-622.
[173] Inkinen S., Hakkarainen M., Albertsson A.C., Sodergard A., *From Lactic Acid to Poly(lactic acid) (PLA): Characterization and Analysis of PLA and Its Precursors*. Biomacromolecules. 2011; 12(3): 523-532.
[174] Dorgan J.R., Janzen J., Clayton M.P., Hait S.B., Knauss D.M., *Melt rheology of variable L-content poly(lactic acid)*. J Rheol. 2005; 49(3): 607-619.
[175] Dorgan J.R., Rheology of Poly(Lactic Acid), in: Auras R, Lim LT, Selke SEM, Tsuji H, (Eds.), *Poly(Lactic Acid): Synthesis, Structures, Properties, Processing and Applications*, Wiley, Hoboken (USA); 2010. p. 125-139.
[176] Stadler F.J., Munstedt H., *Numerical description of shear viscosity functions of long-chain branched metallocene-catalyzed polyethylenes*. J Non-Newton Fluid. 2008; 153(2-3): 203-203.
[177] Chatillon M., Santana O.O., *Modificación estructural de poli(ácido láctico) mediante extrusión reactiva: estudio del comportamiento reológico*. Master Thesis, Universitat Politècnica de Catalunya; Barcelona (2012).

[178] Ferri D., Lomellini P., *Melt rheology of randomly branched polystyrenes*. J Rheol. 1999; 43(6): 1355-1372.
[179] Carreau P.J., Tabatabaei S.H., Ajji A., *Rheological Long-Chain Properties of Blends of Linear and Branched Polypropylenes*. Polym Eng Sci. 2010; 50(1): 191-199.
[180] Dealy J.M., Larson R.G., Nonlinear Viscoelasticity, in: Dealy JM, Larson RG, (Eds.), *Structure and Rheology of Molten Polymers: From Structure to Flow Behavior and Back Again*, Hanser Publisher, Munich; 2006. p. 329-413.
[181] Havriliak S., Negami S., *A Complex Plane Representation of Dielectric and Mechanical Relaxation Processes in Some Polymers*. Polymer. 1967; 8(4): 161-210.
[182] Elster C., Honerkamp J., *The role of the error model in the determination of the relaxation time spectrum* J Rheol. 1992; 36(5): 911-927.
[183] Garcia-Franco C.A., Mead D.W., *Rheological and molecular characterization of linear backbone flexible polymers with the Cole-Cole model relaxation spectrum*. Rheol Acta. 1999; 38(1): 34-47.
[184] Young R.J., Lovell P.A., Mechanical Properties, *Introduction to Polymers*, 2 ed, Chapman and Hall, London; 1991. p. 310-428.
[185] Kinloch A.J., Young R.J., Glassy Polymers I-Thermoplastics, *Fracture Behaviour of Polymers*, Applied Science Publishers, Essex (England); 1995. p. 229-285.
[186] Kinloch A.J., Young R.J., Crazing, *Fracture Behaviour of Polymers*, Applied Science Publishers, Essex (England); 1983. p. 147-181.
[187] Kinloch A.J., Young R.J., Shear Yielding, *Fracture Behaviour of Polymers*, Applied Science Publishers, Essex (England); 1983. p. 107-146.
[188] Narisawa I., Ishikawa M., *Crazing in semicrystalline thermoplastics*. Advances in Polymer Science. 1990; 91/92: 353-391.
[189] Plummer C.J.G., Goldberg A., Ghanem A., *Micromechanisms of slow crack growth in polyethylene under constant tensile loading*. Polymer. 2001; 42(23): 9551-9564.
[190] Thomas C., Ferreiro V., Coulon G., Seguela R., *In situ AFM investigation of crazing in polybutene spherulites under tensile drawing*. Polymer. 2007; 48(20): 6041-6048.
[191] Donald A.M., Crazing, in: Haward RN, Young RJ, (Eds.), *The Physics of Glassy Polymers*, 2 ed, Chapman & Hall, London; 1997. p. 295-341.
[192] Hsiao C.C., Sauer J.A., *On Crazing of Linear High Polymers*. J Appl Phys. 1950; 21(11): 1071-1083.
[193] Bessonov M.I., Kuvshinskii E.V., *Cracks in Transparent Plastics - Their Growth and Structure*. Sov Phys-Sol State. 1960; 1(9): 1321-1328.
[194] Kambour R.P., *Structure and Properties of Crazes in Polycarbonate and Other Glassy Polymers*. Polymer. 1964; 5(3): 143-155.
[195] Deblieck R.A.C., van Beek D.J.M., Remerie K., Ward I.M., *Failure mechanisms in polyolefines: The role of crazing, shear yielding and the entanglement network*. Polymer. 2011; 52(14): 2979-2990.
[196] Kramer E.J., *Microscopic and Molecular Fundamentals of Crazing*. Advances in Polymer Science. 1983; 52-3: 1-56.
[197] Argon A.S., Hannoosh J.G., *Initiation of Crazes in Polystyrene*. Philos Mag. 1977; 36(5): 1195-1216.

[198] Donald A.M., Kramer E.J., *Craze Initiation and Growth in High-Impact Polystyrene*. J Appl Polym Sci. 1982; 27(10): 3729-3741.
[199] Taylor G., *The Instability of Liquid Surfaces When Accelerated in a Direction Perpendicular to Their Planes .1*. Proc R Soc Lon Ser-A. 1950; 201(1065): 192-196.
[200] Fields R.J., Ashby M.F., *Finger-Like Crack Growth in Solids and Liquids*. Philos Mag. 1976; 33(1): 33-48.
[201] Argon A.S., Salama M.M., *Growth of Crazes in Glassy Polymers*. Philos Mag. 1977; 36(5): 1217-1234.
[202] Donald A.M., Kramer E.J., *The Mechanism for Craze-Tip Advance in Glassy-Polymers*. Philos Mag A. 1981; 43(4): 857-870.
[203] Fellers J.F., Kee B.F., *Crazing Studies of Polystyrene .1. New Phenomenological Observation*. J Appl Polym Sci. 1974; 18(8): 2355-2365.
[204] Mcleish T.C.B., Plummer C.J.G., Donald A.M., *Crazing by Disentanglement - Non-Diffusive Reptation*. Polymer. 1989; 30(9): 1651-1655.
[205] Plummer C.J.G., Donald A.M., *The Deformation-Behavior of Polyethersulfone and Polycarbonate*. J Polym Sci Pol Phys. 1989; 27(2): 325-336.
[206] Ling Y., *Uniaxial True Stress-Strain after Necking*. AMP Journal of Technology. 1996; 5: 37-48.
[207] Crist B., Yield processes in glassy polymers, in: Haward RN, Young JB, (Eds.), *The Physics of Glassy Polymers*, Chapman & Hall, London; 1997. p. 155-212.
[208] Al-Jabareen A.I., *Poly(Ethylene Terephthalate)/Polycarbonate Blends Prepared by Reactive Extrusion: Thermal and Mechanical Characterization.* Ph.D. Thesis, Universitat Politècnica de Catalunya; Barcelona (2009).
[209] Vincent P.I., *The Necking and Cold-Drawing of Rigid Plastics*. Polymer. 1960; 1(1): 7-19.
[210] Bowden P.B., *A Criterion for Inhomogeneous Plastic Deformation*. Philos Mag. 1970; 22(177): 455-462.
[211] Bowden P.B., Raha S., *Formation of Micro Shear Bands in Polystyrene and Polymethylmethacrylate*. Philos Mag. 1970; 22(177): 463-482.
[212] Wu J.B.C., Li J.C.M., *Slip Processes in Deformation of Polystyrene*. J Mater Sci. 1976; 11(3): 434-444.
[213] Wellinghoff S.T., Baer E., *Microstructure and Its Relationship to Deformation Processes in Amorphous Polymer Glasses*. J Appl Polym Sci. 1978; 22(7): 2025-2045.
[214] Donald A.M., Kramer E.J., *The Competition between Shear Deformation and Crazing in Glassy-Polymers*. J Mater Sci. 1982; 17(7): 1871-1879.
[215] Perego G., Cella G.D., Mechanical Properties, in: Auras R, Lim LT, Selke SEM, Tsuji H, (Eds.), *Poly(Lactic Acid): Synthesis, Structures, Properties, Processing and Applications*, Wiley, Hoboken (USA); 2010. p. 141-153.
[216] Lainchbury D.L.G., Bevis M., *Crazing and Fracture of Polystyrene .1. Systematic Study of Variations in Craze and Fracture Surface Morphology in a Range of Commercial Polystyrenes*. J Mater Sci. 1976; 11(12): 2222-2234.
[217] Grijpma D.W., Penning J.P., Pennings A.J., *Chain Entanglement, Mechanical-Properties and Drawability of Poly(Lactide)*. Colloid Polym Sci. 1994; 272(9): 1068-1081.
[218] Wu S.H., *Control of Intrinsic Brittleness and Toughness of Polymers and Blends by Chemical-Structure - a Review*. Polym Int. 1992; 29(3): 229-247.

[219] Wu S.H., *Chain Structure, Phase Morphology, and Toughness Relationships in Polymers and Blends*. Polym Eng Sci. 1990; 30(13): 753-761.
[220] Ward I.M., Sweeney J., *An Introduction to The Mechanical Properties of Solid Polymers* Wiley, West Sussex (England); 2004.
[221] Roylance D. Introduction to Fracture Mechanics. In: Engineering DoMSa, editor. Cambridge (USA)2001.
[222] *Griffith Theory of Brittle Fracture*. http://mechanical-materialstechnology.blogspot.com.es/2011/08/griffith-theory-of-brittle-fracture.html (Accessed Date: 09/05/2015).
[223] Inglis C.E., *Stresses in a Plate Due to the Presence of Cracks and Sharp Corners*. Transactions of the Institute of Naval Architects. 1913; 55: 219-241.
[224] Anderson T.L., *Fracture Mechanics: Fundamentals and Applications*. Third edition ed. CRC Press, Boca Raton (USA); 2005.
[225] McCrum N.G., Buckley C.P., Bucknall C.B., Yield and Fracture, in: McCrum NG, Buckley CP, Bucknall CB, (Eds.), *Principles of Polymer Engineering*, Oxford Science Publications, New York (USA); 1988. p. 167-208.
[226] Hertzberg R.W., *Deformation and Fracture Mechanics of Engineering Materials*. Fourth ed. John Wiley & Sons, New York (USA); 1996.
[227] Kinloch A.J., Young R.J., Fracture Mechanics, in: Kinloch AJ, Young RJ, (Eds.), *Fracture Behaviour of Polymers*, Springer-Science, Salem (USA); 1983. p. 74-106.
[228] Ward I.M., Sweeney J., Breaking phenomena, *Mechanical Properties of Solid Polymers*, Third ed, Wiley, Chichester (United Kingdom); 2013. p. 381-447.
[229] Wells A.A., *Application of fracture mechanics at and beyond general yielding*. British Welding Journal. 1963; 10: 563-570.
[230] Zhu X.K., Joyce J.A., *Review of fracture toughness (G, K, J, CTOD, CTOA) testing and standardization*. Eng Fract Mech. 2012; 85: 1-46.
[231] Dugdale D.S., *Yielding of steel sheets containing slits*. Journal of the Mechanics and Physics of Solids. 1960; 8(2): 100-104.
[232] Burdekin F.M., Stone D.E.W., *The Crack Opening Displacement Approach to Fracture Mechanics in Yielding Materials*. Journal of Strain Analysis. 1966; 1: 145-153.
[233] Rice J.R., Rosengren G.F., *Plane strain deformation near a crack tip in a power-law hardening material*. Journal of the Mechanics and Physics of Solids. 1968; 16(1): 1-12.
[234] Broberg K.B., *Crack-growth criteria and non-linear fracture mechanics*. Journal of the Mechanics and Physics of Solids. 1971; 19(6): 407-418.
[235] Broberg K.B., *On stable crack growth*. Journal of the Mechanics and Physics of Solids. 1975; 23(3): 215-237.
[236] Cotterell B., Reddel J.K., *The essential work of plane stress ductile fracture*. Int J Fracture. 1977; 13(3): 267-277.
[237] Mai Y.L., Cotterell B., *On the essential work of ductile fracture in polymers*. Int J Fracture. 1986; 32(2): 105-125.
[238] Gamez-Perez J., Santana O., Martinez A.B., Maspoch M.L., *Use of extensometers on essential work of fracture (EWF) tests*. Polym Test. 2008; 27(4): 491-497.

[239] Hashemi S., *Work of fracture of PBT/PC blend: Effect of specimen size, geometry, and rate of testing*. Polym Eng Sci. 1997; 37(5): 912-921.
[240] Lach R., Schneider K., Weidisch R., Janke A., Knoll K., *Application of the essential work of fracture concept to nanostructured polymer materials*. Eur Polym J. 2005; 41(2): 383-392.
[241] Gamez-Perez J., Velazquez-Infante J.C., Franco-Urquiza E., Pages P., Carrasco F., Santana O.O., et al., *Fracture behavior of quenched poly(lactic acid)*. Express Polym Lett. 2011; 5(1): 82-91.
[242] Mazidi M.M., Aghjeh M.K.R., Abbasi F., *Evaluation of fracture toughness of ABS polymers via the essential work of fracture (EWF) method*. J Mater Sci. 2012; 47(17): 6375-6386.
[243] Maspoch M.L., Henault V., Ferrer-Balas D., Velasco J.I., Santana O.O., *Essential work of fracture on PET films: influence of the thickness and the orientation*. Polym Test. 2000; 19(5): 559-568.
[244] Karger-Kocsis J., Czigany T., Moskala E.J., *Deformation rate dependence of the essential and non-essential work of fracture parameters in an amorphous copolyester*. Polymer. 1998; 39(17): 3939-3944.
[245] Clutton E.Q., Essential Work of Fracture, in: Moore DR, Pavan A, Williams JG, (Eds.), *Fracture Mechanics Testing Methods for Polymers, Adhesive and Composites*, Elsevier, Oxford; 2001. p. 177-202.
[246] Martinez A.B., Gamez-Perez J., Sanchez-Soto M., Velasco J.I., Santana O.O., Maspoch M.L., *The Essential Work of Fracture (EWF) method - Analyzing the Post-Yielding Fracture Mechanics of polymers*. Eng Fail Anal. 2009; 16(8): 2604-2617.
[247] Ferrer-Balas D., Maspoch M.L., Martinez A.B., Ching E., Li R.K.Y., Mai Y.W., *Fracture behaviour of polypropylene films at different temperatures: assessment of the EWF parameters*. Polymer. 2001; 42(6): 2665-2674.
[248] Ferrer-Balas D., Maspoch M.L., Martinez A.B., Santana O.O., *Influence of annealing on the microstructural, tensile and fracture properties of polypropylene films*. Polymer. 2001; 42(4): 1697-1705.
[249] Karger-Kocsis J., Barany T., Moskala E.J., *Plane stress fracture toughness of physically aged plasticized PETG as assessed by the essential work of fracture (EWF) method*. Polymer. 2003; 44(19): 5691-5699.
[250] Karger-Kocsis J., Czigany T., *Strain rate dependence of the work of fracture response of an amorphous poly(ethylene-naphthalate) (PEN) film*. Polym Eng Sci. 2000; 40(8): 1809-1815.
[251] KargerKocsis J., Moskala E.J., *Relationships between molecular and plane-stress essential work of fracture parameters in amorphous copolyesters*. Polym Bull. 1997; 39(4): 503-510.
[252] Santana O.O., Rodriguez C., Belzunce J., Gamez-Perez J., Carrasco F., Maspoch M.L., *Fracture behaviour of de-aged poly(lactic acid) assessed by essential work of fracture and J-Integral methods*. Polym Test. 2010; 29(8): 984-990.
[253] Hill R., *On discontinuous plastic states, with special reference to localized necking in thin sheets*. Journal of the Mechanics and Physics of Solids. 1952; 1(1): 19-30.
[254] Santana O.O., *Estudio de las Fracturas de Mezclas de Policarbonato con Acrilonitrilo-Butadieno-Estireno.* Ph.D. Thesis, Universidad Politechnica de Cataluña; Barcelona (1997).

[255] Martinez A.B., Delgado A., Segovia A., Sanchez-Soto M.A., Salazar A., *Fracture behaviour of an EPBC film. Study of the relationships between J0 and EWF*. XXVII Encuentro del Grupo Español de Fractura, (2010).
[256] Sheeladevi A., Ramanathan N., *Lactic Acid Production Using Lactic Acid Bacteria under Optimized Conditions*. International Journal of Pharmaceutical & Biological Archives. 2011; 2(6): 1686-1691.
[257] Lowe C.E., *Preparation of high molecular weight polyhydroxyacetic ester*. US Patent US2668162 A, DuPont (1954).
[258] Gruber P.R., Hall E.S., Kolstad J.J., Iwen M.L., Benson R.D., Borchardt R.L., *Continuous process for the manufacture of lactide and lactide polymers*. US Patent US6326458 B1, Cargill Incorporated (2001).
[259] Benson R.D., Borchardt R.L., Gruber P.R., Hall E.S., Iwen M.L., Kolstad J.J., *Continuous process for manufacture of lactide polymers with purification by distillation*. US Patent US5357035 A, Cargill Incorporated (1994).
[260] *Dow and Cargill in Venture*. The New York Times, New-York (November 1997)
[261] *Bioplastic development increases with new applications*. (Accessed Date:
[262] Rasal R.M., Janorkar A.V., Hirt D.E., *Poly(lactic acid) modifications*. Prog Polym Sci. 2010; 35(3): 338-356.
[263] Henton D.E., Gruber P., Lunt J., Randall J., Polylactic Acid Technology, in: Mohanty AK, Misra M, Drzal LT, (Eds.), *Natural Fibers, Biopolymers, and Biocomposites*, Taylor & Francis, Boca Raton (Florida); 2005. p. 527-577.
[264] Vink E.T.H., Rabago K.R., Glassner D.A., Gruber P.R., *Applications of life cycle assessment to NatureWorks™ polylactide (PLA) production*. Polym Degrad Stabil. 2003; 80(3): 403-419.
[265] Gupta B., Revagade N., Hilborn J., *Poly(lactic acid) fiber: An overview*. Prog Polym Sci. 2007; 32(4): 455-482.
[266] *Select Committee on GRAS Substances (SCOGS) Opinion: Lactic acid*. http://www.fda.gov/food/ingredientspackaginglabeling/gras/scogs/ucm260449.htm (Accessed Date: 10/12/2013).
[267] Södergtård A., Stolt M., Industrial Production of High Molecular Weight Poly(Lactic Acid), in: Auras R, Lim LT, Selke SEM, Tsuji H, (Eds.), *Poly(Lactic Acid): Synthesis, Structures, Properties, Processing and Applications*, Wiley, Hoboken (USA); 2010. p. 27-42.
[268] Ajioka M., Enomoto K., Yamaguchi A., *Polyhydroxycarboxylic acid and preparation process thereof*. US Patent US5310865 A, Mitsui Toatsu Chemicals Incorporated (1994).
[269] Shen L., Haufe J., Patel M.K. Product overview and market projection of emerging bio-based plastics Utrecht (Netherland): Universiteit Utrecht; 2009.
[270] Drumright R.E., Gruber P.R., Henton D.E., *Polylactic acid technology*. Adv Mater. 2000; 12(23): 1841-1846.
[271] Gruber P.R., Hall E.S., Kolstad J.H., Iwen M.L., Bendson R.D., Boerchardt R.L., *Continuous process for manufacture of lactide polymers with controlled optical purity*. US Patent US5142023 A, Cargill Incorporated (1992).
[272] Endres H.J., Siebert-Raths A., Manufacture and Chemical Structure of Biopolymers, *Engineering Biopolymers: Markets, Manufacturing, Properties ans Applications*, Hanser, Munich; 2011. p. 71-148.

[273] Sodergard A., Stolt M., *Properties of lactic acid based polymers and their correlation with composition*. Prog Polym Sci. 2002; 27(6): 1123-1163.
[274] Okoro H.K., Fatoki O.S., Adekola F.A., Ximba B.J., Snyman R.G., Opeolu B., *Human Exposure, Biomarkers, and Fate of Organotins in the Environment*. Reviews of Environmental Contamination and Toxicology. 2011; 213: 27-54.
[275] Alvarez-Chavez C.R., Edwards S., Moure-Eraso R., Geiser K., *Sustainability of bio-based plastics: general comparative analysis and recommendations for improvement*. Journal of Cleaner Production. 2012; 23: 47-56.
[276] Jacobsen S., Fritz H.G., Degée P., Dubois P., Jérôme R., *New developments on the ring opening polymerisation of polylactide*. Industrial Crops and Products. 2000; 11: 265-275.
[277] Jacobsen S., Fritz H.G., Degee P., Dubois P., Jerome R., *Continuous reactive extrusion polymerisation of L-lactide - An engineering view*. Macromol Symp. 2000; 153: 261-273.
[278] Maharana T., Monhanty B., Negi Y.S., *Melt–solid polycondensation of lactic acid and its biodegradability*. Prog Polym Sci. 2009; 34: 99-124.
[279] Ovitt T.M., Coates G.W., *Stereoselective Ring-Opening Polymerization of rac-Lactide with a Single-Site, Racemic Aluminum Alkoxide Catalyst: Synthesis of Stereoblock Poly(lactic acid)*. Journal of Polymer Science Part A: Polymer Chemistry. 2000; 38: 4686-4692.
[280] Avérous L., Pollet E., Biodegradable Polymers, in: Avérous L, Pollet E, (Eds.), *Environmental Silicate Nano-Biocomposites*, Springer-Verlag, London; 2012. p. 13-39.
[281] Ingeo-4032D, *PLA Polymer 4032D*. Polymer Technical Data Sheets, NatureWorks LLC, Minnetonka, MN (2005).
[282] Ingeo-2002D, *PLA Polymer 2002D*. Polymer Technical Data Sheets, NatureWorks LLC, Minnetonka, MN (2005).
[283] Lim L.T., Cink K., Vanyo T., Processing of Poly(lactic acid), in: Auras R, Lim LT, Selke SEM, Tsuji H, (Eds.), *Poly(Lactic Acid): Synthesis, Structures, Properties, Processing and Applications*, Wiley, Hoboken (USA); 2010. p. 191-216.
[284] NatureWorks, *Sheet Extrusion Processing Guide*. Polymer Processing Guides, NatureWorks LLC, Minnetonka, MN (2005).
[285] Natureworks, *Production of Ingeo™ Film on Blown Film Equipment Designed for Low Density Polyethylene (LDPE) Film*. Polymer Processing Guides, NatureWorks LLC, Minnetonka, MN (2003).
[286] *Brittleness at ambient temperatures makes thermoforming of PLA different*. http://plastics-technical-information.blogspot.com.es/2010/12/brittleness-at-ambient-temperatures.html (Accessed Date: 21/03/2014).
[287] NatureWorks, *Processing Guide for Thermoforming Articles*. Polymer Processing Guides, NatureWorks LLC, Minnetonka, MN (2005).
[288] Bigg D.M., *Polylactide copolymers: Effect of copolymer ratio and end capping on their properties*. Adv Polym Tech. 2005; 24(2): 69-82.
[289] Cam D., Marucci M., *Influence of residual monomers and metals on poly (L-lactide) thermal stability*. Polymer. 1997; 38(8): 1879-1884.
[290] Hyon S.H., Jamshidi K., Ikada Y., *Effects of residual monomer on the degradation of DL-lactide polymer*. Polym Int. 1998; 46(3): 196-202.

[291] Nishida H., Mori T., Hoshihara S., Fan Y.J., Shirai Y., Endo T., *Effect of tin on poly(L-lactic acid) pyrolysis*. Polym Degrad Stabil. 2003; 81(3): 515-523.
[292] Taubner V., Shishoo R., *Influence of processing parameters on the degradation of poly(L-lactide) during extrusion*. J Appl Polym Sci. 2001; 79(12): 2128-2135.
[293] Yu H.X., Huang N.X., Wang C.S., Tang Z.L., *Modeling of poly(L-lactide) thermal degradation: Theoretical prediction of molecular weight and polydisversity index*. J Appl Polym Sci. 2003; 88(11): 2557-2562.
[294] Aoyagi Y., Yamashita K., Doi Y., *Thermal degradation of poly[(R)-3-hydroxybutyrate], poly[epsilon-caprolactone], and poly[(S)-lactide]*. Polym Degrad Stabil. 2002; 76(1): 53-59.
[295] Sodergard A., Nasman J.H., *Stabilization of Poly(L-Lactide) in the Melt*. Polym Degrad Stabil. 1994; 46(1): 25-30.
[296] Wachsen O., Reichert K.H., Kruger R.P., Much H., Schulz G., *Thermal decomposition of biodegradable polyesters .3. Studies on the mechanisms of thermal degradation of oligo-L-lactide using SEC, LACCC and MALDI-TOF-MS*. Polym Degrad Stabil. 1997; 55(2): 225-231.
[297] Gupta M.C., Deshmukh V.G., *Thermal Oxidative-Degradation of Poly-Lactic Acid .1. Activation-Energy of Thermal-Degradation in Air*. Colloid Polym Sci. 1982; 260(3): 308-311.
[298] Kopinke F.D., Remmler M., Mackenzie K., Moder M., Wachsen O., *Thermal decomposition of biodegradable polyesters .2. Poly(lactic acid)*. Polym Degrad Stabil. 1996; 53(3): 329-342.
[299] Zhang X.C., Wyss U.P., Pichora D., Goosen M.F.A., *An Investigation of the Synthesis and Thermal-Stability of Poly(Dl-Lactide)*. Polym Bull. 1992; 27(6): 623-629.
[300] Wang Y.M., Steinhoff B., Brinkmann C., Alig I., *In-line monitoring of the thermal degradation of poly(L-lactic acid) during melt extrusion by UV-vis spectroscopy*. Polymer. 2008; 49(5): 1257-1265.
[301] Santonja Blasco L., *Contribution to the study of thermal, biological and photo degradation of polylactide*. Ph.D. Thesis, Universitat Politècnica de València; València (2012).
[302] Lipik V.T., Widjaja L.K., Liow S.S., Abadie M.J.M., Venkatraman S.S., *Effects of transesterification and degradation on properties and structure of polycaprolactone-polylactide copolymers*. Polym Degrad Stabil. 2010; 95(12): 2596-2602.
[303] Wachsen O., Platkowski K., Reichert K.H., *Thermal degradation of poly-L-lactide - Studies on kinetics, modelling and melt stabilisation*. Polym Degrad Stabil. 1997; 57(1): 87-94.
[304] Korhonen H., Helminen A., Seppala J.V., *Synthesis of polylactides in the presence of co-initiators with different numbers of hydroxyl groups*. Polymer. 2001; 42(18): 7541-7549.
[305] Signori F., Coltelli M.B., Bronco S., *Thermal degradation of poly(lactic acid) (PLA) and poly(butylene adipate-co-terephthalate) (PBAT) and their blends upon melt processing*. Polym Degrad Stabil. 2009; 94(1): 74-82.
[306] Jamshidi K., Hyon S.H., Ikada Y., *Thermal Characterization of Polylactides*. Polymer. 1988; 29(12): 2229-2234.

[307] Najafi Chaloupi N., *Development of Polylactide-Clay Nanocomposites for Food Packaging Applications*. Maîtrise ès Sciences Appliquées Thesis, Ecole Polytechnique de Montréal; Montréal (2011).
[308] Gogolewski S., Jovanovic M., Perren S.M., Dillon J.G., Hughes M.K., *The Effect of Melt-Processing on the Degradation of Selected Polyhydroxyacids - Polylactides, Polyhydroxybutyrate, and Polyhydroxybutyrate-Co-Valerates*. Polym Degrad Stabil. 1993; 40(3): 313-322.
[309] McKee M.G., Unal S., Wilkes G.L., Long T.E., *Branched polyesters: recent advances in synthesis and performance*. Prog Polym Sci. 2005; 30(5): 507-539.
[310] Zhao J.X., Xiao H.Y., Qiu G., Zhang Y.W., Huang N.X., Tang Z.L., *Solid-state polycondensation of poly(ethylene terephthalate) modified with isophthalic acid: kinetics and simulation*. Polymer. 2005; 46(18): 7309-7316.
[311] Villalobos M., Awojulu A., Greeley T., Turco G., Deeter G., *Oligomeric chain extenders for economic reprocessing and recycling of condensation plastics*. Energy. 2006; 31(15): 3227-3234.
[312] Dubois P., Raquez J.M., Degee P., Nabar Y., Narayan R., *Biodegradable materials by reactive extrusion: From catalyzed polymerization to functionalization and blend compatibilization*. Cr Chim. 2006; 9(11-12): 1370-1379.
[313] Pilla S., Kim S.G., Auer G.K., Gong S.Q., Park C.B., *Microcellular Extrusion-Foaming of Polylactide with Chain-Extender*. Polym Eng Sci. 2009; 49(8): 1653-1660.
[314] Mihai M., Huneault M.A., Favis B.D., *Rheology and Extrusion Foaming of Chain-Branched Poly(lactic acid)*. Polym Eng Sci. 2010; 50(3): 629-642.
[315] Di Y.W., Iannace S., Di Maio E., Nicolais L., *Reactively modified poly(lactic acid): Properties and foam processing*. Macromol Mater Eng. 2005; 290(11): 1083-1090.
[316] Liu J.Y., Lou L.J., Yu W., Liao R.G., Li R.M., Zhou C.X., *Long chain branching polylactide: Structures and properties*. Polymer. 2010; 51(22): 5186-5197.
[317] Yang S.L., Wu Z.H., Yang W., Yang M.B., *Thermal and mechanical properties of chemical crosslinked polylactide (PLA)*. Polym Test. 2008; 27(8): 957-963.
[318] Carlson D., Nie L., Narayan R., Dubois P., *Maleation of polylactide (PLA) by reactive extrusion*. J Appl Polym Sci. 1999; 72(4): 477-485.
[319] Cicero J.A., Dorgan J.R., Garrett J., Runt J., Lin J.S., *Effects of molecular architecture on two-step, melt-spun poly(lactic acid) fibers*. J Appl Polym Sci. 2002; 86(11): 2839-2846.
[320] Baratian S., Hall E.S., Lin J.S., Xu R., Runt J., *Crystalization and solid-state structure of random polylactide copolymers: Poly(L-lactide-co-D-lactide)s*. Macromolecules. 2001; 34(14): 4857-4864.
[321] Fambri L., Migliaresi C., Crystallization and thermal properties, in: Auras R, Lim LT, Selke SEM, Tsuji H, (Eds.), *Poly(Lactic Acid): Synthesis, Structures, Properties, Processing and Applications*, Wiley, Hoboken (USA); 2010. p. 113-124.
[322] Kawai T., Rahman N., Matsuba G., Nishida K., Kanaya T., Nakano M., et al., *Crystallization and melting behavior of poly (L-lactic acid)*. Macromolecules. 2007; 40(26): 9463-9469.
[323] Di Lorenzo M.L., *Crystallization behavior of poly(L-lactic acid)*. Eur Polym J. 2005; 41(3): 569-575.

[324] Hoogsteen W., Postema A.R., Pennings A.J., Brinke G., *Crystal Structure, Conformation and Morphology of Solution-Spun Poly(L-lactide) Fibers*. Macromolecules. 1990; 23(2): 634-642.
[325] Tsuji H., *Poly(lactide) stereocomplexes: Formation, structure, properties, degradation, and applications*. Macromol Biosci. 2005; 5(7): 569-597.
[326] Takahashi K., Sawai D., Yokoyama T., Kanamoto T., Hyon S.H., *Crystal transformation from the alpha- to the beta-form upon tensile drawing of poly(L-lactic acid)*. Polymer. 2004; 45(14): 4969-4976.
[327] kobayashi J., Asahi T., Ichiki M., Oikawa A., Suzuki H., Wtanabe T., et al., *Structural and optical properties of poly lactic acids*. J Appl Phys. 1995; 77(7): 2957-2973.
[328] Zhang J.M., Duan Y.X., Sato H., Tsuji H., Noda I., Yan S., et al., *Crystal modifications and thermal behavior of poly(L-lactic acid) revealed by infrared spectroscopy*. Macromolecules. 2005; 38(19): 8012-8021.
[329] Zhang J.M., Tashiro K., Domb A.J., Tsuji H.T., *Confirmation of disorder a form of poly(L-lactic acid) by the X-ray fiber pattern and polarized IR/Raman spectra measured for uniaxially-oriented samples*. Macromol Symp. 2006; 242: 274-278.
[330] Pan P., Zhu B., Kai W., Dong T., Inoue Y., *Effect of crystallization temperature on crystal modifications and crystallization kinetics of poly(L-lactide)*. J Appl Polym Sci. 2008; 107(1): 54-62.
[331] Zhang J., Tashiro K., Tsuji H., Domb A.J., *Disorder-to-order phase transition and multiple melting behavior of poly(L-lactide) investigated by simultaneous measurements of WAXD and DSC*. Macromolecules. 2008; 41(4): 1352-1357.
[332] Pan P.J., Zhu B., Kai W.H., Dong T., Inoue Y., *Polymorphic transition in disordered poly(L-lactide) crystals induced by annealing at elevated temperatures*. Macromolecules. 2008; 41(12): 4296-4304.
[333] Pan P., Inoue Y., *Polymorphism and isomorphism in biodegradable polyesters*. Prog Polym Sci. 2009; 34: 605-640.
[334] Eling B., Gogolewski S., Pennings A.J., *Biodegradable materials of poly(l-lactic acid): 1. Melt-spun and solution-spun fibres*. Polymer. 1982; 23(11): 1587-1593.
[335] Brizzolara D., Cantow H.J., Diederichs K., Keller E., Domb A.J., *Mechanism of the stereocomplex formation between enantiomeric poly(lactide)s*. Macromolecules. 1996; 29(1): 191-197.
[336] Puiggali J., Ikada Y., Tsuji H., Cartier L., Okihara T., Lotz B., *The frustrated structure of poly(L-lactide)*. Polymer. 2000; 41(25): 8921-8930.
[337] Cartier L., Okihara T., Ikada Y., Tsuji H., Puiggali J., Lotz B., *Epitaxial crystallization and crystalline polymorphism of polylactides*. Polymer. 2000; 41(25): 8909-8919.
[338] Saeidlou S., Huneault M.A., Li H.B., Park C.B., *Poly(lactic acid) crystallization*. Prog Polym Sci. 2012; 37(12): 1657-1677.
[339] Kolstad J.J., *Crystallization Kinetics of Poly(L-lactide-co-meso-lactide)*. J Appl Polym Sci. 1996; 62(7): 1079-1091.
[340] Schmidt S.C., Hillmyer M.A., *Polylactide stereocomplex crystallites as nucleating agents for isotactic polylactide*. J Polym Sci Pol Phys. 2001; 39(3): 300-313.

[341] Fukushima K., Furuhashi Y., Sogo K., Miura S., Kimura Y., *Stereoblock poly(lactic acid): Synthesis via solid-state polycondensation of a stereocomplexed mixture of poly(L-lactic acid) and poly(D-lactic acid)*. Macromol Biosci. 2005; 5(1): 21-29.
[342] Dargent E., Arnoult M., Mano J.F., *Mobile amorphous phase fragility in semi-crystalline polymers: Comparison of PET and PLLA*. Polymer. 2007; 48(4): 1012-1019.
[343] Auras R.A., Singh S.P., Singh J.J., *Evaluation of Oriented Poly(lactide) Polymers vs. Existing PET and Oriented PS for Fresh Food Service Containers*. Packaging Technology and Science. 2005; 18: 207-216.
[344] Jacobsen S., Fritz H.G., *Plasticizing Polylactide-The Effect of Different Plasticizers on the Mechanical Properties*. Polym Eng Sci. 1999; 39(7): 1303-1310.
[345] Velàzquez infante J.C., *Relación Estructura-Propiedades de Films de Nanocompuestos de PLA*. Ph.D. Thesis, Universidad Politechnica de Cataluña-Barcelona Tech; Terrassa (2012).
[346] Lim L.T., Cink K., Vanyo T., Processing of Poly (Lactic Acid), in: Auras R, Lim LT, Selke SEM, H. T, (Eds.), *Poly(Lactic Acid): Synthesis, Structures, Properties, Processing and Applications*, Wiley, Hoboken (USA); 2010. p. 191-216.
[347] Park S.D., Todo M., Arakawa K., *Effect of annealing on the fracture toughness of poly(lactic acid)*. J Mater Sci. 2004; 39(3): 1113-1116.
[348] Nascimento L., Gamez-Perez J., Santana O.O., Velasco J.I., Maspoch M.L., Franco-Urquiza E., *Effect of the Recycling and Annealing on the Mechanical and Fracture Properties of Poly(Lactic Acid)*. J Polym Environ. 2010; 18(4): 654-660.
[349] Perego G., Cella G., Bastioli C., *Effect of molecular weight and crystallinity on poly(lactic acid) mechanical properties*. J Appl Polym Sci. 1996; 59(1): 37-43.
[350] Grijpma D.W., Altpeter H., Bevis M.J., Feijen J., *Improvement of the mechanical properties of poly(D,L-lactide) by orientation*. Polym Int. 2002; 51(10): 845-851.
[351] Park S.D., Todo M., Arakawa K., Koganemaru M., *Effect of crystallinity and loading-rate on mode I fracture behavior of poly(lactic acid)*. Polymer. 2006; 47(4): 1357-1363.
[352] NatureWorks, *Crystallizing and Drying Ingeo™ Biopolymer*. Polymer Processing Guides, NatureWorks LLC, Minnetonka, MN (2007).
[353] *Materials Additives & Blends Take PLA Upscale*. (Accessed Date: 22/04/2013).
[354] Joncryl-ADR-4300, *Joncryl ADR-4300*. Technical Data Sheets, (2006).
[355] Bikiaris D.N., Karayannidis G.P., *Chain extension of polyesters PET and PBT with two new diimidodiepoxides .2*. J Polym Sci Pol Chem. 1996; 34(7): 1337-1342.
[356] Takahashi K., Kuriyama T., *The effect of annealing on deformation and fracture behaviour of inyection molded PLA*. Antec 2010: 1294-1297.
[357] Wu C., *Handbook of Size Exclusion Chromatography and Related Techniques*. 2nd ed. Taylor & Francis e-Library, New-York; 2003.
[358] Gaborieau M., Castignolles P., *Size-exclusion chromatography (SEC) of branched polymers and polysaccharides*. Anal Bioanal Chem. 2011; 399(4): 1413-1423.
[359] Van Krevelen D.W., Te Nijenhuis K., Typology of Polymers, in: Van Krevelen DW, Te Nijenhuis K, (Eds.), *Properties of Polymers; Their correlation with chemical*

structure; Their numerical estimation and prediction from additive group contributions, fourth ed, Elsevier, Amsterdam; 2009. p. 7-47.
[360] Young R.J., Lovell P.A., *Introduction to Polymers*. Second ed. Chapman & Hall, Hong Kong; 1991.
[361] Lorenzo A.T., Arnal M.L., Muller A.J., Lin M.C., Chen H.L., *SAXS/DSC Analysis of the Lamellar Thickness Distribution on a SSA Thermally Fractionated Model Polyethylene*. Macromol Chem Physic. 2011; 212(18): 2009-2016.
[362] Perez C.J., Villarreal N., Pastor J.M., Failla M.D., Valles E.M., Carella J.M., *The use of SSA fractionation to detect changes in the molecular structure of model ethylene-butene copolymers modified by peroxide crosslinking*. Polym Degrad Stabil. 2009; 94(10): 1639-1645.
[363] Tchir W.J., Saucier P.C., *Accuracy in Linear Viscoelastic Property Measurement - Effects of Instrument Compliance and Inertia Revisited*. Antec 94 - Plastics: Gate Way to the Future, Vols 1-3. 1994: 1205-1211.
[364] Gabriel C., Munstedt H., *Creep recovery behavior of metallocene linear low-density polyethylenes*. Rheol Acta. 1999; 38(5): 393-403.
[365] Najafi Chaloupi N., *Development of Polylactide-Caly Nanocomposites for Food Packaging Applications.* MSc Thesis, Ecole Polytechnique de Montréal; Montréal (2011).
[366] DeRuiter J., Carboxylic Acid Structure and Chemistry: Part 1, *Principles of Drug Action 1*2005.
[367] Redl A., Morel M.H., Bonicel J., Guilbert S., Vergnes B., *Rheological properties of gluten plasticized with glycerol: dependence on temperature,glycerol content and mixing conditions*. Rheol Acta. 1999; 38: 311-320.
[368] Pretsch E., Bühlmann P., Affolter C., Herrera A., Martinez R., *Determinación estructural de compuestos orgánicos*. Springer-Verlag Ibérica, Barcelona; 2001.
[369] Kister G., Cassanas G., Vert M., *Effects of morphology, conformation and configuration on the IR and Raman spectra of various poly(lactic acid)s*. Polymer. 1998; 39(2): 267-273.
[370] Goncalves C.M.B., Coutinho J.A.P., Marrucho I.M., Optical properties, in: Auras R, Lim LT, Selke SEM, Tsuji H, (Eds.), *Poly(Lactic Acid): Synthesis, Structures, Properties, Processing and Applications*, Wiley, Hoboken (USA); 2010. p. 97-112.
[371] Meng Q.K., Heuzey M.C., Carreau P.J., *Control of thermal degradation of polylactide/clay nanocomposites during melt processing by chain extension reaction*. Polym Degrad Stabil. 2012; 97(10): 1-11.
[372] Espartero J.L., Rashkov I., Li S.M., Manolova N., Vert M., *NMR analysis of low molecular weight poly(lactic acid)s*. Macromolecules. 1996; 29(10): 3535-3539.
[373] Zell M.T., Padden B.E., Paterick A.J., Thakur K.A.M., Kean R.T., Hillmyer M.A., et al., *Unambiguous determination of the C-13 and H-1 NMR stereosequence assignments of polylactide using high-resolution solution NMR spectroscopy*. Macromolecules. 2002; 35(20): 7700-7707.
[374] Liu W., Ray III D.G., Rinaldi P.L., *Resolution of Signals from Long-Chain Branching in Polyethylene by 13C NMR at 188.6 MHz*. Macromolecules. 1999; 32: 3817-3819.

[375] Crosby B.J., Mangnus M., de Groot W., Daniels R., McLeish T.C.B., *Characterization of long chain branching: Dilution rheology of industrial polyethylenes*. J Rheol. 2002; 46(2): 401-426.
[376] Kim E.S., Kim B.C., Kim S.H., *Structural effect of linear and star-shaped poly(L-lactic acid) on physical properties*. J Polym Sci Pol Phys. 2004; 42(6): 939-946.
[377] Hatzikiriakos S.G., *Long chain branching and polydispersity effects on the rheological properties of polyethylenes*. Polym Eng Sci. 2000; 40(11): 2279-2287.
[378] Kasehagen L.J., Macosko C.W., Trowbridge D., Magnus F., *Rheology of long-chain randomly branched polybutadiene*. J Rheol. 1996; 40(4): 689-709.
[379] Najafi N., Heuzey M.C., Carreau P.J., Wood-Adams P.M., *Control of thermal degradation of polylactide (PLA)-clay nanocomposites using chain extenders*. Polym Degrad Stabil. 2012; 97(4): 554-565.
[380] Kratochvil P., *Characterization of branched polymers*. Macromol Symp. 2000; 152: 279-287.
[381] Lagendijk R.P., Hogt A.H., Buijtenhuijs A., Gotsis A.D., *Peroxydicarbonate modification of polypropylene and extensional flow properties*. Polymer. 2001; 42(25): 10035-10043.
[382] Agilent-Technologies, *A guide to multi-detector gel permeation chromatography*. Application Library, (2012).
[383] Ngai K.L., Roland C.M., *Intermolecular Cooperativity and the Temperature-Dependence of Segmental Relaxation in Semicrystalline Polymers*. Macromolecules. 1993; 26(11): 2688-2690.
[384] Zorn R., Mckenna G.B., Willner L., Richter D., *Rheological Investigation of Polybutadienes Having Different Microstructures over a Large Temperature-Range*. Macromolecules. 1995; 28(25): 8552-8562.
[385] Plazek D.J., Zheng X.D., Ngai K.L., *Viscoelastic Properties of Amorphous Polymers .1. Different Temperature Dependences of Segmental Relaxation and Terminal Dispersion*. Macromolecules. 1992; 25(19): 4920-4924.
[386] Plazek D.J., *Temperature-Dependence of the Viscoelastic Behavior of Polyvinyl Acetate)*. Polym J. 1980; 12(1): 43-53.
[387] Hepperle J., Munstedt H., Haug P.K., Eisenbach C.D., *Rheological properties of branched polystyrenes: linear viscoelastic behavior*. Rheol Acta. 2005; 45(2): 151-163.
[388] Ferry J.D., *Viscoelastic properties of Polymers*. 3rd ed. Wiley, New-York; 1980.
[389] Kang S.H., Zhang G.Z., Aou K., Hsu S.L., Stidham H.D., Yang X.Z., *An analysis of poly(lactic acid) with varying regio regularity*. J Chem Phys. 2003; 118(7): 3430-3436.
[390] Palade L.I., Lehermeier H.J., Dorgan J.R., *Melt rheology of high L-content poly(lactic acid)*. Macromolecules. 2001; 34(5): 1384-1390.
[391] Graessley W.W., Roovers J., *Melt Rheology of 4-Arm and 6-Arm Star Polystyrenes*. Macromolecules. 1979; 12(5): 959-965.
[392] *Branced on branched software*. http://sourceforge.net/projects/bob-rheology (Accessed Date: 15/05/2015).
[393] Das C., Inkson N.J., Read D.J., Kelmanson M.A., McLeish T.C.B., *Computational linear rheology of general branch-on-branch polymers*. J Rheol. 2006; 50(2): 207-235.

[394] Gross B., *Mathematical structure of the theories of viscoelasticity*. Hermann, Paris; 1953.
[395] Kim S.H., Kim Y.H., *Direct condensation polymerization of lactic acid*. Macromol Symp. 1999; 144: 277-287.
[396] Ikada Y., Tsuji H., *Biodegradable polyesters for medical and ecological applications*. Macromolecualr Rapid Communications. 2000; 21(3): 117-132.
[397] Gracia-Fernandez C.A., Gomez-Barreiro S., Lopez-Beceiro J., Naya S., Artiaga R., *New approach to the double melting peak of poly(L-lactic acid) observed by DSC*. J Mater Res. 2012; 27(10): 1379-1382.
[398] TA_Instrument, *Thermal Analysis Investigation of a Poly(Lactic Acid) Biodegradable Plastic*. Application Library, TA Instrument, (2007).
[399] Yasuniwa M., Tsubakihara S., Murakami T., *High-pressure DTA of poly(butylene terephthalate), poly(hexamethylene terephthalate), and poly(ethylene terephthalate)*. J Polym Sci Pol Phys. 2000; 38(1): 262-272.
[400] Inoue Y., Pan P., Kai W., Zhu B., Dong T., *Polymorphous crystallization and multiple melting behavior of Poly(L-lactide): Molecular weight dependence*. Macromolecules. 2007; 40(19): 6898-6905.
[401] Nofar M., Zhu W., Park C.B., Randall J., *Crystallization Kinetics of Linear and Long-Chain-Branched Polylactide*. Ind Eng Chem Res. 2011; 50(24): 13789-13798.
[402] Cai H., Dave V., Gross R.A., McCarthy S.P., *Effects of physical aging, crystallinity, and orientation on the enzymatic degradation of poly(lactic acid)*. J Polym Sci Pol Phys. 1996; 34(16): 2701-2708.
[403] Struik L.C.E., Physical Aging: Influence on the Deformation Behavior of Amorphous Polymers, in: Brostow W, Corneliussen RD, (Eds.), *Failure of plastics*, Hanser, Munich; 1986. p. 209-234.
[404] TA_Instrument, *DMA Modulus Equations*. Application Library, TA Instrument, (2005).
[405] Xiao C.D., Jho J.Y., Yee A.F., *Correlation between the Shear Yielding Behavior and Secondary Relaxations of Bisphenol a Polycarbonate and Related Copolymers*. Macromolecules. 1994; 27(10): 2761-2768.
[406] Engelberg I., Kohn J., *Physicomechanical Properties of Degradable Polymers Used in Medical Applications - a Comparative-Study*. Biomaterials. 1991; 12(3): 292-304.
[407] Stoclet G., Seguela R., Lefebvre J.M., Rochas C., *New Insights on the Strain-Induced Mesophase of Poly(D,L-lactide): In Situ WAXS and DSC Study of the Thermo-Mechanical Stability*. Macromolecules. 2010; 43(17): 7228-7237.
[408] Velazquez-Infante J.C., Gamez-Perez J., Franco-Urquiza E.A., Santana O.O., Carrasco F., Maspoch M.L., *Effect of the Unidirectional Drawing on the Thermal and Mechanical Properties of PLA Films with Different L-Isomer Content*. J Appl Polym Sci. 2013; 127(4): 2661-2669.
[409] Hay J.N., *The Physical Aging of Amorphous and Crystalline Polymers*. Pure Appl Chem. 1995; 67(11): 1855-1858.
[410] Duan K., Hu X.Z., Stachowiak G., *Modified essential work of fracture model for polymer fracture*. Compos Sci Technol. 2006; 66(16): 3172-3178.
[411] Karger-Kocsis J., Moskala E.J., *Molecular dependence of the essential and non-essential work of fracture of amorphous films of poly(ethylene-2,6-naphthalate) (PEN)*. Polymer. 2000; 41(16): 6301-6310.

[412] Wu J.S., Mai Y.W., *The essential fracture work concept for toughness measurement of ductile polymers*. Polym Eng Sci. 1996; 36(18): 2275-2288.
[413] Cailloux J., Santana O.O., Franco-Urquiza E., Bou J.J., Carrasco F., Gamez-Perez J., et al., *Sheets of branched poly(lactic acid) obtained by one step reactive extrusion calendering process: Melt rheology analysis*. Express Polym Lett. 2013; 7(3): 304-318.
[414] Karger-Kocsis J., Microstructural and molecular dependence of the work of fracture parameters in semicrystalline and amorphous polymer systems, in: Williams JG, Pavan A, (Eds.), *Fracture of Polymers, Composites and Adhesives*, Elsevier, Les Diablerets (Switzerland); 2000. p. 213-230.
[415] Karger-Kocsis J., Moskala E.J., Shang P.P., *Work of fracture and strain-induced cold crystallization behavior of amorphous copolyester sheets*. J Therm Anal Calorim. 2001; 63(3): 671-678.
[416] Chen H.B., Wu J.S., *Understanding the underlying physics of the essential work of fracture on the molecular level*. Macromolecules. 2007; 40(12): 4322-4326.
[417] Yang X.Z., Sun J., *Coil extension stage in the cold drawing of glassy polymers*. J Polym Sci Pol Phys. 2002; 40(23): 2646-2652.
[418] Hill J.W., *Studies on polymerization and ring formation XVII Friedel-Crafts syntheses with the polyanhydrides of the dibasic acids*. J Am Chem Soc. 1932; 54: 4105-4106.
[419] Hull D., *Fractography: Observing, Measuring and Interpreting Fracture Surface Topography*. Cambridge University Press, Cambridge; 1999.
[420] Basu S., Mahajan D.K., Van der Giessen E., *Micromechanics of the growth of a craze fibril in glassy polymers*. Polymer. 2005; 46(18): 7504-7518.
[421] Costello B., Doe N., Foster P., Smith R., *A Magnetic Bearing Rheometer with Unprecedented Low Torque Performance*. Annual Transactions of the Nordic Rheology Society, TA Instrument (2005).
[422] Gabriel C., Kaschta J., *Comparison of different shear rheometers with regard to creep and creep recovery measurements*. Rheol Acta. 1998; 37(4): 358-364.
[423] Davies A.R., Anderssen R.S., *Sampling localization in determining the relaxation spectrum*. J Non-Newton Fluid. 1997; 73(1-2): 163-179.